VOLUME 2

AFWAL-TR-86-3059

①

DAMPING 1986 PROCEEDINGS

May 1986

Summary Report for Period February 1984 - February 1986

DTIC
ELECTED
NOV 1 2 1986
E

FLIGHT DYNAMICS LABORATORY
AIR FORCE WRIGHT AERONAUTICAL LABORATORIES
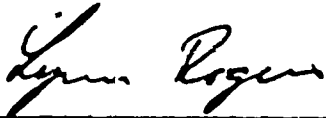AIR FORCE SYSTEMS COMMAND
WRIGHT-PATTERSON AIR FORCE BASE, OHIO 45433

86 11 12 173

AD-A178950

REPORT DOCUMENTATION PAGE

1a. REPORT SECURITY CLASSIFICATION UNCLASSIFIED		1b. RESTRICTIVE MARKINGS			
2a. SECURITY CLASSIFICATION AUTHORITY		3. DISTRIBUTION/AVAILABILITY OF REPORT Approved for public release; distribution unlimited.			
2b. DECLASSIFICATION/DOWNGRADING SCHEDULE					
4. PERFORMING ORGANIZATION REPORT NUMBER(S) AFWAL-TR-86-3059		5. MONITORING ORGANIZATION REPORT NUMBER(S)			
6a. NAME OF PERFORMING ORGANIZATION Advanced Metallic Structures Adv. Development Prog. Office	6b. OFFICE SYMBOL (If applicable) AFWAL/FIBAA	7a. NAME OF MONITORING ORGANIZATION			
6c. ADDRESS (City, State and ZIP Code) Wright-Patterson Air Force Base OH 45433		7b. ADDRESS (City, State and ZIP Code)			
8a. NAME OF FUNDING/SPONSORING ORGANIZATION	8b. OFFICE SYMBOL (If applicable)	9. PROCUREMENT INSTRUMENT IDENTIFICATION NUMBER			
8c. ADDRESS (City, State and ZIP Code)		10. SOURCE OF FUNDING NOS			

		PROGRAM ELEMENT NO.	PROJECT NO.	TASK NO.	WORK UNIT NO.
11. TITLE (Include Security Classification) (UNCLASSIFIED) ...ping 1986 Proceedings		63211F	486U	11	02

12. PERSONAL AUTHOR(S)

13a. TYPE OF REPORT Summary	13b. TIME COVERED FROM Feb 84 TO Feb 86	14. DATE OF REPORT (Yr., Mo., Day) 1986 May	15. PAGE COUNT 1319

16. SUPPLEMENTARY NOTATION

17. COSATI CODES			18. SUBJECT TERMS (Continue on reverse if necessary and identify by block number)
FIELD	GROUP	SUB. GR.	Vibration damping, controls/structure interaction.

19. ABSTRACT (Continue on reverse if necessary and identify by block number)

Individual papers of Damping 86 held 5-7 March 1986 in Las Vegas NV are presented. The subjects included: mechanical properties of polymers, experimental methods, damping in metal matrix composites, friction damping, design of damping structure, modal damping values, and applications of damping, etc.

20. DISTRIBUTION/AVAILABILITY OF ABSTRACT UNCLASSIFIED/UNLIMITED ☒ SAME AS RPT. ☐ DTIC USERS ☐	21. ABSTRACT SECURITY CLASSIFICATION UNCLASSIFIED	
22a. NAME OF RESPONSIBLE INDIVIDUAL Dr Lynn Rogers	22b. TELEPHONE NUMBER (Include Area Code) (513) 255-5664	22c. OFFICE SYMBOL AFWAL/FIBAA

DD FORM 1473, 83 APR   EDITION OF 1 JAN 73 IS OBSOLETE.

FOREWORD

This publication includes the individual papers of Damping 86 held
5-7 March 1985 in Las Vegas NV. The Workshop was sponsored by the Flight
Dynamics Laboratory, Air Force Wright Aeronautical Laboratories, Structures
and Dynamics Division, Advanced Metallic Structures, Advanced Development
Program Office (AFWAL/FIBAA).

It is desired to transfer vibration damping technology in a timely
manner within the aerospace community thereby stimulating research,
development, and applications.

iii

TABLE OF CONTENTS

*Not available for publication.

TABLE OF CONTENTS (Continued)

*Not available for publication.

→ Partial

TABLE OF CONTENTS (Continued)

*Not available for publication.

TABLE OF CONTENTS (Continued)

*Not available for publication.

TABLE OF CONTENTS (Continued)

*Not available for publication.

DAMPING CHARACTERISTICS OF THE SOLAR ARRAY FLIGHT EXPERIMENT

E. D. Pinson[*]

ABSTRACT

Accelerometer data from the on-orbit dynamic testing of the Solar Array Flight
Experiment (SAFE) structure are analyzed to determine the level and source of
modal damping present in the structure. Several innovative features in the
design and manufacture of the SAFE payload are described prior to a discussion
of the tests performed during the STS-41-D Space Shuttle mission. Planned and
unplanned deviations from the standard test procedure are discussed in detail
because of their rather significant impact on procedural aspects of the data
analysis which was performed at Lockheed Missiles and Space Co.

Approximations of the accelerometer records for a given test are based on
modal data obtained from a SPAR finite-element model of the deployed SAFE
structure. These data and trial estimates of the modal
input to a linear, transient response analysis algorithm. Trial damping
values are then iteratively improved to yield the most accurate simulation of
the measured accelerometer traces. The validity of various assumptions made
in the course of this analysis is examined and justification is provided for
several non-standard facets of the procedure. As a part of this discussion,
reasons for including and excluding certain finite-element model refinements
are explained. Also of interest is the validity and effect that assuming zero
initial displacement and velocity for the structure has on the final modal
damping estimates.

Information is traced step-by-step from the NASA/Marshall Space Flight Center
thruster firing data to final estimates of the damping present in the first
six modes of the SAFE module. These damping data are presented for each of
the fourteen dynamic tests performed and several aspects of those results are
discussed in detail. Unexpected modal damping estimates arising from this
analysis suggest that further component testing is required to explain
adequately the source(s) of the damping which was demonstrated during the
on-orbit tests.

_____
* Lockheed Missiles and Space Co., Sunnyvale, CA

DAMPING CHARACTERISTICS OF THE SOLAR ARRAY FLIGHT EXPERIMENT

E. D. Pinson[*]

INTRODUCTION

The National Aeronautics and Space Administration (NASA) launched Space
Shuttle mission STS-41-D on August 31, 1984. On this mission, the crew of the
Space Shuttle performed various tests on the largest structure to be deployed
in orbit and brought back to earth - the Solar Array Flight Experiment (SAFE,
see Figure 1). While this experiment demonstrated advanced technology in many
other areas, a major goal of the SAFE was to verify and improve present
methods of dynamic response prediction for large, lightweight, flexible
structures. Since the SAFE represents a type of construction considered
necessary for the success of future large space structures, this on-orbit
testing is an important milestone in the development and enhancement of
present dynamic response prediction and analysis tools. This paper relates
the SAFE configuration, procedures involved in the on-orbit dynamic testing,
and describe the analysis of accelerometer data performed at Lockheed Missiles
and Space Company, Inc. (LMSC).

PRE-FLIGHT ACTIVITIES

Design and Construction

The SAFE structure was designed and built at LMSC in Sunnyvale, CA under
contract to NASA/Marshall Space Flight Center (MSFC) in Huntsville, AL
(contract number NASB-31352). The mast assembly, produced by Able Engineering
Company, Inc. of Goleta, CA, incorporates a canister deployment mechanism
which allows the entire mast length of 32 m (105 ft.) to be coiled into a
cylinder 1.5 m (5 ft.) long. The triangular mast, only 36 cm (14.4 in.) in
circumscribed diameter, can be deployed/retracted at a nominal rate of
4 cm/sec. (1.5 in./sec.) and has an effective EI of 43.6 kN-m^2
(15.2 X 10^6 lbs-in^2).

The solar array blanket weighs 1.35 kN (303 lbs.) and consists of 84
rectangular panels each 4.0 m (13.125 ft.) by 37 cm (14.49 in.) and
structurally capable of supporting solar cells. However, only one of these
panels, located near the top of the blanket, was populated with active solar
cells during on-orbit testing - all others were fitted with aluminum plates
which simulated the thickness and mass of solar cells. The panel which
contained active solar cells was constructed of two 25.4 micro-meter (1.0 mil)
Kapton substrates with copper circuitry sandwiched between. Five of the
panels were stiffened by a graphite-epoxy framework (all others were stiffened
by an aluminum framework) and joined to adjacent panels along the longest
sides utilizing an s-glass fiber which formed the rib of a "piano-hinge"
construction. Small springs were placed at discrete points along the
hinge-line to guarantee that the panels would fold in the proper directions
during retraction. Although they have little effect in a 1-g environment,
these springs were quite effective during the on-orbit tests.

---

* Lockheed Missiles and Space Co., Sunnyvale, CA

During launch and landing, the blanket was folded into a containment box which exerted a 13.3 kN (3000 lb.) compressive force on the 9.0 cm (3.5 in.) stack of panels. The entire jettisonable structure (including the canister, mast and blanket) weighs approximately 3.0 kN (673 pounds), approximately one-third the weight of conventional solar arrays. Since the SAFE also occupies only one-tenth the volume of conventional designs, several significant technological advances are represented in this relatively unconventional design.

The SAFE wing was dynamically tested at full and 70% deployment. During full deployment, approximately 23.1 N (5 lbs.) of tensile force was applied to the lower edge of the blanket through springs attached to a tension bar and then to two parallel tension wires. Additionally, a similar apparatus applied approximately 55.6 N (12.5 lbs.) to the upper 70% of the blanket. During 70% deployment, only the latter tensioning system was used. The forces transmitted through the tension bars were regulated by two separate pairs of constant-torque mechanisms which were designed to provide constant tension on the blanket during all structural motions. To guide and lightly hold the position of the blanket, three stainless-steel guide-wires, placed in the middle and to either side of the centerline of the blanket, were connected to the containment box lid, laced through eyelets in the blanket, and connected to three separate constant-torque mechanisms in the containment box. Each of these devices applied approximately 8.9 N (2 lbs.) tension to the guide-wires.

Modeling and Pre-Flight Testing

Two finite-element (FE) models of the deployed SAFE structure existat LMSC. One model simulates the wing at 70% extension while the other simulates full deployment of the array. Both models were written using the EAL/SPAR FE code and were used to obtain natural frequencies and mode shapes as well as predict the on-orbit transient response under simulated Space Shuttle excitation scenarios.

Since the structure of the SAFE was not designed to withstand the 1-g effects at the surface of the earth, some of the extensive dynamic testing involving the entire structure could not be performed. Because of this limitation, several components of the SAFE were tested independently. Static tests of the mast alone yielded various strength and deformation parameters and a modal test of the mast alone provided a damping prediction - 1.5% of its critical damping value. Tests that were performed on sections of the blanket shed light on the shear and normal strengths of the Kapton/framework combination seen in each panel. All of the available data concerning material properties of the SAFE structural elements, from these tests and other sources, were incorporated into the FE models.

Instrumentation

The SAFE structure was instrumented with six accelerometers (see Figure 2). Three base accelerometers were located on the support structure which held the mast canister, and three additional accelerometers were located on the blanket containment box lid. The accelerometers located on the support structure of the SAFE were virtually ignored for analysis purposes becaus they sensed an unmanageable amount of noise, but the upper accelerometer records possessed a higher signal-to-noise ratio and were therefore much more useful. The two upper accelerometers placed at the center of the box lid were labeled X1 and Y sensing STS fore/aft and port/starboard accelerations respectively. A single

accelerometer labeled X2 was placed 1.75 m (68.75 in.) starboard of the
longitudinal axis of the mast and also sensed fore/aft accelerations. The box
lid to which these accelerometers were mounted was attached to the tip of the
SAFE mast by a rather complex mechanism which restricted relative
displacements and rotations. This implies that the traces obtained from the
X1, X2, and Y accelerometers are estimates of the accelerations of the tip of
the mast as well as the top of the blanket.

Affixed to the blanket and mast were several targets for two separate
displacement measuring systems used by NASA/Langley Research Center (LaRC) in
Hampton, VA and MSFC. The LaRC targets, located on the blanket, reflected
sunlight into video cameras placed in the four corners of the Space Shuttle
cargo bay, making the system useful only when the array was exposed to a
moderate level of light (Reference 1). The targets used by MSFC, located on
the mast and the blanket, reflected the light emitted by laser diodes into a
field-tracker similar to some new TV cameras (Reference 2). Since the laser
diodes emit such low intensity light, this displacement measuring system was
useful only when the array was exposed to very little direct and reflected
light from extraneous sources.

Excitation

The Space Shuttle Vernier Reaction Control System (VRCS, see Figure 3) was
used to excite the SAFE in very specific directions and tightly regulated
magnitudes. The firing sequences and durations were determined by
C. S. Draper Laboratories in conjunction with Rockwell Intl. to excite
in-plane, out-of-plane, and multi-modal responses of the wing while minimizing
the net angular acceleration of the orbiter. These intended firing histories
(the durations of which were programmed into the VRCS computer) are listed in
Table 1.

TEST PROCEDURE

Overview

Three classes of dynamic tests were performed by the Space Shuttle crew
on-orbit: out-of-plane (O/P), in-plane (I/P), and multi-modal (M/M). A total
of fourteen such tests were performed during the mission (see Table 2). All
but two of these tests were conducted at the 70% deployment length - only one
out-of-plane and one multi-modal test was performed on the fully deployed
structure. Each test consisted of three distinct periods: a quiescent period
of ten minutes prior to VRCS initiation, an excitation phase when the
thrusters were executing pre-programmed firing sequences, and a free-response
period beginning when the VRCS thrusters ceased firing and ending when the
SAFE structural motion was sufficiently small (up to eight minutes allotted).
During all three phases of the test procedure, the automatic attitude control
system of the Space Shuttle was disabled, crew motions were restricted, and
the Space Shuttle was in the "gravity-gradient" orientation (shown in
Figure 4).

Test Plan Deviations

As mentioned previously, several firing durations were programmed into the
VRCS computer prior to launch. However, the original test plan (precisely
specified thruster firing intervals and durations) was implemented for only
the first ten dynamic tests. After the first few tests had been performed,
and the SAFE response had been observed by mission control specialists, it was

obvious that the tip displacements were much smaller than anticipated. A decision was made to repeat the pre-planned excitation phase of the last four tests while decreasing the duration of each thruster pulse and slightly altering the intervals. This method of excitation was intended to boost the tip displacement by 50%, but did not achieve this goal due to the excessive damping in the structure. The shorter duration pulse used throughout these extended duration tests was available on the VRCS computer, thus the thruster durations during all fourteen dynamic tests were computer-controlled. The intended extended firing histories are presented in Table 1.

Although the VRCS computer dictated the duration of the thruster pulses for all dynamic tests, the astronauts were responsible for the initiation of each pulse. On a few occasions, there were deviations from the planned firing schedule (i. e., thrusters were not fired at the pre-designated times). Fortunately, these deviations from the original schedule were recorded by a flight computer and were fairly easy to accomodate in the attendant analyses. The flight computer recorded on/off times for each of the VRCS thrusters and, upon decoding by Rockwell, these records were digitized and incorporated into the analysis as the actual thruster firing histories. These records were subsequently used in the derivation of a forcing function for the appropriate test.

DATA ANALYSIS PROCEDURE

Assumptions and Anomalies

The SAFE structure was assumed to behave in a manner consistent with Hooke's Law allowing standard modal analysis techniques to be employed in the post-flight analysis of the accelerometer records conducted at LMSC. In the absence of more reliable information, the SAFE was assumed to have no initial displacement or velocity prior to each of the fourteen dynamic tests. This assumption was under suspicion from the onset of the post-flight analysis. As verified independently by LaRC, neither the mast tip nor the blanket reached total quiescence prior to dynamic testing. Results from the reduction of LaRC photogrammetric data found peak to peak motions of the mast tip during the "quiescent" period to be as much as 1.5 and 0.44 cm (0.59 and 0.175 in.) in the X and Y directions respectively (see Reference 1). Since the extremely dominant first mode amplitude is approximately 7.6 cm (3 in.) in the 70% deployed configuration, this "low-amplitude" residual oscillation is roughly the same size as that which could be expected of higher mode contributions. This lack of quiescence makes damping factors and the associated contributions of higher modes very difficult and in some cases impossible to determine. In the analysis performed at LMSC, modal damping factors for modes other than the fundamental I/P and O/P modes are given only to identify the recognizable participation of other modes. When given, these "identification factors" are usually 0.25% or 0.5% of the critical damping value and are not intended to reflect the actual amount of modal damping present in the structure.

When the SAFE was deployed, it became obvious that the mast-blanket structure was twisted along its longitudinal axis with respect to theSTS cargo bay. This twisting could not be ignored in the LMSC data reduction process because the accelerometers, which were intended to sense accelerations orthogonal to VRCS thrust directions, actually sensed accelerations at a slightly skewed angle (approximately 7.8° at the accelerometer locations). Some consideration was given to incorporating this twist into the FE model by relocating individual nodes according to their respective locations along the longitudinal axis of the structure. This procedure would yield slightly

different frequencies and mode shapes in addition to producing non-planar finite elements. The idea was discarded in view of the good agreement between simulated and measured frequencies and the difficulties involved in the analysis of the resulting warped elements. Therefore, in an effort to account for the unintended twist, two adjustments (discussed in the following paragraphs) were made to the data reduction process:

1. The model was altered slightly to account for the inertial effects introduced by the twist, and

2. A post-processing module was added to the analysis to transform the simulated orthogonal (to STS coordinates) acceleration histories into simulated accelerometer records (sensed in the slightly skewed directions of the SAFE box lid accelerometers).

Since the array blanket and attendant hardware were offset from the mast by approximately 25.4 cm (10 in.) as well as twisted, any I/P or O/P motion of the array would also cause a slight torsion about the longitudinal axis of the mast (approximately coincident with the twist axis of the structure). This torsion was simulated by the attachment of a lumped mass to the starboard end of the box lid. The size of this mass was determined by equating the torque produced by the twisted structure to the torque produced by the outboard mass. For the fully deployed wing, 23.6 N (5.3 lbs.) was added and for the 70% deployed configuration, 20.0 N (4.5 lbs.) was added. However, since increasing the mass of the structure by any amount reduces the associated natural frequencies, the pre- and post-refinement frequency values were compared to confirm that this change was sufficiently small. In Table 3, this comparison is presented for the first six natural frequencies of the structure, predicted by the FE models discussed earlier.

The justification for and accuracy of the coordinate transformation technique lies in the fact that the amplitude of the I/P accelerometer record during O/P dynamic tests coincides very closely with that which is produced by the transformation procedure. It is felt that this assumption, and the attachment of the lumped mass, introduces minimal error into the final results and adequately accounts for the unexpected twisting of the SAFE.

At various times during the mission, the astronauts noticed that, in addition to the twist discussed above, the array blanket also tended to deform in a "hammock" shape with the edges of the blanket displaced toward the crew cabin. A recent test, which attempted to duplicate this behaviour in the laboratory, indicated that thermal expansion of the aluminum blanket panel frames probably exceeded the allowable growth margin during in-flight testing and caused the panel to deform. Intuitively, the hammock shape would give rise to slightly greater O/P and I/P rigidity in the blanket, and therefore have some small influence on the natural frequencies of the structure. In the LMSC analysis, this "hammocking" is not modeled, nor is it considered to have a significant impact on the dynamic response characteristics of the structure.

Analysis Procedure Overview

On the basis of the above assumptions, the following procedure was implemented to identify the modal damping coefficients of the SAFE:

MSFC provided Lockheed with graphs of the thruster firing histories for each of the fourteen dynamic tests, and multiplication factors representing the accelerations (both translational and rotational) at the base of the SAFE due

to the firing of each individual thruster (see Table 4). The acceleration factors provided by MSFC were based on the following assumptions:

1. When firing, the thrusters provide constant thrust,

2. The Space Shuttle is a rigid link between all thrusters and the base of the SAFE, and

3. The rotational moments of inertia of the Space Shuttle are constant.

During most of the dynamic testing, two or more VRCS thrusters fired simultaneously to provide the proper excitation. The total base acceleration of the SAFE in those cases was determined by superimposing the contributions of each active thruster, justified by the second assumption listed above.

The thruster firing data, which were decoded by Rockwell from the flight recorder, were digitized in the form of ones and zeros, designating on and off, respectively. For each dynamic test, these "on/off vectors" were linearly interpolated using a step-size of 0.1 sec., implicitly assuming that the thrusters achieve maximum thrust and decrease to zero thrust in 0.1 sec. The interpolated thruster time histories were then placed in a matrix with dimensions of time by four (one column for each of the four VRCS thrusters participating in the dynamic tests). This thruster array was post-multiplied by a matrix containing the acceleration factors provided by MSFC. The resulting matrix (with dimensions of time by six) was a time history of the base acceleration of the SAFE, in STS coordinates, during the dynamic test in question. A transformation matrix converted the acceleration histories into FE model coordinates prior to the transient response analyses.

Once the above preparations were completed, data were input to a program which calculated the structural response histories at specified nodes of the model (at or near accelerometer locations). This result was obtained by integrating the following equation over time:

$$[m]\ddot{q} + [c]\dot{q} + [k]q = -[\phi]^T[M][R][\ddot{x}] \qquad (1)$$

where: $[m]$ = the diagonal generalized mass matrix (identity matrix),
$[c]$ = the diagonal generalized gain matrix,
$[k]$ = the diagonal generalized stiffness matrix,
$[\phi]$ = the vibrational modes orthogonalized to the mass matrix,
$[M]$ = the consistent mass matrix,
$[R]$ = the rigid-body transformation matrix (about the base node of the SAFE),
$[\ddot{x}]$ = the base acceleration matrix, and
q = the generalized coordinate vector (with dots denoting time derivatives).

All of the diagonal matrices listed above have dimensions of fifteen by fifteen, corresponding to the number of modes used in the transient response analysis. The generalized gain matrix contains $1/(2\zeta_i)$ factors along its diagonal, where ζ_i corresponds to the per-cent of critical damping for the ith mode, and the generalized stiffness matrix contains the SAFE natural frequencies squared along its diagonal. The vibrational modes, consistent mass, and rigid-body matrices were computed by SPAR. Orthogonal vibrational modes were obtained by an iterative algorithm within SPAR composed of a Stodola matrix iteration technique alternating with a Rayleigh-Ritz procedure. The

consistent mass matrix accounts for the rotational inertias of joints and the rigid-body transformation matrix represents the displacement caused at each node in the SAFE structure by unit translations and rotations of the chosen reference node (in this case, the base of the SAFE).

Integration of the equations of motion was accomplished using a closed-form recursive algorithm. This algorithm approximates the excitation force as a linear change between adjacent time steps as it progresses in time. Since the base acceleration of the SAFE was input as a linerly varying function, the integration algorithm was very effective.

The result of the integration was a set of generalized response histories consisting of acceleration and displacement data. These generalized response histories were backtransformed into structural coordinates by pre-multiplying the histories with the appropriate rows of the modal matrix. This multiplication yielded the structural response histories of specific degrees-of-freedom at certain nodes of the SAFE model. The structural acceleration histories produced by the integration process were relative accelerations of the nodes of interest with respect to the base of the structure. Therefore, the base acceleration histories were added to the integrated results to produce the absolute accelerations which would have been sensed by the box lid accelerometers had they been orthogonal to VRCS thrust directions.

Due to the twist in the SAFE structure, the computer-simulated orthogonal acceleration histories were rotated to simulate the accelerations sensed by the slightly skewed accelerometers. Pre-multiplication by another coordinate transformation matrix accomplished this task. For the purpose of presentation and consistency, the units of the simulated accelerometer records were then changed to milli-g's from in./sec.^{2} by multiplying the entire group of acceleration histories by a conversion factor of 2.588.

The location of nodes along the box lid did not coincide with the placement of the accelerometers. To accomodate this incompatibility between the model and the structure, a linear interpolation was performed between the two nodes adjacent to the outboard accelerometer location. Since the box lid incorporates a fairly rigid graphite-epoxy design, this approximation is considered quite valid.

Utilizing the method described above, the accelerometer records were approximated based on trial modal damping values and analytically derived natural frequencies and mode shapes. The above procedure was iterated, varying the approximations of these damping values, until an acceptable estimate of the measured accelerometer records were produced. In evaluating the acceptability of the damping estimates, accelerometer traces were examined in the region of peak response and shortly thereafter. Magnitudes from the computer simulated records were compared to those obtained during on-orbit testing and the modal damping values yielding the smallest overall residuals were accepted as final estimates. Computer simulated displacements of the mast tip were used only to verify maximum excursions and were not considered while evaluating the acceptability of modal damping estimates.

In addition to monitoring the accelerations and displacements of the nodes near the accelerometer locations, the motions of two nodes at the base of the blanket were monitored. This provided a record of the amount of motion experienced by the blanket tensioning devices. Since the damping attributable to these tensioners was not estimated prior to flight, they were considered to

be a possible source of the higher I/P damping factors. During computer simulations, the reels never deployed more than 12.8 cm (0.5 inch), but a recent test involving one of these mechanisms has shown that a significant level of damping was contributed by these devices, even with such minute displacements (see References 3 and 4).

RESULTS AND ANALYSIS PROCEDURE DEVIATIONS

Out-of-plane and in-plane test files were analyzed as information pertaining to the respective files was made complete. An additional attempt was made to analyze cases appearing to possess relatively few modes before the more complicated tests were investigated. Out-of-plane tests were performed on-orbit more frequently than any other, resulting in several comparable sets of data. For this reason, all informationally complete O/P tests were analyzed before attempting the simplest I/P simulations. Upon approximating all O/P and I/P modal damping values (including those for the files which were originally incomplete), the M/M test cases were analyzed. In this way, all available information and experience could be incorporated into the most complicated analyses.

Table 5 shows the modal damping factors which produced the best computer simulation of the three accelerometer histories (X1, X2, and Y) for each file analyzed. Although not presented in this table, the non-participatory modes (O/P modes during an I/P test and I/P modes during an O/P test) were damped in an inconsistent manner: When the first files were analyzed, no prior knowledge was assumed in setting the damping factors for non-participatory modes, however, as experience was gained, the trial damping factors began to reflect all knowledge accumulated to that point. For this reason, O/P modal damping factors should be taken only from O/P tests and I/P damping factors should be taken only from I/P tests. The M/M damping factors should reflect both cases equally well. Generalized coordinate time histories were examined near the end of the analysis procedure to verify that the non-participatory modal damping factors assumed during the early stages of the analysis were adequate. This examination showed that the non-participatory modal damping values are almost irrelevent, strengthening the basis for extracting damping factors from the proper test data.

During the data reduction process for each file considered, the initial displacement and velocity of the structure was assumed to be zero. However, for one case an attempt was made to estimate the actual initial conditions - file six. This file, the first to be analyzed in the LMSC post-flight data reduction procedure, documents an O/P test performed on the dark side of the orbit at 70% deployment. Considerable time was spent in this initial analysis case to gain an understanding of parameter sensitivities in the algorithms used, therefore, this particular file was chosen for the initial condition approximation process based on a greater familiarity with its features.

Difficulty was encountered while attempting to estimate the initial conditions for O/P displacements and velocities because modes one and four of the SAFE differ only in the phasing of motion between the blanket and the mast (see Table 3 for descriptions of the first six modes of the structure). MSFC provided LMSC with displacement and velocity histories integrated from the accelerometer records - but the accelerometers were located only at the mast/blanket tip. It was thus impossible to distinguish the separate contributions of modes one and four from this data. Due to the lack of information concerning the initial conditions of all nodes in the SAFE, it was decided that modal (rather than structural) initial conditions would be

approximated. The starting point for this iterative process was the
integrated displacement andvelocity histories provided by MSFC. The
displacement and velocity values at the time the VRCS began firing were read
from the integrated histories and assumed modal initial conditions were input
to the transient response analysis. This procedure was used only as a
starting point for an iterative process of estimating the initial conditions.
Subsequent iterations produced refinements in the magnitude and distribution
(between the first and fourth modes) of the modal initial conditions
originally assumed.

Acceptability of an adequate fit was subjective. Initial transient features
of the structural response are modeled more accurately in the curves
incorporating initial condition approximations, as was expected. However, as
these transients decay, the simulation curves where zero initial conditions
were assumed predict the actual structural response with equal or greater
accuracy. Based on these observations, the modal damping values obtained as a
result of the initial condition approximation process are not considered to be
an accurate reflection of the damping actually present in the structure.
Also, since the advantageous effects of accurately representing initial
displacement and velocity are confined to only the first few seconds of the
simulation, it was not considered time-efficient to attempt this initial
condition estimation for each file.

Power Spectral Densities of the accelerometer traces provided by MSFC were
somewhat useful in determining modal participation. As work progressed, modal
damping estimates were calculated from the digital representations of these
PSDs by the half-power method. At the same time, estimates of the frequency
peaks corresponding to the damping factors were obtained (see Table 6). The
frequencies presented in Table 6 were divided into categories (i. e., 70%
deployed, 0/P, daytime test, first mode) and averaged, for the purpose of
comparison. As shown in Table 3, the resulting average values correspond
quite closely with modal analysis predictions.

Four of the final approximations are included in this paper - files 10, 12,
20, and 28. Also included in Figures 5, 6, 7, and 8 are the accelerometer
records provided by MSFC corresponding to these sample cases. These cases
represent the following categories: O/P (file 12), I/P (file 28), and M/M
(file 10) at 70% deployment and M/M at full deployment (file 20). Further
information concerning these sample cases may be obtained by referring to
Table 2. When comparing the simulations to the measured data, note that only
gross features of each curve are approximated well and that modal phasing is
inaccurately simulated in all cases. This inaccuracy is probably due to the
similarities between modes one and four and the inability to distinguish
between their respective contributions and relative phasing.

SUMMARY AND CONCLUSIONS

Since this structure is a product of new technologies in several areas, it is
not surprising that the analysis presented above did not resolve all questions
concerning the structural response of the SAFE. Prior to on-orbit
experimentation involving the structure, damping characteristics were unknown
and therefore conservatively estimated at 0.5% of critical during pre-flight
test simulations. The actual amount of damping found in the structure is
considerably higher than the pre-flight value. This fact should be explained
and understood, as should the unexplained differences in the damping factors
between O/P and I/P modes, orbital night and day, etc. Since space structures

anticipated for the future will probably be large and lightweight, any knowledge that can be gleaned from the SAFE hardware should prove immediately useful.

The reduction and analysis of accelerometer data obtained from the on-orbit testing of the SAFE has been completed by LMSC. Modal damping factors which provide the best analytical simulation of the actual accelerometer records were found by successively improving estimates of these factors. Considering all test cases, for 70% SAFE deployment, the O/P damping estimate is approximately 4.4% while the I/P estimate is approximately 9.8%. For the fully deployed structure, the O/P damping estimate is approximately 2% and the I/P estimate is approximately 4%, based on only one sample. These large differences were not expected, nor are they easily explained. Further, the damping factors for the torsional modes of the structure were not approximated in this analysis. The damping factors of the first O/P and first I/P modes were estimated to within 0.5% (assuming zero initial displacement and velocity) whereas other modes were only detected and flagged if they were found to participate in the structural response. This flagging is indicated by a damping factor of 0.5% or 0.25% in Table 5. Structural damping was found to increase during the orbital nighttime tests for the 70% deployment case - no nighttime tests were performed using the fully deployed array.

Since the frequencies which were approximated prior to flight match quite closely with the average frequencies determined from accelerometer traces, a high level of confidence exists with regard to the FE models used in this analysis. Also, since the analytical simulations of the accelerometer records were found to be fairly accurate, confidence is gained in the ability of presently existing dynamic tools to predict the transient response of large, flexible space structures. This ability is contingent, however, on accurate knowledge of the structural and damping characteristics of the assembly as well as its initial conditions. These contingencies dictate that extensive static and dynamic testing ofstructural components be conducted and that some way of monitoring the on-orbit displacement and veolcity of the structure be implemented.

ACKNOWLEDGEMENTS

During the course of this analysis, the FE models discussed throughout this paper proved to be indispensible tools. Coding for both of these models was accomplished by B. A. Simpson and modified by T. J. Venator and E. D. Pinson (all employed by LMSC, Structural Dynamics). The author wishes to acknowledge the assistance of M. D. Menning and G. J. Welik (LMSC, Solar Array Projects) for their help in gathering design data and specifications for the SAFE. Appreciation is also due to H. C. Pack, Jr. of MSFC, who served as a technical interface and resource for the duration of the contract.

REFERENCES

1. Orbital Dynamics of the OAST-1 Solar Array using Video Measurements, by H. L. Brumfield, et. al., paper presented at the AIAA/ASME/ASCE/AHS 26th Structures, Structural Dynamics and Materials Conference, Orlando, FL, April 15-17, 1985, paper number AIAA-85-0758-CP.

2. Solar Array Flight Dynamic Experiment, by Richard W. Schock, paper presented at the AAS Guidance and Control Conference, Keystone, CO, Feb. 1-5, 1986, paper number AAS 86-050.

3. <u>Procedure for the Post-Flight ... (constant-torque mechanism) ... Test</u>,
    by M. D. Menning. LMSC Document number FO27194, approved August 9, 1985.

4. <u>Discrete Mechanism Damping Effects in the Solar Array Flight Experiment</u>,
    by E. D. Pinson, paper to be presented at the 20th Aerospace Mechanisms
    Symposium, NASA/Lewis Research Center, Cleveland, OH, May 7-9, 1986.

Table 1. Intended VRCS Thruster Firing Durations

70% Deployment O/P Test (Files 5, 6 & 12)

Thruster(s)	Time	Duration
F5L & F5R	0.0	3.6
L5D & R5D	8.4	8.0
F5L & F5R	16.88	3.6
L5D & R5D	25.28	8.0

70% Deployment I/P Test (File 13)

Thruster(s)	Time	Duration
F5L	0.0	3.36
L5D	0.0	7.36
F5R	7.52	3.36
R5D	7.52	7.36

70% Deployment M/M Test (Files 10, 11, 14 & 15)

Thruster(s)	Time	Duration
F5L	0.0	4.0
R5D	4.96	8.8
F5R	32.72	4.0
L5D	40.72	8.8

100% Deployment O/P Test (File 17)

Thruster(s)	Time	Duration
F5L & F5R	0.0	4.32
L5D & R5D	15.04	9.52

100% Deployment M/M Test (File 20)

Thruster(s)	Time	Duration
F5L & F5R	0.0	4.0
R5D	0.0	5.52
L5D	10.0	8.8
R5D	10.0	3.28

Extended Duration Tests

70% Deployment I/P Test (Files 28 & 29)

Thruster(s)	Time	Duration
F5L	0.0	2.0
L5D	0.0	4.4
F5R	7.52	2.0
R5D	7.52	4.4
F5L	14.96	2.0
L5D	14.96	4.4
F5R	22.48	2.0
R5D	22.48	4.4

70% Deployment M/M Test (Files 26 & 27)

Thruster(s)	Time	Duration
F5L	0.0	2.48
R5D	4.96	5.44
F5R	32.72	2.48
L5D	40.72	5.44
L5D	56.0	5.44
F5R	65.04	2.48
F5L	100.0	2.48
R5D	108.0	5.44

NOTES:

1. All times and durations are given in seconds.
2. All values in the "Time" column are referenced to the starting time of the test.
3. For thruster locations, see Figure 3.

Table 2.   Index of STS-41-D Dynamic Tests

File	Day/Night	Type	GMT	MET	Notes
5	Daytime Test	O/P	245:19:25:44.6	2: 6:43:53.6	
6	Nighttime Test	O/P	245:20:13:45.9	2: 7:31:54.9	
10	Daytime Test	M/M	246:13:29:43.7	3: 0:47:52.7	
11	Nighttime Test	M/M	246:14:22: 9.9	3: 1:40:18.9	
12	Daytime Test	O/P	246:15: 0:42.4	3: 2:18:51.4	
13	Nighttime Test	I/P	246:15:52:50.1	3: 3:10:59.1	
14	Daytime Test	M/M	246:16:30:43.8	3: 3:48:52.8	
15	Nighttime Test	M/M	246:17:23:23.6	3: 4:41:32.6	
17	Daytime Test	O/P	246:18: 6:44.3	3: 5:24:53.3	100% Deployed
20	Daytime Test	M/M	246:19:31:47.4	3: 6:49:56.4	100% Deployed
26	Nighttime Test	M/M	247:16: 2:20.7	4: 3:20:29.7	Increased Duration
27	Daytime Test	M/M	247:16:37:49.4	4: 3:55:58.4	Increased Duration
28	Nighttime Test	I/P	247:17:32:58.4	4: 4:51: 7.4	Increased Duration
29	Daytime Test	I/P	247:18: 7:45.6	4: 5:25:54.6	Increased Duration

NOTES:

1. In the "Type" column, O/P designates an out-of-plane bending test, I/P designates an in-plane bending test, and M/M designates a multi-modal test.
2. GMT refers to the Greenwich Mean Time at the start of the test.
3. MET refers to the Mission Elapsed Time at the start of the test.

Table 3. Frequency Comparisons and Modal Descriptions

70% Deployment

Frequencies [Hz.]

Mode	Pre-Flight	Twist-Comp.	Experimental Day	Night
1	0.0593	0.0587	0.058	0.061
2	0.0664	0.0653	0.063	0.064
3	0.0764	0.0759	0.075	0.072
4	0.1191	0.1178	0.105	0.093
5	0.1454	0.1413	N/A	0.130
6	0.1961	0.1956	0.161	N/A

100% Deployment

Frequencies [Hz.]

Mode	Pre-Flight	Twist-Comp.	Experimental Day
1	0.0344	0.0339	0.0375
2	0.0371	0.0365	N/A
3	0.0576	0.0571	0.0577
4	0.0966	0.0956	N/A
5	0.1119	0.1094	N/A
6	0.1528	0.1507	0.144

Modal Descriptions

Mode	Dominant Motion(s)
1	O/P Bending (Mast & Blanket in phase)
2	I/P Bending
3	Torsion about Longitudinal Axis
4	O/P Bending (Mast & Blanket out of phase)
5	Second Torsion Mode
6	O/P Bending and Torsion

NOTES:

1. Entries in the "Pre-Flight" and "Twist-Comp." columns were determined by analyzing finite-element models of the SAFE structure.
2. Entries in the "Experimental" columns reflect average frequency values corresponding to peaks in the accelerometer PSDs (furnished by MSFC).
3. N/A indicates that no data was obtained for the test category in question.
4. All tests on the fully deployed SAFE wing were performed during orbital daytime.
5. Modal descriptions apply to both the 70% and 100% deployment cases.

Table 4. Accelerations at the Base of the SAFE Structure due to VRCS Thruster Firings

Thruster Designation	Acceleration Direction	Magnitude
F5R	X	0.0
	Y	-0.077707686
	Z	0.076541882
	Theta-X	5.3369698E-04
	Theta-Y	1.5153303E-03
	Theta-Z	1.4480092E-03
F5L	X	0.0
	Y	0.077707686
	Z	0.076541882
	Theta-X	-5.3369698E-04
	Theta-Y	1.5153303E-03
	Theta-Z	-1.4480092E-03
R5D	X	0.0
	Y	0.0
	Z	0.002182001
	Theta-X	1.3407100E-03
	Theta-Y	-6.9923789E-04
	Theta-Z	0.0
R5L	X	0.0
	Y	0.0
	Z	0.002182001
	Theta-X	-1.3407100E-03
	Theta-Y	-6.9923789E-04
	Theta-Z	0.0

NOTES:

1. Translational accelerations are given in in./sec.^{2}.
2. Rotational accelerations are given in rad./sec.^{2}.
3. If thrusters fire simultaneously, respective accelerations may be superimposed.
4. All accelerations are referenced to the STS coordinate system shown in Figure 3.

Table 5. Post-Flight Modal Damping Estimates

Modal Damping [Per-cent of Critical]

File	Mode	LMSC Estimate	File	Mode	LMSC Estimate
5	1	3	15	1	4.5
	4	0.5		2	11
				3, 4 & 5	0.25
5	1	6			
	4	0.25	17	1	2
				4	0.25
6	1*	9			
	4*	1	20	1	2
				2	4
10	1	7		4 & 6	0.25
	2	8			
	4	0.5	26	1	6
				2	11
11	1	3		3, 4 & 5	0.25
	2	11			
	3, 4 & 5	0.25	27	1	3
				2	9
12	1	4.5		4	0.5
	4	0.25		5 & 6	0.25
13	2	11	28	1	6
	4	0.5		2	15
				4	0.25
14	1	4.5			
	2	11	29	2	11
	4	0.25		4	0.5

NOTES:

1. Damping for modes marked with an asterisk was determined based on estimated initial conditions (displacement and velocity), all others were based on zero initial conditions.
2. Damping factors of 0.5% and 0.25% of critical indicate participation of the mode in question and do not reflect the actual damping present in the mode.

Table 6. Frequencies and the Corresponding Damping Factors Taken From Accelerometer Power Spectral Densities

File	Frequency [Hz.]	Damping Factor [Per-Cent of Critical]
5	0.056	7
	0.103	0.9/2.6*
	0.11	0.9
	0.165	1.8
6	0.058	11
	0.125	3.7
10	0.058	6
	0.075	3.6
11	0.062	10
12	0.056	8.6
	0.099	3.7
	0.157	1.8
13	0.065	1.4
	0.071	3.8
14	0.059	4.5
	0.075	2.4
15	0.064	1.4
	0.068	1.3
17	0.0375	6.9
	0.152	1.5
20	0.0375	7.2
	0.0577	7
	0.144	1.6
26	0.061	6.7
	0.076	3
	0.135	2.1
27	0.06	4.5
28	0.066	1.4
	0.093	3.3
29	0.063	4.4
	0.108	2

NOTES:

1. All information in this table was furnished by MSFC.
2. All damping values were estimated using the half-power method.
3. Modal damping factors marked with an asterisk were estimated from the X/Y accelerometer traces respectively.

Figure 1. Solar Array Flight Experiment Viewed from STS Crew-Cabin
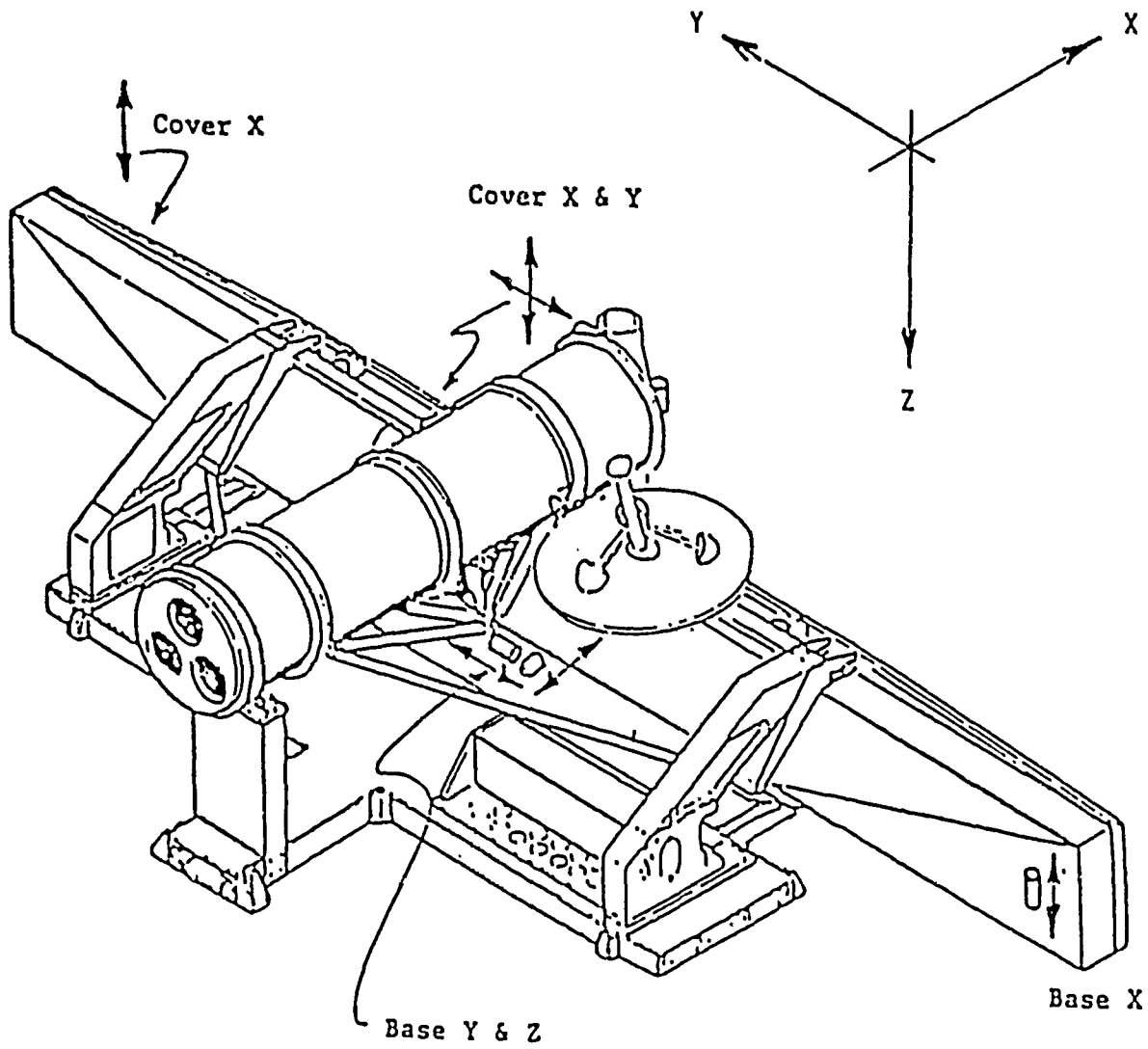
Figure 2. SAFE Model Coordinate Axes and Accelerometer Locations
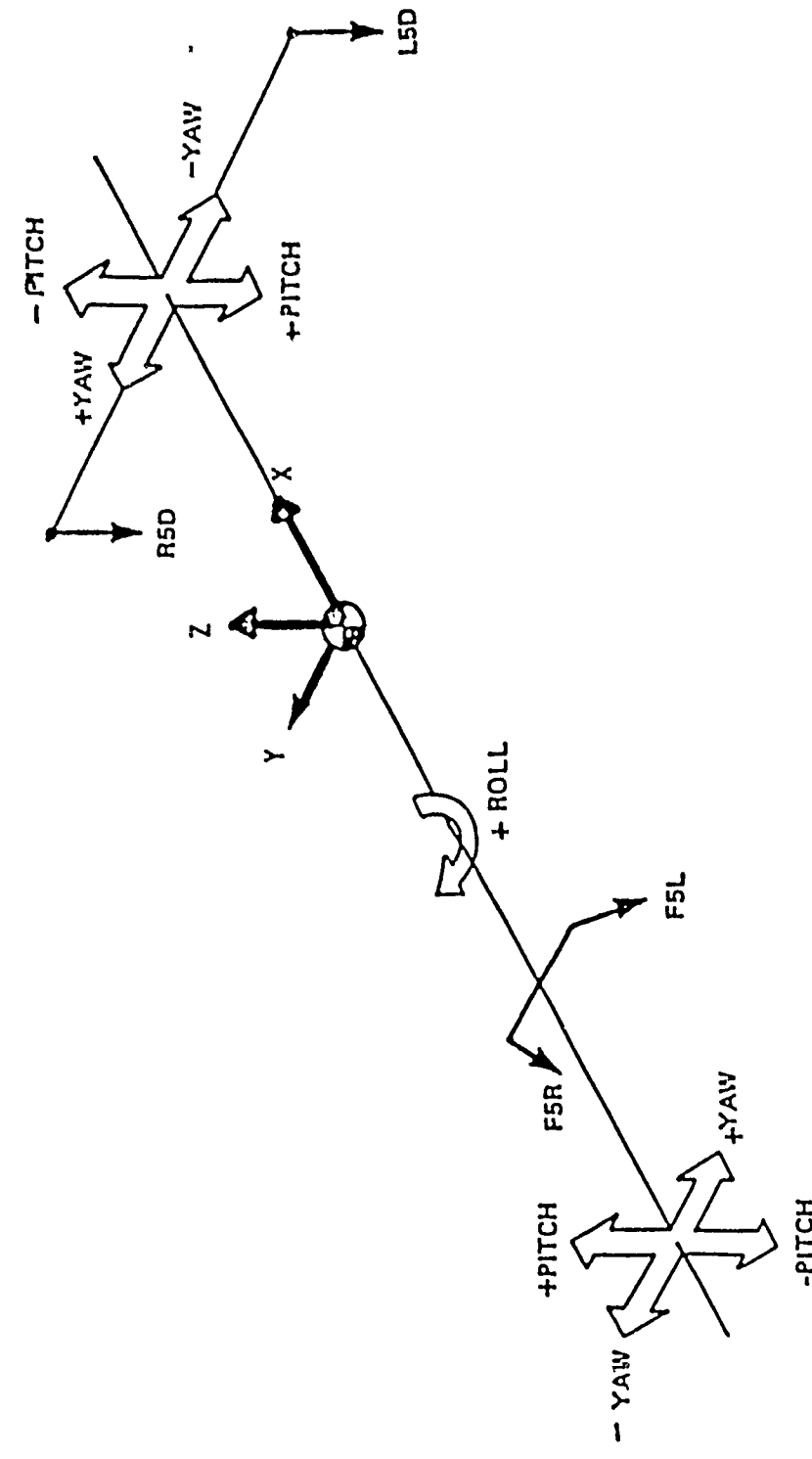
Figure 3. STS Coordinate Axes and VRCS Thruster Locations
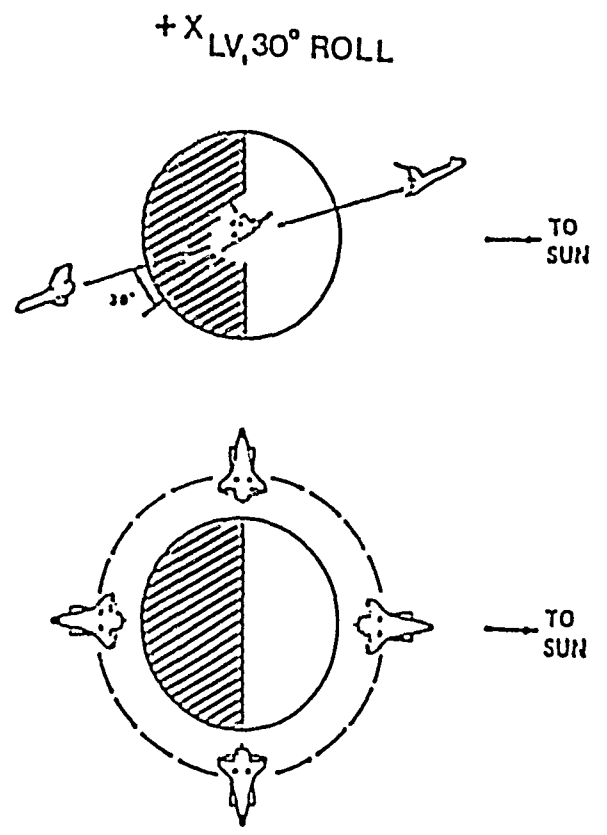
Figure 4. STS Gravity-Gradient Orientation
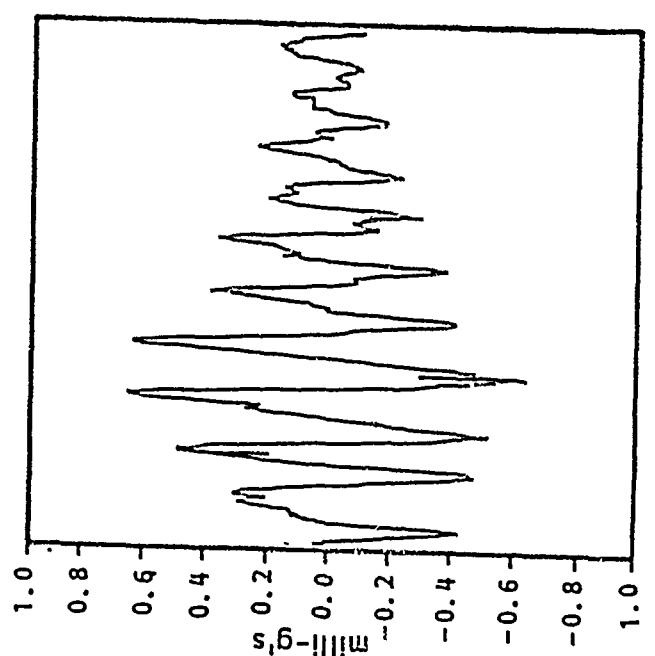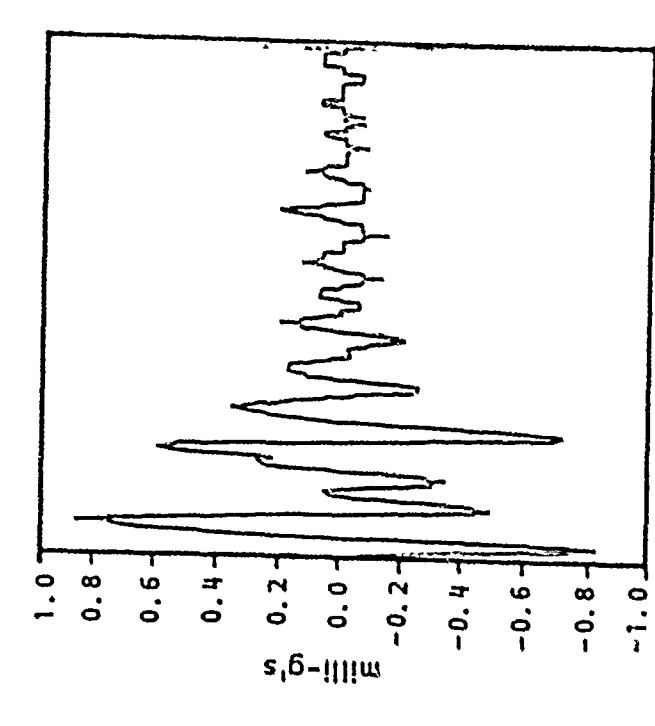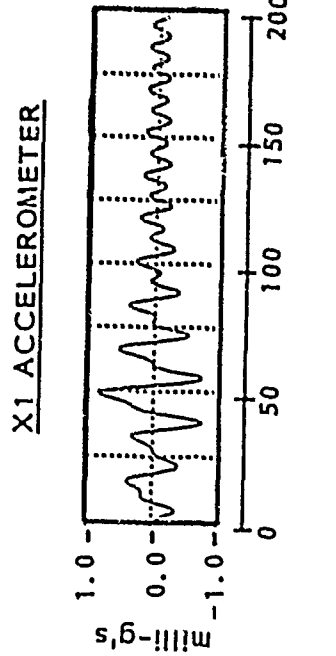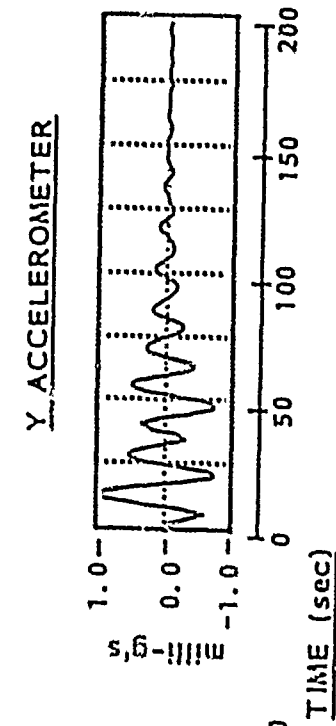
Figure 5.   File 10 Mast-Tip Acceleration History Comparison
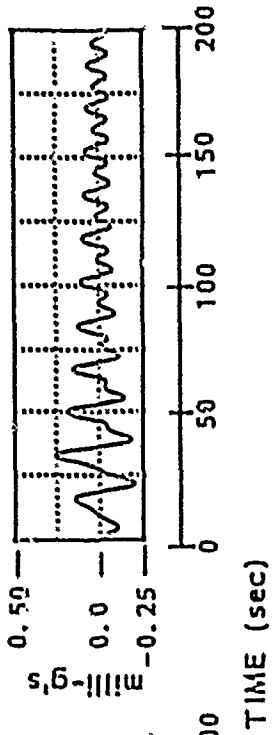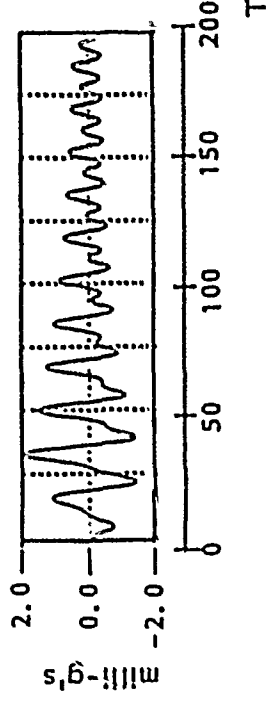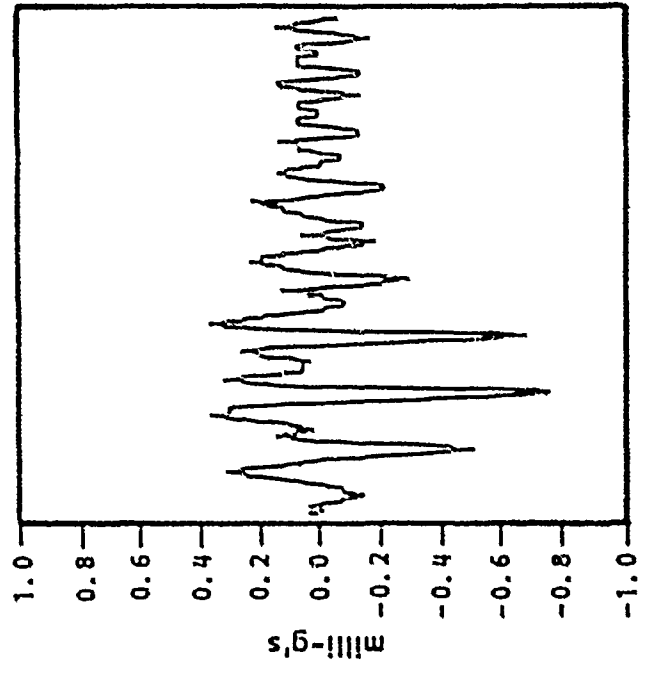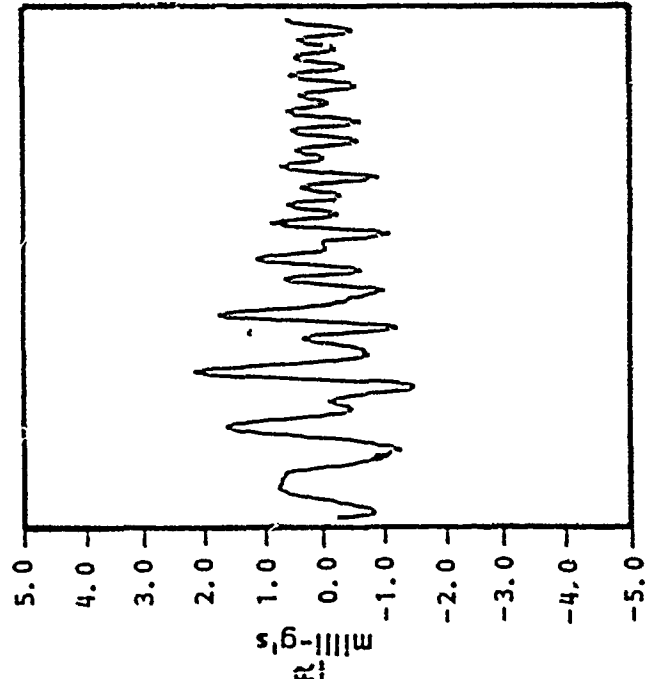
Figure 6. File 12 Mast-Tip Acceleration History Comparison
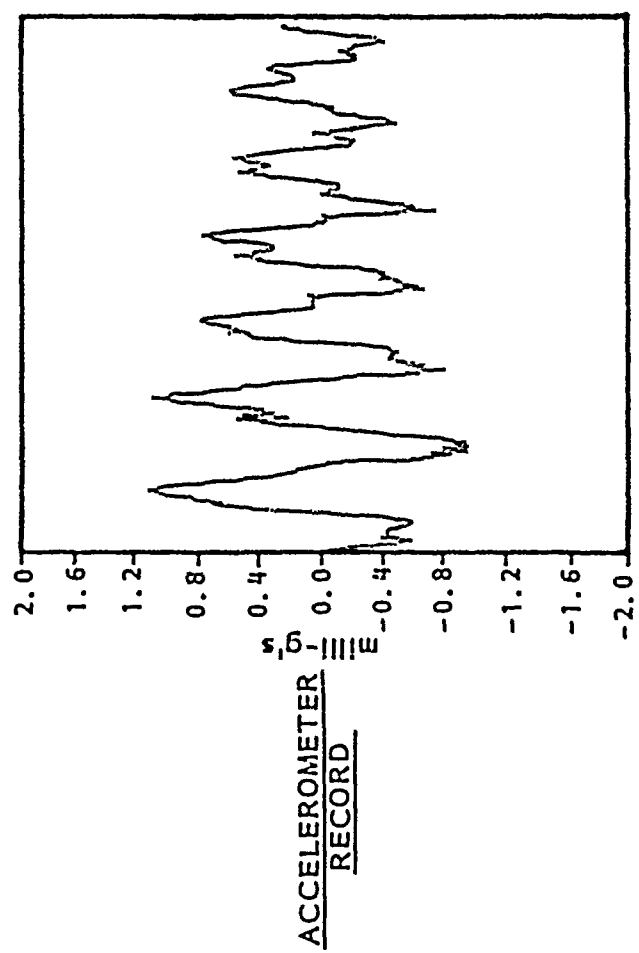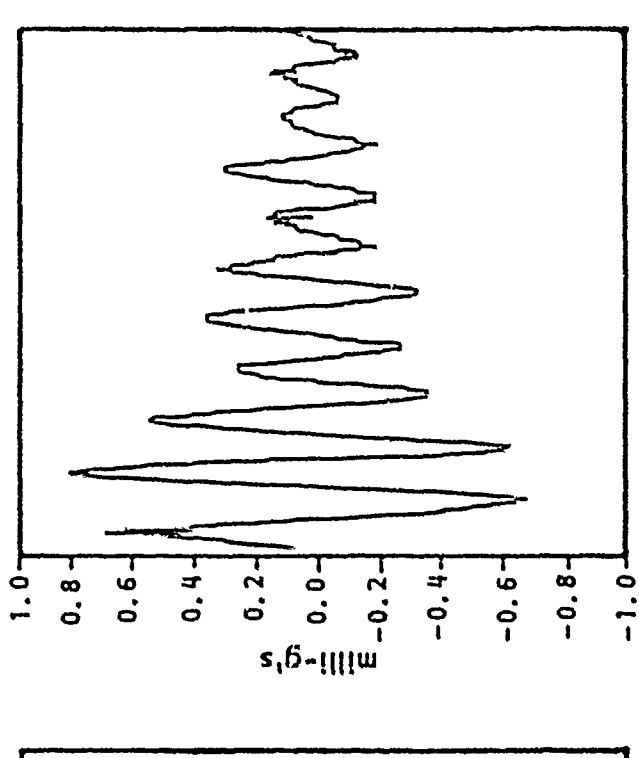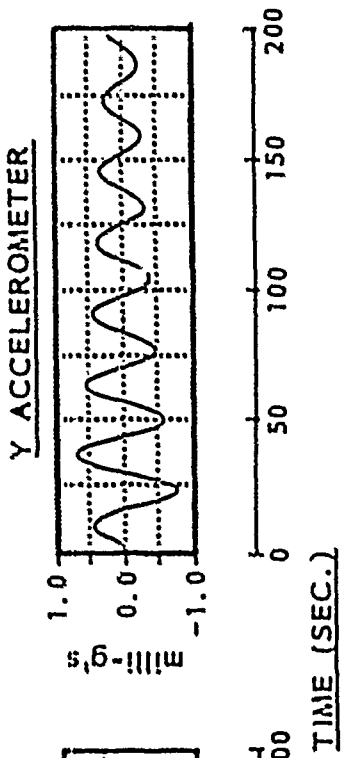
Figure 7. File 20 Mast-Tip Acceleration History Comparison
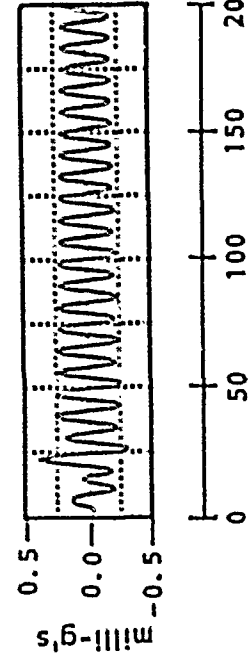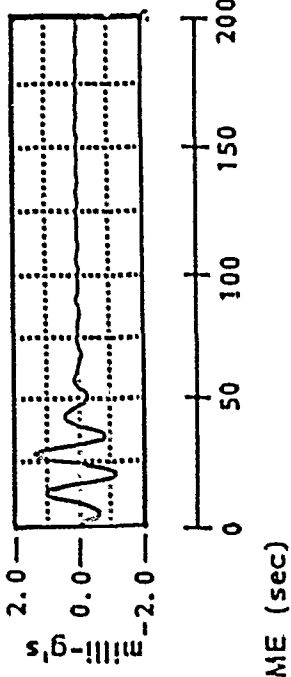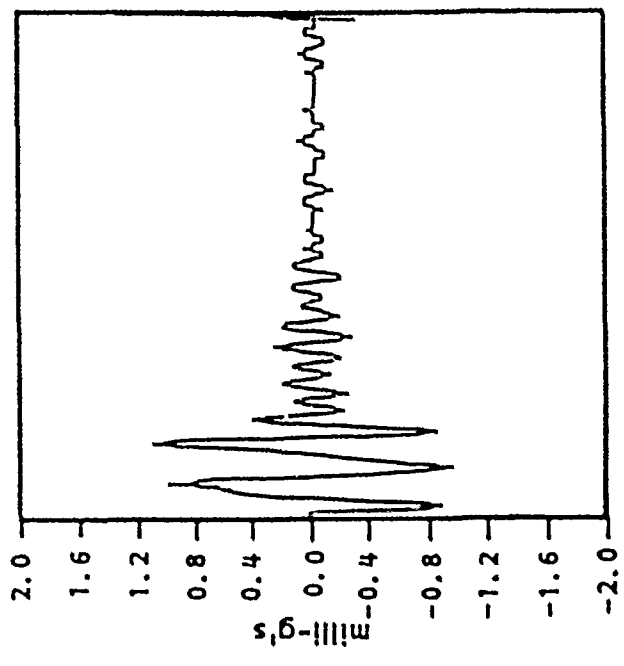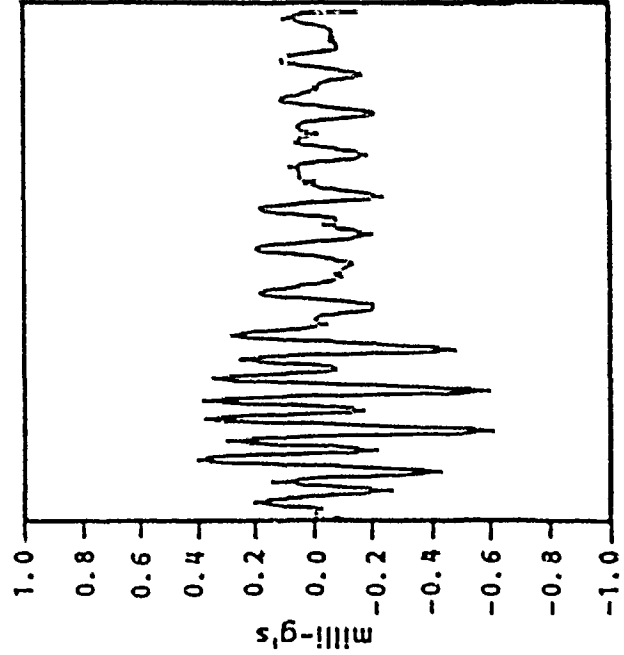
Figure 8. File 28 Mast-Tip Acceleration History Comparison

RESONANT SHIFT MODAL TESTING METHOD FOR VISCOUS DAMPING COEFFICIENT ESTIMATION

D.W. NICHOLSON   ASSOCIATE PROFESSOR
M.G. PRASAD   ASSOCIATE PROFESSOR
R.H. LIN   GRADUATE STUDENT

DEPARTMENT OF MECHANICAL ENGINEERING
STEVENS INSTITUTE OF TECHNOLOGY
CASTLE POINT, HOBOKEN, NEW JERSEY 07030

SUMMARY

An apparently new method has been introduced for experimental estimation of the
effective viscous damping coefficient of lightly damped materials such as
aluminum. The method is based on resonant shifts induced by 'perturbations' of
the inertial and structural properties of a clamped-free cantilever beam with a
variable exposed length and a variable concentrated mass at its free end. A
simple one-element finite element model leads to a very simple relation between
the damping coefficient and a 'weighted resonant shift'. The method merely
requires the accurate experimental estimation of the resonant peaks, which is
accomplished using experimental modal analysis. These peaks are believed to be
more accurately estimated than quantities, especially the damping coefficient,
derived from 'curve fits' to the experimental transfer function in the vicinity
of the resonant peak. In the current investigation extensive data are collected
and analyzed 'pairwise' in accordance with the theoretical model. Overall, the
quality of the data appears reasonable, but it is clear that a more elaborate
analytical model is needed.

INTRODUCTION

The objective of the work reported here is to introduce a method for eval-
uation of damping in lightly damped materials such as aluminum, which is (i)
accurate and (ii) exploits the powerful instrumentation and software used in
experimental modal testing facilities. We confine our attention to viscous
damping, although minor extensions of the test technique will permit estimation
of hysteretic damping.

More concretely, our intent is to introduce a test technique based on
resonant shifts, as discussed below. The work reported here should be viewed as
'work in progress', relying on very simple test designs and analytical models.
Both of these will be upgraded in future investigations.

Typically, in experimental modal analysis the damping coefficient is
estimated directly by fitting single degree-of-freedom equations to the
experimental transfer function, especially near resonant peaks. This
fitting is frequently done by means of the 'circle fit' technique [1].
It is general knowledge that damping coefficient estimates based on direct
curve fitting can produce highly scattered data.

The method proposed in this investigation relies on experimental modal
analysis to identify the resonant frequencies accurately. But it does not
otherwise depend on the accuracy of the experimental transfer function or
on the success of the curve fitting algorithm used. In particular, a simple
clamped cantilever beam technique is used (Fig. 1). Now the exposed length of
the beam is varied. Also there is a variable concentrated mass at the free end

of the beam. As the length of the beam and/or the endpoint mass is varied, the resonant frequencies will shift in a manner sensitive to damping. As discussed in subsequent sections, these shifts can be used to estimate the damping coefficient. The main underlying problem is that, in a certain sense, damping represents a small effect in comparison to stiffness. For example, low levels of damping have a minor effect on the shape of the response curve near resonance, except right at the peak. Likewise, a low level of damping will only produce a slight relative shift in the resonant frequencies. However, as will be shown later, suitably 'weighted' resonant frequency shifts ,induced for example by alteration of boundary conditions, may be quite sensitive to low levels of damping.

An important check is provided by this method. If the damping coefficient is an authentic material property, and not simply a property of the test configuration, its estimated value should prove to be independent of the particular test conditions. In direct curve-fitting tests, this independence is seldom verified. But verification is relatively convenient in the current test since variable boundary conditions are used throughout to produce the shifts. (But regardless of the particular theoretical model being used, the data to be presented here is valuable by virtue of providing test data under a variety of boundary conditions.) Estimates based on the proposed method are compared with modal fit data.

In the subsequent sections (i) we recapitulate the analysis underlying the resonant shift technique, (ii) we describe a sequence of tests leading to damping coefficient estimation by resonant shifts, and (iii) we compare the numbers with results of circle fitting. While we consider the overall results encouraging, several areas of improvement are needed, including a more general analytical model and a more strenuous effort to remove contributions from the holding fixture.

A general discussion of damping is provided in a recent monograph [2], and experimental modal analysis is the subject of another recent monograph [1]. A review of damping evaluation techniques is given in [3], and an earlier study on aluminum damping, based on amplitude decay, has been reported in [4]. Based on a review of this and other literature, it appears that the method introduced here is new.

ELEMENTARY ANALYTICAL MODEL

1. Single element finite element model for a viscoelastic beam

Referring to Fig 1, we assume that the beam material is composed of a Kelvin-Voigt material described by

$$s = Ee + \eta e \qquad (1)$$

where s denotes the stress, e denotes the strain, E denotes the Young's modulus and η denotes the viscosity. The beam equation arising from the Euler-Bernoulli assumptions is simply

$$\frac{EI}{L^3}\frac{\partial^4 w}{\partial z^4} + \frac{I}{L^3}\frac{\partial^4 w}{\partial t \partial z^4} + AL\frac{\partial^2 w}{\partial t^2} = 0 \qquad (2)$$

$$w = y/L \qquad\qquad z = x/L.$$

Here M_c denotes the concentrated mass, A denotes the beam cross-sectional area, denotes the mass density, L denotes the total exposed length of the beam, and I denotes the bending moment of inertia.

He now assume the general approximation

$$w(z,t) = N^T(z)a(t) \qquad (3)$$

where $N(z)$ is a 'shape function' vector and $a(t)$ is a vector of parameters to be determined. The superscript T implies the transpose. Using conventional variational methods [5], the beam equation (2) is approximated by

$$K_{=2}\,[\,\frac{EI}{L^3} + \frac{I}{L^3}\frac{\partial}{\partial t}\,]\,a + AL\,K_{=0} = -M_c\,\ddot{w}(1) \qquad (4)$$

in which

$$K_{=2} = \int_0^1 \underline{N}'' \underline{N}''^T \, dz \qquad\qquad K_{=0} = \int_0^1 \underline{N}\, \underline{N}^T \, dz$$

where the accent mark denotes differentiation with respect to z.

We now assume that the fundamental frequency can be accurately reproduced using a one-element finite element model with a third order shape function. In particular

$$w = \langle\, 1 \quad z \quad z^2 \quad z^3 \,\rangle \begin{Bmatrix} a_0 \\ a_1 \\ a_2 \\ a_3 \end{Bmatrix} \tag{5}$$

The conditions on w are:

$z = 0:$ $\quad w = w' = 0$

$z = 1:$ $\quad w'' = 0$ $\hfill$ (no moments)

$z = 1:$ $\quad \dfrac{1}{L^3}[\, EI + I \dfrac{\partial}{\partial t}\,]\, w''' = -M_c \ddot{w}$ $\hfill$ (equilibrium with the inertial force)

Omitting the intermediate manipulations, the equation of the beam reduces to

$$m \ddot{w}(1) + c \dot{w}(1) + k w(1) = 0 \qquad (6)$$

$$k = \frac{3EI}{L^3} \qquad c = \frac{3 I}{L^3} \qquad m = M_c + \frac{33}{140} M_o$$

where $M_o = AL$ is the total mass of the beam. From equation (6) the resonant frequency is simply:

$$\omega_r^2 = k/m - \tfrac{1}{2}(c/m)^2 \qquad (7)$$

2. Identification of the viscous damping coefficient

Now suppose that two different test configurations are compared, the first with concentrated mass M_1 and the second with concentrated mass M_2. Further, suppose that the measured resonant frequencies for the two configurations are ω_{r1} and ω_{r2}. Simple manipulations using (6) lead to

$$Q c^2 = R \qquad (8)$$

where

$$Q = \tfrac{1}{2} [(M_2 + \frac{33}{140} M_o)^{-1} - (M_1 + \frac{33}{140} M_o)^{-1}] \qquad (9)$$

$$R = [M_1 + \frac{33}{140} M_o]\omega_{r1}^2 - [M_2 + \frac{33}{140} M_o]\omega_{r2}^2 \qquad (10)$$

DD-7

4-

Also,

$$\eta = c L^3 /3I.$$

The equations (8-10) for estimating the damping coefficient require knowing the statically measurable quantities E, I, M_o, M_1, M_2 and L. They also require knowing the resonant frequencies, which are measured here by experimental modal analysis. We view the function R in (10) as a 'weighted resonant frequency shift'. In our view, experimental modal analysis provides relatively accurate estimates of resonant frequencies, and less accurate estimates of the shape of the transfer function in the vicinity of the resonant peaks. In the current method, there is minimal reliance on 'curve fitting'. A major difficulty generally underlying damping evaluation is the fact that its effects are often 'small' in comparison to stiffness effects. However, as seen above, suitably 'weighted' resonant frequency shifts, induced for example by altering the mass, can be highly sensitive to damping.

EXPERIMENTAL RESULTS

The experimental investigation was coducted in the Noise and Vibration Control Laboratory at Stevens Institute of Technology. The modal analysis system includes a ZONIC 6080 Multichannel Fast Fourier Transform Analyzer, a Zonic 6081 Real Time Display Terminal, a modal hammer and an accelerometer from PCB Company. The material tested was 2024-T4 aluminum. The beam width and thickness were 1.5" and .25". In all cases the accelerometer position and the impact point were 6" and 5" from the built-in end, respectively. Five different exposed lengths and three different mass levels were used, as shown in Table I. The beam length was measured from the fixture to the cut end, and the concentrated mass was assumed to be located at the cut end. The average from five impacts was used.

ND-8

The test pairs used and the estimates of c obtained from Eq. (8) are given in Table II. Finally, Table III gives a comparison of the viscosity estimates obtained by the new method and obtained directly from the modal analysis system based on the 'circle fit' method. Overall, in terms of reproducibility, consistency of trends, etc, the data appear to be of reasonable quality.

As can be readily observed in Table 3, the viscosity estimates by the new method are generally four or five times higher than those based on the circle fit method. In addition, both in the new and in the circle fit method, there is discernible dependence on exposed length. Both of these features seem to us to be unrealistic. Quite likely, the finite impedance of the holding fixture has some effect on the quality of the data. Similarly, the rotary intertia of the beam and of the concentrated mass has some effect. Third, what we have been calling a beam is actually intermediate between a beam and a plate. (However, aerodynamic damping is not likely to be significant owing to low amplitudes.) The possible sources of error simply require a more sophisticated model for for the data analysis, for example accounting for the holding fixture. In our view they represent no challenge to the fundamental innovation proposed here, namely the use of resonant shifts to evaluate damping.

CONCLUSION

An apparently new method has been proposed for experimental estimation of the effective viscous damping coefficient of lightly damped materials, such as aluminum. The method is based on resonant shifts induced by 'perturbations' of the inertial and structural properties of the test specimen. A simple one-element finite element model leads to a very simple relation between the damping coefficient and a 'weighted resonant shift'. Experimental modal

analysis is used to identify the resonant frequencies, which are believed to more accurately estimated than quantities, in particular the damping coefficient, derived from 'curve fits' to the experimental transfer function in the vicinity of the resonant peak. Extensive data are collected and analyzed 'pair-wise' in accordance with the model. Overall, the quality of the data appears reasonable. But the damping coefficient estimates appear to be too high, and they exhibit an appreciable dependence on exposed length. However, it is expected that a more sophisticated analytical model will produce improved estimates.

REFERENCES

1. Ewins,D.J., et al, MODAL TESTING:THEORY AND PRACTICE, John Wiley and Sons, N.Y., N.Y., 1984.

2. Nashif, A., Jones, D.I.G., and Henderson, J.P., et al, VIBRATION DAMPING, John Wiley and Sons, N.Y., N.Y., 1984.

3. Kluesener, M.F., 'RELSAT - Task 2: Selection of Test Procedure', Report UDR-TR-86-15, University of Dayton Research Institute, 13 Feb 1986.

4. Baker, H.E., et al, 'Air and Internal Damping of Thin Cantilever Beams', Int'l J Mech Sci, Vol 9, pp. 743-766, 1967.

5. Reddy, J.N., AN INTRODUCTION TO THE FINITE ELEMENT METHOD, McGraw-Hill Book Company, N.Y., N.Y., 1984.

TABLE I

TEST CONDITIONS AND MEASURED FREQUENCIES

TEST NO.	LENGTH	M_{beam}	M_1^*	M_2^*	ω_{r1}
	in	lbf	lbf	lbf	rad/sec
1	10.5	.00105	0.	0.00026	402
2	"	.00105	0.	0.00048	286
3	"	.00105	0.00026	0.00048	240
4	10.75	.00107	0.	0.00026	377
5	"	.00107	0.	0.00048	270
6	"	.00107	0.00026	0.00048	227
7	11.0	.00110	0.	0.00026	355
8	"	.00110	0.	0.00048	259
9	"	.00110	0.00026	0.00048	219
10	11.25	.00122	0.	0.00026	340
11	"	.00122	0.	0.00048	252
12	"	.00122	0.00026	0.00048	213
13	11.5	.00147	0.	0.00026	330
14	"	.00147	0.	0.00048	348
15	"	.00147	0.00026	0.00048	210

$\star$ The total weight of the concentrated mass is M_1 plus M_2.

TABLE II

ESTIMATED DAMPING VALUE PARAMETERS

test pair no.	ω_{r1}	ω_{r2}	c
	sec^{-1}	sec^{-1}	$\dfrac{lbf\text{-}sec}{in}$
1	402	286	.056
2	402	240	.057
3	286	240	.059
4	379	270	.042
5	379	226	.045
6	270	226	.053
7	355	259	.060
8	355	218	.067
9	259	218	.067
10	340	252	.077
11	340	213	.074
12	252	213	.060
13	330	248	.085
14	330	210	.079
15	248	210	.057

TABLE III

COMPARISON OF DAMPING COEFFICIENT ESTIMATES

test no.	NEW METHOD		CIRCLE FIT
	$\overset{\star}{c}$	η	c
	$\dfrac{lbf\text{-}sec}{in}$	$\dfrac{lbf\text{-}sec}{in\text{-}in}$	$\dfrac{lbf\text{-}sec}{in}$
1	.057	8014	.010
2	.057	8014	.010
3	.057	8014	.011
4	.046	8605	.014
5	.046	8605	.011
6	.046	8605	.011
7	.067	10729	.014
8	.067	10729	.011
9	.067	10729	.009
11	.070	12086	.012
12	.070	12086	.008
13	.073	13540	.017
14	.073	13540	.013
15	.073	13540	.011

*average estimate by new method for the exposed length
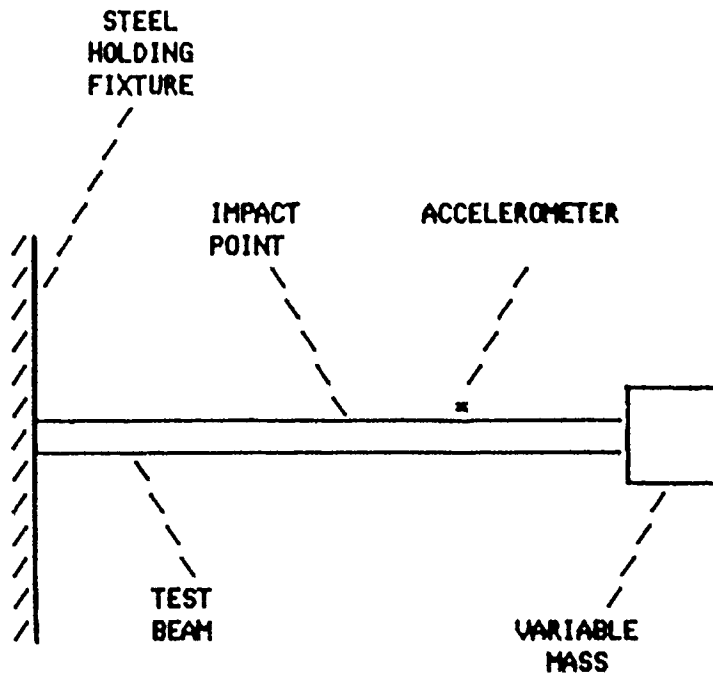
FIG. 1   TEST CONFIGURATION

Prediction of Spacecraft Damping*

Ben K. Wada

Deputy Manager

Applied Technologies Section

Jet Propulsion Laboratory

California Institute of Technology

Abstract

The paper presents the author's observations on the state-of-the-art in the prediction of spacecraft damping for use in launch loads analysis. Experimental spacecraft damping values from the Viking, Voyager, Galileo, and Centaur programs are presented; most of the damping results were obtained using a variety of the state-of-the-art modal test methods. A comparison of the various modal test methods used to extract modal damping from one spacecraft is presented to illustrate the discrepancies. Based upon the available data, the capability to predict damping and experimentally determine modal damping from on-orbit tests for the control of large space structures are discussed.

Introduction

Since a large uncertainty in the prediction of modal damping exists, the designer is required to assume a very conservative value of damping for the design of the spacecraft to eliminate the possibility of a redesign. Often the measured damping values are much larger than the damping assumed in the design of the structure which resulted in a conservative structure designed to conservative loads. The need for a method to more accurately predict modal damping or devise approaches to minimize the influence of modal damping on the design of the structure has been recognized.

In an attempt to reduce conservatism to reduce the structural weight, a modification was made in the design process to minimize the dependency of design loads on damping. This was accomplished by changing the forcing functions used to establish the design loads from a sinusoidal test input, which simulated the anticipated forces, to the expected transient forces. Until the eary part of the 1970's, modal damping was obtained from exponential decay data of individual modes excited by the multiple point sine dwell (MPSD) method. Improvements were made in the prediction of damping at the anticipated level of excitation by obtaining data at a minimum of three levels for each mode in order to estimate the damping at the predicted design levels. The general consensus was that damping increased as the modal frequency increased.

In the mid-1970's, several new modal test techniques were introduced which could be used to determine modal damping. These included the single point random (SPR) and the Ibrahim Time Domain (ITD) modal test methods. Using test results from the Voyager spacecraft, the MPSD, SPR, and the ITD methods were used to estimate modal damping. A comparison of the modal damping data indicated a large deviation between the methods. The deviation was partially attributed to the "newness" of the test methods and the lack of experience by the test personnel.

In the 1980's, another opportunity existed to evaluate the state-of-the-art in measuring modal damping.

In addition to the modal test methods used in the Voyager program, the Simultaneous Frequency Domain (SFD), Polyreference using several sets of random shakers, Swift excitation, Chirp excitation, and the Eigensystem Realization Algorithim (ERA) test methods were used to extract modal damping data from the Galileo test. To preclude errors in the application of the methods, the developers of the various modal test techniques extracted the modal damping data from the test data. A similar set of analyses was also performed on the Centaur G Prime modal test. The resuits from both the tests indicate that the various test methods do not extract consistent modal damping data from the test data. The scatter in the test data resulted in some confusion regarding the trends in damping as a function of frequency. Contrary to past observations and engineering judgement, the damping appears to decrease with increasing frequency. The test data help confuse the effort to improve the prediction of modal damping.

The objective of this paper is to present the results of tests to measure modal damping of space structures using the various modal test and analysis methods. From the observations, the potential ability to experimentally measure on-orbit damping and to predict modal damping will be discussed.

Background

Period from 1960-1970

The original motivation to improve the estimation of modal damping was to improve the ability to predict the anticipated structrual design loads resulting from the dynamic excitations. Since the dynamic excitation was defined as an equivalent sinusoidal vibration test, the structural design loads were directly proportional to damping. Also because the damping couldn't be accurately predicted, a lower bound estimate of damping was used for all the vibration modes to minimize the potential for a redesign late in the program when test hardware was available to experimentally measure damping.

Typical estimates of the lower bound of damping was 1% critical damping. The uncertainty in damping often resulted in an overdesign and overtest by up to an order of magnitude. Specific experimental studies were initiated to determine if damping values could be assigned to different types of joints which were used for various classes of spacecraft structures. The objective was to help establish a means by which damping of structures could be better determined by evaluating the types of joints in the structure. After testing several types of joints, the entire effort was abandoned because the variation in the joint damping was greater due to the manufacturing variability of a specific joint design than to the differences in the joint designs. The highest damping was achieved when the fabrication of the structure was "sloppy".

Period from 1970-1975

The next improvement to minimize the dependence of damping on the entire design process was to establish the design loads and the test program by using the results of a transient loads analysis. The process was initially incorporated on the Viking Program in 1970. Special attention was taken to measure modal damping data at a minimum of three excitation levels for each mode using the MPSD to allow estimation of damping at the excitation levels corresponding to the design loads. In some modes the damping didn't vary with acceleration while in others they varied substantially. The modes with non-linear damping couldn't be predetermined. Figure 1 shows the damping values which were measured for Viking. A line was drawn through the data points reflected our engineering judgement that damping increased with increasing frequency. This curve was used subsequently in the estimation of spacecraft damping. Confidence existed in the accuracy of the modal damping data obtained from the MPDS.

In order to improve the estimation of damping for dynamic response analysis, an effort was initiated to partition the entire structure into subsystems whose damping may be more accurately estimated because of past test data or they were made of similar materials and construction procedures. The Viking structure was comprised of various subsystems which were interconnected at a few points as schematically shown in Figure 2. For each substructure, a set of displacement functions were selected to represent the dynamic motion in the frequency range of interest and the anticipated load distribution in the final structural response. The displacement functions included both normal modes and other static displacements. Modal damping for the subsystems were either estimated and/or obtained from modal tests, whereas the damping for the static displacements could only be estimated because they could not be

experimentally determined. When the equations of motion of the total structure were developed from the subsystem displacement functions, the coupling of the damping matrix resulted in a first order differential equation as shown in Equation 1.

$$A\dot{\eta} + B\eta = F(t)$$

where

$$A = \begin{bmatrix} 0 & K \\ M & C \end{bmatrix}, \quad B = \begin{bmatrix} -M & 0 \\ 0 & K \end{bmatrix}, \quad \eta = \begin{Bmatrix} \dot{x} \\ x \end{Bmatrix}, \quad F(t) = \begin{Bmatrix} 0 \\ f(t) \end{Bmatrix}, \quad (1)$$

M = mass matrix,
C = damping matrix,
K = stiffness matrix,
x = vector of subsystem modal coordinates and
f(t) = forcing function.

Using the complex eigenvalue solution resulting from Equation 1 as the generalized coordinates in the forced response solution, the resulting responses appeared to be erroneous based upon previous analysis and flight data. The apparent error could only be attributable to the coupling in the damping matrix. The final solution was based upon eliminating the off-diagonal damping elements and retaining the diagonal terms which was equivalent to estimating the modal damping. A comparison of the predicted flight loads and accelerations, using our best estimate of modal damping based upon test data, with the Viking flight data indicated an excellent agreement. Using modal damping corresponding to the system modes proved to be a better estimate of the physical system.

The subsystem approach was very beneficial in estimating the response of the total structure when a small finite number of subsystems were connected by nonlinear stiffness and damping elements. The nonlinearity was either a result of the dependency of the connecting element on amplitude or temperature. A forced response solution in the time domain was used with the linear portion of the structure represented as generalized coordinates incorporated with the nonlinear elements with its physical degrees of freedom.

As a result of the Viking program confidence existed that modal damping could be reliably measured by ground testing. In specific cases, such as large area low mass solar panels, experimental measurements of damping must be made in a vacuum chamber.

Period 1975-1980

During the development, analysis, test, and flight of the Voyager spacecraft, another opportunity existed to establish a set of reliable measured modal damping data to help improve the capability to predict modal damping for the design loads analysis. The significant aspect of the Voyager modal data is that although the MPSD was used to obtain the "official" modal damping, an opportunity existed to use other new modal test techniques which had become available. They included modal data analysis using two different Single Point Random (SPR) methods and the Ibrahim Time Domain (ITD) method. The results of

the analysis are presented in Figure 3; the shaded hatched lines encompass the range of modal damping obtained by the MPSD for the various amplitudes of excitation. Comparison of the results of the measured damping values from the various methods is poor. Possible reasons attributed to the differences included the inexperience of the personnel performing the SPR analyses and the immaturity of the methods as applied to realistic structures. The other potential problem which appeared to exist is that possibly the predicted modes with the newer methods may not exist in the structure; this misinformation would result in problems in updating the analytical model to correlate with the test data.

Imagine attempting to update a linear mathematical model representing the physical structure to include modes which may be related to electronically generated or mechanically noisy data.

Period 1980-1984

During the summer of 1983, another opportunity existed to measure modal damping using the various state-of-the-art modal test methods as a part of the Galileo program. Although many of the newer techniques had been used by many organizations, the MPSD technique was selected to obtain the modal parameters to help validate the mathematical model for the loads analysis. Rather than to introduce the potential of misusing the newer techniques, the developers of the techniques participated in obtaining the modal data from tests performed on the Galileo spacecraft. The test data indicated that the Galileo spacecraft structure was locally linearly; thus the test data was ideal to compare results from the various test methods. Although the structure was locally linear, nonlinearity with respect to amplitude was evident in a few select modes.

The modal test methods evaluated included the MPSD, SPR, 3-shaker Polyreference (3-PR), 4-shaker Polyreference (4-PR), Simultaneous Frequency Domain (SFD), Eigensystem Realization Algorithm (ERA), analysis using the CHIRP forcing function, and analysis using the SWIFT forcing function. Although the eigenvectors and eigenvalues were similar for all the test methods, the comparison of damping was not good; the data is shown in Figure 4. Even more disturbing was that when using the same modal analysis technique on data obtained by exciting the structure at different locations in different directions, the resulting damping data were not consistent. The 3-PR and 4-PR data are shown in Figure 5 and the SFD results are shown in Figure 6. The evaluation of all the data indicates that the damping values tend to decrease with increasing frequencies which is contrary to the observations made on many of the previous modal tests. Note that the higher frequencies are not necessarily associated with higher bending type modes but modes of subsystems which are suspended from the main spacecraft.

With the large discrepancies in modal damping, confidence in the measured damping becomes even more difficult. Again the damping values using the MPSD were obtained at a minimum of three levels to help estimate the damping at the higher levels of excitation.

Period 1984-1986

Another unique opportunity existed to measure damping using the state-of-the-art modal test methods by the developers of the methods on a structure which was supported by sliding trunions, the Centaur G Prime. This test was conducted by General Dynamics Convair (GDC) under contract to Lewis Research Center (LeRC).

The structure included the nonlinearities of the sliding joints in part of the test program. The structure was excited by both a low level random excitation as well as a high level sine dwell and sine sweep. Difficulties existed in obtaining good modal data at the low excitation levels; probably due to the nonlinearities. However at the higher excitation levels approaching 1/3 the design levels, good linearized modal results were obtained. A plot of all the damping data obtained are illustrated in Figure 7. Again note the scatter between the results from the various modal test methods which included the SFD, MPSD, Polyreference, and analysis of the frequency response function from the sine sweep data. The trend of the damping is to decrease with increasing frequency.

The difference in the damping results using the same modal analyses methods on data obtained by exciting the structure in different directions and at different locations is shown in Figure 8 for the SFD and in Figure 9 for the analysis of the frequency response function obtained from the sine sweep data.

The conclusion drawn from the data indicates the methods for extracting reliable damping data from the test data is very poor. Again no progress has been made in establishing a method to predict modal damping data because of the inability to establish a reliable base of experimental modal damping.

Period 1986 and Beyond

The future need for large space structures is apparent based upon the projected missions. In many of these structures, the structure must be controlled in order to establish an effective mission. Since damping is an important parameter to help establish an effective control system, and reliable testing of the structure on the ground appears to be virtually impossible, many are advocating on-orbit testing to experimentally measuring the dynamic characteristics including damping. On-orbit testing appears to be more limited than ground testing because of the limited number of excitors and sensors and the inability to check suspect instrumentation or to adjust them during the test. Based upon our experience using state-of-the-art modal test techniques, which is more suitable for on-orbit testing than the MPSD, reliable damping cannot be measured. Also more problems are anticipated with nonlinearities at the low excitation levels which are of interest during the on-orbit operation.

Conclusion

As indicated by the above data, prediction of modal damping by analytical means appears to be very difficult because the current test methods cannot be used to establish a reliable set of experimental modal damping data. Emphasis in research should be placed on understanding the basics of why the various modal test analysis predictions for damping are inconsistent and establish a means to determine the degree of uncertainty in the damping data. Once an experimental data base is established, then predictive techniques for damping can possibly be improved.

Figure 1. DAMPING
VIKING MODAL TEST
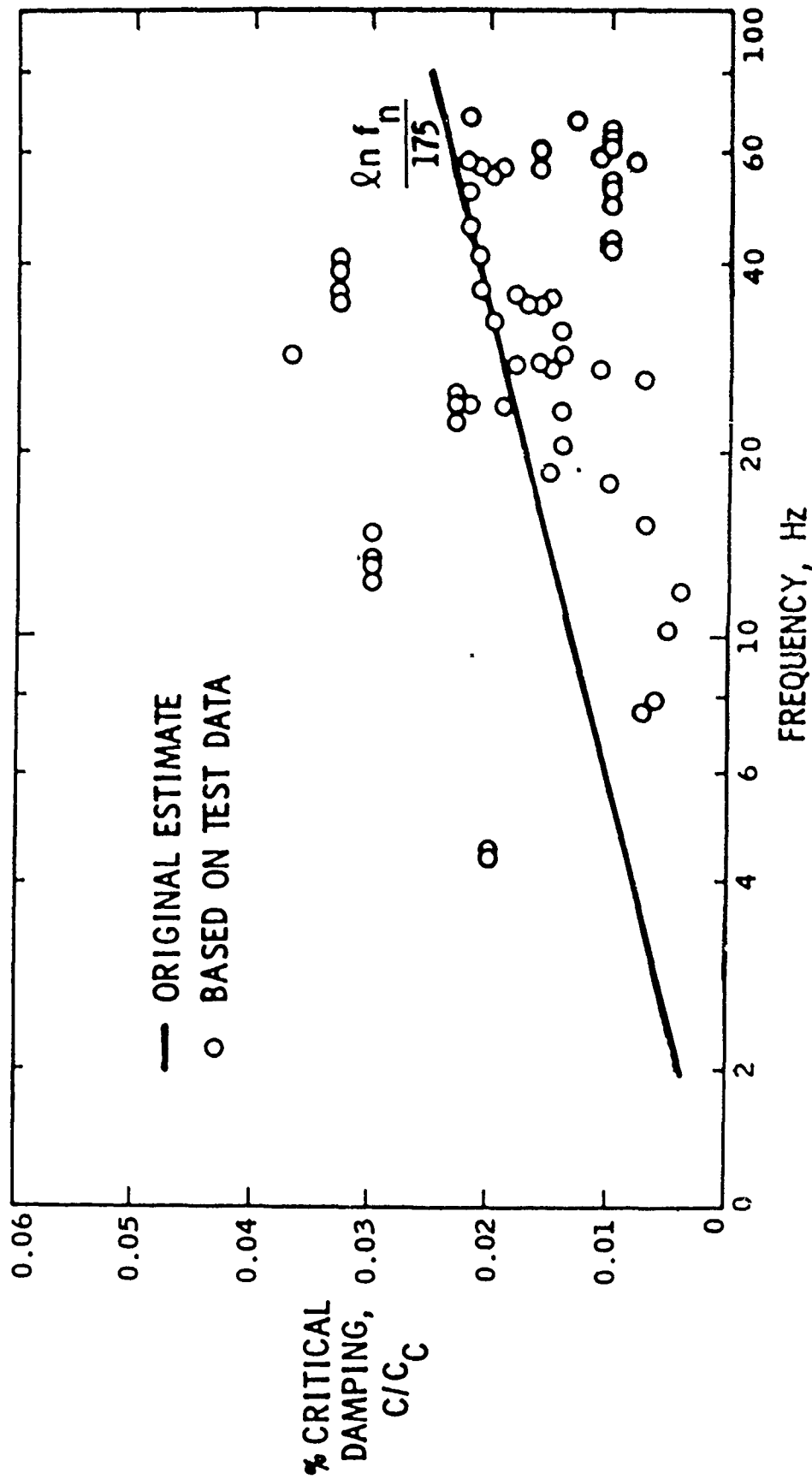
Figure 2. Representation of Total System by Substructures
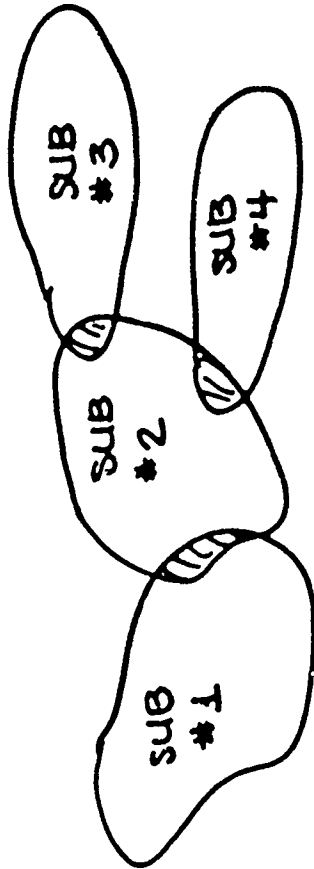
Figure 3. All Damping Data for Voyager
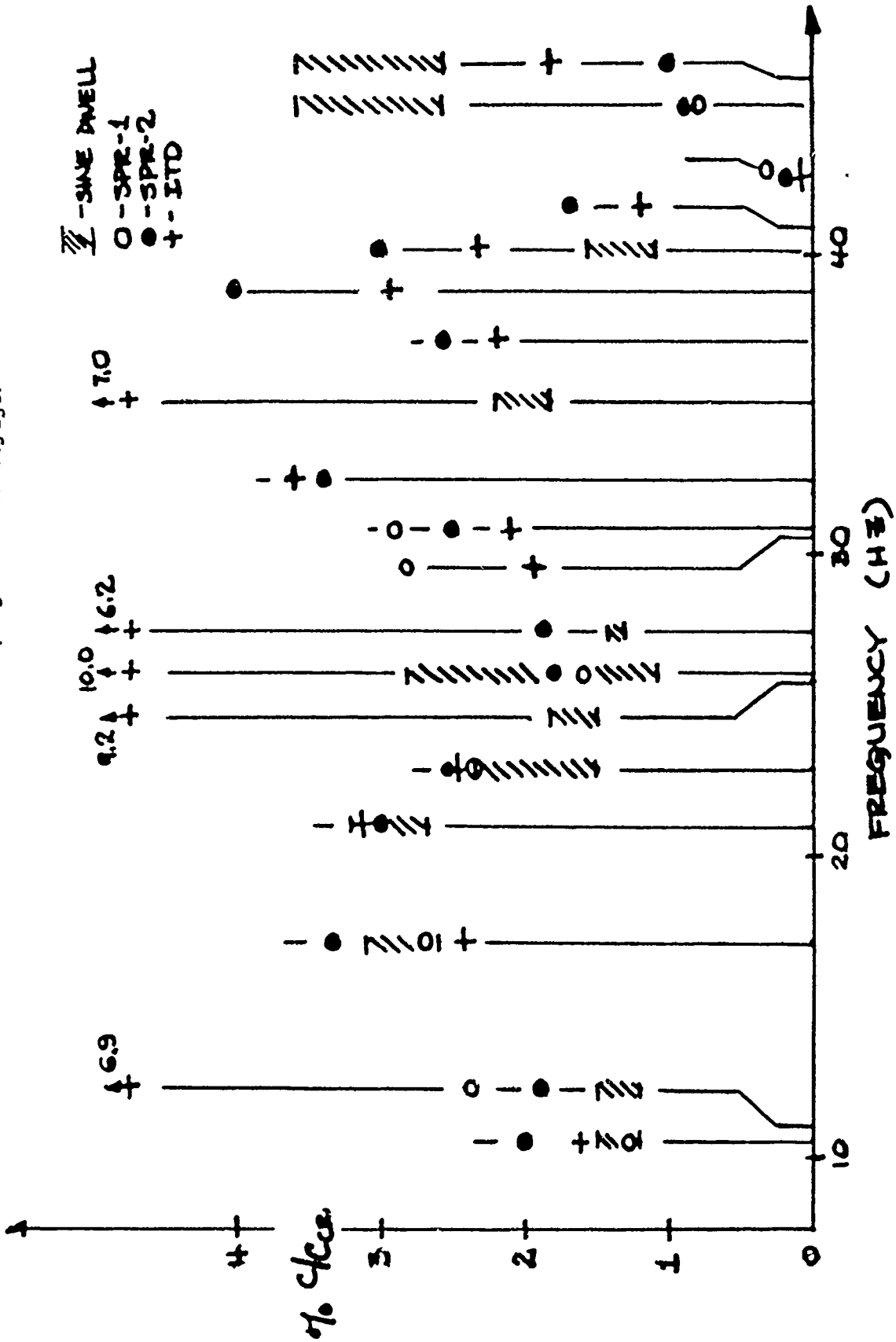
Figure 4. All Damping Data for Galileo
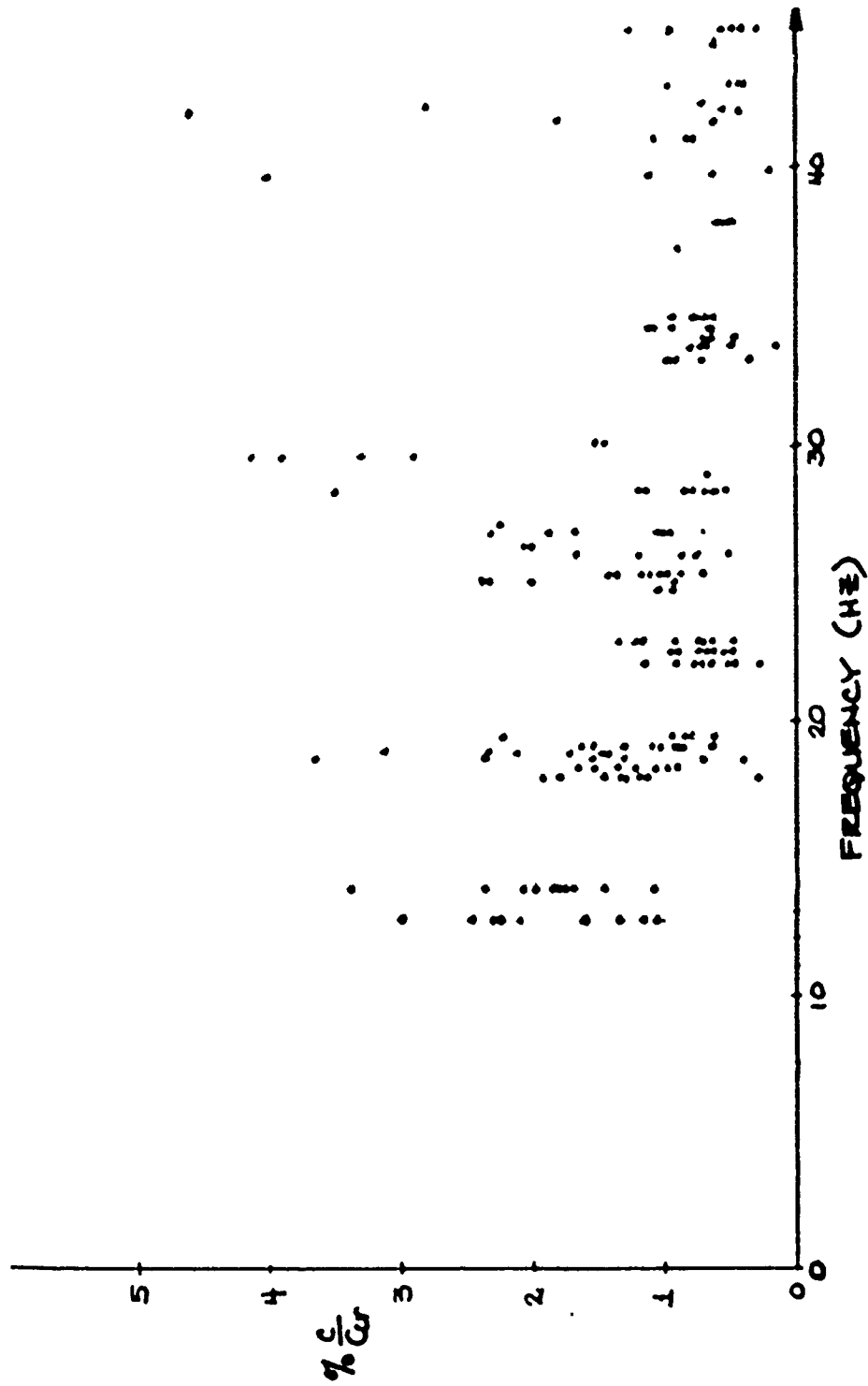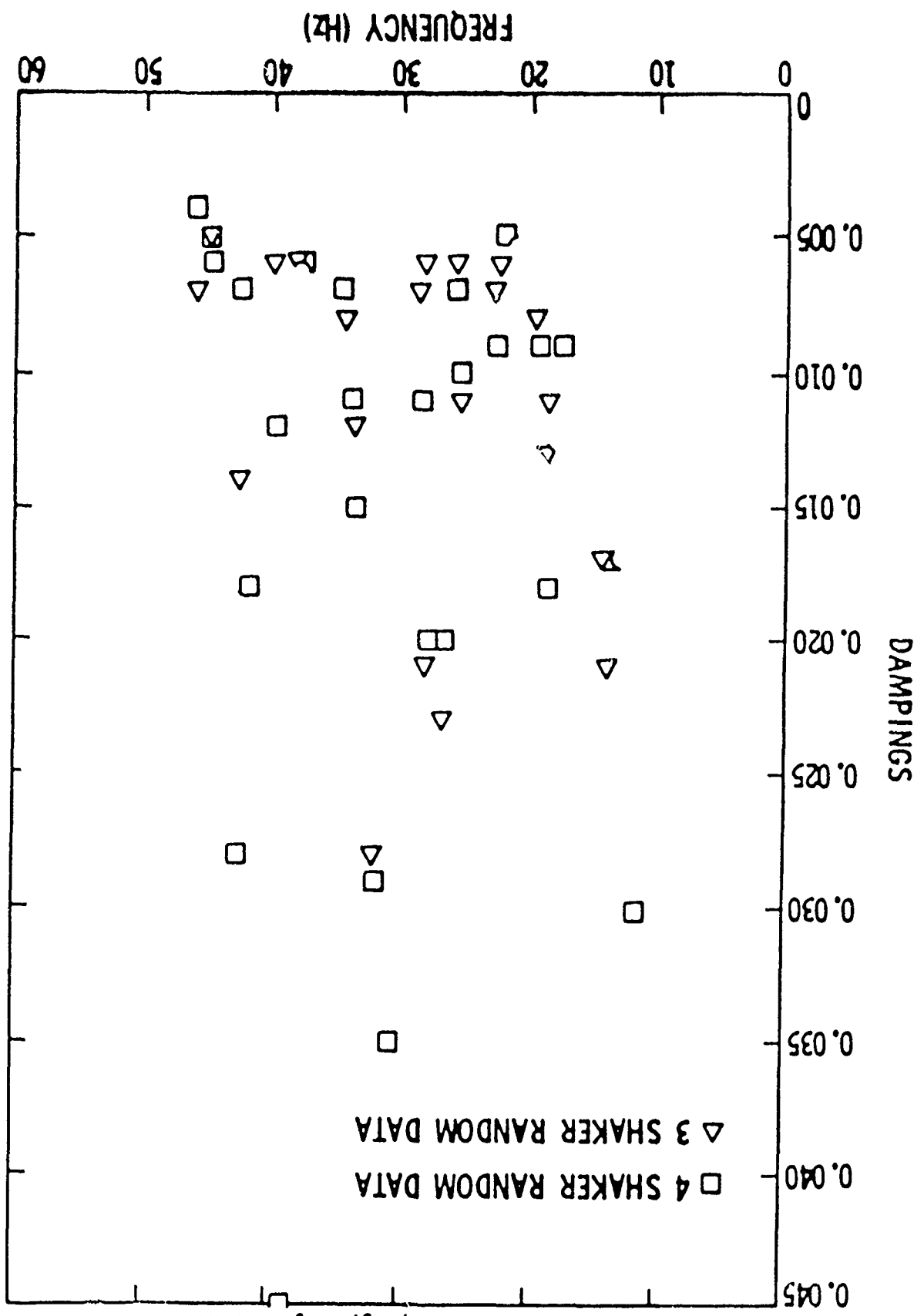
Figure 5. Galileo Modal Damping, Polyreference

Figure 6. Galileo Modal Damping, Simultaneous Frequency Domain
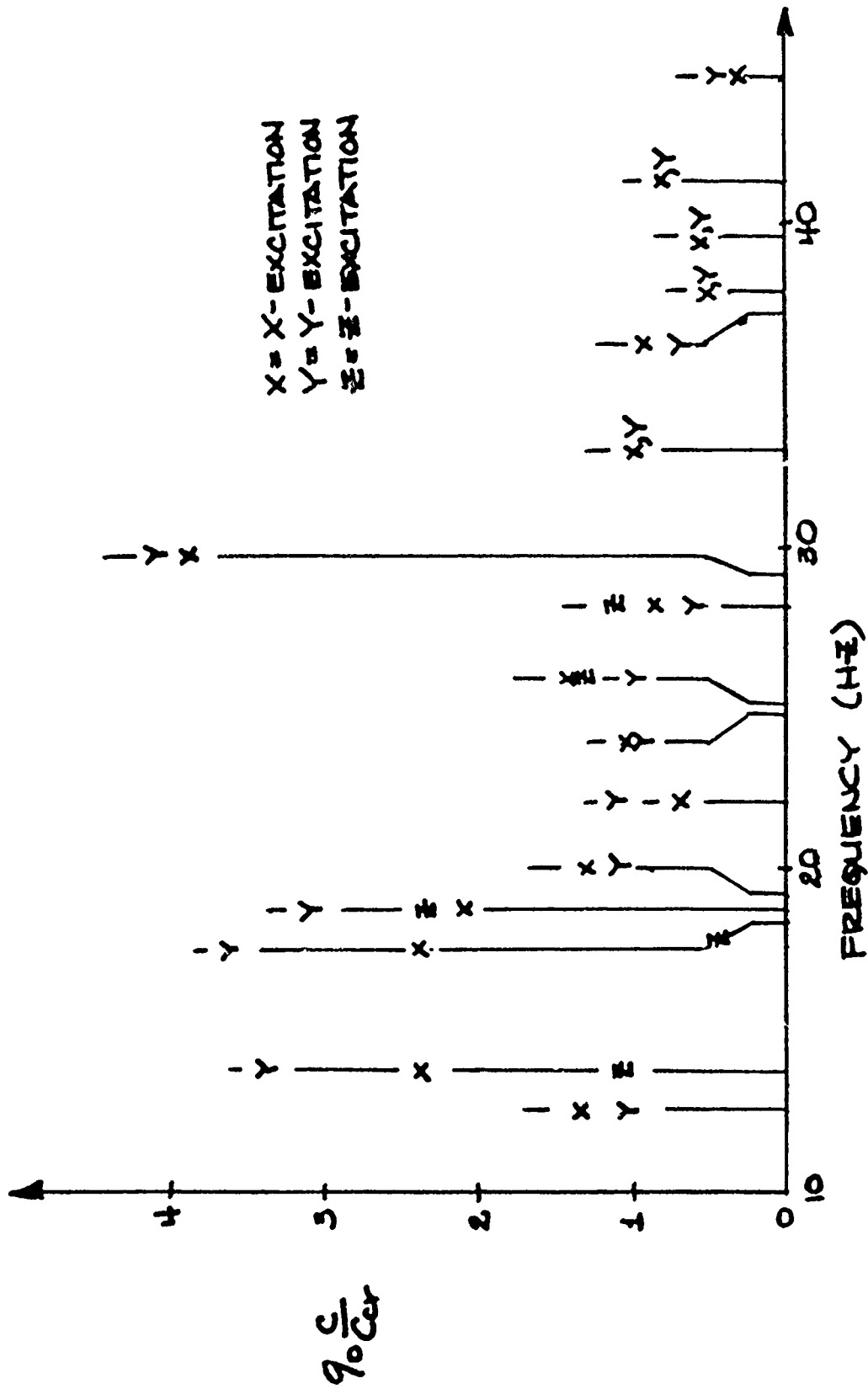
Figure 7. All Damping Data for Centaur G Prime

DE-13
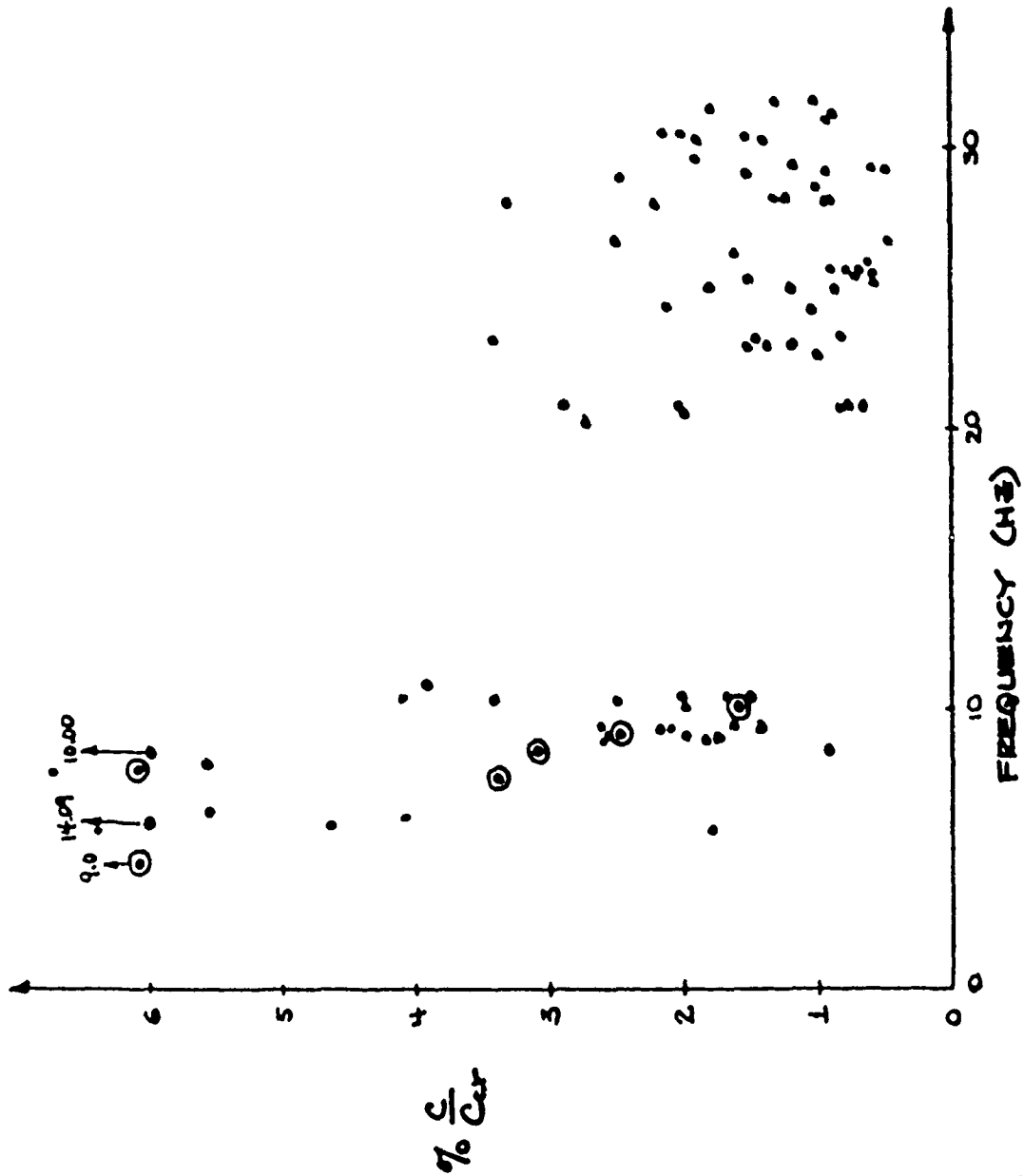
Figure 8. Damping Data for Centaur G Prime, Simultaneous Frequency Domain
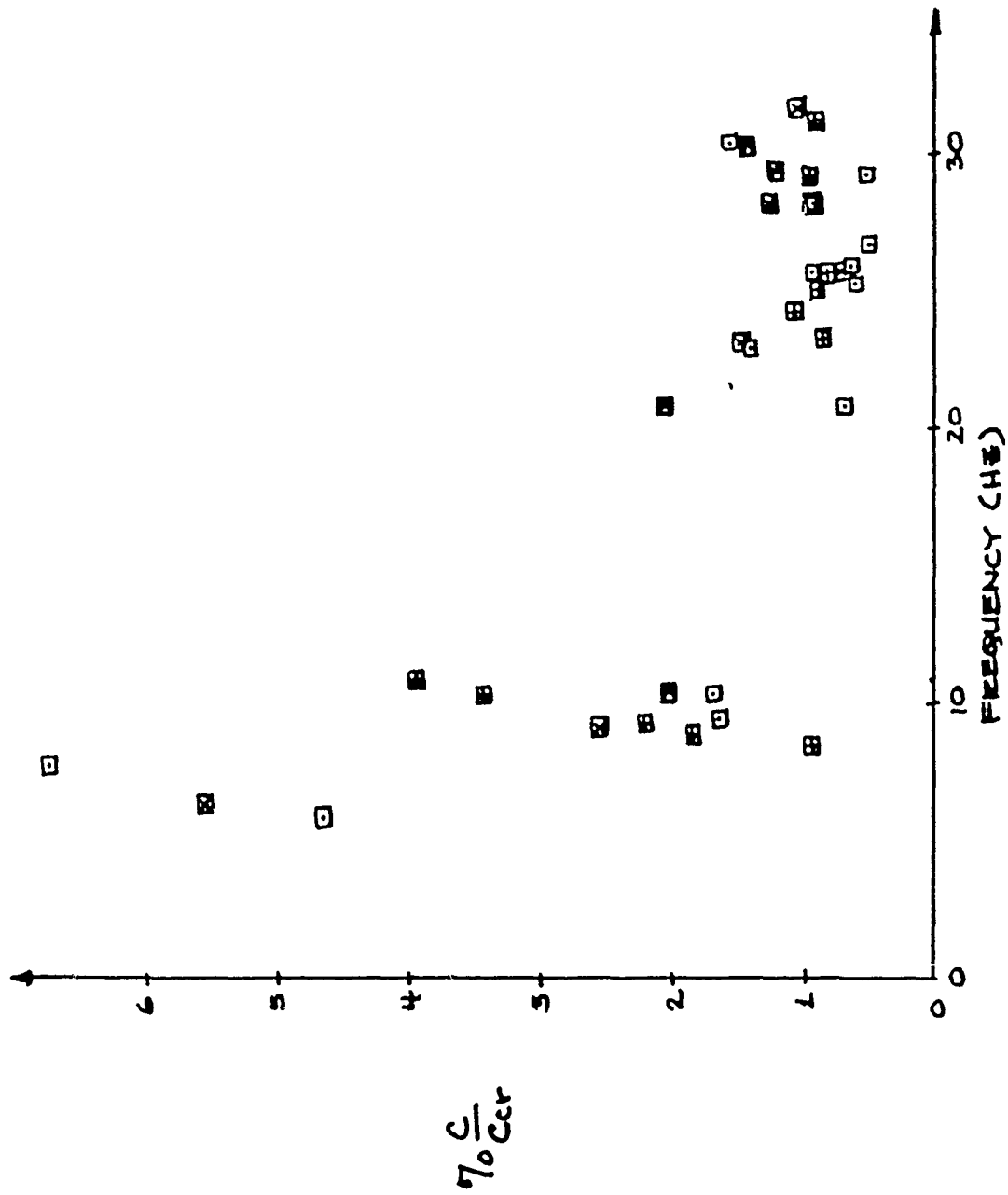
Figure 9. Damping Data for Centaur G Prime, Analysis of Frequency Response Function Generated by High Level Sine Sweep Data

DE-15
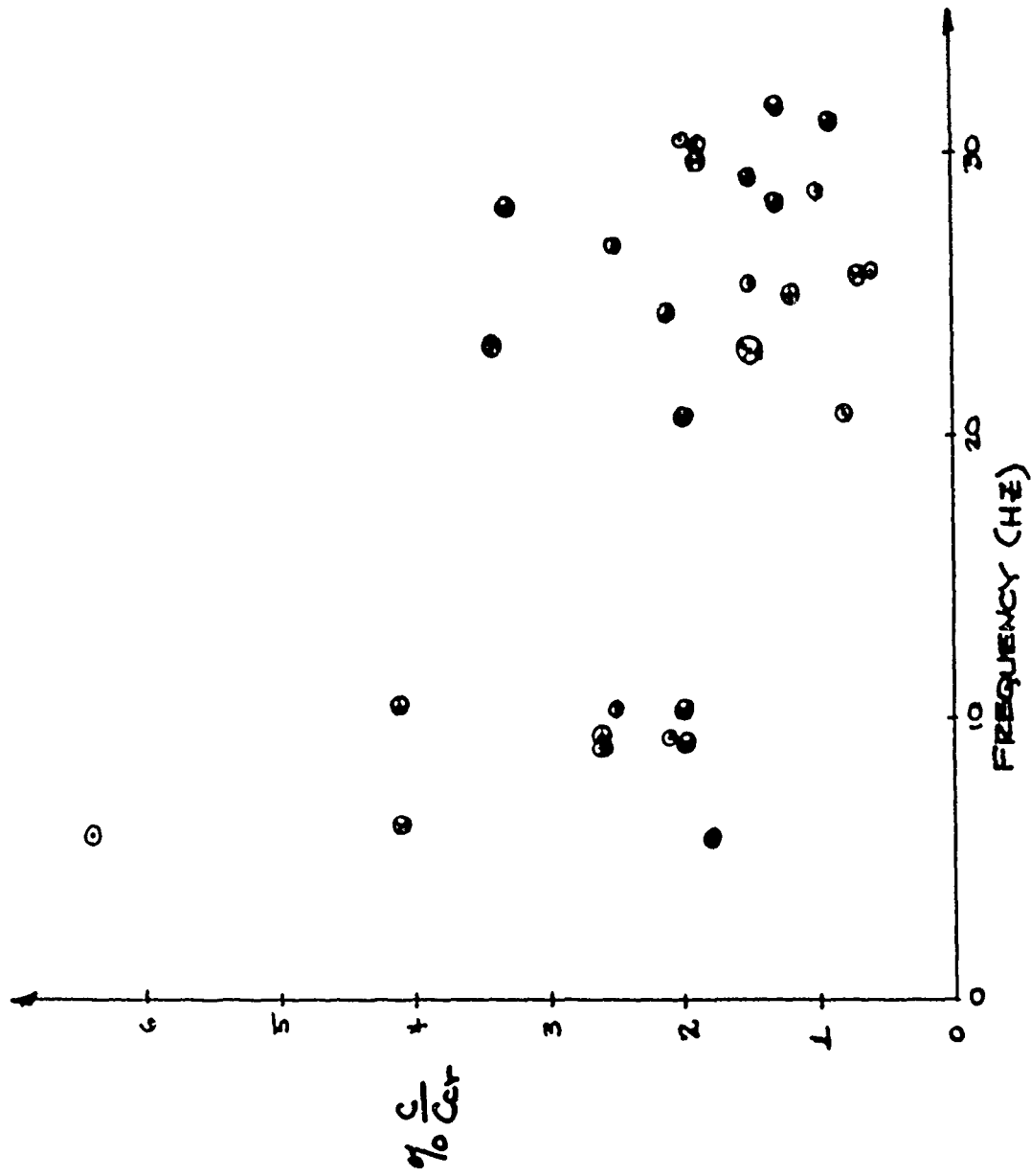
ON-ORBIT FLEXIBLE BODY PARAMETER IDENTIFICATION
FOR SPACE STATION

F.Y. Hadaegh, D.S. Bayard, D.R. Meldrum and E. Mettler

Jet Propulsion Laboratory
California Institute of Technology
4800 Oak Grove Drive
Pasadena, CA 91109

ABSTRACT

This paper is concerned with the Maximum Likelihood identification of modal frequencies of the Space Station "Power Tower" reference model. The identification is carried out on a 15 degree-of-freedom model (a) by utilizing the Station's impulsive disturbances as the main source of excitation and (b) by implementing a set of multi-directional thruster pulses in the form of forces and torques. Different identification problems which arose from inadequate excitation and sensing are discussed. The sensitivity of the identification results to the initial values of the unknown parameters is evaluated, and it is shown that low frequency modes may be identified with excellent accuracy despite considerable error in their initial estimates.

1. INTRODUCTION

Conventional approaches to system identification and on-line control which have previously been applied to numerous classical problems are not adequate for the Space Station project. The complex composite structure of such a flexible system can not be ground-tested because of various physical limitations. However, the structural dynamic characteristics of the Space Station must be known accurately in order to accomplish active vibrational control and to perform other tasks. Hence, the Space Station project requires advancements in modeling flexible structures, on-line system identification (ID) techniques and development of closed-loop control schemes. On-orbit system identification capability is essential for various phases of the Space Station development and operation. Such capability can also be used to automate performance verification/monitoring and to characterize/identify various disturbances. These considerations motivate the current research activities aimed at developing a system identification functional capability for the Space Station. In this paper, the problem of identifying the modal frequencies for NASA's Space Station Power Tower configuration is investigated. The reference configuration primarily consists of a vertical keel and a transverse support truss which supports four solar panels, pressurized modules and supporting structures, and docking facilities for the Shuttle. The station is designed for modular growth and is controllable from a combination of control moment gyros, magnetic torques, and reaction control system capabilities. The identification strategy here is to utilize the Station's internal impulsive disturbance forces and torques such as the astronaut push-off and landing and the console motion noise as the primary source of excitation. The Space Station identification process is treated in Section 2. Different sources of identification problems arising from inadequate excitation are discussed. A methodology is proposed for the system ID input design using thruster pulses to identify the modal frequencies of a 15-degree-of-freedom model of the Space Station. Section 3 presents the results of several case studies for different model orders and different experiment configurations. The sensitivity of parameter estimates to the variations of initial values is studied in Section 4 by evaluating the likelihood functionals and surfaces for all frequencies. Section 5 presents conclusions and the future research for the parameter identification of flexible structures.

2. IDENTIFICATION PROCESS

The Space Station parameter identification is the process of extracting numerical values for the structural and other subsidiary parameters from a set of data. The principal elements involved (See Fig. 1) are: (1) modeling (2) the identification algorithm (3) input system and (4) measurement system. All of these elements together determine the success of the identification process during the main phases of preparation, estimation and validation. A brief discussion of each element follows.

2.1 The Maximum Likelihood Algorithm

In this study, Maximum Likelihood Estimation (MLE) technique is used for the determination of modal frequencies. One reason for using the MLE is that it has good asymptotic properties. As the number of observation increases, then MLE tends to be consistent, normal and efficient. Moreover, MLE can be applied to a large variety of model structures and experimental condition. Consequently, it has been used extensively in practice for process identification[1,2], determination of aircraft stability and control derivatives[3-6] and identification of power system dynamic equivalents[7].

EXTERNAL DISTURBANCES

INPUTS

SPACE STATION

ACTUAL RESPONSE

INPUT DESIGN

SPACE STATION MODEL

MEASUREMENT SYSTEM

ID ALGORITHM

MODAL PARAMETERS
ID ERRORS
MODELING ERROR
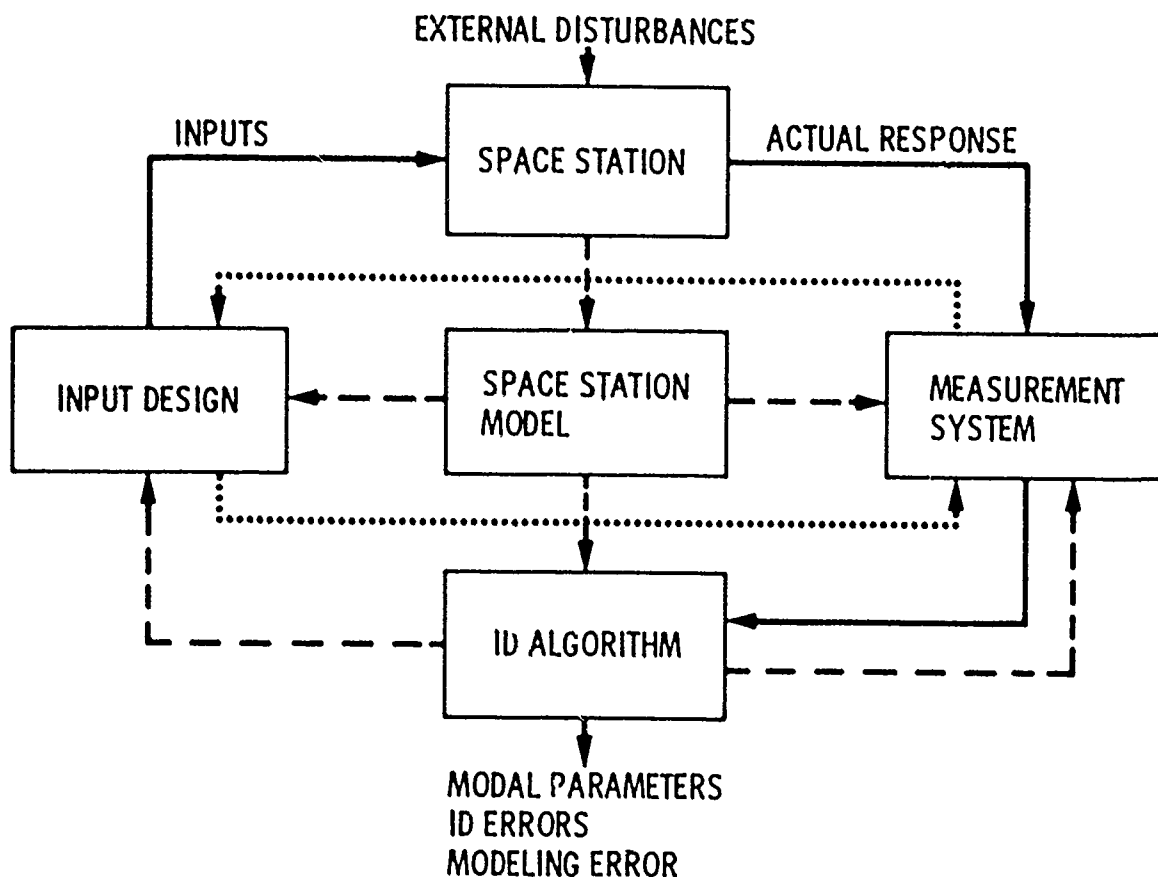
Figure 1. The Space Station Identification Process

Let us assume that a system is described by a continuous time system of equation with discrete observations given by:

$$\dot{x}(t) = A(\Theta)x(t) + B(\Theta)u(t) + F(\Theta)\omega(t) \tag{2.1a}$$

$$z(t_i) = C(\Theta)x(t_i) + D(\Theta)u(t_i) + G(\Theta)v(t_i) \tag{2.1b}$$

where $x(t)$ is $n \times 1$ state vector, $u(t)$ is $p \times 1$ input vector, $\omega(t)$ is $q \times 1$ process noise vector and $z(t_i)$ is $r \times 1$ measurement vector which are taken at discrete instants of time t_i, $i = 1, \ldots, N$. The matrices A, B, C, D, F, and G are assumed to be parameterized by an unknown parameter vector Θ. The process noise $\omega(t)$ is assumed to be white Gaussian with zero mean and identity PSD matrix. The measurement noise sequence of vectors $\{v(t_i)\}$ is a sequence of independent Gaussian vectors with zero-mean and identity variance. The idea behind the MLE is to infer the value of Θ which makes the observed values $Z(t_i)$ the most probable one to have occurred. This value of Θ is obtained by minimizing the likelihood function,

$$L(\Theta) = \sum_{i=1}^{N} [\hat{z}_\Theta(t_i) - z(t_i)]^T \Omega_\Theta^{-1} [\hat{z}_\Theta(t_i) - z(t_i)] + N \log |\Omega_\Theta| \tag{2.2}$$

where $\hat{x}_\Theta(t_i)$ is the output of a Kalman Filter state estimation for a given Θ,

$$\hat{x}_\Theta(t_i) = \Phi \hat{x}(t_{i-1}) + \frac{1}{2}\psi B\left[u(t_i) + u(t_{i-1})\right] \qquad (2.3a)$$

$$\hat{x}_\Theta(t_i) = \hat{x}_\Theta(t_i) + K\left[z(t_i) - \hat{x}_\Theta(t_i)\right] \qquad (2.3b)$$

$$\hat{z}(t_i) = C\hat{x}_\Theta(t_i) + Du \qquad (2.3c)$$

and where

$$\Phi = e^{A\Delta t}; \qquad \psi = \int_O^{\Delta t} e^{As}ds; \qquad \Delta t \equiv t_i - t_{i-1} \qquad (2.4)$$

$$K = PC^T(\Omega_\Theta)^{-1} \qquad (2.5)$$

$$\Omega_\Theta = GG^T + CPC^T \qquad (2.6)$$

$$P = \Phi\left[P - PC^T(GG^T + CPC^T)^{-1}CP + \Gamma\right]\Phi^T \qquad (2.7)$$

$$\Gamma \cong \Delta t FF^T \qquad (2.8)$$

The likelihood functional is highly nonlinear in terms of the parameters and has several local minima. The direct minimization of (2.2) by the Newton-Raphson method often leads to numerical difficulties usually related to non-positive definitness of the estimates of F and G. In addition, a direct application of Newton-Raphson requires the generation of derivatives of Ω_Θ and K with respect to Θ, which gives rise to fairly complicated expressions in light of (2.5), (2.6) and the dependence of the discrete Riccati equation (2.7).

An alternative approach, denoted as that "innovations formulation" arises if one estimates K and Ω_Θ directly in place of F and G, respectively. In this case, minimization of (2.2) with respect to Ω_Θ gives the following expression,

$$\Omega_\Theta = \frac{1}{N}\sum_{i=1}^N \left[\hat{x}_\Theta(t_i) - z(t_i)\right]\left[\hat{x}_\Theta(t_i) - z(t_i)\right]^T \qquad (2.9)$$

A relaxation method for minimizing (2.2) arises naturally by successively minimizing (2.2) with respect to A, B, C, D and K using Newton-Raphson assuming Ω_Θ is fixed (this simplifies the expressions for the required derivatives) and then evaluating (2.9). These two steps are repeated until convergence is obtained. The innovations formulation have been found to work poorly in practice due to the fact that the parameter estimates have not been constrained to satisfy the Riccati equation (2.7). Imposing such constraints, however, irrevocably complicates the minimization, and destroys the usefulness of the method.

The approach used herein for minimization of (2.8) estimates Ω_Θ instead of G as in the innovations formulation (hence taking advantage of closed-form estimate (2.9)) but avoids the pitfalls of the latter method by estimating F instead of K directly. This approach was first advocated by Maine and Iliff [7]. Since K is not estimated directly, the sensitivity matrices of K with respect to Θ must be generated. This requires the solution to a set of Lyapunov equations for each term in the gradient at each iteration. The derivation of likelihood functional becomes much more difficult when the observations are correlated. This is the case for example if the random inputs are used.

DF-4

2.2 Modeling

Accurate modeling of the Space Station is the most important element of the identification process. Consistent with the goal of the identification, the Space Station is assumed to have a linear representation with constant coefficients. Thus, the Space Station is modeled using finite element analysis. Although the system contains infinite number of modes and has, in general, a distributed parameter representation, it is however represented as a lump system. Hence, the infinite dimensional system is approximated by a constant coefficient differential equation of finite dimension which is more tractable and has fewer modes.

Let the plant be represented by the equation of motion:

$$M\ddot{Z} + D\dot{Z} + KZ = F \tag{2.9}$$

where M, D, and K are the mass matrix, damping factor matrix, and stiffness matrix respectively, F is a vector of payload and other forcing functions and Z is the system's displacement vector. The keel is assumed to be relatively stiff so the main flexibiliy will be due to the solar panels and transverse truss. Let Φ be the normalized eigenvector matrix also known as the modal matrix such that

$$\Phi^T M \Phi = I \tag{2.10a}$$

$$\Phi^T K \Phi = \Lambda \tag{2.10b}$$

where I is the identity matrix and Λ is the diagonal eigenvalue matrix. From (2.9) and (2.10), one obtains the system's modal representation. In this paper, a 15-degree-of-freedom model of the Space Station is used as the plant model. This model consists of 3 rigid body modes, 12 flexible modes, and a uniform modal damping of $\varsigma = .5\%$. The continuous time dynamics are given as in (2.1). Here, the state vector is given by,

$$x = \left[\phi_{1r}, \phi_{2r}, \phi_{3r}, \phi_{1f}, \ldots, \phi_{12f}, \dot{\phi}_{1r}, \dot{\phi}_{2r}, \dot{\phi}_{3r}, \dot{\phi}_{1f}, \ldots, \dot{\phi}_{12f}\right]^T$$

where ϕ_{ir} and $\dot{\phi}_{ir}$, $i = 1, 2, 3$ are the rigid body modal amplitudes and modal rates, and ϕ_{if}, $\dot{\phi}_{if}$ $i = 1, \ldots, 12$ are the flexible body modal amplitudes and modal rates. Corresponding to the definition of the state vector x, matrix A has the following form,

$$A = \begin{bmatrix} 0 & I \\ -\Lambda & -\Sigma \end{bmatrix}$$

where,

$$\Lambda = \text{Diag}\left[\omega_{1r}^2, \omega_{2r}^2, \omega_{3r}^2, \omega_{1f}^2, \ldots, \omega_{12f}^2\right]$$

$$\Sigma = \text{Diag}\left[2\varsigma\omega_{1r}, 2\varsigma\omega_{2r}, 2\varsigma\omega_{3r}, 2\varsigma\omega_{1f}, \ldots, 2\varsigma\omega_{12f}\right]$$

The modal frequencies are given in Hertz as follows, $\omega_{if} = .1298, .1636, .1728, 1787, .3433, .3576, 1.657, 1.751, 2.117, 2.123, 4.214, 4.219$. The feedforward matrix D arises from the use of accelerometer sensing and is determined by the relative location of the sensors and actuators. As a function of mode shapes, the input matrix B and the output matrix C are determined by the location of actuators and sensors respectively.

2.3 Input System and Experiment Design

The idea behind an identification experiment design is to enhance the accuracy of estimates of the unknown parameters. Input signal design is one of the various experimental conditions under which system identification may be performed. The importance of input selection has been recognized for a long time and has been the subject of several studies[9,10]. Although the theoretical methods developed are applicable to multi-input multi-output systems, for large scale systems with many unknown parameters analytical approaches have proved to be computationally involved and in practice have been substituted by engineering judgement. When unbiased estimators such as MLE are used, a general approach to optimal input design is to optimize the Fisher[10] information, thus reducing the uncertainty regarding the unknown parameters. The theoretical issues involved in this process as applied to this study will appear in a future paper[11]. Here, some practical problems which arise from inadequate excitations and sensing are addressed.

One of the most significant problems related to the choice of input in an identification experiment is the parameter identifiability problem. For the structural systems where all the modes are decoupled, parameter identifiability is related to the degree of excitation in the particular modes of the system and the ability to obtain meaningful estimates of their modal parameters. Identifiability also relates to the existance and uniqueness of the parameters to be identified. Parameters may be unidentifiable for number of different reasons. For example, if the input does not adequately excite some of the modes or if inputs from different directions interact, thereby suppressing some of the modes, or if the model chosen to get the input-output data is inadequate and consequentely the parameters of the model are forced to account for unmodeled effects, then unrealistic parameter estimates may result with large associated error covariances. Other contributing factors such as too short a data length, local minima in the cost functional, over parameterization of the model, attemps at identifying too many parameters and poor initial estimates may also result in non-physical parameter values.

A method to improve the identifiability of parameters is to enhance the sensitivity of their associated modes to the variation of parameters by increasing the amplitude, energy and power of the input signals. Another approach to alleviate identifiability problems for a structural system is to fix some of the parameters which indicate dependencies and appear to be unidentifiable. These parameters are then treated as a known constant. Clearly, (a) it is difficult to decide on the particular parameter to be fixed and (b) fixing a parameter affects the results of the identification, since the nominal values are not known a-priori and any deviation from the correct values contributes to a bias in the estimate of the unknown parameters.

A second problem arises as the result of inadequate sensing. This problem is sometimes referred to as the resolvability problem and arises when the motions of two or more modes cannot be adequately distinguished due to similarities in mode shape characteristics at the sensing locations. The following case studies are aimed at exploring the identifiability and resolvability problems involved and present an approach to identify the parameters under different environmental and experimental conditions.

3. CASE STUDIES

An approach to real-time on orbit identification is to use environmental dynamic disturbances as the main sources of excitation. For example, the crew motion, console motion noise, thrusters and shuttle dockings contain frequencies higher than 10^{-2} Hz and therefore can be used for identifying the flexible modes. In this section, different aspects of modal frequency identification are investigated. First, the Space Station internal disturbances are used as inputs and the experiment is carried under restricted sensing. Then inputs are designed which incorporate thruster pulses in the form of forces and torques to overcome the practical problems discovered in the first phase of the experiment. Inputs are also designed to improve the quality of the identification results. A 15 degree-of-freedom model is also chosen for the Space Station Power Tower reference configuration. To identify the frequencies, an environmental dynamic disturbance of 25 lb. force such as a man push-off/landing (MPO/L) and console motion noise (C) is applied to the system and the response of the system is sensed through 3 accelerometers and a gyro as shown in Fig. 2(a). The initial estimates of the unknown parameters are set to be 20% off the nominal values. The rigid body modes are assumed to be known and the data is observed over a 40-second time interval. The results for this experiment set up and for different model orders and inputs are shown in Table 1. The identification results indicate that (a) there is no sign of excitation in modes with frequencies higher than 2Hz (b) there is a strong dependency between modes 2 and 6 leading to unrealistic estimates indicated in the Table by a sign "?". The model order is reduced to 12 and finally 10, eliminating modes which are not identifiable either as the result of structural dependencies or lack of excitation (i.e. modes 2, 6 and 10 through 12 indicated in the Table by a sign "X"). The two modes 3 and 4 which are seen to be unresolvable for this sensing configuration (cf. Fig. 3) are identified by fixing one and estimating the other and repeating the process. It is seen that for such a system identification configuration, modes 1 and 3 are estimated accurately where the high frequency modes are not generally identifiable. In order to improve the sensitivity and identifiability of modes 2 and 6, additional excitation represented as a torque at a degree-of-freedom orthogonal to those previously applied are used. Hence, the experiment consists of a 15 degree-of-freedom model with three inputs in the form of a force F, two thruster pulses as torques T_1 and T_2, 9 sensors consisting of 7 accelerometers and two gyro as shown in Fig. 2(b).

The results of this experiment configuration is compared against a reference idealized input model. The reference inputs are three independent Gaussian white noise with a PSD of 800 lb² Hz in each of the three directions, two angular (T_1 and T_2) and one linear direction (F). The noise power level is beyond the practical limitations for any implementable input signals in the space environment. However, it will be used to evaluate the ability of recovering the frequencies in the higher regime and the degree of accuracy which one may obtain in the most ideal situation. This experiment allows the incorporation of different input configurations with a power and magnitude within the practical limitation to be acted on the system and a candidate test signal be decided. The results for a single pulse, doublet, and the staggered pulse configuration are shown in Fig. 4. It is seen that the staggered pulse experiment is superior to the other configurations. This appears to be the consequence of a resultant force effect. In order that certain modes be excited, the input must be in the three directions allowed by the model. A resultant force, when projected in each of the three directions, may insufficiently excite a given mode or be introduced in a phase which cancels the structure effect, e.g., mode 3 in case of a synchronous single thruster pulse and doublet thruster pulse inputs. With this setting, there is no delay between the thrusters firing in each direction. If the pulses are staggered, however, it is seen that mode 3 is identified with

SPACE STATION REFERENCE CONFIGURATION

(a)

(b)

THRUSTERS

ACTUATION		
F	–	FORCE
T_1	–	TORQUE
T_2	–	TORQUE

SENSING

● ACCELEROMETER

✗ GYRO
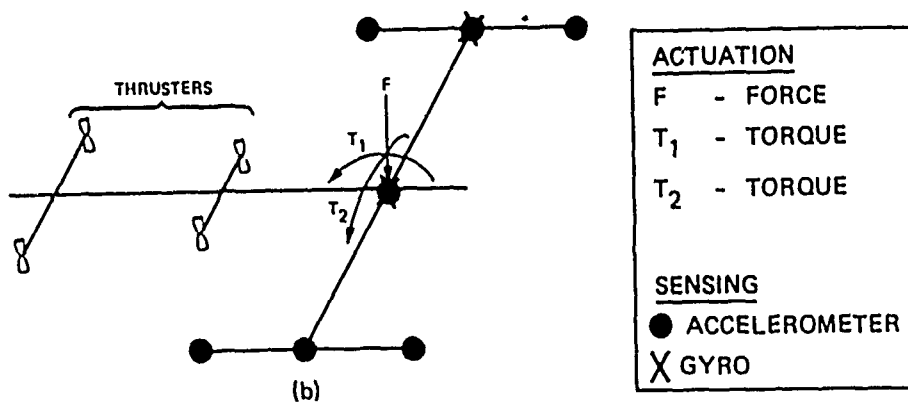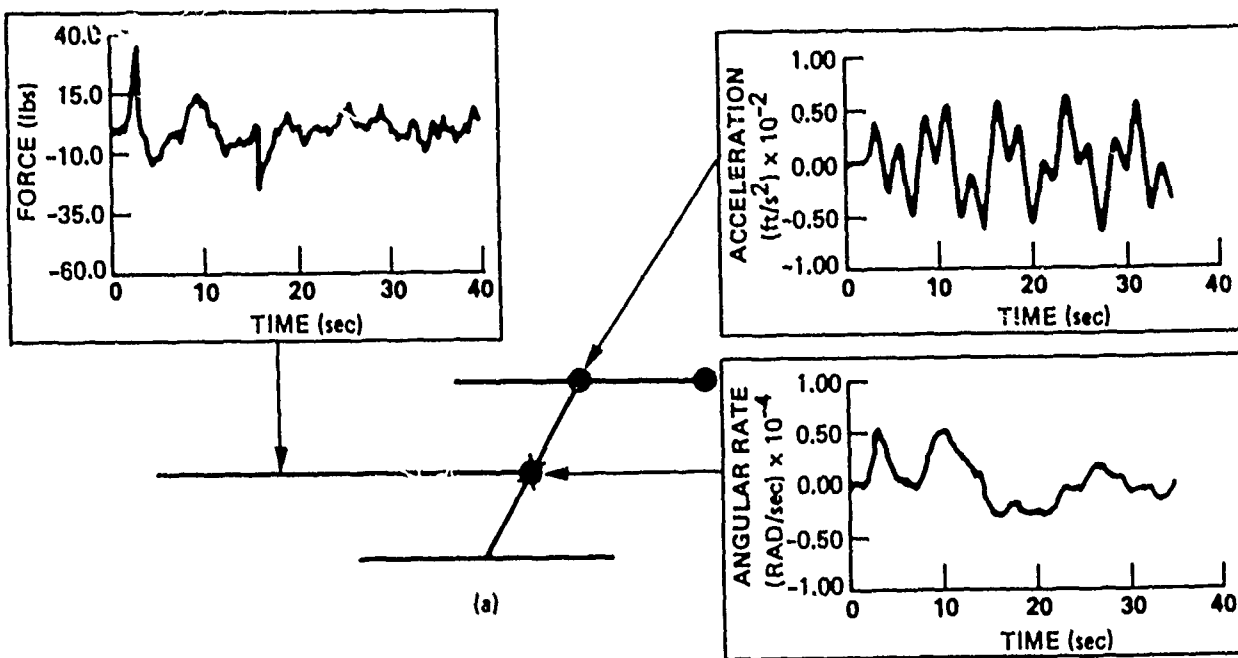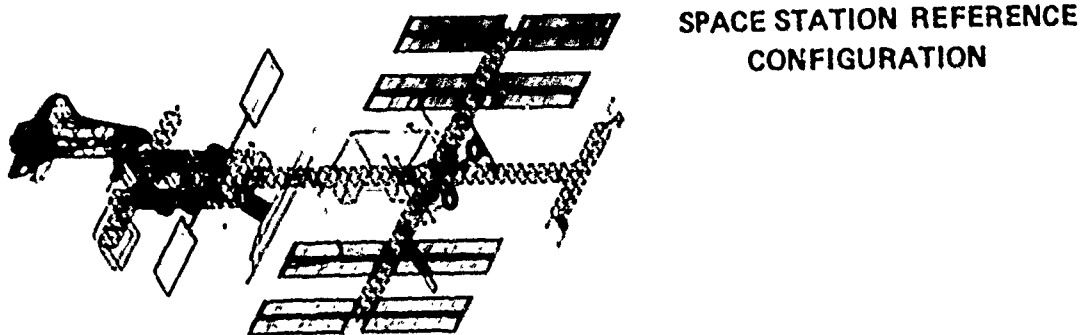
Figure 2. Space Station Identification Experiment Using (a) Impulsive Disturbances from Man Push-Off/Landing and Console Motion Noise (MPO/L+C), and (b) Multidirectional Thruster Pulses with Additional Sensors

MODE 1
$\omega_{1f} = 0.12983$ Hz

MODE 2
$\omega_{2f} = 0.16355$ Hz

MODE 3
$\omega_{3f} = 0.17288$ Hz

MODE 4
$\omega_{4f} = 0.17876$ Hz

MODE 5
$\omega_{5f} = 0.34327$

MODE 6
$\omega_{6f} = 0.35708$ Hz
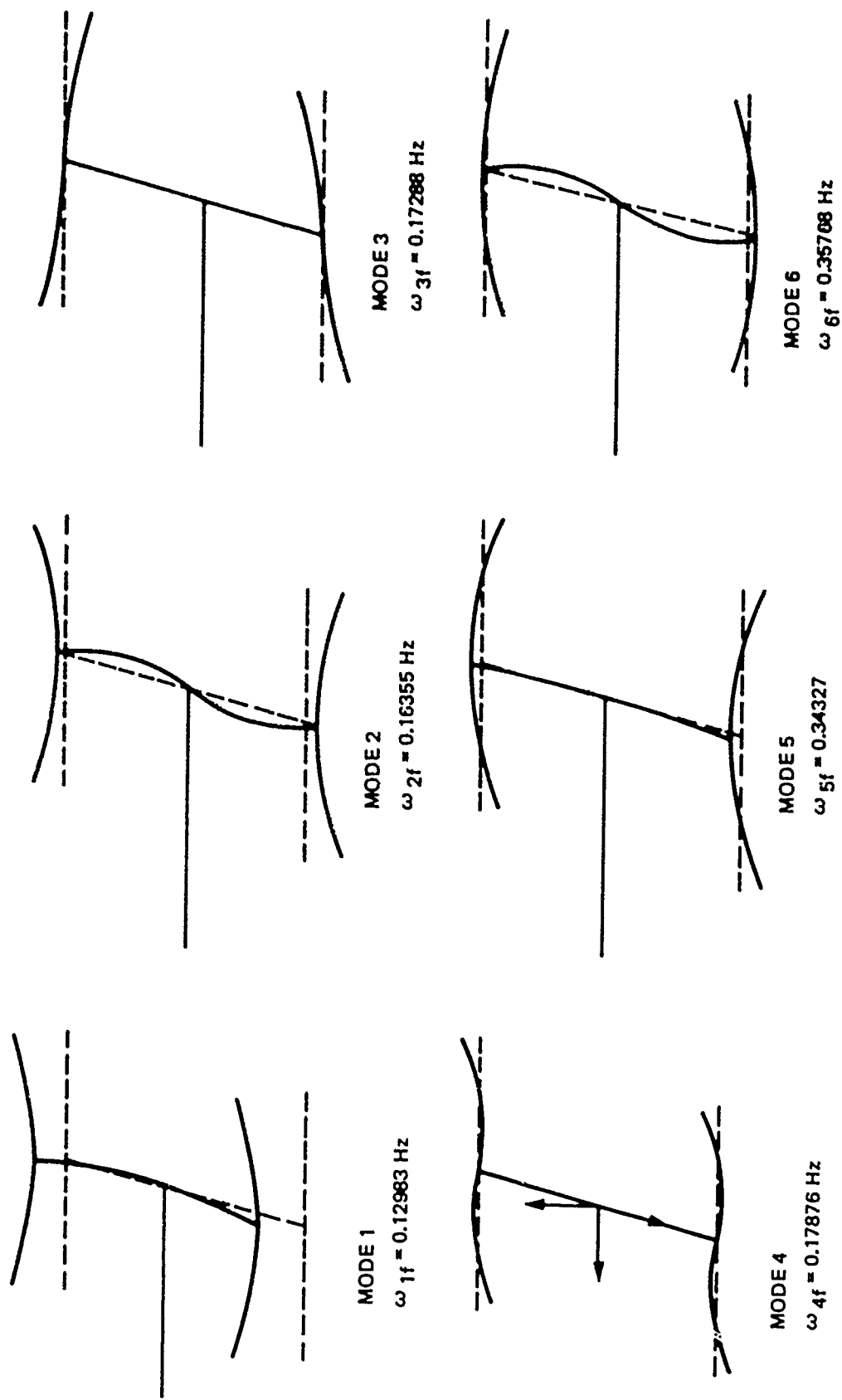
Figure 3. Mode Shapes of Power Tower Model-First Bending Group

TABLE 1. IDENTIFICATION OF MODAL FREQUENCIES (Hz)

			1	2	3	4	5	6	7	8	9	10	11	12
TRUE FREQ.(Hz) ω_{if}			.12983	.16355	.17288	.17876	.34327	.35768	1.6563	1.7509	2.1171	2.123	4.217	4.219
#	INPUT	MODEL												
	ω_{if} 20% ERROR		.1175	.1423	.1543	.1765	.3040	.3203	1.499	1.567	1.890	1.901	3.753	3.755
1	HPO/L+C	15 DOF	.1284	?	.1404	.2332	.2860	?	1.502	1.574	1.890	1.901	3.753	3.755
2	HPO/L	12 DOF	.1283	?	.1471	.2348	.2867	?	1.506	1.574	1.900	X	X	X
3	HPO/L	10 DOF	.1282	X	.1466	.2179	.2871	X	1.502	1.574	1.823	X	X	X
4	HPO/L+C	10 DOF	.1293	X	.1407	.0809	.3077	X	1.500	1.565	1.891	X	X	X
5	HPL/L	10 DOF	.1290	X	.1724	F	.2883	X	1.507	1.574	1.890	X	X	X
6	HPO/L+C	10 DOF	.1298	X	.1724	F	.3125	X	1.500	1.565	1.890	X	X	X

excellent accuracy. It is also noted that single thruster pulses appear to be better than doublet pulses in exciting modes for the identification. When the staggered single pulses are applied, the first 4 modes are identified with no error. Modes 5, 6, and 7 are estimated within 15% of their true values. High frequency modes have not been excited and show no sensitivity to the parameter variations.

4. INITAL ESTIMATES AND LIKELIHOOD FUNCTIONALS

The degree of success in obtaining a good estimate of unknown parameters depends on the closeness of the initial estimates to the true values. If the parameters are identifiable, then under mild regularity conditions, maximum likelihood estimates have been shown to be asymptotically unbiased, consistent and efficient. However, if a mode is not excited then the numerical algorithm for minimizing $L(\Theta)$ finds local minimums far from the nominal values. In such cases, the likelihood functional may show no sensitivity to the variation of the unknown frequencies or the estimates may have no physical significance. The likelihood functionals for all 12 flexible modes and for the staggered thruster pulse input are shown in Fig. 5. For low frequency modes which are the most sensitive to the variations of the associated frequencies, it is observed that the initial estimates may be set up to 50% off the nominal values and still be able to recover the parameters without difficulty. This range will be reduced as the frequency increases. High frequency modes (greater than .3 Hz in the model) are insufficiently excited by the pulse train and are poorly identified. Hence, small deviation from the nominal value will result the associated likelihood functional to converge to a local minimum other than the true one. It is also seen that the cost functionals increase faster to the right of the true parameter values. The behavior of likelihood surfaces for parameters associated with the low and high frequency modes are shown in Fig. 2a and 2b, respectively. The likelihood
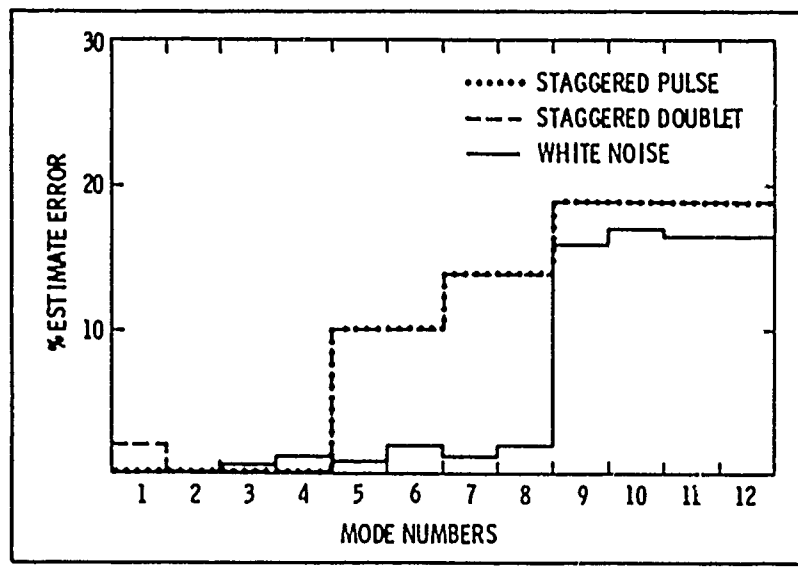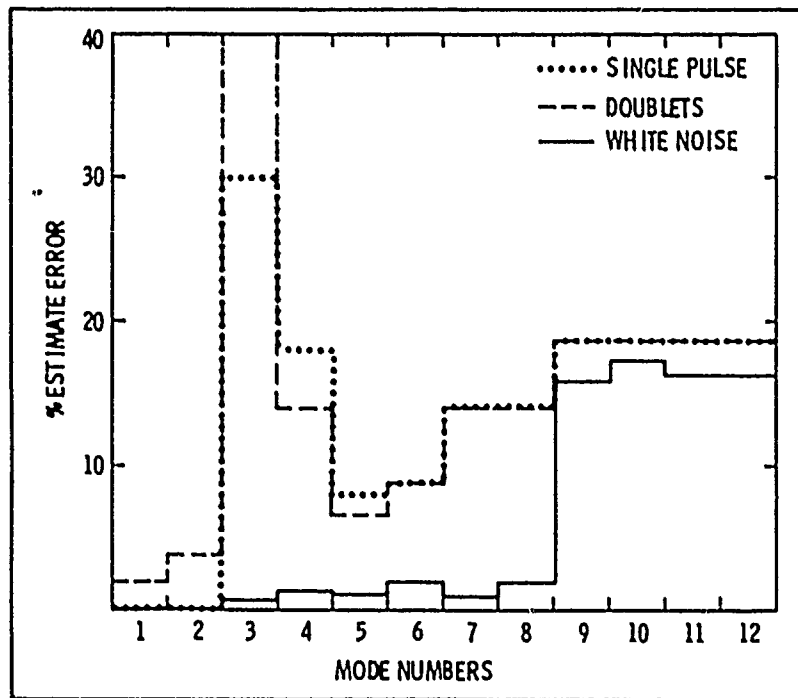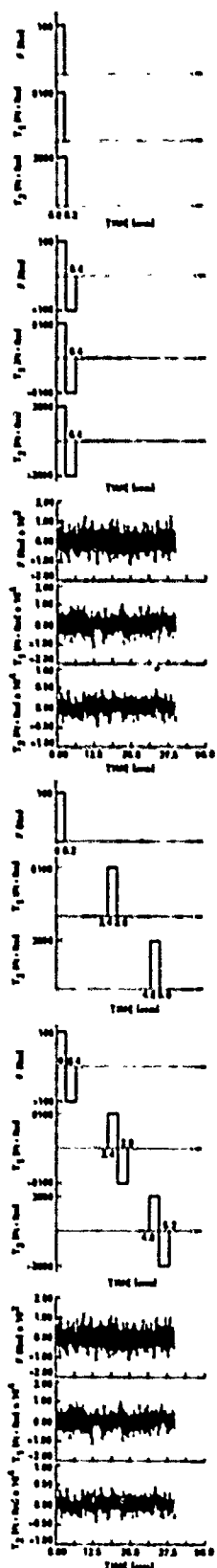
Figure 4. Identification Experiment Using Synchronous and Staggered Inputs
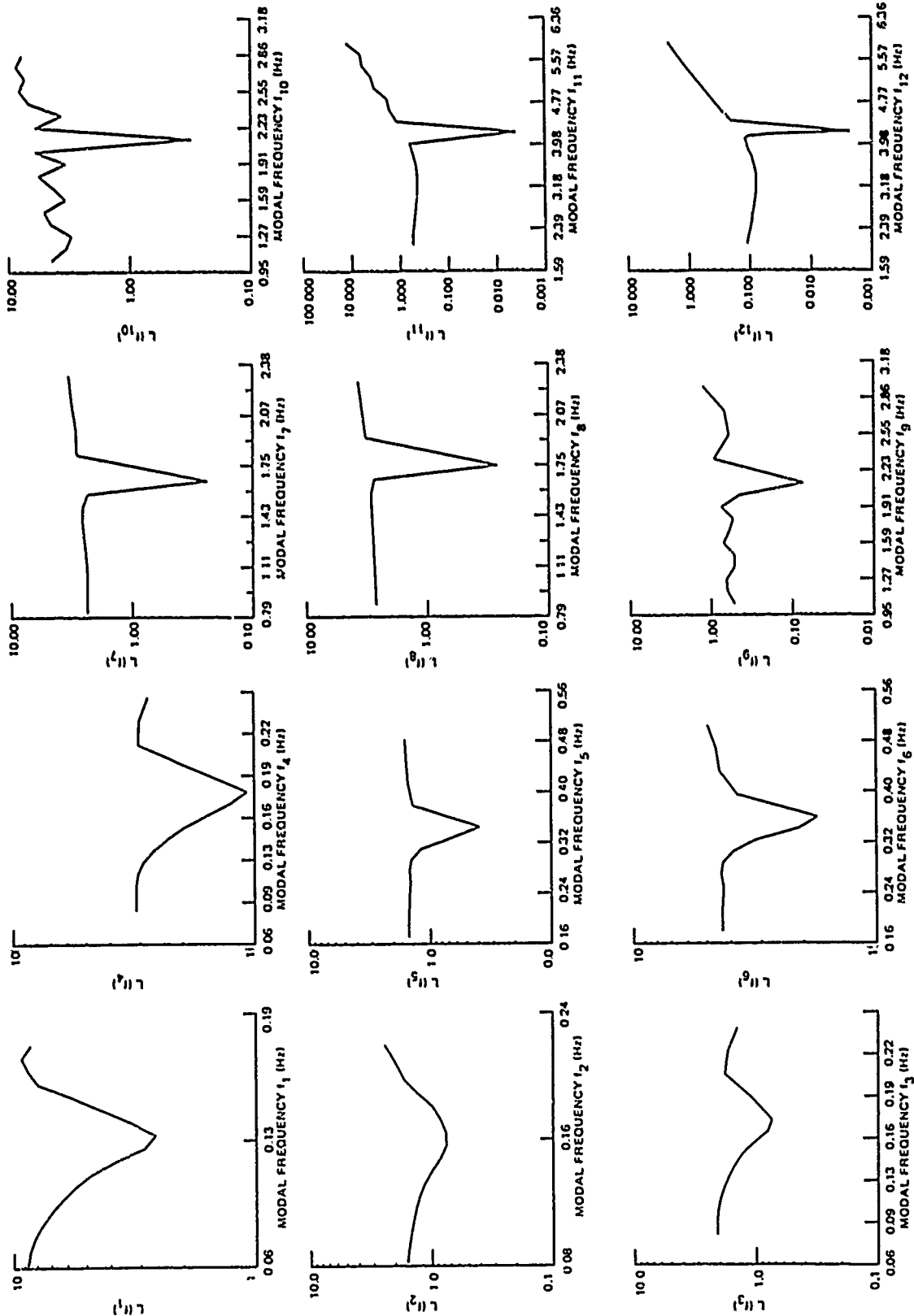
Figure 5. Maximum Likelihood Functionals for all Modal Frequencies
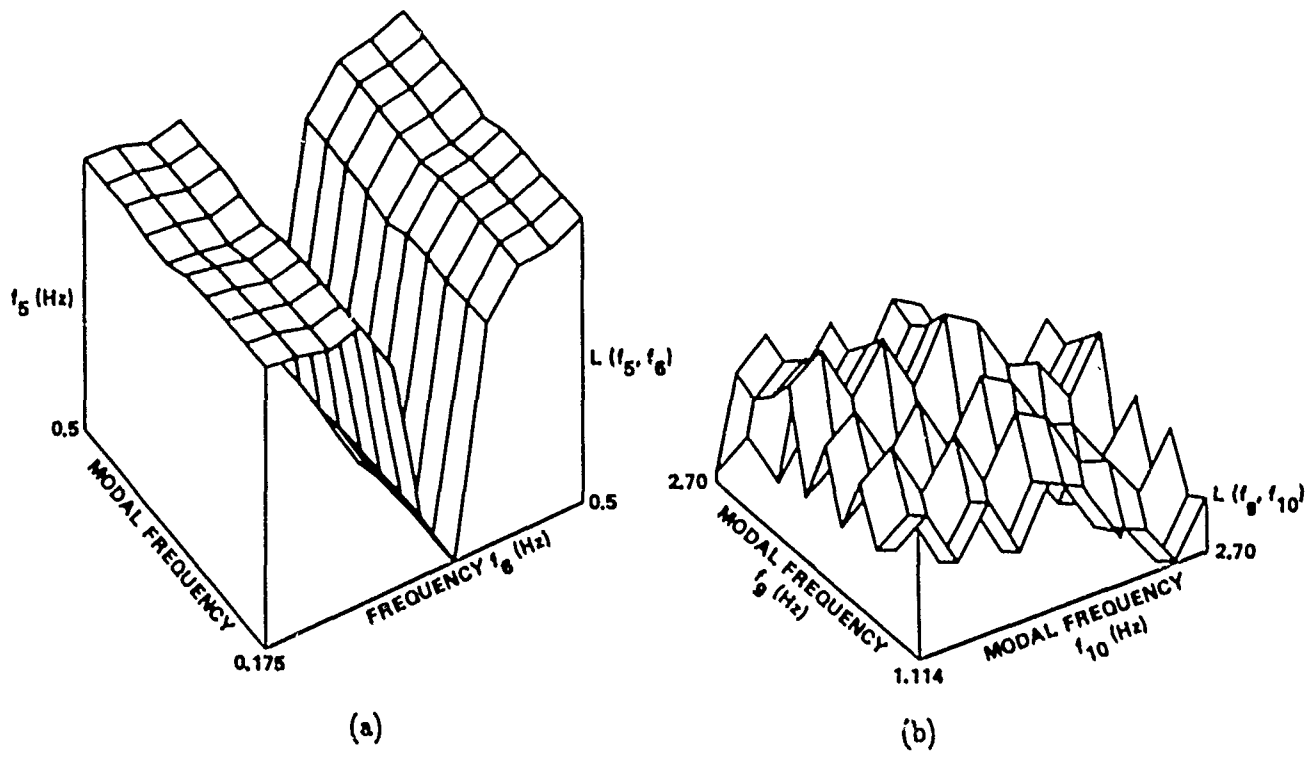
Figure 6. Liklihood Surface for (a) Identifiable Modes and (b) Unidentifiable Modes
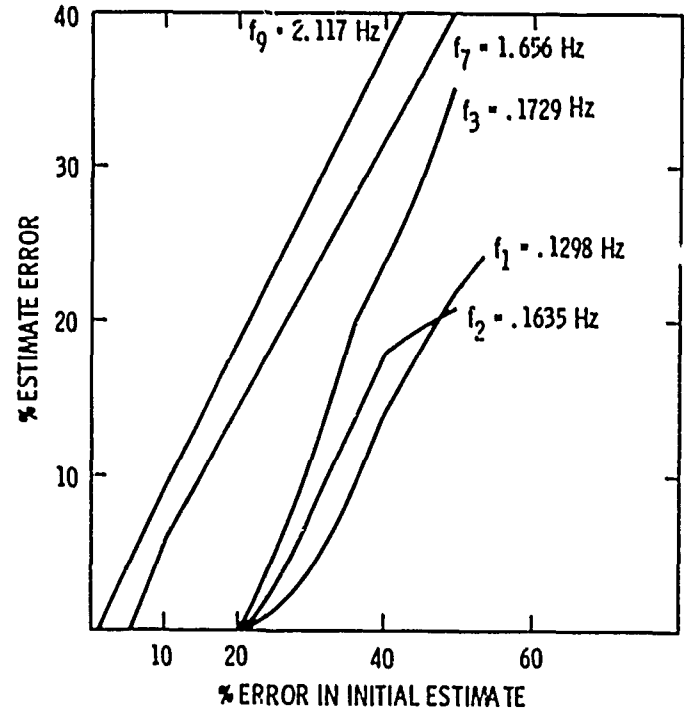
Figure 7. The Sensitivity of the Parameter Identification to the Initial Estimates

surface for the modes 9 and 10 is seen to have a nest of local extrema about the true values of the frequencies. For modes 5 and 6, the likelihood surface is smooth and the identification may tolerate the initial estimate deviations of up to 50% from the nominal values. The sensitivity of the identification results to the initial estimate of the parameters is shown in Figure 7.

5. CONCLUSIONS

On-orbit identification of modal frequencies of a 15 degree-of-freedom Power Tower model of the Space Station is considered. The implementation of environmental dynamic disturbances as the only source of excitation for the maximum likelihood identification is shown to present identifiability and resolvability problems. Therefore, unrealistic parameter estimates may result with large error covariences. It is shown that low frequency modes can successfully be identified by the proper application of multi-directional inputs in the form of force and torques in orthogonal spaces. High frequency modes, however, are insufficiently excited to permit accurate estimation due to thruster power and bandwidth limitations. Among all the inputs considered, it is concluded that staggered pulse sequences are superior for obtaining a more accurate estimate of the unknown parameters. When staggered thruster pulses are used, it is seen that the identification process may tolerate an initial parameter estimate error of up to 50% of the nominal values. Further research is needed for the identification of modal dampings. Since there is no correlation between the identifiability of dampings and frequencies, experiments should be designed to carry the dual frequency-damping identification and address the difficulties arising from indistinguishability problems.

ACKNOWLEDGEMENT

REFERENCES

1. Aström, K.J. and Källström, C.G., "Application of System Identification Techniques to the Determination of Ship Dynamics," Automation 12, pp. 9-22, 1973.

2. Källström, C.G. and Aström, K.J., "Experiences of System Identification Applied to Ship Steering Dynamics," Case Study CSI, 5th IFAC Symposium on Identification and System Parameter Estimation, Darmstadt, 1979.

3. Iliff, K.W. and Maine, R.E., "Maximum Likelihood Estimation with Emphasis on Aircraft Flight Data," proceedings of the workshop on Identification and Control of Flexible Space Structures, Vol. III, pp. 197-24 6, April 1985.

4. Hamel, P., "Determination of Stability of Control Parameters From Flight Testing," AGARD-LS-114, pp. 10-1 to 10-42, 1981.

5. Iliff, K.W., "Aircraft Identification Experience," AGARD-LS- 104, pp. 6-1 to 6-35, 1979.

6. Mehra, R.K., "Maximum Likelihood Identification of Aircraft Parameters," JACC, Atlanta, Georgia, 1970.

7. Price, W.W., Schwepp, F.C., Gulachenski, E.M. and Silva, R.F., "Maximum Likelihood Identification of Power System Dynamic Equivalents," Proc. of Decision and Control Conference, Phoenix, Arizona, pp. 579-586, 1974.

8. Maine, R.E. and Iliff, K.W., "Formulation and Implementation of Practical Algorithm for Parameter Estimation with Process and Measurement Noise," SIAM J. Appl. Math., Vol. 41, pp. 558-578, Dec. 1981.

9. Nahi, N. and Napjus, G. "Design of Optimal Probing Signals for Vector Parameter Estimation," Proc. IEEE Conf. on Decision and Control, Miami, Florida, pp. 162-168, 1971.

10. Mehra, R.K. "Optimal Input Signal for Parameter Estimation in Dynamic Systems-Survey and New Results," IEEE Trans. Automat. Control., Vol. AC-19, pp. 753-768, 1974.

11. Bayard, D.S., Hadaegh, F.Y. and Meldrum, D.R., "Optimal Experiment Design for On-Orbit Identification of Flexible Body Parameters in Large Space Structures," Fourth IFAC Symposium on Control of Distributed Parameter Systems, Pasadena, California, 1986.

DESIGN AND ANALYSIS
OF THE
PACOSS REPRESENTATIVE SYSTEM

Daniel R. Morgenthaler
and
Russell N. Gehling
Martin Marietta Denver Aerospace
Denver, Colorado

ABSTRACT

The PACOSS (Passive and Active Control of Space Structures) program has as a goal the development of analytical and design techniques to incorporate a predictable amount of passive damping into large space structures. The level of passive damping required is determined from system performance studies, wherein an efficient mix of passive and active damping can be found.

This paper describes the development and analysis of the PACOSS Representative System Article (RSA), a generic large space structure consisting of substructures found in large families of future spacecraft. The RSA will serve as an analytic test bed for damping technology developed under the PACOSS program, and a baseline structure for controls development for use on first-generation LSS.

1.0 INTRODUCTION

Many future large space structures, whether military or civilian, exhibit similar dynamic characteristics and performance requirements. The structures themselves typically exhibit dense modal spectra at relatively low frequencies. Performance measures generally include stringent pointing accuracies, relatively short settling dynamics, and fast response requirements which provide a challenge for the most accomplished control system engineer, who frequently finds that even providing a stable system is a challenge.

The PACOSS (Passive and Active Control of Space Structures) program is directed toward developing technology that integrates passive damping techniques with active control design to provide systems which can meet performance objectives, are more tolerant to uncertainties in plant design and disturbances, are less costly to produce, and require less on-orbit maintenance to assure operation. Special consideration is being given to passive damping techniques to reduce the bandwidth over which damping must be provided by active means, to reduce the number of controlled modes by the active system over the complete bandwidth, and to provide increased stability margins. This approach will result in less complicated control systems with fewer sensors and actuators, lower cost, and enhanced reliability.

To provide an analytic test bed for the development of PACOSS technology, a Representative System Article (RSA) has been developed. The RSA is intended to represent system dynamics generic to planned and conceptual space systems. The RSA is not a mission-specific spacecraft but a representation of several missions and requirements in one system. Associated performance measures are taken from the applicable missions.

An important aspect of the RSA design process is that the substructures were designed to permit the incorporation of passive damping treatments. This approach is essential to successful and efficient damping treatment and will be described in some detail.

2.0 . MISSION SURVEY

Definition of the RSA required a survey of planned and conceptual space systems whose initial development will occur during the next decade. Designs for future large space systems are quite general in nature, consisting primarily of qualitative descriptions of performance goals and basic system parameters such as overall dimensions and weight. However, survey of Air Force and NASA mission models revealed a strong requirement for relatively large, lightweight structures possessing the ability for precise pointing and, in some instances, rapid retargeting. Attainment of these characteristics requires structural vibration control through active and/or passive means and, thus, such systems are the target for PACOSS technology. The following paragraphs summarize a survey of military and civilian systems where structural control will play a significant role in accomplishing mission goals.

2.1 Military Systems

The 1983 Military Space Systems Technology Model (MSSTM) lists more than 30 mission concepts requiring advanced space systems. At least 13 of these missions will require structural control and damping augmentation in order to achieve their performance goals. The missions directly applicable to PACOSS technology are categorized in Table 2-1.

The missions identified in Table 2-1 as candidates for PACOSS technology are generally large structures characterized by high modal density at relatively low frequencies. These systems involve components which require low jitter levels and fast settling time in order to function well. Additionally, missions 2, 3, and 10-12 must maneuver or slew rapidly while maintaining coherent electromagnetic paths and stable line of sight (LOS).

2.2 Civilian Systems

The civilian counterpart to the MSSTM is the NASA Space Systems Technology Model. This document lists many mission concepts which are similar in nature to military missions. Again, missions where PACOSS technology can be greatly beneficial are generally large, lightweight systems whose performance is degraded by dynamic structural deformation. Table 2-2 lists planned or conceptual NASA missions which will require structural vibration control.

2.3 Survey Summary

Results of the survey of future space systems and requirements indicated that systems most affected by structural vibration involve electromagnetic reflector systems. The overall size of such systems varies greatly as listed in Table 2-3.

Based on the results of the mission survey, the performance requirements considered in definition of the RSA are primarily those of surveillance, radar, and optical systems. The quantities of primary importance with regard to the RSA are line of sight (LOS) stability (jitter), stability rate, and settling time.

Just as the dimensions of the systems listed in Table 2-3 vary over an order of magnitude, so do the performance requirements. For example, a large space-based surveillance system may be required to slew several degrees over a period of minutes while a space-based laser must retarget in a few seconds. Similarly, jitter requirements are far more stringent for an optical system than for a large radar. The RSA must address a composite of performance requirements, yet demonstrate traceable results to all the space systems of interest.

Table 2-1   1983 MSSTM Concepts for Future Military Space Systems
Benefitting from PACOSS Technology

Ballistic Missile Warning

    1   Staring IR Missile Tracking

Atmospheric Surveillance and Warning

    2   IR Step-Stare Mosaic Surveillance
    3   Mechanically Steered Space-Based Radar
    4   Medium Altitude Surveillance Radar
    5   Synchronous Altitude Active Lens Radar

Surface Target Reconnaissance

    6   Intermediate Phased Array Reconnaissance Radar
    7   Millimeter Wave Radiometer Surveillance

Space Vehicle Detection, Track

    8   Medium Altitude Space Surveillance

Communications

    9   Blue-Green Laser

Force Application

    10   Long-Range Space-Based Laser
    11   Space-Based Laser Interceptor
    12   Space-Based Neutral Particle Beam

Space Operations Support

    13   Modular Space Station

Table 2-2 NASA Mission Concepts with PACOSS Requirement

Earth Observation Satellite

Large Deployable Reflector

Mobile Communications Program

Geostationary Platform

Space Station

Pinhole Occulter Facility

Table 2-3 Size Range of Future LSS

SYSTEM	SIZE	
Space-Based Radar	50 - 100ᵐ	Mesh Reflector
Communications	20 - 70ᵐ	Mesh Reflector
IR Surveillance	15 - 30ᵐ	Solid Mirror
Optical Surveillance	5 - 20ᵐ	Solid Mirror
Space-Based Laser	5 - 20ᵐ	Solid Mirror

3.0   THE MODAL STRAIN ENERGY METHOD AS A DAMPING DESIGN TOOL

The modal strain energy (MSE) method identifies the locations in a structure where viscoelastic materials would be effective in dissipating energy. The motivation for this method lies in the coupled stiffness and damping properties of viscoelastic materials. Additionally, MSE provides a useful tool to estimate modal loss factors throughout the design process. The major implication of this approach is that the locations and types of damping treatments must be addressed via the MSE method in the initial design stages and carried through into final system fabrication.

3.1   The MSE Design Method

The MSE method has its basis in the properties of the viscoelastic materials which generally will be used in the damping treatment of large space structures. Each material modulus is characterized by two parameters: material elastic modulus which describes resistance to deformation, and loss factor which describes energy dissipation.

$$G_{VEM} = G_{ELASTIC} (1 + i \, N_{LOSS})$$

The strain energy stored in a material during deformation is defined as:

$$SE = \int_V \frac{1}{2} \sigma \cdot \varepsilon \, dV = \frac{E}{2} \int_V \varepsilon^2 \, dV$$

The MSE method assumes real eigenvectors from a normal modes analysis approximate the system damped complex eigenvectors. Using this assumption, the above integral written in i^{th} modal coordinates becomes:

$$SE = \sum_{j=1}^{NE} \phi_i^T K_j \phi_i = \omega_i^2 \qquad \text{for unity mass normalized system}$$

where ϕ_i = i^{th} real eigenvector

K_j = stiffness matrix for j^{th} element

NE = number of elements

ω_i^2 = i^{th} natural frequency squared.

Because material or element loss factors relate energy losses to energy stored in the element, the ith modal loss factor may be defined as:

$$\eta_i = \sum_{j=1}^{NE} \eta_j \, \phi_i^T K_j \, \phi_i / \omega_i^2$$

where η_j = j^{th} element loss factor.

By examining this equation, it can be concluded that the goal for the structural designer in the initial stages of design is to arrive at a configuration in which a large portion of the structure's modal strain energy is in elements which allow damping treatment, since each modal loss factor depends on percent strain energy in high loss materials (VEM). Special consideration must be given to locate the damped members out of direct load paths, however, since viscoelastics are relatively soft, will not sustain high stresses, and creep under sustained loading. Because viscoelastics have relatively low moduli and high density, these materials must also be utilized efficiently or a significant increase in system weight and corresponding decrease in achievable modal damping will result. The designer is therefore faced with a trade-off between damping, integrity, and weight of the final structure.

3.2   Implications of MSE on Structural Design Process

To achieve an efficient design for a damped structural system, MSE and damping mechanisms must be addressed in the early stages of configuration selection and member sizing if the aforementioned constraints are to be met. If not considered in the preliminary design the damping designer will be faced with drastic structural modifications since there is no guarantee that any members of the structure will contain high modal strain energy in troublesome modes without high loading unless the structure has been specifically designed with these requirements in mind.

Achieving a satisfactory design even when approaching a specific problem in the initial stages is often difficult, and typically will take several design iterations to arrive at member sizes which will allow significant structural damping. The design of future LSS must therefore include the structural dynamicist in the preliminary design if an efficient overall system design is to be realized.

Selection and design of the RSA configuration utilized the MSE method throughout and energy distribution was a primary design consideration in all aspects of the initial design phases.

4.0 RSA SELECTION

Drawing from the mission survey discussed in Section 2, a structural configuration for the RSA was selected to represent the widest range of characteristics of future space systems where structural vibration control is critical to accomplishing mission goals. Compromises were required in order to develop a viable configuration which would remain representative of the wide range of systems requiring PACOSS technology. Overall dimensions were selected to be of intermediate size to allow adequate demonstration of damping treatments applicable to both very large antennas and smaller truss structures applicable to a Space Based Laser (SBL) or Space Station.

The selected configuration, shown in Figure 4-1, consists of a variety of components, each of which is traceable to one or more future Air Force space systems. Also, each component poses specific challenges for passive or active control and lends itself to unique applications of passive damping. Table 4-1 summarizes the RSA components, and Table 4-2 presents candidate damping technologies applicable to each. This configuration serves as a bridge between the experimental analysis and verification of damping treatments to be performed using a dynamic test article (DTA), and evaluation of the developed technology on future space systems. Section 5 qualitatively describes and justifies the selection of each component of the RSA and gives quantitative design and analysis results.

Table 4-1 Overview of RSA Components

Component	Dimension (m)	Mass (kg)	Function	Applicable Systems
1) Box Truss	20x20x2.5	2395	Primary reflecting surface support and/or spacecraft subsystem carrier	Space Based Radar Large Earth Observing System Mobile Communications Satellite Space Station
2) Ring Truss	Diameter: 22.4	1113	Central support holds system components together	Generic Truss Structure
3) Tripod	Diameter at Base: 20 Height: 30	840	Secondary reflecting surface support	Space Based Laser Large Deployable Reflector
4) Equipment Platform	Length: 12	2634	Support/isolate sensitive equipment or experiments away from main structure	Space Station Strategic Defense Initiative (SDI)
5) Antenna	Diameter: 5	345	Earth communications: command and control	Space Based Radar Space Station Satellites
6, Solar 7) Arrays	Length: 20	786	Power generation, sized for ≈20 kW	Space Based Radar Space Station Satellites

DG-8
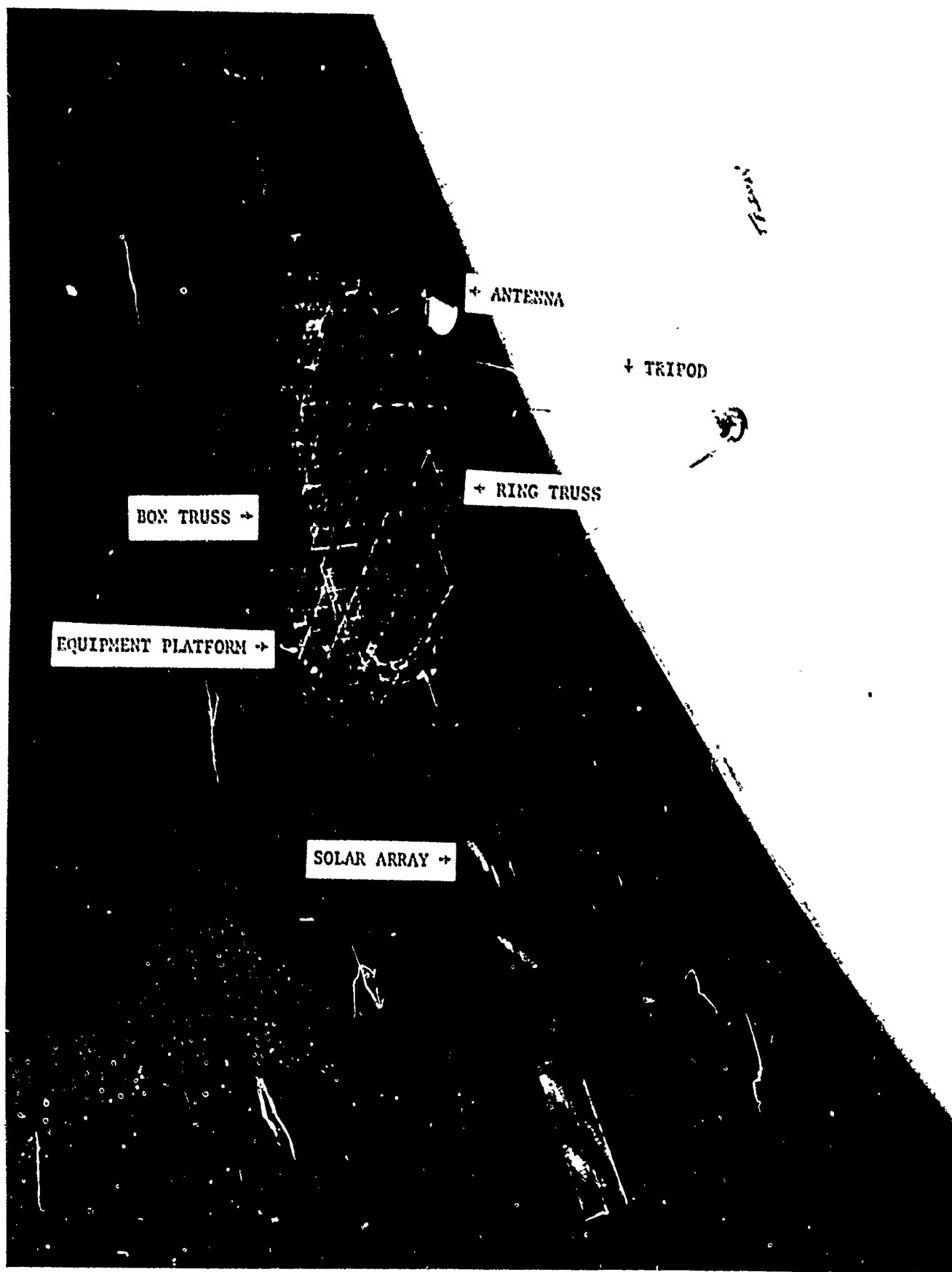
Figure 4-1   RSA Configuration

DG-9

Table 4-2   RSA Component Damping Concept Summary

DAMPING CONCEPT	APPLICABLE COMPONENTS
Constrained Layer Treatment	Antenna Support Tubes Tripod Legs
Joint Damping	Box Truss Corner Joints Box Truss/Ring Truss Interface
Elongational Damping Element	Tension Members
Extensional Shear Damper	Equipment Platform Support Truss
Tuned Mass Damper	Solar Arrays

4.1   Passive/Active Control Issues

The RSA control system was conceived to be simple yet representative of the systems to be used on the first generation of large space structures. Attitude and vibration control were addressed through simple rate and position feedback. Actuator and sensor dynamics were considered in the overall modeling and simulation. Details on the approach to, and design of the RSA control system are given in Section 5.3.

Analysis of the RSA used an assumed modal viscous damping ratio for all system modes. More detailed consideration of passive and active control modeling and evaluation will be addressed in the PACOSS program, but is beyond the scope of this report.

4.2   RSA Performance Goals

The majority of systems listed in Section 2 are required to execute slewing maneuvers. Thus, settling time is critical to performance of these systems which include infrared and optical surveillance, space-based lasers, and smaller radars. Typically, a maximum angular acceleration is available (or allowable) and fast settling time following conclusion of the slew maneuver is the goal. For a system of the RSA's size, 0.1 rad/sec^2 is a representative angular acceleration limit and a LOS settling time to within 0.5 μrad in 1.0 seconds are the corresponding requirements. The jitter response goal was selected as 0.1 μrad response to noise input of a level typical of on-board disturbances. These quantities are characteristic of a system envisioned for operation by 1995.

5.0 RSA DESIGN AND ANALYSIS

Design and analysis of the RSA required a relatively detailed finite element model to allow subsequent Modal Strain Energy (MSE) distribution calculations. Structural integrity and viability, while not primary design drivers, were kept in mind throughout the design process. Component mode synthesis was used to compute the frequencies and mode shapes of the RSA shown in Figure 5-1. In the interest of simplifying control design and overall system analysis, the RSA design was kept symmetric about the Z-axis denoted in Figure 5-1. This impacted component design in that each component was required to be symmetric about the Z-axis when oriented on the RSA, or occur in a pair as in the case of the solar arrays. The finite element modeling and analysis was performed using the MSC/NASTRAN program.
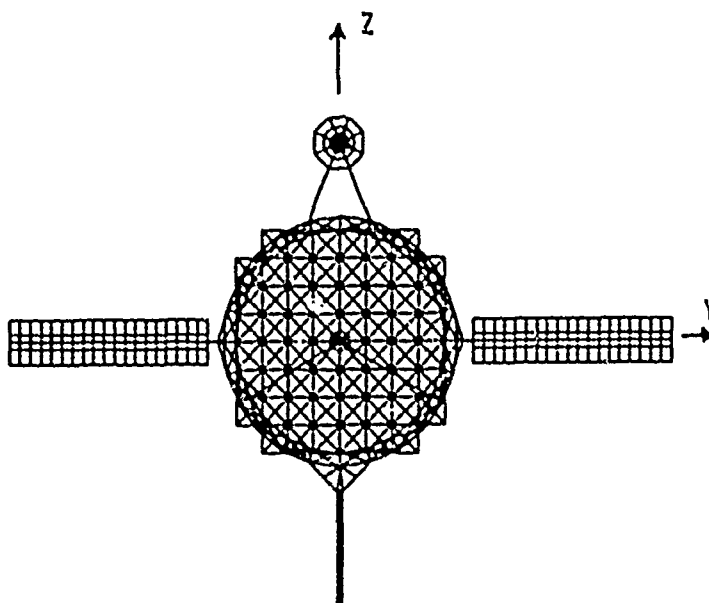
Figure 5-1 RSA Coupled Finite Element Model

As discussed in Section 4, each component was designed as representative of structures required for future LSS. Strain energy distribution, weight, and frequency content were design considerations at the component level. Structural members were designed as realistic and accurate representations of those that will be used in future systems. Generally, the properties of the structure were taken to be those of the metal matrix composite, graphite-magnesium. However, the results from this study are not greatly dependent on the material characteristics. While structural members were modeled in detail, spacecraft subsystems such as propulsion, electronics and so forth were simply modeled as lumped masses. Similarly, reinforcement at component interface regions was crudely modeled using rigid elements. This approach allowed loads to be realistically distributed through the structure while avoiding the "nuts and bolts" details of joining the components.

The Craig-Bampton method of component reduction and coupling was used as the analysis approach. This method consists of reducing each component to a set of generalized coordinates consisting of interface degrees of freedom and a truncated set of component normal modes with all interface degrees of freedom grounded. The normal modes were truncated at a cutoff frequency of 15 Hz for all components with the exception of the solar arrays for which an 8.0 Hz cutoff was used. The following section describes the details of each component design.

5.1   RSA Component Design

Component 1, the box truss, is shown in Figure 5-2. This structure provides a support for a reflecting surface or antenna, and the truss size of 20m is characteristic of optical, infrared, and communication reflectors. The design of this component is quite similar to that described in Reference 5 utilizing pinned-end horizontal members and pretensioned diagonals. This configuration resulted in a very efficient structure; large, lightweight yet relatively stiff.

Lumped mass and inertia was used to represent equipment and coupling hardware at joints. A mass of 50 kg was placed at each corner of the truss to represent station-keeping thrusters. Also, mass and inertia of 10.5 kg and 5 kg-m^2, respectively, was placed at each interior grid point on the upper surface of the truss to represent a reflecting mirror element such as that of the Large Deployable Reflector.

Element dimensions were designed such that the diagonals carry a significant percentage of strain energy in the lower frequency modes, thereby providing candidate locations for passive extensional dampers. This component was coupled to the ring truss in 6 translational degrees of freedom and 34 normal modes were retained for system coupling.

The ring truss (component 2) is shown in Figure 5-3. Designed primarily as a generic truss to tie the other components together, the ring is comparatively stiff with welded joints joining all elements, and typically would be unsuitable or unavailable for damping treatment. Propulsion and maneuver systems, as well as attitude control sensors and actuators, are located on the ring truss. Interface regions on the ring were reinforced with rigid elements to avoid extreme stress concentrations at the component interface points. Further, all coupling was designed such that bending moments are transferred through force couples rather than member bending stiffness. These design approaches gave the ring a fundamental free-free mode of 5 Hz which is rather high for a structure 20m in diameter.

All RSA components are attached to the ring truss giving the ring 87 interface degrees of freedom. The high number of interface coordinates gave the first constrained interface normal mode a frequency far above the 15 Hz cutoff. Therefore, the representation of the ring in the system model includes only the 87 interface degrees of freedom and their associated constraint modes.
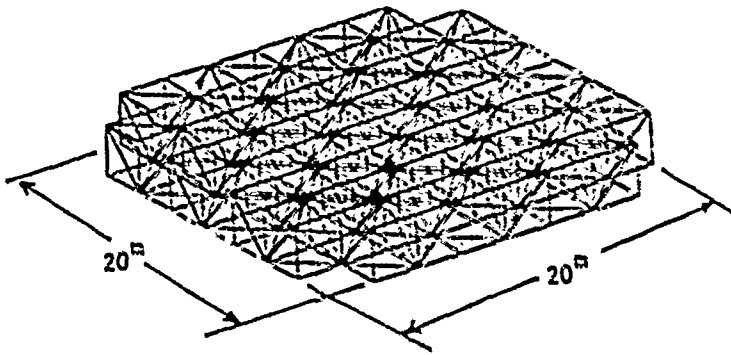
Figure 5-2
RSA Component 1: Box Truss

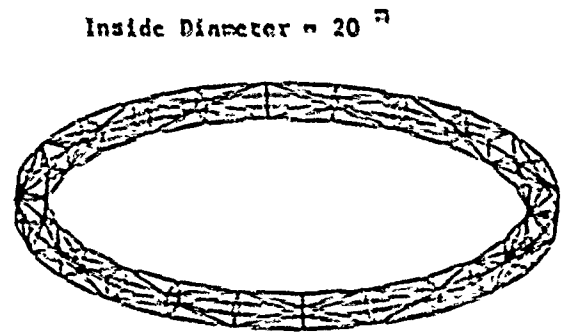Inside Diameter = 20 ᵐ

Figure 5-3
RSA Component 2: Ring Truss

10m

2m
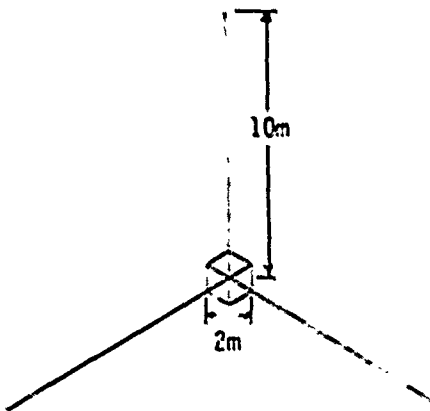
Figure 5-4
RSA Component 3: Tripod

10m
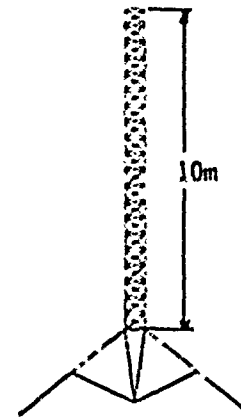
Figure 5-5
RSA Component 4: Equipment Platform

Support Ring

Dish

Support Leg

5.36ᵐ   45°

Figure 5-6
RSA Component 5: Antenna

19 ᵐ

Blanket
Wire
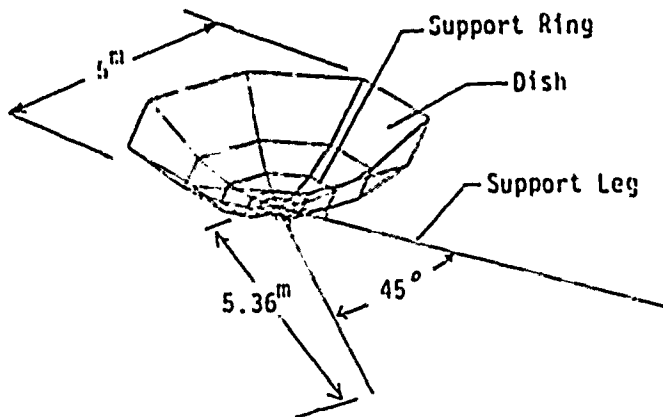Astre-Mast
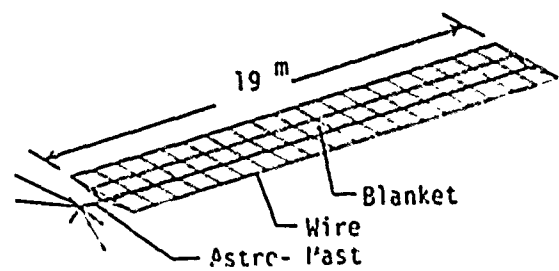
Figure 5-7
RSA Components 6 and 7: Solar Arrays

The third component of the RSA is a tripod structure representative of the secondary reflecting surface support in a Cassegrain system, shown in Figure 5-4. This type of structure is envisioned on Strategic Defense Initiative (SDI) related satellites such as a SBL or radar, as well as many scientific space systems. The tripod supports a secondary reflecting surface, the motion of which has a significant effect on the LOS performance of an electromagnetic system.

Tapered, hollow tubes which allow coolant flow to instruments on the secondary mirror model the tripod legs, while a stiff planar truss and lumped mass represent a gimbal support for the secondary mirror. Flexible modes of the tripod legs have a significant effect on the LOS performance of the system and therefore are candidates for passive damping. Effective damping of this structure requires the support truss to be relatively stiff, thereby placing a high percentage of strain energy of the lower modes in bending of the tripod legs. This allows passive damping treatments utilizing constraining layers to be applied to the legs in an efficient manner.

The tripod was connected to the ring truss at three points. Each interface point was clamped in 5 degrees of freedom, being free to rotate about an axis tangential to the ring truss. This arrangement resulted in 13 normal modes retained in the coupled system model.

Representative of the long trusses planned for future space systems, the fourth component of the RSA is an equipment platform consisting of a high aspect ratio (length to width) truss structure with lumped mass at its tip. The truss design is similar to the towers described in Reference 6. The design goals included a fundamental cantilever frequency of 1 Hz for a 10m long truss with square bays.

For effective damping, it is desirable for this structure to have high axial modal strain energy in the diagonal members. This was accomplished by designing the diagonals to be relatively soft compared to the other members. Graphite-epoxy material characteristics were used for the diagonals as use of metal matrix properties required wall thicknesses unreasonably thin. The platform consists of 20 bays which are 0.5m square and has a tip mass of 91 kg. Single diagonals are used in one plane and double diagonals in the other, thus giving the component a single plane of symmetry. The first bending mode has 31% of the modal strain energy in the diagonals. These diagonals are not pretensioned and thereby allow direct application of the extensional shear damper previously tested and reported in Reference 6. The platform mounts to the ring truss at six points through ball and socket joints thus avoiding moment transfer to the ring truss. The mounting structure was designed to be relatively stiff such that it did not contain significant modal strain energy in low frequency modes. Ten normal modes of the equipment platform were retained in the coupled system.

Component 5 is a communications antenna modeled as an enlarged version of those used by space probes such as Venus Radar Mapper, and is typical of S-band antennas used for ground control of satellites. Modeled as a honeycomb core composite structure, the antenna dish has a relatively low fundamental frequency of 1.5 Hz, which makes this structure a candidate for damping technology applied to plate-like structures. The interface to the ring truss is a simple cantilever arrangement, thus giving 12 interface degrees of freedom to the component. Figure 5-6 presents graphically the antenna design. This component possessed nine constrained interface normal modes below the 15 Hz cutoff frequency. The fundamental mode is simply a bending of the support legs while the second mode involves deformation of the dish.

The solar arrays (components 6 and 7) were modeled after the deployable concept demonstrated in the Solar Array Flight Experiment (SAFE). The arrays are sized for roughly 20kW of power, and these relatively large arrays represent a worst-case situation. Modeling and design parameters were taken from Reference 7. They consist of a mast modeled as a beam which supports a tensioned blanket and wires. Out-of-plane stiffness of the wires and blanket was generated from a differential stiffness analysis in which a temperature shrink was used to produce 33.1 N tension in the blanket and 20.2 N in each wire. Figure 5-7 depicts the design. Damping of the arrays, if necessary, may be accomplished by tuned mass dampers.

This type of array possesses a frequency content much lower than that of the previously described components. However, the degree of modeling used was equivalent to that of the other components. Therefore, the frequency cutoff, below which normal modes were kept, was 8.0 Hz rather than 15.0 Hz as used for the other RSA components. The lower cutoff frequency resulted in the retention of 79 constrained interface modes in the coupled system. Each array was coupled to the ring truss at six points through an interface structure of relatively stiff beams included in the array model. The interface degrees of freedom included only the three translations at each interfaced grid point so as to avoid concentrated stress due to bending moments.

5.2   Coupled System Analysis

The coupled RSA model consists of 87 independent interface degrees of freedom and 224 modal coordinates. System modes were computed for frequencies below 10 Hz, and component participation based on both kinetic and strain energies was found. The analysis shows that a majority of the 210 system modes below 10 Hz primarily involve the solar arrays. However, a relatively high number of system modes are global in character, that is, several components possess significant kinetic and potential (strain) energy in a given system mode. The component participation factors computed on the basis of kinetic and strain energy are roughly equivalent for the RSA design. This indicates that measures taken to reinforce interface regions and avoid stress concentrations were successful in that the kinetic and strain energy was distributed in the components attached to the ring truss. Interface modes, or modes primarily involving deformation of interface regions on the ring truss would have been indicated had a system mode shown high participation of an appendage and relatively low interface participation based on kinetic energy but high ring truss participation based on strain energy.

System modes which are global in character are likely to be important in control design and performance evaluation. Table 5-1 lists system modes in which no single component possessed 92% or more of the modal strain energy. This table also lists the percent of strain energy in each component and indicates the high modal density in the RSA. An important fact is that these modes are global, not merely appendage modes. This characteristic, which will occur in future LSS, complicates the design process and leads to the need for passive and active structural control. Accomplishment of the goal of designing the RSA to facilitate a modal strain energy approach to passive damping is shown by Table 5-2. This table presents strain energy distribution on a component element level in selected global system modes. Note that modes with high box truss participation possess a high percentage of strain energy in the diagonals as was the goal. Similar conclusions may be drawn for other system components.

The primary figure of merit applicable to the RSA is LOS response to disturbances and maneuver commands. Figure 5-8 defines the LOS in terms of discrete motion of the RSA. Note that LOS response due to motion of the primary reflecting surface is approximated by an average of rotations of selected grid points on the box truss. Analysis of modal participation in the LOS showed that many modes are significant to the LOS response. The 20 most significant modes about both the Y and Z axes, together with their relative participation are listed in Table 5-3 (the gimbal modes of the secondary mirror have been excluded as they are nearly uncoupled from the rest of the system).

5.3   Control System Design and Analysis

The control system for the RSA is a simple model of those currently in use on spacecraft and likely to be implemented on first generation large space systems. Design of an active system for control of structural vibrations is beyond the scope of this report, but active vibration control acting in concert with passive damping will be addressed in subsequent studies performed under the PACOSS program.

5.3.1 Baseline Control System Design

The approach taken for the RSA control design was to achieve attitude control and small angle slew maneuvers without excessive excitation of structural modes. Symmetry of the structure decoupled rotation about the pitch axis which is the Y-axis denoted in Figure 5-1. This allowed the dynamics about the pitch axis to be considered separately from the roll-yaw (X and Z axes, respectively, in Figure 5-1) dynamics and thus facilitated uncoupled control systems for pitch and roll-yaw motion.

Investigation of sensor and actuator dynamics indicated that for purposes of the RSA, the effects were not of importance due to the relatively high roll-off frequencies of components such as rate gyros and torque wheels. Such instruments have bandwidths on the order of 50 to 100 Hz and thus the effects of their dynamics are quite minor in the 0 to 10 Hz frequency range covered by the RSA model.

Table 5-1 MSE Distribution in Selected Modes

PERCENTAGE OF SYSTEM MODE STRAIN ENERGY
IN COMPONENTS

System Mode No.	f (Hz)	Box Truss	Ring Truss	Tripod	Equipment Platform	Antenna	Solar Arrays
23	0.72R	·	31.3	5.71	6.75	47.4	R.70
20	1.02	-	14.0	3.37	36.5	23.7	22.2
32	1.03	·	5.7R	-	11.2	5.41	7R.0
33	1.08	69.4	5.12	1.2R	23.9	·	
34	1.14	22.9	2.R	·	73.3	·	
43	1.42	13.4	31.2	3.12	·	49.7	2.0
44	1.50	·	5.15	2.24	5.R2	1.52	R5.0
48	1.53	-	29.5	13.R	31.8	R.32	16.0
51	1.63	18.4	29.2	1.91	1.12	4R.R	·
97	2.44	9.6R	16.4	69.7	-	-	3.5R
124	2.7R	7.36	15.1	70.8	-	3.27	3.2R
129	2.86	R7.5	7.R7	2.62	1.77	-	·
142	3.51	27.3	35.9	27.R	-	6.29	2.56
145	3.60	-	7.79	90.8	-	-	·
158	4.03	15.0	48.1	23.5	·	12.R	
165	4.22	2.R6	9.6	77.2	-	9.99	·
176	4.3R	2.36	10.0	4.11	·	R1.4	2.06
182	4.55	4.1	8.5R	R6.R		·	
185	5.11	12.3	48.R	2.06		35.9	
188	5.45	25.4	3R.9	34.2			
187	5.6R	37.0	18.1	30.6		13.0	·
190	6.30	R7.2	6.0R	1.07	5.44		
191	6.45	7.06	19.4	2.27	60.71	10.3	
122	6.49	8.13	46.7	9.1	17.11	1R.5	
196	6.96	91.3	1.7R	4.04	1.86		
198	7.15	70.5	5.47	17.6	·	5.94	
199	7.31	78.1	12.0	2.99	6.34		
200	7.31	77.5	11.1	9.R4	1.46	·	
201	7.3R	2R.5	42.2	10.5	12.R	5.12	
204	7.90	32.9	45.8	19.8	·		
205	8.3R	25.8	30.5	42.R			
206	8.77	44.8	15.6	32.6	2.05	4.R1	
207	8.R9	81.2	1.47	17.3			
208	9.05	28.1	5.93	65.5			

Table 5-2   Element Level MSE Distribution for
Selected Modes and Components

COMPONENT ELEMENT SET	SYSTEM MODE # / % STRAIN ENERGY IN ELEMENT SET			
Box Truss Diagonals	33 / 64.4	129 / 81.1	190 / 81.0	207 / 77.8
Tripod Legs	97 / 65.2	124 / 67.8	165 / 67.9	206 / 62.7
Equip. Plat. Diagonals	30 / 11.7	33 / 7.4	34 / 23.2	191 / 43.8
Antenna Support Legs	23 / 47.1	43 / 16.3	51 / 11.8	176 / 1.78
Antenna Dish	23 / 0.25	43 / 33.4	51 / 37.0	176 / 79.6
Solar Array Masts	30 / 0.99	32 / 11.0		
Solar Array Cross Members	30 / 20.8	32 / 66.5		

Table 5-3   Relative Modal Participation in LOS

Y-AXIS			Z-AXIS		
SYSTEM MODE #	f (Hz)	RELATIVE PARTICIPATION	SYSTEM MODE #	f (Hz)	RELATIVE PARTICIPATION
209	9.53	1.0	207	8.89	1.0
187	5.68	0.87	190	6.30	0.77
129	2.86	0.79	33	1.10	0.73
196	6.96	0.73	142	3.51	0.64
201	7.38	0.69	34	1.14	0.53
206	8.77	0.66	43	1.14	0.49
199	7.31	0.61	51	1.63	0.47
124	2.78	0.52	195	6.84	0.44
185	5.11	0.49	208	9.05	0.44
158	4.03	0.46	204	7.90	0.40
191	6.45	0.37	97	2.44	0.34
192	6.49	0.25	183	4.66	0.23
198	7.15	0.16	193	6.62	0.19
182	4.55	0.14	145	3.60	0.16
165	4.22	0.13	181	4.52	0.10
30	1.02	0.12	20	0.683	0.10
176	4.38	0.09	140	3.47	0.06
23	0.728	0.08	184	5.00	0.06
118	2.72	0.07	95	2.44	0.06
32	1.03	0.07	42	1.40	0.05
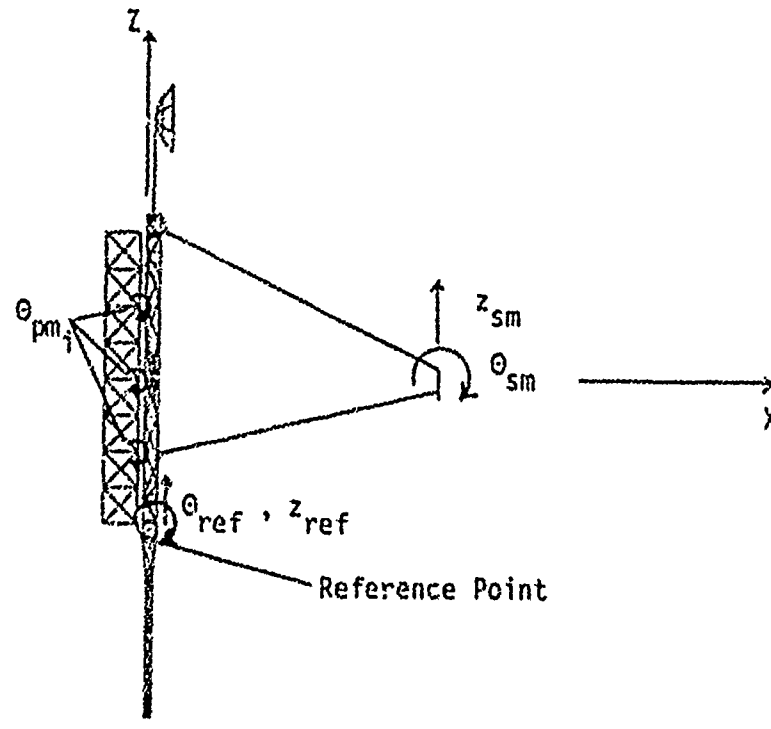
$$LOS_y = (2\frac{f_s}{f_p} - 1)\Theta_{ref} + \frac{2}{13}\sum_{i=1}^{13}\Theta_{pm_i} - 2\frac{f_s}{f_p}\Theta_{sm} - \frac{1}{f_p}(z_{ref} - z_{sm})_{flex}$$

Where,

f_s = Focal length of secondary mirror

f_p = Focal length of primary mirror

$(z_{ref} - z_{sm})_{flex}$ = Relative z deflection of secondary mirror to reference point due to structural deformation

NOTES:

Sum over   represents an average primary mirror deformation

LOS about z-axis has sign change on relative translation term;

$$-\frac{1}{f_p}(z_{ref} - z_{sm})_{flex} \implies +\frac{1}{f_p}(y_{ref} - y_{sm})_{flex}$$

Relative LOS is defined as : Inertial LOS - Rigid Body Motion

Figure 5-8   RSA LOS Definition

DG-19

Attitude/slew control was accomplished by sensing angular rate and position at a reference point on the ring truss, passing the signals through a low pass filter, and feeding the filtered signal equally back to four torque wheels mounted on the ring truss.

The low pass filters were modeled as second order systems and given a 1.0 Hz cutoff frequency with 0.707 damping ratio. The choice of filter cutoff frequency represents a trade between the contamination of altitude/slew information with flexible motion at the sensor point and degraded closed-loop rigid body performance. A higher filter bandpass results in greater chances of closed-loop instability due to flexible modes while a lower bandpass leads to far slower attitude correction.

The feedback gains were designed by classical root locus methods using the filter and rigid body dynamics. Pitch control involved sensing of inertial pitch angle and rate with feedback to pitch torque wheels. The feedback gains were chosen to give closed-loop poles such that the rigid body system would complete a maneuver in 3 to 4 seconds. Similarly, roll-yaw control was accomplished through sensing inertial yaw angle and rate and roll rate. These signals were fed through a coupled gain matrix to four yaw torque wheels and one roll torque wheel. Feedback gain was selected using the same criterion as for the pitch axis control system. Impulse response of the two systems is shown in Figure 5-9 demonstrating good rigid body maneuver response.

In addition to the attitude control system, a simple co-located stiffness and damping was implemented across the secondary mirror gimbal to represent passive or active isolation and damping. The stiffness and damping coefficients were selected to give the secondary mirror a natural frequency of 0.5 Hz and damping ratio of 0.707 in rotation on its gimbal about both the Y and Z axes. Motion of the secondary mirror relative to the gimbal is uncoupled from the rest of the system and therefore this simple control does not affect the attitude control dynamics.

5.3.2 Control System Analysis

Analysis of the control system required determination of the important flexible modes to be retained in the closed-loop model. This was accomplished by determining the participation of the open loop system modes in the primary figure of merit, the line of sight. Additionally, modal controllability, which is simply a consideration of displacement at actuator locations in each mode, was used to assure that all modes which would be significantly excited by the actuators were included in the closed-loop model. Tables 5-4 and 5-5 list the system modes retained for the flexible system analysis and simulation.
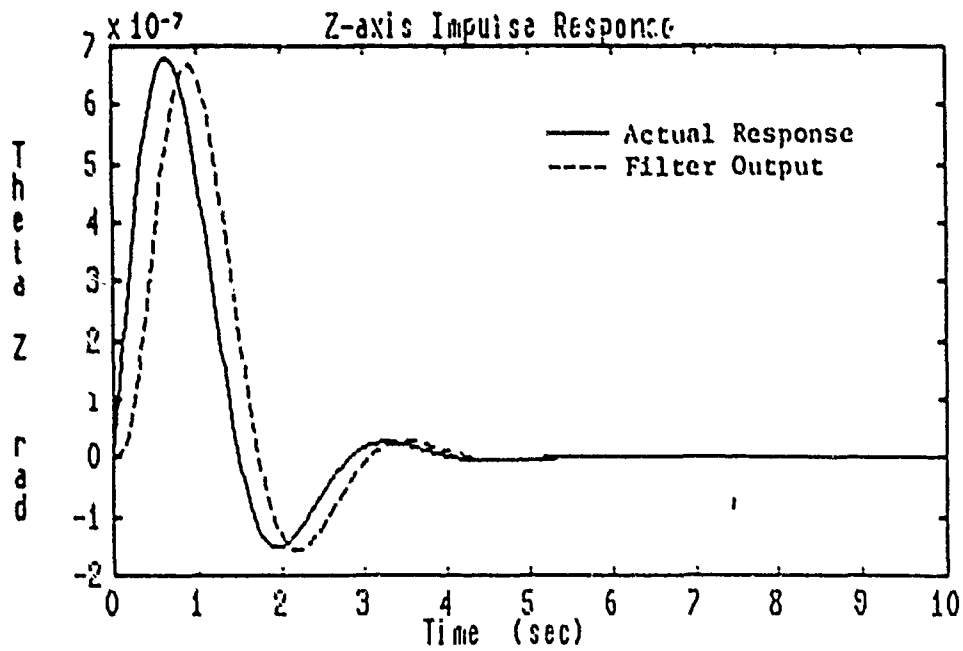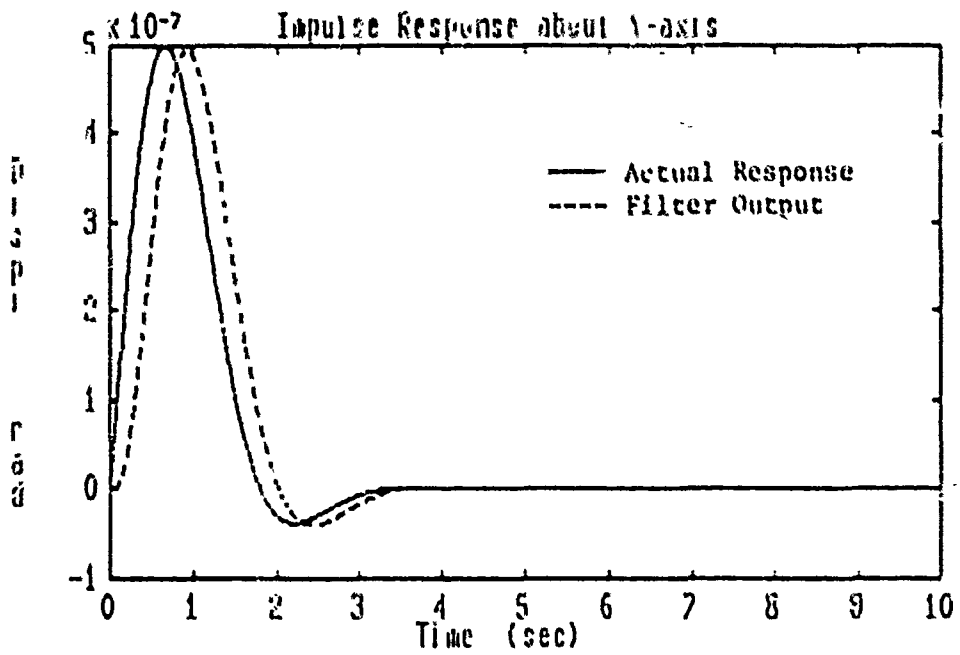
Figure 5-9 Rigid Body Impulse Responses

DG-21

Table 5-4   Pitch-Axis Closed-Loop Modal Summary

MODE #	OPEN LOOP f_n (Hz)	ζ	CLOSED LOOP f_n (Hz)	ζ	STRAIN ENERGY DISTRIBUTION %: BOX TRUSS 1	RING TRUSS 2	TRIPOD 3	EQUIP. PLAT. 4	ANT. 5	SOLAR ARRAYS 6, 7	RANK IN LOS OBSER. (OPEN LOOP)
Filter	1.0	0.707	0.463	0.601	-	-	-	-	-	-	-
-5	0	0	0.544	0.813	-	-	-	-	-	-	-
7	0.01	0.002	0.50	0.707	-	-	100	-	-	-	1
23	0.728		0.767	.0167	0.058	31.3	5.71	6.75	47.4	8.70	19
38	1.016		.965	.0141	0.14	14.0	3.37	36.5	23.7	22.3	17
32	1.035		1.02	.00205	0.040	3.78	0.86	11.9	5.41	78.0	21
48	1.53		1.51	.0101	0.58	29.5	13.8	31.8	8.22	16.0	23
118	2.72		2.72	.00203	0.14	0.29	1.33	-	0.055	98.2	20
124	2.78		2.78	.00456	7.36	15.1	70.8	0.19	3.27	3.28	9
129	2.86		2.87	-.00147	87.5	7.87	2.62	1.77	0.21	-	4
156	4.03		4.04	-.00047	15.0	48.1	23.5	0.26	12.8	0.43	11
165	4.22		4.22	.00169	2.86	9.60	77.3	0.02	9.99	0.25	16
176	4.38		4.38	.00195	2.36	10.0	4.11	0.04	81.4	2.05	18
182	4.55		4.55	.00160	4.10	8.68	86.8	0.21	0.05	0.13	15
185	5.11		5.12	.000754	12.3	48.8	2.06	0.74	35.9	0.20	10
187	5.68		5.68	.00169	37.0	18.1	30.6	0.46	13.0	0.82	3
188	5.81		5.81	.002	0.12	0.13	0.35	-	0.55	98.8	22
191	6.45		6.45	.00103	7.06	19.4	2.27	60.7	10.3	0.29	12
192	6.49		6.49	.00204	8.13	46.7	9.10	17.1	18.5	0.42	13
196	6.96		6.96	.00182	91.3	1.78	4.04	1.85	0.97	0.02	5
198	7.15		7.15	.00184	70.5	5.47	17.6	0.40	5.94	0.09	14
199	7.31		7.31	.0015?	78.1	12.0	2.99	6.34	0.32	0.24	8
201	7.38		7.38	-.00097	28.5	42.2	10.5	12.8	5.12	0.77	6
206	8.77		8.77	.00311	44.8	15.6	32.6	2.05	4.81	0.14	7
209	9.53	0.002	9.53	.00201	96.5	2.50	0.84	0.03	0.13	0.022	2

Table 5-5   Roll-Yaw Closed-Loop Modal Summary

MODE #	OPEN LOOP f_n (Hz)	ζ	CLOSED LOOP f_n (Hz)	ζ	STRAIN ENERGY DISTRIBUTION %: BOX TRUSS 1	RING TRUSS 2	TRIPOD 3	EQUIP. PLAT. 4	ANT. 5	SOLAR ARRAYS 6, 7	RANK IN LOS OBSER. (OPEN LOOP)
Filter	1.0	0.707	0.867	0.706	-	-	-	-	-	-	-
Filter	1.0	0.707	0.442	0.341	-	-	-	-	-	-	-
4	0	0	0	(-4.204)	-	-	-	-	-	-	-
6	0	0	0.379	0.955	-	-	-	-	-	-	-
8	0.01	0.002	0.50	.707	-	-	100	-	-	-	1
10	0.269		0.264	.011	0.013	0.12	-	-	-	99.9	42
33	1.10		1.08	.0005	69.4	5.12	1.28	23.9	0.06	0.22	4
34	1.14		1.14	.00132	22.9	2.80	0.60	73.3	0.14	0.20	6
43	1.41		1.44	-.00653	13.4	31.2	3.12	0.56	49.7	2.0	7
51	1.63		1.67	-.0204	18.4	29.2	1.91	1.12	48.8	0.60	8
97	2.44		2.44	.00229	9.69	16.4	69.7	0.06	0.54	3.57	12
140	3.47		3.47	.00201	0.38	0.46	0.29	-	0.11	98.8	18
142	3.51		3.50	.00335	27.3	35.9	27.8	0.17	6.29	2.57	5
145	3.60		3.60	.00210	0.05	7.79	90.8	0.04	0.02	1.29	15
181	4.52		4.52	.002	0.64	1.76	0.59	-	97.0	-	16
183	4.66		4.66	.00219	2.29	3.42	93.5	-	0.70	0.04	13
186	5.45		5.45	.00371	25.4	38.9	34.2	0.17	0.69	0.66	36
190	6.30		6.30	.00192	87.2	6.08	1.07	5.44	0.20	-	3
193	6.62		6.62	.00199	6.99	0.61	0.04	92.3	0.06	-	14
195	6.84		6.84	.002	98.7	0.31	0.36	0.01	0.64	-	9
200	7.31		7.31	.002	77.5	11.1	9.84	1.46	0.09	0.05	17
204	7.90		7.90	.000602	32.9	45.8	19.8	0.52	0.36	0.65	11
205	8.38		8.38	.00380	25.8	30.5	42.8	0.43	0.14	0.28	32
207	8.89		8.89	.00201	81.2	1.47	17 3	-	0.06	-	2
208	9.05	0.002	9.05	.00238	28.1	5.93	65.5	0.13	0.13	0.16	10

Closed-loop roots for the flexible system using the previously described control system were calculated assuming C.2% modal viscous damping. This value of damping is typical of spacecraft structures with no passive damping augmentation. Frequencies and damping ratios of the closed-loop system indicate serious stability problems. The attitude control system caused a reduction in damping for several system modes and drove a few modes unstable. This situation is unacceptable. At best the system would have a lengthy settling time and high jitter level, at worst it would shake itself apart. These results indicate that even for simple attitude or slew maneuvering, a complex space system requires a sophisticated control system or passive damping augmentation to accomplish its mission.

5.4   System Analysis and Performance

Overall system analysis and performance evaluation was performed using the flexible closed-loop system described in Section 5.3.2. As previously mentioned, LOS settling time and jitter response are the measures most appropriate for system evaluation. The following paragraphs describe a comparison of the nominal system (0.2% modal viscous damping) performance to a system having 5% modal damping. Previous studies performed under the PACOSS program (Reference 6) have shown that a modal damping ratio of 5% in structures of LSS size is attainable through passive damping augmentation using discrete viscoelastic dampers. This comparison demonstrates the performance improvements possible through passive damping.

Significantly lower jitter response due to increased modal damping is shown in Figures 5-10 and 5-11. These figures show the open loop relative LOS response (LOS without rigid body motion) to a noise disturbance applied through the ring truss. In order to simulate response to wide band noise, the disturbance torques were generated as a sum of randomly phased sinusoidal signals at frequencies corresponding to the natural frequencies retained in the pitch and roll-yaw models respectively. Random noise was added to the signal and the disturbance was scaled to a RMS level of 1 NM.

The nominally damped system (0.2%) reached a steady state response level approximately 4 seconds following initiation of the disturbance signal. As shown in Figure 5-10, the RMS response level in the pitch plane was reduced by over 91% when the modal damping was increased from 0.2% to 5%. The corresponding results for response about the yaw axis show a 64% reduction in jitter level.

Transient response to an impulsive disturbance is shown in Figures 5-12 and 5-13. These figures give the inertial LOS response to an impulsive torque acting on the ring truss about the Y and Z axes respectively and demonstrate the advantage of passive damping augmentation with regard to setting time. The pitch axis response graphically shows that as little as 5% modal damping can virtually eliminate transient response of modes above the control bandwidth.
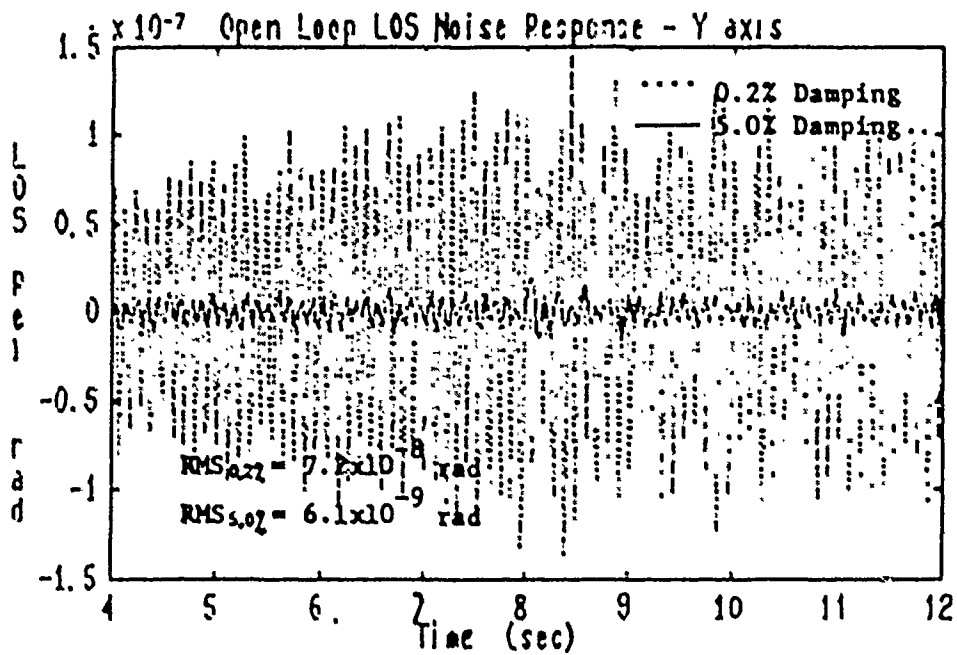
DG-23

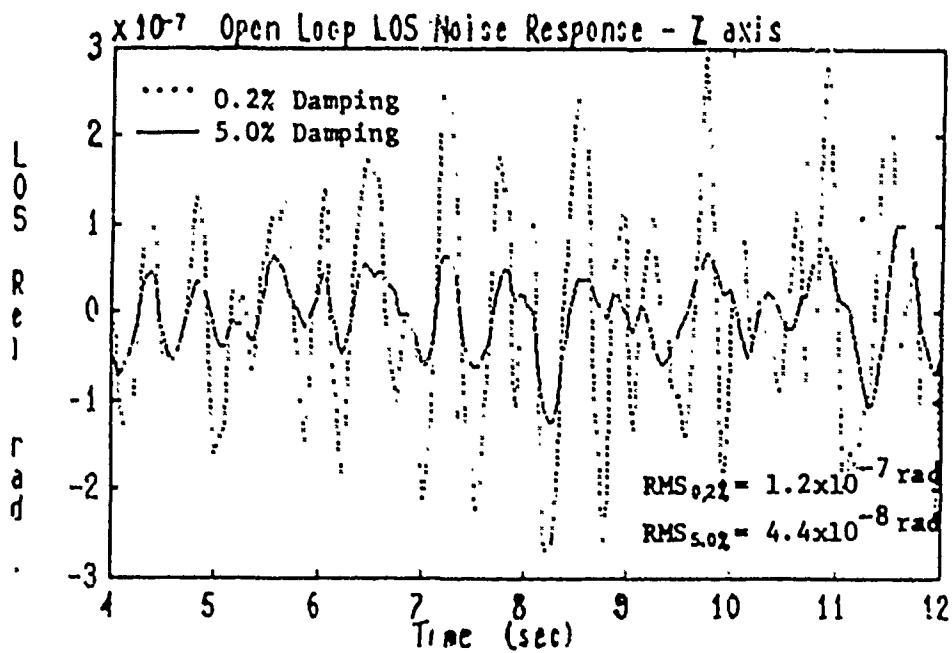**Figure 5-10 Pitch Axis Relative LOS Response to Noise Input**

Figure 5-11 Yaw Axis Relative LOS Response to Noise Input
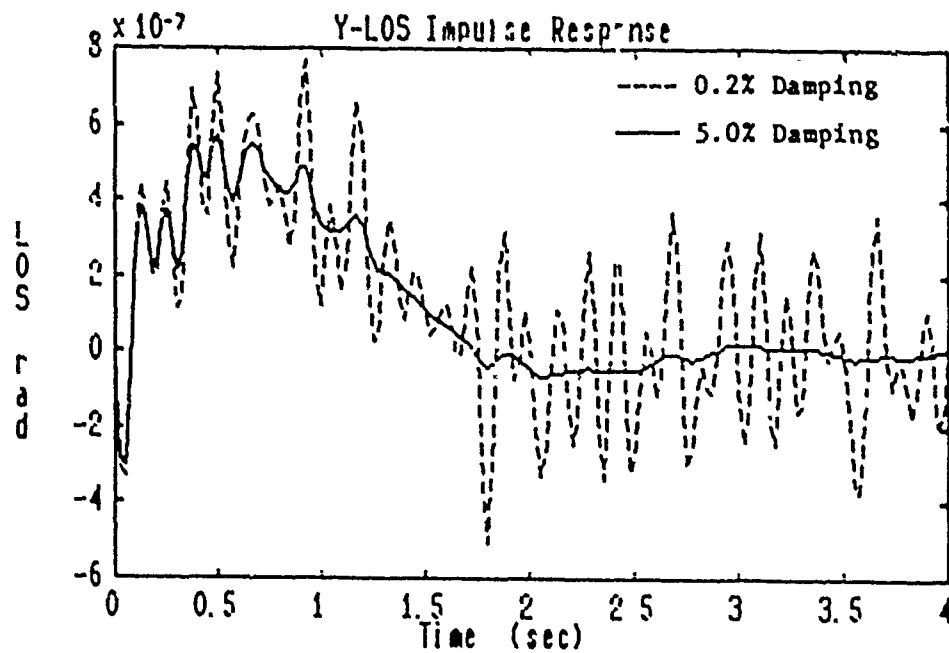
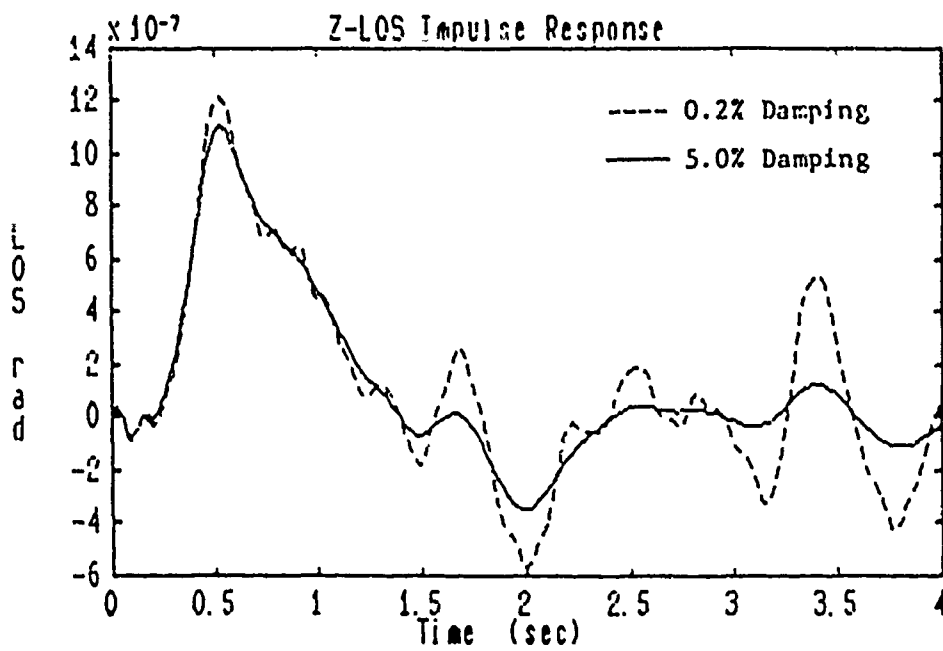**Figure 5-12 Pitch Axis LOS Impulse Response**

Figure 5-13 Yaw Axis LOS Impulse Response

Maneuver or slew performance is also closely associated with settling time. In this case, passive damping benefits are best evaluated through consideration of the relative line of sight or the deviation of the LOS due to structural deformation. Relative LOS response to a 0.01 radian slew maneuver generated by the attitude control system is shown for the pitch and yaw axes in Figures 5-14 and 5-15, respectively. Slewing about the pitch axis with 0.2% modal damping shows a long settling time due to the response of several modes. However, 5% modal damping demonstrates a faster settling time with response dominated by a single mode. Therefore, if further performance improvement using active control were desired, the active system would be required to control only a single flexible mode. The slew maneuver response about the yaw axis given in Figure 5-15 shows the closed-loop instability of the nominal system. Passive augmentation giving 5% modal damping effectively eliminates the instability and again gives a response dominated by a single mode.

These results quantitatively indicate the performance improvement achievable with just 5% modal damping. The primary goal of the PACOSS program is to demonstrate the ability to give a LSS 5% or more modal damping in selected critical modes. Section 6 addresses this concern and other implications of the foregoing results.
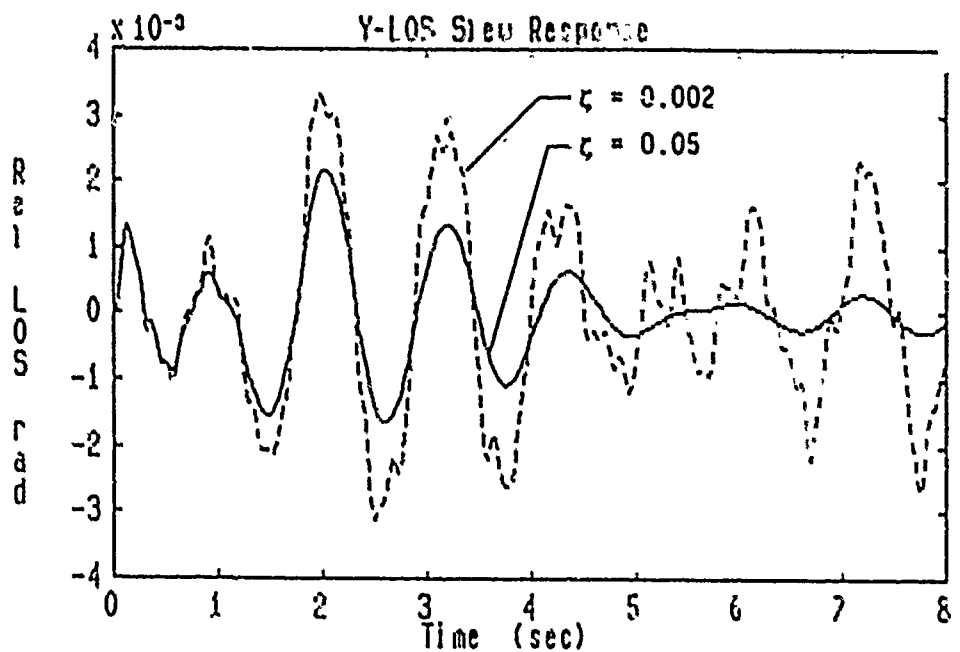
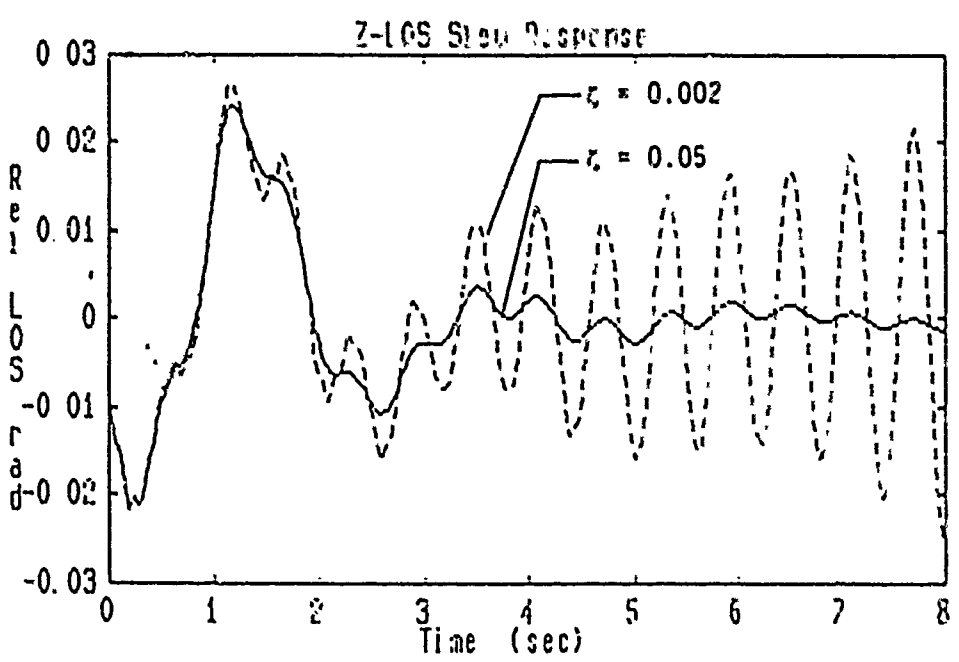Figure 5-14 Relative LOS Slew Response (Pitch Axis)

Figure 5-15 Relative LOS Slew Response (Yaw Axis)

6.0 IMPLICATIONS OF RSA ANALYSIS

Design and analysis results described in the previous sections point to several implications regarding the role passive damping will play in design and development of future large space systems. Specifically, passive damping technology can work in concert with other technologies to allow future Air Force and civilian space systems to meet their performance goals. This complementary behavior can be enhanced if considered throughout the design process.

6.1 Structural Design

To achieve effective damping design, system structural design must be conducted with consideration of passive damping application in the preliminary design phase, continuing through fabrication. The RSA demonstrates that if as little as 5% modal damping can be achieved in troublesome structural modes, significant improvement is realized in system performance.

Consideration of passive damping in the design process is quite naturally accommodated through consideration of modal strain energy distribution. This involves design of members which will allow efficient application of passive damping treatments. The system should include members which possess high modal strain energy in flexible modes expected to have a detrimental impact on system performance. Use of viscoelastic materials usually requires that these members not be in primary load paths of the structure due to their stiffness to weight, but further development of passive damping mechanisms may eliminate this design constraint. Other damping techniques such as viscous and tuned mass dampers should also be considered during the structural design process.

6.2 Control Design

The closed-loop analysis results presented in Section 5 show that passive damping augmentation can alleviate stability problems due to structural modes whose frequency is within, or near, the control bandwidth. Alternatively, an active vibration control system designed for the nominally damped RSA would have to contend with a high number of modes. This includes modes to be actively damped and modes which, while not controlled, must not be driven unstable. Passive damping can ensure stability and reduce modal response levels such that an active control need only be designed to control one or two structural modes. Thus, the passive augmentation fills the role of low authority control in an integrated high authority - low authority control (HAC/LAC) design approach.

In addition to simplified control design, benefits include less expensive and elaborate control systems leading to more reliable and robust performance. Overall, the implication of the closed-loop results is that passive and active control of structural vibrations will both play a major role in future Air Force space systems.

6.3   The Structural Design Process

As mentioned, modal strain energy distribution is the primary means of determining where passive damping treatments would be most effective in a structure. Passive damping of a complex structural system, such as the RSA, is best approached via modal strain energy, when the structure was originally designed with damping in mind. Each component of the RSA was designed to facilitate application of passive damping. Thus, when the coupled system was analyzed, troublesome modes could be identified and targeted for damping. Tables 5-4 and 5-5 list the RSA closed-loop frequencies and damping ratios together with the component level MSE distribution for each mode. As an example of effective structure design for passive damping, consider the unstable closed-loop damping ratio of system mode 129 listed in Table 5-4. This highly unstable mode has 87.5% of its strain energy in the box truss. Table 5-2 shows that the diagonals, which were intended to be passively damped, contain most of this mode's strain energy present in the box truss. Thus, damping treatment of the box truss diagonal elements would solve the stability problem. Similar conclusions can be drawn for other modes and components. This is the essence of the MSE approach: to simply and efficiently damp troublesome modes through judicious location of damping treatments on structures designed to allow such treatment.

7.0 CONCLUDING REMARKS

The mission survey described in this report indicated that future military space systems will be required to perform missions involving atmospheric surveillance and warning, communications, navigation, space vehicle detection and tracking, and space-based defense. These systems will be relatively large and possess high modal density at low frequencies yet must meet stringent pointing performance requirements in the presence of on-board disturbances and spacecraft maneuvering.

As demonstrated by the analysis results presented in this report, the selected RSA design achieves the goal of representing future Air Force space systems which will require passive and active vibration control. This was accomplished through the development of a system having high modal density within the control bandwidth on an intermediate-size structure consisting of components representing a variety of systems.

Closed-loop analysis including an attitude control system demonstrated that high modal density in, or near, the control bandwidth can result in serious instabilities. This reduced or negative stability is most effectively handled through a combination of passive and active vibration control. Passive damping augmentation will lead to reliable and robust systems with simplified active controls.

8.0 REFERENCES

1. Gehling, R. N., and Morgenthaler, D. R., "Representative System Report," MCR-84-541, Martin Marietta Denver Aerospace, Denver, Colorado, November 1985.

2. "NASA Space System Technology Model", Fifth Issue, January 1984, NASA Headquarters, Washington, D.C.

3. "Alpha I Design Program", Rockwell International, Rocketdyne Division, RI/RD79-347P-3.

4. Rogers, L. C. et al, "Passive Damping in Large Precision Space Structures", AIAA Paper 80-0677, presented at the AIAA/ASME/ASCE/AHS 21st Structures, Structural Dynamics and Materials Conference, Seattle, WA, May 1980.

5. Herbert, J. J., Postuchow, J.R., and Schartel, W.A., Martin Marietta Denver Aerospace, Denver, CO, "Technology Needs of Advanced Earth Observation Spacecraft", NASA Contractor Report 3698, January, 1984.

6. White, C. W., Martin Marietta Denver Aerospace, Denver, CO, "Analysis of Damped Twin Towers", The Shock and Vibration Bulletin, No. 55-Part 1, June, 1985, pp. 119-130.

7. "Power Extension Package", Users Handbook, MDC G8546, McDonnell Douglas Astronautics Company, Huntington Beach, CA, June, 1980.

8. Gayman, W. H., Trubert, M.R., Abbott, P.W., "Measurement of Structural Transfer Functions Significant to Flight Stability of the Surveyor Spacecraft", NASA Technical Memorandum 33-389, Jet Propulsion Laboratory, Pasadena, CA, May 1969, Appendix A.

9. "Large Space Antenna Systems Technology - 1982", proceedings held in Hampton, VA, Nov. 30 - Dec. 3, 1982, NASA CP-2269.

10. "Large Space Antenna Systems Technology - 1984", proceedings held in Hampton, VA, Dec. 4-6, 1984, NASA CP-2368.

ROBUST CONTROL DESIGN FOR VIBRATION SUPPRESSION OF

LARGE SPACE STRUCTURES

by

Rama K. Yedavalli
Department of Electrical Engineering
The University of Toledo
Toledo, OH 43606

Abstract

This paper addresses the aspect of designing controllers for robust stability for linear systems having finite parameter variations. The development of upper bounds on the perturbation of an asymptotically stable linear system to maintain stability is extended to the problem of vibration suppression of Large Space Structure (LSS) models with modal frequencies and mode shape slopes at actuator locations taken as uncertain parameters. The uncertainty associated with the parameters in LSS models is modeled in a specific way and is used to obtain bounds which are in turn used to obtain the robust controller.

Introduction

In recent years, 'Control of Large Space Structures' (LSS) has become an active topic of research. Interesting accounts of LSS control trends are reported by Balas[1] and Skelton[2]. One fundamental problem of LSS control is the control of a large dimensional system with a controller of much smaller dimension (model/controller truncation) compounded with modal data uncertainty (parameter errors). Thus 'robustness' is an extremely desirable (sometimes necessary) feature in the active control of LSS. In this study, we address the aspect of stability robustness with respect to parameter errors alone. The recently developed elemental perturbation bounds for robust stability of linear systems with structured uncertainty[3,4,5] is extended to the problem of vibration suppression of LSS. Towards this direction, the fact that modal data uncertainty increases with mode number is incorporated in the characterization of uncertainty in LSS model parameters and this model is used to obtain upper bounds for robust stability which are in turn used to get a robust controller.

LSS Models and Nominal Control Design

Consider the standard state space description of LSS evaluation model with N elastic modes:

$$\dot{x} = Ax + Bu \qquad x(0) = x_0; \quad x \to R^n = 2N , \quad u \to R^m \qquad (1a)$$

$$y = Cx \qquad y \to R^k \qquad (1b)$$

where

$$x^T = [x_1^T, x_2^T, \ldots x_N^T]; \quad x_i = \begin{bmatrix} \eta_i \\ . \\ \dot{\eta}_i \end{bmatrix} \qquad (1c)$$

$$A = \text{Block diag. } [\ldots A_{ii} \ldots], \quad A_{ii} = \begin{bmatrix} 0 & 1 \\ -\omega_i^2 & -2\zeta\omega_i \end{bmatrix} \qquad (1d)$$

$$B^T = [B_1^T, B_2^T, \ldots B_N^T]; \quad B_i = \begin{bmatrix} 0 \\ b_i^T \end{bmatrix} \qquad (1e)$$

$$C = [C_1 \ C_2 \ldots C_N] \qquad (1f)$$

The performance index for vibration suppression problem may be written as

$$J = \int_0^\infty [(\sum_{i=1}^N \omega_i^2 \ \eta_i^2 + \dot{\eta}_i^2) + \rho \ u^T u] dt \qquad (2a)$$

which can be written in the form

$$J = \int_0^\infty (y^T Qy + \rho \ u^T u) dt = \int_0^\infty (x^T C^T QCx + \rho \ u^T u) dt = J_y + \rho \ J_u \qquad (2b)$$

where the matrix C of (1f) is given by

C = Block diag. [... C_i ...]

and

$$C_i = \begin{bmatrix} \omega_i & 0 \\ 0 & 1 \end{bmatrix} \qquad (2d)$$

Let the nominal control law be designed by minimizing the performance index of (2) which results in[6]

$$u = Gx \qquad (3a)$$

where

$$G = -\frac{1}{\rho} B^T K \qquad (3b)$$

$$KA + A^T K - \frac{KBB^T}{\rho} K + C^T QC = 0 \qquad (3c)$$

The closed loop system matrix

$$\overline{A} = (A + BG) \qquad (4)$$

is assymptotically stable. In the nominal design situation, an appropriate value for ρ (and hence G) is determined such that a reasonable trade off between J_y and J_u is obtained. However, in LSS models, the parameters of the plant matrix A, namely the modal frequencies and modal damping as well as the parameters of the control distribution matrix B, namely the mode shape slopes at actuator locations are known to be uncertain. It is also known that the uncertainty in these parameters tends to increase with increase in mode number. Thus with variations ΔA and ΔB in the matrices A and B of (1), the nominal control G of (3) cannot guarantee stability of the closed loop system. Thus one needs to design a control gain G that guarantees stability for a given range of perturbations ΔA and ΔB. Towards this direction, in the next section we briefly review the upper bounds developed for linear systems with structured perturbation and use these bounds to obtain a controller that accommodates perturbations within the given bounds.

Perturbation Bounds for Robust Stability and Robust Control Design Algorithm

Let us consider the following liner dynamic system,

$$\dot{x}(t) = A(t) \, x(t) \qquad (5a)$$

$$= [A_0 + E(t)] \, x(t) \qquad (5b)$$

A_0 is an nxn nominally asymptotically stable matrix and E is an nxn 'Error' matrix. In the case of 'structured' perturbation, the elements of E are such that

$$E_{ij}(t) < \epsilon_{ij} \overset{\Delta}{=} \underset{t}{V} |E_{ij}(t)|_{max} \text{ and } \epsilon \overset{\Delta}{=} \underset{i,j}{Max} \epsilon_{ij}$$

Thus ϵ is the magnitude of the maximum deviation expected in the entries of A.

<u>Theorem</u>: The system of (5) is stable if

$$\epsilon < \frac{1}{\sigma_{max} (P_m U_e)s} \equiv \mu \quad \text{or} \quad \epsilon_{ij} < \mu \, U_{eij} \tag{6}$$

where U_e is an nxn matrix whose entries are such that

$$U_{eij} = \frac{\epsilon_{ij}}{\epsilon} \tag{7}$$

Thus $U_{eij} = 0$ if the perturbation in Ao_{ij} is known to be zero (i.e., $\epsilon_{ij} = 0$). Similarly $U_{2ij} = 1$ if one doesn't explicitly know ϵ_{ij} for some i,j thereby accommodating the worst case situation. Hence, it can be seen that

$$0 < U_{eij} < 1 \tag{8}$$

Here P is the solution of the Lyapunov matrix equation

$$A_o^T P + PA_o + 2I_n = 0 \quad (I_n \text{ is an nxn identity matrix}) \tag{9}$$

$\sigma[\cdot]$ = singular value of the matrix $[\cdot]$

   = $\{\lambda([\cdot][\cdot]T)\}1/2$

$[\cdot]_s$ = symmetric part of a matrix $[\cdot]$

$|(\cdot)|$ = modulus of the entry $(\cdot)$

$[\cdot]_m$ = modulus matrix = matrix with modulus entries

Now let ΔA and ΔB be the perturbation matrices formed by the maximum modulus deviations expected in the individual elements of matrices A and B respectively. Then one can write

$$\left. \begin{array}{l} \Delta A = \epsilon_a \, U_{ea} \\ \\ \Delta B = \epsilon_b \, U_{eb} \end{array} \right\} \quad \text{Absolute variation} \tag{10}$$

where ϵ_a is the maximum of all deviations in A and ϵ_b is maximum of all deviations in B. Then the total perturbation in the linear system matrix of (4) with nominal control $u = Gx$ is given by

$$\Delta = \Delta A + \Delta BG_m = \epsilon_a \, U_{ea} + \epsilon_b \, U_{eb} \, G_m \tag{11}$$

Assuming the ratio $\epsilon_b/\epsilon_a = \bar{\epsilon}$ is known, we can extend the main result of (6) to the linear state feedback control system of (4) and obtain the following design observation.

<u>Design Observation 1:</u>

The perturbed linear system is stable for all perturbations bounded by ϵ_a and ϵ_b if

$$\epsilon_a < \frac{1}{\sigma_{max}[P_m U_{e_a} + \bar{\epsilon} \ U_{e_b} \ G_m]_s} \equiv \mu \tag{12a}$$

and $\epsilon_b < \bar{\epsilon} \ \mu$ where

$$P(A+BG) + (A+BG)^T \ P + 2I_n = 0 \tag{12b}$$

Alternately, we can write

$$\left.\begin{array}{l} \Delta A = \delta_a \ A_m \\[2mm] \Delta B = \delta_b \ B_m \end{array}\right\} \quad \text{Relative variation} \tag{13}$$

where $A_{m_{ij}} = |A_{ij}|$ and $B_{m_{ij}} = |B_{ij}|$ for all those i,j in which variation is expected and $A_{m_{ij}} = 0$, $B_{m_{ij}} = 0$ for all those i,j in which there is no variation expected. For this situation, assuming $\delta_b/\delta_a = \bar{\delta}$ is known, we get the following bound on δ_a for robust stability.

<u>Design Observation 2:</u>

The perturbed linear system is stable for all relative (or percentage) perturbations bounded by δ_a and δb if

$$\delta_a < \frac{1}{\sigma_{max}[P_m(A_m + B_m G_m)]_s} \equiv \mu r \tag{14}$$

and $\delta_b < \bar{\delta} \ \mu_r$ where P satisfies the equation (12b).

We now define, as a measure of stability robustness, an index called stability robustness index $\beta_{S.R.}$ as follows:

<u>Case a)</u>: L.H.S. of (12 or 14) is known (i.e. checking stability for given perturbation range). For this case

$$\beta_{S.R.} \overset{\Delta}{=} \mu - \epsilon_a \ (\text{or } \mu_r - \delta_a). \tag{15}$$

Thus $\beta_{S.R.} > 0$ corresponds to the stability robustness region.

<u>Case b)</u>: L.H.S. of (12 or 14) is not known (i.e. specifying the bound). For this case

$$\beta_{S.R.} \overset{\Delta}{=} \mu \ (\text{or } \mu_r). \tag{16}$$

EA-5

With this definition, the control design algorithm for robust stability consists of picking a control gain (i.e. ρ) that achieves a positive $\beta_{S.R.}$ (for case a) or high value of $\beta_{S.R.}$ (for case b).

Thus the design algorithm involves determining the index $\beta_{S.R.}$ and the costs J_y and J_u for different values of the design parameter ρ and plotting these curves. The algorithm thus provides a simple constant gain state feedback control law (using the standard optimal LQ regulator format) that is robust from stability point of view. The algorithm, for given perturbations, can be used for selecting the range of control weighting (control effort) for which the system is stability robust or alternatively for given control effort, can be used to determine the range of allowable perturbations for stability.

In the next section, we present a specific characterization of uncertainty for LSS models and use the above methodology to design a controller for the Purdue model[7] of a two dimensional LSS.

<div align="center">

Characterization of Parameter Uncertainty in L.S.S. Models and Application to Purdue Model

</div>

In L.S.S. models having the structure given by (1) the uncertainty in the modal parameters such as modal frequency dampings and mode shape slopes at actuator locations tend to increase with increase in mode number. One way of modeling this information in the uncertainty structure is given in the following (specifically we employ the relative variation format of (13))

$$\Delta A = \delta_a \begin{bmatrix} 0 & 0 & & & & \\ (x_1) & (x_1) & & & & \\ & & 0 & 0 & & \\ & & 2(x_2) & (x_2) & & \\ & & & & 0 & 0 \\ & & & & 3(x_3) & 3(x_3) \end{bmatrix} \qquad (17a)$$

$$\Delta B = \delta_b \begin{bmatrix} 0 \\ b_1 T \\ 0 \\ 2b_2 T \\ 0 \\ 3b_3 T \\ \cdot \\ \cdot \\ \cdot \end{bmatrix} \qquad (17b)$$

where (x_i) indicate the nominal entries corresponding to the ith mode. We assume $\delta_a = \delta_b$ which are not known.

With the above proposed uncertainty structure, we apply the robust control design methodology of previous section to the Purdue model[7]. The model used consists of the first five elastic modes. The numerical values of the model are given in ref. 7.

Since δ_a (and δ_b) are not known, the present design corresponds to case b in which case we pick a control gain that gives high βS.R. = μ_r. The plot of μ_r vs. ρ is given in Fig. 1. The robust control gain is the gain corresponding to ρ = 0.12.

Figs. 2 and 3 present the variation of μ_r with control effort (i.e. ρ) assuming ΔA = 0 and ΔB = 0 respectively. From these plots it can be concluded that the control effort range available for guaranteed stability for mode shape ($\Delta B \neq 0$, ΔA = 0) variation is limited in comparison to the range available for model frequency variation. Thus mode shape (slopes at actuator location) variations are more critical from control point of view than modal frequency variations.

Conclusions

Using the recently developed elemental perturbation bounds for robust stability of linear systems, a robust control design algorithm is presented for the vibration suppression problem of LSS models. The algorithm employs the characterization of parameter uncertainty in LSS models that reflects the fact that the modal data uncertainty increases with increase in mode number. The algorithm addresses only stability robustness aspect and more research is needed to incorporate performance robustness into the design procedure.

References

1. Balas, M.J.: "Trends in Large Space Structure Control Theory: Fondest Hopes, Wildest Dreams," IEEE Trans. on Autom. Control, Vol. AC-27, 1982, pp. 522-535.

2. Skelton, R.E.: "Control Design of Flexible Spacecraft," Agardograph on Theory and Applications of Optimal Control in Aerospace Systems, 1981, Ed. P. Kant.

3. Yedavalli, R.K.: "Improved Measures of Stability Robustness for Linear State Space Models," IEEE Trans. on Autom. Control, Vol. AC-30, June 1985, pp. 577-579.

4. Yedavalli, R.K.: "Perturbation Bounds for Robust Stability in Linear State Space Models," The International Journal of Control, Vol. 42, No. 6, Dec. 1985, pp. 1507-1517.

5. Yedavalli, R.K.: "Time Domain Control Design for Robust Stbility of Linear Regulators: Application to Aircraft Control," Proceedings of the 1985 American Control Conference, Boston, June 1985, pp. 914-919.

6. Kwakernaak, H. and Sivan, R.: "Linear Optimal Control Systems," Wiley Interscience, 1972.

7. Hablani, H.: "Generic Model of a Large Flexible Space Structure for Control Concept Evaluation," Journal of Guidance & Control, Vol. 4, No. 5, Sept.-Oct. 1981, pp. 558-561.
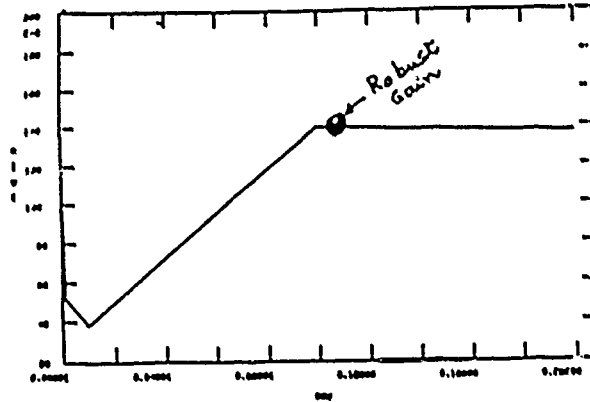
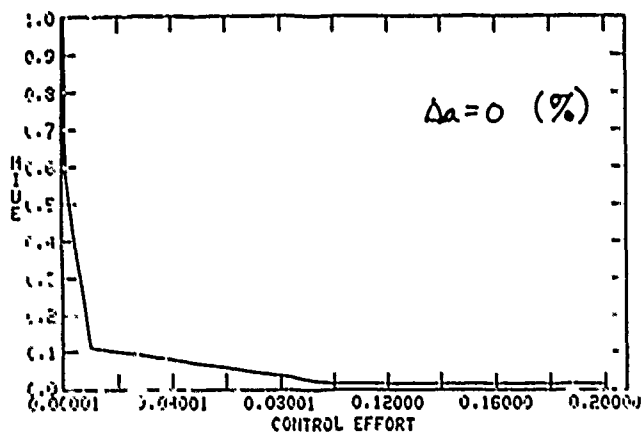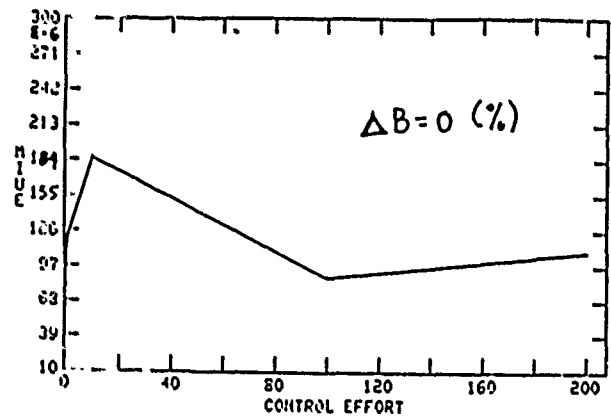## Acknowledgement

Fig. 1

Fig. 2

Fig. 3

ACTIVE AUGMENTATION
OF A PASSIVELY DAMPED
REPRESENTATIVE LARGE SPACE SYSTEM

Russell N. Gehling
Martin Marietta Denver Aerospace
Denver, Colorado

ABSTRACT

Fine-pointing and retargeting requirements of future large space structures (LSS) lead to a need for structural vibration control. The Representative System Article (RSA), developed under the Passive and Active Control of Space Structures (PACOSS) program of the Air Force and Martin Marietta Denver Aerospace, serves as an analytical test bed for passive and active vibration control techniques.

This paper demonstrates the benefits of passive damping with regard to active control implementation and retargeting performance of an LSS. A passive and active control approach was applied to a truncated model of the RSA, and performance was evaluated in terms of a small-angle slew maneuver. Feasible damping values were determined from modal strain energy calculations and applied to the RSA along with an active control system. Results demonstrate that if passive damping is designed into the system, the amount achievable in a representative future LSS will reduce the requirements for active control. Savings can be realized in terms of number of control system components and energy expenditure for vibration control.
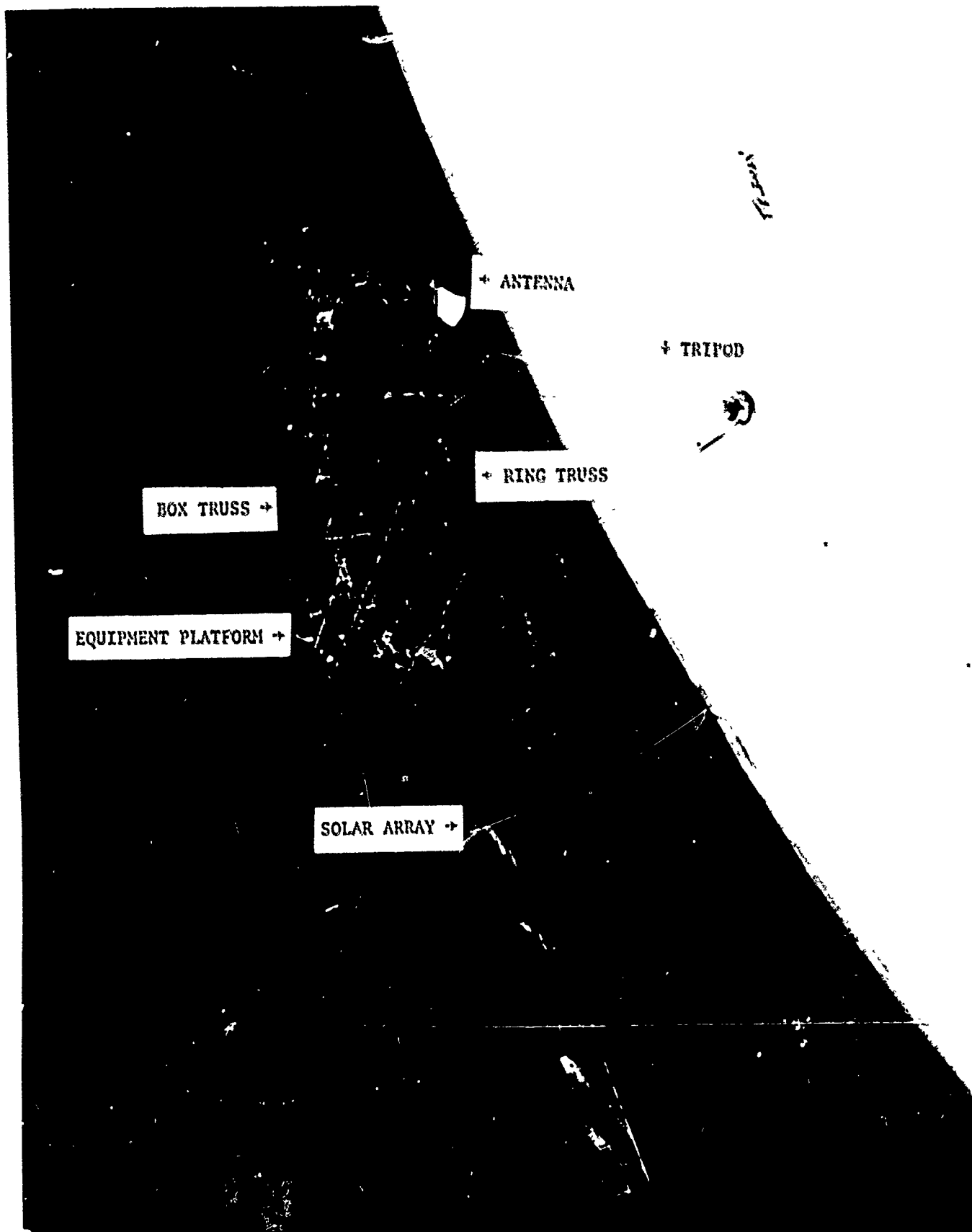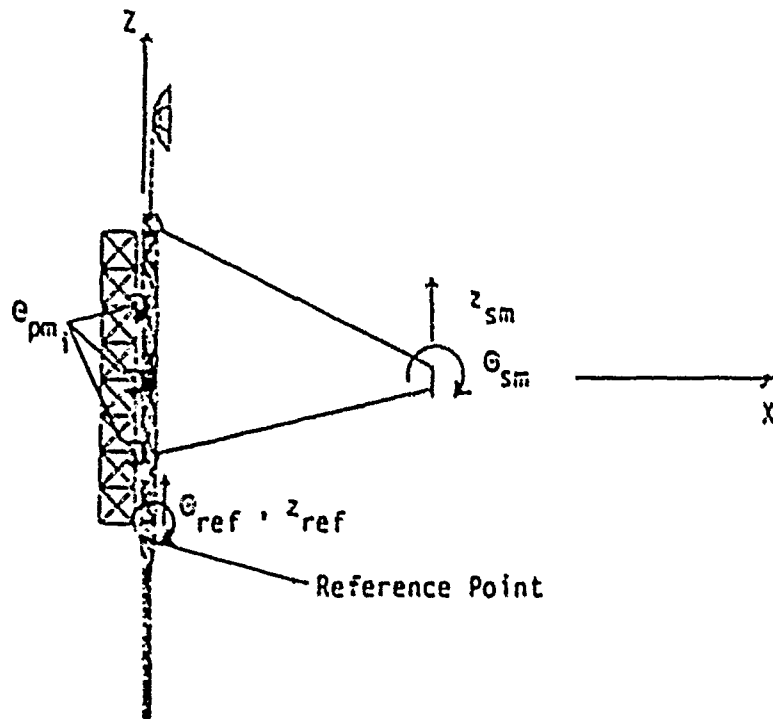
Figure 1 RSA Configuration

EB-3

$$LOS_y = (2\frac{f_s}{f_p} - 1)\theta_{ref} + \frac{2}{13}\sum_{i=1}^{13}\theta_{pm_i} - 2\frac{f_s}{f_p}\theta_{sm} - \frac{1}{f_p}(z_{ref} - z_{sm})_{flex}$$

Where,

f_s = Focal length of secondary mirror

f_p = Focal length of primary mirror

$(z_{ref} - z_{sm})_{flex}$ = Relative z deflection of secondary mirror to reference point due to structural deformation
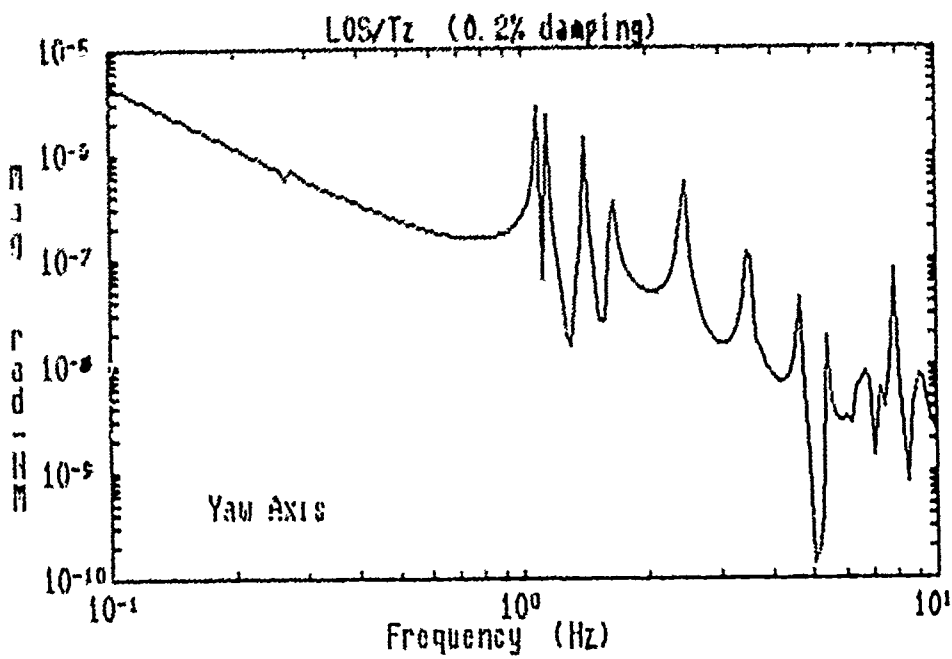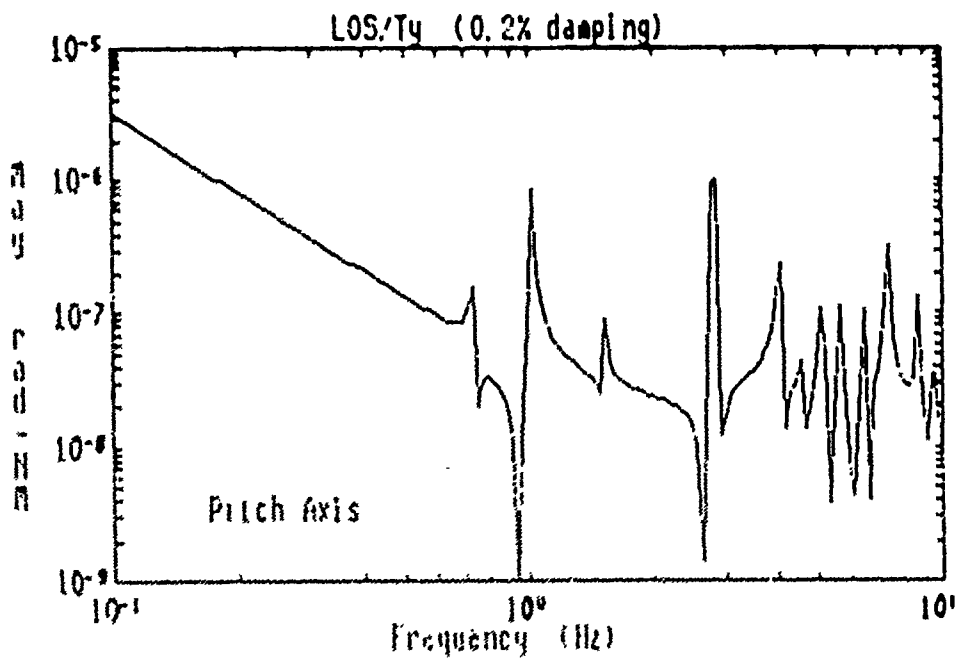
Figure 2 LOS Definition

EB-4

Figure 3   LOS/T_{ring} Transfer Functions

Analysis of the closed-loop dynamics involved the retention of important flexible modes. For purposes of this study, the ten flexible modes possessing the greatest magnitude in the pitch LOS/T_{ring} transfer function of Figure 3 were included in the pitch-axis analysis model. Similarly, nine modes were retained in the yaw-axis model. Closed-loop roots of the system with no vibration control were calculated assuming 0.2% modal viscous damping. This value of damping is typical of spacecraft structures with no passive damping augmentation. Table 1 lists the natural frequencies and damping ratios of the closed-loop system and indicates serious stability problems. The attitude control system caused a reduction in damping for several system modes and drove a few modes unstable. This situation is unacceptable. At best the system would have a lengthy settling time and high jitter level, at worst it would shake itself apart. These results indicate that even for simple attitude or slew maneuvering, a complex space system requires a sophisticated control system and/or passive damping augmentation to accomplish its mission.

Baseline system performance simulation was performed using the flexible closed-loop systems described above. As previously mentioned, LOS settling time is the measure most appropriate for system evaluation. Maneuver or slew performance is closely associated with settling time. LOS response to a 0.01 radian slew maneuver generated by the attitude control system is shown in Figure 4. Slewing about the pitch axis with 0.2% modal damping shows a long settling time due to the response of several modes while the yaw-axis slew response indicates instability in the nominal system.

The data presented in Figure 4 and Table 1 indicate that vibration control is required if the RSA is to achieve acceptable retargeting performance. The following sections present an analytical demonstration of vibration control design for the RSA analysis models described above using both active and passive control. Performance results using this control approach are compared with two alternate approaches: active control alone, and passive damping alone.

Table 1 Nominal System Closed-Loop Modal Frequencies and Damping Ratios

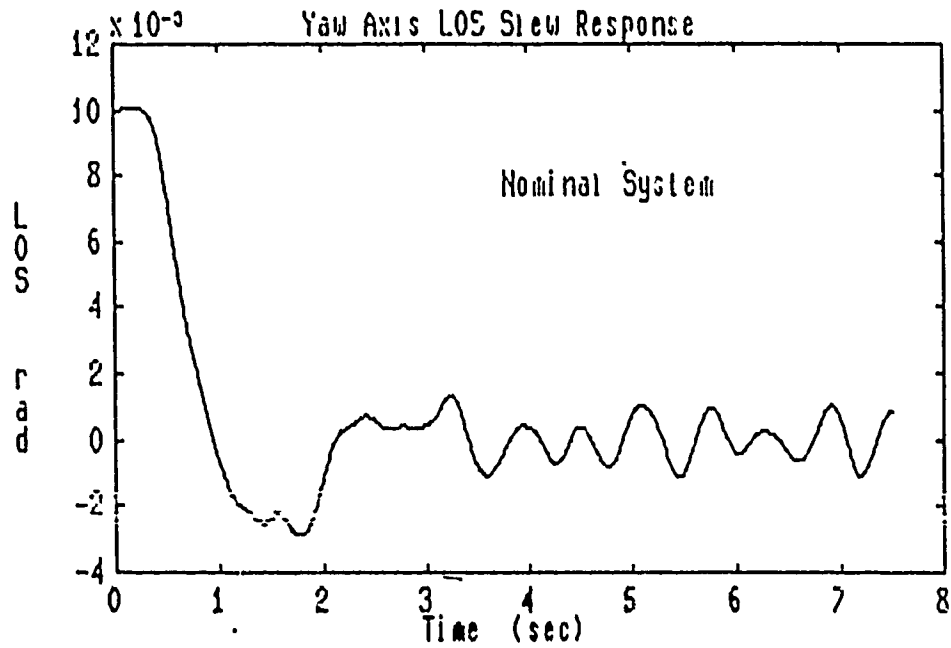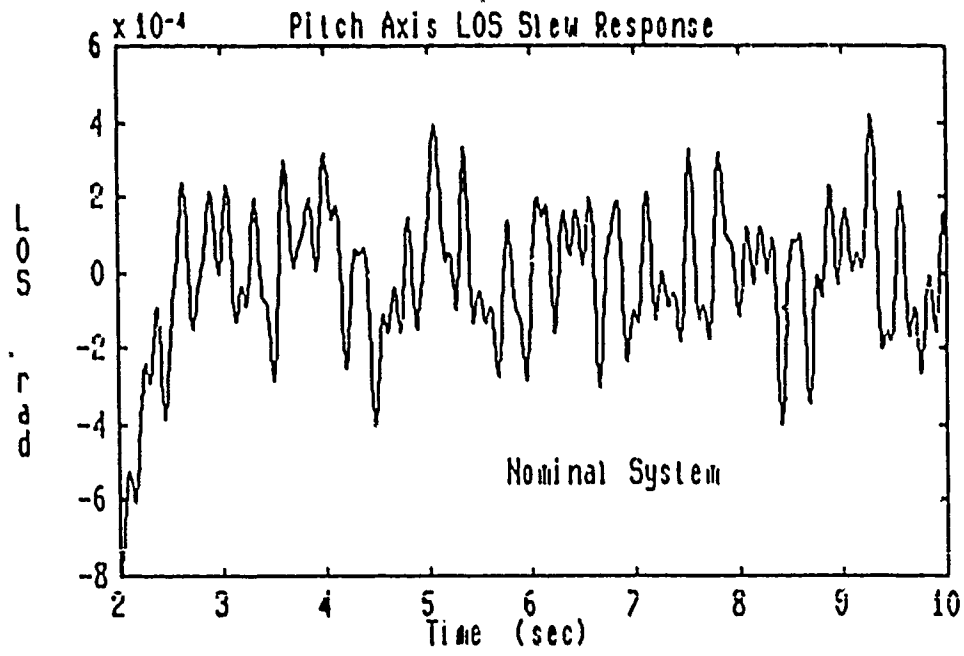| PITCH-AXIS MODEL			
MODE NO.	MODE NO. IN FULL RSA MODEL	f_n(Hz)	ζ (%)
1	RB/Filter	0.454	57.6
2	RB/Filter	0.550	84.1
3	23	0.765	1.52
4	30	0.976	1.18
5	48	1.51	1.02
6	129	2.87	-0.19
7	158	·4.04	-0.05
8	185	5.12	0.08
9	187	5.68	0.16
10	191	6.45	0.11
11	201	7.38	-0.09
12	206	8.77	0.45
YAW-AXIS MODEL			
1	RB/Filter	Overdamped	
2	RB/Filter	0.370	95.0
3	RB/Filter	0.429	34.6
4	RB/Filter	0.874	70.1
5	33	1.08	0.05
6	34	1.14	0.13
7	43	1.44	-0.64
8	51	1.67	-2.0
9	97	2.44	0.23
10	142	3.50	0.33
11	183	4.66	0.22
12	186	5.45	0.37
13	204	7.90	0.06

EB-7

Figure 4   Nominal System LOS Slew Response

VIBRATION CONTROL APPROACH

As previously mentioned, LOS settling time is the critical performance measure with regard to RSA retargeting. For purposes of comparison, an LOS vibration amplitude of 100 μrad (zero-peak) was selected as the level at which the LOS was considered settled. The slew angle was nominally selected to be 100 mrad and the maneuver torque was generated by the RSA attitude control system. The rigid body performance in this scenario gives a retargeting time of approximately 3.25 and 5.0 seconds for the pitch and yaw models, respectively. However, as shown in Figure 4, the flexible systems with nominal damping (and mild instability) require vibration control to achieve the required LOS settling performance.

Approaching vibration damping through both passive and active control is an attractive option in the quest to achieve rapid retargeting through fast LOS settling. The approach used here involved first applying feasible passive damping to the RSA. Modal damping ratios were determined based upon modal strain energy (MSE) distribution and several assumptions regarding the passive damping treatments. The modal strain energy approach is described in Reference 8. Certain elements of the RSA were designed to facilitate viscoelastic damping technology. Specifically, the diagonals of the box-truss and equipment platform are suitable for application of the extensional shear damper described in Reference 8, while the tripod legs and antenna support legs can be damped through a constrained viscoelastic layer treatment.

The calculation of approximate damping ratio of a specific mode is as follows:

$$\frac{1}{2} \sum_{i=1}^{NS} (P_{1i})(P_{2i})(MSE_i)(\eta_i) = \zeta$$

where NS = number of element sets

P_{1i} = fraction of MSE in damped elements

P_{2i} = fraction of element strain energy in viscoelastic material

MSE_i = fraction of MSE in element set

η_i = loss factor of viscoelastic material

ζ = modal damping ratio

Table 2 lists the values assumed for the quantities listed above. These values are consistent with results documented in Reference 8. The modal damping values for the RSA analysis models, as calculated from the above equation, are listed in Table 3.

The addition of passive damping on the order of 5% typically results in response dominated by one or two modes which require further damping. The additional damping is provided through an active control system specifically designed to damp the remaining dominant modes.

Table 2 Assumed Values for Damping Ratio Calculation

	BOX TRUSS DIAGONALS	EQUIPMENT PLATFORM DIAGONALS	TRIPOD LEGS	ANTENNA SUPPORT TUBES
P_1	0.5	0.5	1.0	1.0
P_2	0.9	0.9	0.1	0.1
η	0.7	0.7	0.7	0.7

Table 3 Modal Damping Ratios from Passive Control

MODE NO.	PITCH-AXIS MODEL (%)	YAW-AXIS MODEL (%)
3	2.2	–
4	2.8	–
–	2.3	11.0
6	13.0	7.0
7	2.7	2.6
8	2.6	3.2
9	6.5	3.7
10	8.3	5.8
11	6.3	3.3
12	8.1	4.8
13	–	5.4

The active control algorithm implemented was a form of modal space control using colocated sensors and actuators. As noted in Reference 9, the use of velocity feedback with colocated sensors and actuators gives an unconditionally stable system (assuming ideal sensors and actuators). However, observation and control spillover effects can seriously degrade closed-loop performance. In order to avoid spillover into the rigid body mode, the algorithm was cast such that only relative velocities were sensed and no net torque was applied to the system. The sensor signal was thus the relative angular velocity between each vibration control sensor point and the angular velocity of the reference attitude control sensor located on the ring truss. Similarly, a torque was applied at the attitude control system reference point which exactly negated the torques applied at the vibration control points, so that zero net torque was applied to the system. The feedback gain matrix is thus given by:

$$K = -\left[\phi_{REL}\right]_C^{-T} \left[\,2\zeta\omega_n\,\right]_C \left[\phi_{REL}\right]_C^{-1}$$

where $\left[\phi_{REL}\right]_C$ is the relative open-loop modal matrix and $\left[\,2\zeta\omega_n\,\right]_C$ is the desired diagonal modal damping matrix for the controlled modes. Note that there must be as many sensor/actuator pairs as controlled modes in the approach. Also, the control actions involved torques alone since linear, continuous force actuators (e.g., proof mass actuators) require excessive mass or stroke for low frequency, high force operation.

As previously mentioned, the damped system will typically require active control targeted for only one or two modes. Therefore, a small number of sensor/actuator pairs are required. Sensor/ actuator locations were selected so as to achieve acceptable values in the gain matrix K. This was accomplished through determining the required actuator locations from a set of over 300 candidate locations which give $\left[\phi_{REL}\right]_C$ the largest determinant.

The active control was implemented through the following rather simple relation:

$$u_C = K y_{rel}$$

Results in the form of closed-loop damping ratios and LOS slew response are given in the next section and compared with the performance of systems using the passive damping alone and the active control alone with more modes targeted for control.

PERFORMANCE RESULTS AND COMPARISON

Design of the passive and active control system first involved analysis of the RSA with passive damping alone. The LOS response of the passively damped pitch and yaw analysis models is shown in Figure 5. Note that the time scale in the LOS response figures starts at the initiation of the slew maneuver. This figure shows that, as expected, the response is dominated by one or two relatively low frequency modes. Therefore, the active control was designed to provide an additional 10% damping to modes 3 and 4 in the pitch-axis model and 5% damping to modes 7 and 8 of the yaw-axis system.
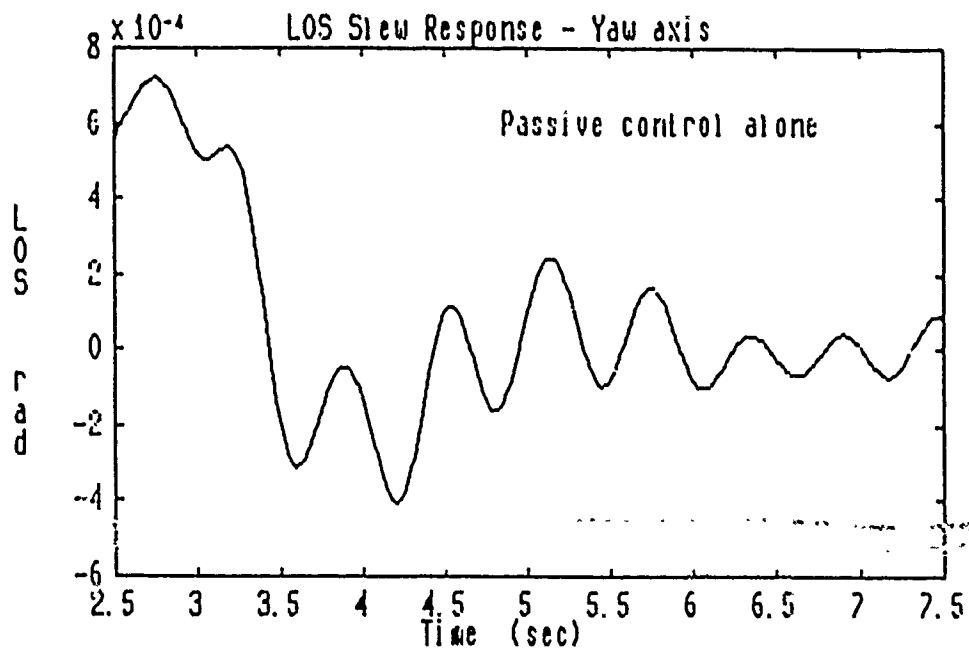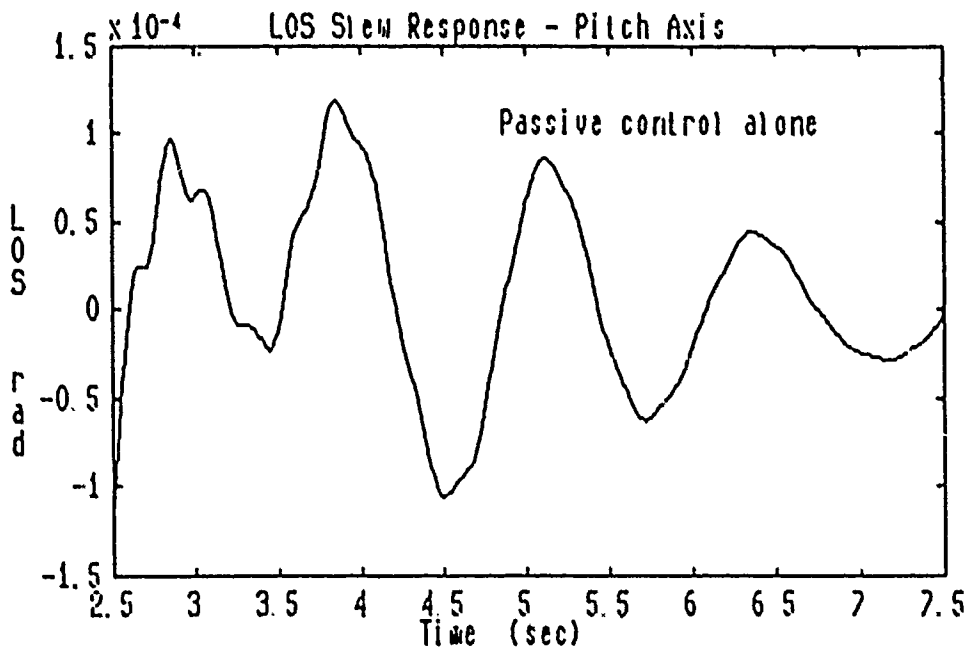
Figure 5   LOS Slew Response — Passive Damping Alone

For purposes of comparison, a system using only active control was designed. In this case, the modal space control method previously described was used to provide acceptable LOS settling performance. Consideration of the transfer function of Figure 3 and the nominal slew response indicated that six modes required active damping in both the pitch and yaw models. Table 4 lists these modes and the design damping ratio.

Table 5 lists the closed-loop damping ratios for the passive and active system along with those of the RSA controlled by passive or active means alone. Note that spillover has a very significant effect on the performance of the modal space control approach. Several modes not intended to receive active damping augmentation are significantly damped, while some controlled modes possess damping ratios which are less than the design value. This can be interpreted as an inefficient use of control energy in that control effort is used to damp modes of little importance to system performance.

Figure 6 shows the LOS slew response of the pitch-axis model using active and passive control and active control alone. The equivalent yaw-axis response is shown in Figure 7. These figures demonstrate that the two approaches yield equivalent system performance. In both cases, the settling time approaches the rigid body retarget time which is the best achievable, given the RSA attitude control system.

Further benefits of passive damping are seen with the consideration of control energy expenditure or the total work done by the active vibration control system during the slew maneuver. Table 6 lists the work done by the active control and shows significant reduction in control energy expenditure when passive damping is utilized. Thus, the passive and active control system meets the performance requirement using fewer sensor/actuator pairs and less energy than active control alone.

Table 4 Modes Requiring Control in Active Control Alone Approach

PITCH-AXIS MODEL		YAW-AXIS MODEL	
MODE NO.	ζ_{DESIGN} (%)	MODE NO.	ζ_{DESIGN} (%)
3	20	5	10
4	10	6	10
6	10	7	10
7	10	8	10
8	10	9	5
11	10	10	5

Table 5 Closed-Loop Damping Ratios, ζ(%)

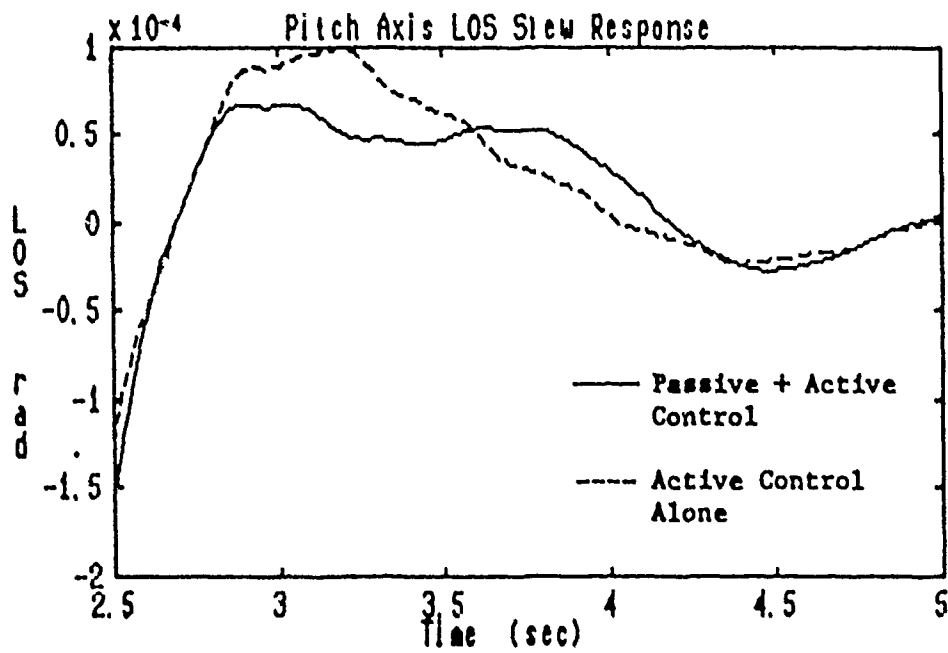|	PITCH-AXIS MODEL				YAW-AXIS MODEL		
MODE NO.	PASSIVE CONTROL ALONE	ACTIVE CONTROL ALONE	PASSIVE + ACTIVE CONTROL	MODE NO.	PASSIVE CONTROL ALONE	ACTIVE CONTROL ALONE	PASSIVE + ACTIVE CONTROL
1	57.5	53.0	57.0	1	Overdamped	98.5	Overdamped
2	84.2	91.5	86.0	2	34.8	36.2	34.8
3	3.7	16.4	13.1	3	95.0	95.7	94.9
4	4.1	9.1	12.1	4	70.2	0.7	70.1
5	3.4	15.3	16.5	5	11.4	9.6	11.5
6	12.6	4.6	14.0	6	7.2	1.4	7.3
7	2.6	8.9	4.6	7	1.9	9.2	6.9
8	2.7	5.2	8.2	8	1.1	7.2	5.7
9	6.7	2.8	7.4	9	3.9	5.2	4.5
10	8.3	Overdamped	85.4	10	6.1	5.3	11.7
11	6.2	8.5	6.4	11	3.5	1.6	3.5
12	8.5	Overdamped	9.0	12	5.2	3.3	5.4
				13	5.5	Overdamped	7.7

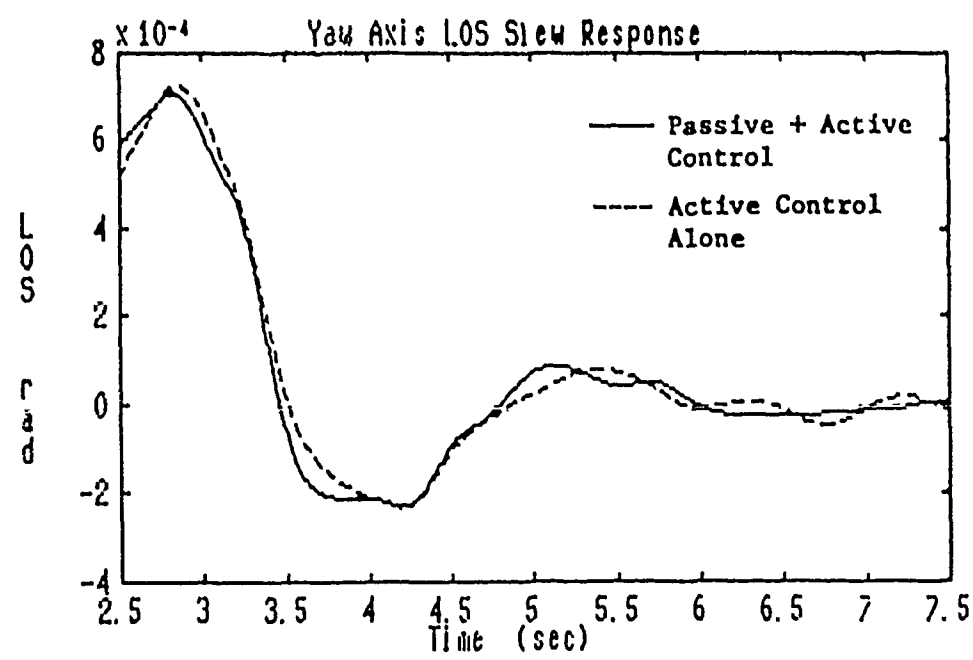**Figure 6 LOS Slew Response - Pitch Axis**

Figure 7 LOS Slew Response - Yaw Axis

EB-15

Table 6 Work Done by Active Control Systems
(0-5 sec Interval of Slew Maneuver)
(N-m)

	PITCH-AXIS MODEL	YAW-AXIS MODEL
Active Control Alone	13.4	76.4
Active + Passive Control	4.4	5.2
% Change	-67%	-93%

CONCLUSIONS

The results presented above demonstrate that the degree of passive damping which can be designed into future LSS can play a major role in improving retargeting performance and simplifying active vibration control systems. Specifically, for a given slew situation and performance requirement, implementation of both passive and active damping in an integrated control approach gives the desired performance while reducing the number of active control components. Also, the total energy expenditure required for vibration control is significantly reduced when passive damping is designed into the system. This can lead to more robust and reliable systems which may be less expensive than those required for active control alone. Table 7 summarizes the advantages and disadvantages, as shown by the analysis results, of the three approaches considered.

This study indicates that much experimental work on the application of vibration control to complex structures remains to be done with regard to the actual implementation of both active and passive control techniques. This conclusion is amplified in light of the fact that ideal sensors and actuators were used in the control design and analysis. Sensor/actuator dynamics must be considered when attempting to achieve the stringent performance suggested for future LSS.

The RSA serves as an analytic test bed for passive and active control techniques and has shown the difficulties which arise due to the presence of several flexible modes in or near the control bandwidth. This high modal density also gives rise to significant control spillover into flexible modes not intended to be damped. However, if a structure were designed to facilitate passive damping, as was the RSA, the difficulties associated with active control design can be reduced or eliminated.

Table 7

ADVANTAGES AND DISADVANTAGES OF
CONTROL APPROACHES CONSIDERED

	ADVANTAGES	DISADVANTAGES
ACTIVE CONTROL ALONE	o Vibration damping can be approached as an add-on measure o Colocated sensors/actuators give unconditionally stable system (assuming ideal sensors/actuators) o Meets performance requirements	o Many sensors/actuators required, in this case, 6 colocated pairs per axis o Damping goal is not achieved due to spillover o Higher energy and power requirements
PASSIVE CONTROL ALONE	o Unconditionally stable o Robust and reliable	o Fails to meet performance requirements assuming present damping technology o Must be designed into structure
PASSIVE + ACTIVE CONTROL	o Few sensors/actuators (2 per axis) o Colocated sensors/actuators give unconditionally stable system (assuming ideal sensors/actuators) o Lower energy and power requirements o Reliable o Meets performance requirements	o Passive component must be designed into structure

REFERENCES

1. Gehling, R. N., and Morgenthaler, D. R., "Representative System Report," MCR-84-541, Martin Marietta Denver Aerospace, Denver, Colorado, November 1985.

2. Hallauer, W. L., Jr., Skidmore, G. R., and Mesquita, L. C., "Experimental-Theoretical Study of Active Vibration Control," Proceedings of 1st International Modal Analysis Conference, 1982, pp. 39-45.

3. Schaechter, D. B., and Elred, D. B., "Experimental Demonstration of the Control of Flexible Structures," Journal of Guidance, Control, and Dynamics, Vol. 7, No. 5, Sept.-Oct. 1984, pp. 527-534.

4. Juang, Jer-Nan, Horta, L. G., and Robertshaw, H. H., "A Slewing Control Experiment for Flexible Structures," Presented at the Fifth VPI&SU/AIAA Symposium on Dynamics and Control of Large Structures, Blacksburg, Virginia, June 12-14, 1985.

5. Hallauer, W. L., Jr., Skidmore, G. R., and Gehling, R. N., "Modal Space Active Damping of a Plane Grid: Experiment and Theory," Journal of Guidance, Control and Dynamics, Vol. 8, No. 3, May-June 1985, pp. 366-373.

6. Russillo, C. M., "A Study of Actuator Reconfiguration and Related Implementation Issues in Active Vibration Damping," MS Thesis, Virginia Polytechnic Institute and State University, February 1983.

7. Gehling, R. N., and Harcrow, H. W., "Effects of Passive Damping on Active Control Design," Presented at 26th AIAA/ASME/ASCE/AHS Structures, Structural Dynamics, and Materials Conference, Orlando, Florida, 15-17 April 1985. AIAA-85-0776-CP.

8. White, C. W., "Analysis of Damped Twin Towers," The Shock and Vibration Bulletin, No. 55, Part 1, June 1985, pp. 119-130.

9. Skidmore, G. R., "Experimental-Theoretical Study of Velocity Feedback Damping of Structural Vibration," PhD Dissertation, Virginia Polytechnic Institute and State University, May 1985.

ACKNOWLEDGMENT

ACTIVE CONTROL FOR VIBRATION DAMPING

Lt P.J. Lynch
Siva S. Banda

Flight Dynamics Laboratory AFWAL/FIGC
Wright Patterson Air Force Base OH 45433

Active control laws are developed for an LSS-type structure
to damp vibrations. High frequency modelling uncertainties
lead to the necessity for a robust control design. The Linear
Quadratic Gaussian with Loop Transfer Recovery (LQG/LTR)
control design technique is a particular robust design technique
selected for use in designing a damping control system. A
summary of LQG/LTR is given and numerical example using
a two bay truss is presented.

INTRODUCTION

The vibration damping problem is an important aspect of the overall control problem of Large Space Structures (LSS). Vibrations will arise in the structure from external disturbances or from commanded maneuvers like slewing. The amplitude of the vibrations must be controlled to insure the LSS can continue to perform its prescribed mission and not incure structural damage. This requires the reduction of the structural vibrations to zero, or to an acceptable level, within a given time. Techniques to accomplish this damping are often separated into two broad categories; passive damping and active damping. Passive damping[1,2,3] refers to the LSS's ability to damp its own osscillations as a result of its structural design, material properties or the effect of additional devices like coatings and elastomers. Active control implies the use of a feedback control system which incorporates a sensing of structural vibrations and calculation of the control input signals for actuators to damp the vibrations present. While the best solution to the vibration damping problem most likely uses a combination of active and passive damping techniques, this paper assumes a fixed level of damping exists throughout the structure and then explores the use of an active control system. The Linear Quadratic Gaussian with Loop Transfer Recovery (LQG/LTR) technique is used to develop a robust vibration control system.

Use of an active control system provides significant design freedom. Active systems can be designed which not only damp vibrations, but simultaneously accomplish maneuvers like pointing and tracking, which may be requirements of the LSS. Additionally, control systems can be developed to reject disturbances that can be expected in an operational environment. These disturbances may include thermal effects, gravity gradient or the effect of rotating surfaces of the LSS.

The increased design freedom gained through the use of active control does not come without expense. A controller designed to accomplish specific control objectives must be developed based upon a mathematical model of the large space structure. Controllers are often designed to meet system objectives based on a low-order design model. This is a result of computational considerations and the inaccuracies associated with finite-element descriptions of high frequency structural behavior. The more closely the model represents the true system, the better the chance of obtaining a controller that accomplishes the stated control objectives. Differences between the design model and the actual system can lead to faulty performance or even instability. As a result, modelling error considerations and the influence of disturbances previously mentioned lead to the requirement for a robust vibration control system.

Robustness[4,5,6] of control systems examines the performance of the control system with respect to uncertainties present. These uncertainties may include differences between the design model and the actual system (plant uncertainties) and the effects of various disturbances which lead to system uncertainties. Robustness of actively controlled systems can be seperated into two broad categories; stability

robustness and performance robustness. Closed-loop systems which remain stable in the face of uncertainties are stability robust. A closed-loop system that maintains an acceptable level of performance in the face of uncertainties is described as performance robust. Although both are desirable, stability robustness is paramount since performance can't even be considered without stability.

The purpose of this work is to demonstrate the application of the Linear Quadratic Gaussian with Loop Transfer Recovery (LQG/LTR) control design technique in arriving at a robust vibration control system. Following this introduction, Section 2 presents a general description of the structural modelling and control objectives used in this study. Section 3 discusses the basics of the LQG/LTR control design technique. This includes a portion addressing the mathematical tools necessary for computer implementation. References are provided for more in-depth coverage of the LQG/LTR method. Section 4 uses an LSS-type structure in the form of a cantilever beam to demonstrate the use of LQG/LTR. Conclusions appear in Section 5.

STRUCTURAL MODELLING AND CONTROL OBJECTIVES

Finite element methods are used to arrive at a mathematical description of the LSS[7]. The LQG/LTR design technique requires a linear state-space representation of the plant's dynamics. Most problems have a high-order truth model which describes the actual system reasonably well, with some degradation at high frequencies. Large order systems present a problem computationally to the control design engineer from both a design and implementation viewpoint. As a result, low-order models are often used for control design purposes. A model reduction is required to arrive at this low-order design model. Numerous techniques exist to accomplish this model reduction[8,9,10]. The scope of this work does not permit development of the many issues involved in model reduction. Rather this work focuses more on the requirements placed on control system design following a reduction. The differences between the design model and the truth model lead to additional plant uncertainties which must be tolerated by the robust control system. Control objectives must ultimately be achieved against the truth model and even more importantly, the actual system.

The standard second order matrix differential equation, developed through finite element methods, which governs the flexural vibrations of a structure is given in equation (1).

$$[m]\ddot{r}(t) + [c]\dot{r}(t) + [k]r(t) = F(t) \qquad (1)$$

Here, the mass $[m]$, damping $[c]$, and stiffness $[k]$ matrices are n×n dimensional and describe the structure of the LSS. These are a function of the LSS's design and are assumed to be constant matrices for the purposes of this study. The vector $r(t)$ is n×1 dimensional and represents the structure's physical coordinates.

For this study, an active control system will be designed to damp an initial

vibration in the structure. The study is simplified by considering only responses to initial conditions as opposed to persistent excitation or some combination of inputs and initial conditions. This is done simply to limit the scope of the work. A rich initial condition will serve to demonstrate the salient features of the damping control system. Since this is an unforced vibration, $[F(t)]$ on the right hand side of equation (1) is simply the control input distribution matrix $[b]$ multiplied by the control signal $u(t)$. The $[b]$ matrix is n×m dimensional and describes the placement of the m actuators and their effect on the structure. This results in equation (2) relating the structure's physical coordinates to the actuator's control inputs.

$$[m]\ddot{r}(t) + [c]\dot{r}(t) + [k]r(t) = [b]u(t) \tag{2}$$

A state-space representation for this system of n second-order differential equations may be written by selecting the (2n×1) state vector $\tilde{x}$ as

$$\tilde{x} = \begin{bmatrix} \dot{r}(t) \\ r(t) \end{bmatrix}_{2n \times 1} \tag{3}$$

The first n elements of the state vector $\tilde{x}$ are physical rates $\dot{r}(t)$ and the last n elements of $\tilde{x}$ are physical displacements $r(t)$. This results in the state-space realization of equation (4)

$$\dot{\tilde{x}} = \tilde{A}\tilde{x}(t) + \tilde{B}u(t) \tag{4}$$

with

$$\tilde{A} = \begin{bmatrix} [-m^{-1}c] & [-m^{-1}k] \\ [I] & [0] \end{bmatrix}_{2n \times 2n} \tag{4a}$$

$$\tilde{B} = \begin{bmatrix} [-m^{-1}b] \\ [0] \end{bmatrix}_{2n \times m} \tag{4b}$$

For this study, we assume that the system's actuators and sensors are colocated, although this is *not* a requirement of the LQG/LTR technique. It is also assumed that the sensors measure the physical displacements of the LSS. This results in the measurement equation being

$$y = \tilde{C}\tilde{x} \tag{5}$$

with

$$\tilde{C} = \begin{bmatrix} 0 & b^T \end{bmatrix}_{m \times 2n} \tag{5a}$$

Modal analysis[7] is used to transform the set of simultaneous equations given in (4) into an independent set of equations. To achieve decoupling of the equations, we must assume that the damping matrix $[c]$ is a linear combination of the mass $[m]$ and stiffness $[k]$ matrices as shown in equation (6).

$$[c] = \alpha[m] + \beta[k] \tag{6}$$

EC-4

A coordinate transform between the structure's physical coordinates (r) and the modal (or principal) coordinates (η) is given in (7).

$$r = T\eta \tag{7}$$

Here, T is the matrix of eigenvectors obtained from the solution of equation (8).

$$\omega^2[m]T = [k]T \tag{8}$$

These eigenvectors make up the modal matrix and determine the mode shapes. The corresponding values of ω which solve (8) are the modal frequencies or eigenvalues. Substitution of equation (7) into equation (4) results in the state-space representation in modal coordinates of equation (9).

$$\dot{x} = Ax + Bu \tag{9}$$

where

$$A = \begin{bmatrix} [-T^{-1}m^{-1}cT] & [-T^{-1}m^{-1}kT] \\ [I] & [0] \end{bmatrix} \tag{9a}$$

$$B = \begin{bmatrix} [-T^{-1}m^{-1}b] \\ [0] \end{bmatrix} \tag{9b}$$

The state vector (x) is defined as

$$x = \begin{bmatrix} \dot{\eta} \\ \eta \end{bmatrix} \tag{10}$$

Orthoganality of the modal vectors and the definition in equation (11)

$$[-T^{-1}m^{-1}cT] = -2\varsigma\omega_i \tag{11}$$

reduces the A matrix to the form of (12).

$$A = \begin{bmatrix} [-2\varsigma_i\omega_i] & [-\omega_i^2] \\ [I_n] & [0] \end{bmatrix} \tag{12}$$

Each of the four entries in the A matrix of (12) are n×n dimensional and are diagonal. The output equation (5) becomes

$$y = Cx \tag{13}$$

with

$$C = \begin{bmatrix} 0 & b^T T \end{bmatrix} \tag{13a}$$

The size of the plant's truth model must now be reconciled. For control design purposes, a reasonable size model is desirable. Individual perceptions of what is reasonable will vary with the system type, available computational power and the designer's experience. For our purposes, a model reduction will be performed based on an examination of the second-order modes[9]. These indicate the relative combined controllability and observability of the system modes for the given set of inputs and outputs. Modes are selected for retention in the design model that are most

controllable and observable. The system is then reformulated as in (14) where the dynamics in the upper portion will be retained in the design model.

$$\begin{bmatrix} \dot{z}_1 \\ \dot{z}_2 \end{bmatrix} = \begin{bmatrix} A_{11} & A_{12} \\ A_{21} & A_{22} \end{bmatrix} \begin{bmatrix} z_1 \\ z_2 \end{bmatrix} + \begin{bmatrix} B_1 \\ B_2 \end{bmatrix} u \qquad y = \begin{bmatrix} C_1 & C_2 \end{bmatrix} \begin{bmatrix} z_1 \\ z_2 \end{bmatrix} \qquad (14)$$

By assuming small changes occur in z_2 ($\dot{z}_2 = 0$), the states of z_2 may be solved for in terms of x_1. This residualization results in the reduced-order design of (15)

$$\dot{x}_r = A_r x_r + B_r u \qquad y = C_r x_r + D_r u \qquad (15)$$

with

$$A_r = \begin{bmatrix} A_{11} & A_{12} A_{22}^{-1} A_{21} \end{bmatrix} \qquad (15a)$$

$$B_r = \begin{bmatrix} B_1 - A_{12} A_{22}^{-1} B_2 \end{bmatrix} \qquad (15b)$$

$$C_r = \begin{bmatrix} C_1 - C_2 A_{22}^{-1} A_{21} \end{bmatrix} \qquad (15c)$$

$$D_r = \begin{bmatrix} -A_{22}^{-1} B_2 \end{bmatrix} \qquad (15d)$$

Note that although the full-order model was assumed not to have a direct-feed term (D matrix), the reduced-order model may have the outputs directly effected by the inputs.

Control design takes place using the low-order design model of equation (15). The objective of the control system is to reduce the amplitude of vibrations to zero or to an acceptable level in a given time. This will most likely require integral action to achieve the desired tracking characteristics and zero steady-state error. The controller must take into account the fact that differences exist between the design model and the truth model. The robustness of designs are measured in terms of multivariable gain and phase margins[11].

The vibration control system in this paper will be evaluated based upon its ability to damp a vibration to .1 percent of its initial amplitude. Factors which will be considered in evaluation include the settling time, control power requirements relative to the initial condition and overall system robustness. A sufficiently rich initial condition will be used to insure significant excitation of the structure.

LQG/LTR DESIGN METHOD

The Linear Quadratic Gaussian with Loop Transfer Recovery (LQG/LTR) method is just one of several robust control design techniques that have been developed in recent years. The technique was formulated in an attempt to regain the desireable stability margins associated with linear quadratic regulators (LQR) that are lost when a Kalman filter is introduced in a linear quadratic gaussian (LQG) formulation[12]. Doyle and Stein developed a procedure called robustness recovery[13] that allows LQG designs to approach the guaranteed stability margins characteristic of full-state designs. The LQG/LTR method is based on robustness recovery, and was formalized by Stein and Athans[14]. Applications of the technique can be found in References 15 through 17.

The standard LQG problem is well known and has been described in detail[18]. LQG/LTR modifies the conventional LQG problem into a loop-shaping problem. Figure 1 and equations (16) through (19) present the problem set-up.
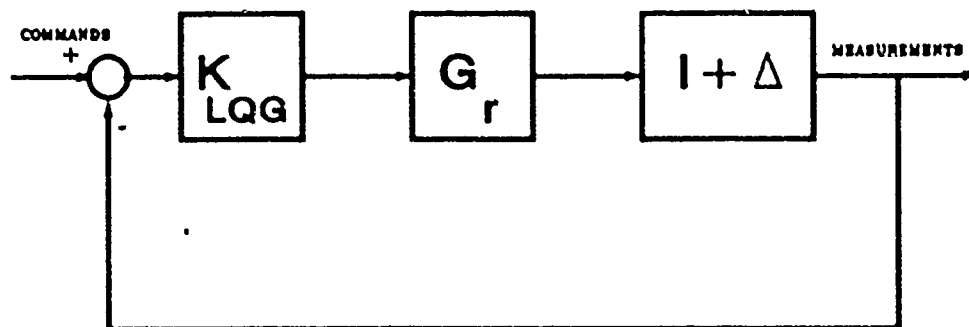
Figure 1. LQG/LTR Problem Block Diagram

$$\dot{x} = Ax + Bu + \Gamma\xi \qquad (16)$$

$$y = Cx + Du + \mu In \qquad (17)$$

$$z = Hx \qquad (18)$$

$$J = E\left\{\lim_{T\to\infty} \frac{1}{T}\int_0^T \left(z^T z + \rho u^T u\right)\right\} \qquad (19)$$

The matrix K_{LQG} in Figure 1 is the controller transfer function matrix obtained by the LQG/LTR methodology. The plant G_r is the reduced-order design model derived from the methods of Section 2.

$$G_r(s) = C(sI - A)^{-1}B + D \qquad (20)$$

$$G = C\Phi B + D \qquad (20a)$$

The subscipts and the Laplace variable s have been dropped for ease of notation. Similarly, Φ is used in equation (20a) in place of $(sI - A)^{-1}$ for convience. The starting point for an LQG/LTR design is the design model's quadruple [A,B,C,D] as shown in equations (16) and (17). In addition, equation (16) includes a noise input distribution matrix (Γ) and a process noise (ξ). Similarly, equation (17) includes a sensor noise distribution matrix (μI) and a sensor noise (n). LQG/LTR considers these noise distribution matrices as tuneable parameters to achieve the desired loop shapes to meet control objectives.

The performance index (J) includes the selected response variables (z) of equation (19) and another free parameter (ρ) which weights the level of control effort. In summary, the LQG/LTR procedure contains four design parameters and a recovery parameter (discussed shortly) which are tuned to achieve desired loop shapes. These include Γ, μ, H, ρ and the recovery parameter. The selection of these parameters in the design process produces the loop-shaping effect. This can be associated with the injection of noise into the system of varying strengths to achieve desired system characteristics.

Given the LSS plant description G, we desire to design a controller (K) to meet the vibration control system objectives. These objectives will be represented in the frequency domain as bounds on the loop transmission GK. The concept of representing the characteristics of a multivariable system through singular values is key to the LQG/LTR methodology[5]. By definition, the singular values of a matrix [P] are given by equation (21).

$$\sigma_i(P) = \sqrt{\lambda_i(P \cdot P)} \qquad (21)$$

The singular values of the loop transmission $\sigma_i(GK)$ are bounded in the frequency domain based on performance requirements and a representation of the system's uncertainty. System uncertainty can be represented as an output multiplicative perturbation[5] $(I + \Delta(s))$ as shown in the block diagram of Figure 1. Uncertainty is reflected at either the input or output of the plant. The LQG/LTR procedure effectively 'breaks' the loop where this uncertainty is assumed to exist and attempts to recover good stability margins at that point. Typical bounds developed from this uncertainty description and performance requirements are shown on the singular value plot of Figure 2.
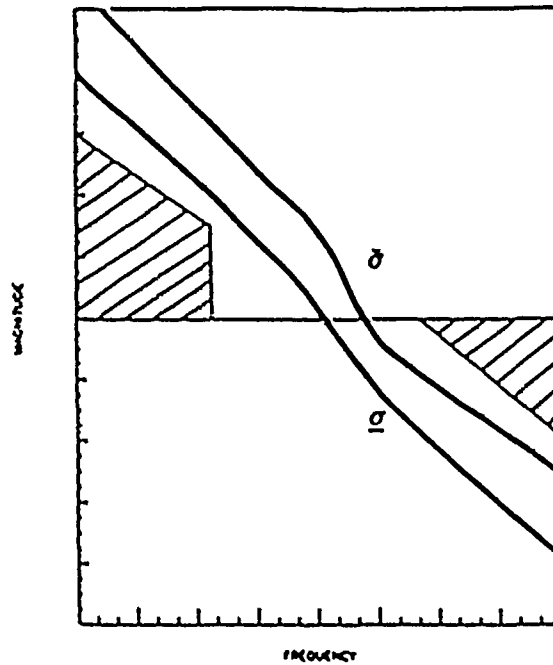
Figure 2. Desired Loop Shapes and Performance and Robustness Bounds

Only the minimum ($\underline{\sigma}$) and maximum ($\bar{\sigma}$) singular value plots of the hypothetical system are shown. These are sufficient since we are concerned with bounds and all other singular values will be bounded if the maximum and minimum singular values are. The system will actually have as many singular values as the lesser of the number of inputs and outputs. In the case of a single-input single-output system, only one singular value plot exists which is identical to the Bode magnitude plot.

The high frequency bound on the system's singular values is related to the description of system uncertainty. The major contribution to uncertainty is usually at high frequencies due to modelling errors and sensor dynamics. This is especially true in an LSS problem where high frequency modes are often neglected in a design model following model reduction. In the case of an output multiplicative System uncertainty is described by a bound $l(\omega)$ on an output multiplicative perturbation matrix $(\Delta(s))$ as shown in equation (22).

$$\bar{\sigma}\left(\Delta(s)\right) \leq l(\omega) \tag{22}$$

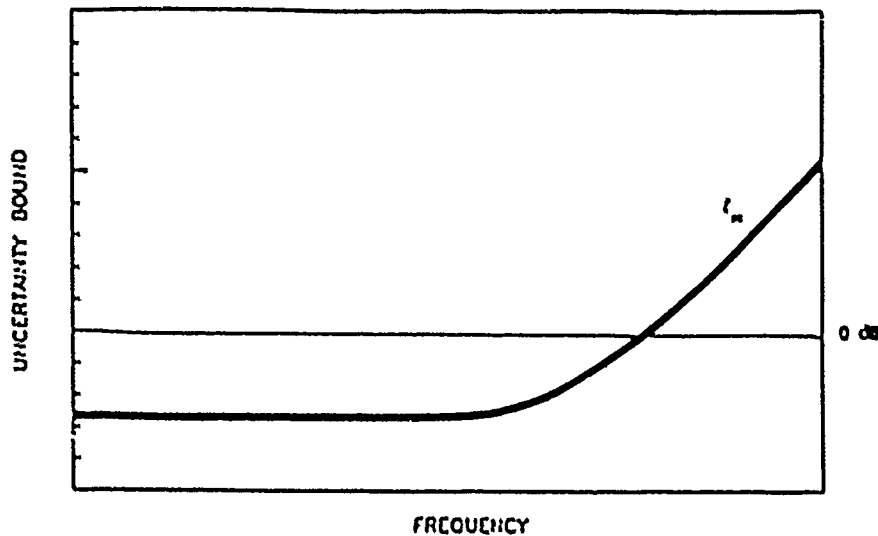Figure 3 shows a typical plot of an uncertainty bound $l(\omega)$.

Figure 3. Typical Uncertainty Profile $l(\omega)$

The uncertainty plot is low at low frequencies indicating that model confidence is high in this frequency range. As frequency increases, uncertainty grows indicating relatively less faith is placed in the system representation. In the typical LSS scenario, the uncertainty profile will increase sharply where modes have been excluded in the design model. The determination of the exact bounds of the uncertainty representation are extremely difficult. Consequently, uncertainty profiles are developed based upon general knowledge of the system's potential limitations.

The high frequency robustness barrier is taken directly from the uncertainty profile. The bound is simply $1/l(\omega)$ and essentially results in an upper bound for the bandwidth of the system. System performance and the bound on uncertainty effect the low frequency bound on the singular values of GK. Traditional control objectives like command following and disturbance rejection demand high gains at low frequencies. These objectives are incorporated into a function $p(\omega)$ resulting in a low frequency bound of $p(\omega)/1 - l(\omega)$. As in the case of the uncertainty profile, no explicit guidance is available on the selection of an appropriate performance function $p(\omega)$. Traditionally, integral control action is a desireable property to achieve zero steady-state error. This requirement and the selection of an appropriate system bandwidth often dominate the development of a low frequency bound.

In order to meet performance requirements, integral action is often required in the system. This is achieved by augmenting the plant with a bank of integrators and designing an LQG compensator (K_{LQG}) based on the new *augmented* plant. Once satisfied with the design performance, the augmented dynamics are cascaded with K_{LQG} to form the overall compensator (K) as shown in Figure 4.
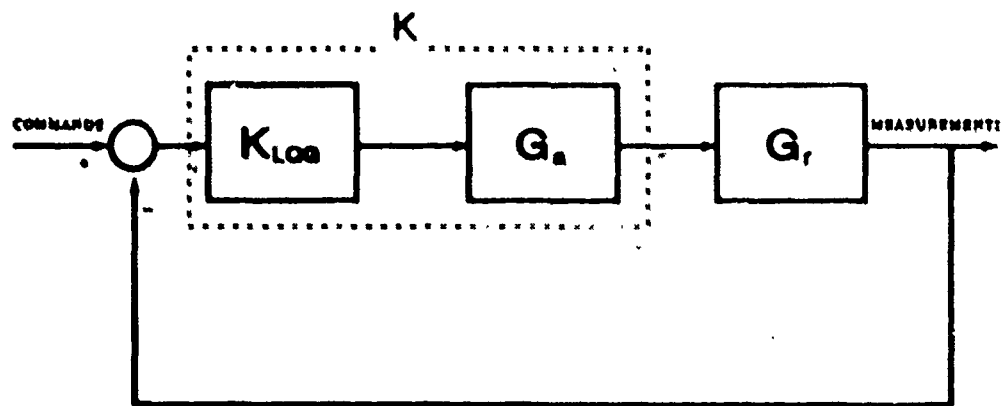
Figure 4. System with Augmented Dynamics

The LQG/LTR procedure effectively breaks the con~.~l ~ ~~ ~ ~ther the plant input or output and attempts to recover full-state stability margins (robustness) at the same location. The design procedures for breaking the loop at the two different locations are duals. A more detailed discussion of the procedures can be found in Reference 17. The LQG/LTR design procedure by breaking the loop at the output is summarized next.

Standard LQG formulations involve the design of a filter-regulator pair. The LQG/LTR design (with loop broken at the output) begins with a modified Kalman filter design. The design is modified in the sense that noi~e statistics which are normally treated as given parameters are now viewed as tunable parameters. The filter weighting matrices are tuned to achieve a filter loop shape $\sigma_i(C\Phi k_f)$ that meets the frequency domain specifications or bounds. Here, k_f is the filter gain matrix. This loop shape is deemed the desired loop shape (as it meets the performance and stability bounds) and posesses guaranteed excellent stability margins.

In order to find the desired loop shape, a Riccati equation must be solved. This can be time consuming computationally while iteratively attempting to find loop shapes that satisfy performance and robustness barriers. Consequently, the low frequency approximation, shown on the left hand side of equation (23), is used which does not involve repeated solution of the Riccati equation.

$$\sigma_i\left(\frac{1}{\sqrt{\mu}}C\Phi\Gamma\right) \approx \sigma_i\left(C\Phi k_f\right) \tag{23}$$

By selecting values for the matrix Γ and scalar μ, the approximate filter loop shapes can be adjusted to attempt to meet the design specifications. Once satisfied with the resulting approximate loop shapes, the values o^r ' and μ are used in the Algebraic Riccati equation of (24).

$$0 = A\Sigma + \Sigma A^T + \Gamma\Gamma^T - \frac{1}{\mu}\Sigma C^T \Sigma \qquad (24)$$

Solution of (24) yields Σ which can be used to find the filter gain k_f.

$$k_f = \frac{1}{\mu}\Sigma C^T \qquad (25)$$

The singular values of the filter loop $\sigma_i(C\Phi k_f)$ are the desired loop shapes. These should now meet performance and robustness bounds. This is a full-state design, and as such has a guaranteed gain margin of at least $[\frac{1}{2},\infty]$ and a phase margin of at least 60 degrees.

The regulator is now designed to attempt to recover to the desired loop shapes of the filter. The state weighting matrix ($[Q_c]$) must be selected as in (26)

$$Q_c = H^T H + q^2 C^T V C \qquad (26)$$

and the control weighting matrix($[R_c]$) as in (27)

$$R_c = \rho[I_m] \qquad (27)$$

to effect recovery. The recovery parameter (q^2) in equation (26) is used to adjust how closely the singular values of GK approach the desired loop shapes. Recovery does not come without expense. Larger control signals are required as recovery continues. The recovery process is halted short of theoretical limits based on available actuator control power. The matrix (V) in equation (26) is a weighting matrix (often selected to be identity). The control weighting (27) consists of an identity matrix of order m (the number of actuators) and a tuneable scalar parameter ρ.

Successive regulator designs with increasing values of the recovery parameter (q^2) cause the system loop shape $\sigma_i(GK)$ to approach the desired loop shape. The selection of an acceptable recovery level through (q^2) results in the controller being completely specified. The Riccati solution (P) from equation (28) can be used to obtain the regulator gain (k_c) from (29).

$$0 = PA + A^T P + Q_c - PBR_c^{-1}B^T P \qquad (28)$$

$$k_c = R_c^{-1}B^T P \qquad (29)$$

The controller (K_{LQG}) is now completely specified by equation (30).

$$K_{LQG} = k_c(sI - A + Bk_c + k_fC)^{-1}k_f \qquad (30)$$

If dynamics (G_a) were augmented to the plant, these are now cascaded with the LQG controller (K_{LQG}) to form the overall compensator (K) as shown in Figure 4 and equation (31).

$$K = G_a K_{LQG} \qquad (31)$$

EC-12

The robustness properties of the resulting design can be verified by checking the multivariable stability margins.

Computer implementation of the LQG/LTR control design technique requires two basic capabilities in addition to standard matrix manipulations and simulation ability; solution of Riccati equations and graphical representaion of system singular values. Routines can be formulated that execute the design procedure interactively with the control engineer being prompted for design parameters and the necessary guidance for system development following initial data entry. Computerization of the technique allows iteration to fully exploit the robustness recovery while remaining within control power limitations.

EXAMPLE AND DISCUSSION

An example active control system for an LSS-type structure is designed using the LQG/LTR control design technique. A simple two-bay truss is used to demonstrate some of the important features of the control system design, without the handling problems associated with typical higher-order LSS systems. The design presented is by no means final. Rather, the design is simply a candidate controller which would be tuned according to specific design goals and constraints.

The cantilevered two-bay truss used for this study is shown in Figure 5. The truss was modified by AFWAL/FIB from a similar structural model[19]. The mathematical structure is 100 inches in length and 18 inches high. The problem considered is a two degree-of-freedom problem with motion allowed in the x and y directions only.
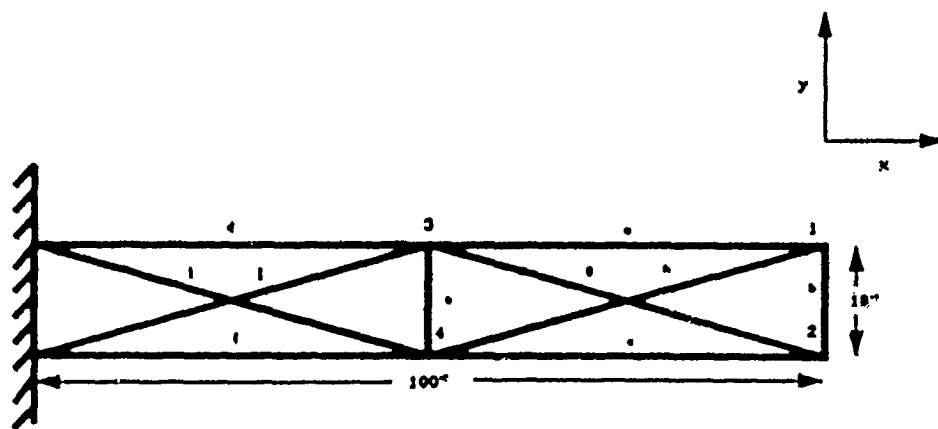

Figure 5. Two Bay Truss Model

Force actuators and position sensors are located at points 1,2,3 and 4 on the truss. Colocation of actuators and sensors is not a requirement of this particular design technique and was selected merely for model simplicity. The actuators act

along the y-axis only and are assumed to be limited to $\pm 100 lb_f$. The sensors measure physical displacements in the y direction at the four locations.

The structure is assumed to be constructed from a material with a modulus $E = 10^7$ psi and a weight density of $\rho = .1 lb_f/in^3$. The cross-sectional areas of the structural members are shown in Table 1.

Table 1. Structural Member's Cross-sectional Areas

Member	Area (in²)	Member	Area (in²)
a	.00321	f	.01049
b	.00100	g	.00328
c	.00321	h	.00328
d	.01049	i	.00439
e	.00100	j	.00439

Non-structural masses are located at positions 1,2,3 and 4. Table 2 indicates the mass at each location. These masses can be associated with the additional mass from the actuators at the four locations. The non-structural mass is large relative to the structural mass to achieve the low frequency structural modes typical of a large space structure.

Table 2. Non-structural Mass

Location	Mass*
1	1.294
2	1.294
3	1.294
4	1.294

$$* = \frac{lb_f\text{-}sec^2}{in}$$

An 8-mode mathematical model of the structure was provided by the Structures Division (AFWAL/FIB). Appendix A contains the matrices of equation (2) required to describe the structural dynamics in physical coordinates. These include the mass ([m]), stiffness([k]) and input distribution matrix ([b]). The damping matrix ([c]) is assumed to be zero temporarily. The solution of the eigenvalue problem of equation (8) results in the matrix of eigenvectors ([T]) also given in Appendix A. This matrix is used to transform the system to modal coordinates using (7). The resulting system is in modal form as described by (9) thru (13).

Once in modal form, some assumptions are now made regarding the level of damping in the structure. For simplicity, we assume uniform damping exists throughout the structure. This can be achieved through the selection of a particular value for damping (ς) and substition into (12). A passive damping level of $\varsigma = .005$ was chosen for this active control study. The modal frequencies and open-loop pole locations for this uniformly damped 8-mode model are shown in Table 3.

Table 2. Open-Loop Characteristics : 8 Mode Model

Mode	Freq. (Hz)	Freq. (r/s)	Real	Imag	Damping
1	.50000	3.1416	-.01571	±3.1415	.005
2	1.6529	10.3857	-.05193	±10.3856	.005
3	3.6134	22.7040	-.11352	±22.7038	.005
4	4.7020	29.5437	-.14772	±29.5435	.005
5	4.9640	31.1894	-.15595	±31.1890	.005
6	5.2315	32.8702	-.16435	±32.8698	.005
7	8.8844	55.8220	-.27911	±55.8213	.005
8	9.3551	58.7790	-.29390	±58.7790	.005

The 8-mode (16th order) truth model is now reduced for design purposes. Examination of the system's second-order modes indicate the system is most controllable and observable with respect to the first two modes. The system is reordered into the form of (14) and reduced to a 4th order system (2 modes). The resulting design model is shown in equation (32).

$$\dot{x} = Ax + Bu \qquad y = Cx + Du \qquad (32)$$

with

$$A = \begin{bmatrix} -.0314 & 0 & -9.8694 & 0 \\ 0 & -.1039 & 0 & -107.86 \\ 1 & 0 & 0 & 0 \\ 0 & 1 & 0 & 0 \end{bmatrix} \qquad (32a)$$

$$B = \begin{bmatrix} .3142 & .3142 & .1161 & .1161 \\ -.1040 & -.1040 & .3337 & .3337 \\ 0 & 0 & 0 & 0 \\ 0 & 0 & 0 & 0 \end{bmatrix} \qquad (32b)$$

$$C = \begin{bmatrix} 0 & 0 & 1 & -.3117 \\ 0 & 0 & 1 & -.3117 \\ 0 & 0 & .3402 & 1 \\ 0 & 0 & .3402 & 1 \end{bmatrix} \qquad (32c)$$

$$D = \begin{bmatrix} .0004 & -.0004 & 0 & 0 \\ -.0004 & .0004 & 0 & 0 \\ 0 & 0 & .0004 & 0 \\ 0 & 0 & -.0004 & .0004 \end{bmatrix} \qquad (32d)$$

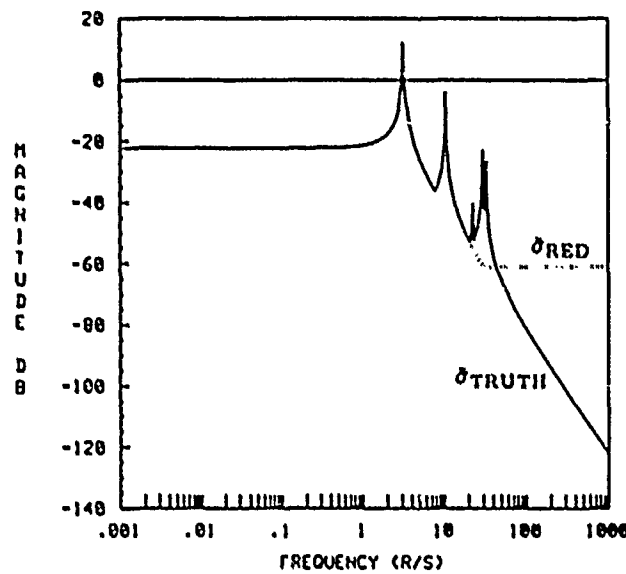The maximum singular values of the truth model and the reduced-order design model are shown in Figure 6.

Figure 6. Singular Values of Truth and Design Models

The maximum singular values of the two models are nearly indentical at low frequency. The same is true for the minimum singular values (not shown). Open-loop initial condition responses (not shown) indicate that the models compare well.

An uncertainty profile is established based on the high frequency modelling uncertainty and the plant uncertainty between the design and truth models. This unstructured uncertainty is modelled as a bound on an output multiplicative perturbation as in equation (22). A bound $l(\omega)$ is shown in Figure 7 which approximates the variations between the design and truth models ($\Delta(s)$) as well as high frequency uncertainties. The LQG/LTR procedure uses the bound $l(\omega)$ during design.
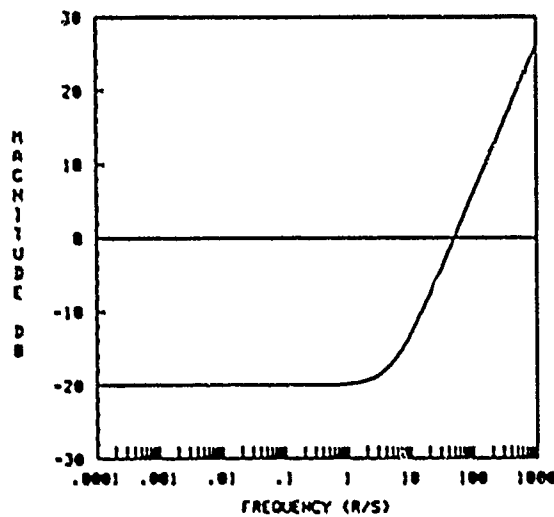
Figure 7. Uncertainty Profile

Uncertainty is low at frequencies below 10 r/s where model confidence is high. The two modes in this frequency range are included in both the truth and design models. Uncertainty increases above 10 r/s due to traditional modelling difficulties at high frequency and the absence of modes 3-8 in the design model.

Evaluation of the control system will be based upon the system response to an initial condition. The particular initial condition was selected to excite a significant number of system modes. Excitation levels were judged by the relative modal amplitudes (η). The initial condition vector of (33) given in physical coordinates excites the first, second, fifth and seventh modes of the structure. This vector corresponds to a tip displacement of approximately one inch and a mid-station displacement of nearly two inches. The initial velocity of the truss is zero.

$$x_0 = [[0]_{1 \times 8} \quad .153 \quad 1.00 \quad -.153 \quad 1.00 \quad -.0785 \quad 1.97 \quad .0785 \quad 1.97\,]^T \tag{33}$$

Examination of Figure 6 indicates that the plant does not have natural integral action. This is seen by from the flat singular values at low frequencies. To achieve zero steady-state error in the system, the design model (G_r) is augmented with a bank of integrators. A controller (K_{LQG}) will be designed upon the augmented plant (G') of equation (34).

$$G' = G_r G_a \tag{34}$$

where

$$G_a = \frac{1}{s}[I]_4 \tag{34a}$$

An approximate filter loop shape is now designed by selecting Γ and μ of equation (23). The upper system bandwidth limit is approximately 10 r/s based on

the uncertainty profile. Through design iteration, values of $\mu = .000025$ and $\Gamma = B$ were found to satisfy the frequency domain bounds with the approximate filter loop shape $\sigma\left(\frac{1}{\sqrt{\mu}}C\Phi\Gamma\right)$ shown in Figure 8.
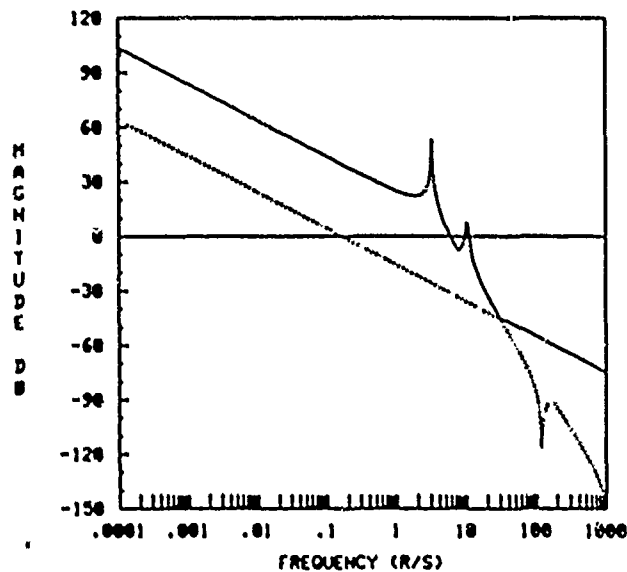

Figure 8. Approximate Filter Loop Shape $\left(\sigma\left(\frac{1}{\sqrt{\mu}}C\Phi\Gamma\right)\right)$

Because of the particular selection of $\Gamma = B$, the loop shape of Figure 8 is simply the open-loop plant augmented with integrators and scaled by $\frac{1}{\sqrt{\mu}}$. The characteristic -20 dB/decade slope from the integral action can be seen at low frequency.

Equations (24) and (25) are solved to obtain the filter gain which results in the closed-loop pole locations shown in Table 4. The seperation principle dictates that these poles are a subset of the system's closed-loop poles.

Table 4. Filter Closed-Loop Poles $\lambda_i[A - k_fC]$

Freq. (r/s)	Real	Imag	Damping
10.4716	-.6697	± 10.4502 i	.064
5.6758	-2.3628	± 5.1606 i	.416
4.7285	-4.7285	0	1
1.3428	-1.3428	0	1
.1766	-.1766	0	1
.1618	-.1618	0	1

The filter loop shape $\bar{\sigma}(C\Phi k_f)$ is plotted in Figure 9 along with its low frequency approximation. The full-state filter loop shows a characteristic -20 dB/decade rolloff at high frequency. This is the desired system loop shape which will now be
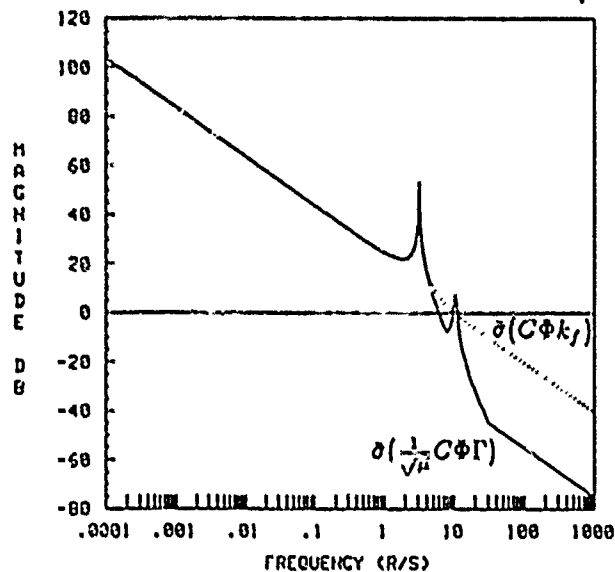
recovered during the regulator design.

Figure 9. Filter Loop Shape and Low Frequency Approximation

The matrices $[Q_c]$ and $[R_c]$ are selected as in equations (26) and (27). The response matrix ($[H]$) is selected as $H = C$ and the scalar (ρ) is chosen to be unity. Designs were accomplished for increasing values of the recovery parameter (q^2). Figure 10 shows how $\bar{\sigma}(GK)$ compares with the desired loop shape $\bar{\sigma}(C\Phi k_f)$ for increasing values of q^2. Only the maximum singular value is plotted for figure clarity. Selection of the final value for the recovery parameter represents a tradeoff between competing issues.
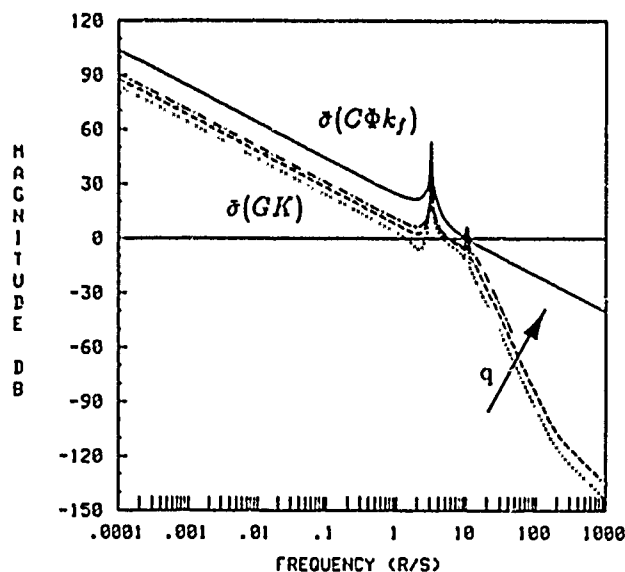
Figure 10. Recovery of Maximum Singular Value

As q^2 is increased during recovery, robustness (as measured by multivariable stability margins) increases. However, the control effort required to accomplish control tasks also increases. Consequently, robustness can be recovered only to that level allowable within the given control power limitations. This tradeoff between robustness recovery and required control power highlights the benefit of computerization of this technique. Computer implementation allows for numerous design iterations that readily allow comparison of performance, robustness and control requirements of competing designs. For this example, actuator limits of $\pm 100 lb_f$ have been imposed. This allows the recovery to continue until $q^2 = 500,000$ without exceeding control limits. Solution of the regulator algebraic Riccati equation (28) is used to find the regulator gain (28). The regulator gain matrix results in the closed-loop regulator poles for the design model shown in Table 5.

Table 5. Regulator Closed-Loop Poles $\lambda_i[A - Bk_c]$

Freq. (r/s)	Real	Imag	Damping
11.1837	-2.0686	$\pm$ 10.9907 i	.185
8.3438	-3.8624	$\pm$ 7.3964 i	.463
7.7350	-7.7350	0	1
4.1624	-4.1624	0	1
.6244	-.6244	0	1
.5719	-.5719	0	1

The poles of Table 4 and Table 5 make up the closed-loop poles of the system. The compensator poles are shown in Table 6. Notice the augmented integrators are included as part of the compensator.

Table 6. Compensator Poles

Compensator Poles
$-5.0720 \pm 12.0064i$
$-2.5881 \pm 11.4316i$
-14.7367
-5.7035
-.8010
-.7336
0
0
0
0

The final system loop shape $\sigma(GK)$ is shown in Figure 11. The bandwidth of the system can be seen to be approximately 10 r/s which is reasonable.
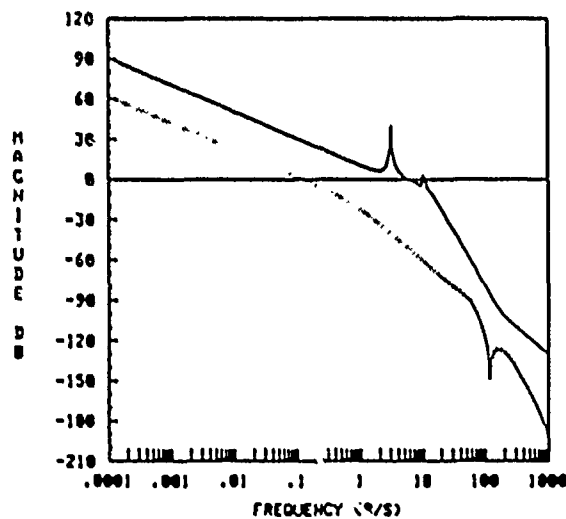
Figure 11. Final System Loop Shape ($\sigma(GK)$)

The control system was developed based upon a *design* model and a description of the differences between this model and the truth model and real world. The performance of the system must be tested against the truth model which is the closest thing to the real world used in this study. Although the controller was *not* specifically designed for the truth model, the system should remain stable and demonstrate acceptable performance. Simulation plots of the *truth model* are shown in Figures (12) through (15). Open and closed-loop plots are shown for comparison. The responses and the control signals at the upper and lower locations are nearly identical. This is a result of the initial condition significantly excited only the longitudinal modes. Breathing (lateral) modes are not directly excited. For convienience, only a single plot is shown at the tip and mid-station locations.
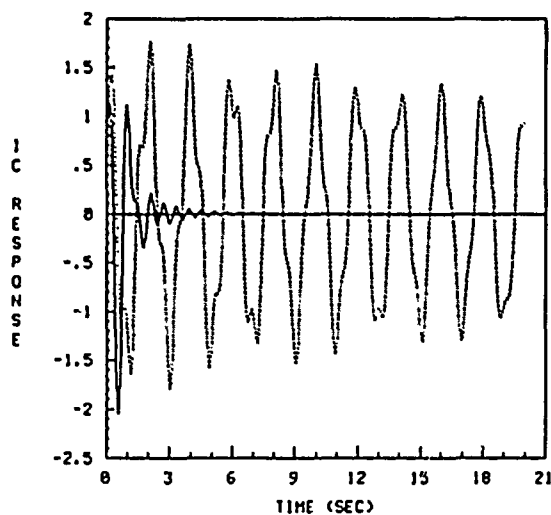
Figure 12. Open and Closed-loop Initial Condition Response (Tip)
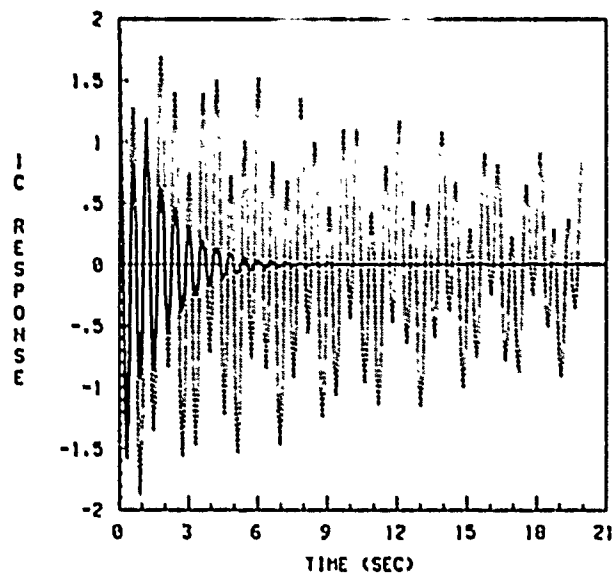
Figure 13. Open and Closed-loop Initial Condition Response (Mid)

The actuator activity required by the control system is linearly related to the magnitude of the initial conditions. The system is driven to relatively high gains by the stringent settling requirements typical of LSS problems. Control effort can be decreased by lengthening the settling time, or reducing the settling criteria and redesigning the control system. Required control power can also be reduced by decreasing the initial condition magnitude. The control signals at the tip and mid-station for this simulation are shown in Figures 14 and 15.
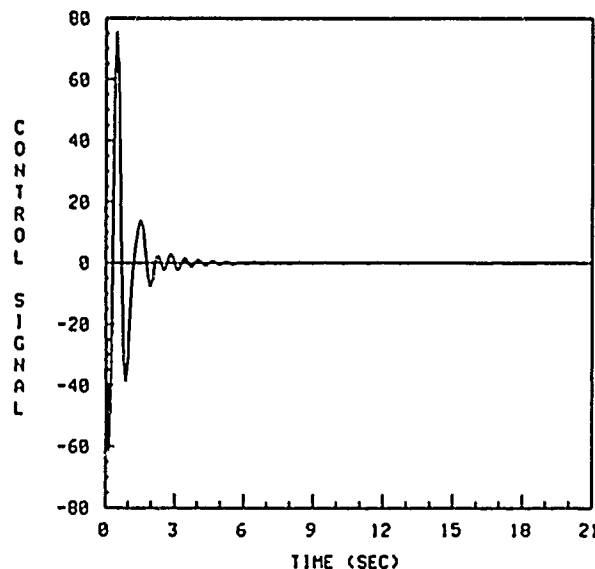
Figure 14. Control Signal for Tip Actuators
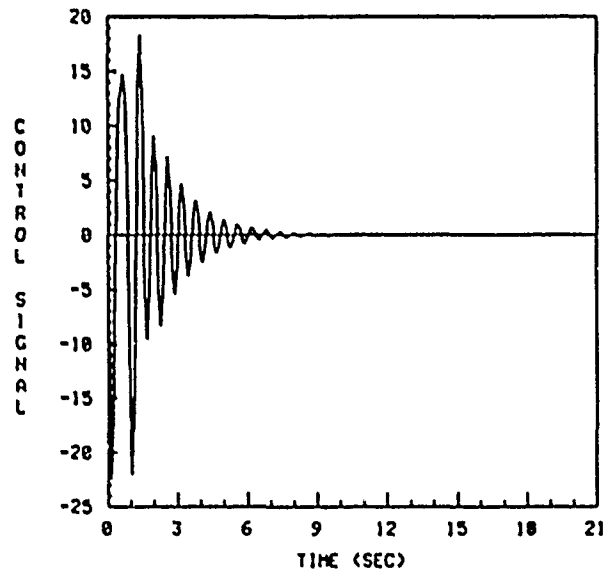
Figure 15. Control Signal for Mid-station Actuators

The initial vibrations are damped to within .1 percent of in initial amplitude in approximately 12 seconds. This is accomplished within the specified control power limits. The design can be altered (fine tuned) for different problem specifications or when design priorities are altered. The design process is always a trade-off between competing requirements. In this problem, a desired loop shape was specified that was expected to give good system performance and robustness. The recovery to that loop shape was halted (full recovery exists only in theory) based on the specified control power requirements. The resulting system robustness is measured in terms of multivariable stability margins.

The vibration control system has a gain margin of [-3.2 dB,+2.75 dB] and a 17.75 degree phase margin. These margins are acceptable for the purposes of this study. Specific application requirements will dictate what acceptable stability margins are for different problems.

CONCLUSIONS

This study has considered the use of active control for vibration damping in the framework of the LSS problem. A uniform level of passive damping was assumed throughout the structure. The authors recognize the potential of both passive and active control techniques and their ultimate synergistic application to solve the vibration damping problem. Assumptions were made concerning the level of passive damping in the structure to limit the scope of the work.

The main contribution of this paper is the demonstration of the use of an active control technique to address the vibration damping problem. The Linear

EC-23

Quadratic Gaussian with Loop Transfer Recovery (LQG/LTR) is an example of a robust design technique that allows the incorporation of a description of system uncertainty in the design. Unfortunately, the available descriptions of system uncertainties often fall short of the potential benefits available from these design methods. However, uncertainty is an important issue in the vibration damping and should be addressed. Continued examination of these issues may provide an impetus for obtaining improved descriptions of uncertainty.

With the use of robustness recovery, the importance of actuation control power in the vibration damping problem is highlighted. As additional robustness is desired, control requirements also increase. A design balance must be struct depending on the specific application. Again, we look for improvements in actuation to parallel the advances in modelling and control techniques to more adequately address the vibration damping problem.

Acknowledgements

REFERENCES

1. J.M. Hedgepeth and M. Mobrem, "Investigation of Passive Damping of Large Space Truss Structures," Vibration Damping Workshop II, Las Vegas, NV, 5-7 March 1986.

2. H. Ashley and D.L. Edberg, "On the Virtues and Prospects for Passive Damping in Large Space Structures," Vibration Damping Workshop II, Las Vegas Nv, 5-7 March 1986.

3. D.R. Morgenthaler and R.N. Gehling, "Design and Analysis of the PACOSS Representative System," Vibration Damping Workshop II, Las Vegas, NV, 5-7 March 1986.

4. J.C. Doyle and G. Stein, "Multivariable Feedback Design Concepts for a Classical/Modern Synthesis," IEEE Transactions on Automatic Control, Vol. AC-26, No. 1, Febuary 1981.

5. M. Vidyasagar and H Kimura, "Robust Controller for Uncertain Linear Multivariable Systems," Proc. IFAC World Congress, Budapest, Hungary, 1984.

6. R.K Yedavalli and S.S. Banda, "Robust Stability and Regulation in the Control of Large Space Structures," Proc. AIAA Guidance and Control Conference, Snowmass, CO. AIAA-85-1969-CP, August 1985.

7. L. Meirovich, "Elements of Vibrational Analysis," McGraw Hill, 1975.

8. R.E. Skelton, "Cost Decomposition of Linear Systems with Application to Model Reduction," International Journal of Control, Vol32, No. 6, pp.1031-1055, 1980.

9. D. Enns, "Model Reduction for Control System Design," PhD Thesis, Stanford University, June 1984.

10. K. Glover, "All Optimal Hankel-Norm Approximations of Linear Multivariable Systems and their L^∞-Error Bounds," International Journal of Control, Vol. 39, No. 6, pp 1115-1193, 1984.

11. M.G. Safonov and M. Athans, "Gain and Phase Margins for Multiloop LQG Regulators," IEEE Transactions on Automatic Control, Vol AC-22, pp 173-179, April 1977.

12. J.C. Doyle, "Guaranteed Margins for LQG Regulators," IEEE Transactions on Automatic Control, Vol. AC-23, No. 4, pp 756-757, August 1978.

13. J.C. Doyle and G. Stein, "Robustness with Observers," IEEE Transactions on Automatic Control, Vol AC-24, No. 4 pp 607-611, August 1977.

14. G. Stein and M. Athans, "The LQG/LTR Multivariable Control System Design Method," Proc. American Control Conference, San Diego, June 1984, also available as MIT LIDS-P-1384, May 1984.

15. M. Athans, P. Kappasouris, E. Kappas, and H. Spang III, "Linear-Quadratic-Gaussian with Loop-Transfer-Recovery Methodology for the F-100 Engine," Journal of Guidance, Control and Dynamics, Vol 9, No. 1, pp 45-52, Jan-Feb 1986.

16. J.A. Mette Jr., "Multivariable Control of a Submarine using the LQG/LTR Methodology," LIDS-TH-1468, M.S. Thesis, MIT, May 1985.

17. D.B. Ridgely and S.S. Banda, "Introduction to Robust Multivariable Control," AFWAL-TR-85-3102, Wright-Patterson Air Force Base, Dayton, OH.

18. H. Kwakernaak and R. Sivan, Linear Optimal Control Systems," Wiley Interscience, New York, 1972.

19. V.B Venkayya and V.A. Tischler, "Frequency Control and the Effects on the Dynamic Response of Flexible Structures," 25th Structures, Structural Dynamics and Materials Conference, AIAA-84-1044-CP, Palm Springs, CA, May 1986.

MASS   =

1.2940	0.0000	0.0000	0.0000	0.0000	0.0000	0.0000	0.0000
0.0000	1.2940	0.0000	0.0000	0.0000	0.0000	0.0000	0.0000
0.0000	0.0000	1.2940	0.0000	0.0000	0.0000	0.0000	0.0000
0.0000	0.0000	0.0000	1.2940	0.0000	0.0000	0.0000	0.0000
0.0000	0.0000	0.0000	0.0000	1.2941	0.0000	0.0000	0.0000
0.0000	0.0000	0.0000	0.0000	0.0000	1.2941	0.0000	0.0000
0.0000	0.0000	0.0000	0.0000	0.0000	0.0000	1.2941	0.0000
0.0000	0.0000	0.0000	0.0000	0.0000	0.0000	0.0000	1.2941

EVECTORS   =

-0.1150	0.2463	1.0000	-0.0003	-1.0000	0.3753	-0.0318	-0.3672
1.0000	-0.3117	-0.2021	1.0000	-0.1812	0.5025	0.0477	-0.0818
0.1150	-0.2463	1.0000	-0.0003	1.0000	0.3753	0.0318	-0.3672
1.0000	-0.3117	0.2021	-1.0000	-0.1812	-0.5025	0.0477	0.0818
-0.0575	0.0047	0.3494	0.0799	-0.0266	0.1823	1.0000	1.0000
0.3402	1.0000	-0.3374	-0.5170	0.1899	1.0000	0.0181	-0.0035
0.0575	-0.0047	0.3494	0.0799	0.0266	0.1823	-1.0000	1.0000
0.3402	1.0000	0.3374	0.5170	0.1899	-1.0000	0.0181	0.0035

STIFF   =

1.0D+03 *

1.1885	0.1966	0.0000	0.0000	-0.6424	0.0000	-0.5461	-0.1966
0.1966	0.6263	0.0000	-0.5556	0.0000	0.0000	-0.1966	-0.0708
0.0000	0.0000	1.1885	-0.1966	-0.5461	0.1966	-0.6424	0.0000
0.0000	-0.5556	-0.1966	0.6263	0.1966	-0.0708	0.0000	0.0000
-0.6424	0.0000	-0.5461	0.1966	4.0191	0.0669	0.0000	0.0000
0.0000	0.0000	0.1966	-0.0708	0.0669	0.7212	0.0000	-0.5556
-0.5461	-0.1966	-0.6424	0.0000	0.0000	0.0000	4.0191	-0.0669
-0.1966	-0.0708	0.0000	0.0000	0.0000	-0.5556	-0.0669	0.7212

SMALLB   =

0	0.	0.	0.
1.	0.	0.	0.
0.	0.	0.	0.
0.	1.	0.	0.
0.	0.	0.	0.
0.	0.	1.	0.
0.	0.	0.	0.
0.	0.	0.	1.

A NEW APPROACH TO MODELING LINEAR VISCOELASTIC DAMPING

FOR SPACE STRUCTURES

P. C. Hughes and D. T. McTavish

Institute for Aerospace Studies
University of Toronto

K. W. Lips and F. R. Vigneron

Communications Research Centre
Department of Communications

ABSTRACT

It is assumed that the reader recognizes that energy dissipation is critically important in modeling the dynamics of large flexible space structures. The program of research reported here seeks to improve upon the more-or-less capricious assignment of "modal damping factors" through an investigation that includes both theoretical and experimental elements. The theory is now nearing completion, and the experiments are in the design stage.

MOTIVATION

Energy dissipation is critically important in modeling the dynamics of flexible space structures. This statement is true with respect to "passive control" designs, in which stabilization relies on the inherent mechanical design of the spacecraft--spinners and dual-spinners, for example. It is equally true for "active control" spacecraft designs, wherein feedback from appropriate sensors is fed, via a computer-based control algorithm, to appropriate actuators. In spite of this agreed importance, the modeling of energy dissipation for spacecraft applications is frequently gi .n short shrift, and is all too often represented by "modal damping factors" that are simply guessed at.

CONTRIBUTION

The program of research reported on briefly here seeks to improve this state of affairs by a combination of theory and experiment. The theory is now relatively complete. It consists of a time-domain finite element formulation, with the damping being material damping of the linear viscoelastic type. The standard structural dynamics form for the equations of motion (linear, matrix-second-order) is retained, but "auxiliary" coordinates are needed to represent the damping. Special results are available if the damping is "light," as it usually is in spacecraft applications.

An experimental program has also recently been begun, in which appropriate material damping data are measured. The material constants needed by the theory are then extracted from these data. A structure of intermediate complexity is now being constructed out of these materials, and the structural damping characteristics measured. These will be compared with predictions based on the theory described in the last paragraph, and inferences made. The experimental half of this short paper will be more in the nature of "work in progress".

THEORY

The objectives of the theory are fourfold:

1. The theory must be conveniently expressible in both the time and frequency domains. (By "frequency domain," we mean the domain of the Laplace variable, herein denoted by s.)

2. The theory must clearly identify material damping parameters to be measured experimentally (in the same manner that Young's modulus is an experimentally determined material parameter used in the analysis of ideally elastic structures).

3. The theory must be readily adaptable to the finite element method, so that the enormous (and enormously successful) body of engineering software for ideally elastic structures can be extended to encompass viscoelastic structures.

4. Consistent with the last requirement, the theory should be expressed in linear matrix-second-order form. (If someone wishes to convert subsequently to linear matrix-first-order form -- i.e., "state-space form," this is of course possible.)

A theory which satisfies these four requirements has recently been published by D. F. Golla and P. C. Hughes ("Dynamics of Viscoelastic Structures -- A Time-Domain Finite Element Formulation," J. Appl. Mech., Vol. 52, Dec. 1985, pp. 897-906). The theory recommends that a space structure be broken down in the following successive steps:

1. overall structure → substructures

2. substructure → finite elements

3. finite element → identify elastic moduli

4. elastic modulus → viscoelastic "dipole pairs"

The first two steps are relatively standard. It is at third step, and particularly at the fourth step, that the present theory has its roots.

THE KERNEL OF THE IDEA

To explain the theory in its simplest terms, we take one substructure, then one finite element of that substructure, then one coordinate of that finite element, and, finally, a single viscoelastic "dipole pair" for an elastic modulus represented by that coordinate. To be more specific, we start with the single degree of freedom, $q(t)$, with which we can associate a mass m and a stiffness k:

$$m\ddot{q} + kq = f(t) \tag{1}$$

Equation (1) represents the ideal elatic situation. The Laplace-transformed version of (1) is

$$(ms^2 + k)q(s) = f(s) \tag{2}$$

With viscoelasticity, we replace the constant parameter k by a function of s:

$$k \rightarrow k(s) = k\left[1 + \frac{a_1 s}{s + b_1} + \frac{a_2 s}{s + b_2}\right] \tag{3}$$

Only two damping poles are included in (3) to maximize simplicity. One pole is not enough because we seek ultimately a second-order form of the structural dynamical equations. Extra pole pairs can be added if needed.

Instead of (3) it is more notationally convenient to use

ED-3

$$k \to k(s) = k \left[1 + \frac{\alpha(s^2 + 2\zeta_d \omega_d s)}{s^2 + 2\zeta_d \omega_d s + \omega_d^2} \right] \tag{4}$$

This notation isolates the (usually small) damping parameter α and also paves the way for a matrix-second-order time realization of the model. Although the expansion (4) involves only three parameters (α, ζ_d, ω_H) instead of the four (a_1, a_2, b_1, b_2) represented in (3), it can be shown (see the Golla/Hughes paper referred to above) that this is the only possibility if a matrix-second-order formulation is to be retained.

To summarize thus far, the "simplest" case has

$$[ms^2 + k(s)]q(s) = f(s) \tag{5}$$

with $k(s)$ given by (4). It is also clear that it is the parameters (α, ζ_d, ω_H) that are to be measured experimentally.

MATRIX-SECOND-ORDER FORM

It will now be shown how a matrix-second-order time-domain realization of (5) can be constructed. The system

$$\underline{M}\,\ddot{\underline{q}} + \underline{D}\,\dot{\underline{q}} + \underline{K}\,\underline{q} = \underline{f}(t) \tag{6}$$

with

$$\underline{M} = m \begin{bmatrix} 1 & 0 \\ 0 & \alpha\omega_e^2/\omega_d^2 \end{bmatrix}; \qquad \underline{D} = m \begin{bmatrix} 0 & 0 \\ 0 & 2\alpha\zeta_d\omega_e^2/\omega_d^2 \end{bmatrix}$$

$$\underline{K} = m\omega_e^2 \begin{bmatrix} 1+\alpha & \alpha \\ \alpha & \alpha \end{bmatrix}; \qquad \underline{q} = \begin{bmatrix} q \\ z \end{bmatrix}; \qquad \underline{f} = \begin{bmatrix} f \\ 0 \end{bmatrix}$$

(with $\omega_e^2 = k/m$) is the form sought. Note that $\underline{M}$ and $\underline{K}$ are symmetric and positive definite, and that $\underline{D}$ is symmetric and positive semidefinite. A mechanical analogy for this system is shown in Fig. 1.

With no damping ($\alpha = 0$) the eigenvalues of (6) are, of course, at $s = \pm j\omega_e$. With light damping ($0 < \alpha \ll 1$) a simple perturbation analysis shows that these two roots move to

$$s = \pm j\omega_v - \zeta\omega_v \qquad (0 < \zeta \ll 1) \tag{7}$$

where

$$\omega_v = \omega_e \left[1 + \frac{1}{2} \alpha\omega_e^2 \frac{(\omega_e^2 - \omega_H^2) + 4\zeta_d^2\omega_d^2}{(\omega_e^2 - \omega_H^2)^2 + 4\zeta_d^2\omega_d^2\omega_e^2} \right] \tag{8}$$
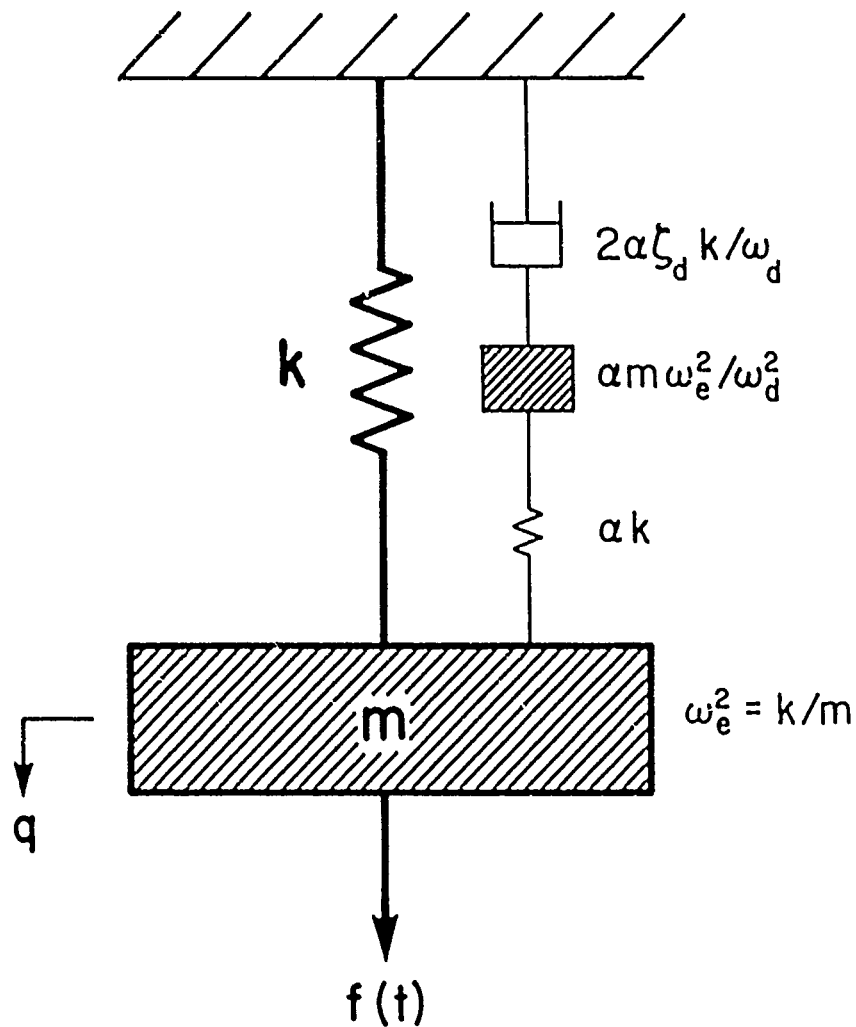
Figure 1: Mechanical Analogy for the Most Elementary Form
of the Theory [no. of finite elements = 1; no. of coords.
in finite element = 1; no. of dipole pairs in Laplace-
generalized modulus = 1]

$$\zeta = \frac{\alpha \zeta_d \omega_d^3 \omega_e}{\left(\omega_e^2 - \omega_d^2\right)^2 + 4\zeta_d^2 \omega_d^2 \omega_e^2} \qquad (9)$$

Of particular interest is the (small) damping factor ζ, which through (9) has been expressed in terms of the material damping parameters (α, ζ_d, ω_d).

GENERALIZATION

As indicated in Fig. 2, the method, in order to be useful, must be generalized to many pole pairs (an extension of Eq. (4)), carried out for all material moduli, for each coordinate, of each finite element of the structure. This has in fact been done (see the reference mentioned in the Theory paragraph above) although the details will not be given here.

PLANNED STRUCTURAL EXPERIMENT

In designing the structure, the principal consideration is that it should be representative of a "typical" space structure. More particularly, it should typify a structure that may contribute in a significant way to the flexibility of a system. This leads naturally to the choice of a lattice type, since it is typical of extendible masts of current design and of connecting beam elements as might be developed for future space structures. The fundamental element of such a structure is the bay, the characteristic properties of which are repeated as many times as necessary. To capture some of the properties of a multi-bay structure, the inclusion of at least two bays is mandatory; additional bays do not add necessarily to the generality of the study and certainly increase model complexity.

In our study, no attempt is made at present to model sources of damping that might arise from the properties of joints or other non-intrinsic material properties; thus, to ensure proper control of experimental variables, the structure is required to b uniform, that is, all joints should exhibit only material properties, and to be non-composite. In addition, desirable properties of the material are that it have linear but significant damping characteristics (though substantially less than critical) and that it facilitate manufacture of a lightweight and reasonalby strong structure of the type required. The selected material is an opoxy resin which has a number of attractive features among which are its ease in moulding and the uniformity of material properties through joints between new and previously moulded material.

Current work is directed to familiarizing personnel with the general mixing and handling properties of the material and the development of moulding techniques. Work will progress into developing sub-components of the intended structure, such as simple slender rods, to review their structural integrity, shape retention and shrinkage. The rods will be tested statically to obtain appropriate moduli for use in the design of the test space structure. Succeeding work will involve the construction of
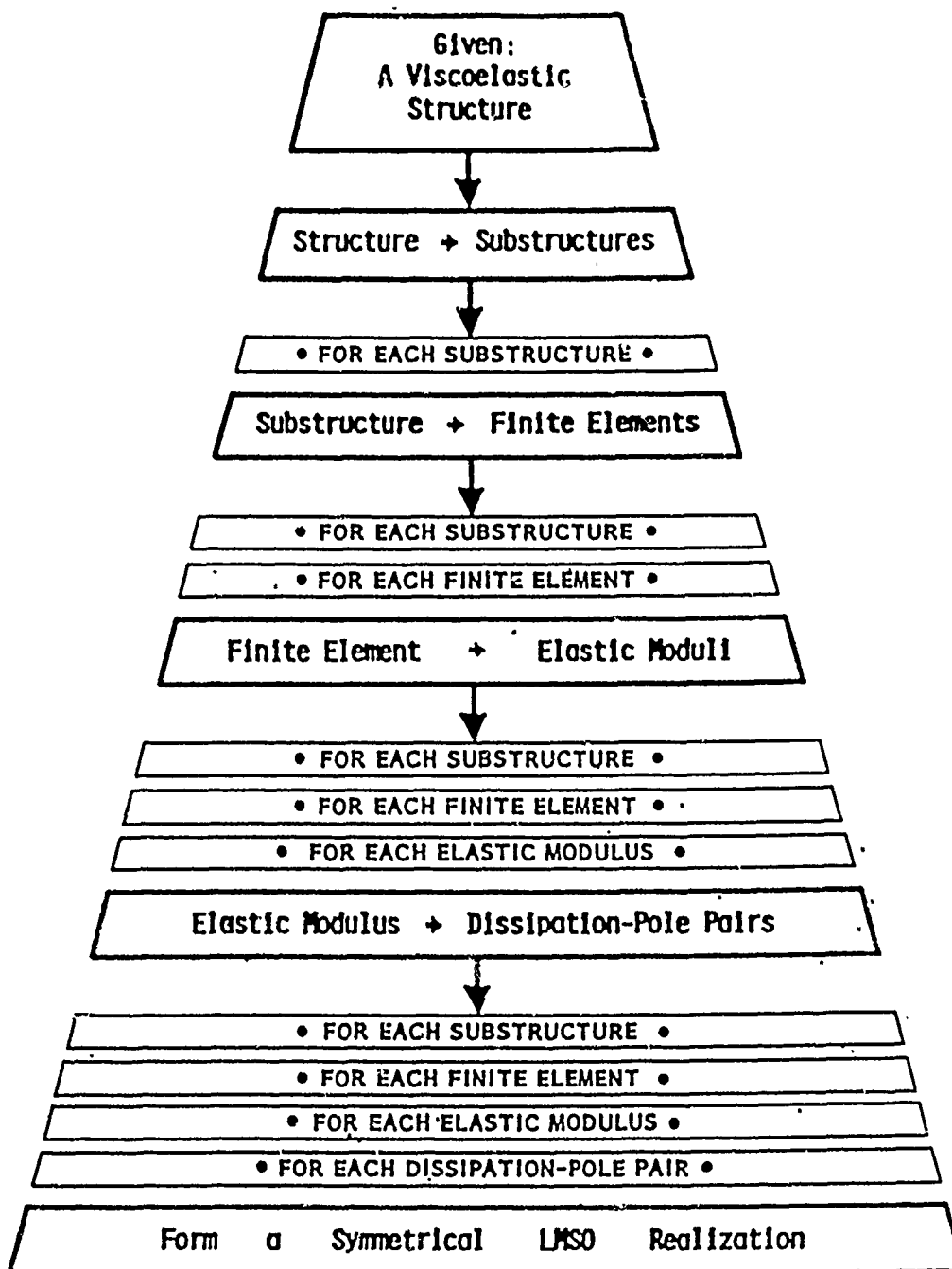
Figure 2: Generalization of the "Most Elementary Form"
of the Theory,[to arbitrary nos. of dipole pairs,
moduli, finite elements, and substructures]

ED-7

member intersections (structure joints) made from one-pour, followed by the construction and assessment of joints from two or more pours.
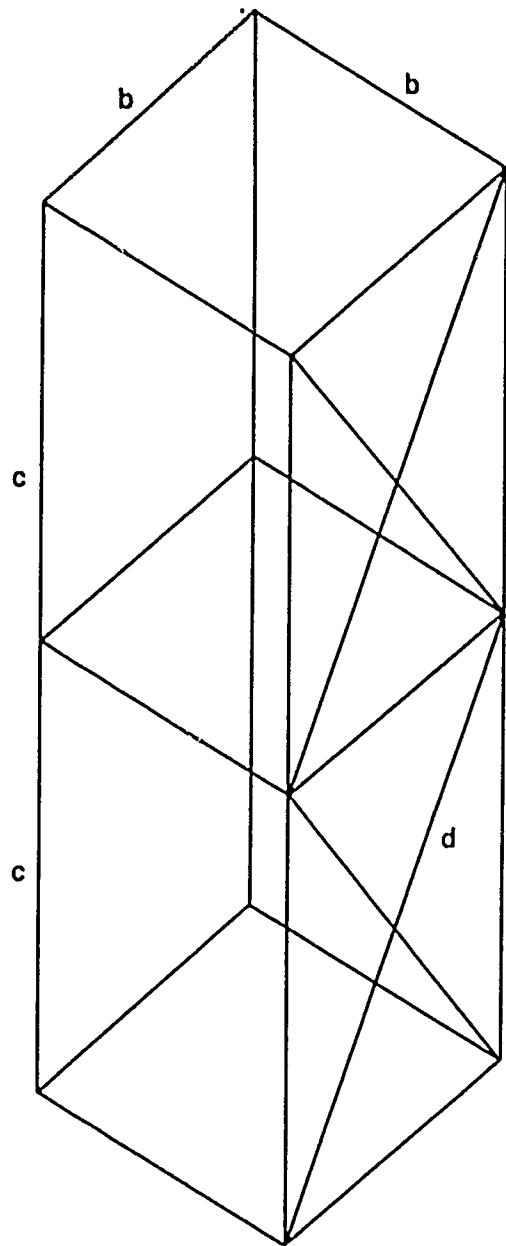
STRUCTURAL DESIGN

The design of the test space structure is not yet finalized; however, the proposed design is shown in Fig. 3. Particular design criteria are relatively loose with respect to size requirements, being little more than to require the model to be easy for an individual to handle ;and, at the same time, to be reasonably robust. This suggests something of about the general height of a person in length and probably not exceeding about two feet in width and depth. Characteristically, lattice-type sub-structural components are slender; however, actual slenderness will be dictated by sub-structure load capacity as well as shape retention capability of the material in such geometries. Because vibration frequencies typical of large spacecraft tend to be very low, it is intended to keep the test space structure's fundamental frequency low also. Recognizing that there are limits to achieving low frequencies with a structure of the chosen size and that accelerometers for use in very low frequency measurements are significantly more heavy and expensive, the lowest fundamental frequency will be selected to be approximately 5 Hz. A further criterion in the design is to ensure that the modes are fairly well separated in the test configuration so that the modal damping factors may be estimated readily from the experimental data. To model the structural and dynamic properties, a finite element analysis will be performed before a final design is accepted.

STRUCTURAL TESTS

Two articles are proposed for testing; one a smple slender rod and the other the test space structure. The slender rod will be essentially similar to typical substructural elements of the test space structure. Modal tests will be performed on both articles. A number of modal tests are planned, each with varying boundary conditions on the test article. For example, in free-free tests it is customary to hang the test article from suitable points on the article by a suspension system which has typical response frequencies well below that of the test article itself. Since modal damping factors are affected by boundary conditions which contain dissipative forces, it is essential that some means of controlling or changing them be provided. Another key issue is the ability of particular parameter identification algorithms to resolve modal damping factors to sufficient accuracy. Several techniques will be applied to provide visibility into this question. In addition, the test data will be investigated for the presence of nonlinearities in the dynamics of the structure.

ACKNOWLEDGEMENTS

MEMBERS	LENGTH (FT)	AREA (IN × IN)
c	2.5	1/2 × 1/2
b	2.0	1/2 × 3/8
d	3.2	1/2 × 3/8

MATERIAL: HYSOL EPOXY
RESIN: TE 6175
HARDENER: HD 3561

Figure 3: Experimental Test Structure [First Draught Design]

merit mention: Mr. William Graham of the Communications Research Centre, Ottawa, is now the responsible technical authority for this contract, replacing Dr. Ken Lips, who is now with Honeywell in Florida. Bill Graham is being assisted on the structural experiments by M. Y. Soucy. The experimental data on materials properties are being collected at the University of Toronto's Institute for Aerospace Studies (UTIAS) by Prof. Jorn Hansen, with the assistance of Peter Floros. Mention should also be made of the contribution of Dr. David Golla, who resolved many of the analytical aspects of the theory as part of his doctoral dissertation at UTIAS. David Golla is now with Spar Aerospace Ltd., Weston, Ontario.

EXPERIMENTAL INVESTIGATIONS INTO

PASSIVE AND ACTIVE CONTROL

USING SPACE-REALIZABLE TECHNIQUES

D. W. Miller
Research Assistant

E. F. Crawley
Associate Professor

Department of Aeronautics and Astronautics
Massachusetts Institute of Technology

Abstract

The selection and design of inertial reaction devices, intended for use as passive absorbers and active control actuators for large flexible space structures, is investigated. Optimal passive vibration absorbers are designed for one and two DOF structural representations using three parameter optimization techniques: minimum maximum steady-state response; pole placement; and quadratic cost minimization. The three techniques yield nearly identical results and indicate that inertial devices should be tuned to the lowest of a set of modes intended to receive increased damping. Control actuators, which incorporate adjustable passive components, are also designed. The optimal passive components of the inertial reaction control actuator are those of the optimal passive vibration absorber. Proof of concept laboratory tests were performed on a modally rich, low fundamental frequency, quasi free-free beam. Electromagnetic, inertial-reaction devices, conceptually capable of functioning in the space environment (space-realizable), were used as passive absorbers providing significant increases in target mode passive damping. These same tuned devices were then used as control actuators in conjunction with positive definite feedback of dual sensor measurements. Best damping performance was achieved by ensuring that each actuator exerted similar levels of control (uniform feedback). Positive definite, dual feedback significantly increased damping in almost all modes without causing beam mode instabilities at any of the feedback gain levels attempted. Additional tests indicated the benefits and limitations of actuator tuning and the necessity of performing realistic experiments using space-realizable techniques.

Nomenclature

A	= state dynamics matrix
b_i	= i^{th} row of control effectiveness matrix
B	= control effectiveness matrix
c	= damper strength
c_{ii}	= i^{th} column of modal measurement matrix
C	= regulated variable matrix
d_i	= i^{th} column of modal disturbance matrix
D	= disturbance effectiveness matrix
D_c	= positive definite desired modal damping matrix
f	= feedback gains
F	= control force
G	= feedback gain matrix
J	= system cost
k_i	= stiffness of ith spring
m_i	= mass of ith mass
M	= measurement matrix
p_a	= decoupled absorber frequency
p_0	= decoupled structural modal frequency
P	= magnitude of disturbance force
P	= Lyapunov equation solution
q_i	= finite element coordinate
Q	= quadratic state penalty
Q_D	= disturbance torque
Q_i	= finite element reaction
R	= quadratic control effort penalty
u	= nondimensional control force
w	= disturbance inputs
x	= state vector
x_i	= displacement of ith mass
x_0	= initial state vector
y	= regulated variables
z	= measured variables
α	= positive gain parameter
β	= absorber-to-structural modal mass ratio
γ	= nondimensional Fourier frequency ratio
γ_{OPT}	= nondimensional modal frequencies
δ	= absorber-to-structure modal frequency ratio
Δ_{ST}	= static deflection of structural mass
θ	= matrix of actuator coordinates
μ	= nondimensional damper strength
σ_i	= second-order modes for internally balanced system
τ	= matrix of actuator torques
Φ_{DEC}	= decimated eigenvector matrix
ζ_i	= damping of ith mode
ω_i	= frequency of ith mode

Introduction

A number of future space structures may require active control of their flexible modes. Because of the lack of passive energy dissipation mechanisms in space, even small disturbances can lead to motions sufficiently large to be detrimental to performance requirements such as precision pointing and

maintenance of a micro-gravity environment. A two level approach to controlling structural vibrations is envisioned. First, the background structural and material damping can be increased by addition of passive damping devices. Secondly, an active control system can be added to further enhance system performance. In this scenario, the purpose of the passive damping device is threefold: to provide a supplementary passive dissipation mechanism; to increase the robustness of the active system; and to provide a fall back in the event of failure of some or all of the active system.

Several options are available for introducing passive and active damping into the structural dynamics. Passive energy dissipation mechanisms which can be implemented in space include: material damping enhancement; viscoelastic dampers; frictional dampers and joints; intermember dampers; and inertial reaction absorbers. Mechanisms for active damping include: piezoelectric devices; interelement actuators; angular momentum exchange devices; and inertial reaction actuators. Common to the list of options for passive dissipators and active actuators are inertial reaction devices. These are conceptually simple devices, easily implemented in space, which offer great promise. Questions associated with such devices include their theoretical optimization and experimental implementation.

Previous investigations have addressed some of the issues concerning the theoretical optimization of passive absorber designs. The classical single degree of freedom vibration absorber solution[1] is well known and has found wide application. Recently, a closed form solution was derived, based on a quadratic regulator formulation, that yields the same design for a one DOF absorber[2] Thus far, vibration absorber theory has primarily been applied toward enhancement of modal damping in a single mode. This work will extend absorber theory to both multi DOF damping and to the selection of the passive components of active inertial control actuators.

Experimentally, one configuration of an inertial reaction actuator is the pivoted, proof-mass actuator, currently being considered for use in active vibration suppression[3][4]. These devices have already been used in experiments involving one and two dimensional structures[5]. The work presented here makes use of similar devices, but incorporates tunable passive components into the design of active control actuators. A second reason for investigating inertial reaction devices is that they are conceptually capable of functioning in the space environment, i.e. they are space-realizable. A distinction of the experiments described below is that no actuation or sensing is performed against the laboratory frame and therefore the space-realizable techniques could be directly applied to spacecraft. This work focuses on the use of tunable inertial reaction devices, which operate through momentum exchange between the structure and a reaction mass, to perform output feedback control[6].

This paper is divided into two main sections which deal with the issues of theoretical optimization and experimental implementation. First, the components of a passive inertial vibration absorber and the passive components of an active inertial control actuator are optimized. The passive vibration absorber, (Fig. 1a) consists of a spring, mass, and damper. For a fixed absorber mass, the parameters to be optimized are the spring and damper values. The passive vibration absorber becomes an active control actuator with the addition of a feedback control force F (Fig. 1b). This actuator is a simplified model of the electromagnetic, inertial-reaction actuator developed at M.I.T., which was based on a concept derived at the Lockheed Palo Alto Research Laboratories[3]. Because of the functional similarities in the inertial absorber and actuator models, the possibility is created of incorporating both concepts into one device. In addition, the availability of adjustable passive parameters allows the passive

and active characteristics of the actuator to compliment each other. Approaches to the topic of absorber and actuator optimization are taken from several criteria including steady-state minimax, pole placement, and quadratic cost minimization.

Experimental verification is used to identify practical approaches and limitations in the use of these devices in the second part of this paper. First, the actuators are experimentally tuned to beam modes as passive vibration absorbers. Once tuned, these devices are used as active control actuators through feedback of dual system measurements. A control test is performed using actuators without optimized passive characteristics in order to demonstrate that improved performance is achieved when the actuators are tuned. A test involving actuation against the laboratory frame is used to demonstrate the relative ease in gaining high performance with a nonspace-realizable technique. By performing analytical and experimental investigations using these devices, the advantages and practical limitations of these space-realizable techniques can be identified.

Optimization of Passive Absorber Parameters

Several different approaches to the optimization of the parameters of a passive vibration absorber will be developed. The systems for which the passive vibration absorbers are optimized are shown in Fig. 2. In Fig. 2a the vibration absorber (m_2, k_2, and c) is attached to a single degree of freedom spring/mass system (k_1 and m_1) which represents the modal stiffness and modal mass of one structural mode. Fig. 2b is a model used for optimizing the absorber to a multi DOF plant. The force P indicates the location of an assumed input disturbance to the structure.

Three different approaches are used to determine the optimal spring and damper values for the passive vibration absorber. First, a steady-state minimax criterion is used to select the optimal passive parameters that minimize the maximum steady-state structural response at the absorber location (e.g. x_1 for the system in Fig. 2a) when subjected to a broad-band disturbance. Secondly, a pole placement solution is used to yield that set of absorber parameters which minimize the maximum transient modal response time. A third optimal solution is found by minimizing a weighted quadratic cost integral of the response. The steady-state minimax criterion is then extended to the selection of optimal absorber parameters for damping of multi DOF systems.

Optimal Absorber Design for a One DOF Structure

The three optimization techniques discussed above are used to examine the system in Fig. 2a. The equations of motion for this one DOF structure and passive vibration absorber are

$$m_1\ddot{x}_1 + c\dot{x}_1 + (k_1+k_2)x_1 - c\dot{x}_2 - k_2x_2 = P \qquad (1a)$$

$$m_2\ddot{x}_2 + c\dot{x}_2 + k_2x_2 - c\dot{x}_1 - k_2x_1 \quad = 0. \qquad (1b)$$

Steady-State Solution. The optimality criterion for this method is that of minimizing the maximum steady-state response (x_1) when the structural mass (m_1) is subjected to a broad-band disturbance (P). The nondimensional transfer function relating input disturbance to response for the model in Fig. 2a is

$$\left|\frac{X_1}{\Delta_{ST}}\right|^2 = [4\mu^2\gamma^2+(\gamma^2-\delta^2)^2]/$$

$$\{[\beta\delta^2\gamma^2-(\gamma^2-1)(\gamma^2-\delta^2)]^2+4\mu^2\gamma^2[\gamma^2(1+\beta)-1]^2\} \qquad (2)$$

where

$\Delta_{ST} = P/k_1$	structure's static deflection	(3a)
$\delta = p_a/p_0$	absorber/structure frequency ratio	(3b)
$p_0 = (k_1/m_1)^{1/2}$	decoupled structural frequency	(3c)
$p_a = (k_2/m_2)^{1/2}$	decoupled absorber frequency	(3d)
$\gamma = \omega/p_0$	nondimensional Fourier frequency ratio	(3e)
$\beta = m_2/m_1$	absorber/structure mass ratio	(3f)
$\mu = c/2m_2p_0$	nondimensional damping	(3g)

The solution based upon minimization of the maximum steady state response, known as the "Classical Vibration Absorber" problem[1], is summarized here. The maximum response of the structural mass (m_1) with an optimally tuned absorber attached is

$$\left.\frac{X_1}{\Delta_{ST}}\right|_{max} = \left[\frac{2+\beta}{\beta}\right]^{1/2} \qquad (4)$$

It is clear that increasing the absorber/structure mass ratio β lowers the maximum steady-state response. Therefore, no "optimal" mass ratio is derived from the absorber optimization, the larger the absorber mass the better. The optimal mass must be determined by a systems analysis which trades off absorber performance versus overall system mass. For the remainder of the present analysis, the mass ratio is assumed fixed and the values of the frequency ratio (δ) and nondimensional damper (μ) are optimized.

For a fixed mass ratio, the optimal frequency ratio (δ_{OPT}) based on the minimax criterion is

$$\delta_{OPT} = \frac{1}{1+\beta} \qquad (5)$$

and the nondimensional damper setting is found by solving an equation of the form

$$\mu_{OPT}^2 = \frac{N - Q(X_1/\Delta_{ST})^2}{L(X_1/\Delta_{ST})^2 - M} \qquad (6a)$$

where

$$N = (\delta_{OPT}^2 - \gamma_{OPT}^2)^2 \qquad (6b)$$

$$Q = [\beta\delta_{OPT}^2\gamma_{OPT}^2-(\gamma_{OPT}^2-1)(\gamma_{OPT}^2-\delta_{OPT}^2)]^2 \qquad (6c)$$

$$L = 4\tau_{0PT}^2(\tau_{0PT}^2(1+\beta) - 1)^2 \qquad (6d)$$

$$M = 4\tau_{0PT}^2 \qquad (6e)$$

and the nondimensional modal frequencies are

$$\tau_{0PT}^2 = \frac{1}{1+\beta}\left[1 \mp \sqrt{\frac{\beta}{2+\beta}}\right]. \qquad (7)$$

Equation 6a is indeterminant at the modal frequencies τ_{0PT}. To determine μ_{0PT}, a limit of Eq. 6a must be taken for values of τ approaching τ_{0PT}.

A numerical example of this steady-state solution is shown in Fig. 3 for a mass ratio of $\beta = 0.02$ (i.e. the absorber mass is 2% of the structural modal mass m_1) and for the optimal frequency ratio $\delta_{0PT} = 0.98$. Given this mass and frequency ratio, Fig. 3 shows the response to broad-band excitation for various nondimensional damper settings. Notice that $\mu = 0.086$ appears to minimize the maximum response, and in fact corresponds to μ_{0PT} derived using Eq. 6a.

Pole Placement Solution. The criterion used to determine the optimal pole placement solution is that of minimizing the maximum modal response time. Fig. 4 shows the upper half of the root locus for the system shown in Fig. 2a as the damper (μ) is varied. A mass ratio of $\beta = 0.02$ has been selected and the particular value of δ which causes the root trajectories to intersect at point A has been used. This is the exact same frequency ratio δ as was calculated in Eq. 5 for the steady-state optimization. The optimal nondimensional damping is that which places both poles at the same position (i.e. point A in Fig. 4). This value is

$$\mu_{0PT\_PP}^2 = \frac{\beta}{(1+\beta)^3}. \qquad (8)$$

The real part of the poles ($S = a \mp bi$) at point A is

$$a\Big|_A = -0.5\left[\frac{\beta}{1+\beta}\right]^{1/2} = Re(S). \qquad (9)$$

As in the steady-state response optimization, performance improves (i.e. $|a|$ increases) monotonically for increasing β. Therefore, a system mass versus performance tradeoff must once again be used to select β. For the numerical example of $\beta = 0.02$, $\delta_{0PT} = 0.98$ from Eq. 5 and the optimal damper value from the pole placement criterion is $\mu_{0PT\_PP} = 0.137$, which is 60% larger than the value for μ_{0PT} derived above using the minimax criterion.

Minimum Quadratic Cost Solution. The third and final criterion for determining optimal passive parameters is to define a cost function that penalizes the undesirable system response. To be consistent with optimal regulator control theory, a quadratic cost function is used. This integral of the quadratic of the system states to be minimized is

$$J = \frac{1}{2} \int_0^\infty x^T Q \, x \, dt \qquad \text{(10a)}$$

where

$$x = \left[\frac{x_1}{A_{sT}} \quad \frac{x_2}{A_{sT}} \quad \frac{\dot{x}_1}{A_{sT}p_0} \quad \frac{\dot{x}_2}{A_{sT}p_0} \right]^T \qquad \text{(10b)}$$

and Q is a non-negative square matrix. In this study, Q is selected so that the quadratic term in x equals the system's total nondimensional energy (kinetic and potential). The unique solution to Eq. 10a is

$$J = \frac{1}{2} x_0^T P \, x_0 \qquad \text{(11)}$$

where P is the solution to the Lyapunov[7] equation for Eqs. 10a and 10b and the system represented by Eqs. 1a and 1b, and x_0 is the nondimensional initial state vector.

A numerical search is used to determine the values of frequency ratio (δ) and nondimensional damper (μ) which result in the lowest cost (J) for a fixed mass ratio (β). The cost function (Eq. 10a) monotonically decreases with increasing β so once again a β must be preselected. An analytical solution exists for this minimization, in the case of a vibration absorber attached to a one DOF system[2]. This solution yields the same optimal frequency ratio δ and a similar nondimensional damping level as was found above for the steady-state optimization.

In this study, a simple heuristic gradient search is performed to determine the optimal spring δ and damper μ as prescribed by the quadratic cost criterion. The initial condition x_0 used to generate these results gives the structural mass (m_1) a unit velocity. The choice of a velocity or displacement initial condition will not significantly affect the results in a lightly damped system.

Optimal solutions using the three methods were compared[8] and found to have identical frequency ratios and similar nondimensional dampers. Thus, all three techniques are considered to yield virtually identical absorber designs, particularly with respect to the accuracy to which these devices can be experimentally implemented.

Optimal Absorber Design for a Two DOF System.

This investigation identifies the possibilities for adding damping to several modes through the use of a single absorber. This is demonstrated by extending the steady-state solution procedure to the design of a passive vibration absorber attached to a two degree of freedom representation of a structural system (Fig. 2b).

Once again, the objective is to minimize the maximum steady-state response. For the multi DOF structure, no simple closed form solution, such as Eqs. 5 and 6, is possible. A nonrigorous extension of the single DOF absorber analysis is presented.

The optimization possibilities are summarized in Fig. 5 where the frequency response of the system in Fig. 2b is shown for two sets of passive absorber parameters. Again, the mass m is fixed at $\beta = 0.02$ where β is defined as the ratio of absorber mass to the mass of the lower structural mode. Curve 1

shows the absorber tuned to the lower structural mode using the relations given in Eqs. 5 and 6 altered to refer to modal properties. In this case the absorber parameters yield a suboptimal result because the response at the high mode frequency is about four times larger than the response of the lower two modes. Increased absorber damper strength reduces apparent damping in the lower two modes while increasing residual damping in the high mode. The term "apparent damping" refers to the damping exhibited by the combined steady-state response of two modes which occur at almost identical frequencies. The apparent damping may not be indicative of the damping in each of the constituent modes. With sufficient additional damping the two peak magnitudes are equated and the minimax criterion is again satisfied (Curve 2).

The absorber frequency can also be tuned to the higher structural mode. However, with this choice of absorber frequency the absorber damper cannot be chosen so as to equate the response magnitudes of the upper and lower modes. This approach is unsuccessful since the damper exerts little influence on the low mode when the absorber frequency is tuned to the high mode.

The important result of this investigation is that when attempting to introduce significant levels of damping into several structural modes, the absorber frequency should be tuned to the frequency of the lowest mode of interest and the damper increased from the value determined through Eq. 6 until desired damping in the higher modes is achieved.

Optimization of Passive Components of an Active Actuator.

Thus far the attention has been focused on optimizing the components of the inertial device only when it is considered as a passive absorber. The next step in the study of inertial reaction devices is to determine the optimal passive components of the active control actuator shown in Fig. 1b. The control force (F) is assumed to be a function of the displacement and velocity states of both the structural mass m_1 and the actuator m_2, i.e. full state feedback is assumed. Both the active feedback gains and the values of the passive components are optimized simultaneously. The objective of this optimization is to determine how different these passive parameters are from the optimal parameters of the passive vibration absorber.

The method used for the simultaneous optimization of the active feedback gains and passive parameters is essentially identical to the previously discussed quadratic cost minimization. The quadratic cost now includes a penalty on the control effort. For example, the quadratic cost penalty for the actuator system in Fig. 2a is

$$ J = \frac{1}{2} \int_0^\infty [x^T Q x + u^T R u] \, dt \tag{12a} $$

where

$$ u = \frac{F}{\Delta_{ST} k_1} = -[\; f_1 \; f_2 \; f_3 \; f_4 \;] \cdot x \tag{12b} $$

and R is a positive, dimensionless constant. By the choice of R=100, the level of control forces are of the same order of magnitude as those generated by the passive components. This is done to prevent domination of the actuator dynamics by either the passive or active components. The solution to this quadratic cost equation is Eq. (11) where P is the solution to the steady-state Matrix Riccati

equation[7]. Again a heuristic gradient search is performed using a matrix map of numerically generated costs for a range of values of frequency ratio (δ) and nondimensional damper (μ). For each choice of δ and μ, the optimal regulator gains are calculated and the cost (Eq. 12a) evaluated. The minimum cost corresponds to the simultaneous optimal actuator design and active gain selection. Note that no penalty is explicitly placed on the passive components, and therefore the optimal solution will be driven towards relying as much as possible on the passive components of the actuator.

The two systems that were optimized for the passive vibration absorber (Fig. 2) were also optimized for the active actuator[*]. One characteristic result throughout the optimizations was that the optimal δ for the actuator is near the optimal δ_{opt} of the passive vibration absorber (17% lower in the worst case). The damper value (μ) is somewhat more sensitive to the presence of active feedback and therefore deviates from μ_{opt} by a greater percentage than do the frequency ratios.

The results of the simultaneous optimization of passive parameters and active feedback gains suggest that sequentially optimizing first the passive and then the active actuator components will yield nearly the same performance. To illustrate this, the frequency ratio (δ) and nondimensional damper (μ) were chosen as those specified by the steady-state minimax criterion, and the optimal regulator gains were calculated for this actuator design. The difference between these two designs is small and may be indistinguishable in actual implementation. Therefore, the inertial reaction control actuator performs most effectively when passively tuned as a vibration absorber. Supplemental passive damping is added to the system, and actuation effectiveness is increased.

Experiments Using Inertial Reaction Control Actuators

In order to investigate the practical implementation and limitations of space-realizable active control, an extensive set of experiments was conducted. The experimental objective was to maximize the damping in a pendulous free-free beam. First, the experimental hardware will be described, followed by a discussion of the model generated to help derive controller gains and predict closed-loop system behavior. Then, the results are given for the test where the inertial reaction devices were experimentally tuned as passive vibration absorbers to various beam modes. Once tuned, these devices were used as active actuators through the feedback of dual system measurements. Finally, the performance of these controllers is compared to the performance of untuned and nonspace-realizable actuators.

Experimental Apparatus.

Control Hardware. The structural plant of a prototypical space structure was simulated by a twenty-four foot brass beam, suspended by wires arranged in six sets of swinging parallelograms (Fig. 6). This simulated the free-free boundary conditions of a space structure by placing the two pendulous modes, at 0.30 and 0.32 Hz., below the first bending mode frequency of 0.37 Hz. There were four modes below 1.0 Hz., including the two pendulous modes, and twelve modes below 10.0 Hz., providing the experimental challenges of modal richness and extremely low frequency. Typical open loop modal damping ratios averaged 0.16% of critical (ζ=0.0016).

Four identical space-realizable Electromagnetic, Inertial-Reaction actuators were used to control the structure (Fig. 7). These devices, which are variations of devices developed at the Lockheed Palo Alto Research Labortory[3],

accelerate a pivoting reaction arm through small angle deflections to generate a control force on the beam[9]. An adjustable spring and damper were included to enable easy adjustment of the natural frequency and passive damping of the device, and allowing them to be used as both tunable vibration absorbers and control actuators with tunable passive components. A momentum wheel was attached to one end of the beam to provide disturbance torques. By rotationally accelerating an unsprung armature inertia, broadband (quasi-white) and sinusoidal torque excitation could be introduced. Eight space-realizable sensors were used to estimate system states. Each actuator contained a tachometer for measuring relative actuator motion. At the location of each actuator, an accelerometer was used to measure coincident inertial beam motion. The beam and actuator states at each sensor location were estimated from the tachometer and accelerometer measurements by an algorithm which filters low frequency signal drift and integrates over a frequency range encompassing the modes of the system. Discrete time processing was accomplished in one master and four slave processors. Interprocessor communication took place through shared memory space. Analog-to-digital and digital-to-analog conversion was used for sensor sampling and issuing control commands. Once this equipment was assembled as illustrated in Fig. 6, a mathematical model of the system was constructed and verified.

System Model. A finite element model, consisting of twelve beam elements and augmented by the dynamics of the four actuators, was formulated (Fig. 8). The model was first formulated with only the momentum wheel (Q_0), beam, and cable suspension properties included, and adjusted to accurately represent the open-loop beam behavior. Then the actuators, with springs set very stiff, were physically added to the beam and mathematically added to the model and the model was again adjusted. Modal damping was then experimentally determined and added to complete the model (Eq. 13).

$$
\begin{bmatrix} \begin{matrix} FEM \\ 26\times26 \end{matrix} & \begin{matrix} \text{ACTUATOR} \\ \text{COUPLING} \\ \text{TO BEAM} \end{matrix} \\ \text{ACTUATOR DYNAMICS} & \end{bmatrix}_{30\times30}
\begin{bmatrix} \ddot{q}_1 \\ \vdots \\ \ddot{q}_{26} \\ \ddot{\theta}_1 \\ \vdots \\ \ddot{\theta}_4 \end{bmatrix}_{30\times1}
+
\begin{bmatrix} \begin{matrix} FEM \\ 26\times26 \end{matrix} & \begin{matrix} \text{ACTUATOR} \\ \text{COUPLING} \\ \text{TO BEAM} \end{matrix} \\ \text{ACTUATOR DYNAMICS} & \end{bmatrix}_{30\times30}
\begin{bmatrix} \dot{q}_1 \\ \vdots \\ \dot{q}_{26} \\ \dot{\theta}_1 \\ \vdots \\ \dot{\theta}_4 \end{bmatrix}_{30\times1}
+
$$

$$
\begin{bmatrix} \begin{matrix} FEM \\ 26\times26 \end{matrix} & \begin{matrix} \text{ACTUATOR} \\ \text{COUPLING} \\ \text{TO BEAM} \end{matrix} \\ \text{ACTUATOR DYNAMICS} & \end{bmatrix}_{30\times30}
\begin{bmatrix} q_1 \\ \vdots \\ q_{26} \\ \theta_1 \\ \vdots \\ \theta_4 \end{bmatrix}_{30\times1}
=
\begin{bmatrix} Q_1 \\ \vdots \\ Q_{26} \\ T_1 \\ \vdots \\ T_4 \end{bmatrix}_{30\times1}
+
\begin{bmatrix} 0 \\ Q_0 \\ 0 \\ \vdots \\ 0 \end{bmatrix}_{30\times1}
\tag{13}
$$

With this refined model, the first seventeen predicted open-loop modal beam frequencies were within 2% of their measured values. The actual actuator

stiffnesses and dampings were determined during the actuator tuning process, i.e. the process of carefully adjusting the passive components of the inertial actuator to their desired optimal values.

Tuned Passive Absorber Experiments

The first set of experiments involved tuning the four actuators, used as passive absorbers, to four "target modes" of the beam, and determining their effectiveness as passive absorbers. Modes targeted for absorber tuning were those most sensitive to the disturbance. Equation 14 defines the modal transmission from disturbance to regulated variables for lightly damped systems in the form of Eq. 15; as derived by internal balancing theory[10]. Equation 13 is manipulated into this form by transformation first to modal coordinates and then to state-space variables. For this example, the regulated variables (y) have been chosen to be the entire state vector (x), i.e. it is desirable to minimize the disturbance to all of the state variables, equally.

$$\sigma^2_{zc_i} = (4\zeta_i\omega_i)^{-1} [d_i d_i^T(\omega_i^{-2} + 1)c_{1i}^T c_{1i}]^{1/2} \tag{14}$$

$$
\begin{aligned}
x &= Ax + Bu + Dw & &\text{state equation} & &(15) \\
z &= Mx & &\text{measurement equation} \\
y &= Cx & &\text{regulated variable equation} \\
u &= -Gz & &\text{feedback equation}
\end{aligned}
$$

In Eq. 14, ω_i is modal frequency and ζ_i is modal damping, and c_{1i} and d_i are columns and rows of the regulated variable matrix C and disturbance matrix D, respectively.

Figure 9 shows the transmission, as defined by Equation 14, from the disturbance to the regulated variables. The result of the analysis above, in which an absorber is tuned to more than one degree of freedom, indicates that it is desirable to tune to the lower frequency modes of interest. Therefore, the four lowest consecutive modes with high disturbance transmission were chosen as the target modes, as shown by the arrows in Figure 9. Once the target modes were selected, the absorbers were placed at positions along the beam where they exerted maximum influence on their respective modes, that is positions which maximized the modal mass ratio. One absorber was placed at each end and one was placed at each 1/3 length position.

One absorber was tuned to each of the four target modes. The optimal passive actuator stiffness and damping, which were shown to be nearly identical to the optimal absorber stiffness and damping, were chosen using the steady-state minimax criterion[9]. The mechanical spring in the actuator was adjusted as accurately as possible to the optimal frequency, and collocated feedback of actuator rotational position and rate was used to fine tune the devices. The performance and limitations of the four "passive" actuators were then assessed.

Once tuned, two types of tests were performed. First, the acceleration transfer function of the beam with tuned absorbers was obtained using a quasi white noise torque input with a constant torque of 0.006 Newton Meters RMS across the frequency range of interest. This disturbance torque level was also used in all subsequent tests. A qualitative comparison of the acceleration transfer function of the beam from the disturbance torque at one end to an accelerometer at the opposite end, is shown in Figure 10. Two traces are shown, one for the case of very stiff absorbers such that there is relatively little

motion, and the second for the case of tuned absorbers. The four target modes are those with frequencies of 1.09, 1.74, 2.61, and 3.78 Hz. Note the reduced response (increased modal damping) in this frequency range as a result of absorber tuning. Additional, or residual damping is also evident in the modes above 4.0 Hz. The existance of residual damping in modes higher than the modes to which the absorbers are tuned is consistent with the observations made from the multi DOF tuning analysis (Fig. 5).

The second set of tests involved initial condition transient decays of the target modes. In Figure 11, the transient responses of the four target modes with tuned absorbers (right column) are compared to the corresponding modal transient responses without the tuned absorbers (left column). Due to the second-order dynamics, tuning of an absorber to a target mode results in two modes close in frequency to the original target mode frequency (e.g. target mode 5 becomes modes 5a and 5b after tuning). The transient decay of the mode with the lesser damping of the two is shown in Fig. 11. As can be seen in the transient decays, stiction would seize the actuator motion at low vibration levels causing marked reductions in damping and limiting low amplitude performance. Table 1 lists information pertaining to the absorber tuning process. As can be seen, by comparison of the modal damping ratios prior to tuning to the case with tuned absorbers, over an order of magnitude increase in critical damping ratio was achieved. Sixty to ninety percent of the predicted damping was obtained. The large deviation between actual and predicted damping in target mode five was due to friction effects, as indicated by the characteristic linear decay in Fig. 11. The low performance in mode eight was due to the low mass ratio which increases tuning sensitivity and difficulty. The absorbers could not be tuned to modes lower than 1 Hz. due to stiction problems and prohibitively large tuned absorber motion.

Several beneficial characteristics occur as a result of absorber tuning. Figure 12 compares the modal disturbance transmissions (Eq. 14) for the beam with tuned absorbers (solid bars) to those shown in Fig. 9 for the beam without the absorbers tuned (hatched bars). Due to double mode behavior, two solid bars occur for each of the four hatched bars corresponding to the original target modes 5 through 8. As can be seen from Fig. 12, the disturbance transmission is significantly reduced in the target mode region.

Controllability of the target modes is also enhanced by tuning the passive components of the actuator to those of the optimal absorber. The modal control transmission from actuator to regulated variables is defined similarly to disturbance transmission in internal balancing theory[10]. The disturbance inputs of Eq. 14 are replaced by control inputs yielding Eq. 16.

$$\sigma^2_{ic} = (4\zeta_i\omega_i)^{-1} \left[b_i b_i^T (\omega_i^{-2} + 1) c_{ii}^T c_{ii} \right]^{1/2} \tag{16}$$

The vector b_i corresponds to a row of the control effectiveness matrix $\bar{B}$. The values for the control transmission for the beam with actuators tuned as absorbers are shown in Fig. 13. Since these values indicate the effect of control action on the states of the system, they are good indicators of relative modal controllability. Note that the target and actuator modes are most controllable. The next most controllable modes are the beam modes above the target modes. Modes lower than the target modes are relatively uncontrollable.

Significant increases in passive damping have been achieved by the addition of the passive absorbers. If these same devices are also used as active actuators, it can be argued that the damping is introduced with no additional mass penalty. While the benefits of adding passive absorbers are substantial,

the limitations are also important. Friction poses a problem in damping low level vibrations where stiction can seize absorber motion. This might be overcome with a high frequency torque dither or bearing improvement. Stroke limitations hinder tuning to low modes and steps to increase stroke often increase friction. Finally, passive tuning of the actuators requires a precise knowledge of the target mode frequency and the difficulty is increased for modes with low absorber mass ratio.

Active Control Experiments

Once the actuators had been passively tuned to the four target modes, three sets of control experiments were performed using negative output feedback (Eq. 15). First, dual rate feedback was used to drive the four tuned actuators from the four tachometers using a fully populated, positive definite gain matrix G. Dual feedback refers to like sensor to like actuator feedback (rotational shaft rate to shaft torque) where each sensor is physically located with an actuator[*]. In the second set of tests, the same dual measurements were fed back to untuned, zero stiffness actuators. This verified the effectiveness of tuning the actuators as absorbers with nonzero stiffness. Finally, a control test was performed using one actuator reacting against the laboratory frame. This investigates the performance differences between space-realizable and nonspace-realizable experiments.

Dual Feedback to Tuned Actuators.

Two different tests were performed in this first set which differed in the method used to derive the feedback gain matrix G. The positive definite, dual feedback was derived using the technique described in Reference 6. In this technique, a matrix D_c is chosen to be a positive definite, diagonal matrix whose entries are the desired increases in damping for a chosen set of modes equal in number to the actuators used. Next, the modal eigenvector matrix of the full system model is decimated while retaining rows corresponding to actuator motion and columns corresponding to the chosen set of modes. This decimated matrix is designated as Φ_{Dec}. The feedback gain matrix is then derived using Eq. 17a. For these tests with four actuators, identical modal damping increases were desired in each of the four chosen modes (Eq. 17b)

$$G = \Phi_{Dec}^{-T} D_c \, \Phi_{Dec}^{-1} \tag{17a}$$

$$D_c = \alpha I . \tag{17b}$$

The quadratic form of Eq. 17a guarentees a positive definite feedback matrix. The two tests performed differed in the four modes chosen to form Φ_{Dec}.

The first test used the lowest two target modes, to which actuators were tuned, and their two corresponding actuator modes (5a, 5b, 6a, and 6b) to create Φ_{Dec}. The second test used the first four beam modes above the target modes (modes 9, 10, 11, and 12) to create Φ_{Dec}.

When the lowest two target and their corresponding actuator modes were chosen to derive the feedback through Equation 17, a feedback matrix resulted which contained highly nonuniform entries. This was due to the relatively large eigenvector entries corresponding to the motion of the two actuators tuned to these two lower target modes (5 and 6). The inversion of the decimated eigenvector matrix Φ_{Dec} in Eq. 17 resulted in high feedback gains for the two actuators not tuned to these two lower target modes (i.e. the actuators tuned to

modes 7 and 8). The highest gain loop was collocated feedback to the actuator which had been tuned to target mode eight. This gain was four orders of magnitude larger than the collocated feedback to the actuator tuned to target mode five. Because of the nonuniform gain matrix, this design only created significant feedback to actuators tuned to the higher two target modes (7 and 8).

Using this feedback, Figure 14 contrasts the transfer function for the beam with only the tuned absorbers (a), with that of the beam with additional nonuniform feedback to tuned actuators (b). Notice that minor increases in damping in the modes above the target modes (modes higher than 4.0 Hz.) occured at the expense of damping in target mode eight (at 3.78 Hz.) of the beam/actuator system. In Fig. 14, hatching indicates modes that exhibited less closed-loop damping than open-loop damping. This behavior can be explained using Fig. 4 to represent the root locus in the vicinity of mode eight. Above a certain level of positive collocated rate feedback, that which places the poles at the equivalent of point A (Figure 4), one of the root trajectories for modes 8a and 8b moves towards the imaginary axis. This results in reduced apparant damping in that mode. The actuator tuned to mode seven is starting to exhibit similar behavior. Recall from above that the collocated rate feedback to the actuators tuned to modes 7 and 8 dominate the feedback gain matrix.

Table 2 lists actual and predicted closed-loop modal characteristics for this test for the feedback gain level chosen. As listed in the table and shown in Fig. 14, only mode 9 (at 4.95 Hz.) exhibited significantly increased modal damping. The model and the data are in fair agreement. The model did not predict reductions in modal damping, due to the feedback, at this gain level but did so at a slightly higher gain level.

An important limitation was realized through this test. The feedback used for the closed-loop case shown in Fig. 14 was at a level just below that which caused onset of a high frequency (67 Hz.) instrumentation/actuator instability, similar in nature to those reported in Reference 4. Only relatively low control performance was achieved prior to the onset of this instability. Due to the nonuniform gain matrix, two of the actuators exerted only negligible control effort, while the other two had relatively high collocated gains. Because this limitation was due to relatively high gains to one actuator causing a local instability before significant control authority could be exerted overall, the corrective step was to create a uniform feedback matrix with positive definite, dual feedback properties.

In the second test, Eq. 17 was again used to derive a positive definite feedback matrix using an eigenvector transformation Φ_{orc} based on the first four beam modes above the target modes (modes 9, 10, 11, and 12). Uniformity in the gain matrix was achieved since the actuator eigenvector entries were of similar magnitudes. Figure 15 compares the acceleration transfer function of the beam with only the tuned absorbers (a) to that of the beam with additional feedback to tuned actuators (b). Significant increases in damping in modes 9 through 12 resulted at a cost of only slight reductions in apparant damping in target modes 5 through 8 (hatching). Table 3 lists the predicted and measured modal characteristics. As can be seen in both Fig. 15 and Table 3, modes 9 and 10 received the largest increases in damping. Better performance was achieved in this case because all four actuators were contributing evenly. In fact, all modes above 4 Hz. exhibited significant increases in damping. Again, an instrumentation/actuator instability limited the feedback gain level. This result verifies that uniform feedback provides better performance since it allows all actuators to contribute before the onset of instability.

Several conclusions can be drawn from this first set of tests. Nonuniform

EE-14

feedback resulted in poor performance while uniform feedback allowed significant increases in higher mode damping at the slight sacrifice of modal damping of the target modes to which the actuators were tuned. This type of rate feedback is simply a more sophisticated form of passive multi DOF absorber tuning. In both tests, positive definite dual feedback proved stable with respect to beam modes for all gain levels tested up to that which caused instrumentation/actuator instability. This type of feedback also guarentees an increase in total system damping but does not necessarily guarentee simultaneous damping increases in all modes at all gains.

Dual Feedback to Untuned Actuators. In the next set of experiments, the same type of dual rate feedback (Eq. 17) was used in conjunction with untuned, almost zero stiffness actuators. This was done to illustrate the benefits of tuning to beam mode frequencies in the range over which control is desired. Figure 16 contrasts the acceleration transfer function of the beam with uniform feedback to untuned, zero stiffness actuators (a), with that of the case using uniform feedback to tuned actuators (b). The previous target modes (modes 5 through 8, 1.09 through 3.78 Hz.) show greater response while closed loop performance is inferior to that shown in Figs. 15. Though the difference between the performances of the systems using tuned and zero stiffness actuators is indistinguishable below 2 Hz. in Fig. 16, Table 4 lists the results which verify, when compared to Table 3, that actuator tuning yields better performance.

Nonspace-Realizable Actuation. The last test involved a nonspace-realizable method of control actuation in which one actuator reacted against the laboratory frame. In this case, simple collocated actuator rate was negatively fed back to the actuator. Figure 17 compares the acceleration transfer function of the beam with tuned absorbers (a) to that of the beam with one actuator allowed to react against the laboratory frame (b), showing how effective this simple feedback is when applied to this actuation arrangement. The level of feedback was again limited by the instrumentation/actuator instability. As is evident from the data, this simple single actuator arrangment resulted in much better performance than any of the space-realizable methods, even those using four actuators. This illustrates the need to conduct space-realizable experiments in order to identify important limitations which may be overlooked when performing nonspace-realizable tests such as this.

Conclusions

Several conclusions can be drawn from the theoretical optimization of these inertial reaction devices. Three different optimization procedures yielded almost identical absorber designs providing confidence in the tuning process. In addition, the optimal passive components of the control actuator were found to be equal to those of the optimal absorber. This allows passive damping to be added without significant mass penalty. Finally, when using an inertial device to increase damping in several modes, it is desirable to tune the frequency of the device to the lowest mode and adjust the damping accordingly.

Experimentally, an inertial reaction device was used effectively as both a passive vibration absorber and a control actuator, passively tuned as an absorber, verifying the results of the tuning analysis that stated that passive tuning compliments active control. This dual purpose device resulted in a mass savings, increased modal controllability, and reduced target mode disturbance transmission. Additional passive damping increases gain margin for feedback

systems that are conditionally stable and allows a form of passive damping enhancement in the event of control system failure. These space-realizable experiments were found to be important in determining performance limitations due to instrumentation instabilities, friction in relative motion actuators, and actuator saturation at low frequencies. In addition, nonspace-realizable tests exhibited excellent damping performance which emphasized the need to investigate the realistic implementation limitations of space-realizable techniques. Uniformity in the positive definite, dual feedback matrix allowed better performance before the onset of instrumentation/actuator instabilities because all actuators were able to exert maximum stable feedback. In deciding whether to apply these tuning procedures to momentum wheel devices, it must be determined whether the increased performance justifies the stroke limitations caused by resonating the devices.

References

1. Timoshenko, S., Young, D.H. and Weaver, W. Jr., Vibration Problems in Engineering, Fourth Edition, John Wiley and Sons, New York, 1974.

2. Juang, J., "Optimal Design of a Passive Vibration Absorber for a Truss Beam," J. Guidance, Control and Dynamics, Nov.-Dec. 1984, p. 733.

3. Aubrun, J.N., Breakwell, J.A., Gupta, N.K., Lyons, M.G., Marguiles, G., ACOSS FIVE (Active Control of Space Structures) PHASE 1A, Lockheed Missiles & Space Co., Inc., Mar.80-Sept.81.

4. Aubrun, J.N., Marguiles, G., "Low-Authority Control Synthesis for Large Space Structures," Lockheed Palo Alto Research Laboratory, Contract Report on Contract NAS1-14887, May 1982.

5. Wang, B.P., Horner, G.C., and Pilkey, W., "Optimal Damping for the Vibration Control of a Two-Dimensional Structure," AIAA Paper 81-1845, Aug. 1981.

6. Skidmore, G.R., Hallauer, W.L.Jr., "Experimental-Theoretical Study of Active Damping with Dual Sensors and Actuators," AIAA Paper no. 85-1921-CP, AIAA Guidance and Control Conference, Aug. 1985.

7. Kwakernaak, H., Sivan, R., Linear Optimal Control Systems, Wiley-Interscience, New York, 1972.

8. Miller, D.W., Crawley, E.F., Ward, B.A., "Inertial Actuator Design for Maximum Passive and Active Energy Dissipation in Flexible Space Structures," AIAA Structural Dynamics and Materials Conference, Paper no. 85-0777, Apr. 1985.

9. Miller, D.W., "Finite Active Control Elements for Large Space Structures," MS Thesis, M.I.T, 1985.

10. Gregory, C.Z.Jr., "Reduction of Large Flexible Spacecraft Models Using Internal Balancing Theory," Journal Guidance, Control and Dynamics, Vol.

Table 1. Experimental Results of Absorber Tuning.

	5	6	7	8
Target Mode Number:	5	6	7	8
Target Mode Frequency (Hz):	1.09	1.74	2.61	3.78
Absorber/Modal Mass Ratio:	0.033	0.011	0.018	0.004
Optimal Frequency Ratio:	0.968	0.990	0.983	0.996
Optimal Nondimensional Damper:	0.111	0.062	0.079	0.039
Predicted Critical Damping Ratio:	0.0637	0.0362	0.0470	0.0231
Measured Critical Damping Ratio:	0.0441	0.0320	0.0438	0.0136
% Achievement (measured/predicted)	69.2%	88.4%	93.2%	59.0%
Damping Ratio Prior to Tuning:	0.0021	0.0018	0.0014	0.0016
Increase in Critical Damping Ratio:	21	18	31	9

Table 2. Test Results for Nonuniform, Positive Definite Dual Feedback to Tuned Actuators

Mode Number	Frequency (Hz)	Modal Damping Ratio			%Achievement measured predicted
		Open Loop (measured)	Closed Loop (predicted)	Closed Loop (measured)	
5a	1.0509	0.0441	0.0441	------	
5b	1.2695	------	0.0479	------	
6a	1.7179	0.0320	0.0329	------	
6b	1.8772	------	0.0392	------	
7a	2.4936	------	0.0709	------	
7b	2.7522	0.0438	0.0715	------	
8a	3.6908	0.0136	CRIT	CRIT	
8b	3.9479	------	0.0173	0.0095	54.9%
9	4.9491	0.0040	0.0055	0.0110	200.0%
10	6.4207	0.0033	0.0042	0.0041	97.6%
11	8.1937	0.0048	0.0055	0.0047	85.5%
12	9.8012	0.0025	0.0029	0.0025	86.2%
------ not measured					

Table 3. Test Results for Uniform, Positive Definite Dual Feedback to Tuned Actuators..

Mode Number	Frequency (Hz)	Open Loop (measured)	Modal Damping Ratio Closed Loop (predicted)	Closed Loop (measured)	% Achievement measured / predicted
5a	1.0508	0.0441	CRIT	-------	
5b	1.2695	-------	0.0233	-------	
6a	1.7173	0.0320	0.8635	-------	
6b	1.8772	-------	0.0470	-------	
7a	2.4936	-------	0.7144	-------	
7b	2.7522	0.0438	0.0546	-------	
8a	3.6908	0.0136	0.4131	-------	
8b	3.9479	-------	0.0259	-------	
9	3.9491	0.0040	0.0155	0.0118	76%
10	6.4207	0.0033	0.0156	0.0129	83%
11	8.1937	0.0049	0.0103	0.0084	82%
12	9.8012	0.0025	0.0075	0.0060	80%
------- not measured					

Table 4. Test Results for Uniform, Positive Definite Dual Feedback to Untuned (Zero Stiffness) Actuators.

Mode Number	Frequency (Hz)	Open Loop (measured)	Modal Damping Ratio Closed Loop (predicted)	Closed Loop (measured)	% Achievement measured / predicted
5	1.0943	0.0021	0.0048	------	
6	1.7423	0.0018	0.0094	------	
7	2.6098	0.0014	0.0056	------	
8	3.7837	0.0016	0.0054	------	
9	4.9217	0.0014	0.0025	0.0018	72%
10	6.4014	0.0015	0.0034	0.0031	91%
11	8.1865	0.0016	0.0023	0.0017	74%
12	9.7930	0.0017	0.0042	0.0030	71%
------- not measured					
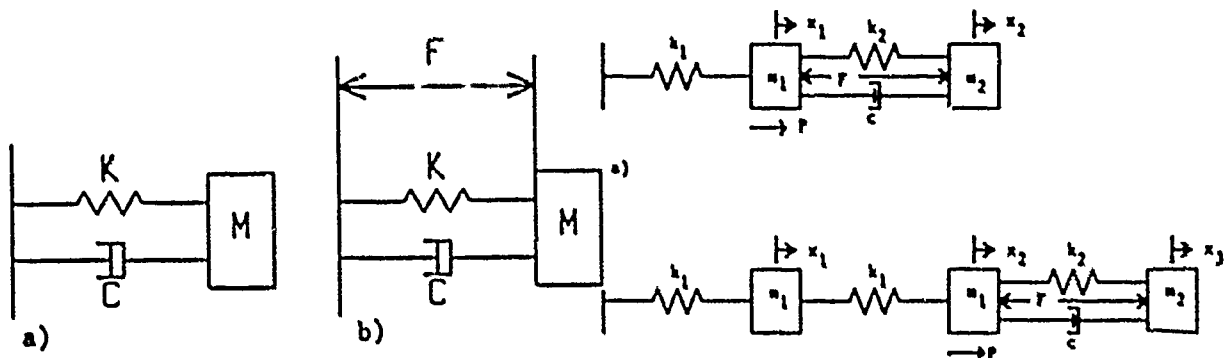
Figure 1. Models of Two Inertial Devices: a) a passive vibration absorber and b) the same device as a control actuator.

Figure 2. A One Degree of Freedom Absorber/Actuator Coupled to a) a one DOF structure and b) a two DOF structure.
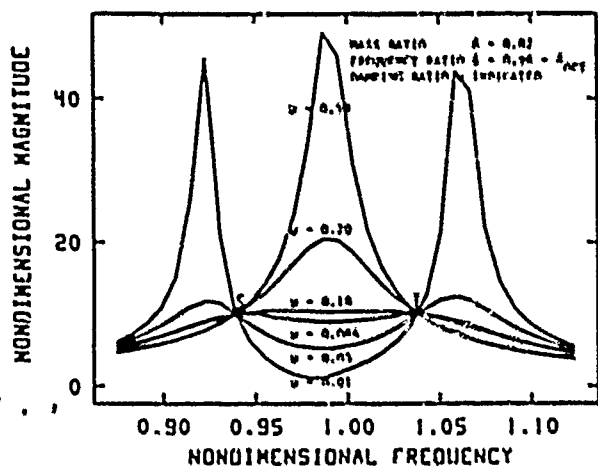
Figure 3. Response (x_1/Δ_{st}) Versus Frequency (ω/p_0) for the System of Fig. 2a for the Optimal Frequency Ratio, the Given Mass Ratio, and the Indicated Damping.
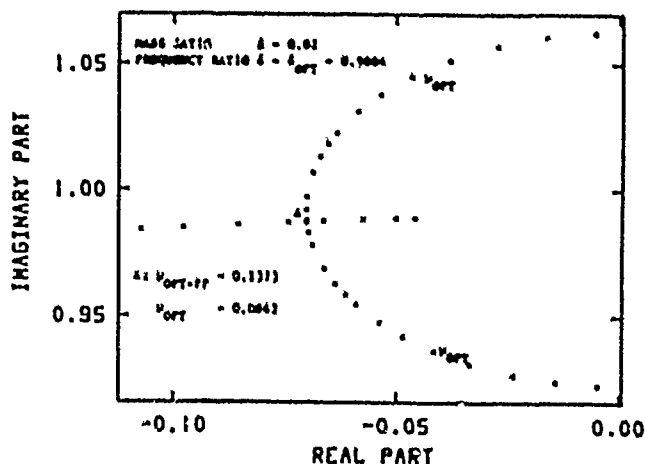
Figure 4. S-Plane Representation of the Poles of the System of Fig. 2a as a Function of Increasing Damper Value.
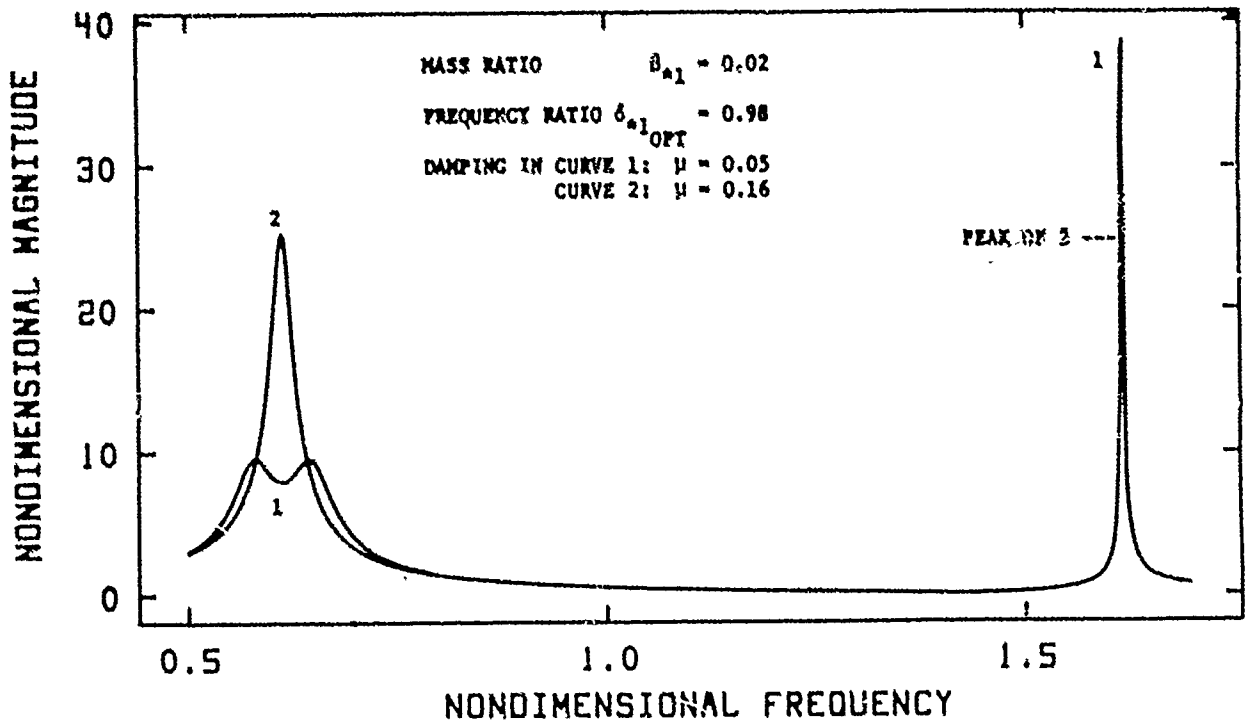
Figure 5. Response (x_i/A_{sr}) Versus Frequency (ω/p_0) for the System of Fig. 2b for the Choice of Damping Which Minimizes the Responses of the Lower Two Modes (Curve 1) and All Modes (Curve 2).
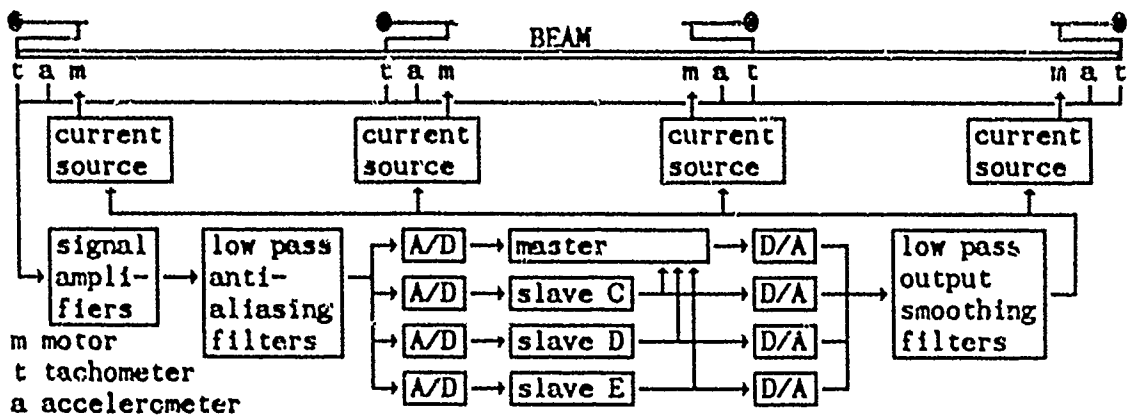
Figure 6. Control Hardware Configuration for Experimental Phase
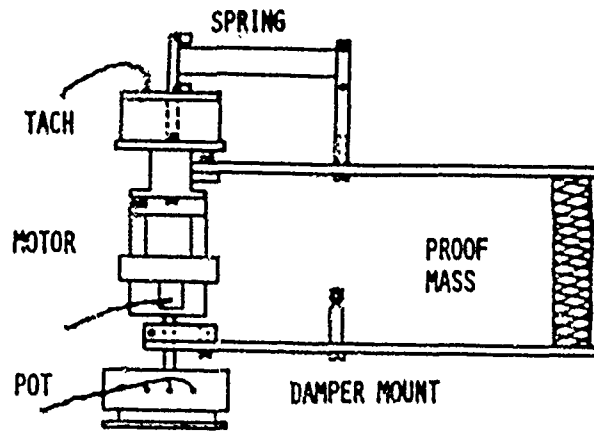
Figure 7. Inertial-Reaction Absorber/Actuator Configuration.
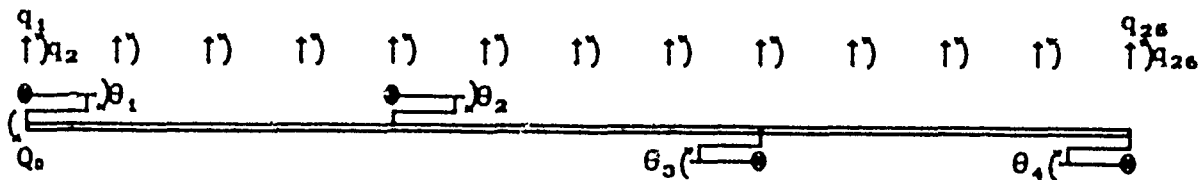
Figure 8. Twelve Element Beam and Actuator Model
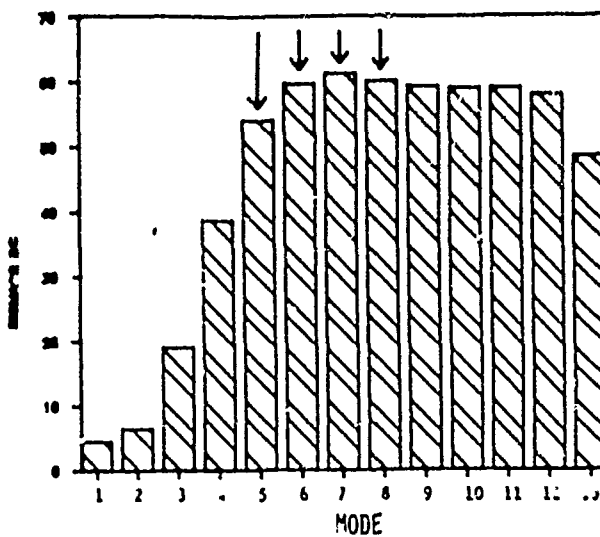
Figure 9. Level of Disturbance Transmission to the Model States for the System Without Absorbers Tuned to Target Modes.
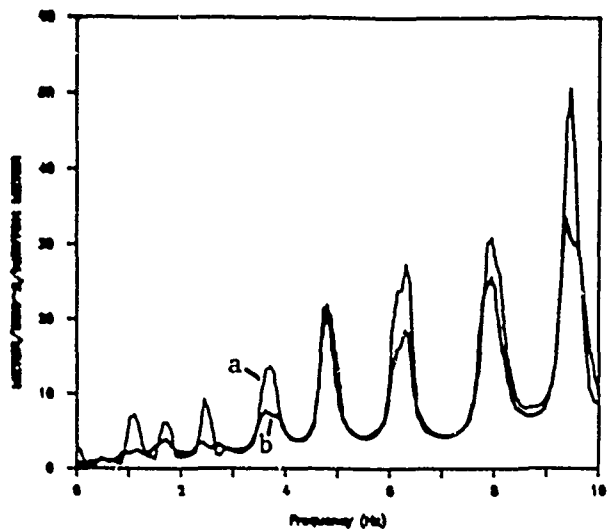
Figure 10. Acceleration Transfer Function a) with very stiff absorbers (higher level response) and b) with tuned absorbers (lower level response).
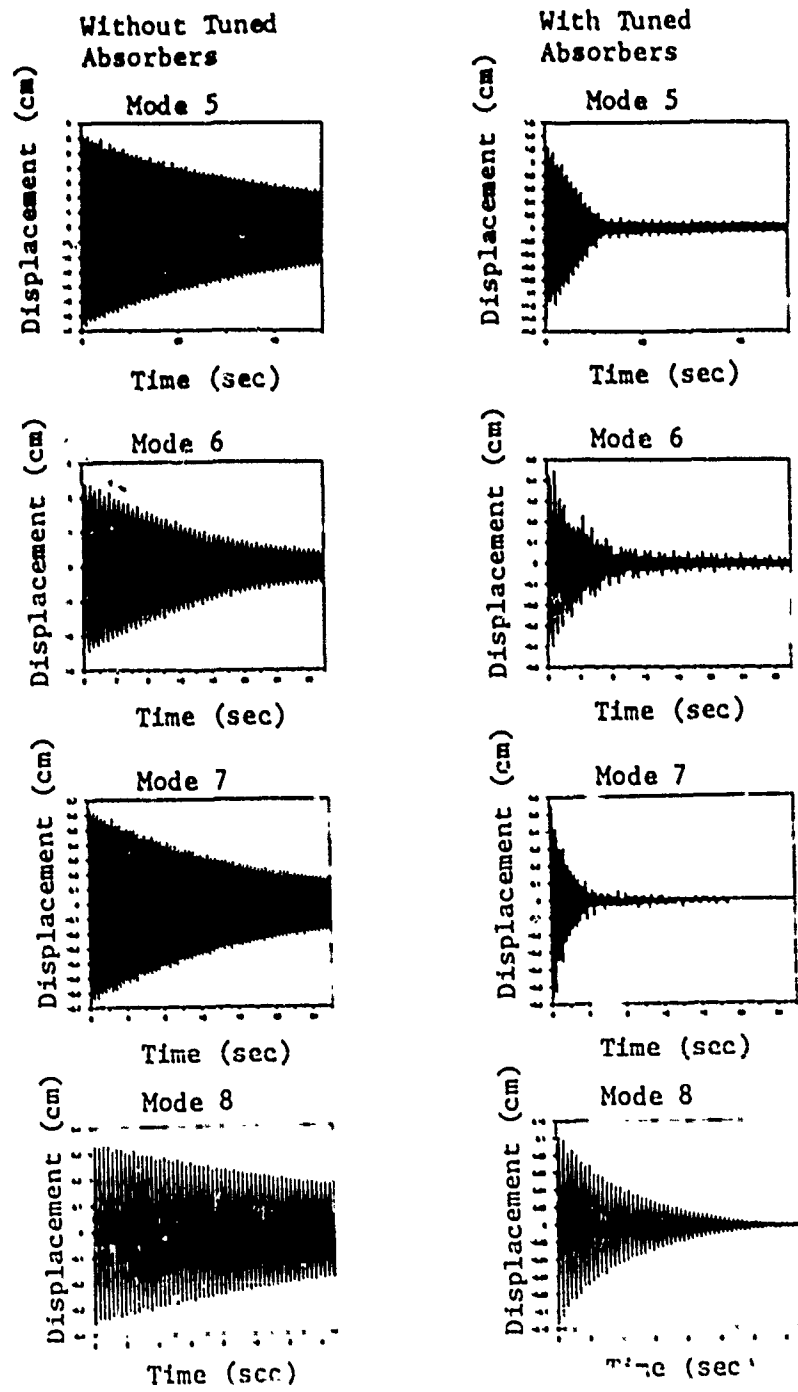
Figure 11. Transient Response of Target Modes Without and With Tuned Absorbers.

EE-22
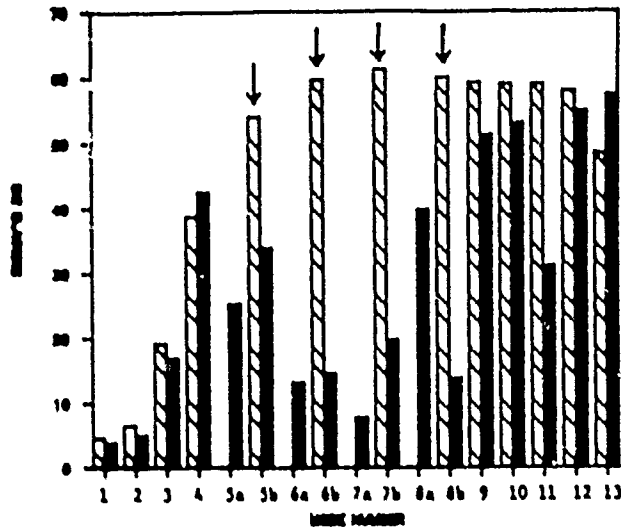
Figure 12. Level of Disturbance Transmission to the Model States for the System Without (hatched) and With (solid) Absorbers Tuned to Target Modes.
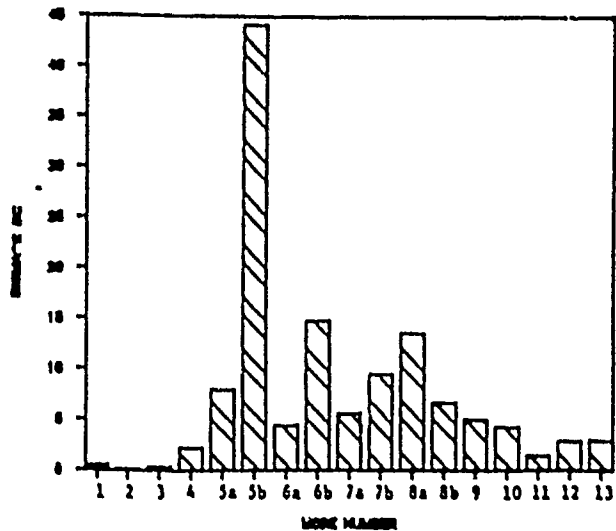
Figure 13. Level of Control Transmission to the Model States for the System With Actuators Whose Passive Components are Tuned to Those of an Optimal Absorber.
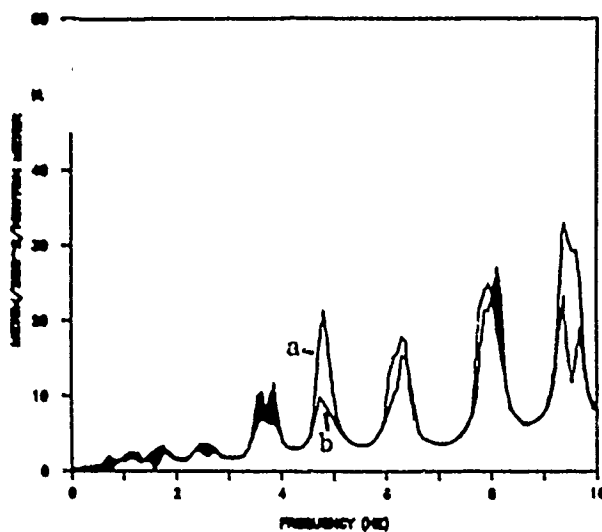
Figure 14. Acceleration Transfer Function a) with tuned absorbers (nominally higher level response) and b) with additional nonuniform dual feedback to tuned actuators (nominally lower level response). Hatching indicates regions in which response is increased in case b.
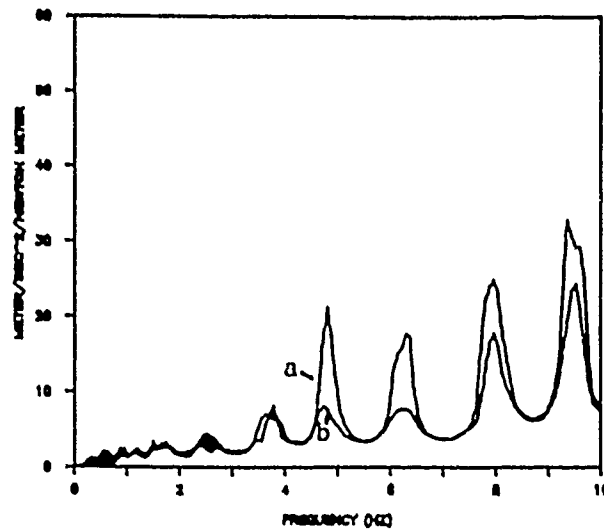
Figure 15. Acceleration Transfer Function a) with tuned absorbers (higher level response). Hatching indicates regions in which response is increased in case b.
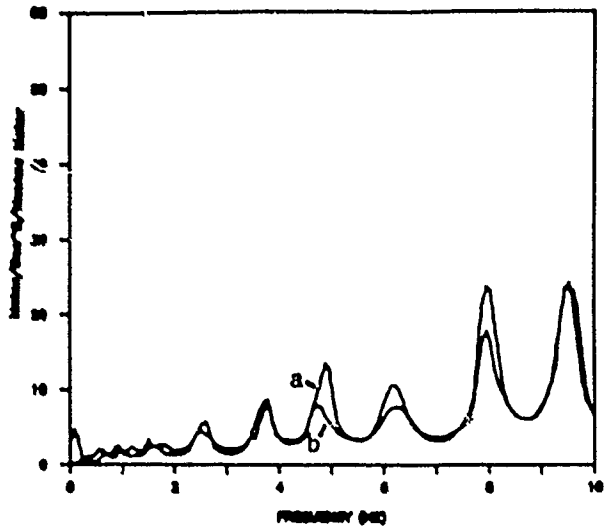
Figure 16. Acceleration Transfer Function a) with additional uniform dual feedback to zero stiffness actuators (higher level response) and b) with additional uniform dual feedback to tuned actuators (lower response).
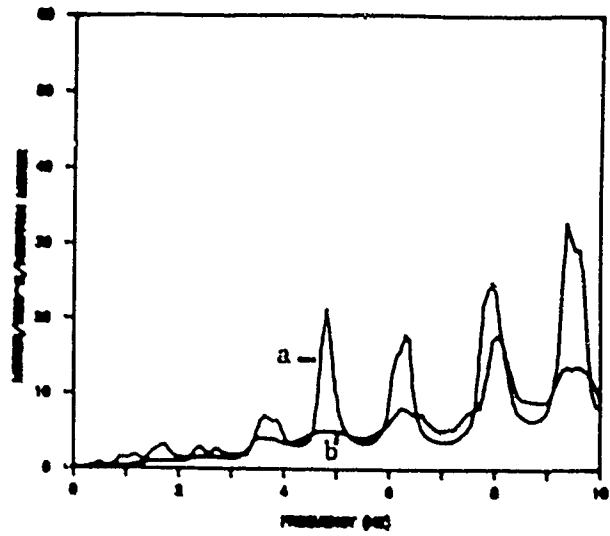
Figure 17. Acceleration Transfer Function a) with tuned absorbers (higher level response) and b) with collocated rate feedback to a single actuator reacting against the laboratory frame (lower level response).

Distributed, Active Damping of Multiple Modes

Dr. T. J. Brennan
P. R. Dahl
J. J. Gerardi

(Not available for publication)

Active Damping Augmentation by Pole Allocation Methods

Dr. E. F. Berkman

(Not available for publication)

A Unified Approach to Model Reduction and Robustness

Dr. L. R. Passeron
B. J. Sevennec

(Not available for publication)

Eigenstructure and Control of Damping and Vibrations

Dr. A. N. Andry, Jr.
Dr. E. Y. Shapiro
Dr. K. M. Sobel

(Not available for publication)

Material Damping in Aluminum
and Metal Matrix Composites

Edward F. Crawley
Associate Professor

Marthinus C. van Schoor
Research Assistant

Department of Aeronautics and Astronautics
Massachusetts Institute of Technology

Abstract

The material damping in beam-like specimens of aluminum and metal matrix composites was measured. A unique apparatus to determine damping by free decay while the specimens are in free fall in a vacuum was used. The specimens tested include 2024-T3 and 6061-T4 aluminum, and unidirectional graphite/metal matrix specimens with P55 and P100 fibers and 6061 Aluminum and AZ91C Magnesium as matrix materials. Tests were conducted to determine the dependence of damping on frequency and stress level. For the aluminum specimens, the material damping followed the Zener model at very low stress levels. Below the Zener relaxation frequency, a strong dependence of damping on stress was found for even moderate stress levels. Damping for the aluminum matrix materials was slightly above that predicted by the Zener model for a homogeneous bar of the matrix aluminum. For the magnesium matrix specimens, damping significantly above the Zener prediction for the homogeneous matrix material was observed.

INTRODUCTION

The increasing interest in large and precision space structures has focused attention on the precise quantification of the passive dynamics and damping of these structures. The mission requirements imposed on these structures often requires active control of their dynamic response. In order to achieve these precise active control requirements in a robust way, sufficient passive energy dissipation characteristics must be present. One of the sources of passive dissipation, material damping, was the subject of this investigation.

The damping characteristics of the materials investigated were determined in this study by recording the free decay response of a beam-like specimen when lofted into free-fall. The tests were performed in vacuum to eliminate the effects of aerodynamic damping [1].

The materials selected for this study were among those anticipated for use in future space structures. Several common aluminum alloys, 2024-T3 and 6061-T4 were chosen for testing, since they have a well documented material damping behavior at low amplitude, and form the matrix for some of the metal matrix specimens subsequently tested. A stress dependence of material damping in 2024-T3 Aluminum had been noted in an earlier study at MIT [2]. By testing the 2024-T3 specimens over a wider range of stress levels, a more complete set of damping versus stress data was obtained. Aluminum 6061-T4 was also tested to investigate the occurrence of stress dependence of damping in this alloy.

The study showed that for very small stresses the material damping of both aluminum alloys can be predicted by the Zener model for frequencies above and below the Zener relaxation frequency. At frequencies below the Zener relaxation frequency, the average material damping in the free-free aluminum specimens increases exponentially with increasing maximum specimen stress level.

A decrease in vibrational frequency with increasing stress was also observed in the aluminum specimens. This phenomenon was found to be due to geometric nonlinearities introduced by the large amplitudes of vibration. The decrease in frequency is therefore a function solely of the amplitude of vibration and is not due to material nonlinearities.

Metal matrix materials with their very high strength to weight ratios are extremely well suited for use in the manufacturing of space structures. Specimens composed of unidirectional plies of P55 and P100 Graphite fibres with either Aluminum 6061-T4 or Magnesium AZ91C as matrix materials were tested. Despite the composite nature of these specimens, their material damping characteristics were compared with Zener's prediction for a uniform homogeneous isotropic metal beam of the same dimensions composed only of the matrix material.

This presentation of the data can be justified in the following way. Material damping losses in metal matrix materials can occur at three locations: in the graphite fiber; in the metal matrix; and at the graphite metal interface. The graphite fiber can be assumed to be lossless [3], reducing to two the possible location of the damping losses. If the experimental data for the metal matrix composite falls on the curve of the damping expected in the homogeneous metal of the matrix, then it can be inferred that the matrix is the primary source of material damping in the composite. If the damping falls above the baseline predicted for the

homogeneous matrix, it can be inferred that significant losses are being generated at the fiber/matrix interface.

The graphite/aluminum matrix composites were found to have a damping level which was slightly above the Zener prediction for the pure aluminum matrix, implying the losses are occuring primarily in the matrix. The graphite/magnesium matrix composites, on the other hand, had a measurably higher damping than could be attributed to just the matrix material, implying the presence of an additional loss mechanism, such as at the fiber/matrix interface.

EXPERIMENT DESCRIPTION

An apparatus for the precise experimental measurement of material and structural damping has been developed in the Space Systems Laboratory at the Massachusetts Institute of Technology. Reference [1] describes the original apparatus and test results obtained for higher frequency aluminum and graphite/epoxy materials. The specimen is lofted into a controlled free fall in a large vacuum chamber. The time history of the vibrational response of the specimen is recorded and analyzed to obtain the damping characteristics. This test method distinguishes itself in that it eliminates the support interferences and excitation interaction encountered in many other test methods. Performing the tests in vacuum also eliminates any aerodynamic drag and damping effects. In future work this test procedure will be used to investigate the dynamics of built up structures in zero gravity, for which the presence or absence of gravity loading on the joints may have a significant effect on the structural damping.

The apparatus to loft the specimen into free fall consists of a test bed, cocking mechanism and launch mechanism (Fig. 1). The test bed supports the specimen near its ends by two vertical stands. The cocking mechanism is a motor driven worm-screw, which draws the test bed downwards compressing a set of four springs in the launch mechanism. The springs provide the force for lofting the specimen vertically upward into free fall. After cocking, the launcher is held in a cocked position by an electromagnet. Upon release of the electromagnet, the launcher translates upwards, guided by linear bearings, until it strikes a hard mechanical stop. The specimen is deflected downward relative to the end supports by the acceleration and is lofted into free fall when the launcher hits the hard mechanical stops.

The construction of the launcher allows the mechanical setting of precompression of the launcher springs, and of the stroke of the launcher prior to striking the hard mechanical stops. Conversely, there are two constraints placed on the launch process, that the specimen leave the launcher with correct rigid body velocity to obtain the maximum time in free fall, and that the initial strain level of the specimen be adjustable. By varying the initial precompression and stroke before each test, the induced elastic strain and rigid body velocity can be varied within limits. The dynamics that couple these parameters are discussed in references 1 and 4.

The time history of the free response of the specimen is measured by a pair of BLH FDE-25-35-ES dynamic strain gauges, mounted on the specimen's lower and upper surfaces at the midpoint. The outputs from the strain gauges are fed via three very fine 39 gauge, enamel-coated signal wires to a small terminal block running on a cable and pulley system (Fig. 1). The motion of the terminal block is controlled to follow the specimen's flight, always keeping the three short signal wires slack. This control of the trajectory of

FA - 3

the terminal is achieved by storing in a digital to analog converter the necessary time history to drive the high torque motor attached to the pulley system. On initiating the test, the electromagnet is deactivated, releasing the specimen, and the digital to analog converter is prompted to send the command signal to the torque motor. The strain gauge signals are fed to a strain gauge amplifier and from there via an analog filter to a high speed analog to digital converter.

By placing all the above mentioned equipment in a 2.2 meter high, 0.6 meter diameter cylindrical vacuum chamber the effects of aerodynamic drag and damping are eliminated. Access to the lofting apparatus and test specimens is achieved by removing the transparent plexiglass upper half of the chamber. The experiment is preprogrammed and controlled by an IBM Personal Computer, via a general purpose interface board (GPIB). The subsequent analysis of the signal was also performed on the Personal Computer.

TEST PROCEDURE AND DATA REDUCTION

The specimens tested were small beams, varying from 152 to 508 mm in length, from 0.79 to 1.57 mm in thickness and from 12.7 to 25.4 mm in width (Tables 1 and 2). To begin a test, the instrumented specimen was placed on the test bed, the top of the vacuum chamber replaced and the chamber pumped down to 1 Torr. of vacuum. While waiting for the vacuum to be achieved, the required precompression and stroke of the launcher were set, the test bed was drawn down, compressing the launcher springs,and the electromagnet was energized.

The computer programmed the D/A with the correct signal to drive the torque motor causing the terminal block to follow the flight of the specimen, and also programmed the A/D for the required sampling rate and number of sampling points. A sampling rate of at least twenty data points per vibrational cycle was used for all tests.

When the required vacuum was reached, the computer initiated the test by deactivating the electromagnet, lofting the specimen upwards. If at any time during the test the fine wires running to the specimen were observed to go taut, the test was discarded. After the test, air was readmitted to the vacuum chamber, the specimen examined for damage and the test sequence repeated. The data from the A/D was stored on a floppy disk.

Once the time response of the specimen was stored, the damping ratio could be calculated. Several methods exist to calculate the damping ratio of such transient decay data. The simple and accurate least-square curve fitting algorithm used in this study fits a decaying sinusoid to the digitized signal [5]. Where possible, an attempt was made to fit sinusoids to an interval of twenty or more cycles of vibration. This was not possible for the specimens with low vibrational frequencies. The use of an exponentially decaying sinusoid in the curve fit assumes that the damping ratio is constant over the interval of the fit. When used on time dependent damping signals, it yields a time averaged damping ratio over the interval of the fit. In such cases, the damping ratio was referenced to the maximum strain amplitude at the start of the interval. The curve fit algorithm also yielded the frequency and strain amplitude of vibration over each interval. Stress was calculated from the corresponding strain assuming Bernoulli-Euler bending.

DISCUSSION OF TEST RESULTS

2024-T3 ALUMINUM

In all, ten 2024-T3 Aluminum specimens have been tested (Table 1). The first free-free natural frequencies of the specimens ranged from approximately one-tenth to ten times the Zener relaxation frequency (ω_R), which is defined as the inverse of the transverse thermal relaxation time constant τ [6]

$$\frac{1}{\omega_R} = \tau = \frac{h^2\, C\, \rho}{\pi^2\, k}$$

where h is the specimen thickness, C the specific heat per mass, ρ the density, and k the thermal conductivity.

Specimens Al-0 through Al-4 and Al-9 were tested for their damping characteristics at frequencies above the relaxation frequency, and at stress levels ranging from 0 to 140 MPa (Table 2). The experimentally measured damping for these specimens was in good agreement with the Zener model, which states that for homogeneous isotropic metals, the damping should go as

$$\zeta = \frac{\alpha^2\, E\, T}{2\, C\, \rho} \left[\frac{\omega\, \tau}{1 + \omega^2\, \tau^2} \right]$$

where E is the Young's Modulus, T the absolute temperature, and ω the frequency of vibration. A comparison of measured damping with the Zener model is shown in Fig. 2. For specimens whose natural frequency is above the peak or relaxation frequency, the mean and standard deviation of the measurements are shown.

However, for tests performed on specimens with natural frequencies below the Zener relaxation frequency, a strong dependence of damping on stress is indicated by the data. For these specimens (Al-5 through 8) the initial stress amplitude was altered from zero to approximately 50% of yield stress (σ_y = 290 MPa). The results for these four specimens are also shown in Fig. 2 for frequencies below the peak or Zener relaxation frequency. The measured damping for these specimens span a much broader range than for the specimens above the relaxation frequency. This broad spread, over an order of magnitude in the case of Al-5, is due to the stress dependence of the damping behavior.

Figure 3 depicts the damping results for specimen Al-6 as a function of measured stress amplitude divided by yield stress. Similar results were obtained for the other low frequency specimens. The Zener theory [6,7] makes no provision for a stress dependence of material damping. In order to quantify the functional dependence of damping on stress, several analytic functions were fit to the data. From among several simple analytical functions which were fit to the data, the following exponential proved to be the best fit.

$$\zeta = a\, exp\left[\frac{b\, \sigma}{\sigma_y} \right]$$

where a and b are constants determined by the least squares fitting routine. The result of such a fit is depicted in Fig. 3 and on a logarithmic scale in Fig. 4. The curves fit to the data clearly indicate that approximately an exponential relationship exists between the damping ratio and the peak stress amplitude in the specimen. It should be noted that throughout this discussion the stress or strain amplitude level refers to the maximum stress or strain in

the specimen, that is the stress or strain at the midpoint of top and bottom surfaces of the specimen while in its first free-free mode.

An important observation is that when the curves of damping versus stress (Fig. 3 or 4) are extrapolated to the zero stress point (i.e., the intercepts of the exponential curves with the vertical axis) the damping ratios obtained agree quite well with the Zener prediction. To illustrate this fact, these intercepts are plotted as triangles on Fig. 3. When a curve is drawn through these points (the dashed line on Fig. 3), the curve follows the Zener prediction closely. It is therefore clear that the Zener transport lag phenomenon serves as a baseline for the material damping in 2024-T3 Aluminum.

However, the experimental results also indicate that a stress dependence of material damping exists even at 20 to 40 percent of the yield stress. It should be noted that for a free-free beam, the stress varies over the thickness and the length. The reported specimen stress, which is the maximum stress, the stress at the top and bottom surfaces of the beam, is just an indication of the average stress state. Therefore, the functional dependence of damping on the peak specimen stress (as reported) may not be synonymous with the dependence of the local damping on the local stress.

Mason [8,9] is one of several researchers [10,11,12] who reported a similar increase in damping ratio with increasing stress for aluminum. It is difficult to determine from these earlier works whether natural frequencies of vibration were above or below the Zener relaxation frequency. Granick and Stern [13] also tested an aluminum specimen at high stress levels. It was observed on initial testing that the material damping remained nearly constant up to 100 MPa, increased slightly between 100 and 240 MPa, and then increased sharply at 240 MPa, which is close to the fatigue limit. In this study, it was also found that the material damping increases rapidly above 140 MPa, but that the transition at this point is a gradual change and not a sharp change, as observed by Granick and Stern. This could be due to the fact that when the damping ratio is calculated by fitting an exponentially decaying sinusoid to the data, a damping ratio is obtained which has the effect of averaging over a small range of stress, reducing the likelihood of finding a sharp change with stress. A theory for stress dependence of material damping has been postulated by Granato and Lucke [12]. On comparison of the data obtained in this study with the Granato and Lucke model, no quantitative agreement could be found [14].

It is almost certain that at least two damping mechanisms are present in specimens tested. The fact that the zero stress damping matches the Zener model so well is a strong indication that the Zener transport lag phenomenon does indeed dominate at low stress levels and higher frequencies. This serves as a baseline for the material damping present in flexural vibration. However, it is also clear that over and above this baseline damping there is a stress dependent phenomenon at frequencies below the relaxation frequency.

A decrease in free-free vibrational frequency with increasing stress was also observed in the aluminum specimens (Fig. 5). However, this was found not to be a material effect, but a nonlinearity due to a large deformation. When the nonlinear effects of large amplitudes of vibration were included in the governing differential equations, the decrease in frequency with amplitude shown in Fig. 5 was predicted. The good agreement between the data and large amplitude model indicates that this is a geometric, not a material effect.

6061-T4 ALUMINUM

Two 6061-T4 Aluminum specimens were tested in exactly the same manner as the 2024-T3 Aluminum specimens. Both the specimens tested had flexural vibrational frequencies below the Zener relaxation frequency. As with the 2024-T3 Aluminum specimens a stress dependent damping was observed and again curve fits indicated that an approximately exponential relationship exists between the material damping ratio and the peak specimen stress. In Fig. 6, the results are compared with the Zener model for damping in 6061-T4. As was the case with 2024-T3 Aluminum the indications are that when extrapolated to zero stress (as shown by the triangles), the Zener transport lag phenomenon is present and serves as a lower limit for the material damping. Thus the presence of both a baseline thermal transport damping, and an additional low frequency stress dependent damping, has been found in at least two of the common aluminum alloys.

GRAPHITE/ALUMINUM METAL MATRIX MATERIAL

Six graphite/aluminum specimens with 6061 Aluminum as matrix were tested for material damping (Table 3). The specimens contained either P55 or P100 graphite fibers. All aluminum matrix specimens were composed of two unidirectional plies, and were faced with 6061 foil on each side. The high stiffness to weight ratio of these specimens reduced the maximum achievable induced specimen strain to the level of 500 microstrain, as compared with a maximum of 2500 microstrain in the aluminum specimens. The strain levels induced in these specimens was far below the levels where significant stress dependent damping was encountered in the pure aluminum specimens making a conclusion concerning the stress dependence of the material damping impossible. By comparison of Fig. 7 with Fig. 2, there was a larger spread in the measured damping ratios for those tests above the relaxation frequency. This can be partially explained by the fact that the specimens were extremely light and damping measurements were affected by the slightest interference of the experimental procedure. Due to the low induced strain, the signal to noise ratio was 15, compared to 200 for the aluminum materials, and the numerical identification of the damping was therefore less precise.

The damping ratios for all the specimens are tabulated in Table 4 and shown in Fig. 7, in comparison with theoretical Zener Values for 6061 Aluminum, the matrix material. In the presence of a nearly lossless fiber, such as graphite [3], the loss must be due to some combination of the matrix material damping, and flaws in the matrix and at the fiber matrix interface. By plotting the damping of the metal matrix composite versus the damping expected from a pure metal bar of the same dimensions, the effects of the matrix can be isolated. In Fig. 7, the Zener curve proved to be approximately a lower limit for the measured damping ratio. The average measured damping ratio was consistantly slightly higher than the values predicted by the Zener model for the matrix. Thus it can be inferred that the dominant source of damping is that of the matrix.

Although specimens of different fiber materials (Graphite P55 and P100) were tested, it is impossible to make any conclusion to the difference in material damping due to the fiber type. Different surface foils were also used, but again no conclusion about their effect on material damping can be drawn from the experimental results.

GRAPHITE/MAGNESIUM METAL MATRIX MATERIAL

Six unidirectional graphite/magnesium metal matrix specimens were tested. As was the case with the graphite/aluminum materials, these specimens were extremely stiff with resultant low induced stresses. The signal to noise level was again in the order of 15. The maximum strain levels induced in these specimens were not high enough for a pattern of stress dependent damping to be observed. When Figs. 8 and 9 are examined, it can be seen that there exists a relatively large spread in the damping ratios measured. In Fig. 9, the frequency axis is expanded for easier interpretation of the results. In Figs. 8 and 9, the damping ratios are compared with the Zener theoretical curve for Magnesium AZ91C, the matrix material for all the specimens.

The small spread in frequencies makes difficult a conclusion on how closely the measured damping ratios follows the Zener curve. The Zener curve again appears to be a lower limit to the measured damping ratios. But now the average value of the damping is significantly higher than the Zener curve, and even the lower bound is measurably higher than the Zener curve. This implies that unlike graphite/aluminum, there is a significant loss mechanism other than the fiber and matrix, probably due to a relatively poor fiber/matrix bond, typical of graphite/magnesium materials [3]. Although different fibers (Graphite P55 and P100) and different foils were tested, no obvious difference in their measured material damping could be observed.

CONCLUSIONS

For small stresses, the material damping of both 6061-T4 and 2024-T3 Aluminum can be predicted accurately by the Zener thermal transport model. For frequencies above the relaxation frequency, the damping is largely independent of the stress level, up to at least 50% of the yield stress. For frequencies below the relaxation frequency an additional loss mechanism is present, causing an approximately exponential increase in damping with peak specimen stress.

In unidirectional graphite/metal matrix materials, the material damping of the matrix metal sets a lower bound on the damping of the composite. For unidirectional graphite/aluminum material the damping agrees quite well with the damping predicted by the Zener model for a homogeneous aluminum beam, implying that losses in the matrix dominate the composite damping. For unidirectional graphite/magnesium material the damping is higher than that predicted for a homogeneous magnesium bar, suggesting the presence of an additional significant loss mechanism at the fiber/matrix interface.

ACKNOWLEDGEMENTS

REFERENCES

1. Crawley, E.F. and Mohr, D.G., "Experimental Measurement of Material Damping in Free Fall with Tunable Excitation," AIAA Journal, Vol. 23, No. 1, January 1985, pp 125-131.

2. Sheen R.F. and Crawley, E.F., "Experimental Measurement of Material Damping for Space Structures," Proceedings of the Vibration Damping Workshop, Long Beach, CA, February 1983.

3. Rawal, S. and Misra, M.S. "Material Damping in Space Structures," Proceedings of the Vibration Damping Workshop II, Las Vegas, NV, March 1986.

4. Mohr, D.G. and Crawley, E.F., "Experimental Measurements of Material Damping of Aluminum and Graphite/Epoxy in Free-Fall with Tunable Excitation", M.I.T. Space Systems Laboratory Report #11-82, June 1982.

5. Marquardt, D.W., "An Algorithm for Least Squares Estimation of Nonlinear Parameters," Journal of the Society for Industrial and Applied Mathematics, Vol. 11, No. 2, June 1963

6. Zener, C.M., Elasticity and Anelasticity of Metals, University of Chicago Press, Chicago, Illinois, 1948.

7. McClintock, F.A. and Argon, A.S., Mechanical Behavior of Materials, Addison Wesley Publishing Company, 1966.

8. Mason, W.P., Piezoelectric Crystals and their Applications to Ultrasonics, Van Nostrand, 1950.

9. Mason, W.P., "Internal Friction and Fatigue in Metals at Large Strain Amplitudes," Proceedings of the 9th International Conference on Applied Mechanics, Vol. 5, Brussels, 1956.

10. Lazan, B.J. "Damping Mechanisms and Phenomenology in Materials," Proceedings of the Eleventh International Congress of Applied Mechanics, Munich, 1964.

11. Niblett, D.H. and Wilkes, J., "Dislocation Damping in Metals,"' Advances in Pysics, Vol. 9, No. 33, January 1960.

12. Granato, A. and Lucke, K., "Theory of Mechanical Damping due to Dislocations," Journal of Applied Physics, Vol. 27, No. 6, June 1956.

13. Granick, N. and Stern, J.E. "Material Damping of Aluminum by a Resonant-Dwell Technique," NASA TN D-2893, August 1965

14. van Schoor, M.C., and Crawley, E.F., "Material Damping in Aluminum and Metal Matrix Materials," MIT Space Systems Laboratory Report #10-85, December 1984.

Table 1 Specifications for the Aluminum Test Specimens

Specimen	Material	Length (mm)	Width (mm)	Thickness (mm)	Fundamental Freq (ω_n) (rad/sec)
Al-0	2024-T3	254.0	25.4	1.55	807.
Al-1	2024-T3	457.2	25.4	1.57	249.
Al-2	2024-T3	355.6	25.4	1.57	411.
Al-3	2024-T3	152.4	25.4	1.57	2246.
Al-4	2024-T3	508.0	25.4	1.57	201.
Al-5	2024-T3	481.1	25.4	.79	111.
Al-6	2024-T3	355.6	25.4	79	203.
Al-7	2024-T3	254.0	25.4	.79	401.
Al-8	2024-T3	203.2	25.4	.79	629.
Al-9	2024-T3	152.4	25.4	.79	1124.
Al-10	6061-T4	455.8	25.4	.86	126.
Al-11	6061-T4	303.4	25.2	.86	292.

Table 2 Results for the Aluminum Test Specimens

Specimen	Material	Frequency Ratio ω_n/ω_r	Average Damping (ζ)	Standard Deviation (ζ)	Minimum Damping (ζ)
Al-0	2024-T3	3.92	.00065	.00003	.00060
Al-1	2024-T3	1.25	.00122	.00006	.00109
Al-2	2024-T3	2.06	.00106	.00007	.00093
Al-3	2024-T3	11.23	.00036	.00011	.00010
Al-4	2024-T3	1.01	.00126	.00006	.00105
Al-5	2024-T3	0.14	.00415[1]	.00267[1]	.00076
Al-6	2024-T3	0.26	.00267[1]	.00165[1]	.00088
Al-7	2024-T3	0.50	.00259[1]	.00125[1]	.00149
Al-8	2024-T3	0.79	.00185[1]	.00028[1]	.00131
Al-9	2024-T3	1.41	.00121	.00012	.00096
Al-10	6061-T4	0.15	.00399	.00256	.00050
Al-11	6061-T4	0.35	.00196	.00030	.00148

Note: 1. Due to strong stress dependence, the average and standard deviation of damping are not meaningful values.

Table 3 Specifications for the Metal Matrix Test Specimens

Specimen	Material	Length (mm)	Width (mm)	Thickness (mm)	Fundamental Freq (ω_n) (rad/sec)
Al-17	[P55/6061]$_2$[1]	202.7	12.7	1.14	1370.
Al-19	[P100/6061]$_2$	203.0	12.7	1.12	1712.
Al-20	[P100/6061]$_2$	208.1	12.7	1.17	1708.
Al-21	[P100/6061]$_2$	192.1	12.7	1.14	1985.
Al-22	[P100/6061]$_2$	405.0	13.0	1.37	428.
Al-23	[P55/6061]$_2$	406.5	13.0	1.32	340.
MG-24	[P55/AZ91C]$_2$[2]	204.0	13.5	1.14	1359.
MG-25	[P55/AZ91C]$_2$	204.0	13.2	1.07	1408.
MG-26	[P100/AZ91C]$_2$	193.6	13.5	1.07	1936.
MG-27	[P100/AZ91C]$_2$	204.0	13.5	1.07	1806.
MG-28	[P100/AZ91C]$_2$	206.0	13.5	1.04	1747.
Mg-29	[P100/AZ91C]$_2$	206.6	13.5	1.07	1742.

Notes:
  1. 6061 matrix specimens had .089mm 6061 foil on each surface.
  2. AZ91C matrix specimens had .051mm Mg foil on each surface.

Table 4 Results for the Metal Matrix Test Specimens

Specimen	Material	Frequency Ratio ω_n/ω_r	Average Damping (ζ)	Standard Deviation (ζ)	Minimum Damping (ζ)
Al-17	[P55/6061]$_2$[1]	2.85	.00117	.00043	.00048
Al-19	[P100/6061]$_2$	3.34	.00085	.00016	.00064
Al-20	[P100/6061]$_2$	3.64	.00128	.00030	.00090
Al-21	[P100/6061]$_2$	4.14	.00070	.00017	.00042
Al-22	[P100/6061]$_2$	1.28	.00205	.00016	.00184
Al-23	[P55/6061]$_2$	0.94	.00209	.00080	.00113
MG-24	[P55/AZ91C]$_2$[2]	4.27	.00128	.00041	.00079
MG-25	[P55/AZ91C]$_2$	4.36	.00165	.00049	.00091
MG-26	[P100/AZ91C]$_2$	5.80	.00114	.00042	.00059
MG-27	[P100/AZ91C]$_2$	5.54	.00139	.00037	.00095
MG-28	[P100/AZ91C]$_2$	5.11	.00115	.00030	.00079
Mg-29	[P100/AZ91C]$_2$	5.34	.00141	.00062	.00052

Notes:
  1. 6061 matrix specimens had .089mm 6061 foil on each surface.
  2. AZ91C matrix specimens had .051mm Mg foil on each surface.

(A) LAUNCHER IN COCKED POSITION   **(B) RELEASE**   **(C) FLIGHT**
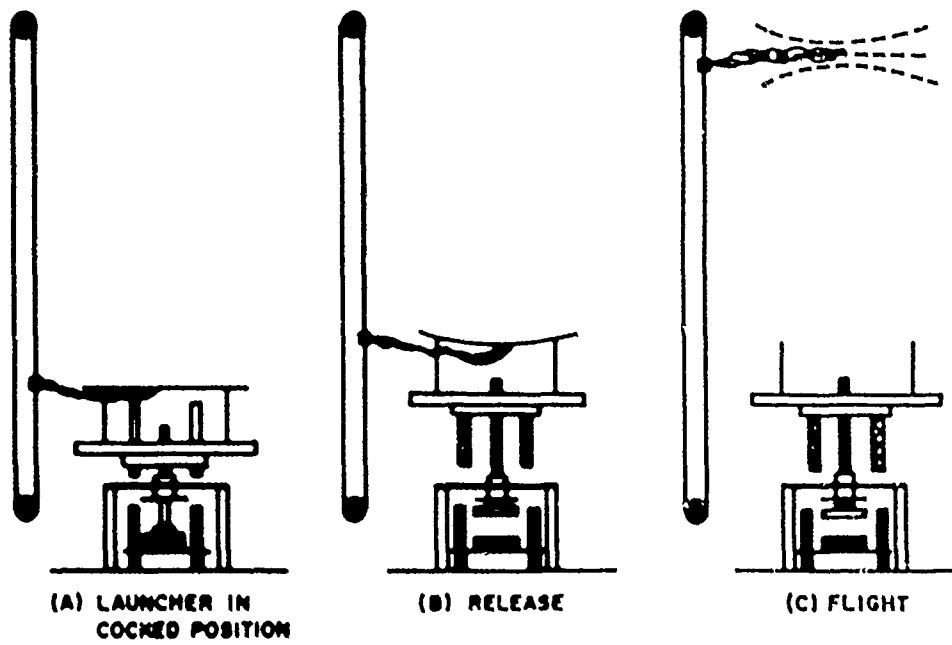
Fig. 1   Schematic of the Experimental Apparatus.
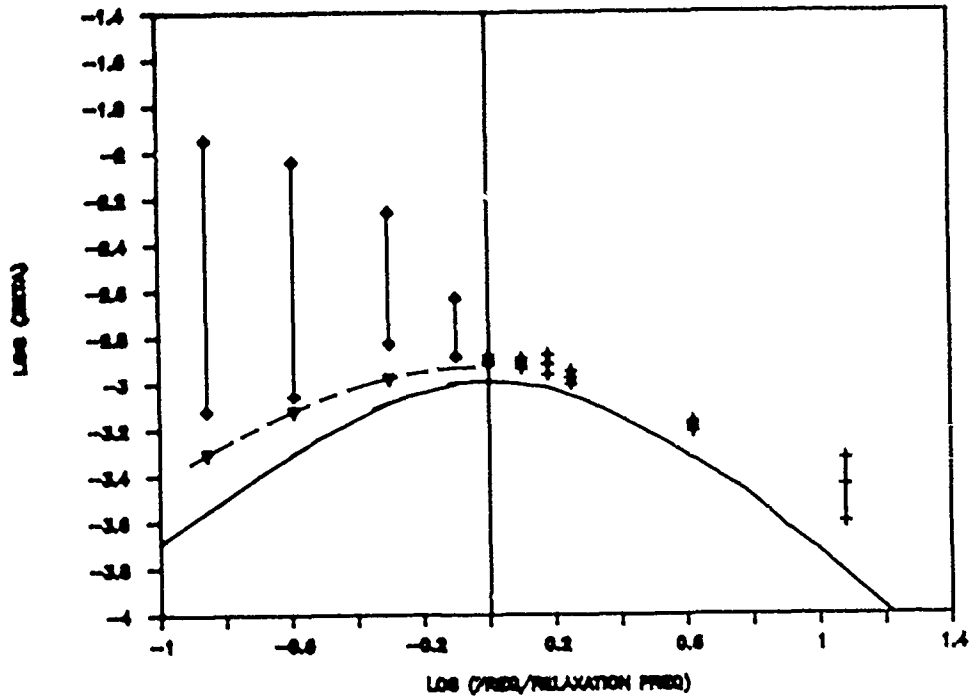
Fig. 2   Damping versus frequency for 2024-T3 Aluminum.
The full range of measured data is shown for
samples to the left, while the mean and standard
deviation are shown for specimens to the right.
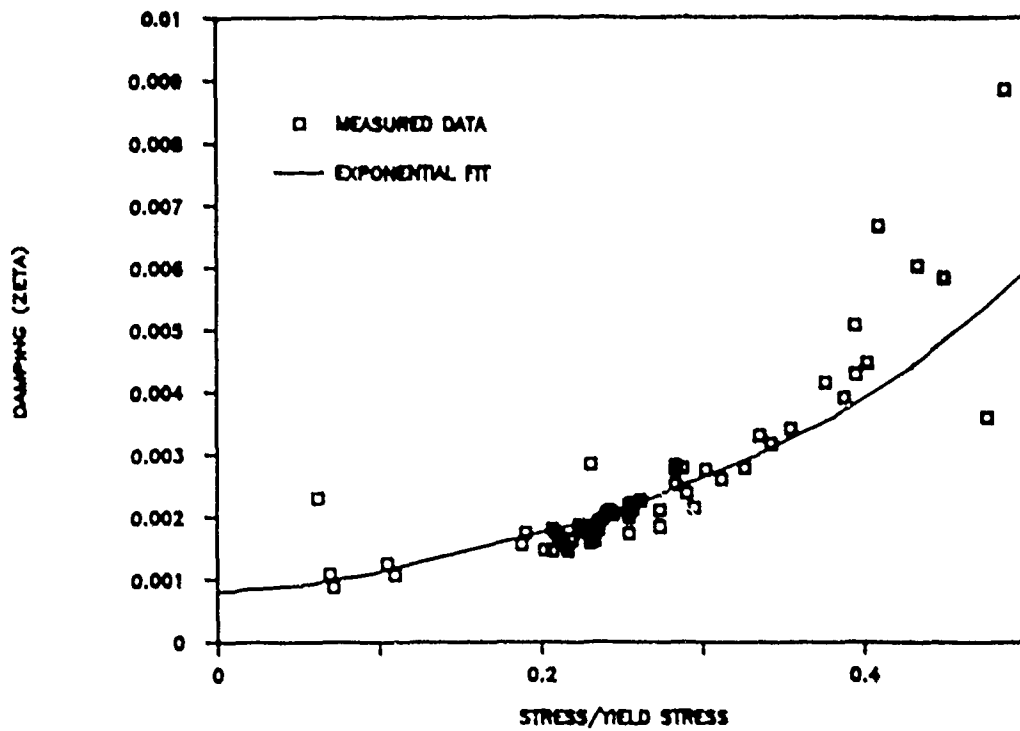
Fig. 3 Damping versus stress for 2024-T3 Aluminum.
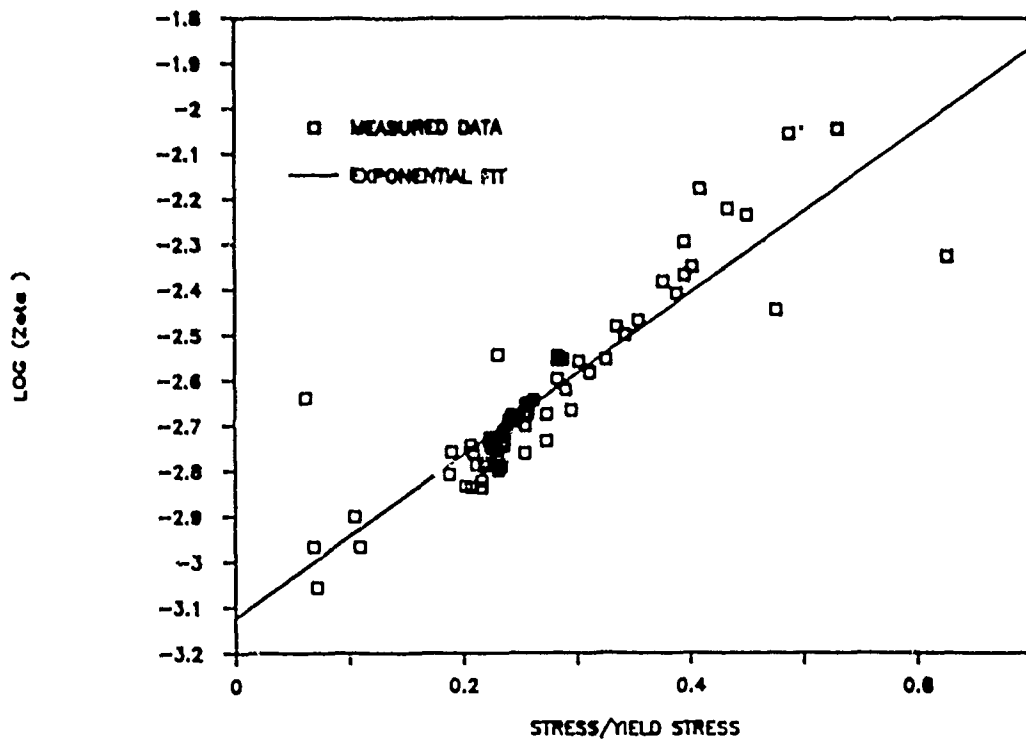
Fig. 4 Damping versus stress for 2024-T3 Aluminum.

FA - 13
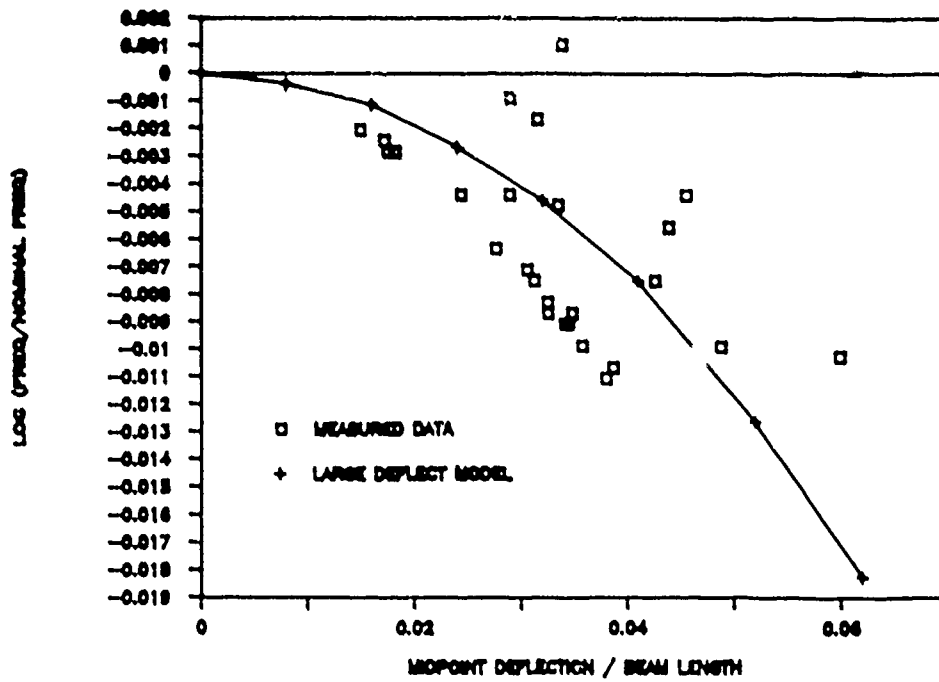
Fig. 5 Specimen frequency versus midpoint deflection.
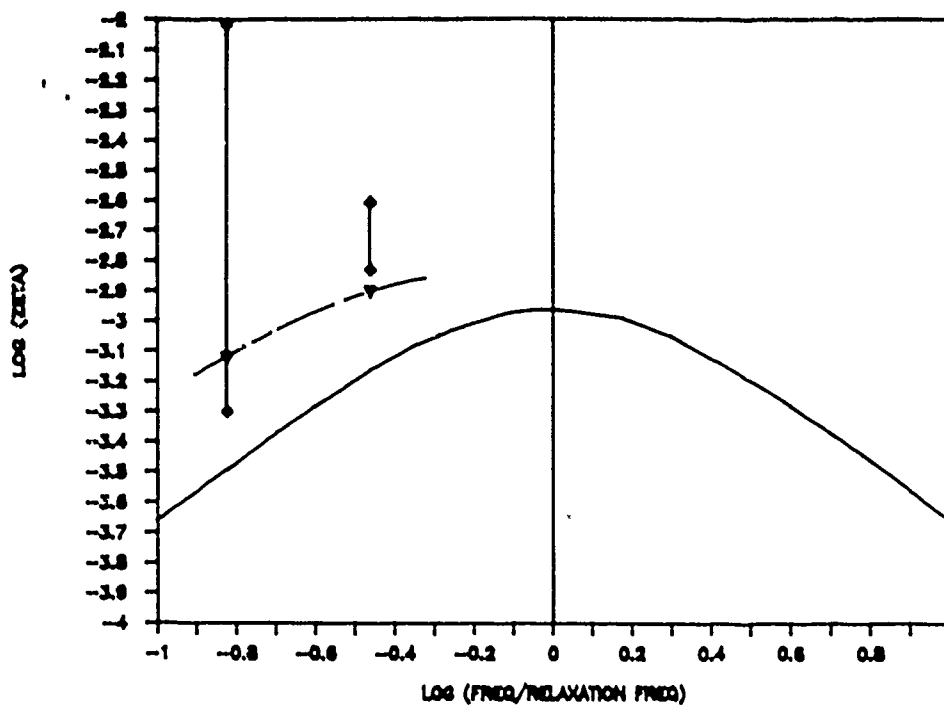
Fig. 6 Damping versus frequency for 6061-T4 Aluminum.

FA - 14
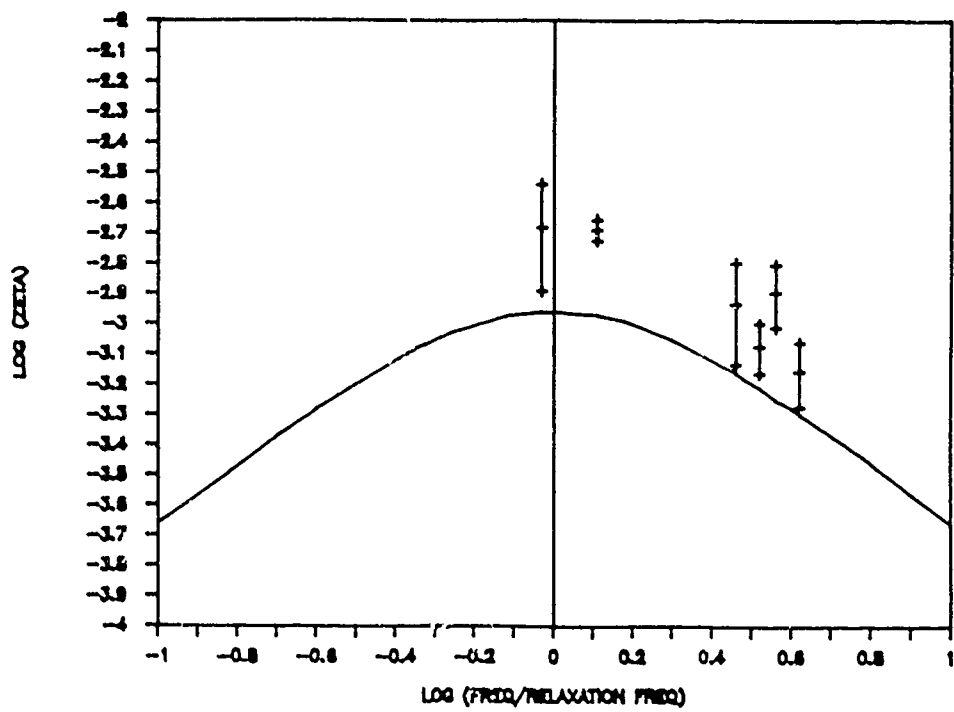
Fig. 7 Damping versus frequency for graphite/6061 Aluminum.
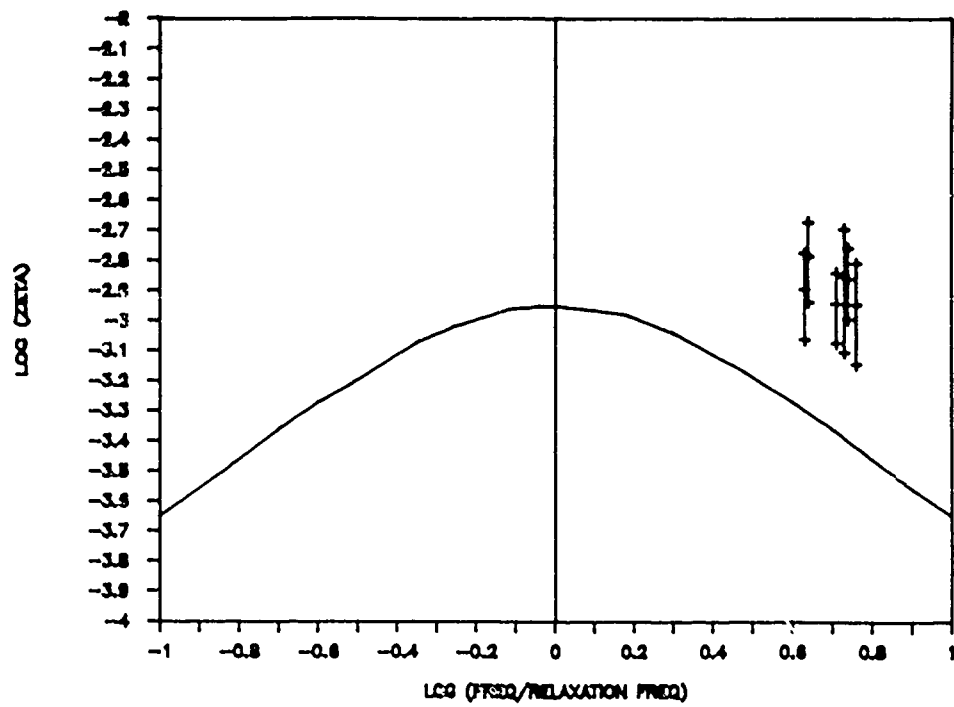
Fig. 8 Damping versus frequency for graphite/AZ91C Magnesium.
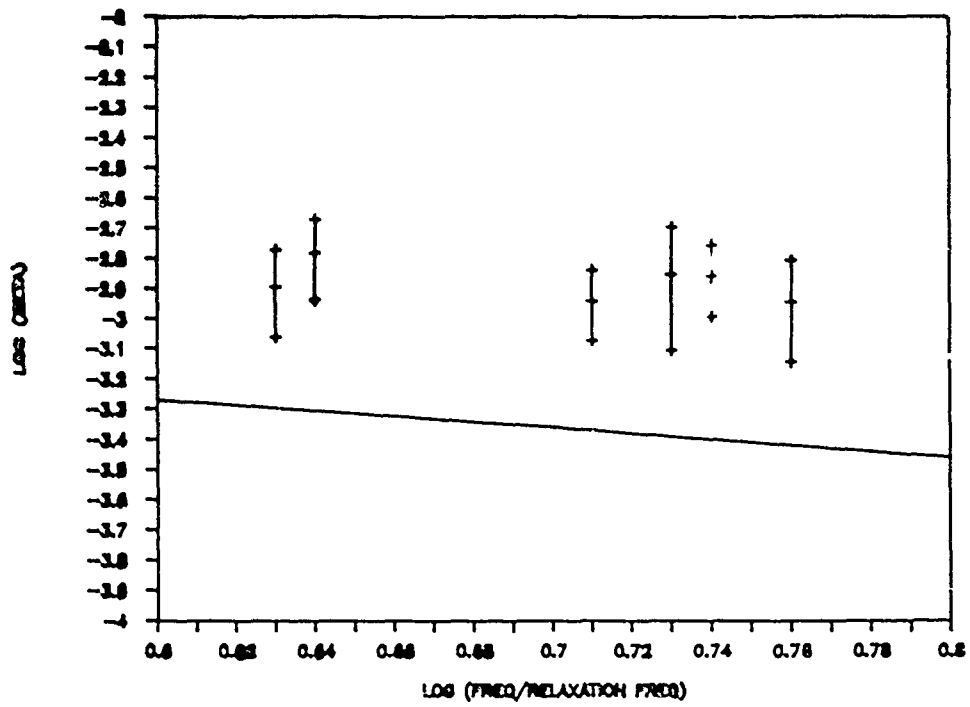
Fig. 9 Damping versus frequency for graphite/AZ91C Magnesium

MATERIAL DAMPING IN SPACE STRUCTURES

S.P. Rawal
Martin Marietta Denver Aerospace

M.S. Misra
Martin Marietta Denver Aerospace

:

ABSTRACT

Material damping contributes significantly to the passive control measures of vibration in space structures. Damping properties of various metallic alloys, viscoelastic materials, polymer matrix and metal matrix composites and their limitations for space application have been reviewed. Viscoelastic materials can be used as discrete dampers which are integrally designed into the structural elements whereas metallic alloys and composites are the candidate structural materials. This paper suggests that metal matrix composites with enhanced material damping will be the ideal material for space structures.

MATERIAL DAMPING IN SPACE STRUCTURES

INTRODUCTION

Damping of vibrations is a critical design and operational requirement in
space structures. Design considerations involve limiting the peak stresses
and extending the fatigue life of structural elements subjected to near
resonant vibrations under suddenly applied forces. Operational concerns
include reduction of settling time to achieve dynamic dimensional precision in
space maneuvers. Damping in space structures can be achieved by active and
passive controls as shown in Figure 1. In the active control of large space
structures, (LSS) the role of material and structural damping is generally
omitted, whereas a small amount of added passive control measures improve the
dynamic stability of the system.[1] In passive control measures, material
damping can be utilized by considering the following two options: 1) using
the inherent capacity of the structural material to dissipate vibrational
energy, and 2) discrete viscoelastic dampers (i.e., artificial dashpots).[2,3]

```
          ┌─────────────────────────────────┐
          │   DAMPING IN SPACE STRUCTURES    │
          └─────────────────────────────────┘
                  │                 │
      ┌───────────────────┐   ┌───────────────────┐
      │  ACTIVE CONTROL   │   │  PASSIVE CONTROL  │
      └───────────────────┘   └───────────────────┘
                                        │
                          ┌─────────────────────────────┐
                          │ MATERIAL AND STRUCTURAL DAMPING │
                          └─────────────────────────────┘
                   │                │                  │
          ┌────────────┐   ┌────────────┐   ┌──────────────┐
          │  MATERIAL  │   │ JOINTS AND │   │  STRUCTURAL  │
          │  DAMPING   │   │  FITTING   │   │  FRICTIONAL  │
          └────────────┘   └────────────┘   │   DAMPING    │
                                            └──────────────┘
```
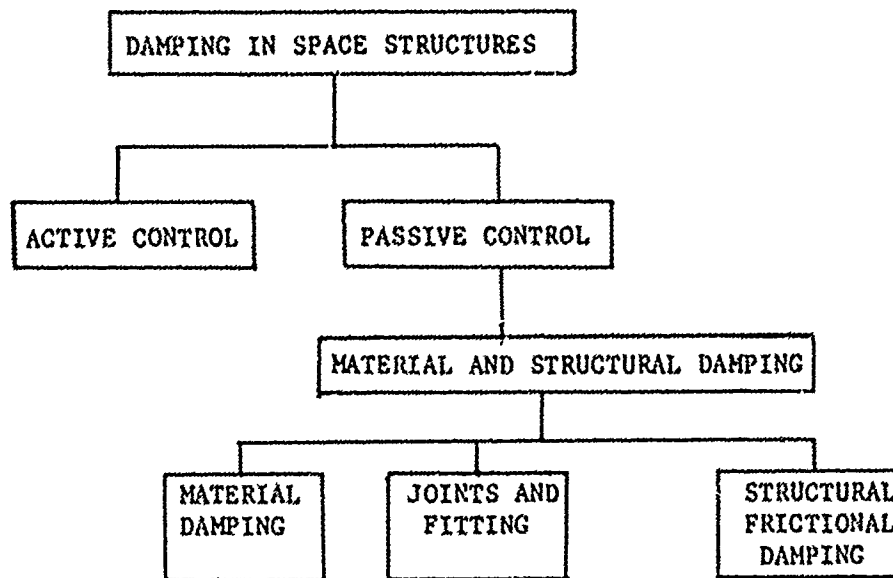
Figure 1   Vibrational Control in Space Structures

If the damping characteristics of structural material(s) used in a LSS can be
enhanced, then the weight and cost of complex active control systems can be
significantly reduced. The methodology incorporating discrete viscoelastic
dampers in LSS designs improves the passive damping by an order of magnitude
than the residual damping present in the original structure by a mere 8
percent penalty in structural weight.[3] Eventually, a large space structure
with less active control and more effective passive control options will
exhibit improvements in performance and reliability. The purpose of this
paper is to discuss space environmental conditions and compare damping
properties of various materials and assess their applicability for space
structures.

SPACE ENVIRONMENT

Dynamic dimensional precision of an orbiting space structure may be affected by disturbances introduced by environmental conditions, such as natural and hostile environments. Natural environment can be subdivided into: a) sources of quasi-static/static disturbances which include gravitational gradients, thermal transients, electromagnetic affects, atmospheric drag, etc. and b) sources of dynamic disturbances, such as thrusters, pumps, motors and generators. Hostile disturbance environments are those induced by foreign power attack, such as nuclear power, laser or particle beam attack. Primarily, natural environment disturbances will influence the system dimensional requirements, whereas hostile environment disturbances are related to system survivability.

Therefore, the material selection process for effective passive damping measures must take into account its suitability in space environment of zero gravity, high vacuum and thermal fluctuations (-250°F to 250°F). Candidate material(s) must also exhibit high damping at low frequency and strain amplitude range levels. Various analyses of structural dynamic models [4,5] of flexible space structures at different thrust levels, indicate that vibrational control in the frequency range 0.1 - 5 Hz and strain amplitude range (10^{-10} - 10^{-4}) is of prime concern. Furthermore, in slewing maneuvers, enhanced structural damping decreases the settling time significantly for a particular thrust level.

MATERIALS IN SPACE APPLICATIONS

Various materials used in space applications can be classified in four categories:

1) Structural metals and alloys
2) Viscoelastic materials
3) Polymer matrix composites
4) Metal matrix composites

Conventional aluminum and titanium base structural alloys used in aerospace systems exhibit low damping. Viscoelastic materials (VEM) have been used to suppress vibration in small and stiff structures and as discrete dampers in large space structures to contribute passive control measures. Fiber reinforced polymer matrix and metal matrix composites are candidate structural materials for space structures.

Damping behavior of materials has been reviewed by Nowick and Berry[6], Lazan,[7] Enwistle,[8] and James.[9] Various measures of damping have been reported such as loss factor (η), loss angle (ϕ), logrithmic decrement (δ), quality factor (Q), specific damping capacity (ψ) and damping ratio (ζ). In the following discussion, damping characteristics of metallic, polymeric and composite materials have been presented in terms of loss factor, η. At low damping levels (i.e., $\eta \ll 1$) their damping parameters are interrelated by the following expression.

$$Q^{-1} = \eta = \tan\phi = \phi = E^I/E^R \qquad (1)$$
$$= \delta/\pi = \psi/2\pi = \Delta W/2\pi W = 2\zeta$$

Damping test data of metallic and non-metallic materials has been obtained at different temperature, frequency and stress (or strain) amplitude levels by various methods depending upon the engineering application of interest. Comparison of their damping behavior becomes particularly difficult as it depends on stress level; however a general trend of damping characteristics of materials can be established from the available data at low stress levels (0.1% tensile yield strength).

STRUCTURAL METALS AND ALLOYS

Damping or internal friction of metallic materials has been used as an effective tool for studying atomic movements at low stress or strain levels ($\leq 10^{-6}$). As a result it is possible to provide insight into fundamental mechanisms in diffusion, ordering, interstitial and substitutional solid solutions and estimation of dislocation densities. Whereas, for engineering applications, dynamic property data has been obtained at intermediate and high strain levels ($\geq 10 \times 10^{-3}$) in order to understand vibrational energy dissipation and extend fatigue life of metallic components.

Table 1 lists loss factor values of various structural alloys at room temperature and low stress levels ($\sigma/\sigma_y \leq 0.1$). Damping at low stress or strain levels is independent of stress or strain amplitude and varies with frequency and temperature. Loss factor, generally increases with increasing stress level and the stress dependence varies widely from metal to metal.

Table 1 Damping Properties of Structural Alloys

Material	Loss Factor	Frequency Range
2024 T-3 Al (10,11)	2.4×10^{-3}	10-100Hz
6061 T-6 Al (10)	2.0×10^{-3}	10-100Hz
1020 Steel (11)	5.0×10^{-4}	50-500Hz
Ti-6Al-4V (12)	2.0×10^{-4}	@ 40 KHZ
310 Steel (13)	1.0×10^{-3}	KHZ Range
403 SS (13)	1.4×10^{-2}	" "
Brass (11,13)	9.0×10^{-5}	" "
NIVCO (13)	3.0×10^{-2}	" "
Nitinol (Ni-45 Ti) (9, 13)	2.8×10^{-2}	" "
Sonoston (Mn-36Cu 4.5Al 2Ni 3Fe) (9, 13)	4.0×10^{-2}	" "
Cast Iron (coarse graphite flake) (13)	5.7×10^{-2}	" "
Fe-12 Cr-3 Al (13)	3.6×10^{-2}	" "
Incramute (Cu-44Mn 1.8 Al) (9, 13)	3.1×10^{-2}	" "
Cast Pure Mg (9)	3.9×10^{-2}	

Copper manganese alloys, nitinol and ferromagnetic materials exhibit high damping, up to even thirty times as large as the damping of an average structural alloy. But these high damping materials possess high density and cannot be recommended for space applications because of weight penalties; though it is possible to use them in metal matrix composites by incorporation in the matrix material.

VISCOELASTIC MATERIALS

Viscoelastic materials have been extensively used in automotive and aircraft industries because of their unique damping properties. VEM exhibit high damping, and their capacity to dissipate vibrational energy is strongly influenced by both temperature and frequency. Damping property data in terms of peak loss factor (η) and effective temperature range at 100 Hz, of a few viscoelastic materials are listed in Table 2.[14]

Table 2 Damping Properties of Viscoelastic Materials

Material	@ 100Hz				Effective Temp °F	
	Density lb/in^3	Temp, °F	Peak Loss Factor	Modulus psi	Min.	Max.
113 (3M)	.0380	0	1.20	1.0×10^3	- 15	45
ISD 113 (3M)	.0340	19	1.50	4.0×10^2	- 25	20
ISD 110 (3M)	.0348	145	1.25	3.5×10^3	125	150
Acrylic Core Foam (3M)	.0210	85	1.20	5.0×10^2	35	135
DYAD 606 (Soundcoat)	.0350	105	1.00	3.5×10^3	98	143
Soundcoat M (Soundcoat)	.0370	90	1.50	7.3×10^2	50	135
Soundcoat N (Soundcoat)	.0620	38	1.40	4.5×10^6	5	100
SMRD-100-F90 (GE)	.0256	80	0.90	6.0×10^3	70	95
IF2012 (Morgan Adhesive)	.0348	62	2.00	5.5×10^1	8	225
National TM119 (National Starch & Chem)	.0360	75	1.50	5.0×10^1	50	115
Plexiglass		70	0.085	5.3×10^5		
Lexan		70	0.010	3.3×10^5		

As Table 2 indicates, viscoelastic materials exhibit high loss factor, but only within an effective transition temperature range of transition region. Temperature variations from thermal cycling in a space environment range from -250°F to 250°F and VEM exhibit poor damping particularly at low temperatures. Furthermore, environmental factors such as vacuum and irradiation along with outgassing have deleterious effect on material and damping properties. Still, the application of VEM in discrete dampers as a passive control measure to suppress low frequency vibrations of generic space truss structures has been widely recognized, wherein VEM can be encapsulated to protect it from space environments.[2-4] In the Passive and Active Control of Space Structures (PACOSS) program at Martin Marietta Aerospace, a discrete damper using acrylic core foam near its peak loss factor conditions, significantly improved damping in a demonstration structure model.

POLYMER MATRIX COMPOSITES

Fiber reinforced polymer matrix composites have been used extensively in space applications. Dr. R. Plunkett and Dr. R. Gibson have designed test techniques[15,16] to obtain reliable damping data. Damping test results recorded in the literature encounter differences in test methods and test conditions. In a few cases the test results may not be valid due to extraneous losses in the test apparatus or air damping. Still, a general trend prevails in the test data, and typical loss factors of organic matrix composites are listed in Table 3.

Table 3 Damping Properties of Polymer Matrix Composites

Material	Peak Loss Factor	Comments
Gr/epoxy $(0)_8$	1.28×10^{-3}	40-140Hz (@700×10^{-6})
Gr/epoxy $(90)_8$	1.10×10^{-2}	" "
Gr/epoxy $(\pm 45)_{25}$	1.10×10^{-2}	" "
Kevlar/epoxy	2.00×10^{-2}	" "
HT-S/epoxy-F	3.00×10^{-4}	" "
HT-S/epoxy-Ly	4.00×10^{-4}	" "
E glass/epoxy Dx21	1.75×10^{-3}	" "
Gr/epoxy $(1/d \approx 20)$(predicted)	2.80×10^{-2}	" "
Gr/epoxy $(1/d \approx 200)$	0.80×10^{-2}	" "

As Table 3 shows, polymer matrix composites exhibit higher damping than conventional aluminum and titanium base structural alloys. Furthermore, the damping behavior of fiber reinforced composites is significantly influenced by its constituents (fiber and matrix) and fiber orientation. Fiber and matrix with high damping enhance the loss factor of the composite[17,18], e.g., Kevlar/epoxy and unidirectional composites exhibit higher damping in the transverse direction than in the longitudinal direction[19]. Theoretical predictions and experiments[18,20] indicate that if the fiber damping is small, then the polymer matrix composite exhibits maximum damping for an optimum fiber aspect ratio and orientation; and when the fiber damping is significant, the optimum fiber aspect ratio approaches continuous fiber reinforcement.

Polymer matrix composites exhibit high enough damping and are considered as structural materials for space structures. The major limitation is introduced by exposure of the matrix to space environmental conditions of high vacuum, radiation and thermal cycling, which may lead to outgassing, material degradation and decrease in damping, particularly at low temperatures.

METAL MATRIX COMPOSITES

Fiber reinforced metal matrix composites (MMC) are candidate structural materials for space applications, because of their unique properties, such as, high specific modulus and specific strength, low thermal expansion, high electrical and thermal conductivity, laser survivability and no outgassing. These material properties meet the design requirements for various components of space structures. In addition, high material damping is recognized as an extremely important requirement for dynamic dimensional precision in space maneuvers.[21] Preliminary investigations of damping measurements suggest

that some metal matrix composites exhibit higher damping than conventional
structural alloys of aluminum and titanium. Table 4 lists the damping data of
metal matrix composites.

Table 4   Damping Properties of Metal Matrix Composites

MATERIAL	LOSS FACTOR	COMMENTS	REFERENCES
B/Al (0°)	1.50×10^{-2}	@ freq. 2000 Hz/450°C	22
P100 Gr/Al (0°)	$4 \times 10^{-3} - 9.00 \times 10^{-3}$	@ freq. 40 Hz/25°C	23, 24, 25
P100 Gr/Al (90°)	2.40×10^{-2}	"	23
B/Al (0°)	5.0×10^{-3}	@ freq. 1 Hz/20°C	22
P100 Gr/Mg (0°)	$2 \times 10^{-3} - 1.20 \times 10^{-2}$	@ freq. 40 Hz/25°C	23, 24
P100 Gr/Mg (90°)	1.80×10^{-2}	"	23
20/SiCw/Al	1.48×10^{-3}	"	23
P55 Gr/Al (0°)	4×10^{-3}	@ freq. 0.1 - 10 Hz/25°C	26
Gr/Mg - 1% Si	8.0×10^{-3}		28

Loss factors of unidirectional B/Al, Gr/Al and Gr/Mg composites is greater
than the loss factors of the matrix alloys. The enhanced damping in boron
reinforced composites has been attributed to high intrinsic damping capacity
of boron fibers.[22] In addition to intrinsic damping of composite
constituents, damping could be influenced by features introduced during
fabrication such as voids, delaminations, fiber twist, fiber alignment and
residual stresses; along with the material parameters, e.g., fiber volume,
fiber orientation, interface and continuous or discontinuous fibers.
Therefore, it is possible to enhance material damping in metal matrix
composites by choosing optimum material and fabrication parameters.

SUMMARY

Material damping contributes significantly to the passive control measures of
vibration control of large space structures. Passive damping can be enhanced
by utilizing high damping materials and design concepts. Viscoelastic
materials, used as a constrained viscoelastic layer or a discrete damper will
definitely improve the vibrational control ᴐ space structures, but material
and property degradation in space environment becomes a limiting factor. In
the case of structural materials, damping measurements need to be conducted
under the following conditions· 1) high vacuum, 2) at temperatures in the
thermal cycling range (~250°F to 250°F), 3) low frequency (0.1 - 10 Hz), 4)
low strain levels ($10^{-7} - 10^{-4}$), 5) flexural (free-free unrestrained), and
6) extensional modes. Metallic structural alloys exhibit low damping.
Polymer matrix composites are candidate structural material as they exhibit
high damping and stiffness, but do encounter problems similar to VEM, because
of the viscoelastic matrix. Metal matrix composites are uniquely qualified as
structural material for precision space structures due to their environmental
resistance. Moreover, the potential exists to enhance their material damping
and tailor-make optimum combination of material properties for space structure
applications.

REFERENCES

1. H. Ashley, "On Passive Damping Mechanisms in Large Space Structures", AIAA Paper No. 82-0639, 23rd Structures, Structural Dynamics and Materials Conference, April 1982, p. 56.

2. "Passive and Active Control of Space Structures", Technical Operating Report MCR-84-541, Martin Marietta Aerospace Denver, April 1984.

3. C.D. Johnson and D.A. Kienholz, "Finite Element Prediction of Damping in Structures with Constrained Viscoelastic Layers", Paper No. 81-0486, 22nd Structures, Structural Dynamics and Materials Conference, April 1981, p. 17.

4. R.W. Trudell, R.C. Curley and L.C. Rogers, "Passive Damping in Large Precision Space Structures", AIAA Paper 80-0677, 21st Structures, Structural Dynamics and Materials Conference, May 1980, p. 124.

5. E.E. Bachtell, S.S. Bettadapur, L.A. Karanian and W.A. Schartel, "System and Structural Dynamic Observations of a Slewed Box Truss Antenna", AIAA Paper No. 85-0821, 26th Structures, Structural Dynamics and Materials Conference, April 1985, p. 735.

6. A.S. Nowick and B.S. Berry, "Anelastic Relaxation in Crystalline Solids", Academic Press, New York, 1972.

7. B.J. Lazan, "Damping of Materials and Members in Structural Mechanics, Pergamon Press Ltd., Oxford, 1968.

8. K.M. Entwistle, "The Damping Capacity of Metals", Physical Examination of Metals, 2nd ed. by B. Chalmers and A.G. Quarrel, Edward Arnold, Ltd. London, 1960, p. 487.

9. D.W. James, "High Damping Metals for Engineering Applications", Materials Science and Engineering, 4, 1969, p. 1.

10. E.F. Crawley, G.L. Sarver and D.G. Mohr, "Experimental Measurement of Passive Material and Structural Damping for Flexible Space Structures", Vibration Damping 1984 Workshop proceedings, AFWAL-TF-84-3064, November 1984, p. A23.

11. J.M. Lee and K.G. McConnell,"Experimental Cross Verification of Damping in Three Metals", Experimental Mechanics, September 1975, p. 347.

12. Alan Wolfenden, 'Damping in Turbine Blade Alloys", Journal of Testing and Evaluation, Vol. 10, No. 1, January 1982, pp. 17-20.

13. R.D. Adams, "The Damping Characteristics of Certain Steels, Cast Irons and Other Metals", Journal of Sound and Vibration (Vol. 23(2), 1972, p. 199.

14. "Passive and Active Control of Space Structures, Task 1.1, Literature Search", Anatrol Corporation, Cincinnati, OH, March 1984.

15. R.F. Gibson and R. Plunkett, 'A Forced-Vibration Technique for Measurement of Material Damping", Experimental Mechanics, August 1977, p. 297.

16. S.A. Saurez, R.F. Gibson and L.R. Deobald, "Random and Impulse Techniques for Measurement of Damping in Composite Materials", Experimental Techniques, 8(5), 1984, p. 19.

17. R.D. Adams, D.G.C. Bacon, "The Dynamic Properties of Unidirectional Fiber Reinforced Composites in Flexure and Torsion", Journal of Composite Materials, Vol. 7, January 1973, p. 53.

18. R.F. Gibson, "Improvement and Optimization of Internal Damping in Fiber Reinforced Composite Materials", 1st Annual Progress Report, Grant No. AFOSR-83-0156.

19. R.D. Adams, and D.G.C. Bacon, "Effect of Fiber Orientation and Laminate Geometry on the Dynamic Properties of CFRP", Journal of Composite Materials, Vol. 7, October 1973, p. 402.

20. R.F. Gibson, S.K. Shaturvedi and C.T. Sun, "Complex Moduli of Aligned Discontinuous Fiber-Reinforced Polymer Composites", Journal of Materials Science, 17, 1982, p. 3499.

21. J. Persh, "Materials and Structures, Science and Technology Requirements for the DOD Strategic Defense Initiative", Ceramic Bulletin, Vol. 64(4), 1985, p. 555.

22. J.A. DiCarlo and J.E. Maisel, 'Measurement of the Time Temperature Dependent Dynamic Mechanical Properties of Boron/Aluminum Composites", Composite Materials: Testing and Design (Fifth Conference), ASTM STP 674, S.W. Tsai, Ed., American Society for Testing and Materials, 1979, pp. 201-227.

23. M.S. Misra and P.D. LaGreca, "Damping Behavior of Metal Matrix Composites", Vibration Damping 1984 Workshop Proceedings, AFWAL-TR-84-3064, Nov. 1984, p. u-1.

24. E.F. Crawley and R.L. Sheen, "Experimental Measurement of Material Damping in Space Structures", Vibration Damping 1984 Workshop Proceedings, AFWAL-TR-84-3064, November 1984, p. F-2.

25. N.S. Timmerman, "Damping Characteristics of Metal Matrix Composites", Army Materials and Mechanics Research Center Report, AMMRC-TR-82-19, April 1982.

26. A.K. Ray and V.K. Kinra, "Measurement of Damping in Continuous Fiber Metal Matrix Composites", presented at the Symposium on the Role of Surfaces and Interfaces in Material Damping, sponsored by the American Society for Metals, Toronto, Canada, Oct. 16, 1985.

27. J.A. DiCarlo, and J.E. Maisel, "High Temperature Dynamic Modulus and Damping of Aluminum and Titanium Matrix Composites", Advanced Fibers and Composites for Elevated Temperatures, edited by I. Ahmed and B.R. Noton, 1979, pp. 55-79.

28. G. Steckel, "Material Damping Behavior of Gr.Mg Composites", Aerospace Corporation, El Segundo, CA, ONR Report No. TOR-0084-A-5726-01 (-1), Oct. 1985.

SPECIFIC DAMPING CAPACITY OF METAL-MATRIX COMPOSITES IN TENSION-TENSION FATIGUE

by

Asok K. Ray
&
Vikram K. Kinra
Mechanics & Materials Center
&
Department of Aerospace Engineering
Texas A & M University
College Station, Texas 77843

Suraj P. Rawal
&
Mohan S. Misra
Martin Marietta Aerospace
Denver, Colorado 80201

ABSTRACT

The dependence of specific damping capacity (Ψ) in metal-matrix composites on frequency and strain amplitudes has been studied experimentally in tension-tension uniaxial fatigue. The strain amplitude and frequency were varied over the range of 150 – 600 microstrains and 0.4 – 10.0 Hz, respectively. The results show that damping depends on both strain amplitude and frequency. For 0°-fiber orientation the damping was found to be sensitive to both strain and frequency whereas for the 90°-fiber orientation the damping was found to be rather insensitive to strain amplitude.

INTRODUCTION

The complexity of control problems of large space structures has given an impetus to the research and development of new high-damping materials. Though the active modal controls remain the primary means of energy dissipation, the active control systems, however, control only some finite number of flexible modes. In the absence of passive damping, active contol systems tend to excite the higher modes which in turn tend to destabilize a space structure with a closed-loop control system. This phenomenon is known as spillover.

High passive damping not only limits vibration amplitudes and reduces transient times but also has other favorable effects on stability and control when it is combined with active controls. Use of viscoelastic materials for the control of structural vibrations has been an approach used in an ever increasing variety of applications as viscoelastic technology becomes well established and more widely known. However most of the viscoelastic elements are not suitable for hostile environment. New materials (fiber-reinforced metal-matrix composites) have been developed to suit this purpose. The stiffness, strength and the damping properties of these materials can be tailored to suit specific purpose by changing the volume fraction of fibers, angle of orientation of fibers with the load axis and the fiber-matrix interface properties.

The components of large space structure are made of repetitive lattice trusses. Therefore the main load experienced by any member of a truss is nothing but the axial tension or compression. Accurate test results are required when the properties of all the components of structure are to be synthesized to predict the overall properties and from these properties designers can predict the overall performance of the structure. It is well known that damping capacity of viscoelastic or crystalline materials depends on the frequency of vibration and the strain amplitude.

Zener's model predicts the material damping in homogeneous crystalline materials quite accurately [1],[3],[7]. This model is based on the assumption that the anelastic behavior of metals is caused by a heat flow mechanism. According to Zener, when the material vibrates at low frequencies i.e., the period of vibration is much larger than the period of thermal conduction, the temperature gradient in the material remains almost zero resulting in an isothermal process. However, at a very high frequency the period of thermal conduction becomes much larger compared to the period of vibration resulting in an adiabatic process. From this theory it is evident that the system with a very low frequency of vibration is completely different from the system with a fairly high frequency from material damping point of view. Global motions of large space structures are expected to occur at extremely low frequencies (below 1 Hz). Therefore, the damping data of specimens at very low frequency is needed to simulate or predict the exact dynamic behavior of the structure.

In this paper an experimental method is described by which one can determine the specific damping capacity of the material at any frequency between 0.4 Hz to 10.0 Hz and at any desired strain amplitudes (at 150 microstrains and above).

THEORY

Material or structural systems that dissipate energy under cyclic load display one phenomenon in common: the cyclic load-displacement (or stress-strain) curve is not a single-valued function but forms a hysteretic loop. Since energy is absorbed by a material system under cyclic loading, the unloading portion of the loop must lie below the loading portion as shown in Fig.1. Therefore the energy dissipated in a specimen under cyclic loading, ΔW, is the area under the hysteresis loop.

We define specific damping capacity of a specimen by

$$\Psi = \Delta W / W \tag{1}$$

Where W is the maximum energy stored in a specimen during a cycle. If the applied cyclic stress on the specimen is represented by

$$\sigma = \sigma_o \, \text{Sin} \omega t \tag{2}$$

Where σ_o = cyclic stress amplitude
ω = frequency of cyclic loading
t = time

and the strain due to cyclic loading is represented by

$$\varepsilon = \varepsilon_o \, \text{Sin}(\omega t - \phi) \tag{3}$$

Where ε_o = cyclic strain amplitude
ω = frequency of cyclic strain
ϕ = angle of phase lag between stress and strain

The energy loss per cycle is given by

$$\Delta W = \Pi M_2 \varepsilon_o^2 \tag{4}$$

and maximum stored energy in the cycle is given by

$$W = (1/2) M_1 \, \varepsilon_o^2 \tag{5}$$

Where M_1 and M_2 are storage modulus and loss modulus of the material, respectively. Therefore specific damping capacity can be written as

$$\Psi = \Delta W / W = 2\Pi \, M_2 / M_1 = 2\Pi \, \text{tan} \phi \tag{6}$$
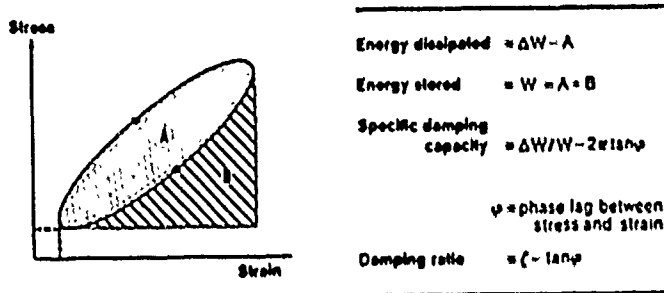
Fig. 1   Ideal stress vs. strain curve for a full cycle
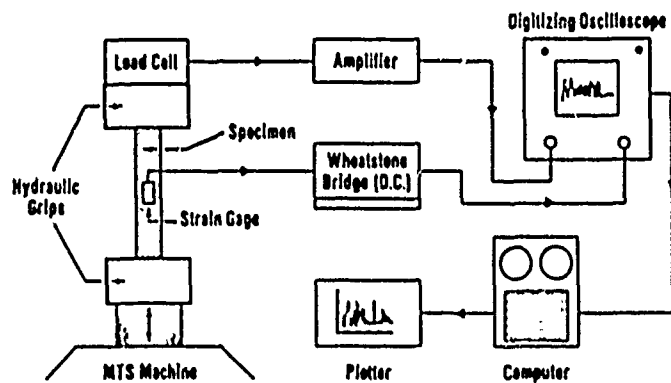
Fig. 2   Schematic Diagram of the Experimental Setup

DESCRIPTION OF THE TEST SPECIMEN

Two specimens S-13 and S-25, which were tested, have rectangular cross-section of thickness 0.026" and width 0.75". The gage length of the specimen S-13 is 7" whereas S-25 has a gage length of 3". Both the specimens have fiber-reinforced plastic (FRP) tabs at the ends for grips to match with the MTS hydraulic friction grips.

The specimens are cut from a plate of graphite-fiber-reinforced aluminum(6061) composites. Fibers used for this plate are continuous. The specimen S-13 has its reinforced fibers oriented along its load axis (i.e. 0° fiber orientation), whereas specimen S-25 has 90° fiber orientation. Typical properties of the material are given in Table 1. The microstructural details and the fiber-matrix interface properties of the material are given in Ref.[5] and [8].

EXPERIMENTAL PROCEDURE

Numerous techniques of damping measurements for a wide range of frequencies and strain levels have been reviewed and discussed in the liturature, see Ref.[1-4],[7] for example. The measurement of specific damping capacity at a low frequency is quite difficult and is prone to fairly high degree of errors. The classical or direct method of measuring damping at low frequency is the hysteresis loop technique. The specific damping capacity of the material was measured by subjecting the specimen to low frequency sinusoidal oscillations in servohydraulic MTS machine. Expression (6) shows that the specific damping capacity can be determined either from the phase lag between the load (stress) and strain signal or from the area enclosed inside the resultant hysteresis loop. The second alternative has been used here.

In order to remove the grip friction losses from the measurement system the machine should be operated in load control mode. Several cycles of loading were allowed to stabilize the hysteresis loops formed by load cell and strain gage bridge signals. The signal from the load cell was first amplified by an amplifier and then digitized and stored in one channel of a dual channel storage oscilloscope. Simultaneously the semiconductor strain gage (mounted on both faces of the specimen) signal is taken through an ordinary D.C. Wheatstone bridge circuit, digitized and stored on the other channel of the oscilloscope. High resistance (2000 ohms) and high gage factor (about 150) semiconductor gages with an excitation of 30 V produce about 1 V bridge output at a strain level of 500 microstrains. Therefore, the amplification of the bridge signal is not needed even at very low strain levels.

A schematic diagram of the experimental set up is shown in Fig.2. The use of amplifiers has been kept at a minimum, because most of the amplifiers cause phase shift of the signal even at very low frequency. Considerable amount of noise is present in the stored signal. It is especially evident at low level of strain where signal to noise ratio is comparatively low. Therefore the noise from both the signals was removed by digital filtering technique.

A typical stored load cell signal with noise as shown in Fig.3(a) was analyzed by Fast Fourier Transform (FFT) and plotted. Fig.3(b) shows the FFT of the noisy signal. From the FFT plot it is easy to identify the signal from the noise. Now performing Inverse Fourier Transform (IFT) keeping only the coefficients regarded as signal, clean signal as shown in Fig.3(c) can be obtained. Similarly the bridge signal which is stored on the other channel can be cleaned up. Fig.4(a),4(b) and 4(c) show the process for the bridge signal. Fig. 5(a) and 5(b) show the load vs strain plots of the noisy signal and clean signal respectively. It should be mentioned here that the small amount of phase shift may occur in the filtered signals due to digital filtering. However, this shift occurs equally in both the load cell and the bridge signals causing no relative phase shift between the two signals. This process may be viewed as filtering of two different signals by two perfectly matched filters.

The area under the hysteresis loop considered to be the energy loss in a cycle of loading and the area under the curve from zero load to the maximum load along the loading path considered to be the maximum stored energy can be measured by numerical integration of load-strain plot of filtered signals as shown in Fig.5(b). The trapezoidal rule has been used for numerical integration.

The phase shift of the load cell signal due to amplifier was anticipated. Therefore, the amplifier of the load cell signal was calibrated to determine the phase shift at test frequencies namely 0.4,1.0,2.0,4.0 and 10.0 Hz by passing the same sinusoidal signal through the amplifier to one channel of the oscilloscope and directly from function generator to other channel of the oscilloscope. The calculation of the phase shift due to amplifier was done exactly the same way as it was done for the real signals. The phase shift due to amplifier alone was subtracted from the phase shift obtained with the specimens.

RESULTS

The typical values of phase shift of load cell amplifier at test frequencies are given in Table 2. The specific damping capacity (Ψ) and loss angle (ϕ) for specimen S-13 and S-25 are given in Table 3 and Table 4 respectively. The values in Table 3 and Table 4 are given after correction of phase shift due to load cell amplifier.

DISCUSSION

In order to check the reliability of the measurement system an aluminum alloy specimen (6061-T625) was tested at a frequency of 1 Hz. The values of loss angle (ϕ) for the aluminum alloy specimen are plotted as shown in Fig.6. It may be seen from the plot that the scatter of data points at low strain level (below 150 microstrains) is quite high. The factor(s) that is causing this wide range of scatter at low strain levels is still unknown. Therefore, the values below 150 microstrains are not considered reliable.

Table 1

Typical Properties of Metal-Matrix Composites [Ref.8]

Specimen	Material	Density	Fiber Volume	Fiber Angle	Young's Modulus	Ultimate Strength
		Lb/in^3	%		MSI	KSI
S-13	Std.P55/6061	0.08714	39.23	0°	22.9	76.97
S-25	Std.P55/6061	0.08714	39.23	90°	5.54	4.42

Note: Further details of the materials are given in Ref.[5] and [8].

TABLE 2

Equivalent specific damping capacity (Ψ) and loss angle due to load cell amplifier phase shift.

TEST FREQUENCIES IN Hz	$\Psi \times 10^{-3}$	STANDARD DEVIATION	$\phi \times 10^{-3}$	STANDARD DEVIATION
0.4	0.701	0.6874×10^{-3}	0.1117	1.0940×10^{-4}
1.0	1.11135	0.5271×10^{-3}	0.1816	0.8390×10^{-4}
2.0	1.9075	0.5023×10^{-3}	0.3036	0.7995×10^{-4}
4.0	3.5578	0.3565×10^{-3}	0.56625	0.5675×10^{-4}
10.0	8.9168	0.4701×10^{-3}	1.41915	0.7483×10^{-4}

TABLE 3

Specific Damping Capacity (ψ) and loss angle (φ)
for specimen S-13 (0° fiber orientation)

Frequencies in Hz

STRAIN AMPLITUDE	0.4		1.0		2.0		4.0		10.0	
	$\psi \times 10^{-3}$	$\phi \times 10^{-3}$	$\psi \times 10^{-3}$	$\phi \times 10^{-3}$	$\psi \times 10^{-3}$	$\phi \times 10^{-3}$	$\psi \times 10^{-3}$	$\phi \times 10^{-3}$	$\psi \times 10^{-3}$	$\phi \times 10^{-3}$
150 μc	19.54	3.11	16.84	2.68	18.56	2.95	21.45	3.41		
195 μc	22.05	3.51	18.41	2.93	18.88	3.01	29.94	4.76	40.34	6.42
242 μc	27.39	4.36	25.32	4.03						
285 μc	32.73	5.21	28.77	4.58						
325 μc	38.71	6.16	33.49	5.31						

TABLE 4

Specific damping capacity (ψ) and loss angle (φ)
for specimen S-25 (90° fiber orientation)

Frequencies in Hz

STRAIN AMPLITUDE	0.4		1.0		2.0		4.0		10.0	
	$\psi \times 10^{-3}$	$\phi \times 10^{-3}$	$\psi \times 10^{-3}$	$\phi \times 10^{-3}$	$\psi \times 10^{-3}$	$\phi \times 10^{-3}$	$\psi \times 10^{-3}$	$\phi \times 10^{-3}$	$\psi \times 10^{-3}$	$\phi \times 10^{-3}$
150 μc	12.41	1.97	7.45	1.19	11.25	1.79	12.13	1.93	20.61	3.28
187 μc	11.09	1.77	7.19	1.14	8.89	1.42	11.00	1.75	21.01	3.35
230 μc	11.41	1.82	10.62	1.69	9.11	1.45			19.51	3.11
307 μc	10.53	1.675	8.95	1.42	9.11	1.45				
381 μc	12.03	1.915	8.20	1.31	7.82	1.25				
455 μc	11.47	1.825	7.66	1.22	8.07	1.27				
525 μc	11.12	1.77	8.42	1.34	8.11	1.26				
566 μc	10.75	1.71	8.32	1.32	7.95	1.26				

FC-8
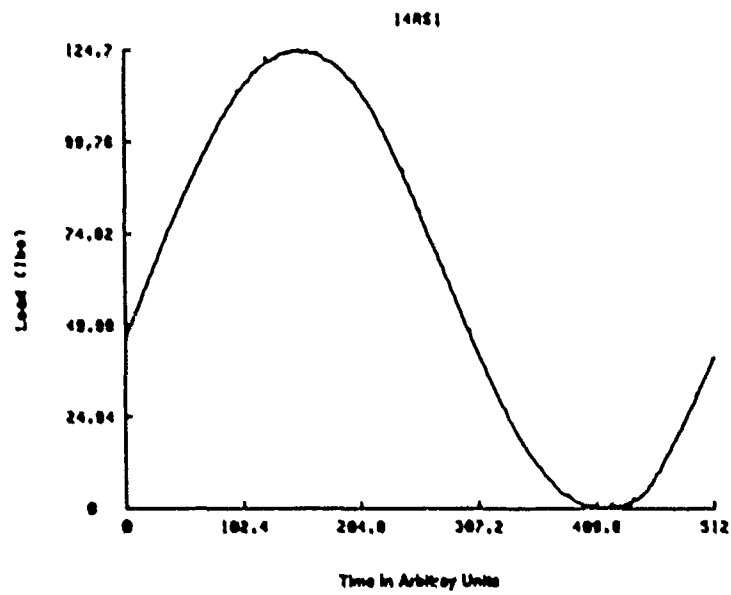
Fig. 3(a) Unfiltered load vs time curve
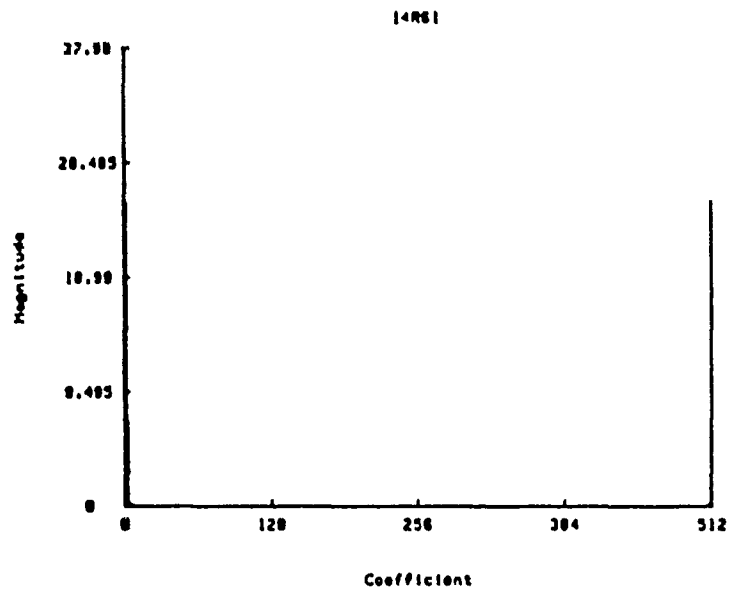
Fig. 3(b) FFT of load-time signal
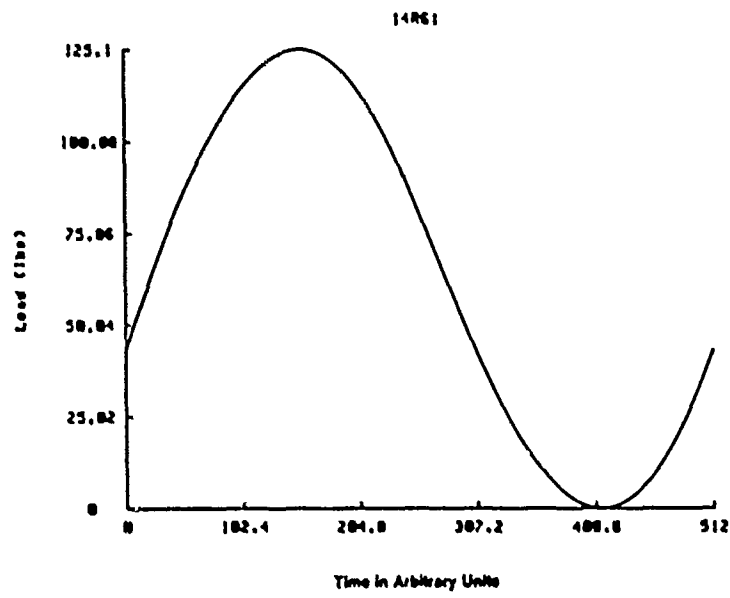
Fig. 3(c) Filtered load vs time curve
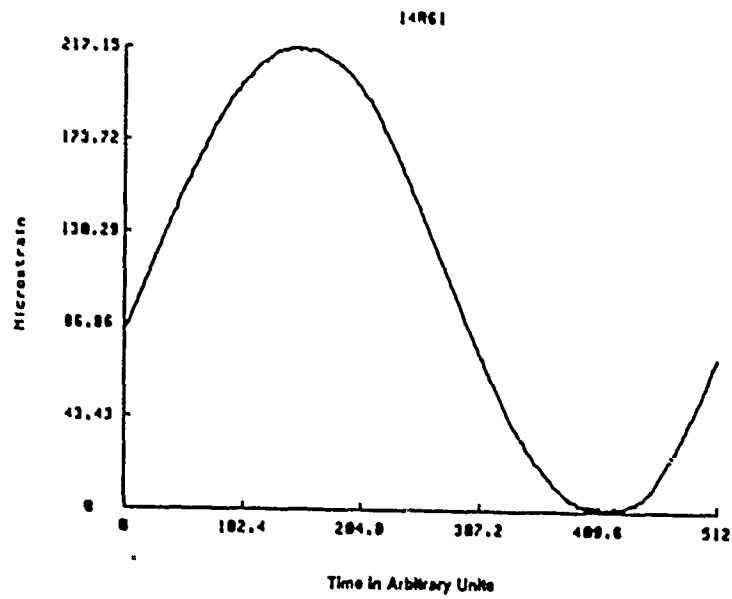
Fig. 4(a) Unfiltered strain vs time curve

FC-10
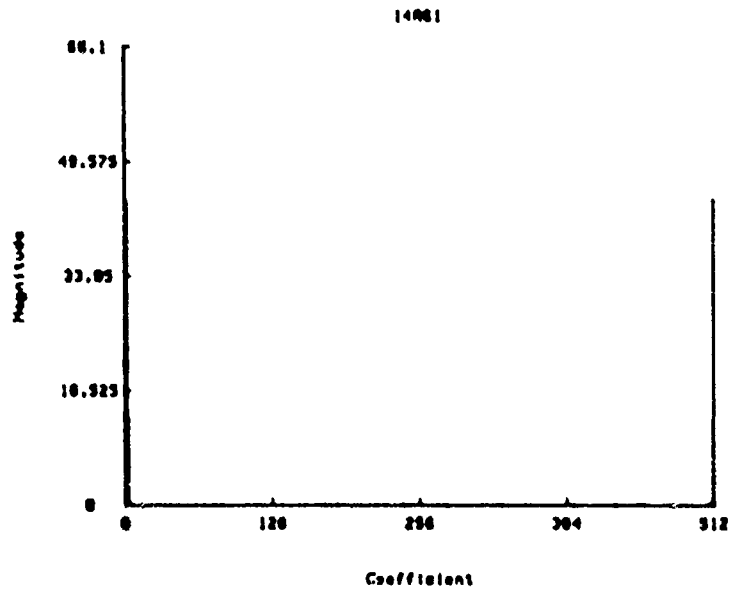
Fig. 4(b) FFT of strain-time signal
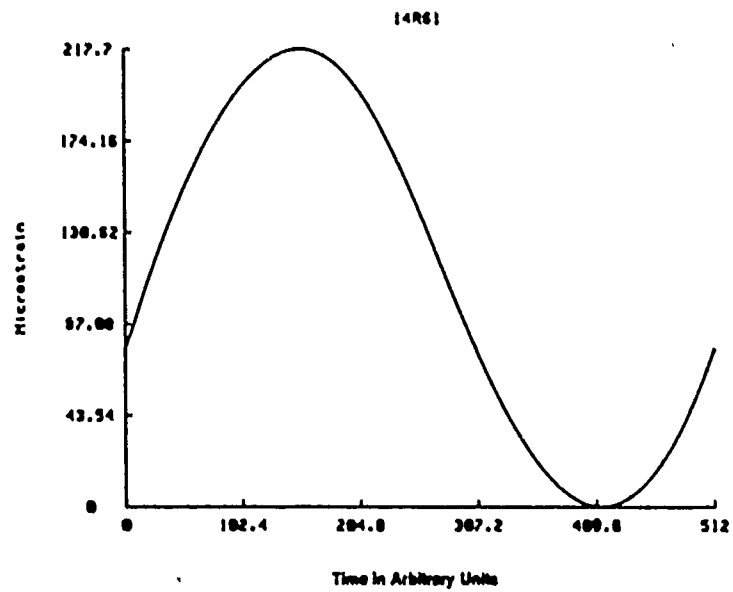
Fig. 4(c) Filtered strain vs time curve

FC-11

451
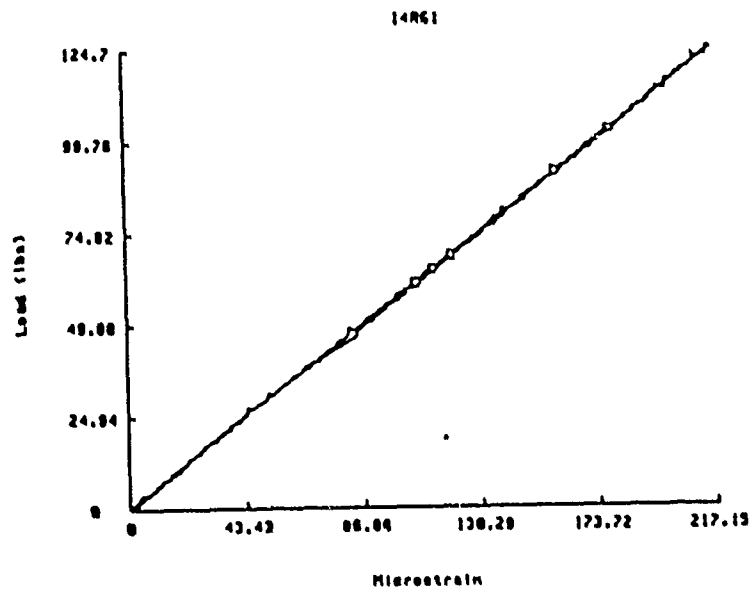
Fig. 5(a) Unfiltered load vs strain curve
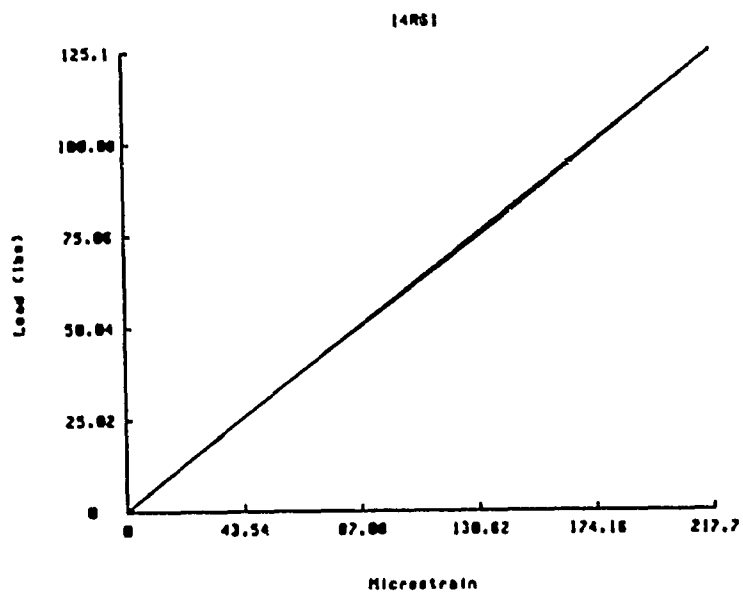
Fig. 5(b) Filtered load vs strain curve

FC-12
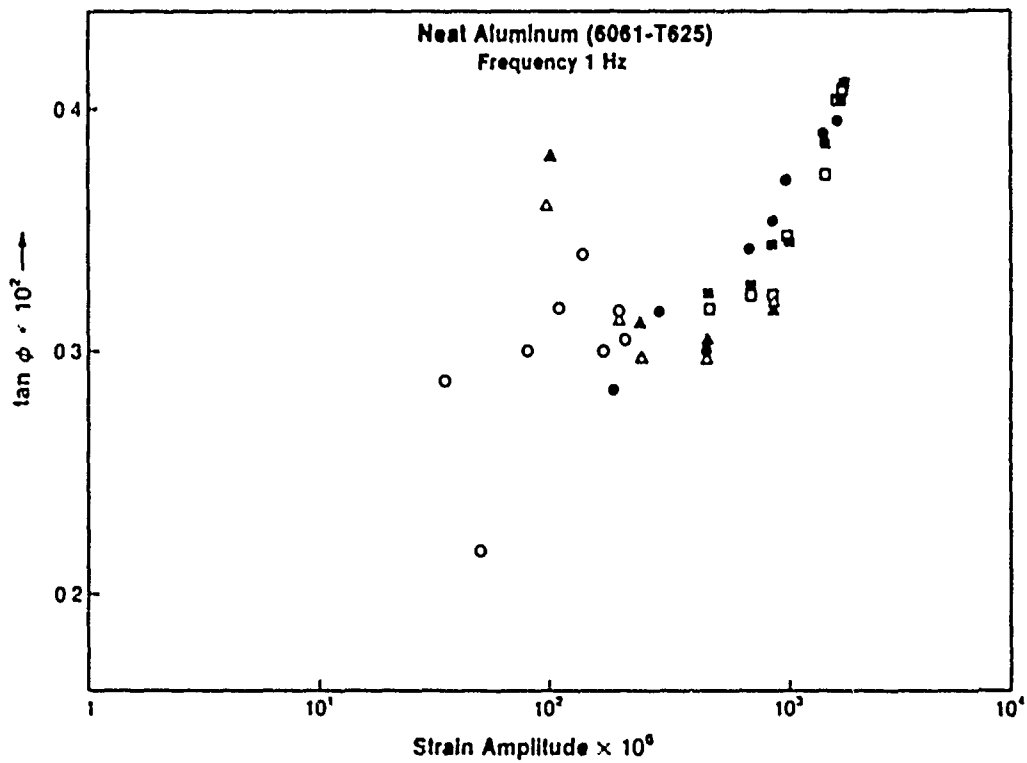
Fig. 6 Loss angle vs strain amplitude for 6061-T625
Aluminum specimen
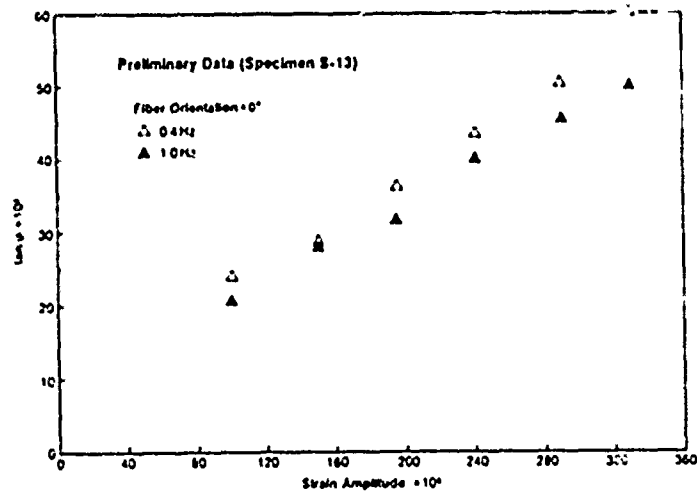
Fig. 7 Loss angle vs strain amplitude for Graphite/
Aluminum composite specimen of 0° fiber orientation

FC-13
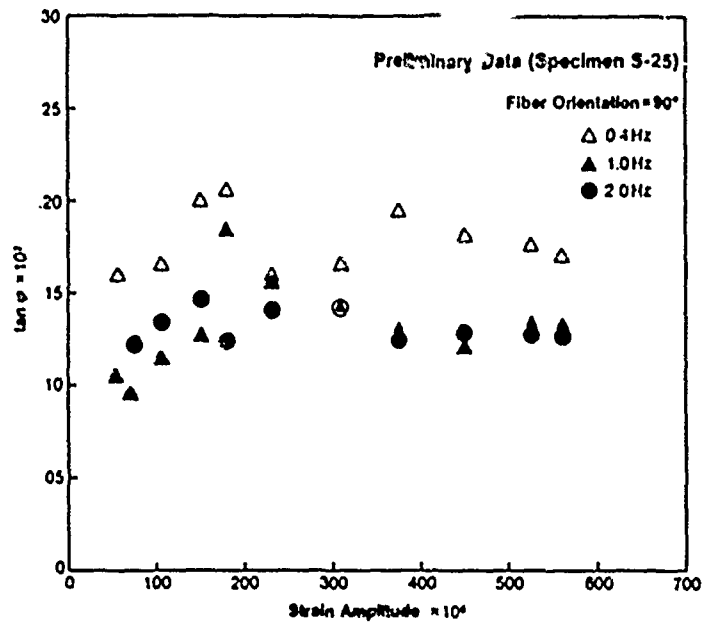
Fig. 8 Loss angle vs strain amplitude for Graphite/
Aluminum composite specimen of 90° fiber orientation
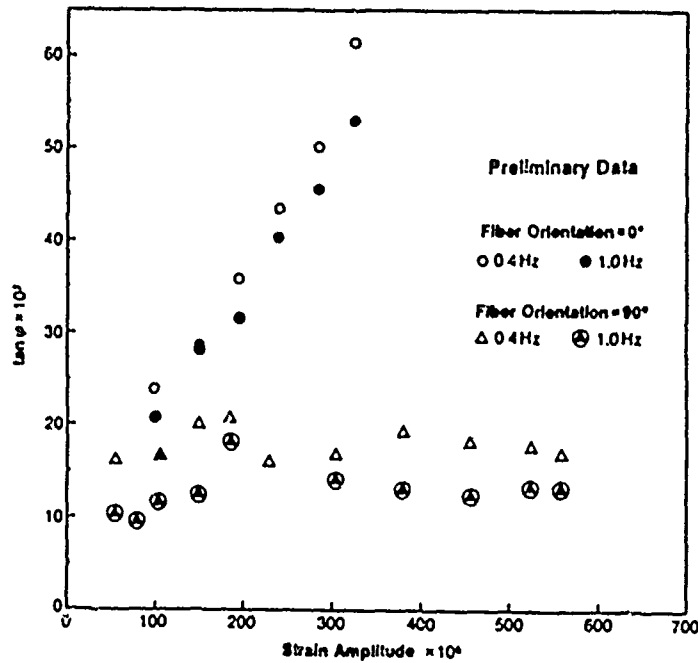
Fig. 9 Comparison of loss angles with the variation of
strain amplitudes between 0° and 90° fiber
orientation in Graphite/Aluminum composites

FC-14
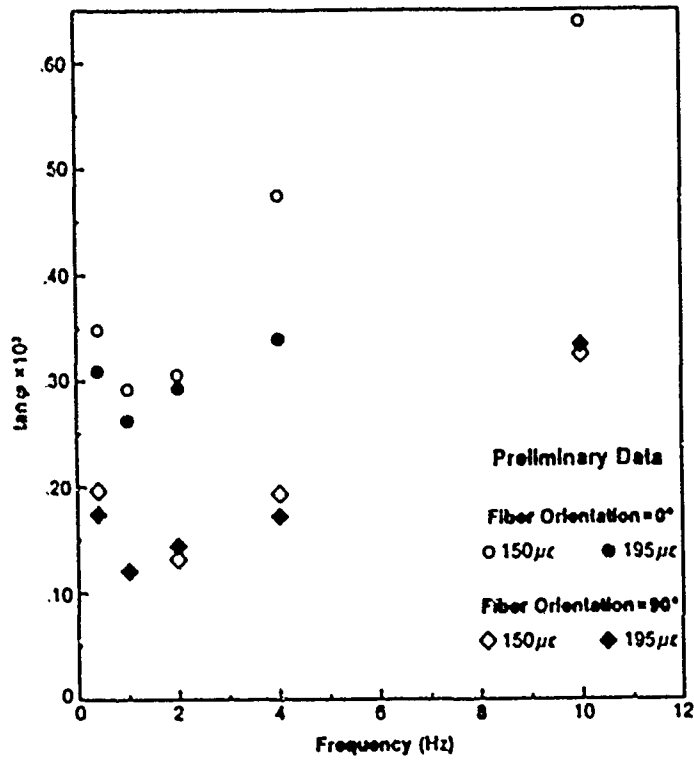
Fig 10 Variation of loss angle with frequency for
Graphite/Aluminum composites

Fig.7 shows the plot of tanϕ vs strain amplitude for specimen S-13. From the plot it is quite evident that the loss angle (tanϕ or ϕ) increases steadily with the increase of strain amplitude for the specimen with $0°$ fiber orientation. Fig.8 shows a plot of tanϕ vs strain amplitude for specimen S-25. Plot shows no noticeable increase of loss angle with the increase of strain amplitudes for the specimen having $90°$ fiber orientation. Fig.9 shows the improvement of loss angle with the fiber orientation in the specimen. Fig.10 shows the variation of loss angle with the variation of frequency as the frequency increases there is noticeable increase in loss angle for both $0°$ fiber and $90°$ fiber specimen.

REFERENCES

1. Nowick, A.S. and Berry, B.S., "Anelastic Relaxation in Crystalline Solids," Academic Press, New York, 1972.

2. Read, B.E. and Dean, G.D.,"The Determination of Dynamic Properties of Polymers and Composites," John Wiley & sons, New York, 1978.

3. Zener, C.,"Elasticity and Anelasticity of metals," University of Chicago Press, Chicago, 1948.

4. Ray, A.K. and Kinra, V.K.,"Damping Capacity in Metal-Matrix Composites- A Liturature Review," Report No. MM RH4-394042-84-20, Mechanics & Materials Center, Texas A & M University, September, 1984.

5. Misra, M.S. and LeGreca, P.D.,"Damping Behavior of Metal-Matrix Composites," Vibration Damping 1984 Workshop proceedings, Ed. L. Rogers, November,1984,pp.U2-13.

6. Gibson, R.F.,"Vibration Damping Characteristics of Graphite/Epoxy Composites for Large Space Structures," Large Space Systems Technology-1981, Third Annual Technical Review, NASA Langley Research Center, Hampton, Virginia.

7. Lazan, B.J.,"Damping of Materials and Members in Structural Mechanics," Pergamon Press, New York, 1968.

8. Rawal, S.P. and Misra, M.S. "Interfaces and Damping in Continuous Gr/Al Composites", Proceedings of 1985 Metals Congress/Role of Surface and Interface on Materials Damping-Session-IV, 14-17 October, 1985.

ACKNOWLEDGMENTS

RESPONSE SUPPRESSION IN COMPOSITE SANDWICH SHELLS

R. Vaicaitis
Dept. of Civil Engineering, Columbia University

D.A. Bofilios
Dept. of Aerospace Engineering, San Diego State University

Abstract

This paper presents an analytical study based on modal methods on response suppression of double wall cylindrical composite shells. Solutions are determined for random point loads acting either on the interior or the exterior shell. The space between the shells is assumed to be filled with a soft viscoelastic material. The shell skins are modeled according to fiber reinforced laminated composite shell theory. Viscous and material damping models are considered. Results indicate that reponse of a double wall shell is controlled by damping of the laminated shells and viscoelastic core, location of the point load action, and reinforcing fiber orientation.

Introduction

The design of many flight structures is impacted by the interaction of various functional requirements such as weight, passenger accommodations, strength, stiffness, reliability, etc. To accommodate these requirements under severe space environment constraints, new design concepts will need to be developed which could lead to lower weight and be more cost efficient. The use of fiber reinforced composite materials could provide weight advantages and improve structural integrity.[1-4] The cylindrical shell configuration is widely used for rockets, missiles, aircraft fuselages, hulls of submersibles, etc. The modules of the proposed space station concept will require configurations of a cylindrical shell. The internal and external random loads impacting on these modules could produce unaccceptable vibration and noise levels. Thus, to satisfy the vibroacoustic environment of these structures, design concepts utilizing various add-on damping mechanisms might need to be introduced. Past studies have demonstrated that a significant amount of response and noise reduction can be achieved by a sandwich type construction.[5-12] Preliminary studies on double wall shell response and noise transmission presented in Refs. 11 and 12 indicate that the reponse levels are strongly controlled by system damping parameters.

This paper presents an analytical method for calculating the response of double wall shells. The solution of the coupled system are obtained by a Galerkin-like procedure. A simplified problem geometry is shown in Figure 1 and Figure 2. The space between the two thin shells is assumed to be filled with a soft viscoelastic material. Such a model allows in phase (flexural) and out of phase (dilatational) motions of the double wall system. The inputs are random point loads acting on the outer or/and the inner shells. The double wall shell skins are modeled according to a laminated composite cylindrical shell theory.[13-16]

Several types of damping models for the viscoelastic core and the face shells are examined. It is shown that the reponse of a double wall fiber reinforced composite shell is strongly dependent not only on the damping values chosen, but also on the type of damping model selected for theoretical study.

Response of a Double Wall Shell

The double wall shell system shown in Figure 1 is composed of two simply supported shells and a soft viscoelastic core. The loads are random point forces acting on the exterior and/or interior shell as indicated in Figure 2. Each shell is constructed from fiber reinforced laminae of uniform thickness. The thin shells are modeled according to the theory presented in Refs. 13-16. This theory is appropriate for many arbitrarily oriented layers, each reinforced with unidirectional fibers. The fiber orientation is defined in Figure 1 with respect to the chosen coordinates. The stiffness coefficients of the composite shell are calculated in terms of directional moduli, Poisson's ratios and fiber orientation angle α.[16] In this approach, the properties of each lamina are proportioned according to the volume ratio of fibers and supporting matrix material. Utilizing the Donell-Mushtari-Vlasov type assumptions[14-16], a single partial differential equation in terms of transverse displacement w can be derived for each shell.[11] These equations are then coupled through the soft viscoelastic core into two partial differential equations for normal deflections of the exterior and interior shells.

$$(_{z}\nabla_{E}^{8} + _{x}\nabla_{E}^{6} + _{y}\nabla_{E}^{4})\, w_{E} + \nabla_{E}^{4}\, (\rho_{E}\ddot{w}_{E} + k_{S}(w_{E} - w_{I})$$

$$+ c_{E}\dot{w}_{E} + (1/3)\, m_{S}\ddot{w}_{E} + (1/6)\, m_{S}\ddot{w}_{I}) = \nabla_{E}^{4}\, p^{e}(x,\theta,t) \qquad (1)$$

$$(_{z}\nabla_{I}^{8} + _{x}\nabla_{I}^{6} + _{y}\nabla_{I}^{4})\, w_{I} + \nabla_{I}^{4}\, (\rho_{I}\ddot{w}_{I} + k_{S}(w_{I} - w_{E})$$

$$+ c_{E}\dot{w}_{I} + (1/3)\, m_{S}\ddot{w}_{I} + (1/6)\, m_{S}\ddot{w}_{E}) = - \nabla_{I}^{4}\, p^{i}(x,\theta,t) \qquad (2)$$

where the subscripts E, I and S denote the external and the internal shells, and the core, respectively. The differential operators $_{z}\nabla^{8}, _{z}\nabla^{6}, _{y}\nabla_{e}^{4}$ and ∇_{i}^{4} are lengthy expressions and given in Ref. 11. The random loads p^{e} and p^{i} are expressed in terms of two point loads F_1 and F_2 as

$$p^{e}(x,\theta,t) = (1/\Lambda_1^{e}\Lambda_2^{e})\, \{F_1^{e}(t)\, \delta(x - x_1^{e})\, \delta(\theta - \theta_1^{e})$$

$$+ F_2^{e}(t)\, \delta(x - x_2^{e})\, \delta(\theta - \theta_2^{e})\} \qquad (3)$$

$$p^{i}(x,\theta,t) = (1/\Lambda_1^{i}\Lambda_2^{i})\, \{F_1^{i}(t)\, \delta(x - x_1^{i})\, \delta(\theta - \theta_1^{i})$$

$$+ F_2^{i}(t)\, \delta(x - x_2^{i})\, \delta(\theta - \theta_2^{i})\} \qquad (4)$$

where the superscripts e and i denote the external and the internal loads, δ is the Dirac delta function, and for a cylindrical shell $\Lambda_1^{e} = 1, \Lambda_2^{e} = R + h_s$, $\Lambda_1^{i} = 1, \Lambda_2^{i} = R$.[16] These point loads are assumed to be independent and each characterized by a force spectral density.

The equations of double wall shell vibrations can be solved by modal methods. To further simplify this procedure and utilize the orthogonality condition, the terms containing odd derivatives of spatial variables x and θ in the operators $_{z}\nabla^{8}, _{x}\nabla^{6}, _{y}\nabla^{4}$ are neglected. The various simplifications of shell equations are discussed in Refs. 13, 15, 16. Then, the solutions for exterior and interior shell normal deflections can be written as

$$w_{E}(x,\theta,t) = \sum_{m=1}^{\infty} \sum_{n=0}^{\infty} \Lambda_{mn}^{E}(t)\, X_{mn}(x,\theta) \qquad (5)$$

$$w_{I}(x,\theta,t) = \sum_{m=1}^{\infty} \sum_{n=0}^{\infty} \Lambda_{mn}^{I}(t)\, X_{mn}(x,\theta) \qquad (6)$$

Λ_{mn}^{E} and Λ_{mn}^{I} are the generalized coordinates of external and internal shells, and X_{mn} are the structural modes. For a simply supported shell, the modes are $X_{mn} = \sin(m\pi x/L)\cos n\theta$. Taking Fourier transformation of equations (1-6) and utilizing the orthogonality principle, solutions for $\Lambda_{mn}^{E}(\omega)$ and $\Lambda_{mn}^{I}(\omega)$ can be determined.[11]

For the analysis presented in this paper, the random point inputs are characterized by spectral densities. Thus, shell deflections need to be expressed in a form of spectral density. Following the procedures given in Ref. 20 and using equations (5) and (6), the spectral densities of normal shell deflections are

$$S_w^{E,I}(x,\theta,\omega) = \sum_{m=1}^{\infty} \sum_{n=0}^{\infty} \sum_{r=1}^{\infty} \sum_{s=0}^{\infty} S_{mnrs}^{E,I}(\omega) X_{mn}(x,\theta) X_{rs}(x,\theta) \qquad (7)$$

where $S_{mnrs}^{E,I}$ are the cross-spectral densities of generalized coordinates A_{mn}^{E} or A_{mn}^{I}. It is convenient to express response on logarithmic scale by defining response levels as

$$RL^{E,I}(x,\theta) = 10 \log (S_w^{E,I}(x,\theta,\omega) \, \Delta\omega/w_{ref}^2) \qquad (8)$$

where $\Delta\omega$ is the frequency bandwidth and w_{ref} is the selected reference deflection.

Damping

Damping in the double wall fiber reinforced composite shell is assumed to be composed of material damping due to internal friction within each of the materials and interfacial slip at the fiber-matrix interfaces, viscous damping due to radiation effects and structural damping of the core material. A detailed discussion on damping of fiber reinforced composite materials is given in Refs. 17-19, 21-23. Using the complex elastic modulus approach, all directional moduli are expressed in the form

$$E_{rs} = E_{rs}^{R} (1 + i \, g_{rs}) \qquad (9)$$

where E_{rs} are the complex directional moduli, E_{rs}^{R} is the real part of E_{rs} and g_{rs} are the loss factors. Damping in the soft core is introduced by expressing the core stiffness as

$$k_s = k_o (1 + i \, g_s) \qquad (10)$$

where k_o is the real part of the unidirectional core stiffness and η_s is the damping loss factor in the core. The viscous damping coefficients C_E and C_I are expressed in terms of modal damping ratios (% of critical) ζ_{mn}^{E} and ζ_{mn}^{I}.

Numerical results are obtained for several different models of ζ_{mn}^{E} and ζ_{mn}^{I}.

Numerical Results

Numerical results presented herein correspond to the double wall shell system shown in Figures 1 and 2. The following parameters are selected: $L = 7.62$ m, $R = 1.473$ m, $h_s = 5.08$ cm, $h_E = 0.813$ mm, $h_I = 2.54$ mm, $k_o = 1.14 \times 10^6$ N/m^3, $\rho_s = 37.40$ Pa-sec^2/m^2, $w_{ref} = h_I$. The outer shell contains three layers while the inner shell is composed of ten layers. Fiberglass and graphite fibers are used to reinforce the Plexiglass material. The ratio of fibers volume to Plexiglass volume is 0.2. The elastic moduli, Poisson's ratios and material densities are, respectively, $E_f = 5.17 \times 10^{10}$ Pa,

$\mu_f = 0.33$, $\rho_f = 2180$ Pa-sec^2/m^2, $E_g = 7.03 \times 10^{11}$ Pa, $\mu_g = 0.33$,

$\rho_g = 1550$ Pa-sec^2/m^2, $E_p = 1.57 \times 10^9$ Pa, $\mu_p = 0.35$, $\rho_p = 1197$ Pa-sec^2/m^2.

The fiber reinforcement for each layer (same pattern is used for inner and for outer shells) is arranged as follows: 1st layer fiberglass, 2nd layer graphite, 3rd layer fiberglass, and so on. The fiber orientation for the three lamina layers of the interior shell are $\alpha = -45°, 45°, -45°$. Similar alternating orientation is used for the ten layers of the inner shell where $\alpha = -45°, 45°, -45°, 45°$, etc. The shell response is computed at $x = L/2$ and $\theta = 45°$.

The input point loads F_j^e, F_j^i ($j = 1,2$) are assumed to be characterized by truncated Gaussian white noise spectral densities

$$S_{F_1, F_2}^{e,i}(f) = \begin{cases} 4.95 \times 10^{-3} \ \text{N/}^2\text{Hz}, & 0 < f < 1000 \ \text{Hz} \\ \\ 0, & \text{otherwise} \end{cases} \tag{11}$$

The random point loads are acting at $x_1^e = x_2^e = 3.81$ m, $x_1^i = x_2^i = 3.81$ m,

$\theta_1^e = -90°$, $\theta_2^e = 90°$, $\theta_1^i = -90°$ and $\theta_2^i = 90°$.

The response levels of the inner shell are given in Figure 3 for several values of core loss factor g_s. Modal damping is assumed to be constant for all modes and equal to 0.01 (percent of critical). The material damping is not included for this case. As can be observed from these results, viscoelastic damping in the core has only a small effect on shell response for frequencies below 100 Hz. The rms (root mean square) response of the outer and inner shells is plotted in Figure 4 versus the core loss factor g_s. Since the rms response is dominated by modes at low frequencies, the increase in loss factor g_s from 0.02 to 0.5, has only a modest effect on reduction of shell response.

The effect of changes in modal damping on shell response is illustrated in Figures 5 and 6. In this case, the core loss factor $g_s = 0.02$, damping is constant for all modes and the material damping is neglected. These results clearly illustrate that shell response is strongly dependent on selected modal damping values for the entire frequency range. The results shown in Figure 7 indicate the sensitivity of shell response to different modal damping models. The f^* and f^λ are the "breathing" ($m = 1, n = 0$) modal frequency and the lowest modal frequency of the coupled shell system. As can be observed from these results, deflection response levels can vary by as much as 25 dB at some frequencies among the different damping models used.

To demonstrate the effect of material damping introduced through the loss factors g_{rs}, results are presented in Fig. 8 for several values of loss factor g_{rs}. The core loss factor $g_s = 0.02$ and constant modal damping is assumed for which $\zeta_o = 0.01$. The same loss factor is used for all directional moduli. By increasing material loss factor g_{rs}, significant attenuation of shell response can be achieved at most frequencies.

Conclusions

Results indicate that deflection response of a double wall composite shell is controlled by damping characteristics of the shell material and reinforcing fiber orientation at different lamina layers. Damping in the soft core does not seem to have much effect on shell response at low frequencies. Response calculations are sensitive to the type of modal damping model used. For fiber reinforced composites, material damping introduced through directional moduli might be a convenient procedure to model structural damping.

Acknowledgment

References

1. Davis, G.W. and Sakata, I.F., "Design Consideration for Composite Fuselage Structure of Commercial Transport Aircraft," NASA CR-159296, March, 1981.

2. Revell, J.D., Balena, F.J. and Koval, L.R., "Analytical Study of Interior Noise Control by Fuselage Design Techniques on High-Speed Propeller-Driven Aircraft," NASA CR-159222, July, 1978.

3. Yang, J.C.S. and Tsui, C.Y., "Optimum Design of Structures and Composite Materials in Response to Aerodynamic Noise and Noise Transmission," NASA CR-155332, December 1977.

4. Durchlaub, E.C., "Minimized Fuselage Vibrations Using Advance Composites," 33rd Annual National Forum of the American Helicopter Society, Paper No. 77.33-84, Washington, D.C., May 1977.

5. Freudenthal, A.M. and Bieniek, M.P., "Forced Vibrations of Sandwich Structures," WADD Technical Report 60-307, U.S. Air Force, January, 1961.

6. Ford, R.D., Lord, P. and Walker, A.W., "Sound Transmission Through Sandwich Constructions," Journal of Sound and Vibration, Vol. 5, No. 1, January 1967, pp. 9-21.

7. Smolenski, C.P. and Krokosky, E.M.," Dilatational-Mode Sound Transmission in Sandwich Panels," Journal of the Acoustical Society of America, Vol. 54, No. 5, December, 1973, pp. 1449-1457.

8. Dym, C.L and Lang, M.A., "Transmission of Sound Through Sandwich Panels," Journal of the Acoustical Society of America, Vol. 56, No. 5, November 1974, pp. 1523-1532.

9. Vaicaitis, R., "Noise Transmission by Viscoelastic Sandwich Panels," NASA TN D-8516, August 1977.

10. Vaicaitis, R. and Hong, H.-K., "Nonlinear Response of Double Wall Sandwich Panels," 24th/AIAA/ASME/ASCE/AHS SDM Conference, Paper No. 83-1037-CP, Lake Tahoe, Nev., May 1983.

11. Vaicaitis, R. and Bofilios, D.A., "Response of Double Wall Composite Shells," 26th AIAA/ASME/ASCE/ASH SDM Conference, Paper No,. 85-0604-CP, Orlando, FL, April 1985.

12. Vaicaitis, R. and Bofilios, D.A., "Noise Transmission of Double Wall Composite Shells," ASME Conference on Vibration and Sound, Cincinnati, Ohio, Sept. 1985.

13. Bert, C.W , Baker, J.L. and Egle, D.M., "Free Vibration of Multilayer Anisotropic Cylindrical Shells," Journal of Composite Materials, Vol. 3, pp. 480-499, 1969.

14. Roth, B.K. and Das, Y.C., "Vibration of Layered Shells," Journal of Sound and Vibration (1973), 28(4), 737-757.

15. Harai, A. and Sandman, B.E., "Vibratory Response of Laminated Cylindrical Shells Embedded in an Acoustic Fluid," Journal of the Acoustical Society of America, Vol. 60, No. 1, July, 1976.

16. Soedel, W., Vibrations of Shells and Plates, Marcel Dekker, Inc., New York, 1981.

17. Chang, S. and Bert, C.W., "Composite Materials in Engineering Design," Proc. 6th St. Louis Symposium, May 1972.

18. Bert, C.W., "Composite Materials: A Survey of the Damping Capacity of Fiber Reinforced Composites," From: Damping Applications for Vibration Control, ed. by P.J. Torvik, ASME, AMD, Vol. 38, Nov. 1980.

19. Bert, C.W., "Material Damping: An Introductory Review of Mathematical Models, Measures and Experimental Techniques," Journal of Sound and Vibration (1973), 29(2), 129-153.

20. Lin, Y.K., Probabilisitc Theory of Structural Dynamics, McGraw-Hill, Inc. 1967.

21. Adams, R.D. and Bacon, D.G.C., "Effect of Fiber Orientation and Laminate Geometry on the Dynamic Properties of CFRP," J. Composite Materials, Vol. 7, pp. 402-428, October 1973.

22. Natarajan, R.T. and Lewis, A.F., "Advanced Composite Constrained Layer Laminates," J. Composite Materials, Vol. 10, pp. 220-230, July 1976.

23. Pulgrano, L.J. and Miner, L.H., "Effects of Fiber and Resin on the Vibration Damping of Composites Reinforced with Fiberglass, Graphite, and Aramid," the 28th National SAMPE Symposium, April 12-14, 1983.

Appendix-Nomenclature

$A_{mn}^{E,I}$	generalized deflection coordinates (m)
c_E, c_I	damping coefficients (Nm·s)
f	frequency (Hz)
h_S	core thickness (m)
h_E, h_I	thickness of external and internal shells (m)
$\underset{\sim}{i}$	$\sqrt{-1}$
k_o	core stiffness (N/m^3)
L	length of shell (m)
m_S	mass density of the core (kg/m^3)
p^e, p^i	external and internal random pressures (N/m^2)
R	radius (m)
w_E, w_I	normal displacements of external and internal shells (m)
x, θ	cylindrical coordinates (m,rad)
$x_j^e, x_j^i, \theta_j^e, \theta_j^i$	locations where the point loads are applied, $j = 1,2$ (m,rad) angle between fiber direction and shell axis (rad)
$\zeta_{mn}^E, \zeta_{mn}^I$	damping coefficients of external and internal shells
ζ_c	a constant value of damping coefficient
ρ_E, ρ_I	mass densities of external and internal shells (kg/m^3)

Superscripts and subscripts:

E	external shell
I	internal shell
E,I	external or internal shell
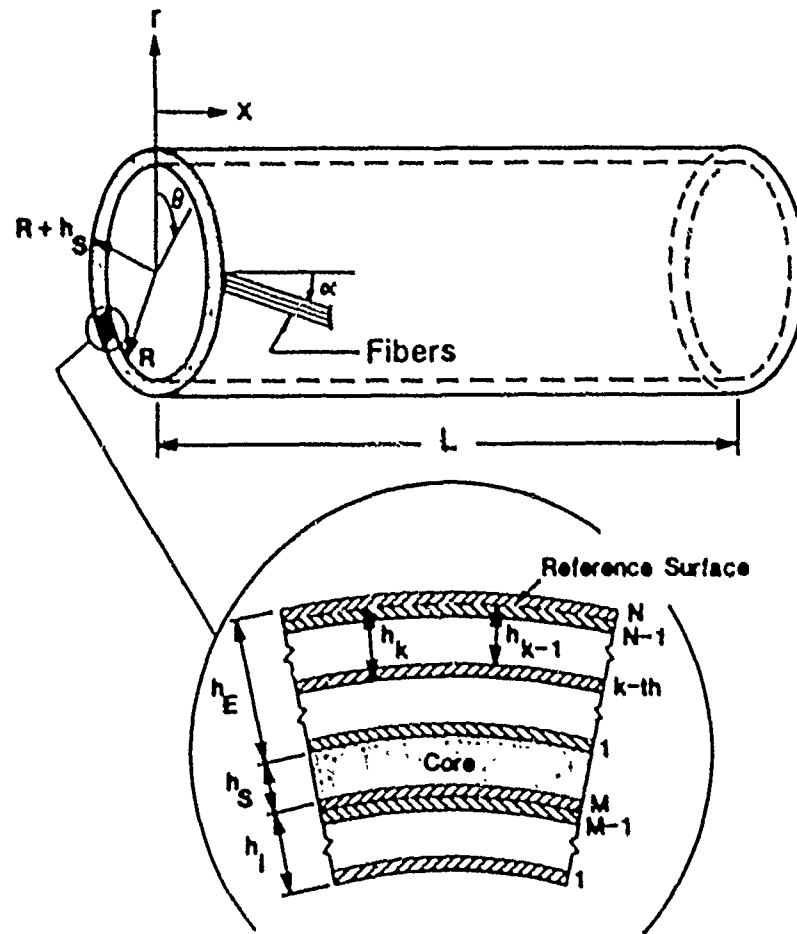
Fig. 1. Geometry of double wall composite shell
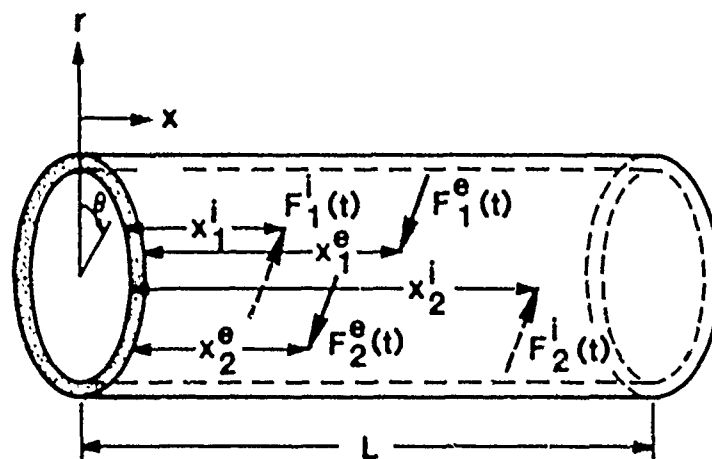
Fig. 2. Random point loads acting on the shell
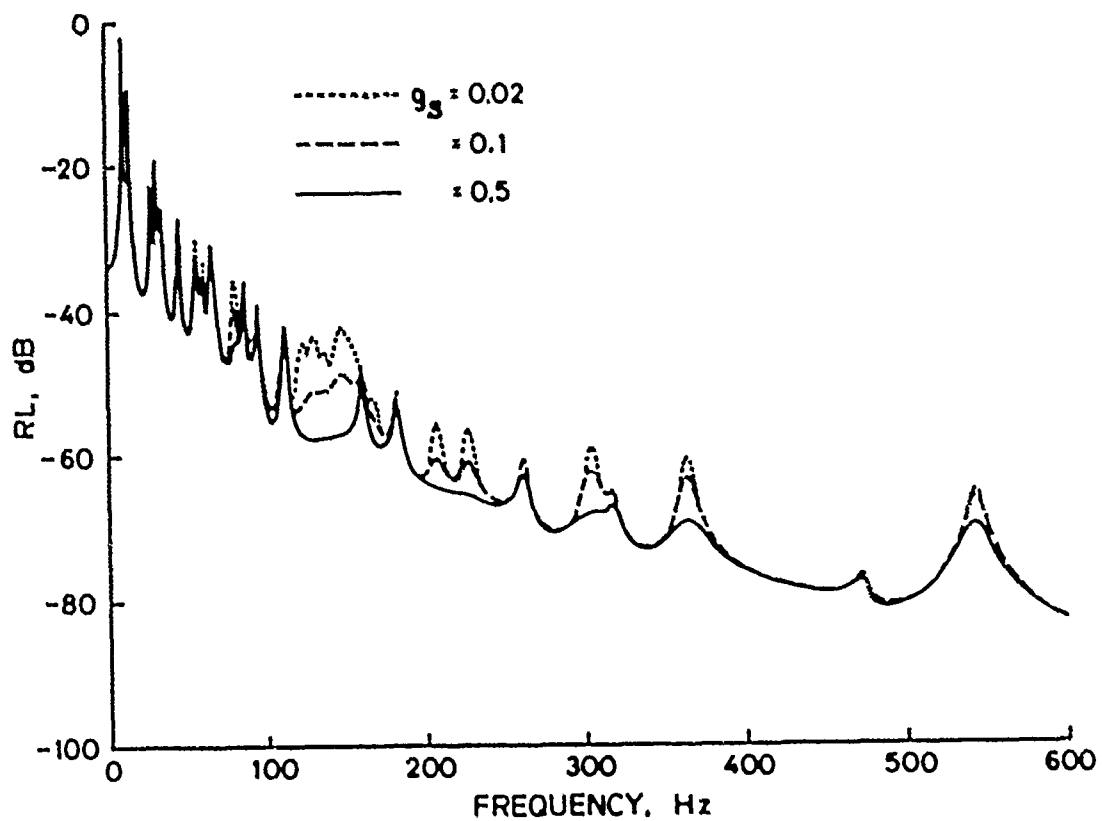
Fig. 3 Response levels of inner shell for different values of loss factor
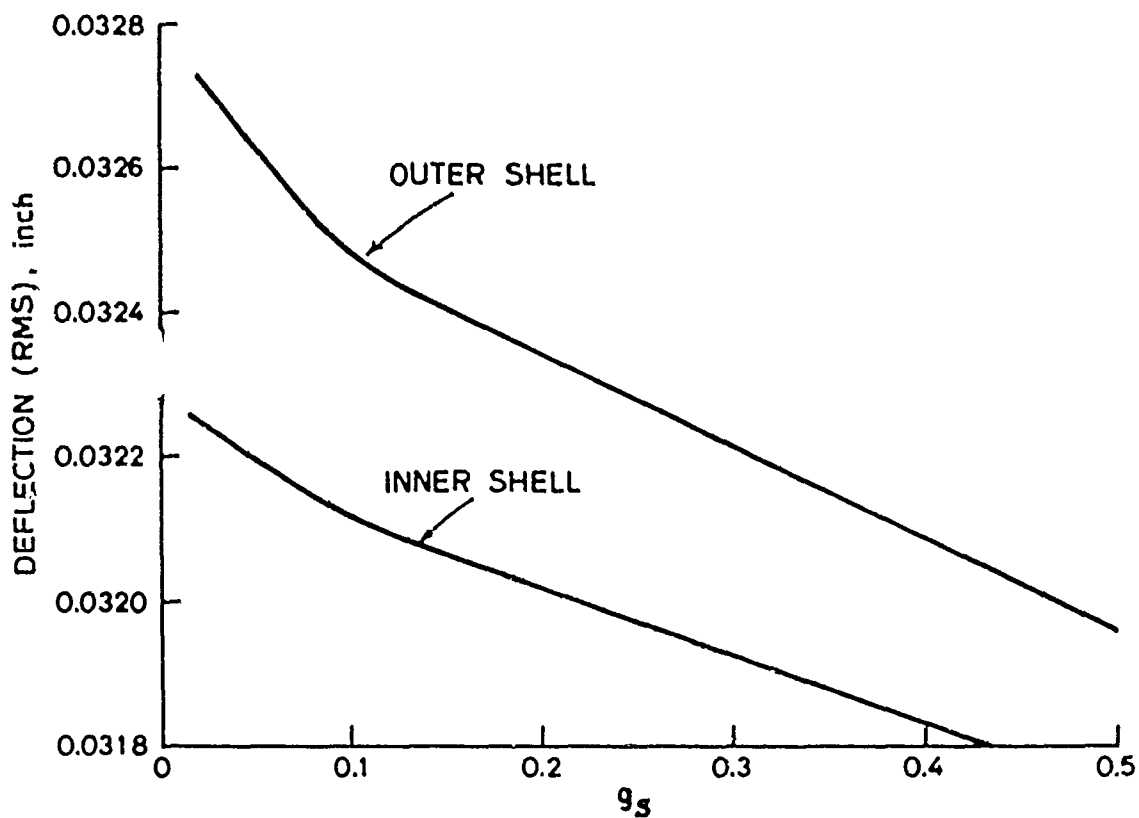
Fig. 4 Root mean square response for different values of loss factor g_s
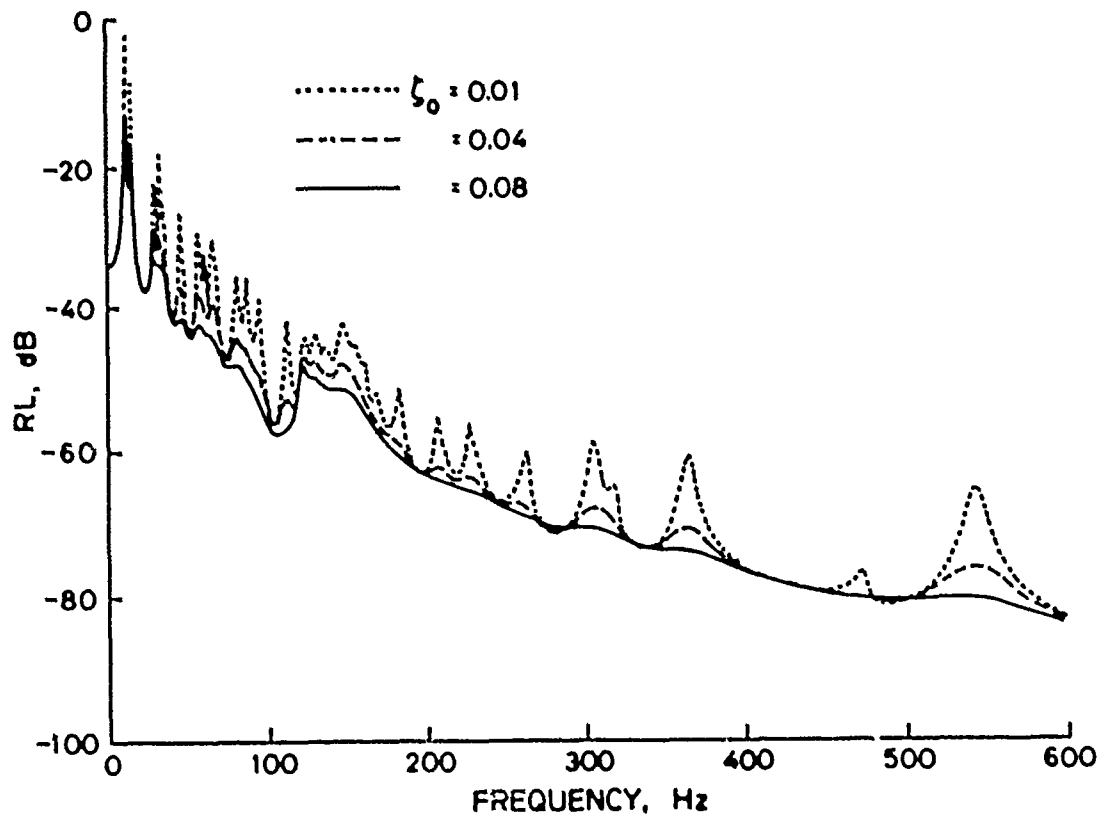
Fig. 5 Response levels of inner shell for different values of modal damping
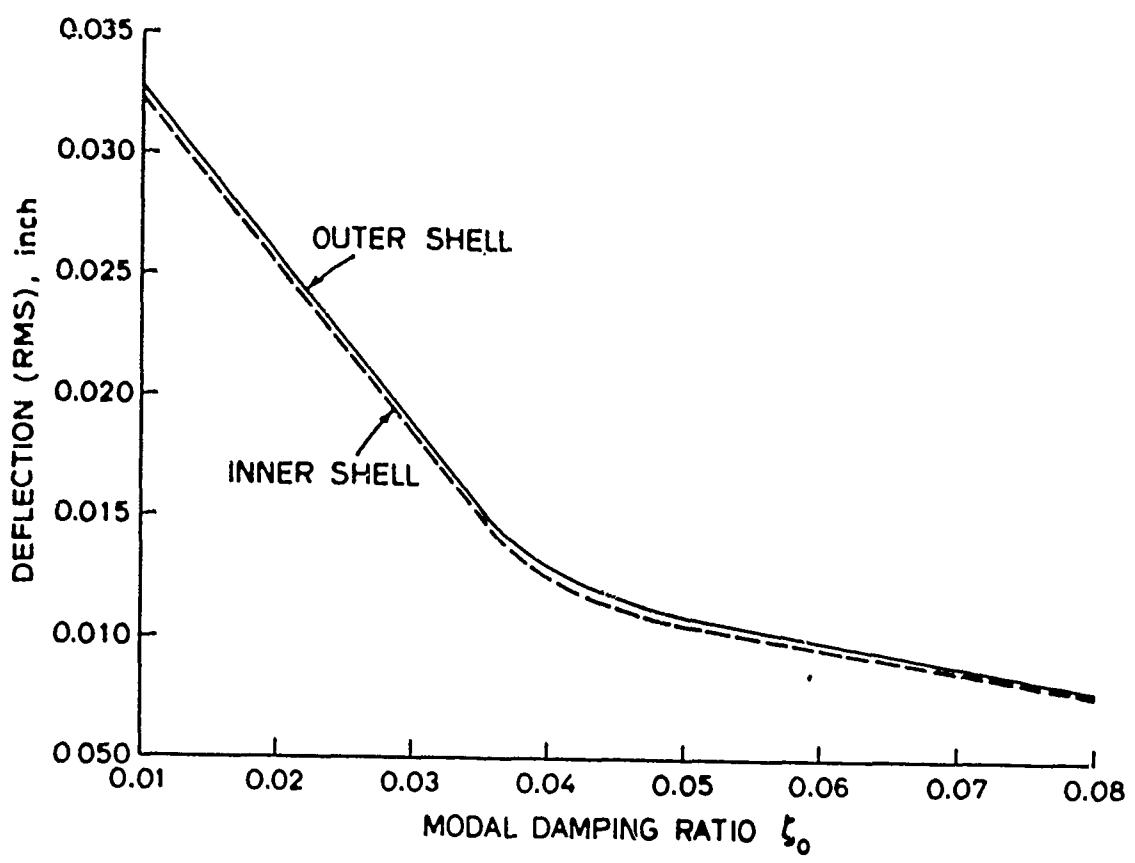
Fig. 6 Root mean square deflections of inner shell for different values of modal damping

FD-11
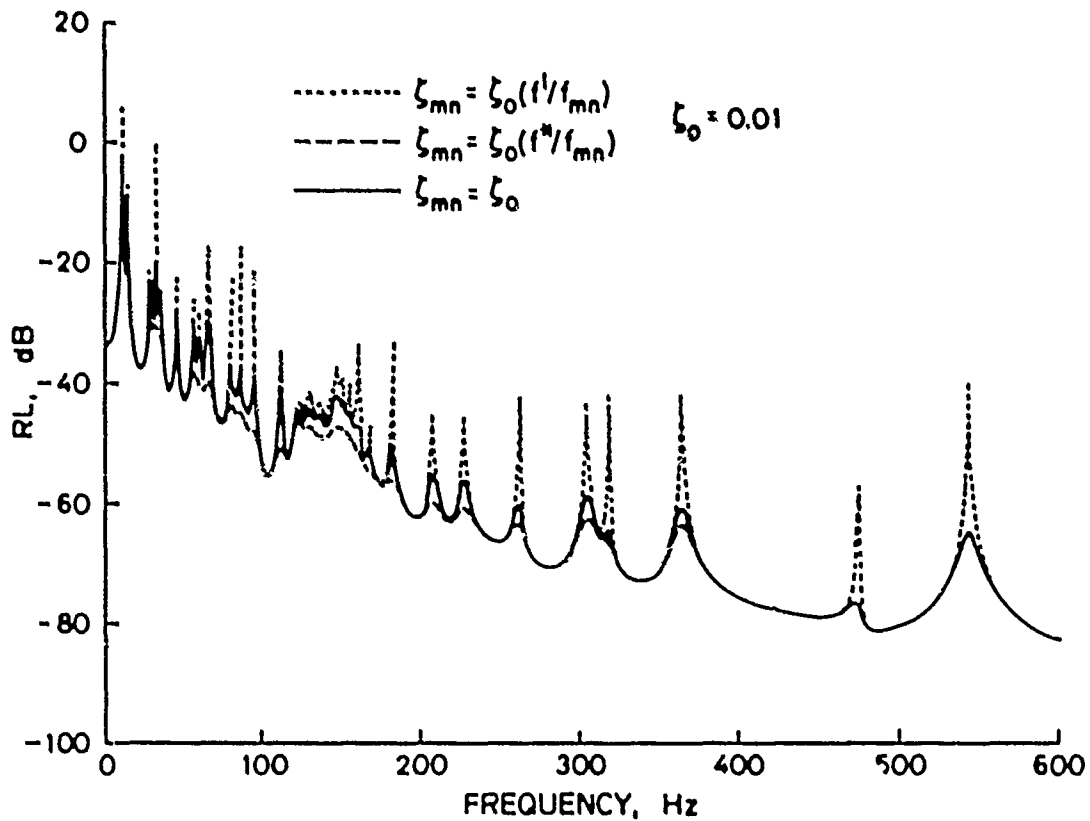
Fig. 7 Response levels of inner shell for different damping models
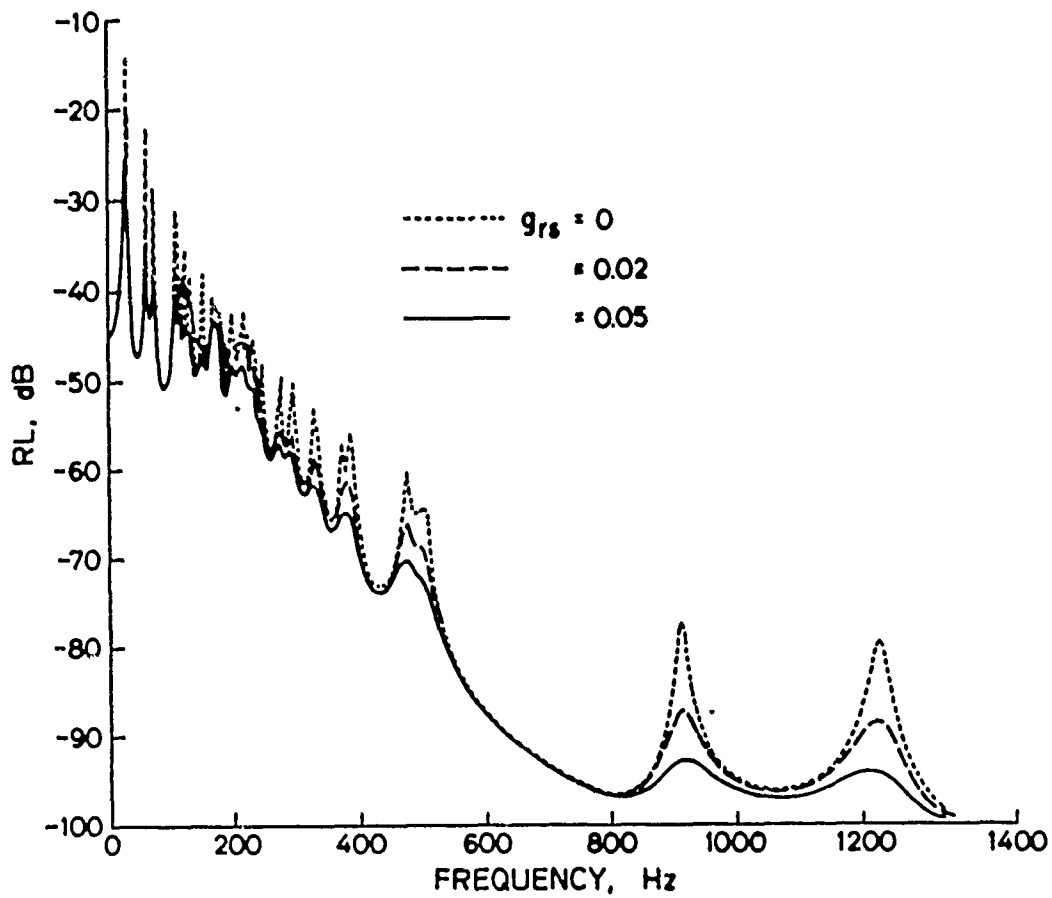
Fig. 8. Response levels for different material
damping models

FD-12

Prediction of Material Damping of

Laminated Polymer Matrix Composites

by

C. T. Sun and J. K. Wu

Department of Engineering Sciences

University of Florida

Gainesville, Florida 32611

and

R. F. Gibson

Department of Mechanical Engineering

University of Idaho

Moscow, Idaho 83843

Abstract

In this study the material damping of laminated composites is derived analytically. The derivation is based on the classical lamination theory in which there are eighteen material constants in the constitutive equations of laminated composites. Six of them are the extensional stiffnesses designated by [A], six of them are the coupling stiffnesses designated by [B], and the remaining six are the flexural stiffnesses designated by [D]. The derivation of damping of [A], [B], and [D] is achieved by first expressing [A], [B] and [D] in terms of the stiffness matrix $[Q]^{(k)}$ and h_k of each lamina and then using the relations of $Q_{ij}^{(k)}$ in terms of the four basic engineering constants E_L, E_T, G_{LT} and ν_{LT}.

Next, we apply elastic and viscoelastic correspondence principle by replacing E_L, E_T ... by the corresponding complex modulus E_L^{*}, E_T^{*}, ..., and [A] by $[A]^{*}$, [B] by $[B]^{*}$ and [D] by $[D]^{*}$ and then equate the real parts and the imaginary parts respectively. Thus, we have expressed A_{ij}', A_{ij}'', B_{ij}', B_{ij}'' and D_{ij}', D_{ij}'' in terms of the material damping $\eta_L^{(k)}$ and $\eta_T^{(k)}$ ... of each lamina. The damping $\eta_L^{(k)}$, $\eta_T^{(k)}$ ... have been derived analytically by the authors in their earlier publications. Numerical results of extensional damping $_I\eta_{ij} = A_{ij}''/A_{ij}'$ coupling damping $_C\eta_{ij} = B_{ij}''/B_{ij}'$ and flexural damping $_F\eta_{ij} = D_{ij}''/D_{ij}'$ are presented as functions of a number of parameters such as fiber aspect ratio ℓ/d, fiber orientation θ, and stacking sequence of the laminate.

1. Introduction

Damping is a kind of energy dissipation. For fiber reinforced composites, damping may be primarily due to one or a combination of the following mechanisms

(a) Viscoelastic behavior of matrix and/or fibers
(b) Thermoelastic damping due to cyclic heat flow
(c) Coulomb fricition due to slip in unbonded regions of the fiber/matrix interface
(d) Dissipation caused by microscopic or macroscopic damage in the composite.

The first two mechanisms are the basic causes of damping for undamaged composites. The objective of this research is to determine analytically the damping of laminated polymer matrix composites.

During the past two years, the authors have engaged in research in damping for composite materials both analytically and experimentally. During the course of research we have successfully developed analytical methods to predict internal material damping for unidirectional composites [1], unidirectional off-axis composites [2,3] and randomly oriented short-fiber composites [4,5].

There are two analytical methods which have been employed by the authors. The first method is to use the force-balance approach in conjunction with Cox's shear-lag analysis [6] to derive the expression for the elastic modulus E_L along the fiber direction of unidirectional aligned short-fiber composites. Then the elastic-viscoelastic correspondence principle is used to obtain the expression for the complex modulus E_L^*. The complex equation for E_L^* then becomes two real equations for storage and loss moduli. The material damping is obtained as the ratio of the loss modulus to the storage modulus.

The second method is the energy approach. In this approach the energy stored in the fiber and matrix, and energy dissipated due to interfacial shear stresses, are used to find the values of storage as well as loss moduli.

By using these approaches, we have obtained numerical results of damping of unidirectional aligned short-fiber composites, unidirectional off-axis short-fiber composites and also randomly oriented short fiber composites. Important parameters which will affect damping are also identified as stiffness ratio E_f/E_m, fiber volume fraction V_f loading angle θ, fiber aspect ratio ℓ/d and damping of the fiber and matrix materials η_f and η_m.

In this paper the internal material damping of laminated composites is studied analytically. In this study, the force-balance approach is used. In the force-balance approach we apply the classical lamination theory to obtain the [A], [B] and [D] stiffness matrices [7]. Damping in laminated composites can therefore be classified as in-plane damping which is defined as the ratio of A_{ij} loss to A_{ij} storage, i.e. A_{ij}''/A_{ij}' coupled damping defined as B_{ij} loss to B_{ij} storage, i.e. B_{ij}''/B_{ij}' and flexural damping defined as the ratio of D_{ij} loss to D_{ij} storage, i.e. D_{ij}''/D_{ij}' (i,j = 1.2.6). A_{ij}, B_{ij}, and D_{ij} are functions of $\overline{Q}_{ij}^{(k)}$ of each lamina which are in turn functions of the four basic engineering material constants E_L, E_T, G_{LT} and ν_{LT} and the angle θ. Therefore, the material damping of laminated composites can be obtained from the definition of A_{ij}, B_{ij} and D_{ij} and the elastic-viscoelatic correspondence principle in the following form

$$A_{ij}^* = A_{ij}' + iA_{ij}'' = \sum_{k=1}^{N} (\overline{Q}_{ij}' + i\overline{Q}_{ij}'')^{(k)}(h_k - h_{k-1})$$

$$B_{ij}^* = B_{ij}' + iB_{ij}'' = \frac{1}{2} \sum_{k=1}^{N} (\overline{Q}_{ij}' + i\overline{Q}_{ij}'')^{(k)}(h_k^2 - h_{k-1}^2) \qquad (1)$$

$$D_{ij}^* = D_{ij}' + iD_{ij}'' = \frac{1}{3} \sum_{k=1}^{N} (\overline{Q}_{ij}' + i\overline{Q}_{ij}'')^{(k)}(h_k^3 - h_{k-1}^3)$$

where $i = \sqrt{-1}$ and both Q_{ij}' and Q_{ij}'', are functions of E_L', E_T', G_{LT}', E_L'', E_T'' and G_{LT}''. The expressions for E_L', E_L'', E_T', G_{LT}' and G_{LT}'' have been derived in [2,3] by the authors.

The material damping in laminated composites is therefore expressed as

$$_I\eta_{ij}(\text{in-plane}) = A_{ij}''/A_{ij}'$$
$$_c\eta_{ij} (\text{coupled}) = B_{ij}''/B_{ij}' \qquad (i,j = 1.2.6) \quad (2)$$
$$_F\eta_{ij}(\text{flexural}) = D_{ij}''/D_{ij}'$$

where A_{ij}'', A_{ij}', B_{ij}'', B_{ij}', D_{ij}'' and D_{ij}' are defined in Eq. (1) in terms of $Q_{ij}'^{(k)}$, $Q_{ij}''^{(k)}$ and the position h_k relative to the mid-surface. For symmetric laminates $B_{ij} = 0$ and $_c\eta_{ij}$ (coupled) also vanish.

2. Analysis

The relations between Q_{ij} ($i,j = 1,2,6$) and the four basic engineering constants are given by the well-known formulae

$$Q_{11} = \frac{E_L}{1 - (\nu_{LT})^2 E_T/E_L}$$

$$Q_{12} = \frac{\nu_{LT}E_T}{1 - (\nu_{LT})^2 E_T/E_L} \qquad (3)$$

$$Q_{22} = \frac{E_T}{1 - (\nu_{LT})^2 E_T/E_L}$$

$$Q_{66} = G_{LT}$$

where

$$E_L = E_f V_f (1 + R) \left[1 - \frac{\text{Tan h }(\beta L/2)}{\beta L/2}\right] + E_m (V_m - V_f R) \qquad (4)$$

R = fiber tip spacing/fiber length   (See Fig. 1)

$$\beta L = 4\; \ell/d\; \left(\frac{G_m}{E_f}\; \frac{1}{\ell n\; \pi/4V_f}\right) \tag{5}$$

$$E_T = E_m\; \frac{1 + 2\eta_1 V_f}{1 - \eta_1 V_f} \tag{6}$$

$$G_{LT} = G_m\; \frac{1 + \eta_2 V_f}{1 - \eta_2 V_f} \tag{7}$$

$$\nu_{LT} = \nu_f V_f + \nu_m V_m \tag{8}$$

$$\eta_1 = \frac{E_f/E_m - 1}{E_f/E_m + 2} \tag{9}$$

$$\eta_2 = \frac{G_f/G_m - 1}{G_f/G_m + 1} \tag{10}$$

Equations (4) and (5) are obtained from Cox's shear lag model [6] and Eqs. (6) and (7) are the well-known Halpin-Tsai equations. If we consider both fiber and matrix materials are viscoelastic materials, then in Eqs. (4) through (8) we have to replace E_L by E_L^*, E_f by E_f^*, i.e.

$$E_L^* = E_L\; (1 + \eta_L) = E_f\; (1 + i\eta_f) V_f R\; \left[1 - \frac{\tan h\; \beta^* L/2}{\beta^* L/2}\right]$$

$$+ E_m\; (1 + i\eta_m)(V_m - V_f R) \tag{11}$$

$$\beta^* L = \beta' L + i\beta_L^{\prime\prime} = 4L/d\; \frac{G_m(1 + i\eta_{mG})}{E_f(1 + i\eta_f)}\; \frac{1}{\ell n\; \pi/4V_f} \tag{12}$$

$$E_T(1 + i\eta_T) = E_m\; (1 + i\eta_m)\; \frac{1 + 2\eta_1^* V_f}{1 - \eta_1^* V_f} \tag{13}$$

$$G_{LT}(1 + i\eta_{LT}) = G_m(1 + i\eta_{mG})\; \frac{1 + \eta_2^* V_f}{1 - \eta_2^* V_f} \tag{14}$$

$$\nu_{LT}(1 + i\eta_{\nu_{LT}}) = \nu_f(1 + i\eta_{\nu_f}) V_f + \nu_m(1 + i\eta_{\nu_m})V_m \tag{15}$$

Upon separation of real and imaginary parts in Eqs. (11) through (15) and

equating the real parts and the imaginary parts respectively we can derive the damping coefficients η_L, η_T, η_{GLT}, and $\eta_{\nu_{LT}}$, i.e. damping along the longitudinal direction, damping along the transverse direction, shear damping and damping of Poisson's ratio for the unidirectional composites in terms of E_f/E_m, G_f/G_m, η_f, η_m, fiber aspect ratio ℓ/d, fiber tip spacing R, fiber volume fraction V_f and fiber orieintation angle θ. The expressions of η_L, η_T, η_{GLT} can be found in the authors earlier publications [1-3]. The derivation of the real and imaginary parts of the Poisson's ratio was based on observation by Gibson and Plunkett [8] that the bulk modulus K is independent of frequency. With this observaiton, for isotropic fiber and matrix materials we can easily derive the real part and the imaginary part of the Poisson's ratio respectively with the result

$$\nu' = 1/2(1 - \frac{E'}{3K})$$

$$\nu'' = -1/2 \frac{E''}{3K}$$

(16)

Substitution of Eqs. (12) through (15) yields the expressions of

$$Q^\star_{11} = Q'_{11} + iQ''_{11} \qquad\qquad Q^\star_{22} = Q'_{22} + iQ''_{22}$$

$$Q^\star_{12} = Q'_{12} + iQ''_{12}$$

$$Q^\star_{66} = G^\star_{LT} = G_{LT} (1 + i\eta_{GLT})$$

(17)

in terms of E_f/E_m, η_f, η_m, V_f, ℓ/d and R. The detail expressions $Q'_{11},...Q''_{66}$ are too lengthy to be presented in this paper, but the derivation is straight forward.

Since [A], [B] and [D] are functions of $\overline{Q}'_{ij}$ and $\overline{Q}''_{ij}$ (i,j = 1.2.6) which are related to Q_{ij} by the following relations [7]

$$\overline{Q}_{11} = Q_{11} \cos^4\theta + Q_{22}\sin^4\theta + 2(Q_{12} + 2Q_{66}) \sin^2\theta\cos^2\theta$$
$$\vdots$$
$$\overline{Q}_{26} = (Q_{11} - Q_{12} - 2Q_{66}) \cos\theta\sin^3\theta - (Q_{22} - Q_{12} - 2Q_{66}) \cos^3\theta\sin\theta$$

(18)

the expressions of

$$A^\star_{ij} = A_{ij}(1 + i_I\eta_{ij})$$

$$\beta^\star_{ij} = \beta_{ij}(1 + i_c\eta_{ij}) \qquad\qquad (i,j = 1.2.6)$$

(19)

$$D_{ij}^\star = D_{ij}(1 + {}_iF\eta_{ij})$$

can be derived from Eqs. (1), (3) and (4) through (16). Again the expressions are too lengthy to be given here. Numerical results of $A_{11}^\star$, $A_{66}^\star$, $D_{11}^\star$ and $D_{66}^\star$ are presented in the next section as functions of the stacking sequence, fiber aspect ratio ℓ/d fiber tip spacing R and fiber volume fraction V_f.

3. Numerical Results and Discussion

The important quantities to be presented are:

$_I\eta_{11}$ = extensional damping along the direction 1

E_{11}^1 = extensional storage modulus along direction 1

$_I\eta_{66}$ = in plane shear damping

E_{66}^1 = in plane shear storage modulus

$_F\eta_{11}$ = flexural damping about the axis 1

D_{11}^1 = flexural storage modulus along direction 1

$_F\eta_{66}$ = flexural shear damping

D_{66}^1 = flexural shear storage modulus

Numerical results of the above quantities are presented in Figs. 2 - 11 in normalized nondimensional form.

In Figs. 2 and 3 $_F\eta_{11}$, D_{11}^1, $_F\eta_{66}$ and D_{66}^1 of quasi-isotropic graphite-epoxy composites are plotted as a function of the fiber aspect ratio L/d. Four different stacking sequences are included. The results are not surprising. Under flexural loading, the bending stiffness D_{11}^1 is the highest when 0° ply is placed on the top and bottom surfaces of the laminate and becomes the lowest when 0° ply is located in the mid-surface of the laminate. For D_{66}^1 the situation is just the opposite. It is maximum for a given ℓ/d for the laminate with ± 45° plies on the top and bottom and is minimum with ± 45° plies on the midsurface. The behavior of damping is just opposite to the corresponding stiffness. This observation is clearly indicated in Figs. 1 and 2, i.e. D_{11}^1 and D_{66}^1 increase as ℓ/d increases and $_F\eta_{11}$ and $_F\eta_{66}$ decrease as ℓ/d increases.

Figures 4 - 7, show the four in-plane extensional properties, i.e. E_{11}^1, $_I\eta_{11}$, E_{66}^1 and $_I\eta_{66}$ of angle-ply graphite-epoxy as a function of the ply angle θ. Maximum E_{11}^1 occurs at 0° and drops sharply as θ increases and

reaches to the same value as $\theta = 90°$ for all value of ℓ/d. This is true since when $\theta = 90°$, E_{11}' appraoches to E_T' which is assumed to be independent of the fiber aspect ratio ℓ/d. The maximum value of $_I\eta_{11}$ depends on the stacking sequence. This observation was also noticed in the authors previous publications [2,3] for unidirectional composites. Again at $\theta = 90°$, $_I\eta_{11}$ reaches the same value regardless of the value of ℓ/d.

E_{66}' and $_I\eta_{66}$ behave just the opposite with the exception that both plots are symmetric with respect to the vertical line of $\theta = 45°$. Maximum E_{66}' occurs at $\theta = 45°$ and larger fiber aspect ratio and maximum $_I\eta_{66}$ also occurs at $\theta = 45°$ but smaller fiber aspect ratio.

Figures 3 - 11, show plot of D_{11}', $_F\eta_{11}$, D_{66}' and $_F\eta_{66}$ of laminated graphite-spoxy composites with four different stacking sequences as a function of ℓ/d. No surprising results were observed. The trend is always the same, i.e. materials with higher damping will have lower stiffness and vice versa. For instance $0_8/s$ laminate has maximum D_{11}' and minimum D_{66}' and $[45/-45/45/-45]_{2S}$ laminate has maximum D_{66}' and minimum D_{11}'. But for dampings, i.e. for $_F\eta_{11}$ and $_F\eta_{66}$ these trends are just reversed.

4. Concluding Remarks

Analytical prediction of extensional stiffness and damping in-plane shear stiffness and damping, flexural stiffness and damping and flexural shear stiffness and damping of laminated composites were obtained from the classical theory of lamination along with the elastic-viscoelastic correspondence principle and separation of the real and imaginary parts. Numerical results for laminated composites indicate similar trends as observed in the unidirectional composites, i.e. damping and stiffness always behave in opposite manners. Designers, thus, should make some compromise in order to achieve optimum performance of composite structures.

Finally the above analysis does not take into account the contribution of the interlaminar stresses. A three dimensional model by using the finite-element approach include the influences of interlaminar stresses has been developed and the results will be published in the near future.

References

[1] R. F. Gibson, S. K. Chaturvedi and C. T. Sun, "Complex Moduli of Aligned Discontinuous Fiber Reinforced Polymer Composites", Journal of Material Sciences, Vol. 17, 1982, p. 3499.

[2] C. T. Sun, S. K. Chaturvedi and R. F. Gibson, "Internal Damping of Short-Fiber Reinforced Polymer Matrix Composites", Computers and Structures, 1985, p. 285.

[3] C. T. Sun, R. F. Gibson and S. K. Chaturvedi, "Internal Material Damping of Polymer Matrix Composites Under Off-Axis Loading", Journal of Material Sciences, Vol. 20, 1985, pp. 2575-2585.

[4] C. T. Sun, J. K. Wu and R. F. Gibson, Prediction of Material Damping in Randomly Oriented Short Fiber Polymer Matrix Composites", Journal of Reinforced Plastics and Composites, Vol. 4, 1985, pp. 262-272.

[5] S. A. Suavez, R. F. Gibson, C. T. Sun and S. K. Chaturvedi, "The Influence of Fiber Length and Fiber Orientation of Damping adn Stiffness of Polymer Composite Materials", presented at the SESA Spring 1985 Conference, June 2-13, 1985, Las Vegas, Nevada and published in the Conference Proceedings.

[6] H. L. Cox, "The Elasticity and Strength of Paper and Other Fibrous Materials", British Journal of Applied Physics, Vol. 3, 1953, p. 72.

[7] B. D. Agarwal and L. J. Broutman, Analysis and Performance of Fiber Composites, John-Wiley Interscience, 1979.

[8] R. F. Gibson and R. Plunkett, "Dynamic Mechanical Behavior of Fiber-Reinforced Composites; Measurement and Analysis", Journal of Composite Materials, Vol. 10, 1976, pp. 325-341.

Acknowledgement
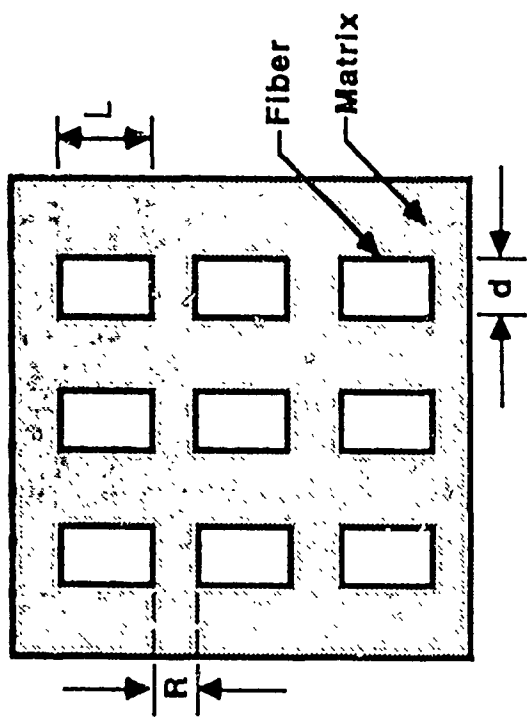
Figure 1. Aligned short fiber composites
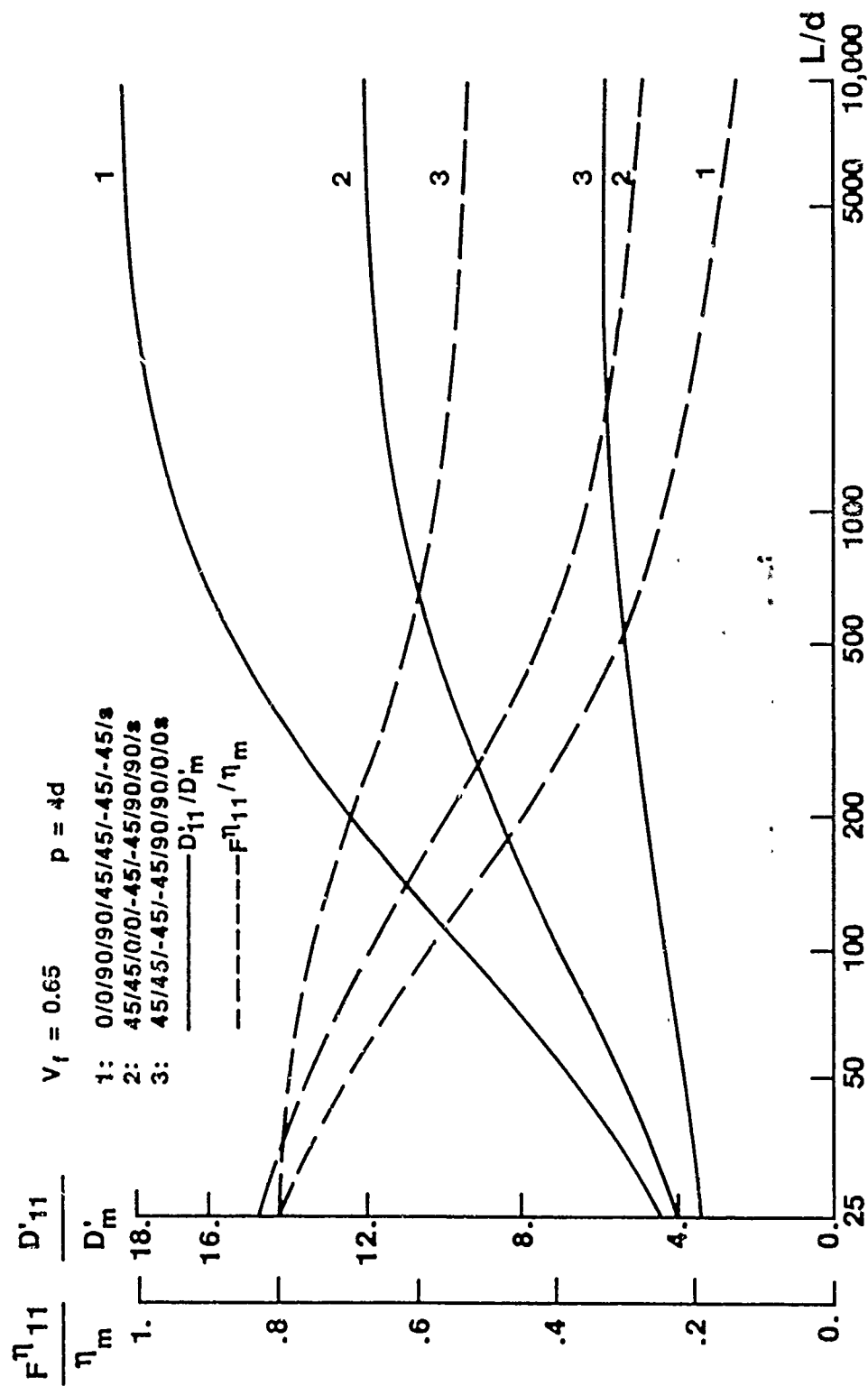
Figure 2. Plots of D'_{11}/D'_m and F^{η}_{11}/η_m vs L/d for Quasi-Isotropic Graphite Epoxy Composites
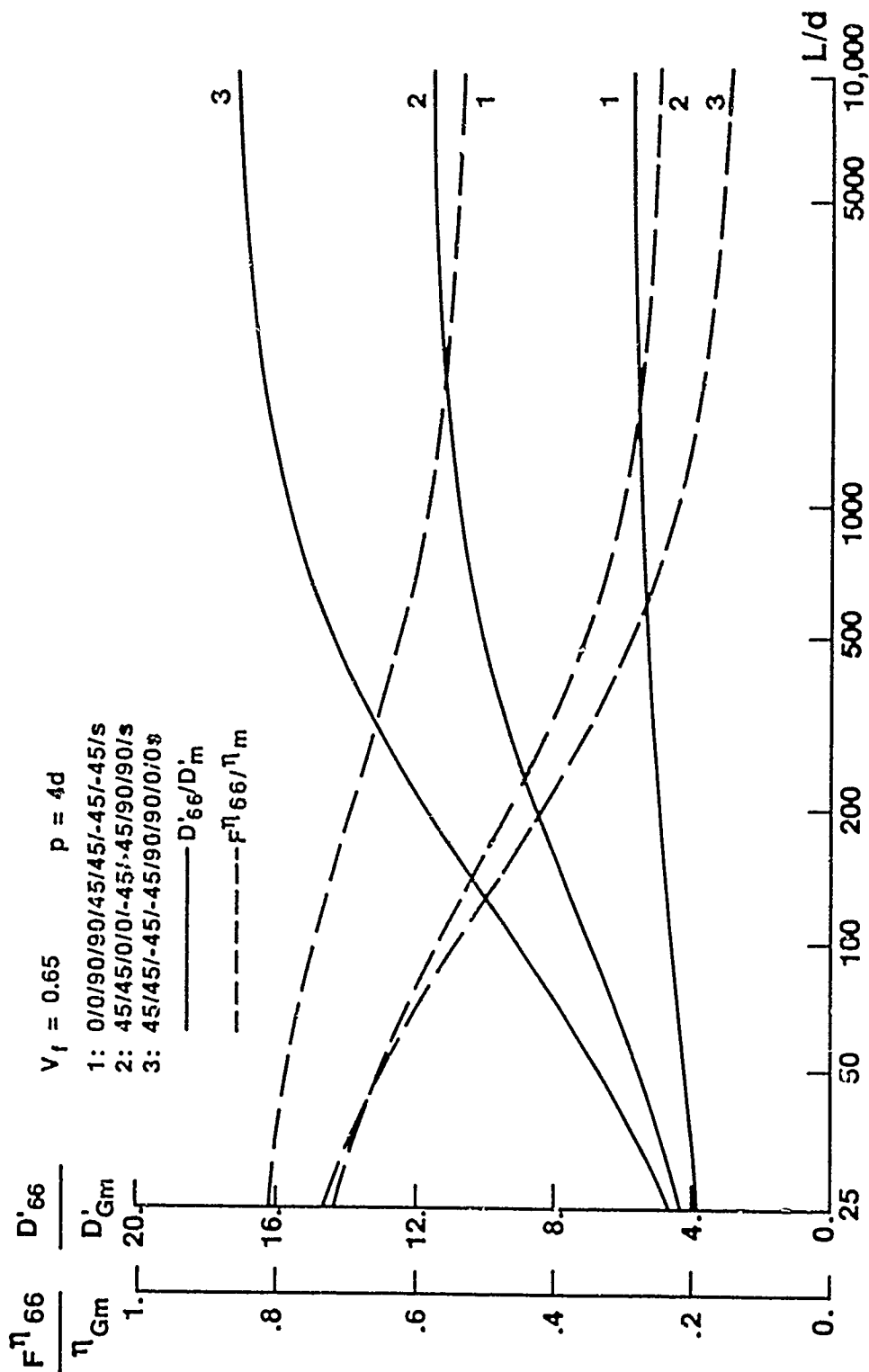
$V_f = 0.65$ $p = 4d$

1: 0/0/90/90/45/45/-45/-45/s
2: 45/45/0/0/-45/-45/90/90/s
3: 45/45/-45/-45/90/90/0/0s

——— D'_{11}/D'_m
- - - F^{η}_{11}/η_m

FE-11

Figure 3. Plots of D'_{66}/D_{Gm} and F^η_{66}/η_{Gm} vs L/d for Quasi-Isotropic Graphite Epoxy Composites

$V_f = 0.65$ $p = 4d$

1: 0/0/90/90/45/45/-45/-45/s
2: 45/45/0/0/-45/-45/90/90/s
3: 45/45/-45/-45/90/90/0/0/s

D'_{66}/D'_m ———

F^η_{66}/η_m ― ― ―

FE-12
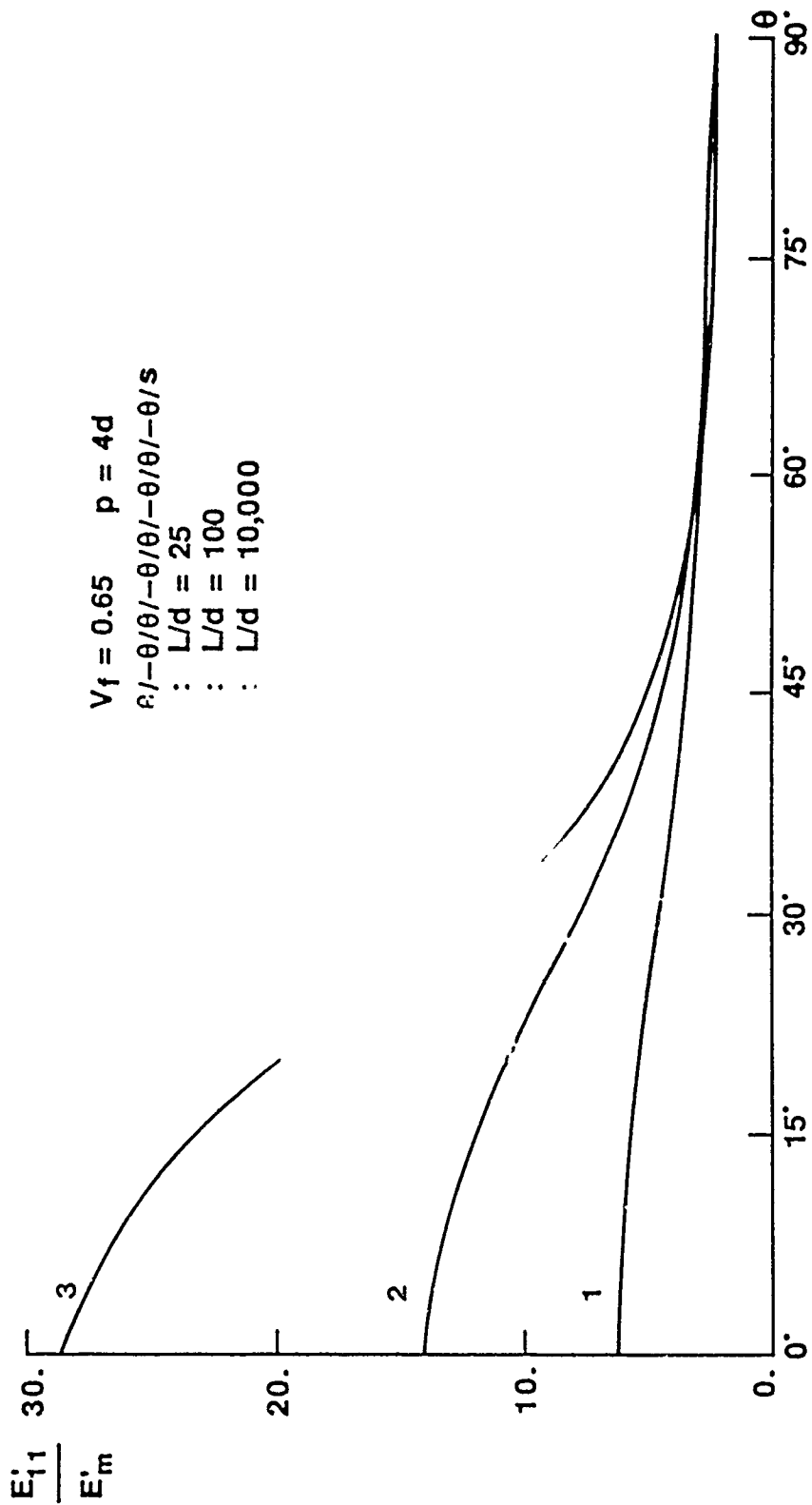
Figure 4. Plots of E'_{11}/E'_m vs θ using L/d as a Parameter for Angle Ply Graphite Epoxy Composites
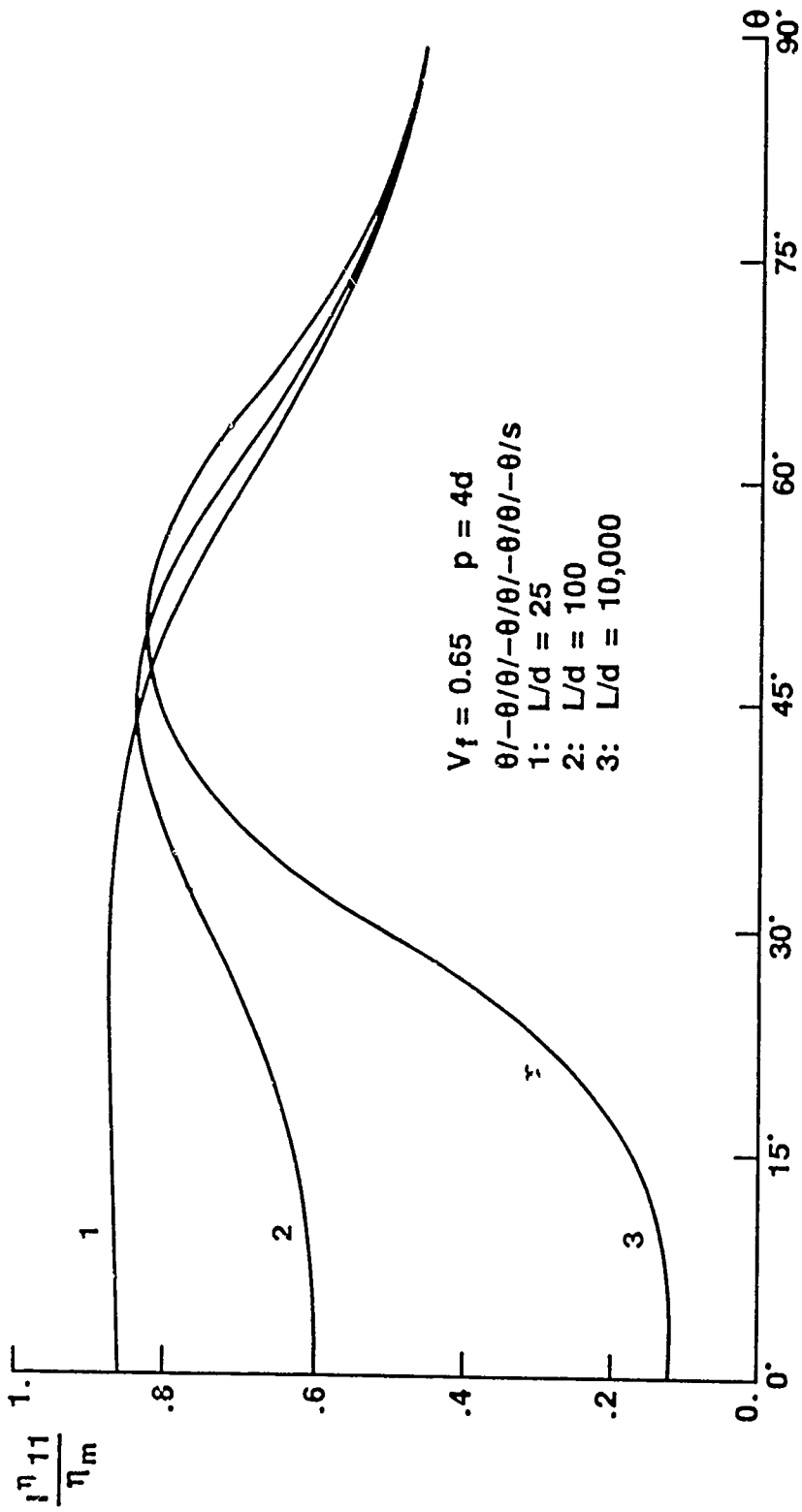
$V_f = 0.65 \qquad p = 4d$

$\theta/-\theta/\theta/-\theta/\theta/-\theta/\theta/-\theta/s$

: L/d = 25
: L/d = 100
: L/d = 10,000

FE-13

Figure 5. Plots of $|^{\eta}{}_{11}/\eta_m$ vs θ using L/d as a Parameter for Angle Ply Graphite Epoxy Composites

FE-14
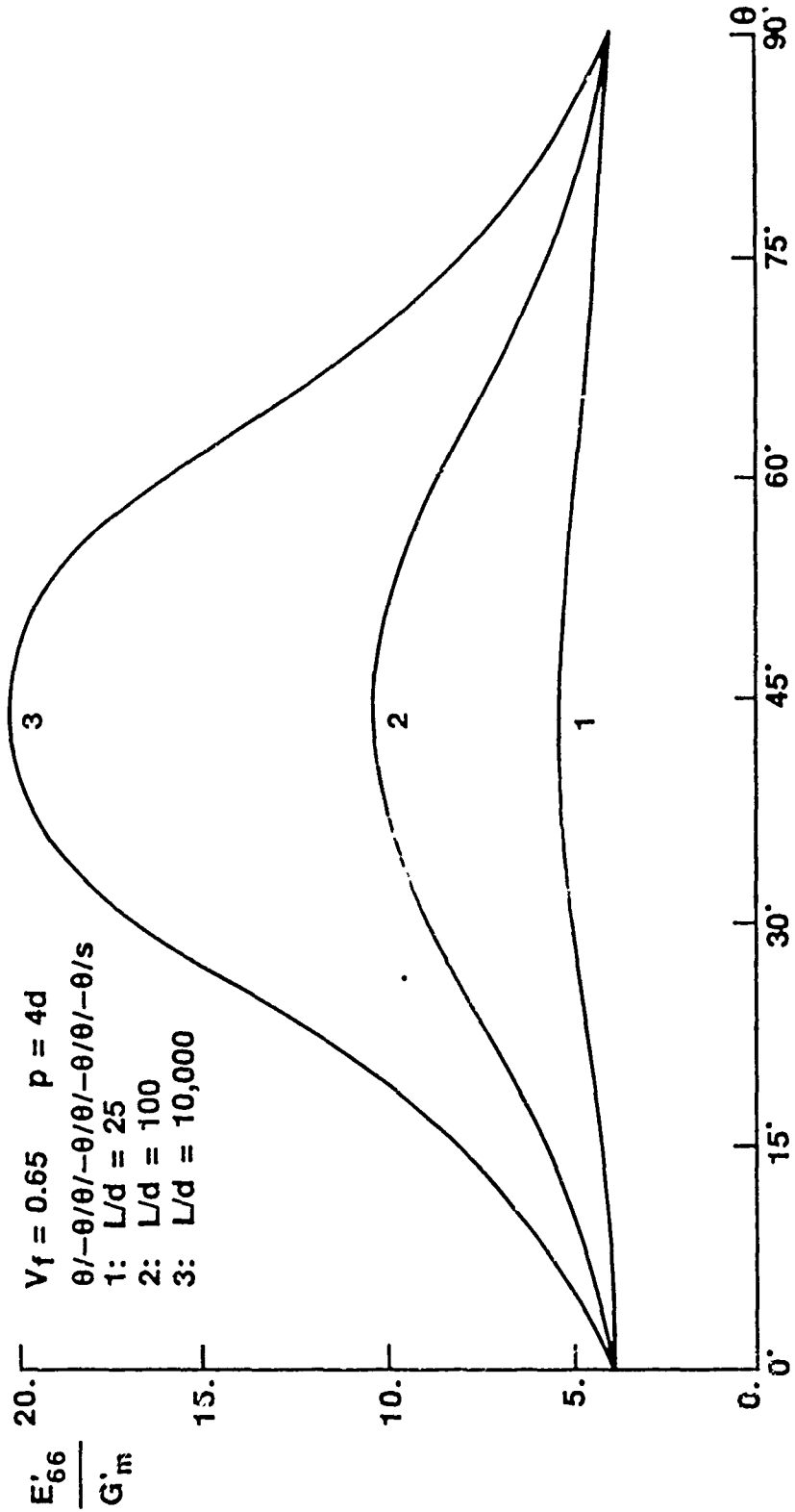
Figure 6. Plots of E'_{66}/G'_m vs θ using L/d as a Parameter for Angle Ply Graphite Epoxy Composites
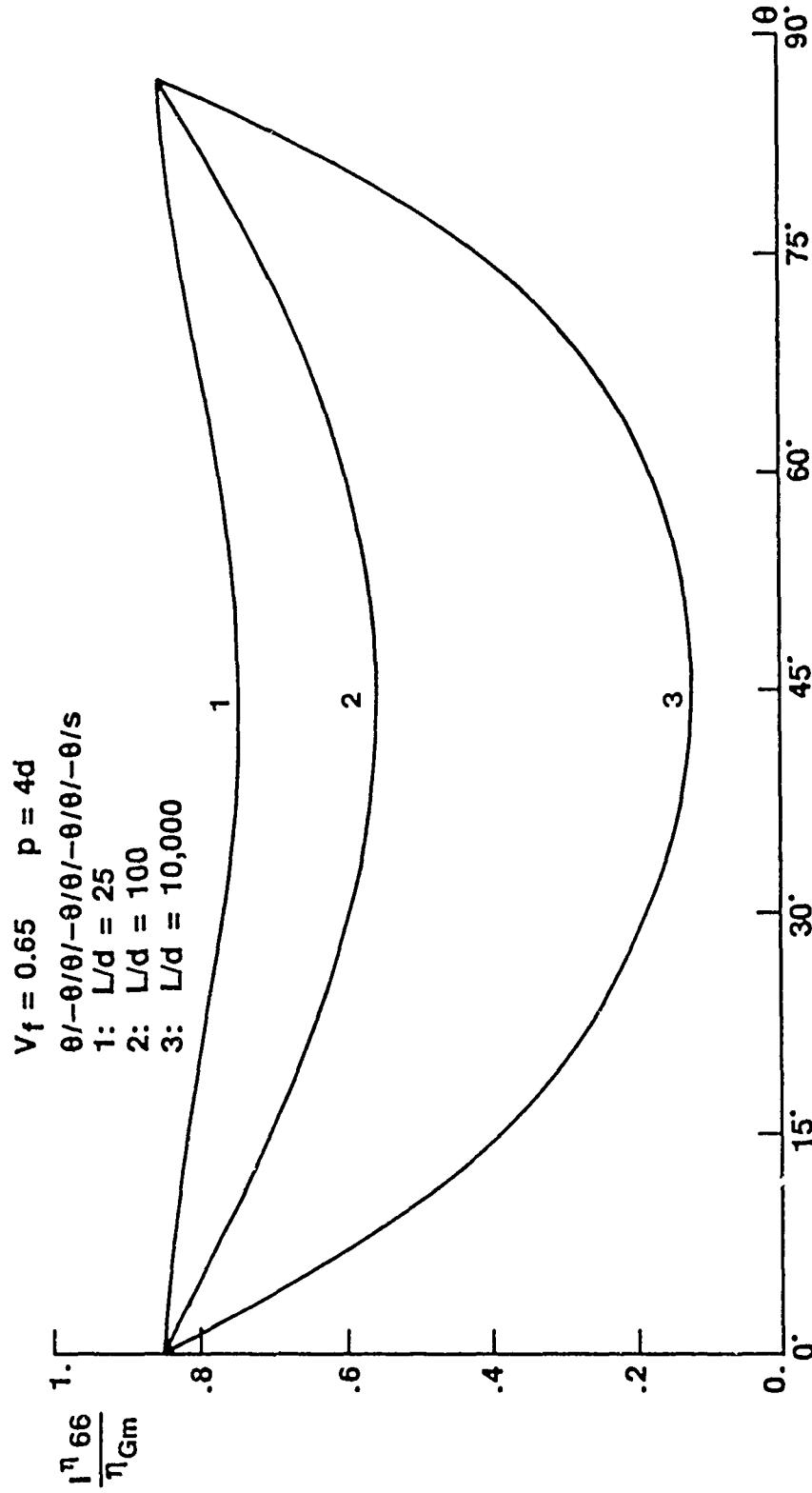
Figure 7. Plots of $I^{\eta}66/\eta_{Gm}$ vs θ using L/d as a Parameter for Angle Ply Graphite Epoxy Composites
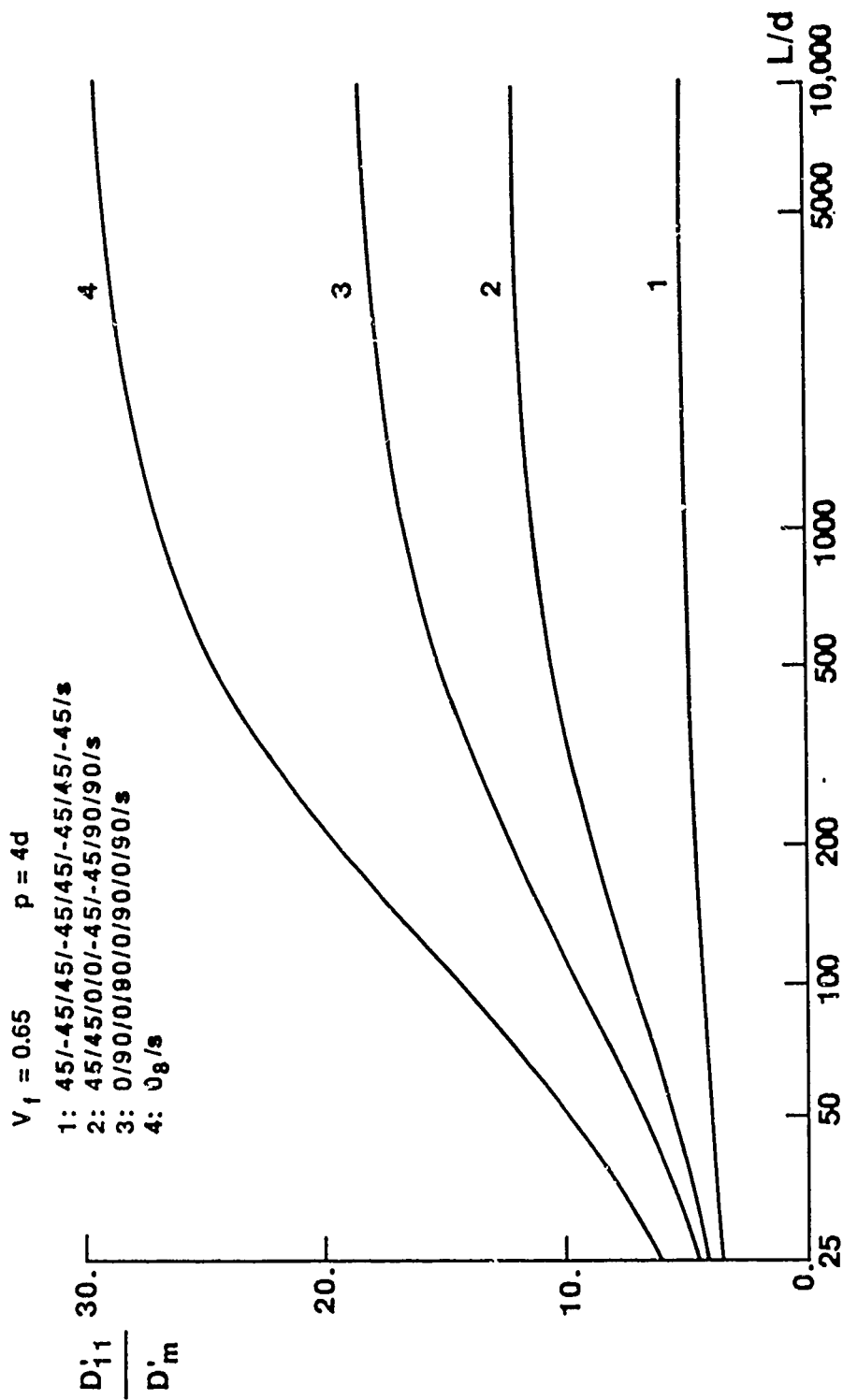
Figure 8. Comparisons of D'_{11}/D'_m vs L/d for Four Kinds of Laminated Graphite Epoxy Composites
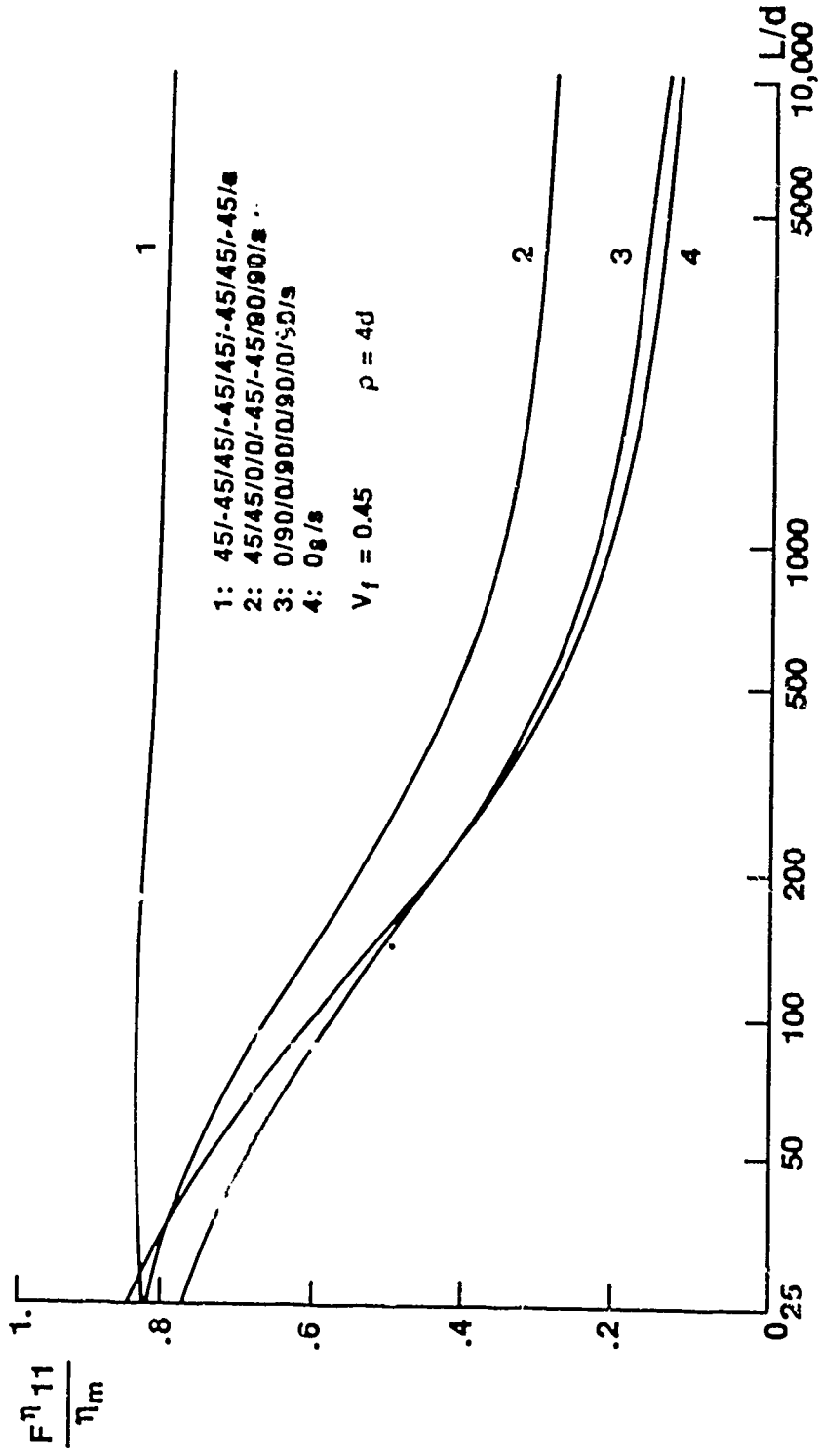
$V_f = 0.65$ p = 4d

1: 45/-45/45/45/-45/45/45/-45/s
2: 45/45/0/0/-45/-45/90/90/s
3: 0/90/0/90/0/90/0/90/s
4: 0_8/s

FE-17

Figure 9. Comparison of $\frac{F\eta_{11}}{\eta_m}$ vs L/d for Four Kinds of Laminated Graphite Epoxy Composites

1: 45/-45/45/45/-45/45/-45/s
2: 45/45/0/0/-45/-45/90/90/s
3: 0/90/0/90/0/90/0/90/s
4: 0₈/s

$V_f = 0.45$ $\rho = 4d$

FE-18
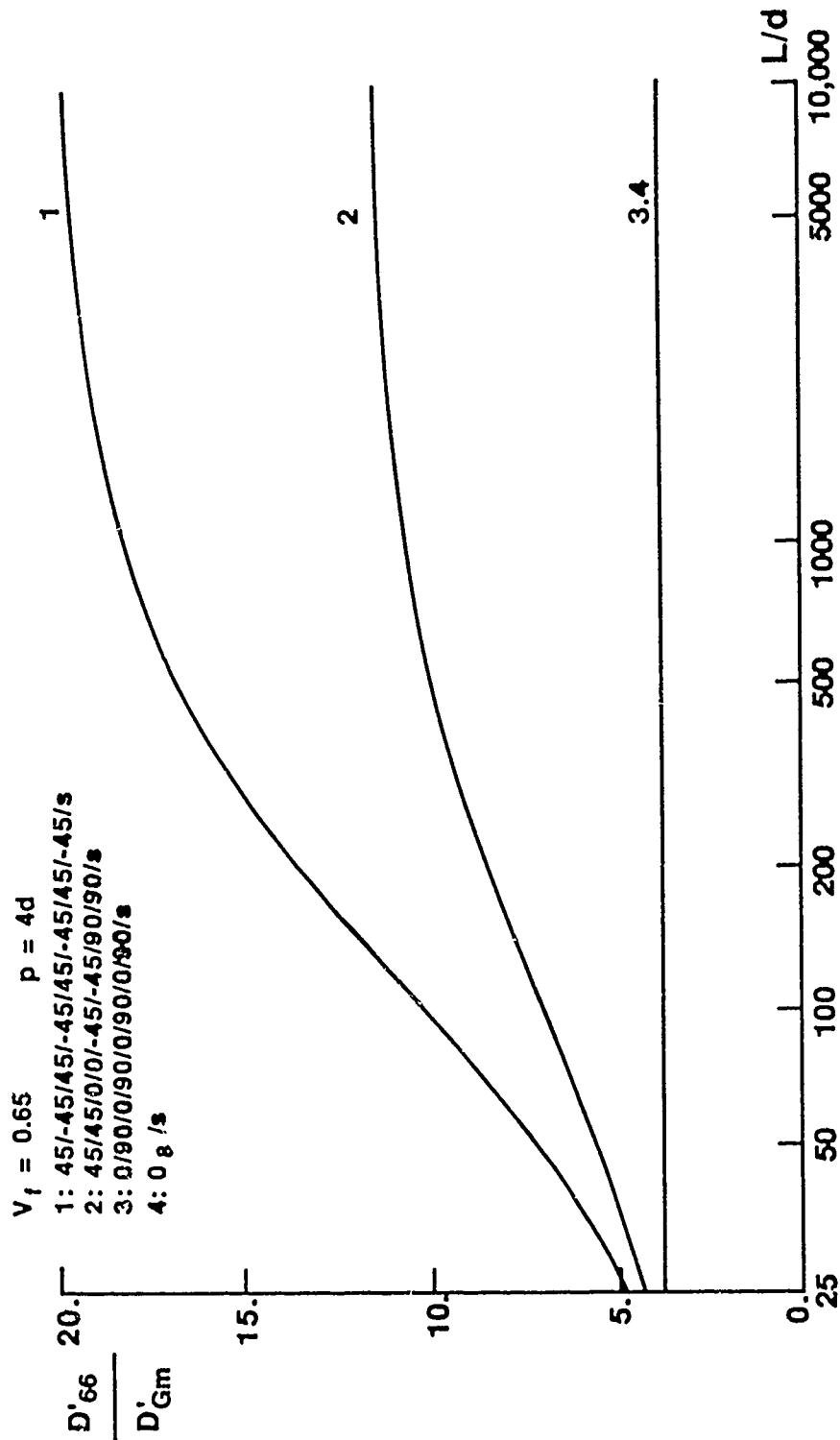
Figure 10. Comparisons of D'_{66}/D'_{Gm} vs. L/d for Four Kinds of Laminated Graphite Epoxy Composites
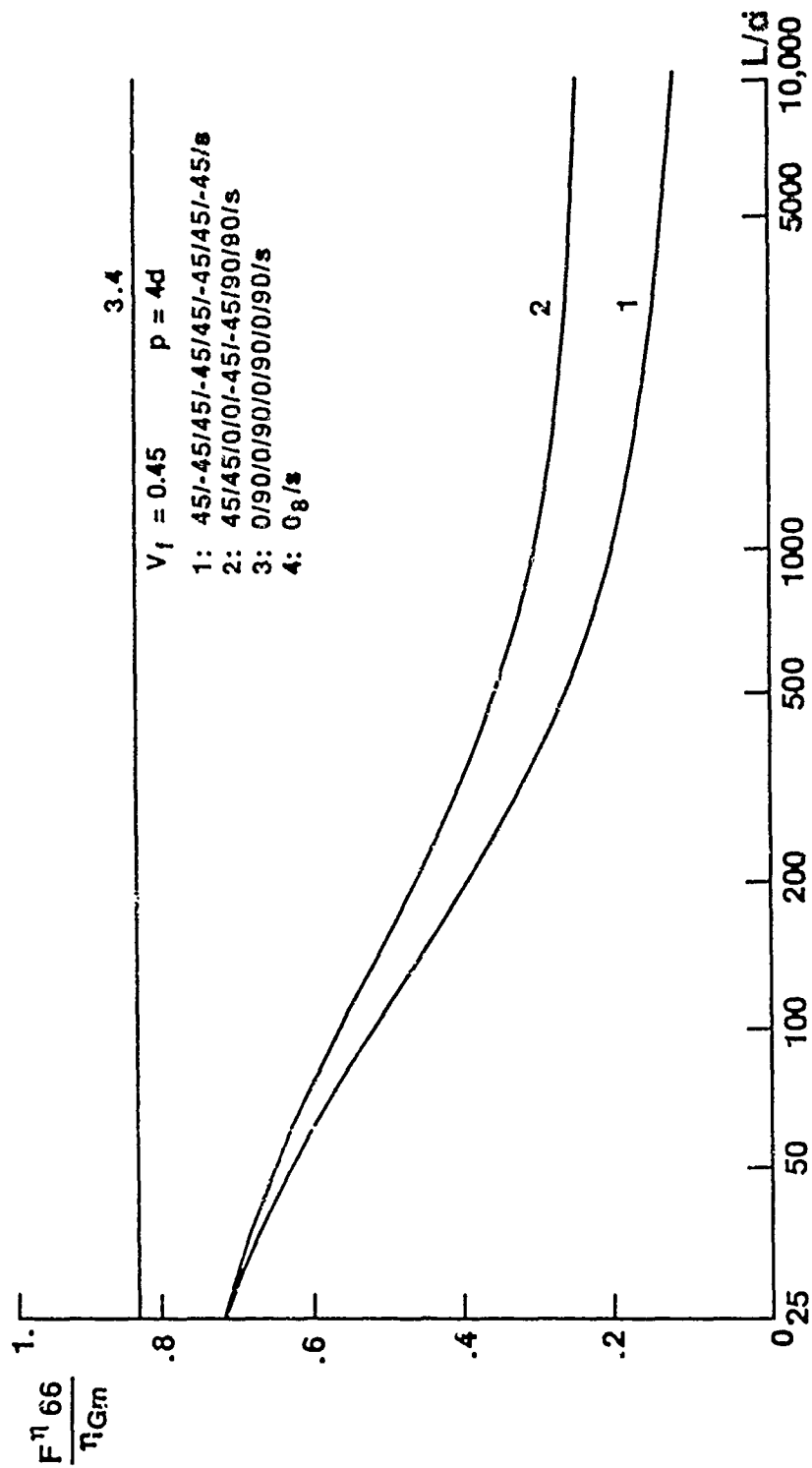
Figure 11. Comparison of $_F\eta_{66}/\eta_{Gm}$ vs L/d for Four Kinds of Laminated Graphite Epoxy Composites

FE-20

THE INFLUENCE OF FIBER LENGTH AND FIBER ORIENTATION ON DAMPING AND STIFFNESS OF POLYMER COMPOSITE MATERIALS

S.A. Suarez and R.F. Gibson
Mechanical Engineering Department
University of Idaho
Moscow, ID   83843

C.T. Sun
Department of Engineering Sciences
University of Florida
Gainesville, FL   32611

S.K. Chaturvedi
Civil Engineering Department
Ohio State University
Columbus, OH   43210

Abstract:

This paper describes the theoretical analysis, the experimental results and the curve-fitting of the analytical model to the experimental results on the influence of fiber length and fiber orientation on damping and stiffness of polymer composite materials. The experimental results show that, as predicted, very low fiber aspect ratios are required to produce significant improvements in damping. Measurements and predictions also indicate that the control of lamina orientation in a continuous fiber-reinforced laminate may be a better approach to the improvement of damping than the control of fiber aspect ratio.

List of Symbols:

E_f^*	Complex extensional modulus for the fiber
E_{fT}^*	Complex transverse modulus for the fiber
E_L^*	Composite extensional complex modulus
E_m^*	Complex modulus for the matrix
E_T^*	Composite transverse complex modulus
E_X^*	Composite complex modulus along the loading direction
E_f', E_f''	Extensional storage and loss moduli for the fiber
E_L', E_L''	Extensional storage and loss moduli for the composite
E_m', E_m''	Extensional storage and loss moduli for the matrix
G_{LT}	In-plane shear modulus for the composite
G_{fLT}^*	Complex in-plane shear modulus for the anistropic fiber
G_m^*	Complex shear modulus for the matrix
K^*	Generalized complex viscoelastic constant, or complex modulus
K'	Generalized storage modulus
K''	Generalized loss modulus
ℓ	Fiber length
(ℓ/d)	Fiber aspect ratio
$(\ell/d)_{eff}$	Effective fiber aspect ratio
M	Composite modulus E_T or G_{LT}
M_f	Fiber modulus E_f or G_f
M_m	Matrix modulus E_m or G_m
r_0	Fiber radius
v_f	Fiber volume fraction
v_m	Matrix volume fraction
Z	Curve fitting parameter for fiber aspect ratio
β	Parameter defined in Eq. 2
n_f	Fiber loss factor
$n_h, n_{h_1}^*, n_{h_2}^*$	Parameters defined in Eqs. 6, 11 and 13
n_m	Matrix loss factor
Θ	Angle of the fibers with respect to the direction of the applied load
ϕ_1, ϕ_2	Functions defined in Eq. 9
ν_f	Fiber Poisson's ratio
ν_m	Matrix Poisson's ratio
ν_{LT}	Composite major Poisson's ratio
ξ, ξ_1, ξ_2	Halpin-Tsai parameters

Introduction:

In a recent paper by one of the authors [1], it was concluded that the use of discontinuous fiber reinforcement appears to be a viable approach to the problem of improvement of internal damping in fiber reinforced polymer composite materials. This conclusion was based primarily on a study of the different damping mechanisms operating in these materials and on the results of an earlier theoretical analysis of damping in aligned discontinuous fiber reinforced composites [2]. The presence of shear stress concentrations at the fiber ends of the discontinuous fibers and the resulting shear stress transfer to the viscoelastic matrix were thought to be responsible for the increased damping. In Ref. [2], it was shown that when the fiber damping is small, there is a theoretically optimum fiber aspect ratio where the loss modulus in a discontinuous aligned fiber composite is maximized. Since the predicted optimum aspect ratios were very low ($\ell/d < 20$), it was expected that only greater-than-optimum values were practically attainable. One of the objectives of the present work was to obtain experimental damping data for composites having fiber aspect ratios that were low enough that significant increases in damping could be generated. Comparisons of these results with predictions would then be used to test the analytical model.

In Ref. [3], the case of off-axis fiber orientation was treated analytically. It was predicted that, since the maximum shear stress occurs at an off-axis angle, maximum damping characteristics could be obtained at off-axis angles. A second objective of the present work was to measure damping in composites under off-axis vibratory loading for comparison with predictions from Ref. [3].

Previous publications have reported on the development of macro-mechanical models for predicting damping in continuous fiber reinforced laminated beams from measured lamina properties, lamina orientation and stacking geometry [4,5,6]. Micromechanical models for prediction of continuous fiber reinforced lamina properties from constituent material properties and volume fractions have also been developed [7,8]. To the best of our knowledge, however, the work reported here is the first experimental and analytical study of the influence of fiber length and orientation on damping in discontinuous fiber reinforced laminates at both the micromechanical and macromechanical levels.

Two variations of a recently developed impulse-frequency response technique [9,10] were used to determine the complex moduli of small composite beam specimens. Graphite/epoxy, Kevlar/epoxy and boron/epoxy materials were tested in flexural vibration for the fiber length studies, while graphite/epoxy and Kevlar/epoxy materials were tested in extensional vibration for fiber orientation studies.

Analysis:

The theoretical analysis of internal damping and dynamic stiffness for aligned discontinuous fiber reinforced composite materials was based on the micromechanics models for the complex moduli, as established in [2]. These analytical models were based on the Cox stress distribution [11]. The basic assumptions were:

a. A round fiber surrounded by a cylindrical matrix under extensional load.
b. Fiber and matrix are isotropic.
c. A perfect bond exists between the fiber and the matrix.
d. There is no load transfer through the ends of the fiber.
e. The transfer of load from the matrix to the fiber depends upon the difference between the actual displacement at a point on the interface, and the displacement that would exist if the fiber were absent [12].

Using the interfacial shear stress and longitudinal fiber stress obtained by Cox as a starting point, Gibson, et al. [2] found the solution for the complex modulus by two methods: the energy method and the force-balance method. The force-balance approach is actually a combination of an elastic "mechanics of materials" analysis and the elastic-viscoelastic correspondence principle [13]. This method was used in the current research because of convenience and ease of use. From Ref. [2] the elastic longitudinal modulus of the aligned discontinuous fiber composite is

$$E_L' = E_f' \left(1 - \frac{\tanh \ell/2}{\beta\ell/2}\right)v_f + E_m' v_m \tag{1}$$

where

$$\beta^2 = \frac{G_m'}{E_f'} \frac{2}{r_o^2 \ln(R/r_o)} \tag{2}$$

The complex modulus, E_L^* was then found by applying the correspondence principle to Eq. (1).

$$E_L^* = E_f^* \left(1 - \frac{\tanh\beta^*\ell/2}{\beta^*\ell/2}\right)v_f + E_m^* v_m \tag{3}$$

By separating real and imaginary parts, two equations for the storage modulus and loss modulus were found. This method predicts an optimum fiber aspect ratio (ratio of fiber length to fiber diameter) for maximum damping [2]. Predictions were checked against experimental values using this model for the case of aligned discontinuous fiber composite materials. The results are shown in a later section of this paper.

For the case of off-axis analysis, again the force-balance approach [2] and the elastic-viscoelastic correspondence principle [13] were used to find the complex moduli of a composite material when the applied load is not parallel to the fiber direction [3]. The apparent elastic modulus, E_X, along the direction of the applied stress is given in Eq. (4) as a function of the longitudinal modulus, E_L, the transverse modulus, E_T, the in-plane shear modulus, G_{LT}, the major Poisson's ratio v_{LT}, and the direction of the applied load, θ [14].

$$\frac{1}{E_X} = \frac{1}{E_L} \cos^4\theta + \left(\frac{1}{G_{LT}} - \frac{2v_{LT}}{E_L}\right)\sin^2\theta \cos^2\theta + \frac{1}{E_T} \sin^4\theta \tag{4}$$

The longitudinal modulus E_L is given by Eq. (1), and the transverse modulus and the in-plane shear modulus can be obtained empirically by using the Halpin-Tsai equations [14].

$$\frac{M}{M_m} = \frac{1 + \xi \eta_h V_f}{1 - \eta_h V_f} \qquad (5)$$

where

$$\eta_h = \frac{(M_f/M_m) - 1}{(M_f/M_m) + \xi} \qquad (6)$$

ξ, which is a measure of fiber reinforcement, depends on the fiber geometry, packing array and loading conditions. For circular fibers in a square array, values for ξ equal to 2 and 1 for transverse modulus and for in-plane shear modulus, respectively, gave good results [14]. The major Poisson's ratio can be obtained by using the rule of mixtures [14]:

$$\nu_{LT} = \nu_f V_f + \nu_m V_m \qquad (7)$$

Using the elastic-viscoelastic correspondence principle, the elastic constants for the composite and for each constituent material can be transformed to complex viscoelastic constants as follows:

$$K^* = K' + iK'' = K'(1 + i\eta) \qquad (8a)$$

where the associated loss factor is

$$\eta = \frac{K''}{K'} \qquad (8b)$$

Introducing the complex elastic constants in Eq. (4), the off-axis composite storage modulus, E_X', and the loss modulus E_X'', can be obtained by separating the real and imaginary parts and neglecting higher order terms in the loss factor. These equations are very long, so only the general form is given here:

$$E_X' = \phi_1 [E_f', E_m', V_f, V_m, (\ell/d), \eta_f, \eta_m, \nu_f, \nu_m, \Theta, \text{packing array}]$$

$$E_X'' = \phi_2 [E_f', E_m', V_f, V_m, (\ell/d), \eta_f, \eta_m, \nu_f, \nu_m, \Theta, \text{packing array}] \qquad (9)$$

The complete equations are given in [15].

The analysis up to this point is based on the assumption that matrix and fibers are each isotropic. As shown later, however, in order to fit the analytical solution to the experimental data, the anisotropic nature of the graphite fibers must be taken into account [16]. Whitney [17] showed that by treating the fiber as an orthotropic, transversely isotropic material, the micromechanics equations can be adapted easily to take care of fiber anisotropy. Thus, the complex composite transverse modulus is given by:

$$E_T^* = E_m^* [\frac{1 + \xi_1 n_{h_1}^* V_f}{1 - n_{h_1}^* V_f}]$$ (10)

where
$$n_{h_1}^* = \frac{(E_{fT}^*/E_m^*) - 1}{(E_{fT}^*/E_m^*) + \xi_1}$$ (11)

and the complex in-plane shear modulus is given by:

$$G_{LT}^* = G_m^* [\frac{1 + \xi_2 n_{h_1}^* V_f}{1 - n_{h_2}^* V_f}]$$ (12)

where
$$n_{h_2}^* = \frac{(G_{fLT}^*/G_m^*) - 1}{(G_{fLT}^*/G_m^*) + \xi_2}$$ (13)

Experimental Results:

Small cantilever beam specimens of Fiberite Hy-E1034C graphite/epoxy, Fiberite Hy-E1734A2 Kevlar/epoxy and AVCO 5505 boron/epoxy (Table 1) were tested under flexural vibration for complex moduli determination of aligned-discontinuous fiber reinforced composites. Specimens were produced by cutting continuous fiber prepreg tapes and curing with an autoclave-style press cure as described in Ref. [18]. The computer-aided impulse-frequency response techniques are described in detail in Refs. [9], [10] and [15], and the apparatus for the flexural vibration technique is shown in Fig. 1. Impulsive excitation and frequency spectrum analysis are used to obtain the frequency response functions, and curve-fitting to these functions yields the desired complex modulus data.

Small free-free beam specimens of graphite/epoxy and Kevlar/epoxy with masses attached at each end (Table 2, Fig. 2) were tested under extensional vibration [10,15] for complex moduli determination of off-axis fiber reinforced composites. The extensional test was used for off-axis specimens in order to eliminate the bending-twisting coupling that would have been present in flexural tests.

The dynamic properties of the matrix were needed as input data for the micromechanics model used to predict the dynamic properties of composite materials. Thus, small specimens of neat resin were tested under flexural and extensional vibration in order to obtain the complex modulus of the matrix as a function of frequency [10,15].

Discontinuous Aligned Fiber Reinforced Composites:

Figs. 3 and 4 show the experimental data for storage modulus and loss factor, respectively, along with the original predicted curves generated from Eq. (3) for graphite/epoxy specimens. The theoretical analysis did not show good agreement with the experimental results, so the parameters which had the greatest uncertainties associated with them were then used as curve-fitting parameters. For example, the elastic modulus of the

fiber given by the manufacturers is based on bare fibers, and apparently there is a reduction in the fiber properties in the pre-preg material. This parameter was used as curve-fitting parameter to shift the curve in Fig. 3 downwards. The fibers contribute some damping [19], but since no information on fiber loss factors for our materials was available, this was used as another parameter for curve-fitting. A non-zero fiber loss factor shifts the curve in Fig. 4 upwards. Since the micromechanical model does not include the effects of the fiber/matrix interface, the "fiber loss factor" parameter probably includes some interface damping as well. The resulting vertical shifts of the theoretical curves in Figs. 3 and 4 were not sufficient to match the experimental data, however. Some horizontal shifting was also necessary in order to get good agreement, as shown in the following paragraph.

The force-balance model is based on a single fiber [2]. However, the influence of contiguous fibers in fiber bundles is not known, so an "effective fiber aspect ratio," $(\ell/d)_{eff}$ was introduced as given in Eq. 14:

$$(\ell/d)_{eff} = Z(\ell/d) \tag{14}$$

where Z is a curve-fitting parameter that shifts the curves of Figs. 3 and 4 to the left or to the right.

By varying these parameters one at a time, a good fit was obtained with the following values. For graphite/epoxy composite (see Figs. 5 and 6):

$E_f' = 25.51 \times 10^6$ psi (175.76 GPa)

Manufacturer's value: 33×10^6 psi (227.36 GPa)

$n_f = 0.0015$

$Z = 0.03$

For Kevlar/epoxy composite (see Ref. [15]):

$E_f' = 14.28 \times 10^6$ psi (99.767 GPa)

Manufacturer's value: 18×10^6 psi (124.026 GPa)

$n_f = 0.011$

$Z = 0.03$

For boron/epoxy composite (see Ref. [15]):

$E_f' = 55.43 \times 10^6$ psi (381.913 GPa)

Manufacturer's value: 58×10^6 psi (399.62 GPa)

$n_f = 0.019$

$Z = 0.4$

No claim is made here regarding the uniqueness of these sets of curve-fitting parameters. There may be other combinations of values that would work equally well. These results should be taken only as a first attempt at explaining the observed discrepancies. We are continuing to work on improved analytical models. For example, the model used here does not consider fiber interaction, since it is based on a single fiber.

In addition, it does not consider interface effects that can have substantial influence on the damping. Research now going on at the University of Idaho involves the use of a finite element model with spacing between the
ends of the fibers as another parameter [20,21]. This parameter has the same effect as the "effective fiber aspect ratio" in the force-balance approach.

Figure 7 shows a tridimensional plot from the "corrected" analytical model. The measured frequency dependence of the matrix loss factor is shown to affect the corresponding composite property, and the best damping characteristics are apparently obtained in low fiber aspect ratio composites which are subjected to high frequency vibrations.

Off-Axis Fiber Reinforced Composites:

Off-axis tests were done on graphite/epoxy continuous and discontinuous fibers and Kevlar/epoxy continuous fiber specimens. These results showed that fiber length only has a significant effect for fiber angles near zero [15]. Thus, the fiber length effect was discussed in the previous section and only the results for off-axis continuous fibers are discussed here. For comparison with the predicted curves from Eqs. (4-8), the dimensionless ratio for E'_X/E'_m and the loss factor are

plotted against fiber direction in Figs. 8 and 9, respectively for graphite/epoxy continuous fiber composite.

Again, the analysis without curve-fitting did not show good agreement with the experimental data. The first attempt at curve-fitting involved the introduction of the parameters that gave the best fit for the aligned discontinuous fiber case: storage modulus, effective fiber aspect ratio and fiber loss factor. These parameters corrected the curves for the 0° fiber direction. The Halpin-Tsai parameters that appear in the equations for the transverse Young's Modulus and shear modulus (Eqs. 5,6) were then changed. These parameters made it possible to fit the off-axis stiffness data, but not the loss factor data. Only by considering the anisotropy of the fibers (Eqs. 10-13), was it possible to obtain good agreement with the loss factor data. The transverse Young's Modulus and the shear modulus of the fiber were used as curve-fitting parameters as follows:

For graphite/epoxy composite:

   Transverse modulus for the fiber: 2×10^6 psi (13.78 GPa)
   Shear modulus for the fiber: 4×10^6 psi (27.56 GPa)
   Halpin-Tsai parameters: 2 for transverse modulus and 4 for shear modulus

For Kevlar/epoxy composite:

   Transverse modulus for the fiber: 1×10^6 psi (6.89 GPa)
   Shear modulus for the fiber: 2×10^6 psi (13.7 GPa)
   Halpin-Tsai parameters: 2 for transverse modulus and 1 for shear modulus

Since the Kevlar fibers have a larger diameter than the graphite fibers and the Kevlar composites had roughly twice the void fraction of the graphite composites (Table 2), it is reasonable to expect that the Halpin-

Tsai interpolation parameters might be different for the two materials. Again, no claim of uniqueness is made regarding the choice of curve-fitting parameters.

Figs. 10 and 11 show the experimental values with the best predicted curves. The stiffness is maximum at 0° and continuously goes down; rapidly up to about 30° and then move slowly from there to 90°. The loss factor increases to a maximum for an optimum fiber direction of approximately 30°, then decreases slowly with increasing fiber direction. These trends are in agreement with those for a different graphite/epoxy composite in a previous paper by Ni and Adams [6]. The same trends were obtained for Kevlar/epoxy specimens, but the experimental values for loss factor were consistently greater than predicted values for fiber angles greater than 45° [15]. The excellent toughness of the Kevlar fibers caused problems during machining of the off-axis specimens, and the resulting delaminations are believed to be responsible for the high apparent damping in these specimens.

The overall trends can be better visualized with the tridimensional plots of $E_X^!/E_m^!$, and loss factor for graphite/epoxy continuous fiber that are shown in Figs. 12 and 13, respectively. Figure 12 shows that maximum stiffness occurs for high fiber aspect ratios and an angle of zero degrees, and these conditions are practically attainable. Figure 13 shows that the maximum damping occurs for very low fiber aspect ratios and an angle of zero degrees, but the very low fiber aspect ratios are not practically attainable for high modulus fibers. A more practical approach to improving damping appears to be the control of fiber orientation at reasonable fiber aspect ratios. This conclusion is also supported by the numerical values tabulated in Table 3. Table 3 shows that the predicted maximum loss factors occur for zero degree fibers with an aspect ratio near 20, but that when the actual minimum attainable aspect ratios are used, the off-axis fibers (continuous or discontinuous) give greater damping. The experimental results also show that Kevlar has twice the damping of graphite for a fiber orientation of zero degrees, but in the off-axis case, the two materials have nearly the same maximum damping.

Current research involves the extension of the work reported here to the more general cases of random short fiber composites and hybrid laminates.

Conclusions:

1. Analytical predictions show that discontinuous fiber composite materials give maximum damping for fiber aspect ratios less than those experimentally attainable in this research. Experimental data did verify the predicted trend of increased damping as the aspect ratio is reduced, however.

2. The results show that the off-axis composite properties are essentially independent of the fiber aspect ratio in the range of practical aspect ratios when the fiber angle is not close to zero.

3. Greater experimental damping values were obtained in graphite/epoxy and Kevlar/epoxy by varying the fiber orientation than by varying the fiber aspect ratio. Thus, the control of lamina orientation in a continuous fiber-reinforced laminate may be a better approach to the improvement of composite damping than the control of fiber aspect ratio.

4. Empirical design equations have been developed for predicting the dynamic mechanical properties of a fiber-reinforced orthotropic lamina in terms of properties and volume fractions of constituent materials, fiber geometry and fiber orientation.

5. Due to the number of parameters involved in the analytical models and the uncertainties associated with numerical values of some of these parameters, the attempts at curve-fitting should only be taken as a first attempt at explaining the discrepancies between experimental data and predictions. Research on improved analytical models is continuing.

References:

[1]   Gibson, R.F., "Development of Damping Composite Materials," 1983 Advances in Aerospace Structures, Materials and Dynamics, AD-06, American Society of Mechanical Engineers (1983), pp. 89-95.

[2]   Gibson, R.F., Chaturvedi, S.K. and Sun, C.T., "Complex Moduli of Aligned Discontinuous Fibre-Reinforced Polymer Composites," Journal of Materials Science, 17 (1982), pp. 3499-3509.

[3]   Sun, C.T., Gibson, R.F. and Chaturvedi, S.K., "Internal Damping of Polymer Matrix Composites Under Off-Axis Loading," Journal of Materials Science, 20 (1985), pp. 2575-2585.

[4]   Schultz, A.B. and Tsai, S.W., "Dynamic Moduli and Damping Ratios in Fiber-Reinforced Composites," Journal of Composite Materials, 2 (3) (1968), pp. 368-379.

[5]   Adams, R.D. and Bacon, D.G.C., "Effect of Fibre Orientation and Laminate Geometry on the Dynamic Properties of CFRP," Journal of Composite Materials, 7 (1973), pp. 402-428.

[6]   Ni, R.G. and Adams, R.D., "The Damping and Dynamic Moduli of Symmetric Laminated Composite Beams - Theoretical and Experimental Results," Journal of Composite Materials, 18 (1984), pp. 104-121.

[7]   Chang, S. and Bert, C.W., "Analysis of Damping for Filamentary Composite Materials," Composite Materials in Engineering Design, American Society for Metals, Metals Park, Ohio (1973), pp. 51-62.

[8]   Gibson, R.F. and Plunkett, R., "Dynamic Mechanical Behavior of Fiber-Reinforced Composites: Measurement and Analysis," Journal of Composite Materials, 10 (1976), pp. 325-341.

[9]   Suarez, S.A., Gibson, R.F. and Deobald, L.R., "Random and Impulse
        Techniques for Measurement of Damping in Composite Materials,"
        Experimental Techniques, 8 (10) (1984), pp. 19-24.

[10]   Suarez, S.A. and Gibson, R.F., "Computer-Aided Dynamic Testing of
        Composite Materials," Proceedings of 1984 Fall Meeting of Society
        for Experimental Mechanics, Milwaukee, Wisconsin (Nov. 1984), pp.
        118-123, Submitted to Experimental Techniques.

[11]   Cox, M.A., "The Elasticity and Strength of Paper and Other Fibrous
        Materials," British Journal of Applied Physics, 3 (1952) pp. 72-79.

[12]   Chamis, C.C., "Mechanics of Load Transfer at the Interface,"
        Composite Materials, 6, Academic Press, New York (1974).

[13]   Hashin, Z., "Complex Moduli of Viscoelastic Composites. I. General
        Theory and Application to Particulate Composites," Int. Journal of
        Solids and Structures, 6 (1970), pp. 539-552.

[14]   Jones, R.M., Mechanics of Composite Materials, Scripto Book Co.
        (1975).

[15]   Suarez, S.A., Optimization of Internal Damping in Fiber Reinforced
        Composite Materials, Ph.D. Dissertation, University of Idaho
        Graduate School (Dec. 1984).

[16]   Hashin, Z., "Analysis of Properties of Fiber Composites with
        Anisotropic Constituents," Journal of Applied Mechanics, 46 (Sept.
        1979), pp. 543-550.

[17]   Whitney, J.M., "Elastic Moduli of Unidirectional Composites with
        Anisotropic Filaments," Journal of Composite Materials, 1 (1967),
        pp. 188-193.

[18]   Gibson, R.F., Deobald, L.R. and Suarez, S.A., "Laboratory
        Production of Discontinuous-Aligned Fiber Composite Plates Using an
        Autoclave-Style Press Cure," Journal of Composites Technology and
        Research, 7 (2) (Summer 1985), pp. 49-54.

[19]   DiCarlo, J.A., "The Fiber Contribution to Composite Damping,"
        Presented at Symposium on the Role of Surfaces and Interfaces
        in Material Damping, 1985 ASM Metals Congress, Toronto, Canada
        (October 1985).

[20]   Hwang, S.L., "Finite Element Modeling of Damping in Discontinuous
        Fiber Composite Materials," M.S. Thesis, University of Idaho
        (1985).

[21]   Hwang, S.L. and Gibson, R.F., "Micromechanical Modeling of Damping
        in Discontinuous Fiber Composites Using a Strain Energy/Finite
        Element Approach," Presented at ASME Winter Annual Meeting, Miami
        Beach, Florida (November 1985).

TABLE 1

Description of discontinuous aligned specimens tested with flexural vibration

No	Fiber Length (in)	(mm)	Width (in)	(mm)	Thickness (in)	(mm)	Density (lb/in³)	(g/cc)	Vf (%)
FIBERITE 934 RESIN CASTING									
6	N/A		0.744	18.898	0.123	3.134	0.0469	1.298	N/A
AVCO 5505 RESIN CASTING									
6	N/A		0.753	19.126	0.119	3.023	0.0445	1.232	N/A
GRAPHITE / EPOXY									
6	7.5	190.5	0.746	18.948	0.062	1.575	0.0571	1.584	66
6	1/2	12.7	0.76	19.304	0.0588	1.494	0.0571	1.584	66.5
6	1/4	6.35	0.733	18.618	0.06	1.523	0.0572	1.586	66.6
6	1/8	3.175	0.749	19.025	0.061	1.554	0.0568	1.574	64.7
6	1/16	1.588	0.753	19.126	0.0625	1.588	0.0567	1.574	63.2
KEVLAR / EPOXY									
5	7.5	190.5	0.755	19.177	0.0528	1.341	0.0492	1.362	65.8
5	1/2	12.7	0.755	19.177	0.0542	1.377	0.0487	1.348	68.1
6	1/4	6.35	0.74	18.796	0.0521	1.323	0.0477	1.323	66.7
6	1/8	3.175	0.749	19.025	0.053	1.346	0.049	1.357	67.1
6	1/16	1.588	0.746	18.948	0.0553	1.405	0.0498	1.382	63
BORON / EPOXY									
6	7.5	190.5	0.745	18.923	0.0459	1.167	0.0743	2.061	63.4
6	2	50.8	0.746	18.923	0.0481	1.221	0.0732	2.031	62.9
6	1	25.4	0.749	19.012	0.0551	1.399	0.0724	2.009	60.4
6	1/2	12.7	0.748	18.991	0.0532	1.351	0.073	2.024	60.2
6	1/4	6.35	0.751	19.075	0.0487	1.237	0.0751	2.084	62
6	1/8	3.175	0.75	19.05	0.0504	1.279	0.0734	2.037	60.3
6	1/16	1.588	0.751	19.075	0.0541	1.373	0.0704	1.954	56

Note.- The length for all the specimens is 7.5 in (190.5 mm)
Vf = Fiber volume fraction

TABLE 2

Description of off-axis fiber specimens tested with extensional vibration

No	Fiber angle	Length (in)	(mm)	Width (in)	(mm)	Thickness (in)	(mm)	Mass 1 (lb)	(kg)	Mass 2 (lb)	(kg)

FIBERITE 934 RESIN CASTING

No	Fiber angle	Length (in)	(mm)	Width (in)	(mm)	Thickness (in)	(mm)	Mass 1 (lb)	(kg)	Mass 2 (lb)	(kg)
1	N/A	8.344	211.938	0.745	18.923	0.124	3.150	0.627	0.285	0.6316	0.287
1	N/A	5.563	141.3	0.746	18.948	0.126	3.2	0.627	0.285	0.6316	0.287
1	N/A	1.875	47.625	0.746	18.948	0.126	3.2	0.627	0.285	0.6316	0.287
1	N/A	0.875	22.225	0.746	18.948	0.126	3.2	0.627	0.285	0.6316	0.287

Note.- The density for resin casting is 0.0469 lb/in³ (1.298 g/cc)

GRAPHITE / EPOXY CONTINUOUS FIBER

No	Fiber angle	Length (in)	(mm)	Width (in)	(mm)	Thickness (in)	(mm)	Mass 1 (lb)	(kg)	Mass 2 (lb)	(kg)
6	0	8.375	212.725	0.746	18.948	0.062	1.575	1.2615	0.573	1.2686	0.577
5	2.5	8.556	217.322	0.741	18.821	0.060	1.524	1.2615	0.573	1.2686	0.577
5	7.5	8.25	209.550	0.729	18.517	0.062	1.575	1.2615	0.573	1.2686	0.577
6	12.5	7.896	200.558	0.73	18.542	0.060	1.524	0.946	0.43	0.9514	0.432
5	20	7.422	188.519	0.728	18.491	0.060	1.524	0.627	0.285	0.6316	0.287
6	45	5.037	127.94	0.731	18.547	0.060	1.524	0.305	0.139	0.3076	0.14
6	60	4.060	103.124	0.729	18.517	0.060	1.524	0.305	0.139	0.3076	0.14
6	75	3.058	77.673	0.729	18.517	0.061	1.549	0.305	0.139	0.3076	0.14
6	90	3.037	77.140	0.729	18.517	0.061	1.549	0.305	0.139	0.3076	0.14

Note.- Density 0.0573 lb/in³ (1.589 g/cc)
      Fiber volume fraction 67.5 %
      Void volume fraction 0.2 %

GRAPHITE / EPOXY DISCONTINUOUS FIBER

No	Fiber angle	Length (in)	(mm)	Width (in)	(mm)	Thickness (in)	(mm)	Mass 1 (lb)	(kg)	Mass 2 (lb)	(kg)
6	0	8.125	206.375	0.733	18.618	0.060	1.524	1.2615	0.573	1.2686	0.577
5	2.5	9.307	236.398	0.73	18.542	0.062	1.575	0.946	0.43	0.9514	0.432
5	7.5	8.863	225.120	0.729	18.517	0.061	1.549	0.946	0.43	0.9514	0.432
6	12.5	6.933	176.098	0.731	18.567	0.061	1.549	0.946	0.43	0.9514	0.432
5	20	5.938	150.825	0.729	18.517	0.063	1.600	0.627	0.285	0.6316	0.287
6	45	4.537	115.240	0.722	18.339	0.061	1.549	0.305	0.139	0.3076	0.14
6	60	3.542	89.963	0.732	18.593	0.062	1.575	0.305	0.139	0.3076	0.14
5	75	3.063	77.788	0.725	18.415	0.062	1.575	0.305	0.139	0.3076	0.14
5	90	3.057	77.648	0.724	18.390	0.063	1.600	0.305	0.139	0.3076	0.14

Note.- The fiber length for these specimens is 1/4 in (6.35 mm),
      Density 0.0573 lb/in³ (1.589 g/cc), and
      Fiber volume fraction 67.8 %
      Void volume fraction 0.67 %

TABLE 2   (continuation)

Description of off-axis fiber specimens tested with extensional vibration

No	Fiber angle	Length (in)	(mm)	Width (in)	(mm)	Thickness (in)	(mm)	Mass 1 (lb)	(kg)	Mass 2 (lb)	(kg)
					KEVLAR / EPOXY CONTINUOUS FIBER						
4	0	8.375	212.725	0.755	19.177	0.053	1.346	1.2615	0.573	1.2686	0.577
4	2.5	7.914	201.016	0.733	18.618	0.053	1.346	1.2615	0.573	1.2686	0.577
4	7.5	7.899	200.635	0.734	18.644	0.054	1.372	0.946	0.43	0.9514	0.432
5	12.5	6.938	176.225	0.742	18.847	0.053	1.346	0.627	0.285	0.6316	0.287
3	20	4.464	113.386	0.753	19.126	0.054	1.372	0.627	0.285	0.6316	0.287
6	45	3.072	78.029	0.75	19.05	0.054	1.372	0.305	0.139	0.3076	0.14
4	60	2.089	53.061	0.742	18.847	0.054	1.372	0.305	0.139	0.3076	0.14
4	75	1.553	39.446	0.75	19.05	0.057	1.448	0.305	0.139	0.3076	0.14
4	90	1.442	36.627	0.762	19.355	0.055	1.397	0.305	0.139	0.3076	0.14

Note.- Density 0.05 lb/in^3 (1.367 g/cc)
      Fiber volume fraction 71.5 %
      Void volume fraction 1.38 %

Table 3

Comparison of Maximum Loss Factors

(a) Based on predicted optimum fiber aspect ratio

Material	Fiber Angle	Fiber Aspect Ratio	Loss Factor
graphite/epoxy	0°	20	0.029
Kevlar/epoxy	0°	20	0.029

(b) Based on minimum attainable experimental fiber aspect ratios and off-axis continuous fibers

Material	Fiber Angle	Fiber Aspect Ratio	Loss Factor
graphite/epoxy	0°	226	0.009
Kevlar/epoxy	0°	133	0.017
graphite/epoxy	37.5^o	continuous	0.024
Kevlar/epoxy	45°	continuous	0.035
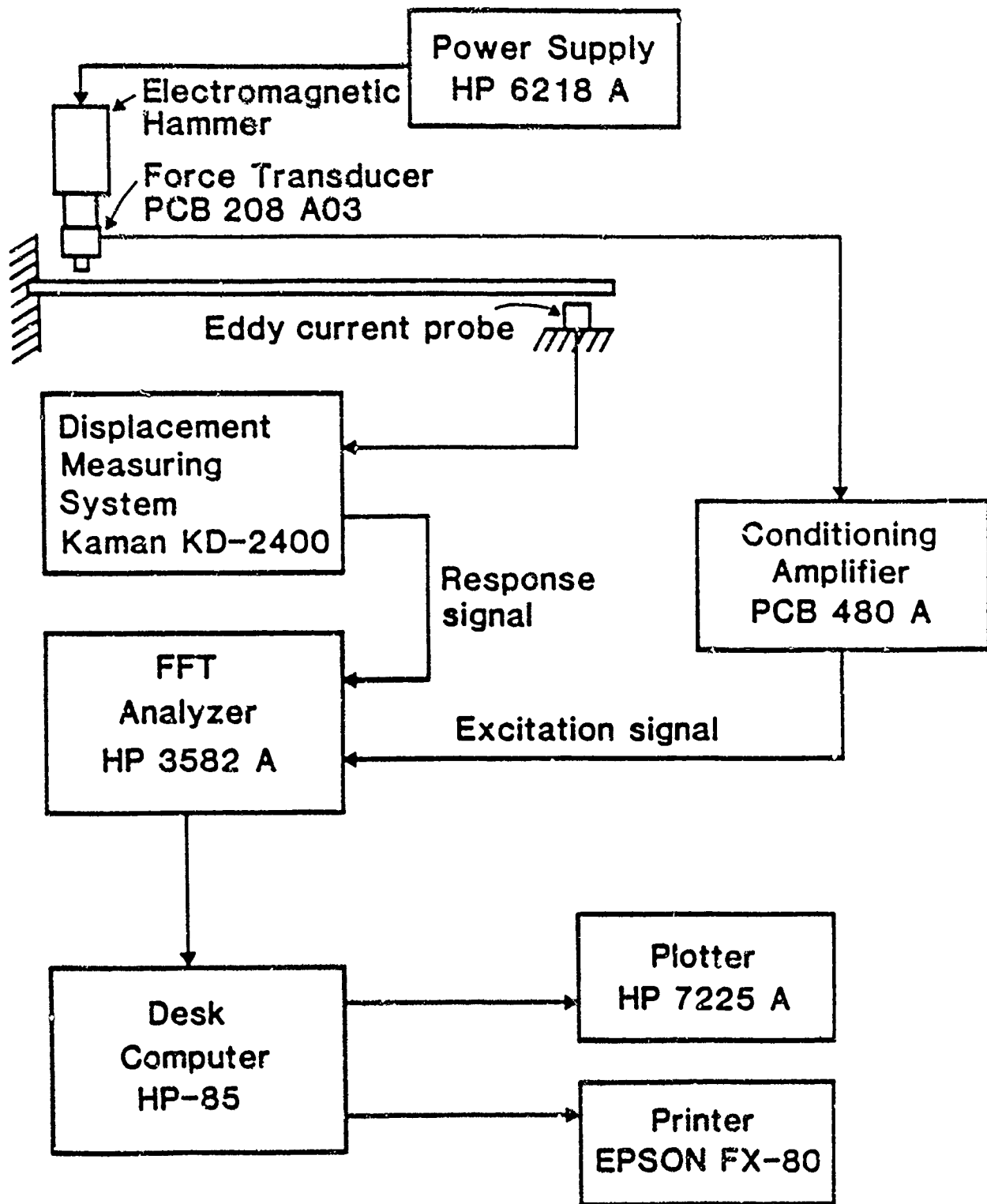
Figure 1. Flexural vibration apparatus.
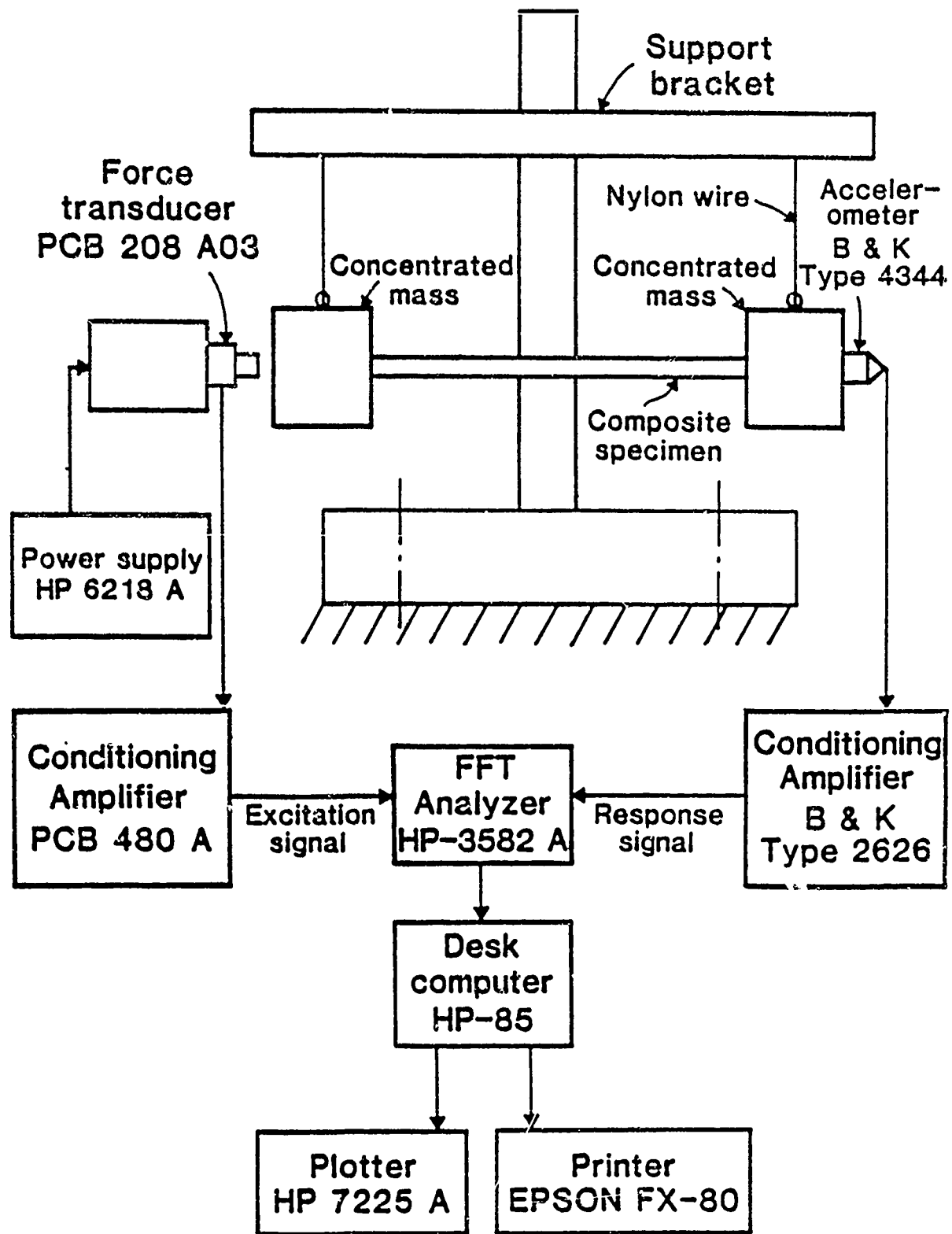
Figure 2. Extensional vibration apparatus.

FF-17
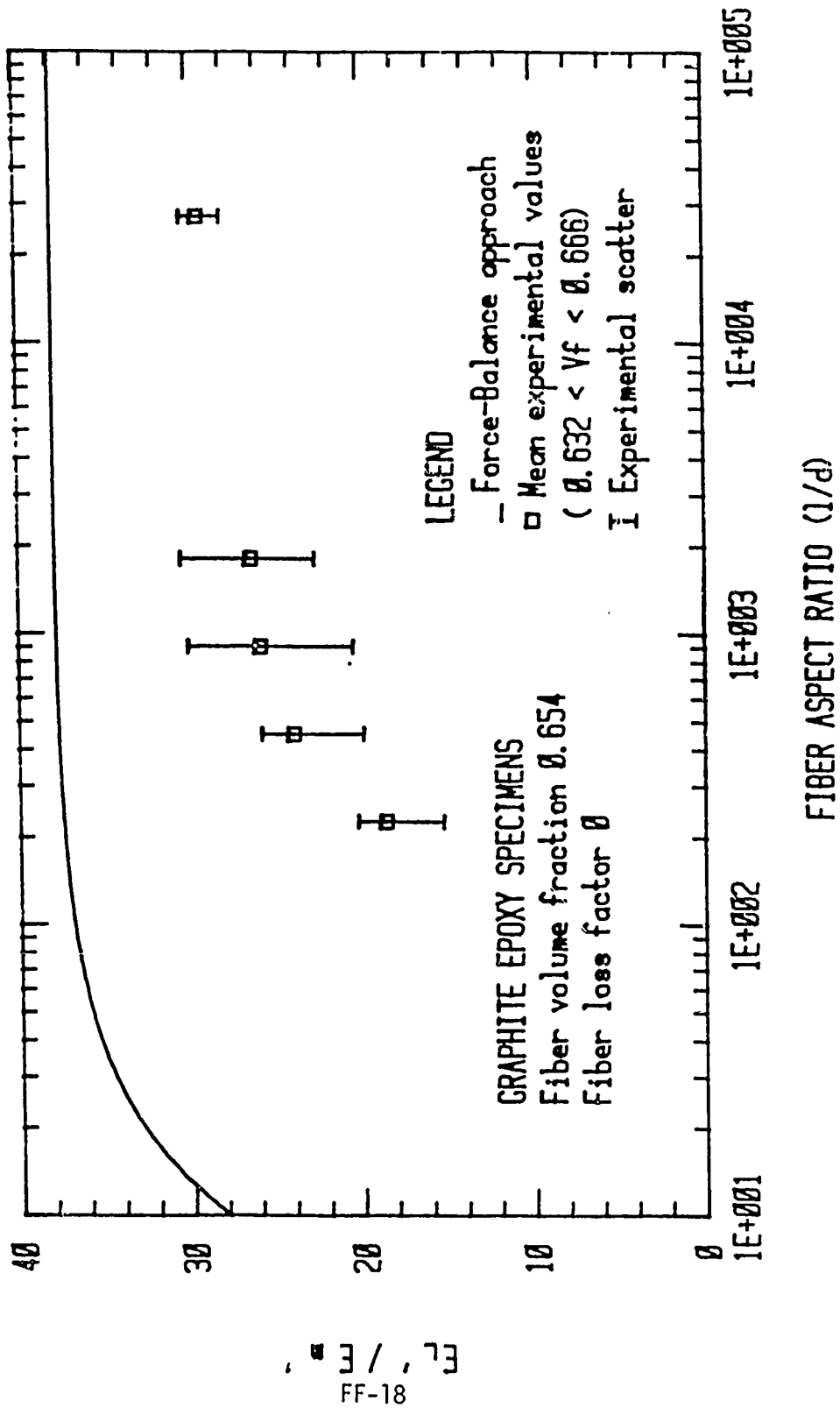
Figure 3. E_L'/E_m' vs. fiber aspect ratio for graphite/epoxy without curve fitting.

FF-18
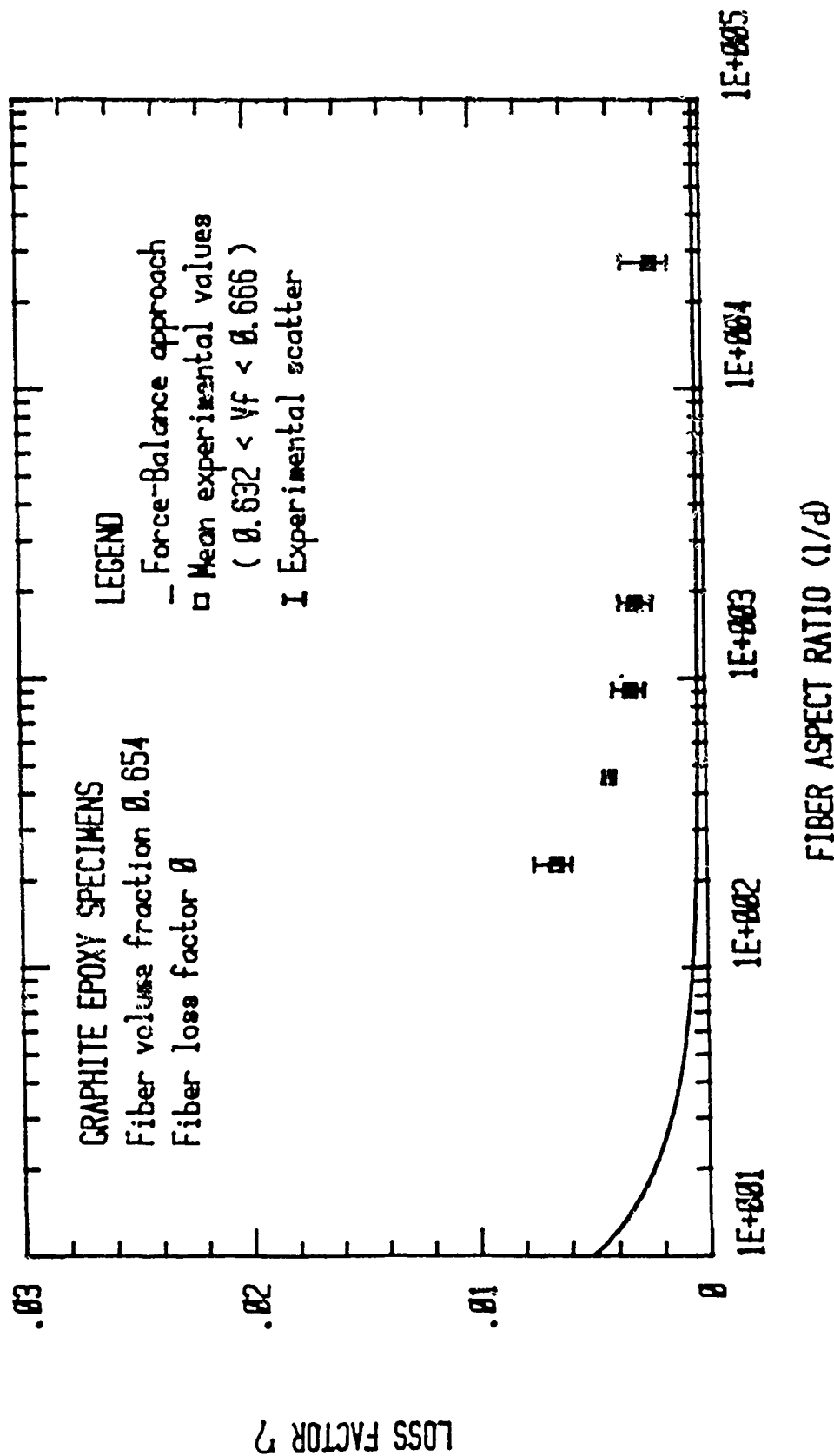
Figure 4. Loss factor vs. fiber aspect ratio for graphite/epoxy without curve fitting.

FF-19
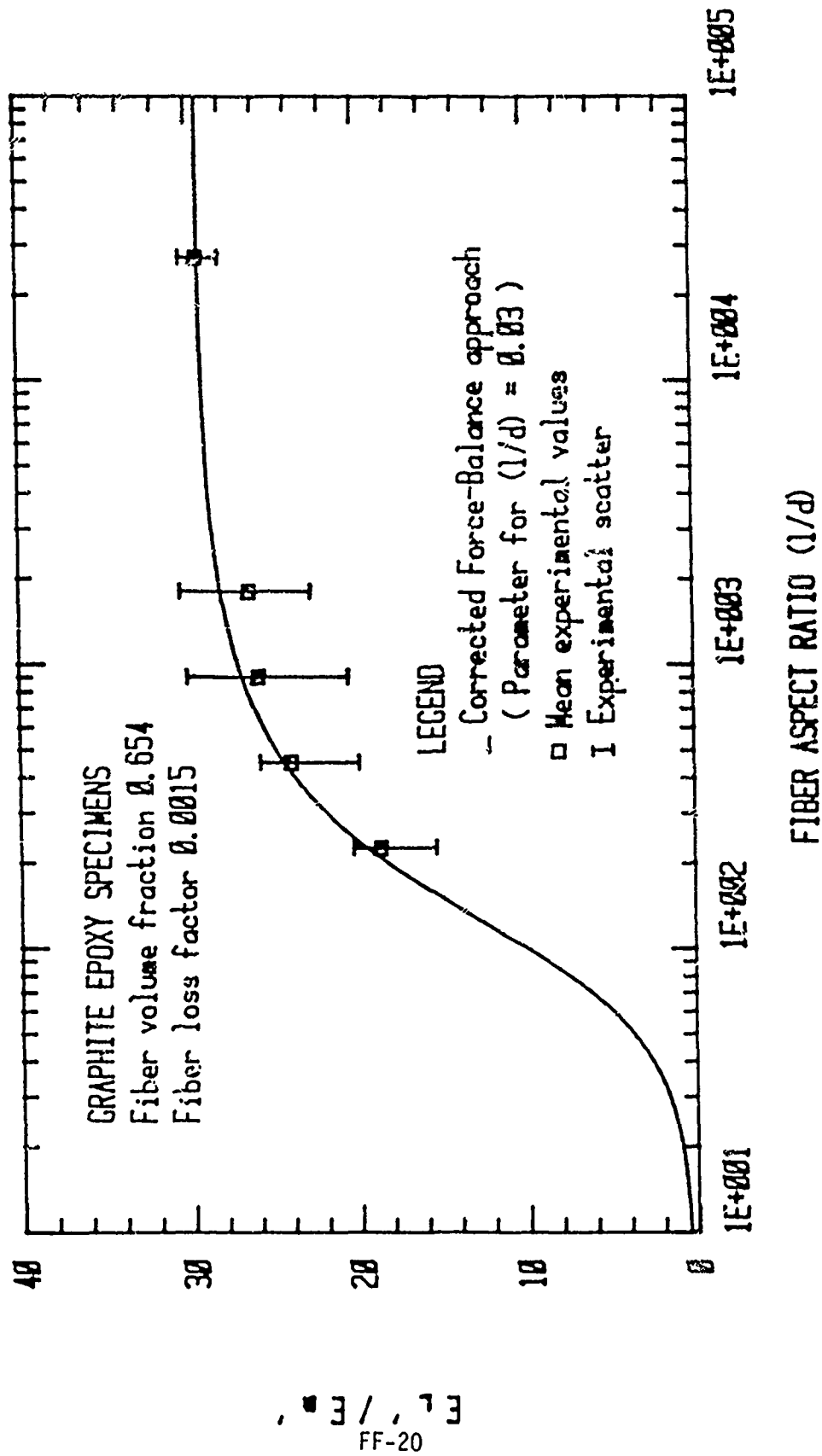
Figure 5. E_L'/E_m' vs. fiber aspect ratio for graphite/epoxy with curve fitting.
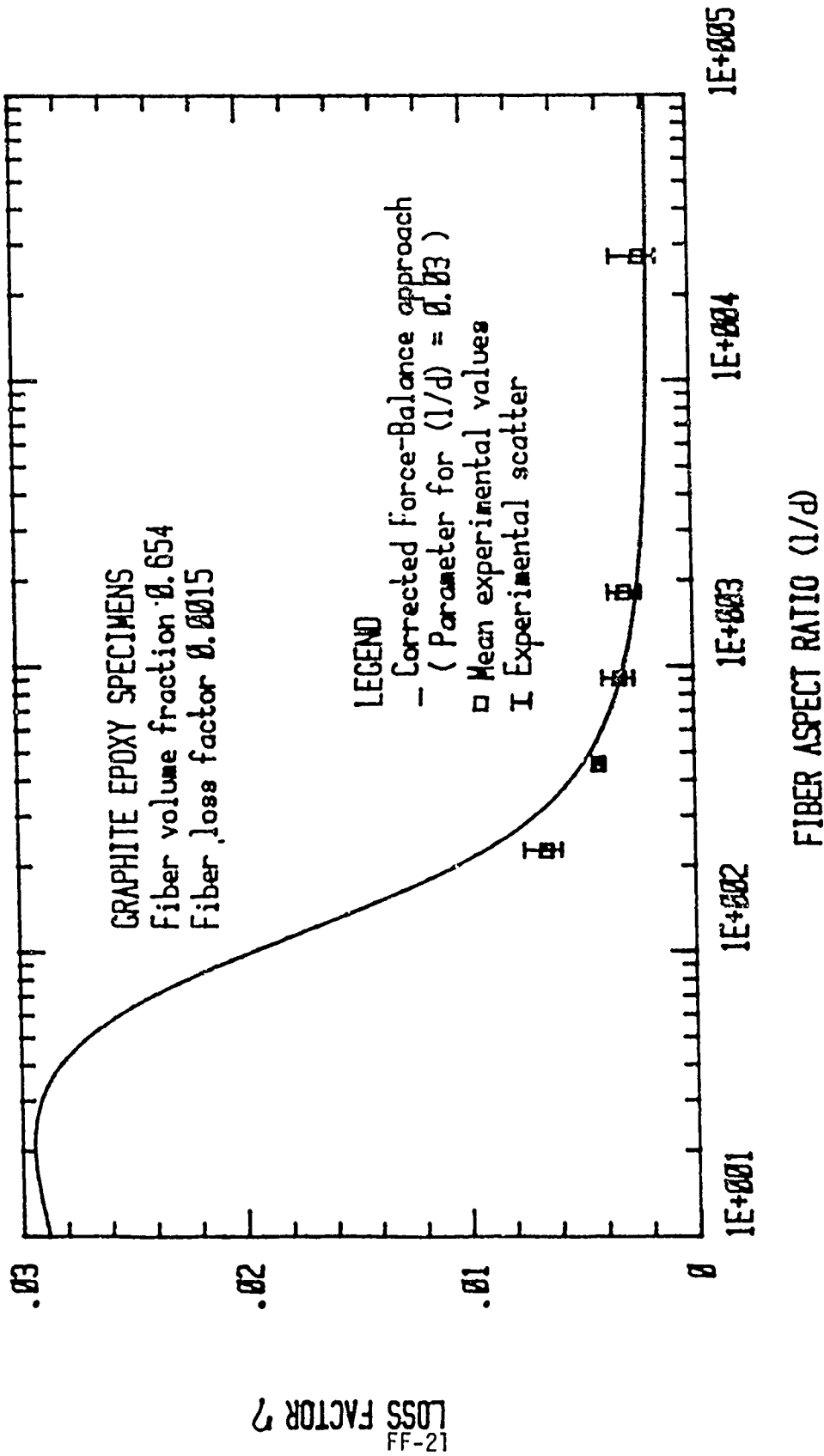
Figure 6. Loss factor vs. fiber aspect ratio for graphite/epoxy with curve fitting.
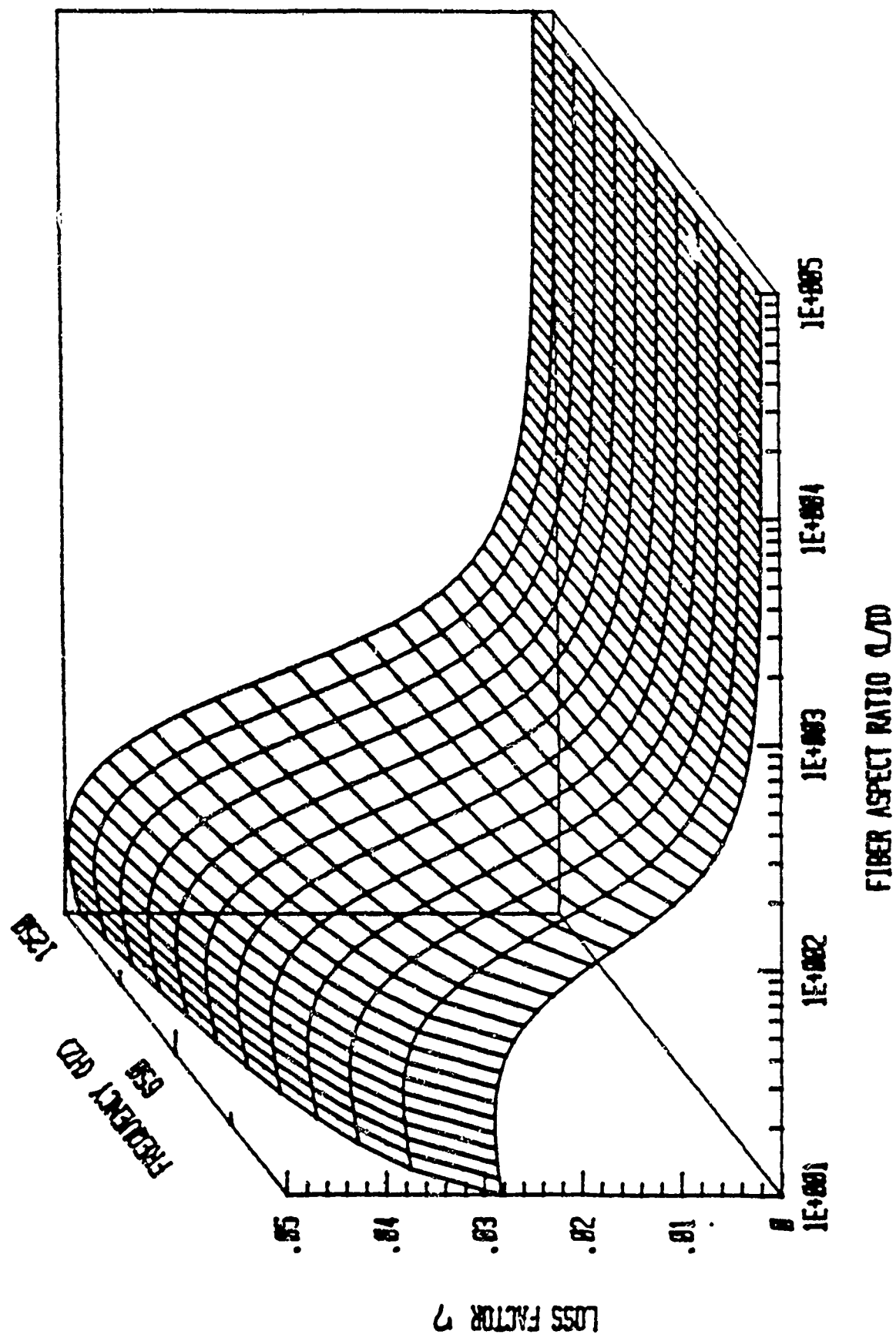
Figure 7. Tridimensional plot of loss factor vs. fiber aspect ratio and frequency, for graphite/epoxy composite.

FF-22
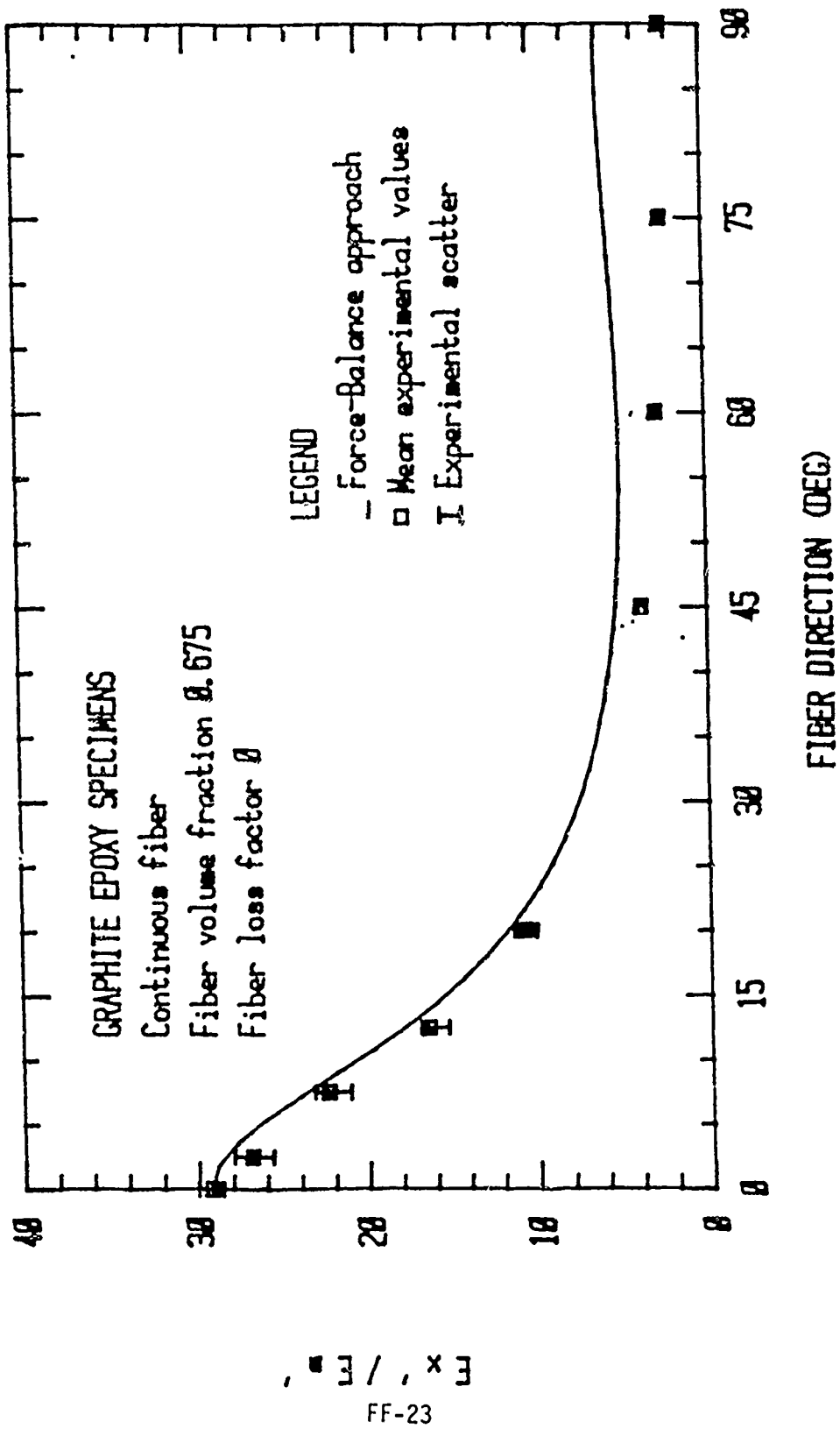
Figure 8. E_X'/E_m' vs. fiber direction for continuous graphite/epoxy, without curve fitting.
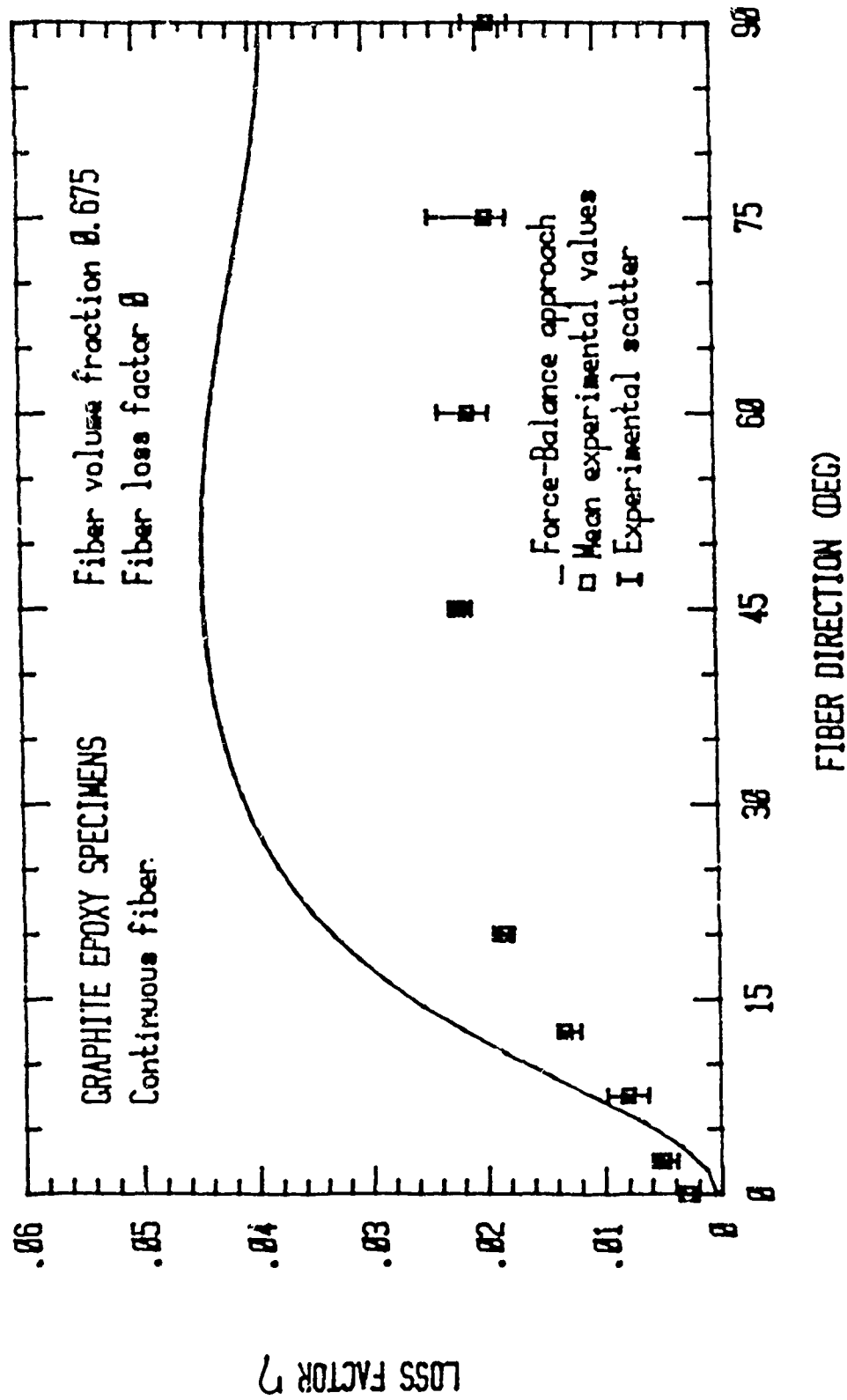
Figure 9. Loss factor vs. fiber direction for continuous graphite/epoxy, without curve fitting.

FF-24
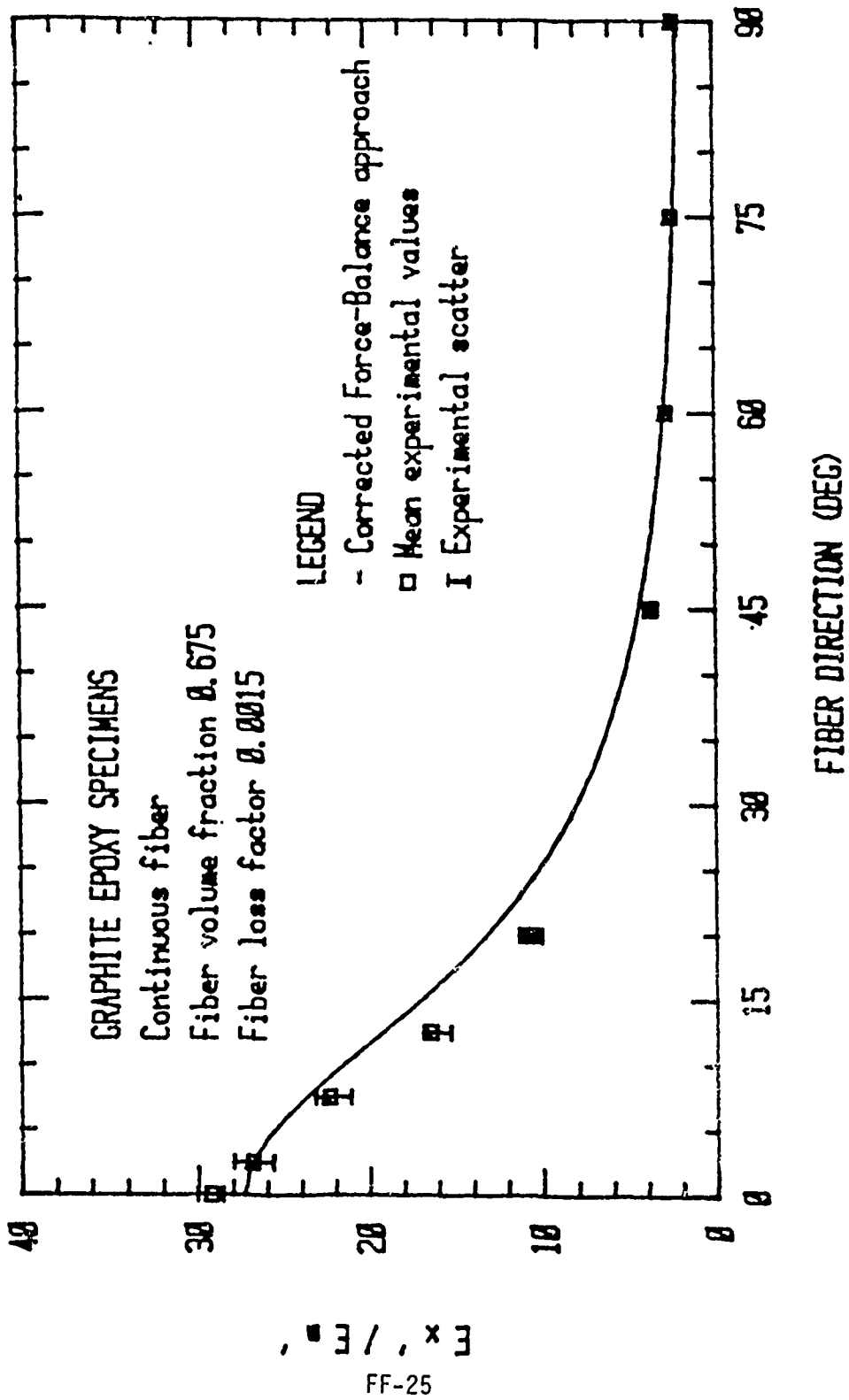
Figure 10. E'_X/E'_m vs. fiber direction for continuous graphite/epoxy, with curve fitting.

FF-25
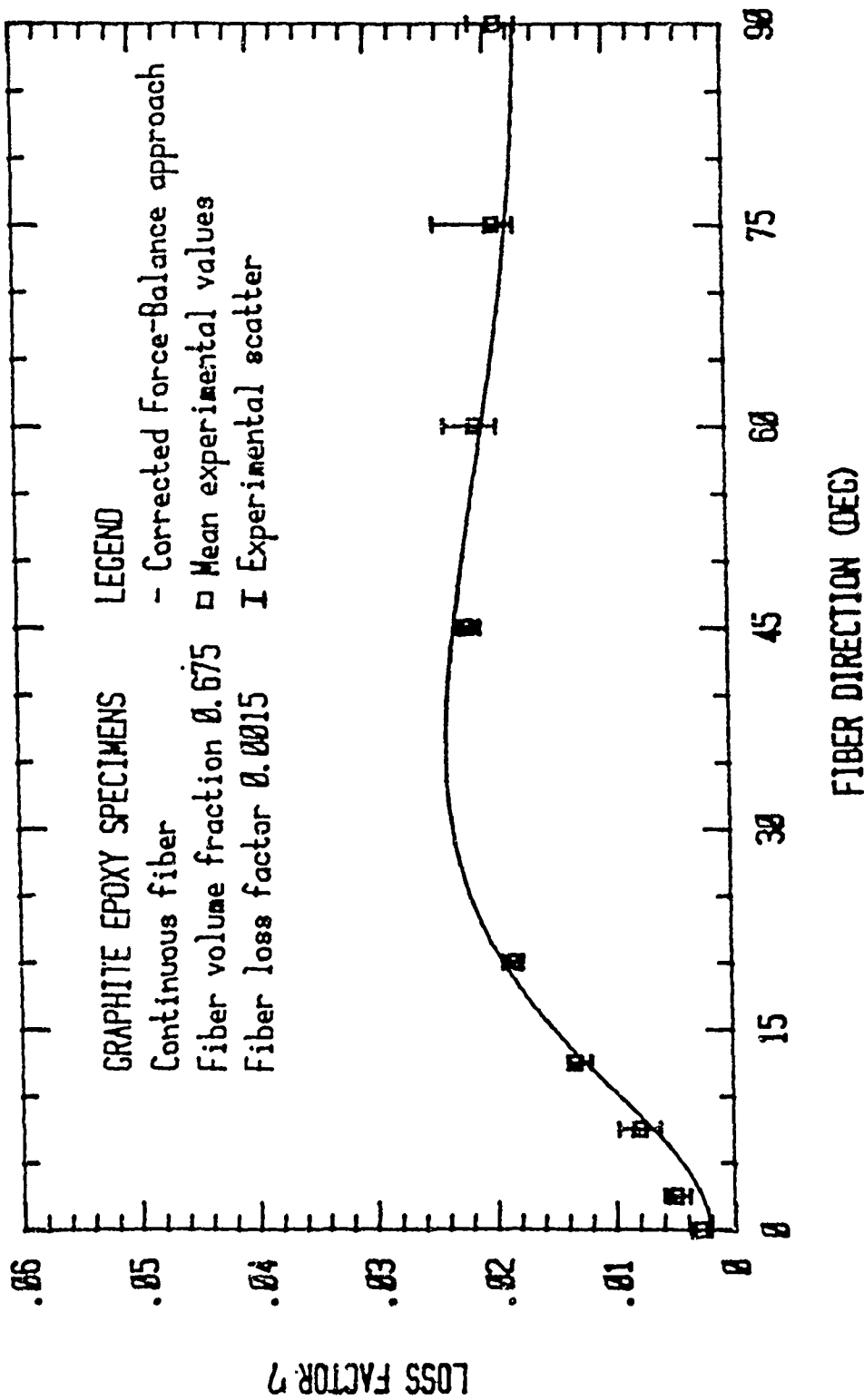
Figure 11. Loss factor vs. fiber direction for continuous graphite/epoxy, with curve fitting.
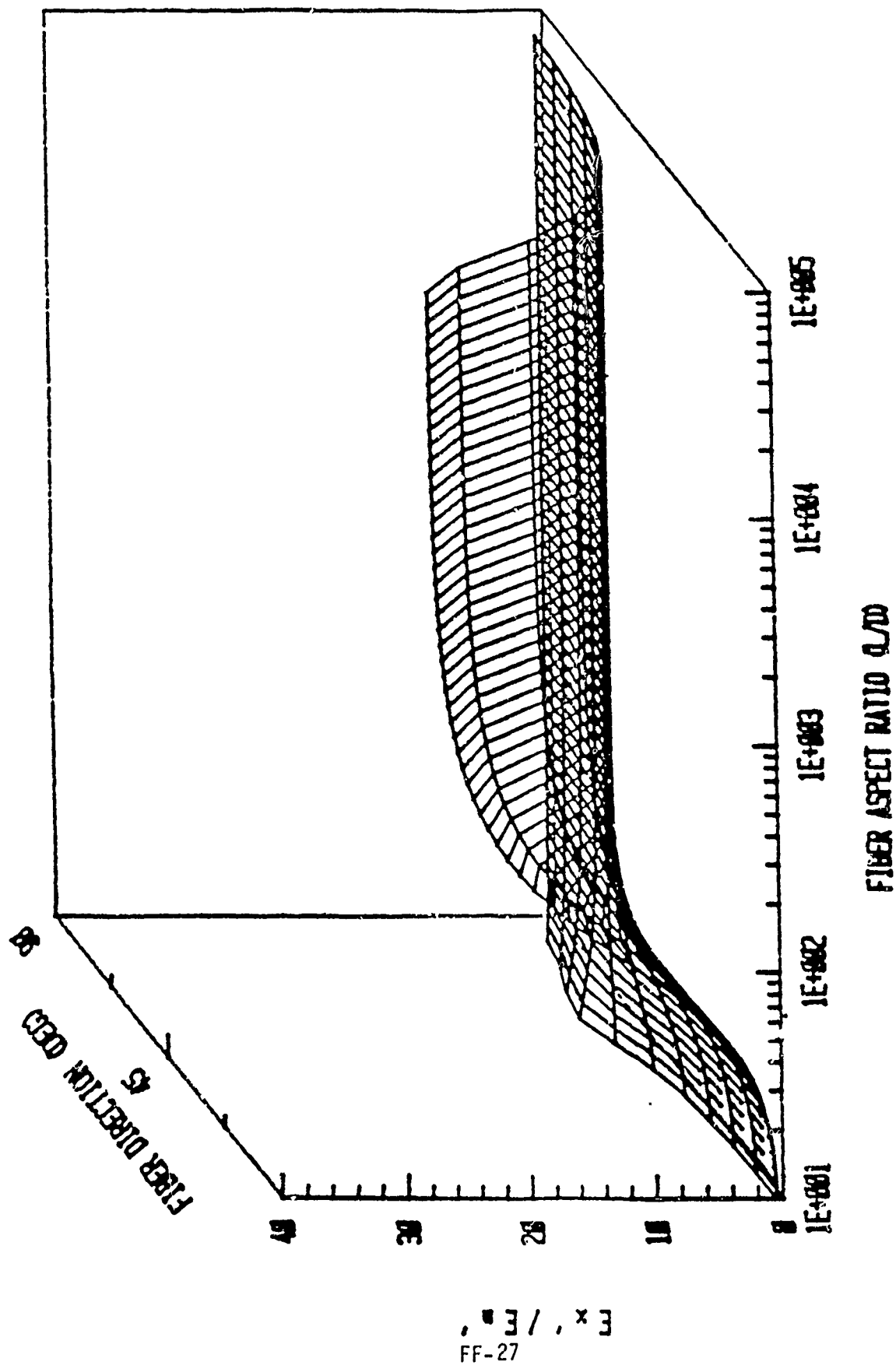
Figure 12. Tridimensional plot of E_X'/E_m' vs. fiber aspect ratio and fiber direction, for graphite/epoxy composite.

FF-27
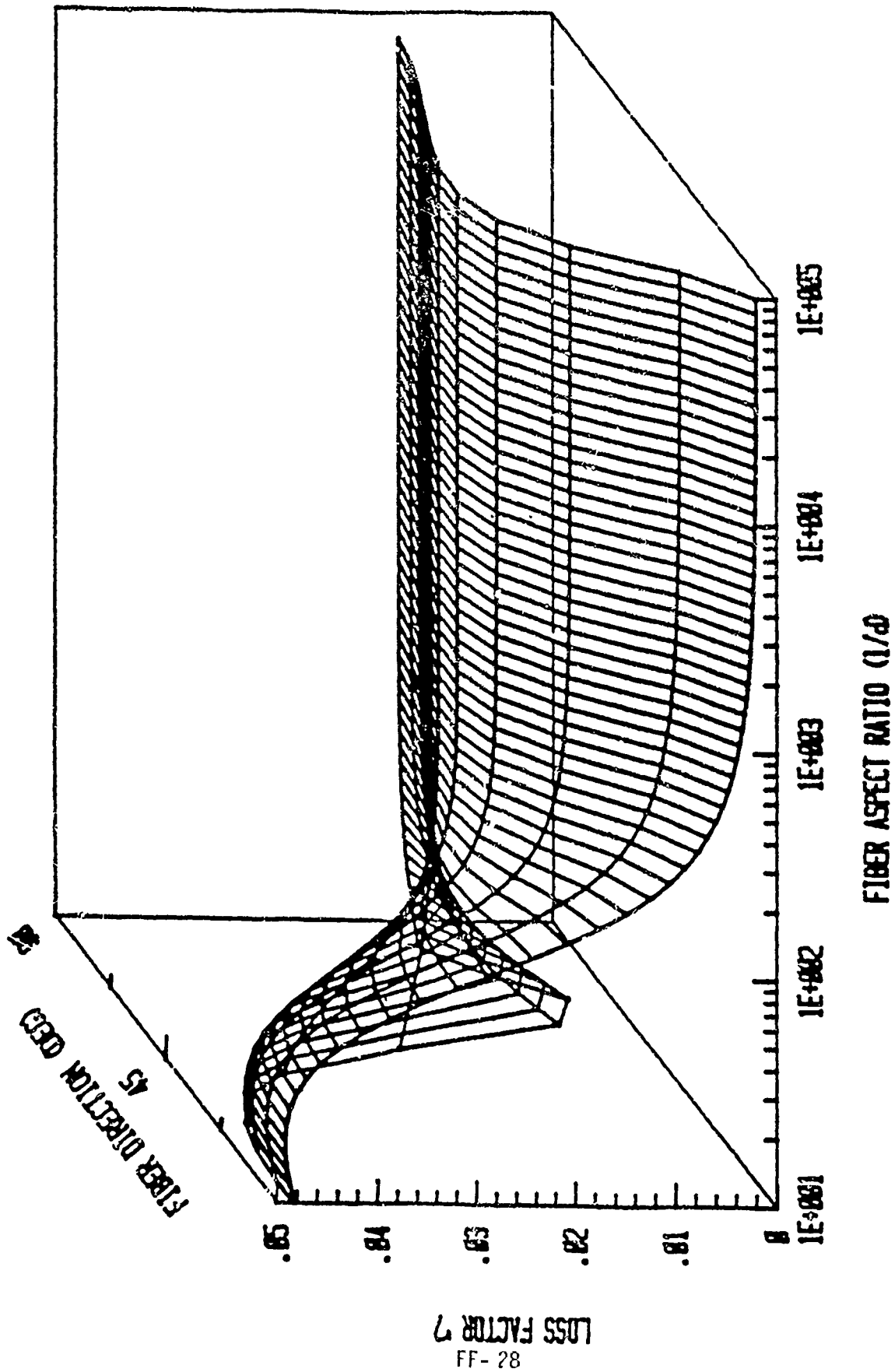
Figure 13. Tridimensional plot of loss factor vs. fiber aspect ratio and fiber direction, for graphite/epoxy composites.

A REVIEW OF THE DAMPING MECHANISMS IN

ADVANCED FIBRE-REINFORCED COMPOSITES

by

Robert D. Adams

Department of Mechanical Engineering
University of Bristol,
Bristol BS8 1TR
England

ABSTRACT

The damping properties and dynamic moduli of fibre-reinforced composite materials are reviewed starting with micromechanics as applied to uni-directional materials, we proceed to the predictions of damping for laminated beams and plates. Theoretical predictions are shown to be in excellent agreement with experimental measurements. Comparisons are also made with light-weight metals.

1. INTRODUCTION

High performance filamentary composite materials are finding increased usage in aircraft, space and propulsion systems, thus complementing the already extensive use of low-performance composite materials in general industrial and shipbuilding applications. The distinguishing features of these new materials are their high specific strength and stiffness, together with a directionality of properties. The first two properties mean that significant weight reductions may be achieved. The directionality factor complicates structural design procedures but, at the same time, leads to a new degree of freedom in that the strength and stiffness of the material may be tailored precisely to the amount and in the direction required for a specific application.

Most early developments work in the field was restricted to glass fibre reinforced materials due to its cheapness and ease of manufacture. Indeed, glass is eminently suitable in terms of its high ultimate strength, being typically in the range of 3 to 3.5 GPa (425-500 x 10^3 psi)*, but it lacks in terms of stiffness (Young's modulus E = 70 GPa (10 x 10^6 psi)) compared with alternative materials. For instance, boron offers a stiffness more than five times that of glass (380 GPa (55 x 10^6 psi)) whilst posessing a similar tensile strength (2.8 GPa (400 x 10^3 psi)). This has led to the development of boron/epoxy and boron/aluminium materials for aerospace applications. One disadvantage of boron is the high cost of manufacture which is predominantly by vapour phase reaction on a tungsten wire substrate. Carbon (or graphite) can be produced in both whisker and fibrous form for inclusion in resin or carbon based composites. In its whisker form, carbon has an ultimate tensile strength of 15 to 20 GPa (2 to 3 x 10^6 psi) and a tensile modulus of 700 GPa (100 x 10^6 psi) but it is even more expensive to produce than boron. However, continuous carbon fibre may be produced relatively cheaply by the controlled pyrolysis of man-made organic fibres. The resulting fibres have a high strength and stiffness (tensile strength 3.5 GPa (500 x 10^6 psi)) and Young's modulus up to 500 GPa (70 x 10^6 psi), and are capable of retaining their strength up to temperatures approaching 3000 °C. The manufacturing processes vary with the type of precursor and the properties desired from the final product and surface treatments may be used to improve the bond between fibre and matrix. Manufacturing costs remain high while quantities are small, but at the present time carbon offers great promise. The various derivatives of Kevlar, which are manufactured from organic polymers, have a tensile strength similar to that of glass, but twice the modulus.

The second component of the composite, the matrix, is most commonly of the resin type, although metal, rubber, ceramic and carbon based materials have occasionally been used. The resin systems available may be divided into two groups, namely thermosetting and thermoplastic resins. Of the former group, by far the most important types are the polyesters and epoxides. Polyesters are low-cost general-purpose resins which cure at room temperature, while epoxides generally require both temperature and pressure during the cure cycle. To ease manufacture, the epoxide/fibre material is usually supplied in sheet or tape form which has been pre-impregnated with partially cured resin, but which retains sufficient flexibility to facilitate moulding. Thermally stable polymers have been developed for continuous operation at up to 300 °C. Thermoplastics such as nylon and polypropylene may be reinforced with fibrous material, especially glass.

* 1 lbf/in^2 (psi) ≡ 6895 N/m^2 = 6895 Pa

In the past, the damping capacity of conventional engineering materials has not generally provided sufficient energy dissipation to limit resonant or near resonant amplitudes of vibration. The position has been further aggravated by the development of high strength alloys such as aluminium and titanium which generally have lower damping than that provided by their weaker counterparts. Conventional structures have many additional sources of energy dissipation such as bolted and rivetted joints, lubricated bearings and so on. In space applications, owing to the absence of a surrounding fluid or gas, aerodynamic damping is essentially zero, thus removing another important source of energy dissipation, especially in thin, sheet structures. However, when using composite materials it is usually necessary to use adhesively-bonded joints, since bolts and rivets tend to pull out. This seriously reduces the structural damping and so makes material damping far more important. This situation can be alleviated in fibre reinforced materials by making a suitable choice of components in that the damping derives essentially from the matrix and matrix/fibre interface. *It is therefore more important to understand the mechanisms of damping in composites than in metallic materials.*

The main sources of internal damping in a composite material arise from microplastic or viscoelastic phenomena associated with the matrix and relative slipping at the interface between the matrix and the reinforcement. Thus, excluding the contribution from any crac   nd debonds, the internal damping of the composite will be influenced by the following factors:

(i) the properties and relative proportions of matrix and reinforcement in the composite (the latter is usually represented by the volume fraction of the reinforcement v);

(ii) the size of the inclusions (particle size, fibre diameter, etc.)

(iii) the orientation of the reinforcing material to the axis of loading;

(iv) the surface treatment of the reinforcement.

In addition, loading and environmental factors such as amplitude, frequency and temperature may also affect the measured damping values.

To cover the dynamic properties of all composite materials is beyond the limited scope of this review. We will therefore restrict the treatment to those advanced composites which are to be found in stress-bearing situations in modern engineering. Unreinforced polymers will not be covered here, except as a component of the composite, nor will composites with randomly-oriented fibres.

The vibration properties which concern us are the damping and the dynamic modulus. These are defined in Fig.1. When taken round a stress cycle, all materials show a non-singular relationship between stress and strain. The modulus is given by the mean slope of the stress-strain loop. For most materials, there is little ambiguity in this definition, since the loop is almost indistinguishable from a straight line. The area, ΔU, of the loop represents the work done against "internal friction" and is the amount of energy dissipated during the cycle.
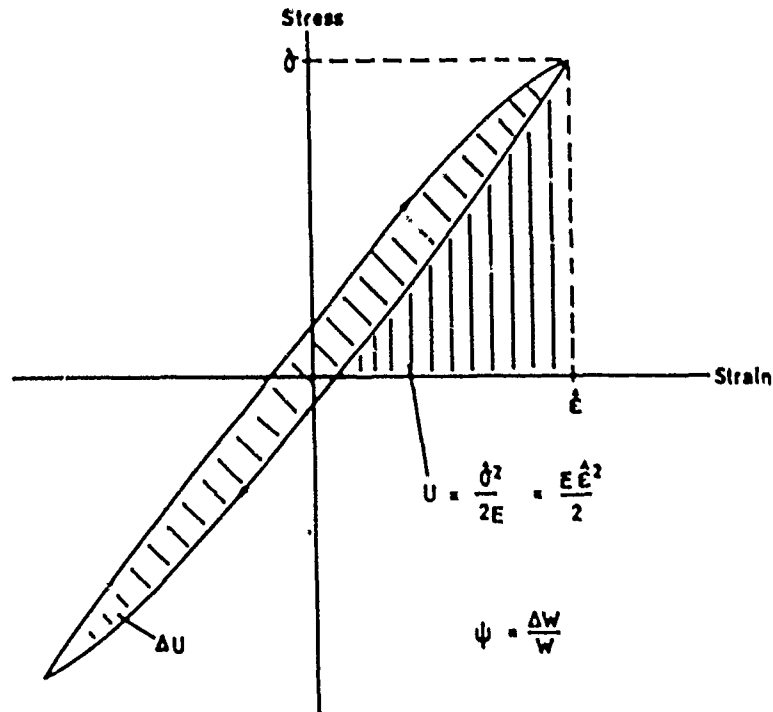
Fig.1. Definition of specific damping capacity, Ψ

Referring to Fig.1, it can be seen that the maximum strain energy stored per unit volume in the cycle is $U = \delta^2/2E = E\hat{\epsilon}^2/2$. We now define the specific damping capacity, Ψ, of the material as

$$\Psi = \frac{\Delta U}{U}$$

This quantity is usually expressed as a percentage. Providing the damping is not large ($\Psi < 100\%$), Ψ is related to other commonly used damping parameters by the relationships

$$\Psi = \frac{2\pi}{Q} = 2\delta = 2\pi\eta = 4\pi C = 2\pi \left(\frac{\omega_2 - \omega_1}{\omega_n} \right) \tag{1}$$

where
$Q =$ quality (amplification) factor,
$\delta =$ logarithmic decrement.
$\eta =$ loss factor
$C =$ proportion of critical damping
$\omega_n =$ natural frequency

ω_1 and ω_2 are the half power (3 dB) points

2. UNIDIRECTIONAL COMPOSITES

In these materials, all the fibres are considered to be parallel and lying in the direction of the major axis of the specimen.

Longitudinal shear concerns the twisting of a bar of such an aligned

composite. Thus, the longitudinal shear modulus of CFRP and GFRP is principally a function of the matrix shear modulus, the fibre shear modulus, and the volume fraction of fibres. None of the existing micromechanics theories accurately fit the experimental data[1], but the numerical prediction of Adams and Doner[2] gives good agreement. From such a curve as is shown in Fig.2. it is possible to determine the volume fraction v_f if the matrix shear modulus G_m is known, and vice versa.

For longitudinal shear loading, it can be shown that for viscoelastic materials[3],

$$\Psi_{LT} = \frac{\Psi_m (1 - v_f)[(G + 1)^2 + v_f(G - 1)^2]}{[G(1 + v_f) + 1 - v_f][G(1 - v_f) + 1 + v_f]} \tag{2}$$

where the suffices f and m mean fibre and matrix, v_f is the volume fraction of fibre, G is the ratio of the shear modulus of the fibre to that of the matrix, and Ψ the specific damping capacity. For many fibre/matrix combinations, G is of the order of 10, and this result leads to a composite specific damping capacity that is little influenced by the volume fraction of fibre. This relationship is shown for a typical carbon fibre composite in Fig.3. together with an alternative solution proposed by Adams and Bacon[1]. In order that these predictions can be compared to the variety of experimental systems, the damping values have been non-dimensionalised. To explain the lower damping measured in their torsional tests, Adams and Bacon cited effects due to fibre misalignment and dilational strains in the material which contribute little to the damping, but significantly to the stored strain energy.

The longitudinal Young's modulus, E_L, (the tensile modulus in the direction of the fibres in a unidirectional composite), is given by the rule of mixtures and is

$$E_L = E_f v_f + E_m (1 - v_f)$$

where E_f, E_m are the fibre and matrix moduli and v_f is the volume fraction of fibre. This rule is well-obeyed experimentally as shown in Fig.4. and may be used as a check on any parameter provided the others are known. This relationship was derived for normal axial loading (tension or compression), but also applies in flexure provided shear effects can be neglected. It is also possible to predict the damping capacity of unidirectional material when stressed in the fibre direction by using the law of mixtures and assuming that all the energy dissipation occurs in the matrix. On this basis, we arrive at the equation

$$\Psi_L = \Psi_m (1 - v_f) E_m/E_L$$

where E is Young's modulus and the suffix L means longitudinal tensile/ compressive properties of the composite.

However, it is found that this expression underestimates considerably the measured value of Ψ_L, even when considerable effort has been made to eliminate extraneous losses (Fig.5). Basically, there are several contributions to the discrepancy. First, the smaller is the fibre diameter, the larger is the surface area of fibre per unit volume. Adams and Short[4] showed that,
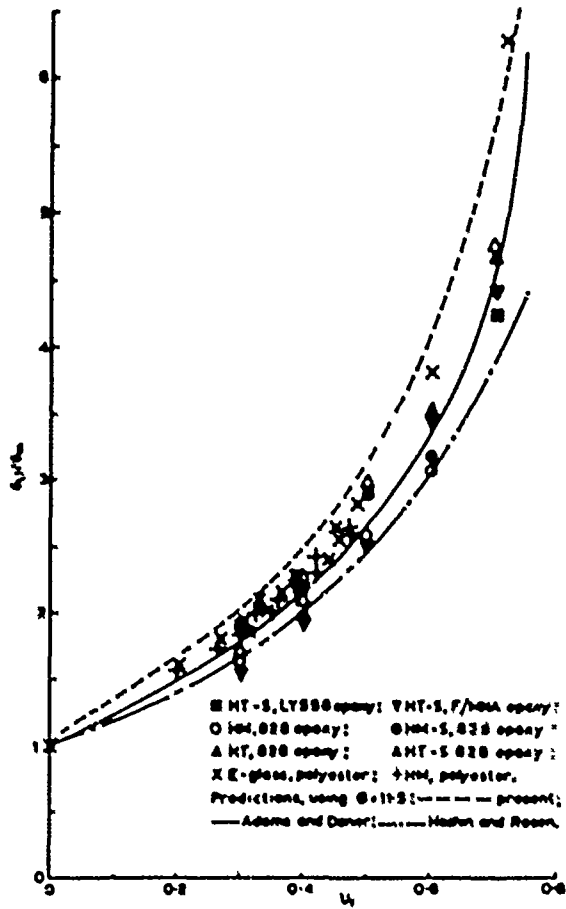
Fig.2. Variation of reduced composite longitudinal shear modulus G_{LT}/G_m with fibre volume fraction, v_f.
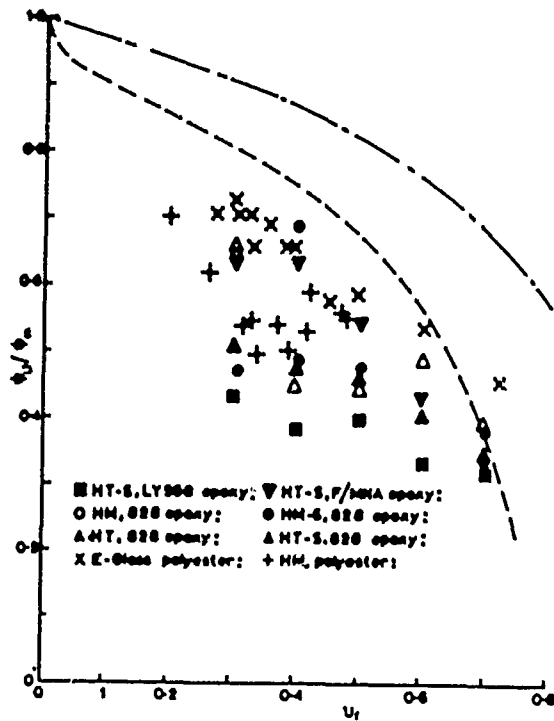
Fig.3. Variation of the ratio of longitudinal shear damping, Ψ_{LT}, to the matrix damping, Ψ_m, with volume fraction v_f.

———— —— Hashin's prediction[3]

—————— Adams and Bacon's prediction[1]
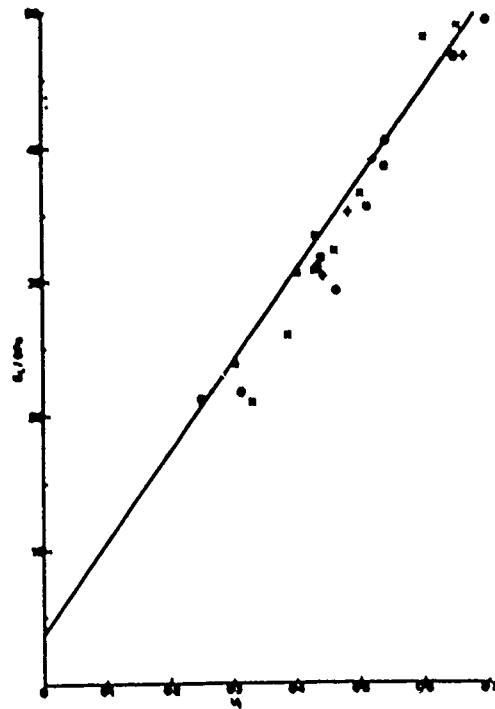
Fig.4. Longitudinal
Young's modulus against
fibre volume fraction for
different fibres:

☐ $d = 10$ μm; + $d = 20$ μm
0 $d = 30$ μm; x $d = 50$ μm
_____ law of mixtures

for glass fibres of 10, 20, 30 and 50μm diameter in polyester resin, there was
a consistent increase in Ψ_L with reduction in fibre diameter.   Second, the
problem of misalignment is not insignificant as is shown below for angle-ply
composites.   Third, any structural imperfections, such as cracks and debonds,
lead to interfacial rubbing and hence to additional losses.   Finally, although
the effect of shear is usually negligible in stiffness measurements, this is
less true for the damping since the shear damping is essentially that of the
matrix and Ψ_{LT} is of the order of 50 - 100 times larger than Ψ_L.   Thus,
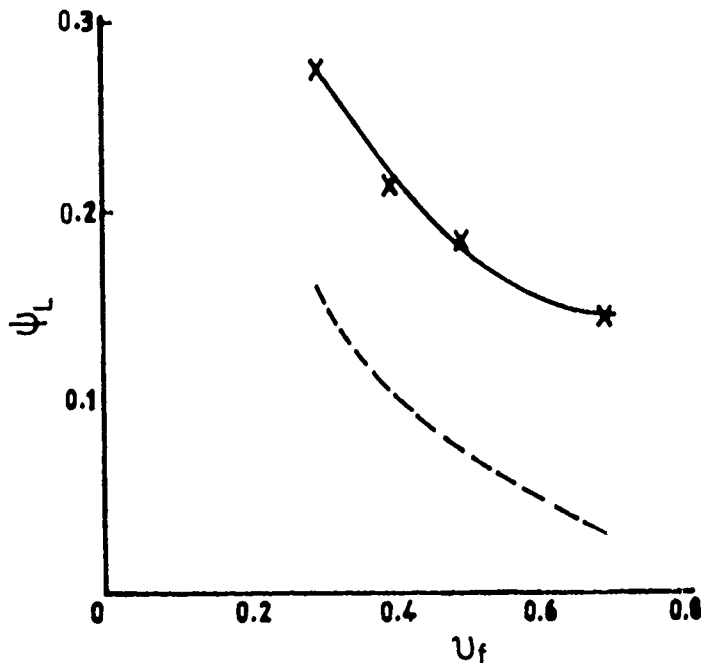
Fig.5. Variation of
Flexural damping Ψ_L, with
fibre volume fraction v_f
for HT-S carbon fibre
in epoxy resin.

——X— Experimental values

—————— Law of mixtures
          plus shear damping

FG-7

although only a few per cent of the energy is stored in shear, this can make a substantial contribution to the total predicted value. Figure 6 shows that as the aspect ratio of a beam was reduced from 90 to 50, the shear damping contribution was increased. Further, by subtracting the shear damping from the experimental values, the effect of aspect ratio is essentially eliminated. *The difference remaining between the law of mixtures prediction and the "Experimental minus shear" values was mainly due to the combination of misalignment, internal flaws and fibre diameter.* It has been suggested that the discrepancy can be accounted for by the composite being modelled such that the damping of the fibres is considered. Unfortunately, this is unlikely to be a realistic solution since the damping of the fibres is extremely small. Adams[5] has measured directly the longitudinal shear damping of a variety of single carbon fibres and found values of the order of 0.13% specific damping capacity. This gives a loss factor of the order of 2×10^{-4}! In tension/compression, the graphite microfibrils which comprise the structure of carbon fibres will be preferentially stressed in their strong direction, with much less interfacial slip than might occur in torsion. Thus, the longitudinal damping (tension/compression) ought to be at least an order of magnitude lower than that measured in torsion, giving a loss factor of 2×10^{-5} or so. There is, therefore, no way in which damping of this level can reasonably be used to explain the discrepancies in the micromechanics models.
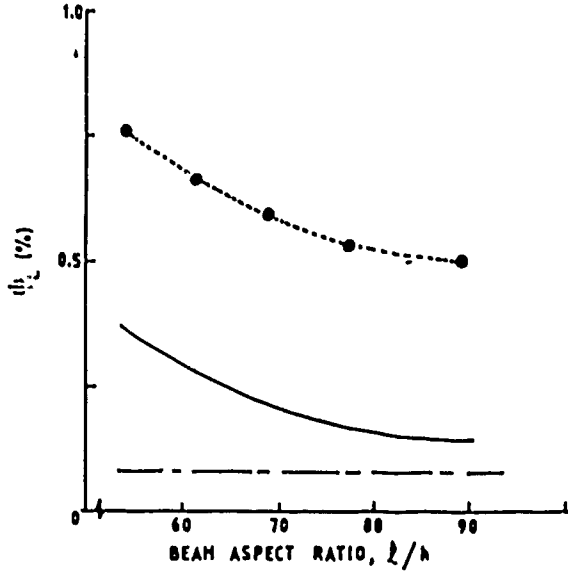
Fig.6.
Variation of flexural damping, Ψ_L with aspect ratio for HM-S carbon fibre in DX 209 epoxy resin; $v_f = 0.5$; ● measured SDC; ——— theoretical shear SDC; — — — theoretical law of mixtures SDC.
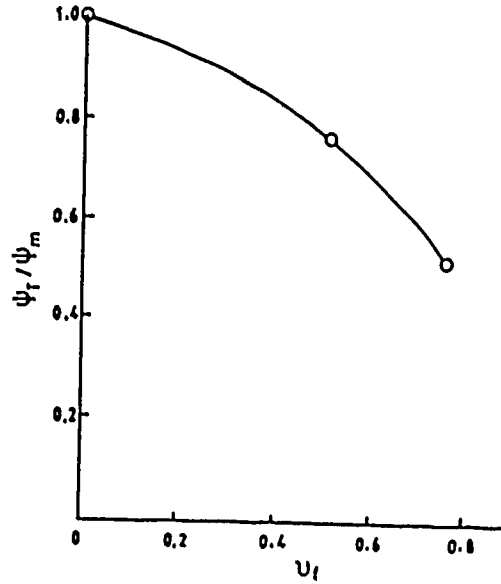
Fig.7.
Variation of ratio of transverse damping, Ψ_T, to matrix damping, Ψ_m, with fibre volume fraction v_f.

In the transverse direction, the damping is, as in shear, very heavily matrix dependent. Also there is again no reliable micromechanics theory for predicting Ψ_T. Experiments covering a wide variety of fibres (from E-glass to HM carbon) showed that the transverse damping is largely independent of both fibre type and surface treatment. Volume fraction does, in a similar way to longitudinal shear, have a significant effect on Ψ_T. Some experimental results to illustrate this point are given in Fig.7. Fig. 8 shows the transverse Young's modulus E_T which is seen to increase markedly with volume fraction.

It can be seen from the above that while the various micromechanics theories are sufficiently accurate for predicting moduli, they are generally poor at predicting damping. This is because the various theories do not contain some of the important factors (such as microcracks, misalignment, surface area, etc) which contribute to the damping of unidirectional materials. Without developing some very complex models, it is unlikely that the situation can be changed in the near future. The only safe feature is that, with the possible exception of Kevlar, there is essentially no damping in the fibres themselves.

Recently, Ni and Adams[6] used a combination of micromechanics and experimental results to produce a series of predictive curves for the variation of the unidirectional moduli and damping values with fibre volume fraction. They also showed the importance of using the correct volume fraction for this basic data. Thus, when making predictions of the damping for laminated plates, it is important to know the volume fraction of both the plates and the unidirectional material used in making the prediction. Guides were given for converting data, and an example showed the errors which can occur if the corrected data is not used. It is suggested that the Ni and Adams approach is far more suitable in practical terms than trying to evolve increasingly complex micromechanics models.

When the specimen axis, and so the direction of loading, is at an angle θ to the fibre direction in a unidirectional composite, we have the off-axis situation. Adams and Bacon[7] showed that, for a unidirectional beam with the fibres at angle θ to the specimen axis, the damping is given by

$$\Psi_\theta = \frac{1}{S_{11}} \left[\sin^4\theta \left(\frac{\Psi_T}{E_T} \right) + \cos^2\theta \, \sin^2\theta \left(\frac{\Psi_{LT}}{G_{LT}} \right) \right] \qquad (3)$$

for $5° \leq \theta \leq 90°$, where S_{11} is the compliance in the direction of the specimen axis. Figure 9 shows the theoretical and experimental values of Ψ_θ for a carbon fibre beam, together with the separate theoretical contributions from stresses in the L, T and LT directions. Figure 9 includes the full theoretical expression for the variation of camping with angle θ and also shows the separate contributions from direct stresses in the direction of the fibres (Ψ_L), transverse to the fibres (Ψ_T) and in shear (Ψ_{LT}). The theoretical prediction and experimental measurement of the variation of Young's modulus, E_θ, with angle is also shown in Fig.9. Excellent agreement between the theory and experiment is shown for both modulus and damping.
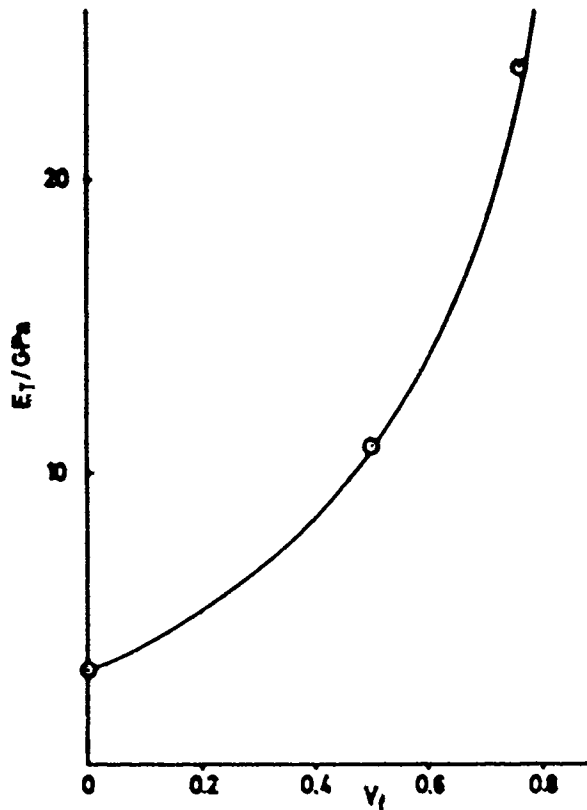
Fig.8.
Variation of the transverse modulus, E_T, with fibre volume fraction, v_f, of GFRP in flexure.

——— Halpin & Tsai's theoretical curve E_{fT} = 70 GPa

E_m = 3.21 GPa

⊙ = experimental points
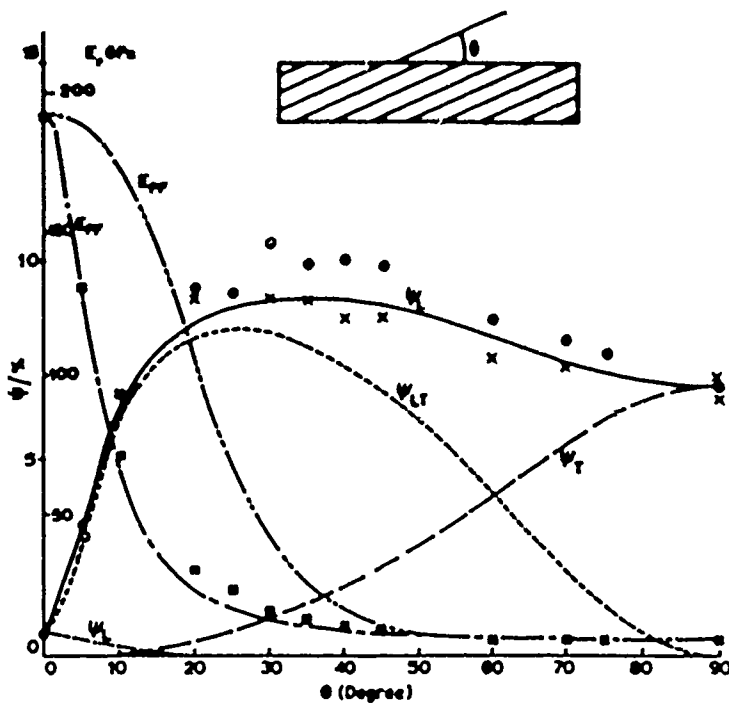
Fig.9.
Variation of flexural Young's modulus and damping with fibre orientation θ for HM-S carbon fibre in DX209 epoxy resin, v_f = 0.5; x Ψ_F (plates 1 and 2) o Ψ_F in vacuo; L_F average for plates 1 and 2(values virtually coincident). Theoretical predictions

— — — ——— E_{PF} (pure flexure);

— — — ——— E_{FF} (free flexure); ——— Ψ_F total

FG-10

3. BEAMS CUT FROM LAMINATED PLATES

Beams and plates are often made from a succession of laminae as shown in Fig.10. It is necessary to use the theory of laminated plates and to evaluate the contributions to damping made by each layer. Beams are a special case of plates, but are better treated separately because the theory of vibrating beams is much easier than that of plates. In any case, the theory can only be outlined in a review of this length.

The constitutive equation relating stresses, σ, and strains, ϵ, in the kth lamina is

$$
\begin{bmatrix} \sigma_1 \\ \sigma_2 \\ \sigma_6 \end{bmatrix}_k = \begin{bmatrix} Q_{11} & Q_{12} & Q_{16} \\ Q_{12} & Q_{22} & Q_{26} \\ Q_{16} & Q_{26} & Q_{66} \end{bmatrix}_k \begin{bmatrix} \epsilon_1 \\ \epsilon_2 \\ \epsilon_6 \end{bmatrix}_k
$$

where the values Q_{ij}^{k} are the stiffness matrix components in the specimen system of axes, 1, 2, 3 of the kth lamina and are obtained from the values in the axes related to the fibre direction x, y, z by using the appropriate geometric transformation. *For a beam specimen, the stresses σ_2 and σ_6 (traverse and interlaminar shear) can be neglected in comparison with σ_1.*

By using the appropriate geometric transformation, these stresses can be converted from the specimen axes to the fibre directions. It is then possible to calculate the stresses in the fibre direction σ_x (i.e. σ_L), normal to it σ_y (i.e. σ_T) and the shear components σ_{xy} (i.e. σ_{LT}). The total energy stored in the x (or L) direction, say Z_L, can then be calculated, and the energy dissipation in this layer and in this direction is then given by

$$\Delta Z_L = \Psi_L \, Z_L$$

For the beam, the overall specific damping capacity Ψ_{ov} is then given by

$$\Psi_{ov} = \frac{\Sigma \Delta Z}{\Sigma Z} = \frac{\Psi_L Z_L + \Psi_T Z_T + \Psi_{LT} Z_{LT}}{Z_L + Z_T + Z_{LT}} \tag{4}$$

If the elastic moduli and damping coefficients are known for unidirectional material, it is possible to calculate the overall damping of a beam. Ni and Adams[8] give the theory for generally-laminated beams and obtained excellent agreement with measured results.
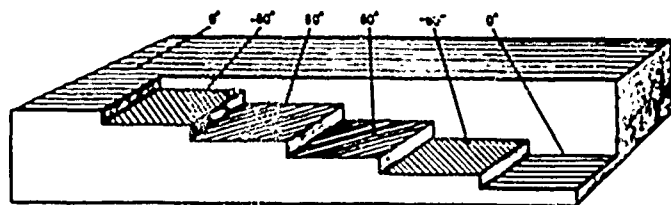
Fig.10.
Lamina stacking arrangement for (0, -60, 60)$_s$ laminate. The suffix 's' indicates symmetry of stacking about the mid-plane.

Whereas specimens with all layers at θ will twist as they are bent, the twisting can be internally restrained by using several layers at $\pm \theta$. The damping contributions can again be assessed and the measured values accounted for[6]. Figure 11 shows theoretical predictions and experimental measurements for the modulus and damping of a series of CFRP beams made with ten layers (of high modulus carbon fibres in epoxy resin) alternately at $\pm \theta$. Note that the modulus is higher than that of the off-axis specimens owing to the internal restraint, while the damping is generally lower.

More generally laminated composites, as shown in Fig.10, are commonly used in practice. Fortunately, the same method can be used as above for predicting the damping, and Fig.12 shows the excellent agreement between theory and experiment for the variation of damping with θ of a symmetrical, high-modulus graphite fibre reinforced epoxy plate. Beam specimens were cut at angles from -90° to +90° relative to the fibre direction in the outer layer of this $(0°, -60°, +60°)_s$ plate.

4. LAMINATED PLATES

Fibre reinforced plates of various shapes and with different boundary conditions (free, clamped, hinged) commonly occur in practice. Designers need to be able to predict the stiffness parameters and damping values of such plates for conditions such as aeroelasticity, acoustic fatigue and so on. Much attention has been devoted to the stiffness predictions, but very little to damping. Our interest here is mainly in damping and the development of a suitable mathematical model which can be used to predict the damping values of plates laminated from fibres of various types at various orientations. Such is the mathematical complexity of the equation of motion of plates (even those made from isotropic materials) that closed-form solutions exist only for special cases such as hinged (simply supported) rectangular plates, and circular plates (involving Bessel functions). The solution is therefore best obtained using finite element techniques which can readily accommodate different shapes, thicknesses and boundary conditions. Some examples are given by Cawley and Adams[9].

All the plates discussed here are mid-plane symmetric so as to eliminate bending-stretching coupling. It is, however, possible to include this effect in the analysis if asymmetrical laminates were to be used.

The first 10 modes of vibration of a typical plate can be adequately described by using a coarse finite element mesh with six elements per side ($6 \times 6 = 36$ elements for a rectangular plate). The essence of the technique is first to determine the values of strain energy stored due to the stresses relative to the fibre axes of each layer of each element. By using modulus parameters determined from unidirectional bars, it is then possible to determine the total energy stored in each layer of each element. These are then summed through the thickness to give the energy stored in each *element*: this is related to the strains and the mean elasticity matrix for the element. It is then possible to use standard finite element programs and avoid the mathematical complication of working in terms of the standard plate equations. This approach provides the stiffness of the plate, the maximum strain energy U stored in any given mode of vibration, the natural frequencies, and the mode shape.

The ener⟨ dissipated in an element of unit width and length situated in the kth layer can also now be determined. This is done by transforming the stress⟨; and strains to the fibre directions and using the damping properties of 0° bars. The energy dissipated in the element in the kth layer is integrated over the whole area of the plate and the contributions of each layer summed to give ΔU, the total energy dissipated in the plate. The overall specific damping capacity Ψ_{OU} is then given by $\Psi_{OU} = \Delta U / U$. Alternatively, the damping can first be summed through the thickness of the damped element to give a damped element stiffness matrix. This can then be treated by standard finite element techniques.
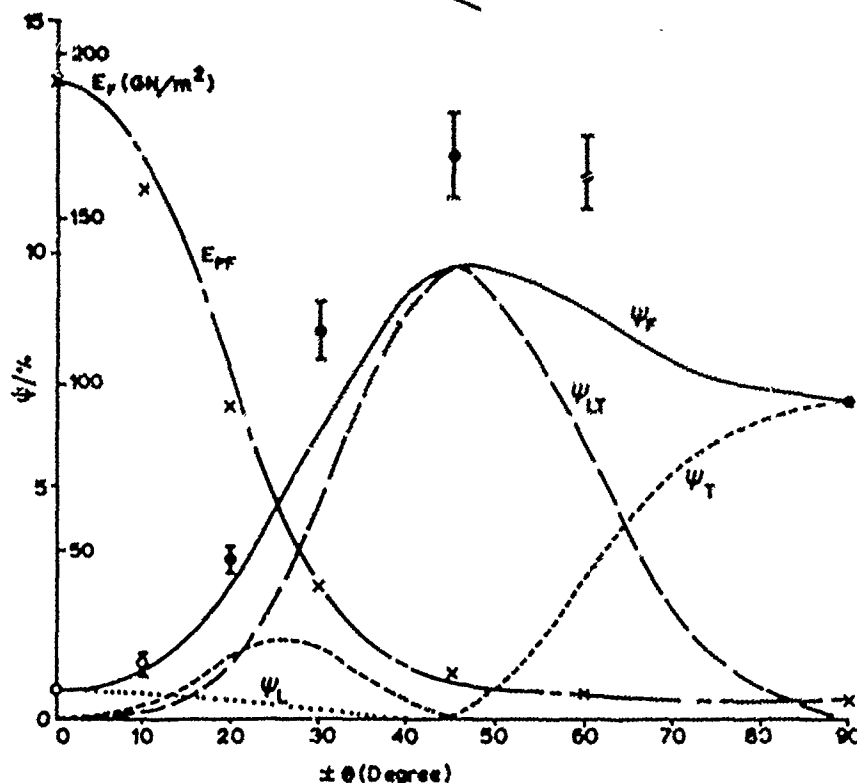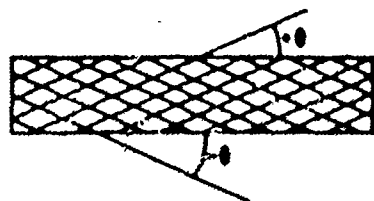
Fig.11.
Variation of flexural Young's modulus E_F and damping Ψ_F with ply angle $\pm \theta$ for HM-S carbon fibre in DX209 epoxy resin, $v_f = 0.5$. Experimental points: x E_F; ● Ψ_F; oΨ_F in vacuo. Free flexure prediction:
— — — E_{FF}
——— total Ψ_{FF};

It is useful to express in mathematical terms the technique described above. The maximum strain energy U is obtained as for an undamped system as follows:

$$U = \tfrac{1}{2} \int_V \{\varepsilon_{ij}\}^T \{\sigma_{ij}\}dV \tag{5}$$

where ε_{ij} and σ_{ij} are the strains and stresses related to the fibre direction. This equation may be reduced to a standard form as

$$U = \tfrac{1}{2}\{\delta\}^T [K] \{\delta\} \tag{6}$$

FG-13

where $\{\delta\}$ is the nodal point displacement matrix. Here, five degrees of freedom for each nodal point and 8 nodal points for each element are used, and $[K]$ is the stiffness matrix. In the evaluation of the maximum strain energy U, the Young's modulus of $0°$ and $90°$ unidirectional fibre reinforced beams, E_L, E_T, and the shear modulus of a $0°$ unidirectional rod G_{LT} are used.
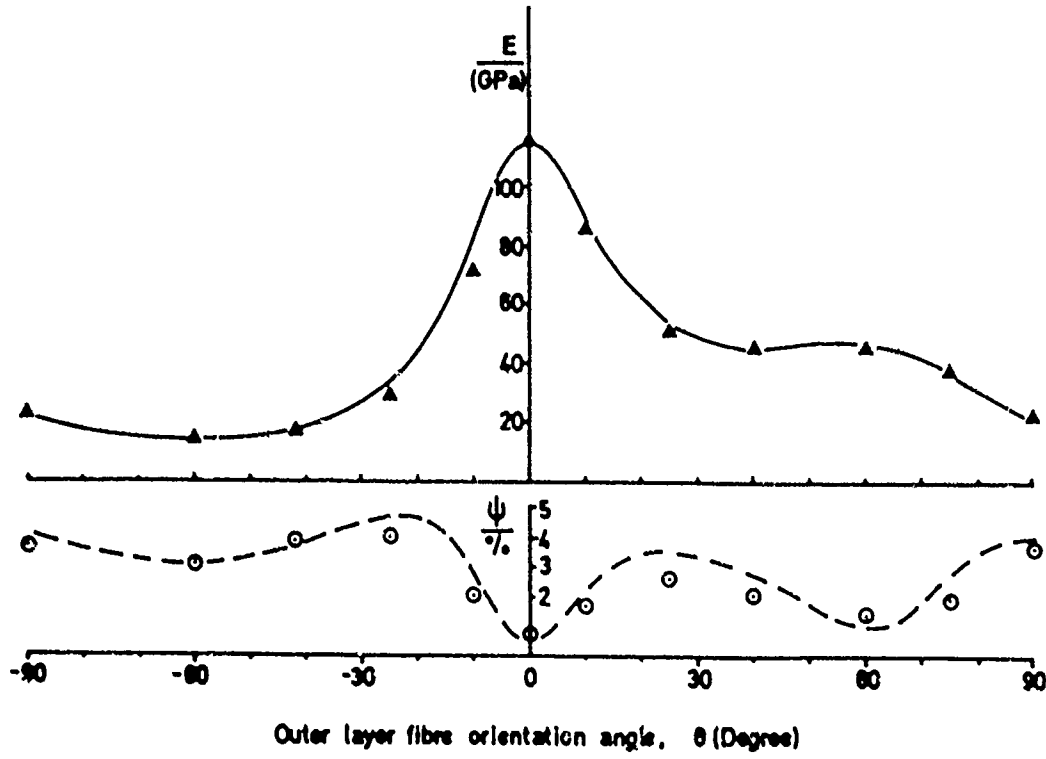
FIG.12   Variation of flexural modulus E, and damping Ψ, with outer layer fibre orientation angle θ, for (0°, -60°, 60°)s in HMS/DX-210

——— theoretical E   Δ experimental E
— — — theoretical Ψ ⊙ experimental Ψ

Now,

$$\Delta U = \int_V \delta(\Delta U) \; dV \tag{7}$$

where $\delta(\Delta U)$ is the energy dissipated in each element, and is defined as

$$\delta(\Delta U) = \delta(\Delta U_1) + \delta(\Delta U_2) + \delta(\Delta U_{23}) + \delta(\Delta U_{13}) + \delta(\Delta U_{12})$$

and

$$\delta(\Delta U_1) = \tfrac{1}{2}\Psi_L \, \varepsilon_{11} \, \sigma_{11}, \quad \delta(\Delta U_2) = \tfrac{1}{2}\Psi_T \, \varepsilon_{22} \, \sigma_{22}$$

$$\delta(\Delta U_{23}) = \tfrac{1}{2}\Psi_{TT} \, \varepsilon_{23}\sigma_{23}, \quad \delta(\Delta U_{13}) = \tfrac{1}{2}\Psi_{LT} \, \varepsilon_{13} \, \sigma_{13}$$

$$\delta(\Delta U_{12}) = \tfrac{1}{2}\Psi_{LT} \, \varepsilon_{12} \, \sigma_{12}$$

Suffix 1 denotes the fibre direction, while 2 and 3 are the two directions transverse to the direction of the fibres. Ψ_L, Ψ_T and Ψ_{LT} are the associated damping capacities which are also obtained from tests on unidirectional beams.

We may now reduce the equation (7) to matrix form as:

$$\Delta U = \tfrac{1}{2} \int_V \{\varepsilon_{ij}\}^T \; [\Psi] \; \{\sigma_{ij}\} \; dV \tag{8}$$

where

$$[\Psi] = \begin{bmatrix} \Psi_L & 0 & 0 & 0 & 0 \\ 0 & \Psi_T & 0 & 0 & 0 \\ 0 & 0 & \Psi_{TT} & 0 & 0 \\ 0 & 0 & 0 & \Psi_{LT} & 0 \\ 0 & 0 & 0 & 0 & \Psi_{LT} \end{bmatrix}$$

Using the sa   e d as with eqn. (5), eqn. (8) may be reduced to

$$\{\delta\}^T \; [K_d] \; \{\delta\} \tag{9}$$

where $\{\delta\}$ is the same matrix as in eqn. (5) and was obtained from the finite element results. $[K_d]$ is the stiffness matrix of the damped system, and it may be evaluated separately. Lin, Ni and Adams[10] described this method in much more detail.

Some results are given for theoretical predictions and experimental measurements on some plates made from glass or HM-S carbon fibres in DX-210 epoxy resin. The plates were made of 8 or 12 layers of preimpregnated fibre to give different laminate orientations; details of the plates used are given in Table 1. The material properties used in the theoretical prediction are given in Table 2. All the values in this table were established either by using beam specimens cut from a unidirectional plate (longitudinal and transverse damping and Young's moduli) or cylindrical specimens (for measuring the shear modulus and damping in torsion). It should be noted that the value of the torsional damping of a 90° fibre orientation rod, Ψ_{23}, is not important in the prediction, since changing it from 6% to 15% gave no significant difference to the theoretical results. In the prediction, Ψ_{23} is taken as the same value as Ψ_{12} which is the value of torsional damping of a

Table 1   Plate Data

Plate number	Material	No of layers	Density kg m^{-3}	v_f	Ply orientation
1	CFRP	8	1446.2	0.342	$(0°, 90°, 0°, 90°)_s$
2	CFRP	12	1636.4	0.618	$(0°, -60°, 60°, 0°, -60°, 60°)_s$
3	GFRP	8	1813.9	0.451	$(0°, 90°, 0°, 90°)_s$
4	GFRP	12	2003.5	0.592	$(0°, -60°, 60°, 0°, -60°, 60°)_s$

N.B.   Suffix s means mid-plane symmetric

Table 2   Moduli and damping values for materials used in the plates

Material	$\dfrac{E_L}{GPa}$	$\dfrac{E_T}{GPa}$	$\dfrac{G_{LT}}{GPa}$	$\dfrac{\Psi_L}{\%}$	$\dfrac{\Psi_T}{\%}$	$\dfrac{\Psi_{LT}}{\%}$	v_1, v_2	v_f
HMS/DX-210	172.1	7.20	3.76	0.45	4.22	7.05	0.3	0.50
Glass/DX-210	37.87	10.90	4.91	0.87	5.05	6.91	0.3	0.50
DX-210/BF$_3$400	3.21	3.21	1.20	6.54	6.54	6.68	0.34	0

unidirectional rod in longitudinal shear.   Because of variations in the fibre
volume fraction of the plates, the material properties used in the theoretical
prediction were each corrected from a standard set given for a 50% fibre volume
fraction, using the method of Ni and Adams[6].

Figures 13 and 14 show for the first six modes the theoretical
prediction and the experimental results of CFRP plates for various fibre
orientations.   On the whole, there is good agreement between the predicted
and measured values.   Mode 6 in plate 3 could not be obtained experimentally
because the input energy from the transient technique used for measuring the
frequency and damping[11] was insufficient.   Figures 15 and 16 give the results
for GFRP plates.   All show good agreement between prediction and measurement.

The effect of air damping and the additional energy dissipation associated
with the supports affect the results of the very low damping modes such as
the 4th mode of plate 1, the 4th mode of plate 3 and so on.   These are
essentially beam modes in which the large majority of the strain energy is
stored in tension/compression in the fibres and not in matrix tension or shear.
However, the results for all the plates used are satisfactory, even when the
specimens have imperfections such as slight variations in thickness and the
nominal angle of the fibres (± 2° to ± 3° error).

No.	Freq. (Hz)	Mode shape	SDC(%)
1	58·10 (64·84)		7·80 (6·65)
2	213·31 (218·9)		0·91 (1·05)
3	243·47 (251·2)		2·50 (2·6)
4	302·51 (305.4)		0·60 (0·92)
5	324·16 (323·5)		1·51 (1·7)
6	441·62 (452·5)		2·74 (3·0)

Outer layer
Fibre direction

No.	Freq. (Hz)	Mode shape	SDC(%)
1	165·17 (155·6)		1·44 (1·40)
2	279·14 (272·0)		0·93 (0·88)
3	347·8 (372·3)		0·63 (0·65)
4	432·57 (407·8)		1·23 (1·26)
5	511·43 (486·1)		0·98 (0·99)
6	800·37 (779)		0·92 —

Outer layer
Fibre direction
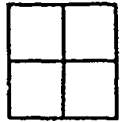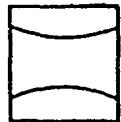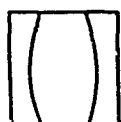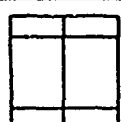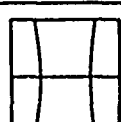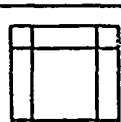
Fig.13
Natural frequency and damping
of various modes of an 8-layer
(0°, 90°, 0°, 90°,90°, 0°, 90°,0°)
carbon FRP plate. (Plate No.1).
Experimental values in brackets.

Fig.14.
Natural frequency and damping of
various modes of a 12-layer (0°, -60°,
60°, 0°, -60°, 60°, 60°, -60°, 0°,
60°, -60°, 0°) carbon FRP plate
(Plate No.2). Experimental values
in brackets.

It can be said that the more the twisting, the higher the damping. For instance, for an 8 layer cross-ply (0°/90°) GFRP plate (see Fig.15) the two beam-type modes, numbers 2 and 3, appear similar, but the relationship of the nodal lines to the outer fibre direction means that the higher mode has much less damping than the lower one. The other modes of vibration of this plate all involve much more plate twisting and hence matrix shear than do modes 2 and 3, and so the damping is higher. *It is important for designers to realise the significance of these results, which show that for all the plates the damping values are different for each mode.*
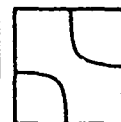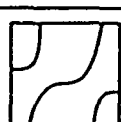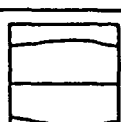
No.	Freq. (Hz)	Mode shape	SDC(%)
1	88.42 (82.21)		7.16 (6.7)
2	131.62 (131.4)		2.47 (2.8)
3	164.46 (159.2)		1.62 (1.9)
4	189.79 (180.5)		4.87 (4.9)
5	208.87 (200.05)		3.73 (3.2)
6	347.16 (326.7)		5.09 (5.8)

Outer layer ——→
Fibre directi‹

No.	Freq (Hz)	Mode shape	SDC (%)
1	108.17 (90.4)		3.74 (4.4)
2	168.64 (144.7)		2.81 (3.5)
3	218.64 (222.3)		1.90 (2.6)
4	280.15 (264.1)		3.40 (3.4)
5	301.00 (281.1)		2.84 (3.0)
6	505.15 (492.6)		2.76 (2.7)

Outer layer ——→
Fibre direction

Fig.15
Natural frequency and damping of various modes of an 8-layer (0°, 90°, 0°, 90°, 90°, 0°, 90°, 0°) glass FRP plate (Plate No.3.). Experimental values in brackets.

Fig.16.
Natural frequency and damping of various modes of a 12-layer (0°, -60°, +60°, 0°, -60°,+60°)$_s$ glass FRP plate (Plate No.4.). Experimental values in brackets.

5. TEMPERATURE

For composites using polymeric matrices, usually eopxy resins, there will exist the usual temperature-frequency relationship. However, unlike most of the high damping polymers used in constrained-layer damping treatments, the influence of frequency is not strong. Fig.17 shows the change of E_L, E_T and G_{LT} of a unidirectional composite over the range -50°C to +200 °C (-60°F to +390°F). A logarithmic scale is used, and it can be seen that the two matrix dependent moduli, E_T and G_{LT} are significantly reduced at temperatures above 150 °C (300°F). Indeed, the transverse specimen (90°) could not be tested at temperatures above this as it sagged under its own weight. In contrast, the 0° modulus was essentially unaffected until the matrix became shear soft: at this point, the deformation became more by shear than by bending and fibre deformation.

The damping behaviour (Fig.18) is also presented in a logarithmic scale,
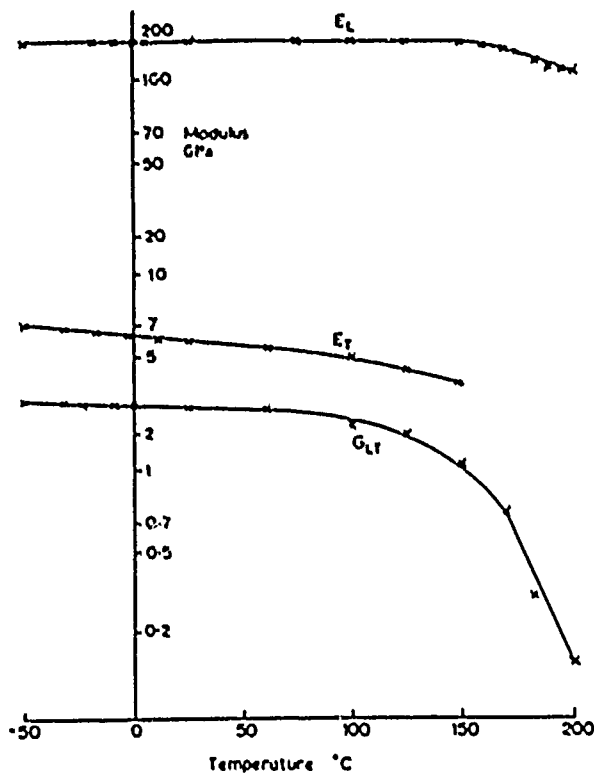
Fig.17. Variation of longitudinal modulus E_L, transverse modulus E_T and longitudinal shear modulus G_{LT} with temperature for HM-S carbon fibre in DX209 epoxy resin; $v_f = 0.5$.
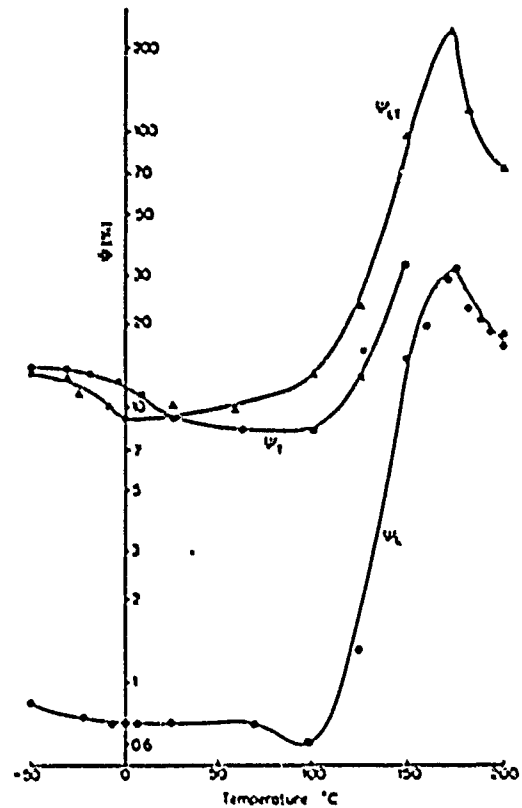
Fig.18. Variation of longitudinal damping Ψ_L, transverse damping Ψ_T, and longitudinal shear damping Ψ_{LT} with temperature for HM-S carbon fibre in DX209 epoxy resin; $v_f = 0.5$.

and shows the very much higher damping levels available in shear and transverse loading than in longitudinal tension/compression. The Ψ_L damping is due not only to increased matrix damping according to the law of mixtures term, but also to the enhanced shear deformation referred to above. The damping peak at about 180°C (360°F) represents classical viscoelastic behaviour. Testing beyond 200 °C (390°F) was impossible owing to charring.

At lower temperatures, there was evidence of an increase in damping: this is related to the β relaxation phenomenon, and is illustrated in Fig.19 for a cryogenic grade woven glass fibre/epoxy material tested down to 4K (−269 °C, −516°F).

6. COMPARISONS WITH METALS

Fig.20 shows the vriation of damping with cyclic stress amplitude for a range of common structural metals. It can be seen that composites provide slightly higher damping than steels, but significantly less than conventional high-damping alloys. On the other hand, low-weight, high-strength alloys such as aluminium and titanium give extremely low damping and values of less than 0.01% SDC have been reported.[12]
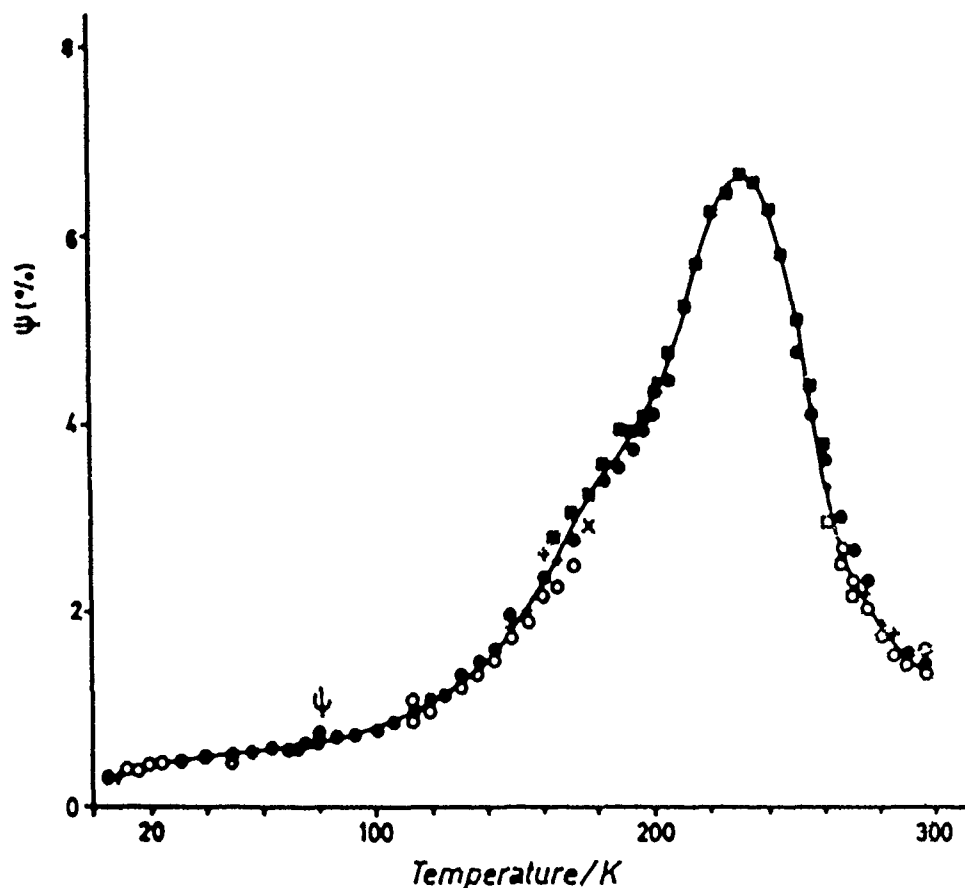
FIG.19.
Variation of specific damping capacity, Ψ, with temperature (°K) for a glass cloth/epoxy G10 CR specimen.
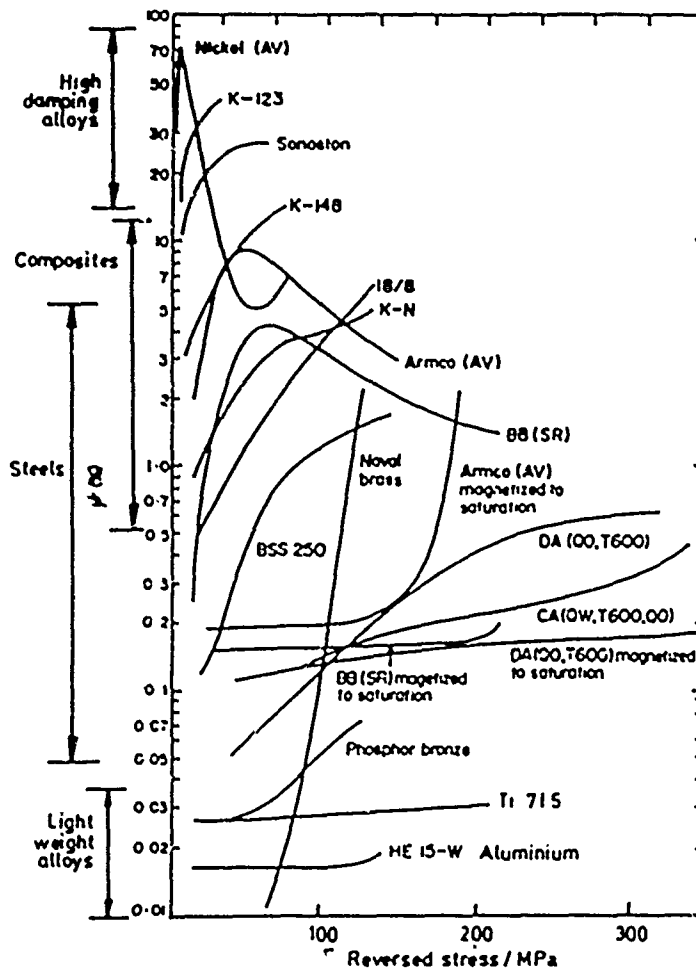
FIG.20.
Damping versus stress for a range of ferrous and nonferrous metals.
Nickel (AV): annealed in vacuum; K-123, K-148, K-N: grades of
cast iron; 18/8: stainless steel; Armco (AV): low carbon iron,
annealed in vacuum; BB(SR): 0.12% carbon steel, stress relieved;
BSS 250, Naval brass, phosphor bronze: copper-based alloys;
CA, DA: high-carbon steels; HE 15-W: Duralumin aluminium alloy;
Ti715: titanium alloy.

REFERENCES

1. R. D. Adams and D. G. C. Bacon (1973). J.Compos.Matls., 7, 53-67.

2. D. F. Adams and D. R. Doner (1967). J.Compos.Matls., 1, 4-17.

3. Z. Hashin (1970). Int.Jnl.Solids & Structs., 6, 797-804.

4. R. D. Adams and D. F. Short (1973). J.Phys.D:Appl.Phys., 6, 1032-1039.

5. R. D. Adams (1975). J.Phys.D:Appl.Phys., 8, 738-748.

6. R. G. Ni and R. D. Adams (1984). Composites, 15, 193-199.

7. R. D. Adams and D. G. C. Bacon (1973). J.Compos.Matls., 7, 402-428.

8. R. G. Ni and R. D. Adams (1984). J.Compos.Matls., 18, 104-121.

9. P. Cawley and R. D. Adams (1978). J.Compos.Matls., 12, 336-347.

10. D. X. Lin, R. G. Ni and R. D. Adams (1984). J.Compos.Matls., 18, 132-152.

11. D. X. Lin and R. D. Adams (1985). J.Phys.E.: Sci.Instr., 18, 161-165.

12. G.A. Cottell, K. M. Entwistle and F. C. Thompson (1948). J.Inst.Metals, 74, 373-424.

A DESIGN METHODOLOGY FOR ESTIMATING THE DAMPING IN LAMINATED AND FIBRE-REINFORCED PLATES

by Dr R.D. Adams
University of Bristol, Bristol, England

and
R.F. Lambert
ESDU International Ltd, London, England

Abstract

The methodology used within a computer program to estimate the damping in laminated and fibre-reinforced plates is described. The simplifying assumptions made to provide rapid estimates of damping are detailed. The damping values, for free-free plates, obtained using the program are compared with measured values and those predicted using a more exact finite element technique. The program is shown to provide damping data suitable for use in engineering design calculations.

1. INTRODUCTION

The use of fibre-reinforced plastics in high performance structures, such as those used in the aerospace industry, gives rise to a need for reliable procedures for estimating the structural properties required for dynamic response calculations. The properties of interest to structural dynamicists are the material elastic properties (e.g. moduli of elasticity) and damping information. Fibre-reinforced panel-type structures are usually manufactured by layering sheets of pre-impregnated fibres together. By varying the relative orientations of the fibres in the different layers, the designer is able to manipulate both the elastic properties and the damping of the structure to meet the requirements for a specific application.

Unlike conventional metallic built-up structures, fibre-reinforced laminated structures are often constructed using adhesive joints where there are fewer additional sources of energy dissipation associated, for example, with bolted or riveted joints. Therefore, for these fibre-reinforced structures, material damping contributes significantly to the overall damping in any mode of vibration. The reduction of the structural component of damping in fibre-reinforced materials may be partly redressed by the suitable choice of matrix and fibre constituents to give optimum material damping.

The purpose of this paper is to outline a methodology for estimating the damping in a multilayered laminate vibrating in one of its lower frequency natural modes. Using this methodology and beam characteristic functions to define mode shapes, a computer program[1] (suitable for running on a desk-top computer) has been developed for balanced symmetric laminates. In plates of this balanced symmetric type, laminae having the same material properties, and orientations of their principal axes of orthotropy, are symmetrically arranged about the plate mid-plane. Damping results for free-free plates, evaluated using the computer program, are compared with those from a finite element method and with measured values.

2. DAMPING IN COMPOSITES

For composite materials, damping is taken to be any process within the body of the material in which energy is dissipated. The principal processes are associated with hysteresis losses within each of the constituent materials and interfacial effects at the fibre-matrix interfaces. Damping is dependent on the cyclic stress amplitude, but it has been shown (see for example Adams and Short[2]) that for small vibration amplitudes the variation of damping with stress amplitude is negligible.

When considering fibre-reinforced laminates it is convenient to express damping in terms of specific damping capacity, ψ. Specific damping capacity is the ratio of energy dissipated in a unit volume per stress cycle to the maximum strain energy per unit volume. The relationship between specific damping capacity and other common measures of damping are given by Bert[3]. For harmonic vibration these relationships are summarised in the table below. The tabulated values are equivalent (e.g. $\psi = 4\pi\delta$) for small values of damping. The relationships are sufficiently accurate for use in most engineering

applications.

Viscous damping ratio	Specific damping capacity	Magnification factor	Logarithmic decrement	Loss factor
δ	$\dfrac{\psi}{4\pi}$	$\dfrac{1}{2Q}$	$\dfrac{\Delta}{2\pi}$	$\dfrac{\eta}{2}$

In this paper the specific damping capacity for an individual lamina is considered in terms of damping components in longitudinal flexure, ψ_L, transverse flexure, ψ_T, and longitudinal shear, ψ_{LT}. For a particular fibre-reinforced lamina it is preferable to obtain values of the three damping components by direct measurement. Typical test procedures are described by Adams[3] et al. If measured values of damping for a particular lamina are not available, approximate values of the damping components may be obtained from curves in [1] where damping values are presented in terms of the volume proportion of fibre in a representative volume of lamina material.

3. ESTIMATION OF DAMPING IN LAMINATED AND FIBRE-REINFORCED PLATES

3.1 Stress-strain relationships for a single layer

Considering a single unidirectional-fibre layer in a laminated plate shown in Figure 1. The stress/strain relationships for the orthotropic k^{th} lamina, referred to the (α, β) coordinates of that layer, are

$$\sigma_i^k = C_{ij}^k \epsilon_j^k , \tag{1}$$

and
$$\epsilon_i^k = S_{ij}^k \sigma_j^k , \tag{2}$$

where C_{ij} and S_{ij} are the lamina stiffness and compliance matrices respectively.

The components of C_{ij} are related to the layer engineering constants E_α, E_β, $G_{\alpha\beta}$, $\nu_{\alpha\beta}$ and $\nu_{\beta\alpha}$ by the following

$$C_{11} = \frac{E_\alpha}{1 - \nu_{\alpha\beta}\nu_{\beta\alpha}} , \quad C_{22} = \frac{E_\beta}{1 - \nu_{\alpha\beta}\nu_{\beta\alpha}} , \quad C_{66} = G_{\alpha\beta}$$

and
$$C_{12} = \frac{\nu_{\beta\alpha}E_\alpha}{1 - \nu_{\alpha\beta}\nu_{\beta\alpha}} = C_{21} = \frac{\nu_{\alpha\beta}E_\beta}{1 - \nu_{\alpha\beta}\nu_{\beta\alpha}} . \tag{3}$$

Since the stresses are related to fibre axes,

$$S_{16} = S_{26} = 0 ,$$

$$S_{11} = \frac{1}{E_\alpha} , \quad S_{22} = \frac{1}{E_\beta} , \quad S_{66} = \frac{1}{G_{\alpha\beta}} ,$$

and
$$S_{12} = S_{21} = -\frac{\nu_{\alpha\beta}}{E_{\alpha}} . \tag{4}$$

In terms of the plate mid-plane reference axes (x, y), the stress-strain relationship is given by

$$\sigma_i^k = b_{ij}^k \epsilon_j^k , \tag{5}$$

where b_{ij}^k is the transformed stiffness matrix of the kth layer whose fibre axis is at an angle θ to the plate reference axis.

$$b_{ij}^k = T_T C_{ij}^k T , \tag{6}$$

where
$$T = \begin{bmatrix} \cos^2\theta & \sin^2\theta & \tfrac{1}{2}\sin2\theta \\ \sin^2\theta & \cos^2\theta & -\tfrac{1}{2}\sin2\theta \\ -\sin2\theta & \sin2\theta & \cos2\theta \end{bmatrix} \tag{7}$$

and T_T is the transpose of the T matrix.

3.2   Stiffnesses of an assembly of layers

In a single plate consisting of an assembly of ℓ layers, the in-plane and flexural load deformation reltionships for the plate (using the load sign convention shown in Figure 2) can be written as follows,

$$\begin{bmatrix} N_x \\ N_y \\ N_{xy} \\ M_x \\ M_y \\ M_{xy} \end{bmatrix} = \begin{bmatrix} A_{11} & A_{12} & A_{16} & B_{11} & B_{12} & B_{16} \\ A_{12} & A_{22} & A_{26} & B_{12} & B_{22} & B_{26} \\ A_{16} & A_{26} & A_{66} & B_{16} & B_{26} & B_{66} \\ B_{11} & B_{12} & B_{16} & D_{11} & D_{12} & D_{16} \\ B_{12} & B_{22} & B_{26} & D_{12} & D_{22} & D_{26} \\ B_{16} & B_{26} & B_{66} & D_{16} & D_{26} & D_{66} \end{bmatrix} \begin{bmatrix} \epsilon_x \\ \epsilon_y \\ \epsilon_{xy} \\ \partial^2 w/\partial x^2 \\ \partial^2 w/\partial y^2 \\ 2\partial^2 w/\partial x\partial y \end{bmatrix} \tag{8}$$

which is usually written in the shortened form,

$$\begin{bmatrix} N \\ M \end{bmatrix} = \begin{bmatrix} A & B \\ B & D \end{bmatrix} \begin{bmatrix} \epsilon \\ K \end{bmatrix} . \tag{9}$$

The plate stiffnesses A, B and D are given by

$$A = \sum_{k=1}^{k=\ell} t^k b^k , \quad B = \sum_{k=1}^{k=\ell} t^k z^k b^k \quad \text{and} \quad D = \sum_{k=1}^{k=\ell} \left[t^k (z^k)^2 + I^k \right] b^k , \tag{10}$$

where $I^k = (t^k)^3/12$ and is usually negligibly small in relation to $t^k(z^k)^2$.

The in-plane and flexural load deformation relationships may alternatively be written as

$$\begin{bmatrix} \epsilon \\ K \end{bmatrix} = \begin{bmatrix} A' & B' \\ B' & D' \end{bmatrix} \begin{bmatrix} N \\ M \end{bmatrix} , \tag{11}$$

where
$$\begin{aligned} A' &= A^{-1} + A^{-1}B(D - BA^{-1}B)^{-1}BA^{-1} , \\ B' &= -A^{-1}B(D - BA^{-1}B)^{-1} , \end{aligned} \tag{12}$$
and
$$D' = (D - BA^{-1}B)^{-1} .$$

The behaviour of the laminate is governed by the strain distribution across the thickness of the laminate. Combining the in-plane strain with the flexural strain, the total strain (linear strain distribution through the laminate thickness) is

$$\varepsilon(z) = \varepsilon_o + zK \quad . \tag{13}$$

For the vibration of a general laminate, in a single mode, a cross-section is subjected to a system of cyclic forces and moments at circular frequency ω. These can be represented as

$$\begin{bmatrix} \bar{N} \\ \bar{M} \end{bmatrix} \sin \omega\tau, \text{ where } \begin{bmatrix} N \\ M \end{bmatrix} \text{ are the peak values.}$$

Under this system, the stresses in the kth layer (referred to the plate axes) are

$$\sigma_1^k = b^k \left[(A' + zB')N + (B' + zD')M\right] \sin \omega\tau \quad . \tag{14}$$

The resultant stress field in the fibre axis can be evaluated using the transformation

$$\sigma_{(\alpha,\beta)} = T \ \sigma_{(x,y)} \quad , \tag{15}$$

i.e.

$$\begin{bmatrix} \sigma_\alpha \\ \sigma_\beta \\ \sigma_{\alpha\beta} \end{bmatrix} = \begin{bmatrix} \cos^2\theta & \sin^2\theta & \tfrac{1}{2}\sin 2\theta \\ \sin^2\theta & \cos^2\theta & -\tfrac{1}{2}\sin 2\theta \\ -\sin 2\theta & \sin 2\theta & \cos 2\theta \end{bmatrix} \begin{bmatrix} \sigma_x \\ \sigma_y \\ \sigma_{xy} \end{bmatrix} \tag{16}$$

3.3 Damping in laminated composite plates

The theory used to estimate the specific damping capacity in laminated composite plates is that developed by Adams and Bacon[4].

Taking an element of the kth layer, of unit width and length and distance z from the midplane, the strain energy associated with σ_α, σ_β and $\sigma_{\alpha\beta}$ in this element can be separated into three components

$$\delta U = \delta U_\alpha + \delta U_\beta + \delta U_{\alpha\beta} \quad , \tag{17}$$

where the strain energy stored in tension/compression in the fibre axis is

$$\delta U_\alpha = \tfrac{1}{2} \sigma_\alpha (S_{11} \sigma_\alpha + S_{12} \sigma_\beta) \ \delta z \quad , \tag{18}$$

the strain energy stored in tension/compression transverse to the fibre is

$$\delta U_\beta = \tfrac{1}{2} \sigma_\beta (S_{12} \sigma_\alpha + S_{22} \sigma_\beta) \ \delta z \quad , \tag{19}$$

and the strain energy stored in longitudinal shear is

$$\delta U_{\alpha\beta} = \tfrac{1}{2} \sigma_{\alpha\beta}^2 \ S_{66} \ \delta z \quad . \tag{20}$$

From the definition of specific damping capacity, the energy dissipated in the element of the kth layer may be written in terms of the layer damping components

FH-5

ϕ_L, ϕ_T and ϕ_{LT}. It is assumed that these damping components are independent of stress amplitude.

Energy dissipated in longitudinal tension/compression is

$$\delta(\Delta U_\alpha) = \tfrac{1}{2} \phi_L \, \sigma_\alpha \, (S_{11} \, \sigma_\alpha + S_{12} \, \sigma_\beta) \, \delta z \ , \tag{21}$$

energy dissipated in transverse tension/compression is

$$\delta(\Delta U_\beta) = \tfrac{1}{2} \phi_T \, \sigma_\beta \, (S_{12} \, \sigma_\alpha + S_{22} \, \sigma_\beta) \, \delta z \ , \tag{22}$$

and energy dissipated in longitudinal shear is

$$\delta(\Delta U_{\alpha\beta}) = \tfrac{1}{2} \phi_{LT} \, \sigma_{\alpha\beta}{}^2 \, S_{66} \, \delta z \ . \tag{23}$$

Hence the total energy dissipated in the element of the kth layer may be written as

$$\delta(\Delta U) = \delta(\Delta U_\alpha) + \delta(\Delta U_\beta) + \delta(\Delta U_{\alpha\beta}) \ . \tag{24}$$

The total energy dissipated in the kth layer of the laminate is given by the volume integral

$$\Delta U = \int_0^a \int_0^b \int_{z_{k-1}}^{z_k} \delta U \; dx \; dy \; dz \ , \tag{25}$$

where a and b are the dimensions of the rectangular plate in the x and y directions respectively, and z_k and z_{k-1} are the ordinates of the upper and lower surfaces of the kth layer.

The total energy dissipated in the plate is found by summing through the layers of the plate

$$\Delta U_{TOT} = \sum_{k=1}^N \Delta U \ . \tag{26}$$

The maximum strain energy stored by the plate under the peak force and moment resultants N and M is

$$U = \tfrac{1}{2} [N] [\epsilon] + \tfrac{1}{2} [M] [K] \ . \tag{27}$$

The specific damping capacity of the laminate, in the mode considered, is

$$\psi = \frac{\Delta U_{TOT}}{U} \ . \tag{28}$$

3.4   Approximate analysis for plate damping

To reduce the complexity of the analysis for damping it is convenient to make a number of simplifying assumptions. Firstly it is assumed that laminates have symmetric layups so that $B = 0$, and the effect of inplane forces on bending is neglected. Neglecting inplane forces, $N_x = N_y = N_{xy} = 0$, the moment

FH-6

resultants are given by Ashton and Whitney[5] as

$$M_x = -D_{11} \frac{\partial^2 w}{\partial x^2} - 2D_{16} \frac{\partial^2 w}{\partial x \partial y} - D_{12} \frac{\partial^2 w}{\partial y^2} ,$$

$$M_y = -D_{12} \frac{\partial^2 w}{\partial x^2} - 2D_{26} \frac{\partial^2 w}{\partial x \partial y} - D_{22} \frac{\partial^2 w}{\partial y^2} , \qquad (29)$$

$$M_{xy} = -D_{16} \frac{\partial^2 w}{\partial x^2} - 2D_{66} \frac{\partial^2 w}{\partial x \partial y} - D_{26} \frac{\partial^2 w}{\partial y^2} .$$

Considering only symmetric laminates (B = 0) the sub-matrices of Equation (11) reduce to

$$A' = A^{-1} , \quad B' = 0 \quad \text{and} \quad D' = D^{-1} . \qquad (30)$$

Using the above relationships, and neglecting in-plane forces (N = 0), Equation (14) giving the stresses in the kth layer of a laminate (referred to the plate x, y axes) becomes

$$\sigma_i^k = z b^k D^{-1} M. \qquad (31)$$

The lamina stresses in the fibre axes are given by Equation (15), i.e.

$$\sigma_{(\alpha,\beta)} = T \sigma_{(x,y)} . \qquad (32)$$

When in-plane forces are neglected the maximum strain energy stored in the plate (from Equation (27)) becomes

$$U = \tfrac{1}{2} [M] [K] . \qquad (33)$$

To evaluate [M] it is necessary to make an assumption of the deflected shape of the plate. It is usual to assume a deflected shape in the form of a series

$$w = \sum_{i=1}^{m} \sum_{j=1}^{n} c_{ij} \Phi_i(x) \theta_j(y) . \qquad (34)$$

In [1], and for the calculation of damping values presented in this paper, the deflected shapes were based on characteristic beam functions. The deflected shapes for the particular plate edge conditions and modes of vibration considered are given in Appendix A.

Having assumed an appropriate mode shape and evaluated the plate and layer stiffness parameters, values of M and K may be obtained from Equation (29) and

$$K = \begin{bmatrix} \partial^2 w / \partial x^2 \\ \partial^2 w / \partial y^2 \\ 2 \partial^2 w / \partial x \partial y \end{bmatrix} \qquad (35)$$

respectively, from which U may be calculated using Equation (33).

Values of the layer stresses, referred to the plate x, y-axes, may be evaluated using Equation (31) and transformed to the fibre axes using Equation (32).

FH-7

These stresses may then be substituted into Equations (21) to (23) to evaluate the components of energy dissipation which are then summed as indicated by Equation (25). Summing the energy dissipation through the plates gives ΔU_{TOT} which may be substituted into Equation (28) to give the specific damping capacity for the mode of vibration considered.

4. COMPARISON BETWEEN ESTIMATED AND MEASURED VALUES OF DAMPING

Tables 1 to 5 show a comparison between estimated and measured values of specific damping capacity in various modes of vibration of square, free-free plates. The measured damping values are given by Lin et al[6]. In the tables, estimated values of specific damping capacity are given for both the method of analysis described in this paper and values obtained using a finite element method. The latter damping values are also taken from Lin's paper.

In Tables 1 and 2 results are presented for an eight layer carbon fibre-reinforced plastic laminate, each layer being reinforced by unidirectional fibres. The relative orientations of the fibres in each layer are given in the table, and in each case the layering is symmetric about the mid-plane of the plate. In Tables 3 to 5 damping values are given for similar laminated plates in which glass fibre is the reinforcing material.

The tabulated data show good agreement between the measured values of damping and the values estimated using both the finite element analysis and the analysis method described in this paper. In the finite element analysis, additional energy dissipation terms are used to account for transverse shear deformation and rotary inertia effects in the laminated plate.

5. DISCUSSION
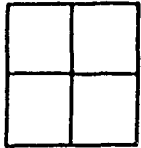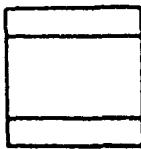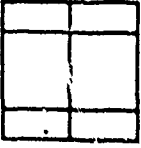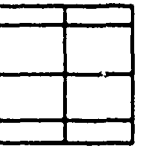
In this paper, it is shown that the method of analysis, described in Section 3, to obtain damping in laminated and fibre-reinforced plates gives values of damping in good agreement with measured values.

The comparison with measured damping values are for square plates where, for clamped or free edge conditions, nodal lines may not be parallel to the plate edges. Such non-parallel nodal lines readily occur, for instance, when a square laminate is constructed from alternative layers with fibre orientations at $\pm 45^0$. For these cases the simple deflected shapes given in Appendix A are not adequate for the prediction of reliable damping values.

The results presented suggest that the simple methodology for damping estimation is suitable for use in engineering design. The method has been programmed in both BASIC and FORTRAN computer languages and may be run on desk-top computers to obtain rapid estimates of damping in a selected mode of vibration. The method has been proved to be viable and its planned extension to provide more reliable damping values for modes in which nodal lines are not parallel to the plate edges is justified.

6. REFERENCES
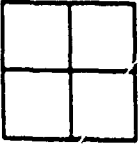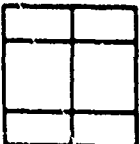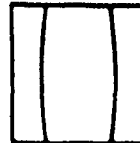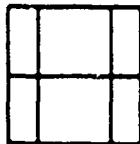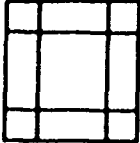
1. ESDU: "Estimation of damping in laminated and fibre-reinforced plates". Item No. 85012, Engineering Sciences Data Unit, London, June 1985.

2. R.D. ADAMS and D. SHORT: "The effect of fibre diameter on the dynamic properties of glass-fibre-reinforced polyester resin". J. Phys. D: Appl. Phys., Vol. 6, pp. 1032-1039, 1973.

3. R.D. ADAMS et al: "The dynamic properties of unidirectional carbon and glass fibre reinforced plastics in torsion and flexure". J. Composite materials, Vol. 3, pp. 594-603, October 1969.

4. R.D. ADAMS and D.G.C. BACON: "Effect of fibre orientation and laminate geometry on the dynamic properties of CFRP." J. Composite Materials, Vol., 7, pp. 402-428, October 1973.

5. J.E. ASHTON and J.M. WHITNEY: "Theory of laminated plates". Progress in Material Sciences Series, Vol. IV. Technomic Pub. Co. Inc., Stamford, USA, 1970.

6. D.X. LIN; R.G. NI and R.D. ADAMS: "Prediction and measurement of virbational damping parameters of carbon and glass fibre-reinforced plastic plates". J. Composite Materials, Vol. 18, No. 2, pp. 132-152, March 1984.

7. R.E.D. BISHOP and D.C. JOHNSON: "Vibration analysis tables". Cambridge University Press, 1956. (Alternative reference: "Mechanics of vibration". Cambridge University Press, 1960.)

Mode numbers m, n	Mode shape	Specific damping capacity %		
		Measured damping	Finite element analysis (Ref. 6)	Analysis method in this paper (Ref. 1)
2, 2		7.0	6.76	6.89
1, 3		4.9	4.28	4.16
2, 3		5.4	5.89	5.21
1, 4		4.7	4.13	4.16
2, 4		4.8	5.11	4.58
3, 1		-	0.47	0.44

Fibre direction ------→

DAMPING IN VARIOUS MODES OF AN 8 LAYER (ALL 0^0) CARBON FRP PLATE
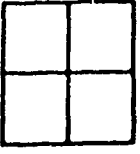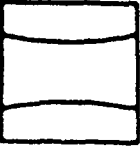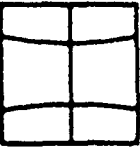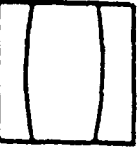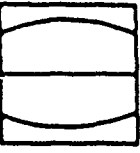
TABLE 1

Mode numbers m, n	Mode shape	Specific damping capacity %		
		Measured damping	Finite element analysis (Ref. 6)	Analysis method in this paper (Ref. 1)
2, 2		6.65	7.80	8.18
1, 3		1.05	0.91	0.97
2, 3		2.6	2.5	1.48
3, 1		0.92	0.60	0.67
3, 2		1.7	1.51	0.94
3, 3		3.0	2.74	2.92

Outer layer
Fibre direction ————→

DAMPING IN VARIOUS MODES OF AN 8 LAYER $(0^0, 90^0, 0^0, 90^0)_s$ CARBON FRP PLATE
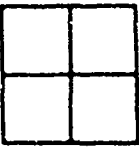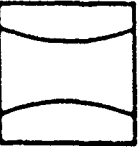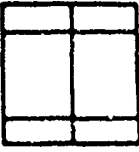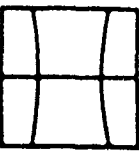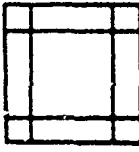
TABLE 2

Mode numbers m, n	Mode shape	Specific damping capacity %		
		Measured damping	Finite element analysis (Ref. 6)	Analysis method in this paper (Ref. 1)
2, 2		6.0	5.99	6.21
1, 3		4.8	4.44	4.71
2, 3		5.8	5.40	5.22
3, 1		1.3	0.93	0.82
3, 2		2.8	2.80	1.55
1, 4		4.0	4.34	4.71

Fibre direction ------->

DAMPING IN VARIOUS MODES OF AN 8 LAYER (ALL 0^0) GLASS FRP PLATE

TABLE 3
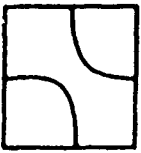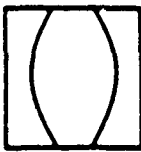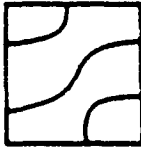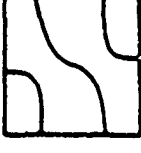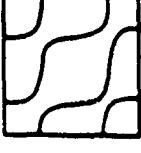
FH-12

Mode numbers m, n	Mode shape	Specific damping capacity %		
		Measured damping	Finite element analysis (Ref. 6)	Analysis method in this paper (Ref. 1)
2, 2		6.7	7.16	7.30
1, 3		2.8	2.47	2.58
3, 1		1.9	1.62	1.41
2, 3		4.9	4.87	3.64
3, 2		3.2	3.73	2.35
3, 3		5.8	5.09	5.39

Outer layer
Fibre direction ———————→

DAMPING IN VARIOUS MODES OF AN 8 LAYER $(0^0, 90^0, 0^0, 90^0)_s$ GLASS FRP PLATE

TABLE 4

FH-13

Mode numbers m, n	Mode shape	Specific damping capacity %		
		Measured damping	Finite element analysis (Ref. 6)	Analysis method in this paper (Ref. 1)
2, 2		5.4	4.97	4.31
1, 3		3.1	2.24	2.91
3, 1		2.5	1.71	1.92
2, 3		4.3	3.81	3.27
3, 2		3.5	3.13	2.41
3, 3		3.8	3.92	3.68

Outer layer
Fibre direction ————→

DAMPING IN VARIOUS MODES OF AN 8 LAYER $(0^0, 90^0, 45^0, -45^0)_s$ GLASS FRP PLATE

TABLE 5
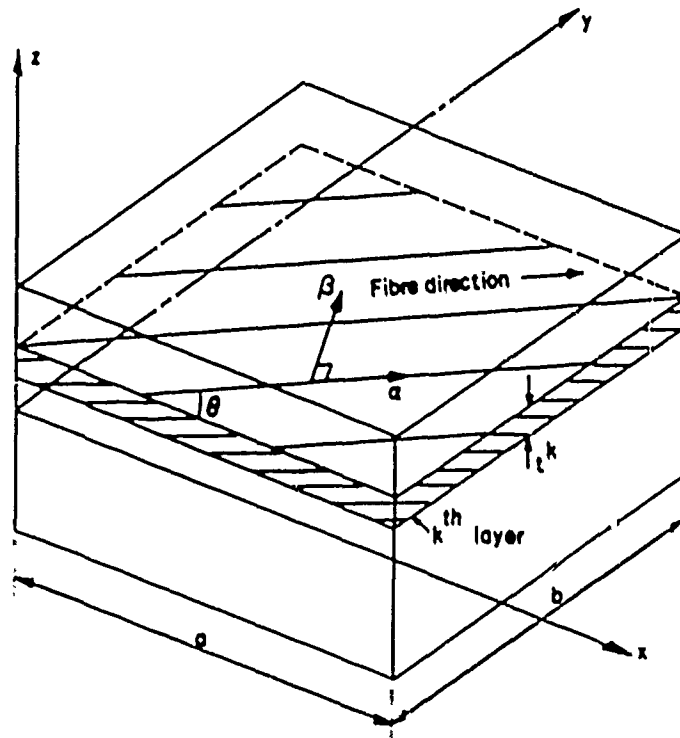
FIGURE 1 LAMINATED PLATE
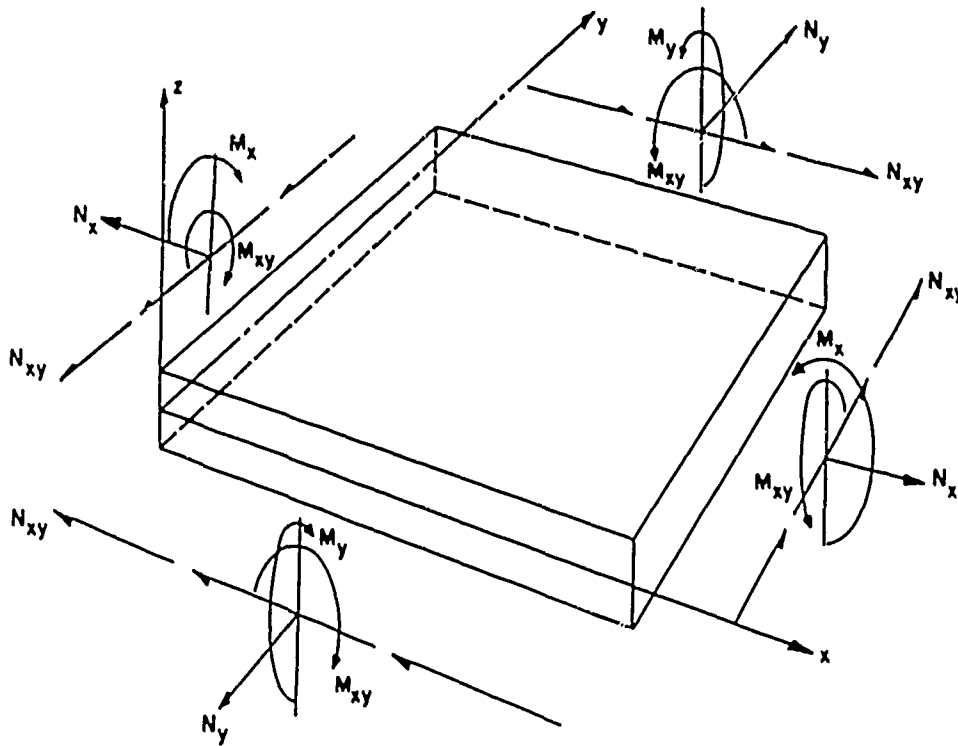
FIGURE 2. LOADING SIGN CONVENTION

FH-15

APPENDIX A

Deflected shapes

The deflected shape in a mode of vibration is defined conveniently in terms of mode numbers m and n. These numbers may be related to the nodal lines, provided that these lines are parallel, or approximately parallel, to the sides of the plate. For these cases m and n are one plus the number of nodal lines crossing any line parallel to the x-axis and y-axis respectively. In this definition plate edges, clamped or simply-supported, are not counted as nodal lines.

In the computer program in [1], the mode shapes are assumed to be products of beam characteristic functions,

$$w = c_{mn} \, \Phi_m(x) \, \Theta_n(y) \, .$$

These shapes, for each of the boundary conditions considered, are defined as follows.

A1. All plate edges simply-supported

$$\Phi_m(x) = \sin \frac{m\pi x}{a} \, ,$$

and

$$\Theta_n(y) = \sin \frac{n\pi y}{b} \, .$$

A2. All plate edges clamped

$$\Phi_m(x) = \cosh \lambda_m x - \cos \lambda_m x - \gamma_m (\sinh \lambda_m x - \sin \lambda_m x) \, ,$$

and

$$\Theta_n(y) = \cosh \lambda_n y - \cos \lambda_n y - \gamma_n (\sinh \lambda_n y - \sin \lambda_n y) \, ,$$

where λ_m and λ_n are the roots of the frequency equations

$$\cos \lambda_m a \, \cosh \lambda_m a = 1 \, ,$$
$$\cos \lambda_n b \, \cosh \lambda_n b = 1 \, ,$$

and

$$\gamma_m = \frac{\cosh \lambda_m a - \cos \lambda_m a}{\sinh \lambda_m a - \sin \lambda_m a} \, ,$$

$$\gamma_n = \frac{\cosh \lambda_n b - \cos \lambda_n b}{\sinh \lambda_n b - \sin \lambda_n b} \, .$$

The constant $\lambda_m a$, $\lambda_n b$, γ_m and γ_n are tabulated for various values of m and n by Bishop and Johnson[7].

A3. All plate edges free

For the plate having all edges free there are a number of combinations of m and

FH-16

n that must be independently considered to account for the rigid-body modes.

$m = n = 1$ rigid-body translation mode.

$m = 1, \quad n = 2$ rigid-body rotation modes

$m = 2, \quad n = 1$

(i) $m > 3$ and $n > 3$

$$\Phi_m(x) = \cosh \lambda_m x + \cos \lambda_m x - \gamma_m (\sinh \lambda_m x + \sin \lambda_m x) \, ,$$

$$\Theta_n(y) = \cosh \lambda_n y + \cos \lambda_n y - \gamma_n (\sinh \lambda_n y + \sin \lambda_n y) \, .$$

Values of $\lambda_m a$, $\lambda_n b$, γ_m and γ_n are the same as for the plate with clamped edges.

(ii) $m > 3$ and $n = 2$

$$\Phi_m(x) = \cosh \lambda_m x + \cos \lambda_m x - \gamma_m (\sinh \lambda_m x + \sin \lambda_m x)$$

$$\Theta_n(y) = \sqrt{3} \left(1 - \frac{2y}{b} \right)$$

(iii) $m = 2$ and $n > 3$

$$\Phi_m(x) = \sqrt{3} \left(1 - \frac{2x}{a} \right)$$

$$\Theta_n(y) = \cosh \lambda_n y + \cos \lambda_n y - \gamma_n (\sinh \lambda_n y + \sin \lambda_n y)$$

(iv) $m = n = 2$

$$\Phi_m(x) = \sqrt{3} \left(1 - \frac{2x}{a} \right)$$

$$\Theta_n(y) = \sqrt{3} \left(1 - \frac{2y}{b} \right)$$

(v) $m > 3$ and $n = 1$

$$\Phi_m(x) = \cosh \lambda_m x + \cos \lambda_m x - \gamma_m (\sinh \lambda_m x + \sin \lambda_m x)$$

$$\Theta_n(y) = 1$$

(vi) $m = 1$ and $n > 3$

$$\Phi_m(x) = 1$$

$$\Theta_n(y) = \cosh \lambda_n y + \cos \lambda_n y - \gamma_n (\sinh \lambda_n y + \sin \lambda_n y)$$

DAMPING MEASUREMENTS BY HILBERT TRANSFORM ON
COMPOSITE MATERIALS

Alessandro Agneni and Luigi Balis Crema

University of Rome "La Sapienza"
Aerospace Department
Via Eudossiana, 16 - 00184 Rome (Italy)

Abstract

This paper deals with the approach to evaluate the damping factor by the Hilbert transform both for the single mode appropriation and for the multi-mode excitation via broadband inputs. The Hilbert transform allows to get an analytic signal, whose envelope permits to evaluate the damping factor either by a statistical approach or by a least squares regression. A particular attention has been paid to low damping factors and frequencies that play a paramount role in the aerospace composite materials. A simple computer program, to perform numerical simulations by using this method, has been set up by means of FFT. Some results gained with the aforementioned program have been presented, they show the flexibility of this approach and its noticeable precision in the damping estimation.

1. Introduction

An accurate evaluation of the structural damping results fundamental in different fields, in particular as regards the aerospace field it seems proper to single out the following items:

i) military aircraft, particularly for aeroelastic problems;

ii) spacecraft on board antennas, where the damping characteristics play a significant role in the directivity loss;

iii) large space structures, for studying the structural dynamic of the system and for choosing the control methodology: active, passive or both.

Generally the damping factor estimation for composite materials, which can be considered as the main components of the aerospace structures, is the basis of all these problems. In fact the material damping is a significant element in the energy dissipation mechanism and represents the main source of energy loss in the space, where the environmental conditions do not permit some dissipation, as sound radiation and air pumping in joints, to work [1]. It follows that a very accurate evaluation of the structural damping, expecially for composite materials, is essential in the development of aerospace designs.

Attention must be paid to the high precision – much higher than that generally required in dynamic analysis – necessary in the damping factor estimation for those structures, as the large space ones, which are characterized by:

i) frequency range which extends below one Hertz, where the fundamental natural frequencies are expected to be;

ii) high modal density, which involves modal coupling problems;

iii) very low decay rates, because of both the damping factors and the angular frequencies are very small; this implies an almost persistent signal over the time interval used for studying it (unless of course one uses a very long time interval) [2].

Several approaches in order to get the modal damping factor can be used, either in the time domain, as for the logarithm decrement, or in the frequency domain, choosing significant points (as the half power ones) on the frequency response. The excitation techniques can be divided into: single frequency, with different approaches to get the modal appropriation, and broadband by impulse or random input signals.

It is possible to point out that the logarithm decrement method can only use few points, unless using a very long time data-block length for signal recording [2]; on the contrary the possible truncation of the structure response at the end of the aforementioned time interval gives rise to the well known leakage effect in the frequency domain; it can be limited by using suitable time "windows" (Hann, Hamming, etc.) [3].

In this paper the technique based on the Hilbert transform, which works in the time domain, is presented. This approach seems to offer some advantages, linked to its capability to get the envelope of the signal, for estimating the damping factor in the cases that present the aforesaid troubles.

2. Hilbert method for estimating damping factor

The Hilbert transform of a generic signal $x(t)$ is obtained by the following expression:

$$\hat{x}(t) = \frac{1}{\pi} \; p.v. \int_{-\infty}^{\infty} \frac{x(\tau)}{t - \tau} \, d\tau \tag{1}$$

where the letters p.v. stand for Chauchy principal value [4]. As it is applied for casual signal, the relation (1) can be considered the convolution between the original signal $x(t)$ with the other $1/\pi t$. This last point of view permits to get the Hilbert transform in an easy and effective way, in fact applying to the convolution the Borel theorem:

$$x(t) * \frac{1}{\pi t} \xleftrightarrow{\;\mathscr{F}\;} - j \frac{1}{\pi} X(\omega) \; sign(\omega) \tag{2}$$

where $\mathscr{F}$ implies the Fourier transform and sign (signum) represents the function

$$sign(\omega) \begin{cases} 1 \\ -1 \end{cases} \quad for \quad \begin{matrix} \omega > 0 \\ \omega < 0 \end{matrix}$$

(its value for $\omega = 0$ is assumed to be zero [5]), it is possible to obtain $\hat{x}(t)$ simply Fourier anti-transforming the right hand side relation in (2). The direct and inverse Fourier transform can be performed via a FFT algorithm, as shown in Figure 1.
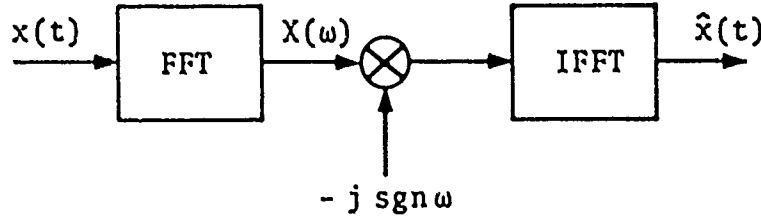
Figure 1: Hilbert transform via FFT

Once the Hilbert transform of the original signal is known it is possible to form the analytic function:

$$z(t) = x(t) + j \, \hat{x}(t) \tag{3}$$

which not only contains all the information we had in $x(t)$, but it also allows to get its envelope point by point:

$$\left| z(t) \right| = \sqrt{x^2(t) + \hat{x}^2(t)} \tag{4}$$

Because we are concerned, in a free vibration of a structure, with functions of the following type [6]:

$$x(t) = |r| e^{-\zeta \omega_n t} sin(\omega t + \phi) \tag{5}$$

(where $|r|$ represents the residue magnitude, ζ the damping factor, ω_n the angular natural frequency, ω the damped angular frequency and ϕ the phase angle of the residue) if only one mode has been excited or with a sum of similar functions if ma

ny modes have been excited with random or impulsive forcing signals, the envelope of a single mode is simply expressed by:

$$|x(t)| = |r| \; e^{-\zeta\omega_n t} \tag{6}$$

Obviously, in the case of broadband excitation, it is first necessary to single out the mode of interest with a passband filter and then to go on with the Hilbert transform, Figure 2.
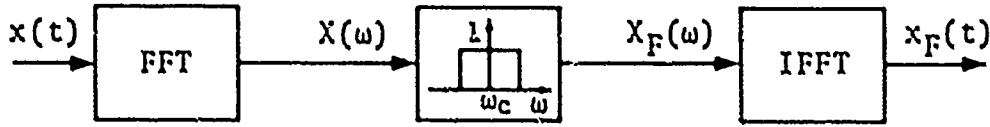
Figure 2: Filtering in the broadband excitation case

In order to evaluate the damping factor, it is necessary to measure the natural angular frequency. If the single mode is appropriated, ω_n is estimated when the mode of interest is excitated.

Two ways are instead possible to get the natural angular frequency, when broad band excitements are used.

The first one consists in the estimation of the decay rate $\sigma = \zeta\omega_n$ from the envelope (6) and of the damped angular frequency from the free response (time domain); from these quantities, which characterize the pole in the s plane, the natural angular frequency is derived:

$$\omega_n = \sqrt{\sigma^2 + \omega^2} \tag{7}$$

In this case an oversampling of the time response is desirable in order to obtain a good estimation of the damped period, even if the number of points generally used in the FFT algorithms entails a time window rather short, i.e. a not good frequency resolution [7]. The second way consists in the evaluation of the natural angular frequency from the spectrum of the original function x(t), and in particular from the peak of the imaginary part or better from the zero crossing of the real part (an improvement of ω_n estimation is possible intersecting the straight line between the two sampled points around the zero and the frequency axis). It is obvious that a good frequency resolution is now necessary and then the time window should be as long as possible, taking into account the Shannon theorem for the sampling rate and the number of points available to perform the FFT and after to process the signals (computer memory).

The use of the frequency domain seems to be the easiest and the most useful, expecially considering that for a broadband excitation it is necessary to filter the mode of interest and therefore the frequency domain permits to decide quickly the characteristics of the filter (central angular frequency, ω_c, and bandwidth).

The envelope (6) allows to get the damping factor for each sampling point (kT_s):

$$\zeta_k = \left(\frac{1}{\omega_n \, kT_s} \right) \ln \left(\frac{|r|}{|z(kT_s)|} \right) \tag{8}$$

(being T_s the sampling interval in seconds) for k that runs from zero up to (N-1), that is all the points in the time window. All these estimated values permit to

use a statistical approach for obtaining the final value $\bar{\zeta}$. Another way to evalua
te the damping factor consists to apply the linear least squares technique on the
data in the semi-logarithm plane $(\ln|z(kT_s)|, kT_g)$ and then to calculate the an-
gle between the obtained straight line and the axis of abscissas [8]. The use of
the least squares approach allows to clean out the noise, always present in the
experimental data, and the possible oscillations due to a small tail, present in
the bandwidth of the filter, of a near mode, Figure 3.
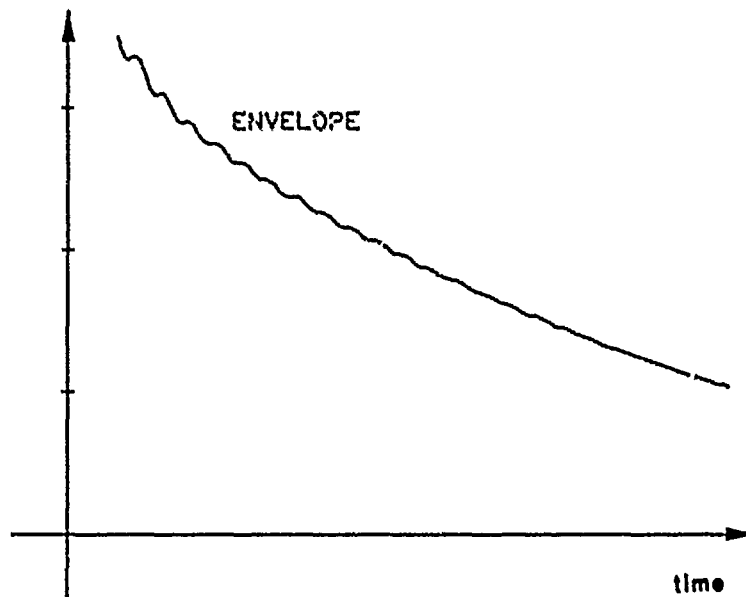
Figure 3: Oscillations due to the tail of a near mode

The procedure for applying the Hilbert transform technique in the case of the
mode appropriation and of the broadband excitation are presented in Figures 4 and 5.
Once the mode of interest has been singled out and its damping factor and natural
angular frequency has been estimated, an evaluation of the error on the damping
factor can be carried out by the Hilbert transform approach and afterwards an im-
proved estimation of the damping factor achieved. This improvement is obtained
multiplying the free response by:

$$e^{\zeta^* \omega_n^* t} = f^*(t) \tag{9}$$

where ζ^* and ω_n^* represents the estimated values.

Multiplying the (5) by $f^*(t)$, an oscillating damped function is still gained,
whose decay rate depends upon both the error made in the angular frequency, $\Delta\omega_n$,
and that in the damping factor, $\Delta\zeta$ (in addition of course to the unknown "true"
damping factor and angular frequency). Supposing the product $\Delta\zeta\Delta\omega_n$ negligeable
respect to the other terms and the ratio $(\Delta\omega_n/\omega_n)$ negligeable respect to the uni-
ty, it is possible to evaluate the error on the damping factor, when its percenta
ge value results greater than that on the angular frequency at least of one order
of magnitude.

The resulting signal has a very small damping and so it certainly gives rise to leakage problems. Nevertheless they do not result of significant consequence, as the angular frequency has been already estimated.
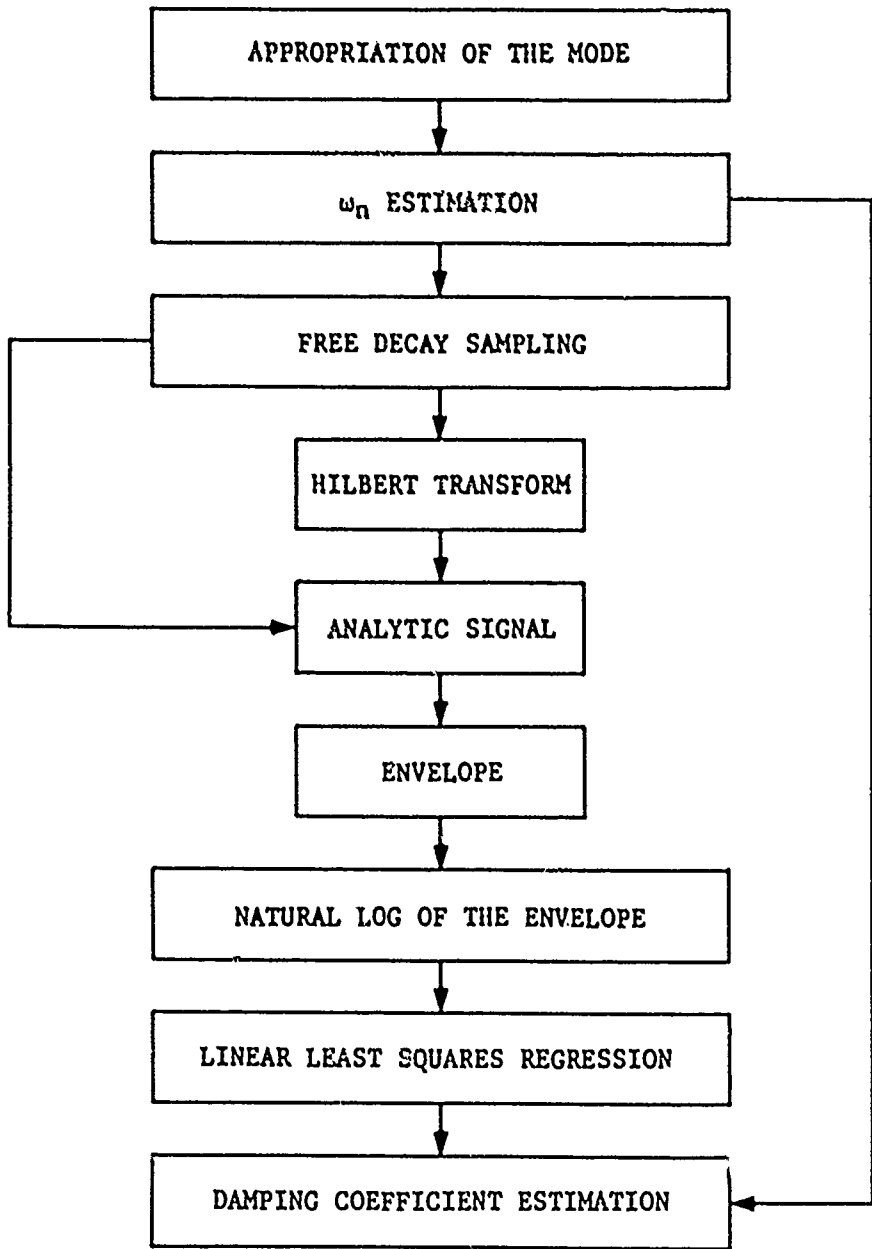
Figure 4: Procedure for the mode appropriation
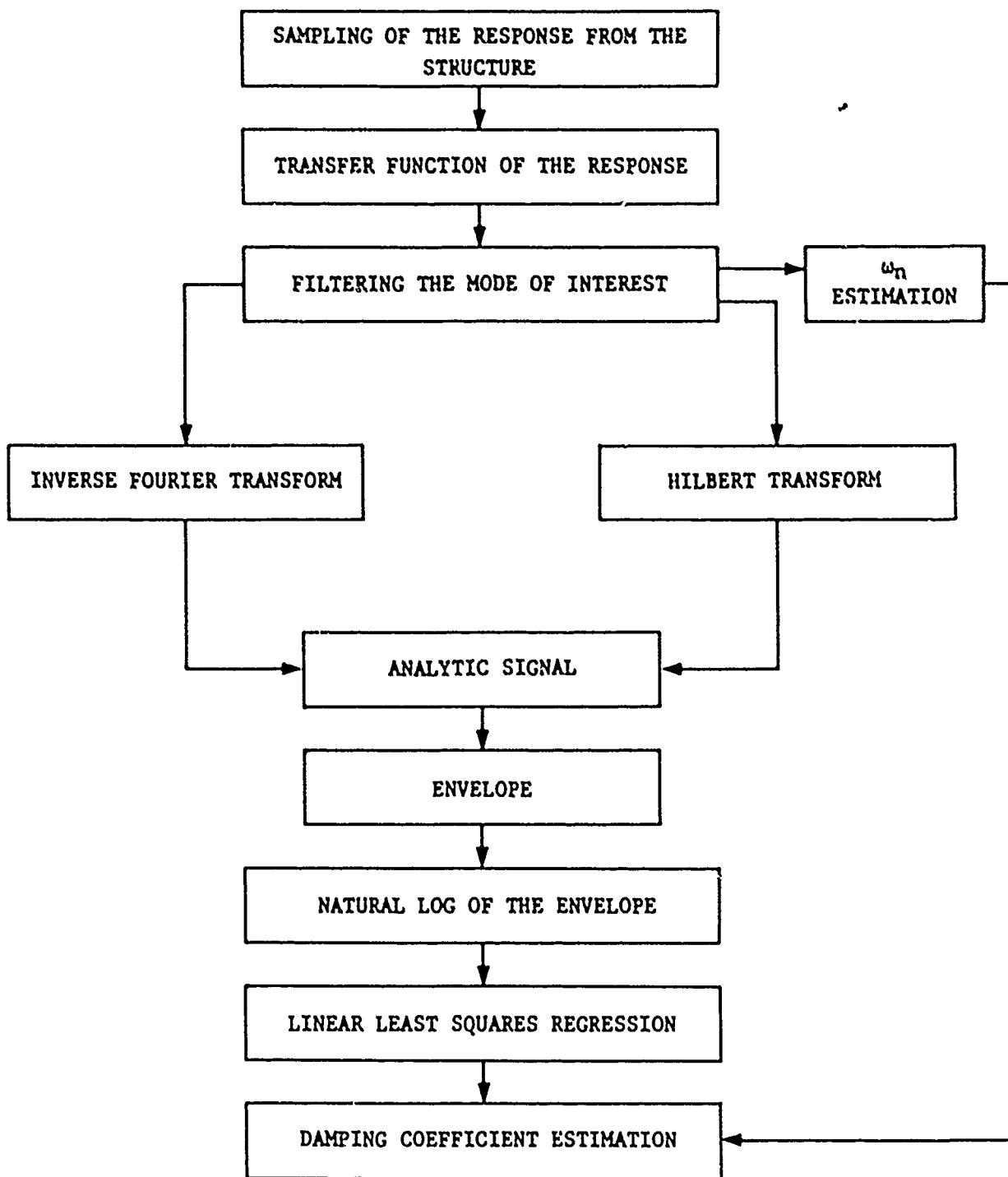
Figure 5: Procedure for the broadband excitation

3. Numerical tests

The Hilbert transform, necessary to get the analytic signal, was performed by a FFT algorithm [9], which uses 2^9 points and a rectangular time window. In the case of broadband excitation, filtering in the frequency domain has been carried out with an ideal bandpass filter, properly chosen with regard to the mode of interest. A HP-9816S computer has been used for the numerical tests.

When the mode appropriation technique is applied the envelope is very smooth, except for the noise always present in an experimental test (in our simulations the noise has been added in order to take into account the characteristics of an experimental system), and considering the large amount of available points a statistical estimation of the damping factor is possible, even if the use of a least squares regression yields better results, as shown in Table 1.

Table 1: Comparison between statistical and least squares regression in the damping factor evaluation

$\zeta = 0.001$; time window: 1 s				
frequency (Hz)	$\bar{\zeta}$	$|\epsilon|$ (%)	ζ^*	$|\epsilon|$ (%)
7.0	0.000773	227.0	0.001001	1.0
10.0	0.000840	160.0	0.000999	1.0
20.5	0.000921	79.0	0.000995	5.0
126.5	0.000987	13.0	0.000998	2.0

However the statistical evaluation comes in handy both when the free decay response is triggered before reaching its steady state and when a non linear damping factor is present. A simulation of stepwise non linear behaviour, due to large oscillations for example, has been carried out and the results are shown in Figure 6. The damping factor has been evaluated with the statistical approach in each time interval where it remains constant. The points in those intervals where the statistical evaluation yields to a constant damping factor estimation can be afterwards used for the least squares approach, in order to decrease the error.

In presence of a short time window, i.e. a scarce frequency resolution, the half power method could not be applicable directly, but it would require a least squares evaluation of the frequency response from the available points. On the contrary the Hilbert approach allows to evaluate the damping factor without problems, in fact it uses, for obtaining the Hilbert transform by the FFT, all the information held by all the lines of the frequency response. A poor frequency resolution involves an error on the angular frequency estimation-which in turn influences the damping factor evaluation-that results to be generally small. In Table 2 three modes with a very narrow bandwidth in comparison with the angular frequency resolution are shown.
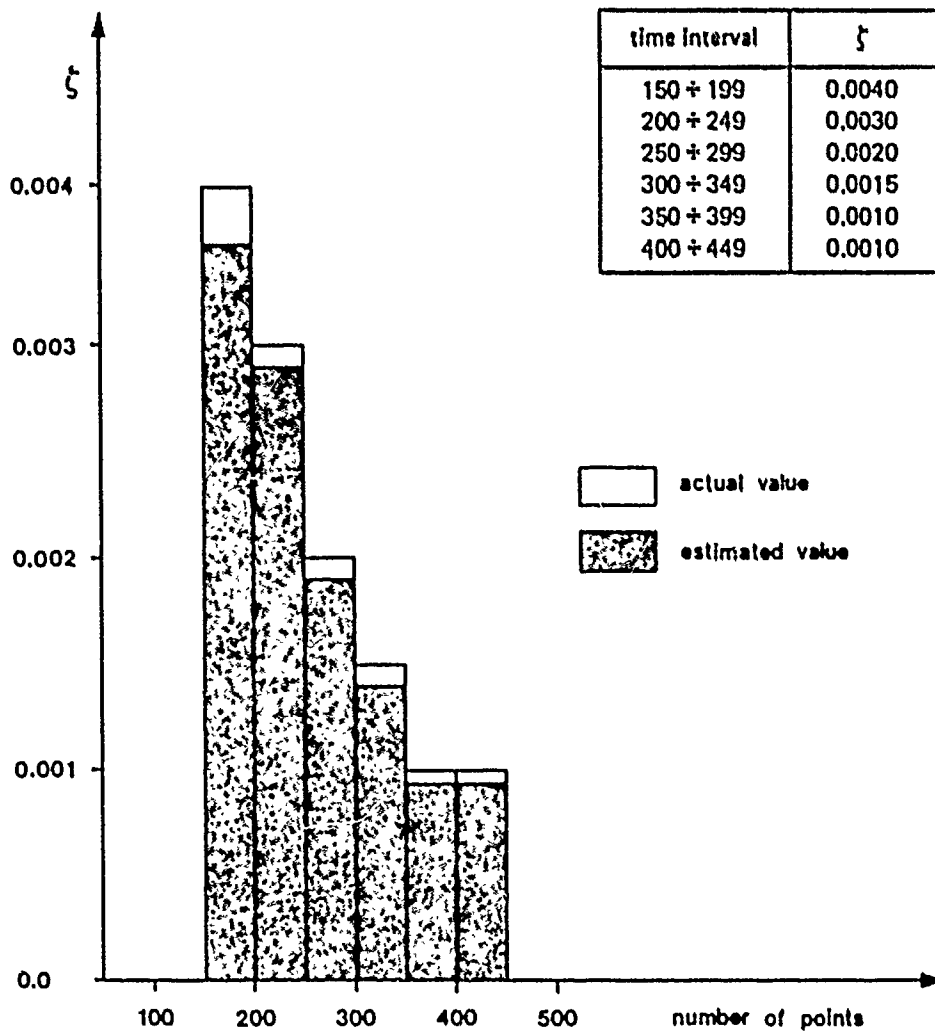
Figure 6: A non linear damping simulation

Table 2: Damping estimation in the case of poor frequency resolution

angular frequency resolution: 3.14 (rad/s)				
f(Hz)	half power bandwith (rad/s)	ζ	ζ*	|ε| (‰)
8.56	0.11	0.0010	0.00102	22.3
10.00	0.06	0.0005	0.00051	12.0
40.00	0.25	0.0005	0.00050	0.2

At any rate a good frequency resolution is always desirable and, if necessary, it can be achieved by the classical zoom technique.

In a previous work [8], an analysis for a non correct mode appropriation was

carried out. In this case the damping factor of the mode with the highest residue, the single that may be evaluated, was obtained with a negligeable error, but getting higher and higher with the increase of the mode residue due to the non correct appropriation. Actually if one filters the mode of interest the error on its damping coefficient results to be smaller than before. Table 3 shows a comparison between the damping factors obtained by filtering or not the data gathered in non correct mode appropriation cases (only two modes are excited) with different residue ratios ($|r_1|/|r_2|$).

Table 3: A comparison between filtered and unfiltered data

$\dfrac{|r_1|}{|r_2|}$	Unfiltered		Filtered	
	ζ_2^*	$|\epsilon_2|$ (%.)	ζ_2^*	$|\epsilon_2|$ (%.)
0.02	0.0010030	3.0	0.0010001	0.1
0.07	0.0010112	11.2	0.0010001	0.1
0.10	0.0010160	16.0	0.0010001	0.1
0.20	0.0010320	32.0	0.0010003	0.3
0.30	0.0010476	47.0	0.0010004	0.4

Besides the filtering technique allows to get both the damping factors of the excited modes. In Table 4 several cases, with residue ratios from 0.02 up to 0.80, are presented along with the maximum of their error magnitude.

Table 4: Damping factor evaluation by filtering

$f_1 = 11$ (Hz); $f_2 = 60$ (Hz); $\zeta_1 = 0.002$; $\zeta_2 = 0.001$			
$\dfrac{|r_1|}{|r_2|}$	ζ_1^*	ζ_2^*	$|\epsilon|_{MAX}$ (%.)
0.02	0.00197	0.00100	15.0
0.07	0.00200	0.00100	1.2
0.10	0.00199	0.00100	6.3
0.20	0.00197	0.00100	15.0
0.30	0.00198	0.00100	9.9
0.50	0.00199	0.00100	7.4
0.80	0.00198	0.00100	9.9

The effects due to an increasing coupling are shown in Table 5; when the coupling gets tighter the error becomes not negligeabie and even a better frequency resolution does not lead to any significant improvement.

Table 5: Coupling modes

$f_1 = 11.5$ (Hz); $\left\|\dfrac{r_1}{r_2}\right\| = 0.8$; $\zeta_1 = 0.005$; $\zeta_2 = 0.002$			
f_2 (Hz)	ζ_1^*	ζ_2^*	$\|\epsilon\|_{MAX}$ (%)
13.5	0.00501	0 00200	1.9
13.0	0.00498	0.00202	8.8
12.5	0.00502	0.00199	4.5
12.0	0.00497	0.00201	6.0
11.9	0.00482	0.00183	87.0

The possible improvement in the damping factor estimation is presented in Table 6, where one can see that the error on the angular frequency limics the attainable precision on the damping factor.

Table 6: Improvement of the damping factor estimation

f(Hz)	ζ	ζ^*	$\|\epsilon\|$ (%)	$\Delta\omega_n^*$ (rad/s)	$\|\epsilon\|$ (%)	ζ_c^*	$\|\epsilon\|$ (%)
11.5	0.040	0.040496	12.4	0.376991	5.2	0.039794	5.2
31.5	0.005	0.004883	23.4	0.314159	1.6	0.005008	1.6
145.5	0.008	0.007310	86.0	3.141593	3.4	0.007954	5.7

Some numerical tests were carried out at a very low frequencies and low damping factors, which are of particular interest in large space structures design. In Table 7 the damping factor evaluation of a single mode is presented, while in Table 8 the influence of two near modes is shown.

Table 7: Damping factor evaluation for low frequencies and $\zeta = 0.001$

Baseband range (Hz)	f(Hz)	ζ^*	$\|\epsilon\|$ (‰)
1	0.530	0.000999	0.6
2	0.535	0.001015	14.8
5	0.530	0.001013	12.56

FI-11

Table 8: Damping factors evaluation for two coupling modes

$\dfrac{\|r_1\|}{\|r_2\|} = 0.8$; $f_1 = 0.237$ (Hz); $\zeta_1 = 0.001$; $\zeta_2 = 0.002$			
f_2 (Hz)	$\zeta_1^{\star}$	$\zeta_2^{\star}$	$\|\varepsilon\|_{MAX}$ (‰)
0.743	0.000998	0.002000	1.9
0.513	0.000997	0.002002	0.9
0.373	0.001010	0.002003	1.3
0.297	0.000983	0.001974	17.3

4. Conclusions

The numerical tests have confirmed the idea that the approach based on the Hilbert transform allows a very accurate evaluation of the damping factor also in the case of broadband excitation.

Moreover, it should be pointed out that a very good precision has been achieved by using even elementary filtering techniques and an unsophisticated algorithm for the FFT evaluation (working on a limited set of points: 2^9). The numerical tests have been concerned with low damping and frequencies that are of interest in studying composite material for aerospace structures.

Even if this approach permits a statistical evaluation the best results have been gained by a least squares interpolation in the plane: logarithm of the envelope (in amplitude) versus time.

The effects due to a non correct mode appropriation or, in the case of broadband excitation, to the presence of "tails" of near modes – on condition that they are not tightly coupled – are very limited by using the least squares interpolation.

For suitable conditions an improvement of the damping factor estimation can be achieved by applying successively the Hilbert transform technique.

Some of the operative problems touched on in this work have been developed with more details in a paper that is now being completed [10].

Further studies will be turned to the possible use of this technique for the damping factor evaluation in the non linear case and for coupled modes.

Acknowledgements

References

[1] E.F. Crawley, R.L. Sheen: "Experimental measurement of material damping for space structures", Vibration damping 1984 Workshop Proceedings, AFWAL-TR-84-3064, F1-F19.

[2] T. Bailey, J.E. Hubbard, Jr.: "Distributed piezoelectric-polymer active vibration control of a cantilever beam", Vibration damping 1984 Workshop Proceedings, AFWAL-TR-84-3064, XX1-XX23.

[3] D.J. Ewins: "Modal testing: theory and practice", Research Studies Press, England, 1984, pp. 120-121.

[4] R.N. Bracewell: "The Fourier Transform and its Applications", Mc Graw-Hill Ko gajusha, Tokyo, 1978, p. 267.

[5] (anon.): "Signal Processing Techniques", Interstate Electronics Corporation, 1979, p. 1-12.

[6] M. Richardson: "Modal analysis using digital test systems", Seminar on understanding digital control and analysis in vibration test systems - NASA TM-X-74637, part 2 of 2 parts; pp. 43-64.

[7] M. Kunt: "Traitement numérique des signaux", Dunod, 1981, p. 121.

[8] A. Agneni, L. Balis Crema: "Misura del fattore di smorzamento con l'impiego della trasformata di Hilbert", Atti del Dipartimento Aerospaziale, DAURS 84.02, Dicembre 1984.

[9] E.A. Robinson: "Multichannel Time Series Analysis with digital computer programs", Holden Day, San Francisco, 1978, pp. 63-64.

[10] A. Agneni, L. Balis Crema: "Damping factor estimation via Hilbert Transform in broadband excitation".
(to be published)

A COMPARISON AMONG DAMPING
COEFFICIENTS ON SEVERAL
AEROSPACE COMPOSITE MATERIALS

Luigi Balis Crema and Antonio Castellani

University of Rome "La Sapienza"
Aerospace Department
Via Eudossiana, 16 - 00184 Rome (Italy)

Abstract

In this work several experimental data on the measurement of the damping coefficient for aerospace composite materials as glass, carbon and Kevlar fiber laminates, Kevlar fabrics and glass short fiber composites are presented.

The effect of pressure and temperature, in order to simulate the aerospace environment, and different frequencies are considered.

A previsional estimation, based on the bounds computed by the correspondence principle, can supply a significant evaluation of the damping factor in different conditions.

1. Introduction

In this work a series of experimental results, gained at the Aerospace Department of the Rome University in these last years, on the damping factor evaluation for different composite materials is presented.

The research in the field of the damping measurements started with damping coefficient evaluations on aluminum samples and studies on joining effects with tests on riveted samples [1], [2].

Successively the effect connected to the space environment, i.e. pressure and temperature, on the damping factors was considered [3].

The attention has been turned to the study of the damping characteristics for composite materials with particular reference to different environmental conditions, i.e. pressure and temperature [4], and to singling out of bounds on the loss modulus [5], [6].

In addition to a synthesis of some experimental results, gained in previous works, some other results, that are now being gained in present researches, on the evaluation of damping factors for short fiber samples and on Kevlar fabrics and laminates are presented.

The interest that is now turned to the Kevlar composite materials in building up some space structures, as feed towers and antennas for spacecraft, has induced to a general study of the thermoelastic characteristics for Kevlar composite materials [7], [8] and in particular to a research on the peculiar damping behaviour.

In fact the damping characteristics show significant differences in comparison with glass or carbon fiber composites and this is probably due to the similar damping characteristics for fiber and resin in Kevlar composites [9].

2. Measurement method

The equipment used for the experimental damping measurements consists of: oscillator, vibration exciter, capacitive detector, amplifier and recorder.

The specimen is clamped on a mounting, while the electromagnetic exciter and the vibration detector can move along a slide which is fixed on the same mounting. A frequency range starting from 2 until 2000 Hz can be examined.

As it is well known several difficulties are involved since the measurement is influenced by vibration amplitudes, transducers position, clamping pressure, specimen characteristics and so on.

A particular attention has been given to keep comparable vibration amplitudes; non dimensional damping coefficients versus specimen vibration amplitude (peak-peak) w, normalized to the specimen thickness h, are reported in Figure 1, which refers to normal test conditions: it can be noted that the vibration amplitude has no effects in the selected working conditions.

The non dimensional damping coefficient is measured by means of the decay transient method; in the range of the damping values on study this method can be considered as more efficient than the frequency sweep method that can also be used with the same available equipment.

A series of tests has been carried out at room conditions for pressure and temperature, and other tests have been made in the environmental chamber of the Ae-

rospace Department where a vacuum level until 10^{-6} torr can be achieved; finally, other tests have been carried out in a temperature range from room conditions to 120 °C.
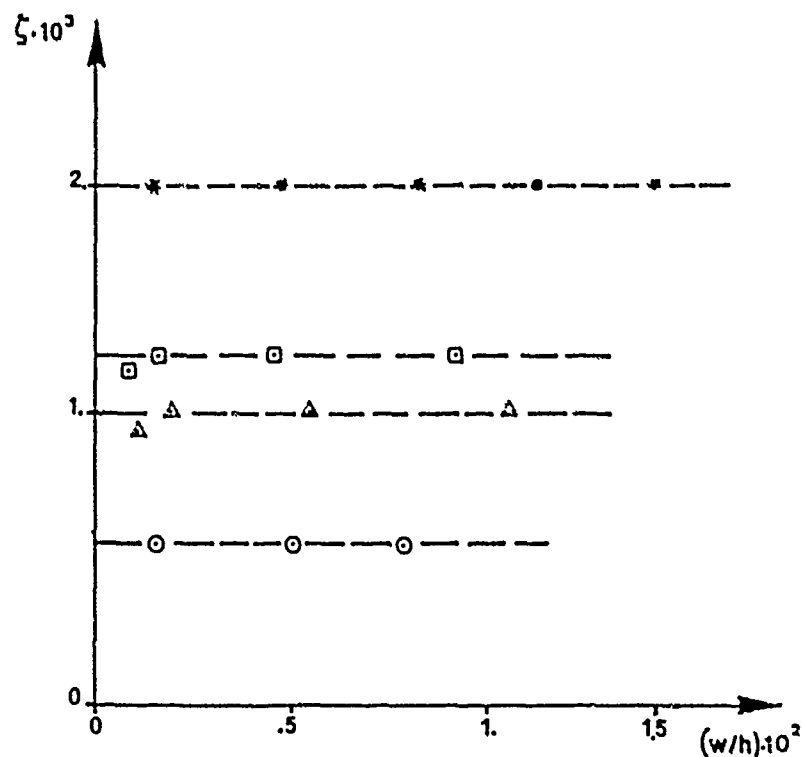
Figure 1: Damping versus vibration amplitude [4].

The various frequencies have been gotten both with various sample geometries,by changing lenght, and with the excitation of the first and second bending mode.

3. Samples of glass and carbon fiber

The test samples in glass and carbon fibers were prepared by the Italian Industry Agusta. For each material eight sets of samples have been used; in Table 1 the specifications of all the samples are reported and in Table 2 the properties of the prepreg by Ciba-Geigy are presented.

In order to evaluate the damping properties of these composite materials in space environmental conditions, the effects due to pressure and temperature have been investigated, together with frequency effect:

i) pressure effect: in Figures 2 and 3 the damping coefficient versus pressure, respectively for the glass and carbon fibers, is shown: a decrease of damping coefficient versus pressure from atmospheric pressure to 10^{-6} torr is pointed out; the effect is more relevant for the thinner specimens that get to a decrease until the 25 per cent of the value at the atmospheric pressure.

FJ-3

Table 1: Specifications of glass and carbon fiber specimens

SPECIMEN		NUMBER OF LAMINAE	LAMINATE LAY-UP	LENGTH (mm)
GLASS FIBER	CARBON FIBER			
A1	A1	8	90/90/90/90	250
A2	A2	8	0/0/0/0	250
B1	B1	8	0/90/90/0	200
B2	B2	8	0/90/90/0	250
B3	B3	8	0/90/90/0	400
C1	C1	16	0/90/90/0	250
C2	C2	16	0/90/90/0	300
C3	C3	16	0/90/90/0	400

Table 2: Properties of Ciba-Geigy prepregs

CHARACTERISTICS		GLASS FIBER	CARBON FIBER
FIBER TYPE		R glass	COURTAULDS E/HM-S
RESIN TYPE		920	920
FIBER DENSITY (kg m^{-3})		2500	1860
RESIN DENSITY (kg m^{-3})		1260	1260
RESIN CONTENT (wt)%		33	42
PLY THICKNESS	NOMINAL (mm)	.1750	.1555
	AVERAGE (mm)	.1862	.2270
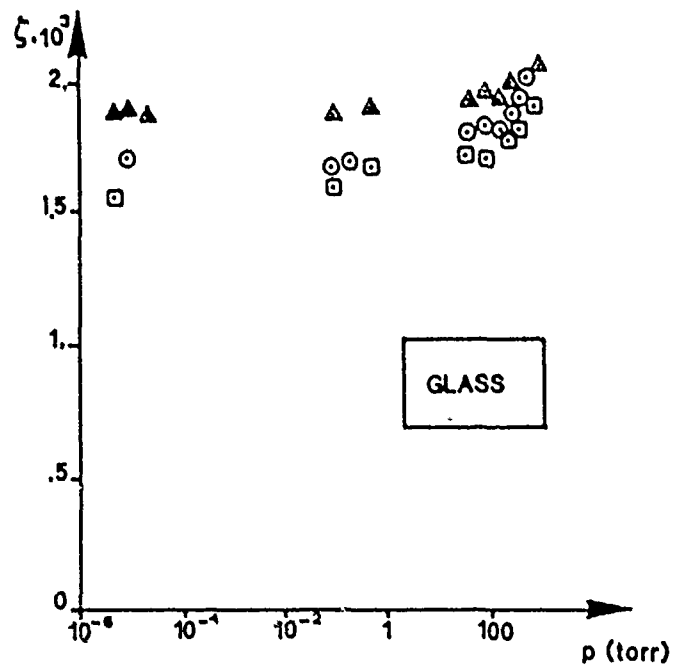
Figure 2: Glass fiber damping coefficient versus pressure [4]
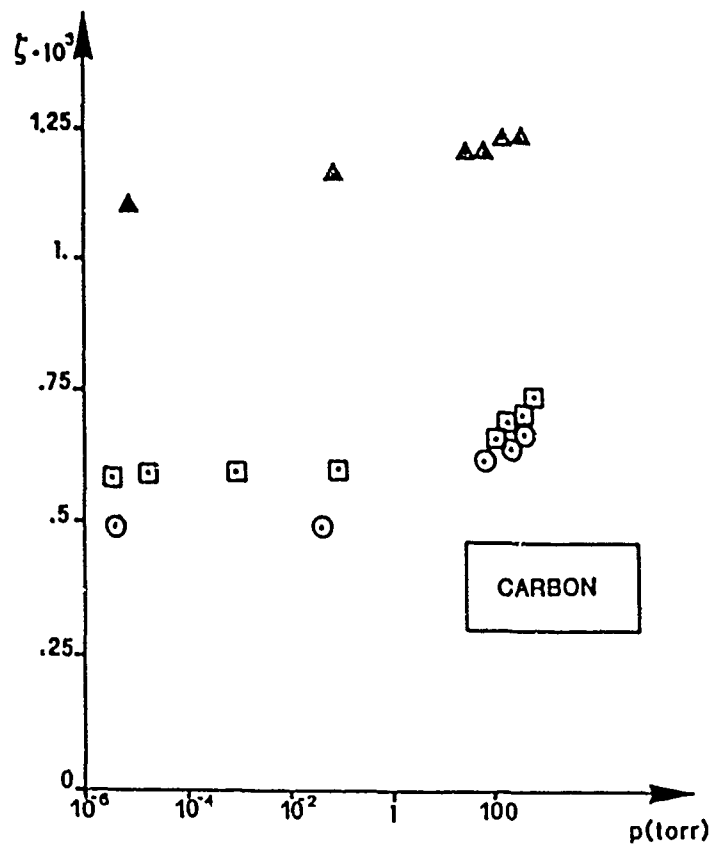
Figure 3: Carbon fiber damping coefficient versus pressure [4]

FJ-5

ii) <u>frequency effect</u>: in Figure 4 the experimental values of the damping coeffi<u>_</u>
cient versus frequency for the glass fiber specimens at the pressure 10^{-3}
torr are displaied.
The same results for the carbon fiber are shown in Figure 5, the behaviour
is like glass fiber but the damping coefficients are, for the whole range of
investigated frequencies, lower than the damping coefficient for the glass
fiber.
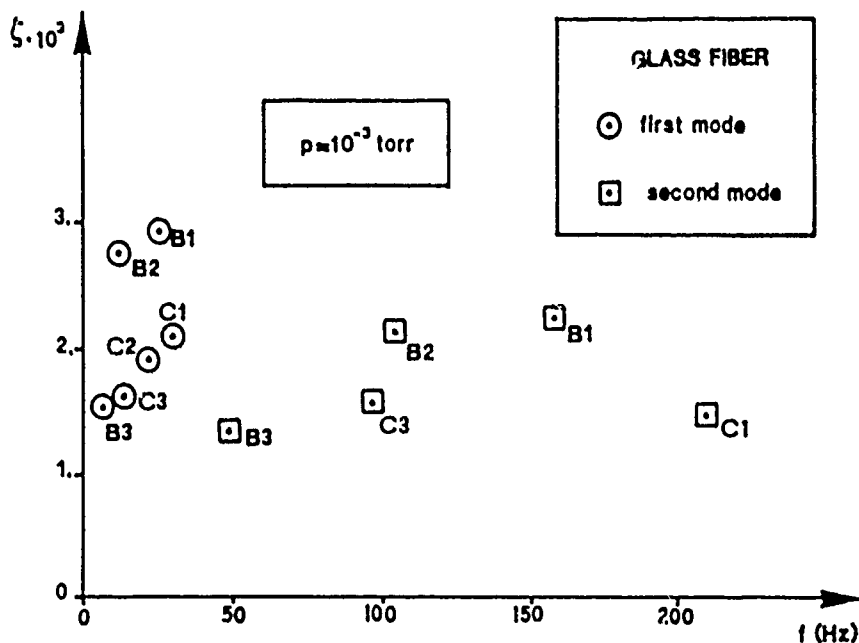
Figure 4: Glass fiber damping factors versus frequency [5]
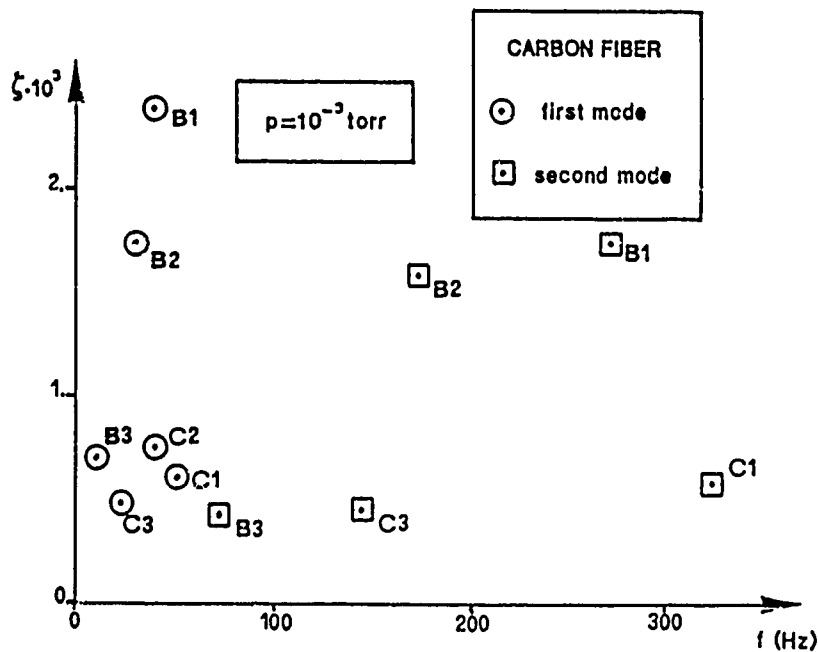
Figure 5: Carbon fiber damping factors versus frequency [5]

FJ-6

iii) temperature effect: some tests have been carried out in the temperature range between room conditions and 120 °C, the experimental results, ζ/ζ_0 ratio
versus temperature, are shown in Figure 6 and 7 respectively for glass and
carbon fibers, where ζ_0 is the damping coefficient at room temperature and
ζ is the damping value at the current temperature.

It is possible to see a remarkable increase on the damping value starting
from temperatures of about 90 °C: this effect is consistent with the cure
cycle of the laminating procedure at 125 °C.
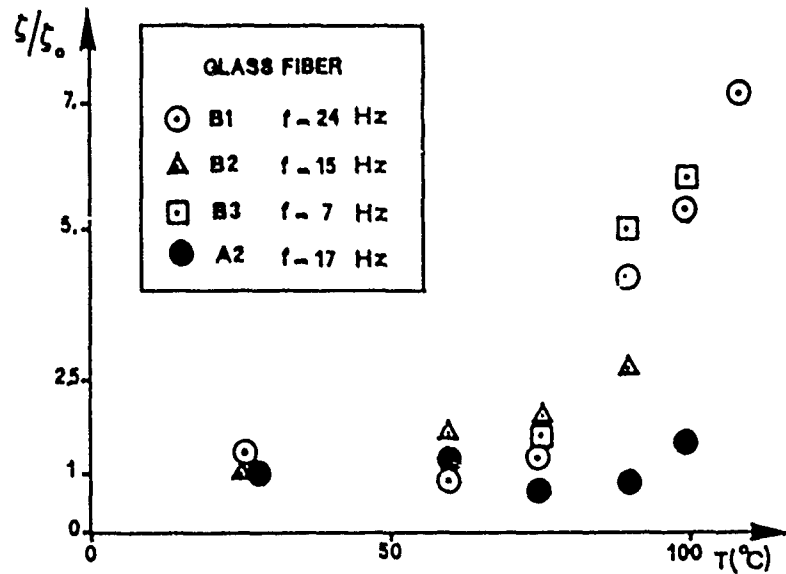
Figure 6: Glass fiber damping versus temperature [5]
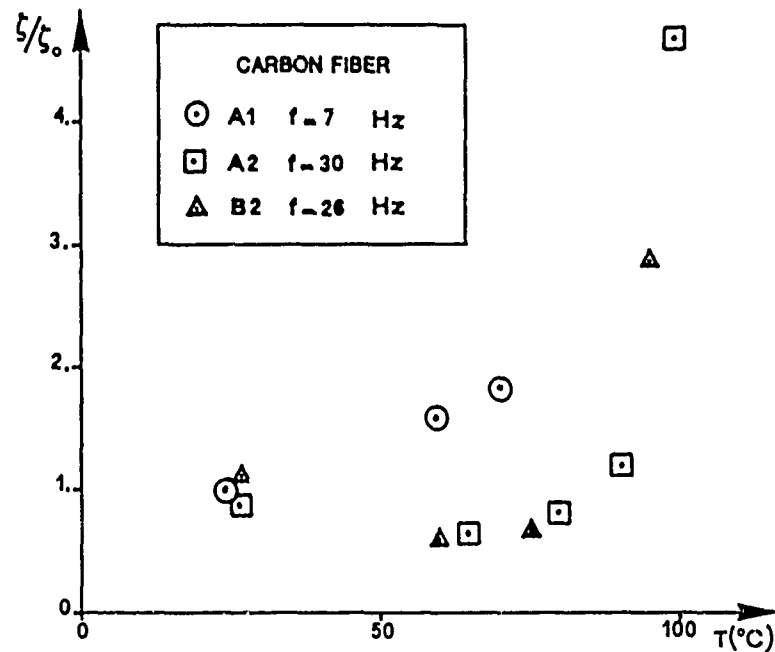
Figure 7: Carbon fiber damping versus temperature [5]

4. Bounds for the damping factor prevision

One of the targets of these researches is in the possibility of getting a pre_vision for the damping characteristics in composite materials.

In order to achieve this point the experimental data of nondimensional damping coefficient on the samples of composite materials have been used to check the bounds on the complex dynamic flexural modulus as computed by the correspondence principle.

The upper and lower bounds for the nondimensional damping coefficient are given by:

$$\frac{V_m \ \zeta_m \ E_m + V_f \ \zeta_f \ E_f}{E_c} < \zeta_c < \frac{V_m \ \zeta_m \ E_m \ E_f^2 + V_f \ \zeta_f \ E_f \ E_m^2}{E_c (V_m \ E_f + V_f \ E_m)^2} \tag{1}$$

where the subscripts c, f, m mean, respectively composite, fiber and matrix.

In Figure 8, as an example, the results gained by room pressure measurements for carbon fiber composites are reported: the experimental values fall in a wide band and some of them go out the proposed bounds, actually it can be due to an error in excess on the measurement of the damping coefficient in the carbon fiber composites because the damping coefficient is very small and the effects of testing in room pressure and of the measurement errors can be relevant.
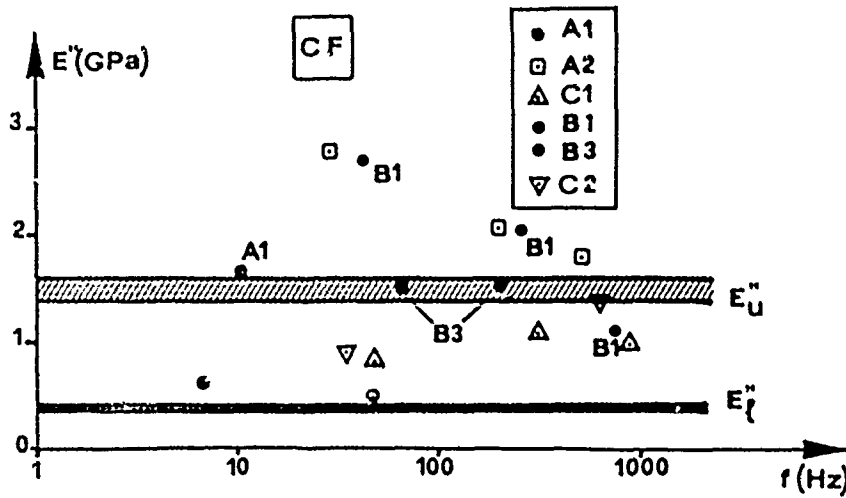
Figure 8: Carbon fiber loss modulus bounds [6]

In Table 3 the experimental values of the flexural modulus in comparison with the values predicted by a classical laminate theory have been reported.

In order to establish an empirical relationship between damping and stiffness properties for laminate composite materials, the adimensional damping coefficients versus the storage modulus, respectively for glass and carbon fibers have been reported in Figures 9 and 10. This correlation corresponds to the general intuitive idea that an increase in the stiffness involves a decrease in the damping coefficient.

Table 3: Experimental and previsional Young modulus

SPECIMEN	EXPERIMENTAL E'(GPa)	PREVISIONAL E'(GPa)
GLASS FIBER		
A1	12.	8.
A2	41.	40.
B2	32.	27.
C3	29.	25.
CARBON FIBER		
A1	4.	6.
A2	158.	160.
B2	103.	98.
C2	78.	87.
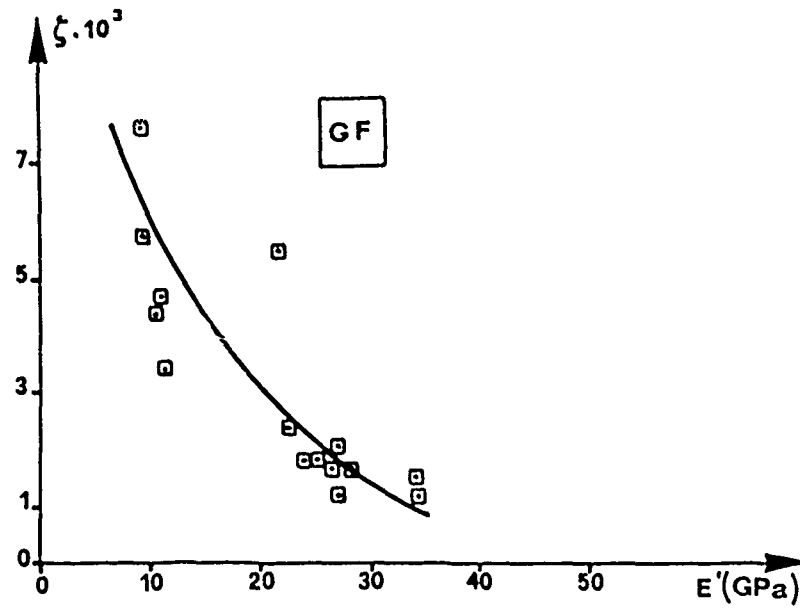
Figure 9: Glass fiber damping versus storage modulus [6]
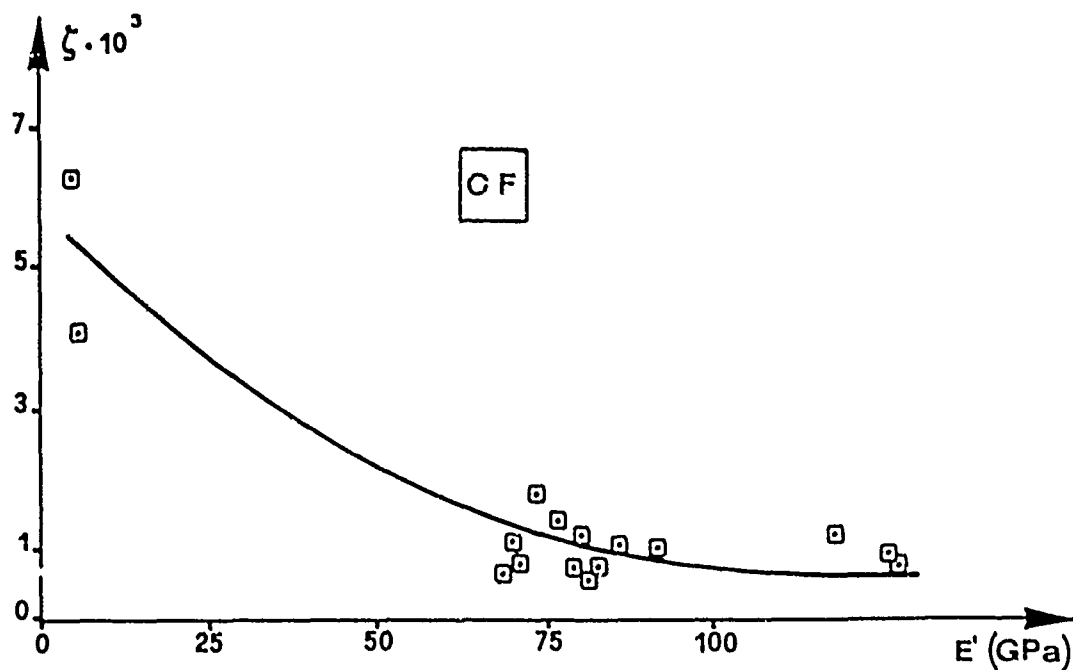
Figure 10: Carbon fiber damping versus storage modulus [6]

5. Short fiber specimens

A large series of short glass fiber specimens built by the Italian Research Laboratory "Istituto Donegani" of Novara has been tested. In Table 4 the specifi cations and the properties of a single type of these specimens, in resin polypro pylen, are reported.

Table 4: Short glass fiber in resin polypropylen

CHARACTERISTICS	GLASS FIBER CP 713	RESIN POLYPROPYLEN
DENSITY (kg m^{-3})	2500	910
RESIN CONTENT (%)	—	86
YOUNG MODULUS (GPa)	70	1.5

SPECIMEN	E (GPa) PREVISIONAL	E (GPa) EXPERIMENTAL
RANDOM	5.4	3.2
TRANSVERSAL	> 2.1	3.1
LONGITUDINAL	< 11.1	7.2

Three different kinds of samples are considered:

i) random short fibers;
ii) transverse short fibers;
iii) longitudinal short fibers.

FJ-10

In Figure 11 the experimental results of the nondimensional damping coeffi-
cient versus frequency for random, transverse and longitudinal samples are shown.
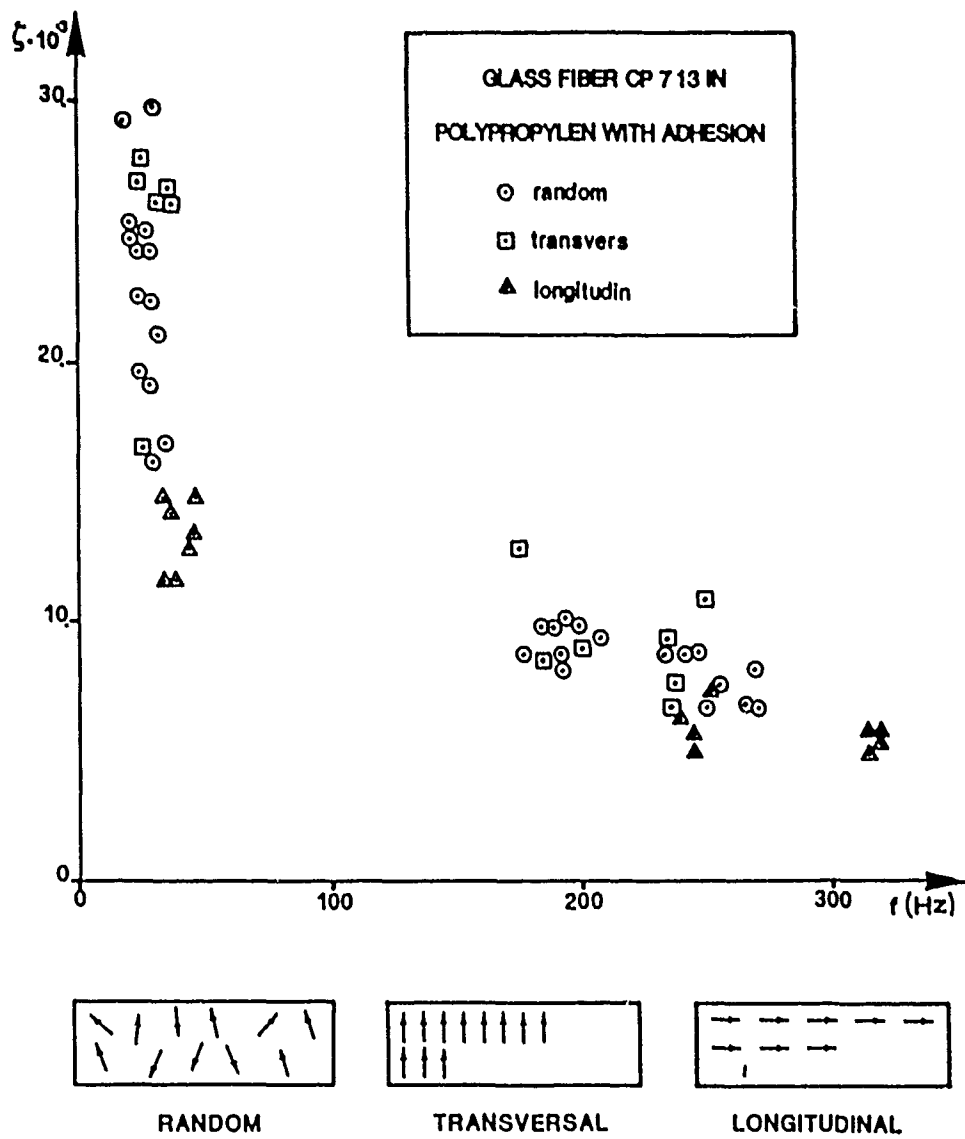
Figure 11: Damping versus frequency [10]

Results corresponding to the ones reported in Figure 11 have been gained for
different types of short glass fiber composites and a complete analysis of all
the results is presented in a research that is now being completed [10].

6. Kevlar specimens

Just now the research is turning to Kevlar samples in epoxy resin prepared by
the Italian Industry Aeritalia for space applications.

Some of the results gained by these tests are presented and precisely on:

  i) laminates;
 ii) fabrics style 120;

iii) sandwiches (fabric style 120).

In the Table 5 the layout and the resin content, that is forty per cent in fa_
brics and sixty per cent in laminates, are presented.

'Table 5: Kevlar samples properties

	Kevlar 49 fabric 120 style	Kevlar 49 laminate
LAYOUT	$[(0/90)_4/0]_S$ $[(0/90/\pm45)_2/45]_S$	$[(0/90)_4/0]_S$ $[(0/90/\pm45)_2/45]_S$
RESIN CONTENT %	40	60

In Figure 12 some preliminary results, as damping factor versus frequency are presented.
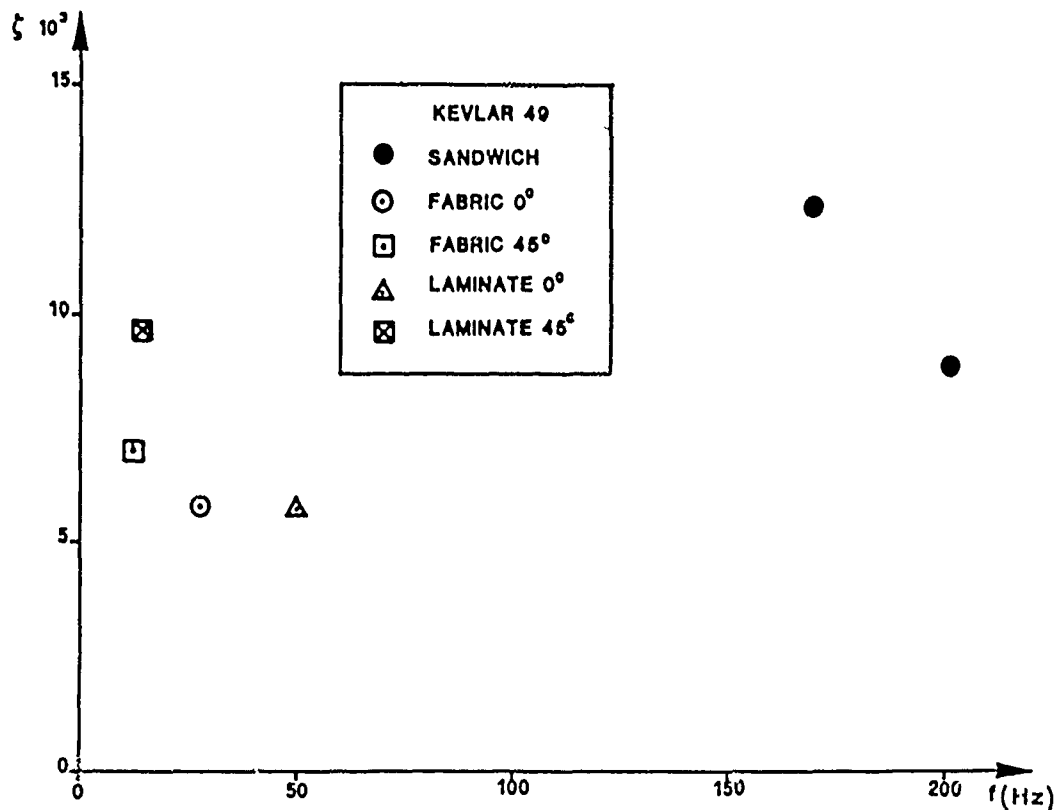
Figure 12: Damping factor versus frequency

No significant difference appears between fabrics and laminates; the damping values result higher for the sandwich samples but also the frequency range is dif_ ferent, and precisely higher, than the one considered for fabric or laminate sam_ ples.

FJ-12

As well for the Kevlar specimens a trend similar at that one presented in Figures 9 and 10, regarding the damping coefficient versus storage modulus for glass and carbon fiber composites, has been achieved as results in Figure 13.
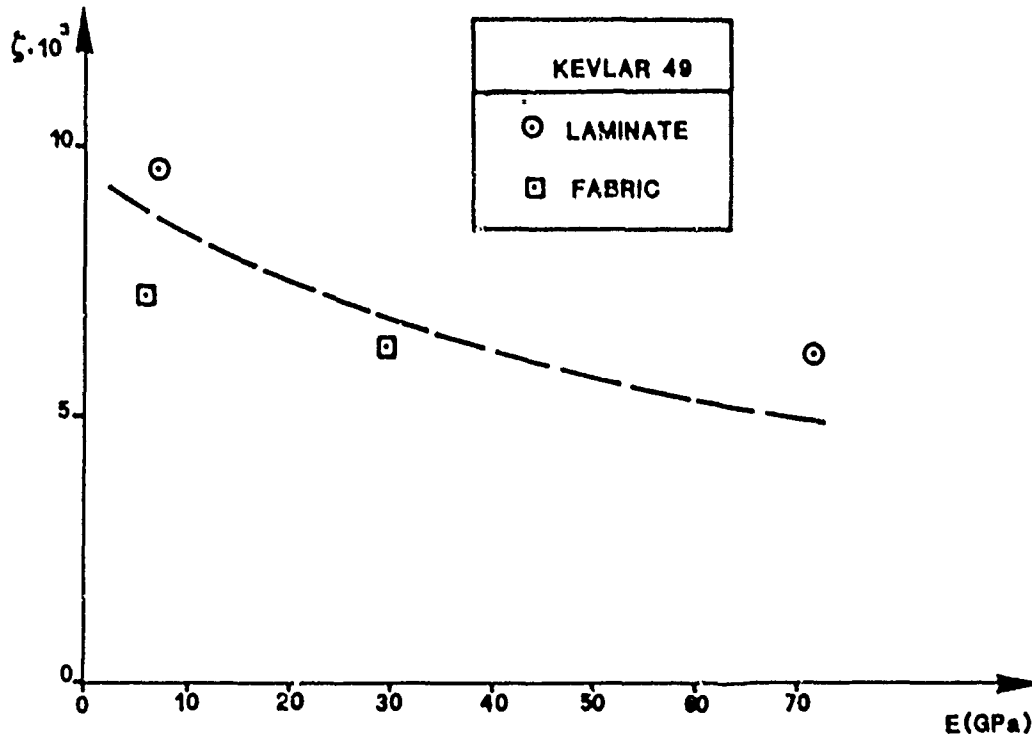
Figure 13: Damping factor versus storage modulus

It should be noted that a peculiar problem for the Kevlar composites is in a high amplitude dependance: this behaviour is much more significant than in the other composite materials.

This non linear characteristic together with damping values higher than in glass and carbon fiber composites are the essential Kevlar features [11].

On course for the space use of this material it is necessary to consider the space environmental effects; the future work is on these items:

  i) vacuum condition testing;
 ii) temperature testing in the range starting from -120 to 120 °C;
iii) low frequency testing (as imposed by the large size of space structures).

7. Conclusions

Experimental evaluations of the damping coefficients for several aerospace composite materials have been presented.

The research has been essentially turned to the singling out of a connection between stiffness and damping characteristics in order to achieve a previsional valuation of the damping factors in composite materials.

At the present the lower bound gained for the damping factor makes it possible to achieve a significant estimation of the damping factors for different com

posite materials and different conditions.

Acknowledgements

References

[1] R. Barboni, L. Balis Crema: "Determinazione Sperimentale delle Caratteristiche Viscoelastiche", L'Aerotecnica Missili e Spazio, N. 2, 1972, pp. 117-128.

[2] L. Balis Crema, A. Castellani, A. Nappi: "Damping Effects in Joints and Experimental Tests on Riveted Specimens", AGARD CP 277, 1980.

[3] L. Balis Crema, A. Castellani, A. Nappi: "Influenza della Temperatura e del Vuoto sul coefficiente di Smorzamento in Giunti Rivettati", L'Aerotecnica Missili e Spazio, Vol. 58, N. 4, 1979, pp. 183-187.

[4] L. Balis Crema, R. Barboni, A. Castellani: "Structural Damping of Composite Materials for Space Applications", AGARD CP 327, 1983.

[5] L. Balis Crema, R. Barboni, A. Castellani, I. Peroni: "Tests and Prediction of Composite Material Viscoelastic Behaviour for Large Space Structure", L'Aerotecnica Missili e Spazio, Vol. 62, N. 4, 1983, pp. 205-210.

[6] L. Balis Crema, A. Castellani, A. Serra: "Experimental Tests on the Loss Modulus Bounds for Composite Materials", Roma, 1984.

[7] L. Balis Crema, R. Barboni, A. Castellani: "Thermoelastic Behaviour of Space Structures in Composite Materials", 35th I.A.F. Congress, Lausanne, 1984, I.A.F. 84-404.

[8] L. Balis Crema, R. Barboni, A. Castellani, I. Peroni: "Thermoelastic Characteristics Testing on Kevlar Samples for Spacecraft Structures", 36th I.A.F. Congress, Stockholm, 1985, I.A.F. 85-215.

[9] "Vibration Damping of Kevlar 49 Aramid, Graphite and Fiberglass Fibers and of Composites Reinforced with these Fibers", PIM 428, Du Pont Company, Wilmington, Delaware, 1981.

[10] L. Balis Crema, A. Castellani, A. Serra: "Experimental Tests for Damping Measurements on Several Short Glass Fiber Composites", to be published.

[11] L Balis Crema, A. Castellani: "Damping Characteristics on Fabric and Laminate Kevlar Samples", to be published.

Vibration Damping of Solid Propellant Rocket Motors

by

Robert A. Heller and Mahendra P. Singh
Department of Engineering Science & Mechanics
Virginia Polytechnic Institute & State University
Blacksburg, VA 24061

Abstract

Solid propellant rocket motors are composite structures consisting of a visco-elastic material with high damping and a metal or other hard case. The two are adhesively attached to each other.

During transportation, whether by ground vehicles, air or space launch systems, these motors undergo high frequency vibrations.

Because the damping characteristics of the propellant, binder and case are temperature and frequency dependent and because the excitation is usually of the random vibration type, analysis of such structures requires knowledge of the complex modulus for the materials involved.

A random vibration analysis is carried out in the frequency domain utilizing power spectral load inputs to a motor which is divided into lumped masses.

The missile is considered to be a composite cylinder with longitudinally variable cross-sectional properties. An acceleration power spectrum for operational conditions is used as excitation. Frequency response functions and output power spectra for bending and shear stresses are presented. The power spectral information is then used to evaluate the statistical properties of the random output.

1. Introduction

During transportation of solid propellant motors stresses are induced due to vehicle vibrations. These stresses vary randomly in time and are in addition to the stresses induced by environmental temperature variations.

Random vibration methodology is used for the evaluation of stresses and associated cumulative damage. Frequency response functions for bending and shear stresses in the motor are developed with the aid of the transfer matrix technique of structural dynamics (1). The motor is modeled as a composite beam with a solid propellant core encased in a steel shell. For analysis purposes the beam is discretized into lumped masses connected by elastic and viscoelastic beam segments. This discretization allows for variable mechanical properties in the longitudinal direction. The frequency response functions are used in conjunction with input power spectra to obain the standard deviations of induced stresses.

2. Analytical Model of Missile

A missile carrying a warhead and guidance system and powered by a solid propellant motor, having the simplified weight distribution shown in Fig. 1 is analyzed. The bending rigidity of the missile is provided by an elastic, steel shell of 1.52 mm thickness and 127 mm outer diameter, the aft portion of which is filled with a viscoelastic solid propellant having a 47 mm diameter smooth circular bore.

The structure is supported at two points on viscoelastic cushions (Fig. 1) and is transported on a truck bed.

To analyze the shear and bending stresses that develop as a result of vehicular vibrationss produced by the terrain, the beam is discretized into a lumped mass system as shown in Fig. 1. The masses, m, and corresponding rotatory inertias, J, of each lump as well as the elastic and viscoelastic bending rigidities, EI are also listed in the figure.

The visco-elastic, complex modulus for the propellant

$$E(\omega) = E'_{(\omega)} + iE''_{(\omega)} \tag{1}$$

is given in terms of the storage modulus

$$E'(\omega) = E_\infty + \sum_{i=1}^{15} \frac{E_i \omega^2 a_T^2 \tau_i^2}{1 + \omega^2 \tau_i^2 a_T^2} \tag{2}$$

and the loss modulus

$$E''(\omega) = \sum_{i=1}^{15} \frac{E_i \omega a_T \tau_i}{1 + \omega^2 \tau_i^2 a_T^2} \tag{3}$$

where E_∞, E_i and τ_i are listed in Ref. 2 and a_T is the shift function

$$\log a_T = - \frac{6.857 \, (T-25)}{146.43 + (T-25)} \quad T^0 C \tag{4}$$

	246.07 N/M	359.51 N/M	233.71 N/M
Weight/Unit Length	.62m	.45m	1.68m

Mass No.	1	2	3	4	5	6	7	8	9
Length, m	.13 .25	.34	.34	.34	.34	.34	.34	.34	.17
Mass, kg	6.22	7.38	11.53	9.98	8.05	8.06	8.05	8.03	8.0
J (kg$-$m^2)	.038	.064	.123	.115	.085	.085	.085	.085	.084

EI (N,M^2)

2.41×10^5
Elastic

$2.41 \times 10^5 + 1.14 \times 10^{-5} \ (E' + IE'')$
Viscoelastic
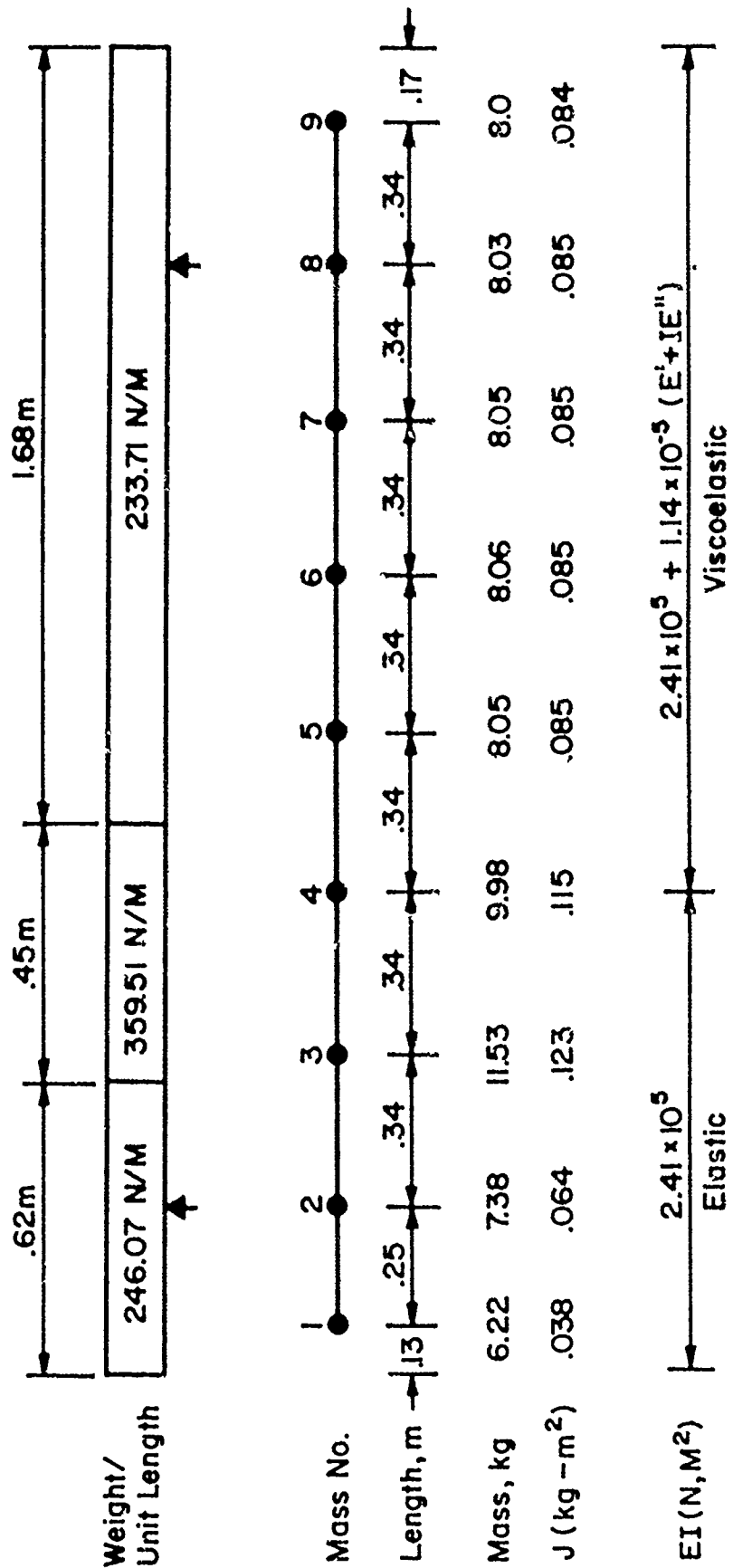
FIG. 1 MASS AND STIFFNESS CHARACTERISTICS OF THE LUMPED MASS MODEL

GA-3

The missile is considered to be a composite cylinder with longitudinally variable cross-sectional properties. Between stations 1 and 4 bending rigidity is supplied by a hollow elastic cylinder. Hence

$$(EI)_1 = E_{steel} \frac{\pi}{32} (d_3^4 - d_2^4) \tag{5}$$

where $E_{steel} = 3 \times 10^7$ psi $(2.07 \times 10^{11} \text{ N/m}^2)$, d_3 and d_2 are the outer and inner diameters of the casing.

Between stations 4 and 9 the viscoelastic propellant in a steel shell is considered. Therefore

$$(EI)_2 = \frac{\pi}{32} (E_{steel}(d_3^4 - d_2^4) + (E' + iE'') \cdot (d_2^4 - d_1^4)) \tag{6}$$

The parameters are presented on Fig. 1 for a temperature of -45°C. At the supports the stiffness constant is assumed as follows:

$$k_j = k' + ik'' = 4 \times 10^4 (1 + .05i) \tag{7}$$

Transfer Matrix Analysis of Lumped Mass System with Multiple Support Inputs

The lumped mass system shown in Fig. 1 consists of masses connected by beam segments.

Fig. 2 shows the free body diagrams for a typical mass element and the adjacent beam segment. Each mass has rotatory inertia, while beam segments have bending rigidities, EI. Beams transfer shears, bending moments, slopes and deflections from the right side of station j to the left side of station j+1 by bending rigidity. Mass elements are loaded in addition to spring supports by shears, bending moments, translational and rotational inertia forces.

The variables of interest at any station: deflection, slope, moment and shear may be expressed in the form of a state vector (z) as follows:

$$(z)_j^r = \left\{ \begin{matrix} y \\ \theta \\ M \\ V \end{matrix} \right\}_j^r \quad \text{on the right (r) side of station j} \tag{8}$$

To transfer the vector from $(z)_j^r$ to $(z)_{j+1}^\ell$, that is across a beam segment, a transfer matrix, [F], is used

$$(z)_{j+1}^\ell = [F]_{j+1} (z)_j^r \tag{9}$$

where

$$[F]_{j+1} = \begin{bmatrix} 1 & \ell & \ell^2/2EI & \ell^3/6EI \\ 0 & 1 & \ell/EI & \ell^2/2EI \\ 0 & 0 & 1 & \ell \\ 0 & 0 & 0 & 1 \end{bmatrix}_{j+1} \tag{10}$$
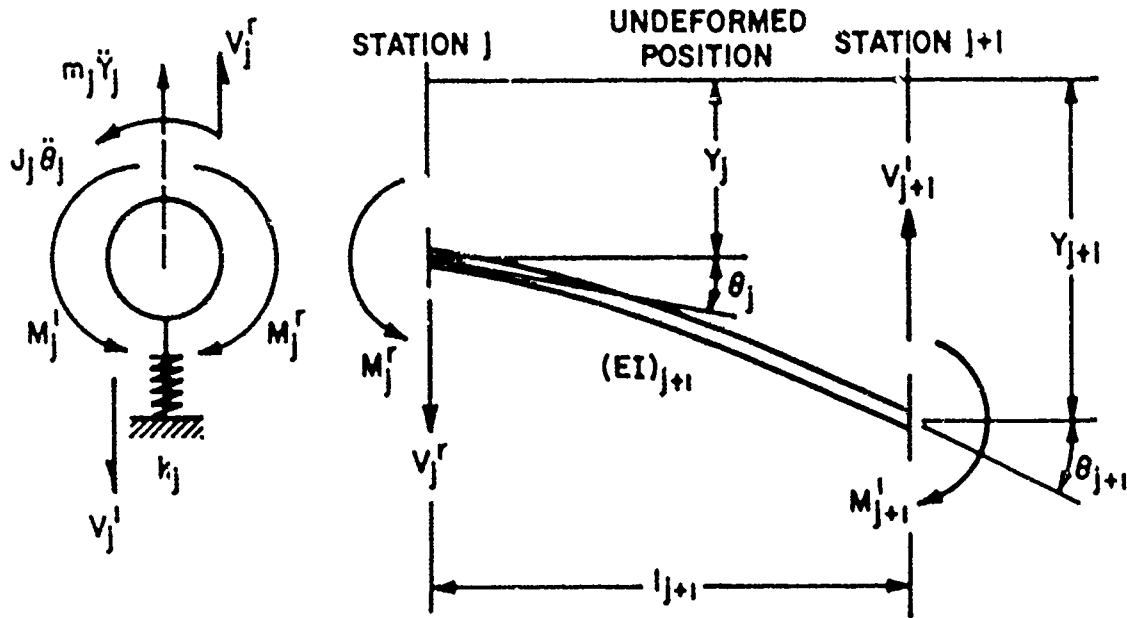
FIG. 2   FREE BODY DIAGRAMS OF A MASS AND ADJACENT BEAM SEGMENT

(a)

(b)
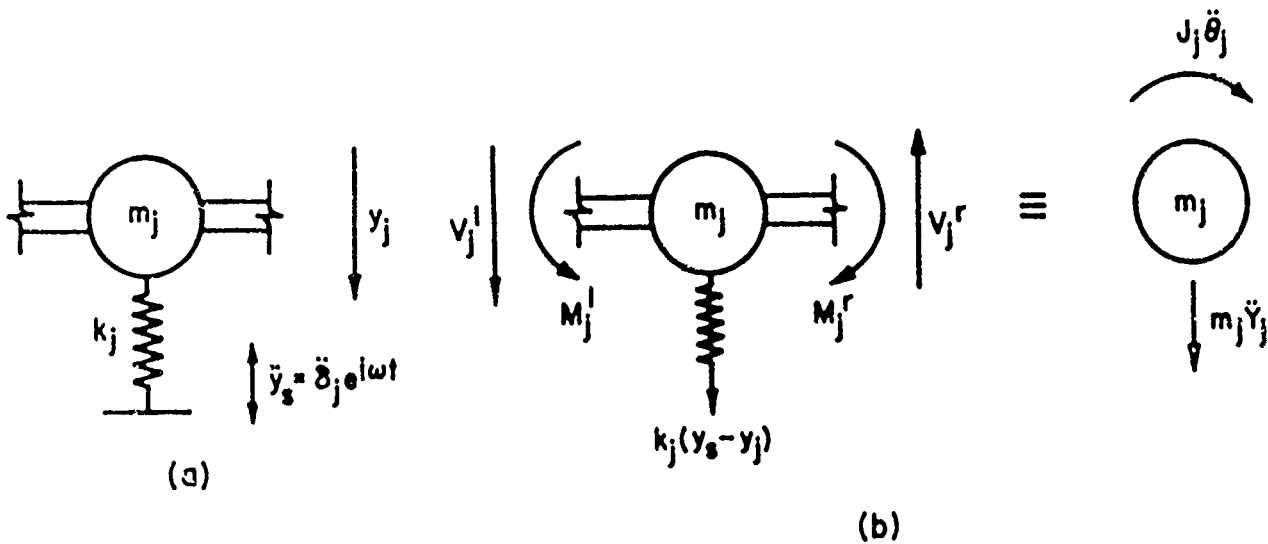
FIG. 3 EQUILIBRIUM OF A LUMPED MASS WITH SUPPORT EXCITATION

To transfer the vector $(z)_j^\ell$ from the left side of a lumped mass j to the right, the equilibrium of forces and moments in Fig. 2 requires

$$(z)_j^r = [U_j](z)_j^\ell + (L)_j \tag{11}$$

where the transfer matrix $[U]_j$ for a sinusoidal support motion with frequency ω is defined as follows:

$$[U_j] = \begin{bmatrix} 1 & 0 & 0 & 0 \\ 0 & 1 & 0 & 0 \\ 0 & -J_j\,\omega^2 & 1 & 0 \\ (m_j\omega^2-k_j) & 0 & 0 & 1 \end{bmatrix}_j \tag{12}$$

and L_j is the input load at j. For sinusoidal loading, $m\ddot{y}$ and $J\ddot{\theta}$ in Fig. 2 become $-m\omega^2 y$ and $-J\omega^2\theta$. $(z)_j^\ell$ may be transferred to the right of station k with the use of transfer matrix $_k^r[T]_j^\ell$, which consists of the products of F and U matrices, as follows:

$$(z)_k^r = {}_k^r[T]_j^\ell (z)_j^\ell \tag{13}$$

where

$${}_k^r[T]_j^\ell = [\ddot{U}]_k[F]_k \times \ldots \times [F]_{j+2}[U]_{j+1}[F]_{j+1}[U]_j \tag{14}$$

similarly

$${}_k^\ell[T]_j^\ell = [F]_k[U]_{k-1} \times \ldots \times [F]_{j+2}[U_{j+1}][F]_{j+1}[U]_j \tag{15}$$

and

$${}_k^\ell[T]_j^r = [F]_k[U]_{k-1} \times \ldots \times [F]_{j+2}[U]_{j+1}[F]_{j+1} \tag{16}$$

2 Mass Supported on a Movable Support

Fig. 3a shows a mass, with a movable support. The response of the system to a unit harmonic acceleration will be calculated. Fig. 3b shows the free body diagram of mass m_j subjected to a support acceleration of $\delta_j e^{i\omega t}$. Writing the equations of equilibrium one obtains the following:

$$\begin{Bmatrix} y \\ \theta \\ M \\ V \end{Bmatrix}_j^r = \begin{bmatrix} 1 & 0 & 0 & 0 \\ 0 & 1 & 0 & 0 \\ 0 & -\omega^2 J_j & 1 & 0 \\ \omega^2 m_j - k_j & 0 & 0 & 1 \end{bmatrix} \begin{Bmatrix} y \\ \theta \\ M \\ V \end{Bmatrix}_j^\ell + \begin{Bmatrix} 0 \\ 0 \\ 0 \\ k_j \end{Bmatrix} \cdot \delta_j \tag{17}$$

or

$$\{z\}_j^r = [U]_j \{z\}_j^\ell + \{f_j\}\delta_j \tag{18}$$

in which $\{f\}_j$ is the forcing function vector and the support displacement, $\delta_j = -\delta_j/\omega_j^2$.

Boundary Conditions - Frequency Response Functions

Using the matrices, the transfer of a state vector at a point in the beam to another point can be easily achieved, by Eq. 13. Thus, if a state vector at a location is known, the state vector at any other location on the beam can also be obtained. It is convenient to obtain the state vector on the left most end of the beam using the zero-force boundary conditions at the ends. This will be illustrated for the beam in Fig. 1 subjected to a unit harmonic motion of its jth support.

The equation relating the state vector on the left end to the one on the right with a harmonic support movement at an intervening support is as follows:

$$\{z\}_n^r = {}_n^r[T]_1^{\ell}\{z\}_1^{\ell} + {}_n^r[T]_j^r\{f_j\}$$ (19)

in which n represents the right most lumped mass and

$$\{f_j\} = \begin{Bmatrix} 0 \\ 0 \\ 0 \\ -1/\omega^2 \end{Bmatrix}$$ (20)

Since moment and shear are zero on the left of mass 1 and on the right of mass n,

$$\begin{Bmatrix} y \\ \theta \\ 0 \\ 0 \end{Bmatrix}_n^r = {}_n^r\begin{bmatrix} T_{11} & T_{12} & T_{13} & T_{14} \\ T_{21} & T_{22} & T_{23} & T_{24} \\ T_{31} & T_{32} & T_{33} & T_{34} \\ T_{41} & T_{42} & T_{43} & T_{44} \end{bmatrix}_1^{\ell} \cdot \begin{Bmatrix} y \\ \theta \\ 0 \\ 0 \end{Bmatrix}_1^{\ell}$$

$$+ {}_n^r\begin{bmatrix} T_{11} & T_{12} & T_{13} & T_{14} \\ T_{21} & T_{22} & T_{23} & T_{24} \\ T_{31} & T_{32} & T_{33} & T_{34} \\ T_{41} & T_{42} & T_{43} & T_{44} \end{bmatrix}_j^r \cdot \begin{Bmatrix} 0 \\ 0 \\ 0 \\ -1/\omega^2 \end{Bmatrix}$$ (21)

Y and θ at station 1 can now be obtained using the last two simultaneous equations as follows:

$$\begin{Bmatrix} y \\ \theta \end{Bmatrix}_1^{\ell} = \frac{1}{\omega^2} \left({}_n^r\begin{bmatrix} T_{31} & T_{32} \\ T_{41} & T_{42} \end{bmatrix}_1^{\ell} \right)^{-1} \cdot {}_n^r\begin{Bmatrix} T_{34} \\ T_{44} \end{Bmatrix}_j^r$$ (22)

Eq. 22 defines the frequency response function of displacement y and rotation, θ, at station 1 due to a harmonic acceleration of the jth support. Using this, the frequency response function for displacement, rotation, moment and shear force on the left and right of a mass can be obtained as follows:
on the left:

$$\{z\}_k^{\ell} = {}_k^{\ell}[T]_1^{\ell}\{z\}_1^{\ell} + {}_k^{\ell}[T]_j^r\{f_j\}$$ (23)

GA-7

and on the right:

$$(z)_k^r = {}_k^r[T]_1^\ell (z)_1^\ell + {}_k^r[T]_j^r (f_j) \tag{24}$$

If the kth mass is on the left of the moving support (jth mass), the second terms on the right hand sides of Eqs. 23 and 24 are then zero.

Frequency response functions for bending and shear stresses in the propellent can be directly obtained as they are linearly related to these forces as follows:

$$s = \frac{M}{I} y \tag{25}$$

$$\tau = \frac{VQ}{Ib} \tag{26}$$

in which M and V are the bending moment and shear forces, I is the total moment of inertia of the cross-section, y the distance of the propellant fibre from the neutral axis, Q is the first moment of the area about the neutral axis and b is the cross sectional thickness at the neutral axis.

Figs. 4 and 5 show some typical frequency response function plots for bending and shearing stresses on the right of station 5 due to a support excitation at Station 2.

3. Input Loading

An acceleration power spectrum for transportation loads is shown in Fig. 6. The excitations are applied at the beam supports of the missile in the vertical direction.

It is assumed that the same input is applied at both supports but with a time delay of T. This is to incorporate the effect that the front and rear wheels of a transportation vehicle go over the same surface except with a time delay of T. In terms of this time delay T the cross correlation and cross spectral density function of the inputs, say at any two supports of Fig. 1 can be obtained as follows.

Since the two supports receive the same input, their autocorrelation functions and spectral density functions are identical. That is:

$$\ddot{Y}_i(t) = \ddot{Y}_j(t + \Delta t_{ij}) \tag{27}$$

in which $\ddot{Y}_i(t)$ is the input at support i at time t and $\ddot{Y}_j$ is the input at support j at a later time $t + \Delta t_{ij}$. Δt_{ij} is the time separation of these two inputs. Thus input auto spectra are

$$S_{ii}(\omega) = S_{jj}(\omega) = S(\omega) \tag{28}$$

The cross correlation function between the inputs at support i and j is given by

$$R_{ij}(\tau) = E[\ddot{Y}_i(t)\ddot{Y}_j(t+\tau)]$$
$$= E[\ddot{y}_i(t)\ddot{Y}_i(t - \Delta t_{ij} + \tau)] \tag{29}$$
$$= R_{ii}(\tau - \Delta t_{ij})$$

GA-8
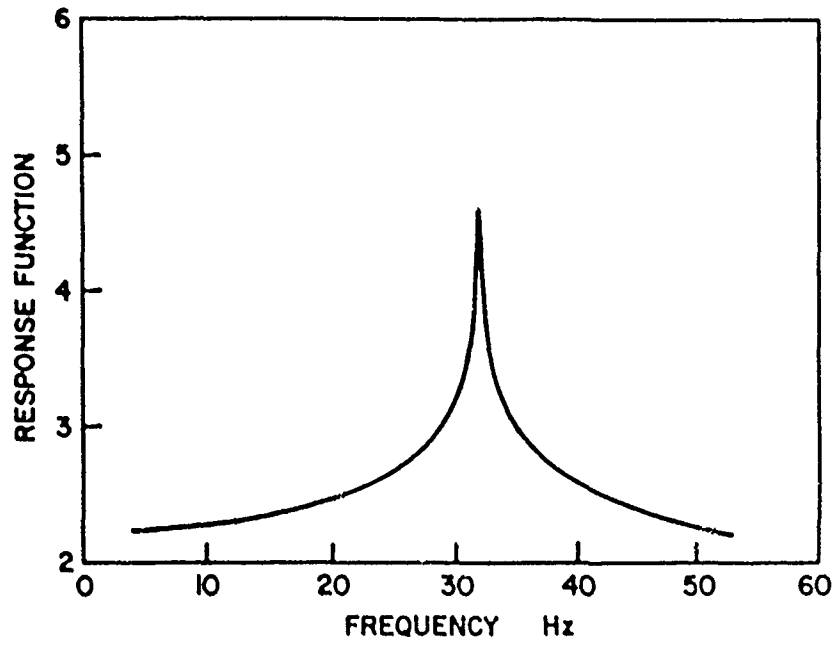
FIG. 4 FREQUENCY RESPONSE FUNCTION FOR BENDING STRESS ON RIGHT OF STATION 5 FOR EXCITATION AT STATION 2
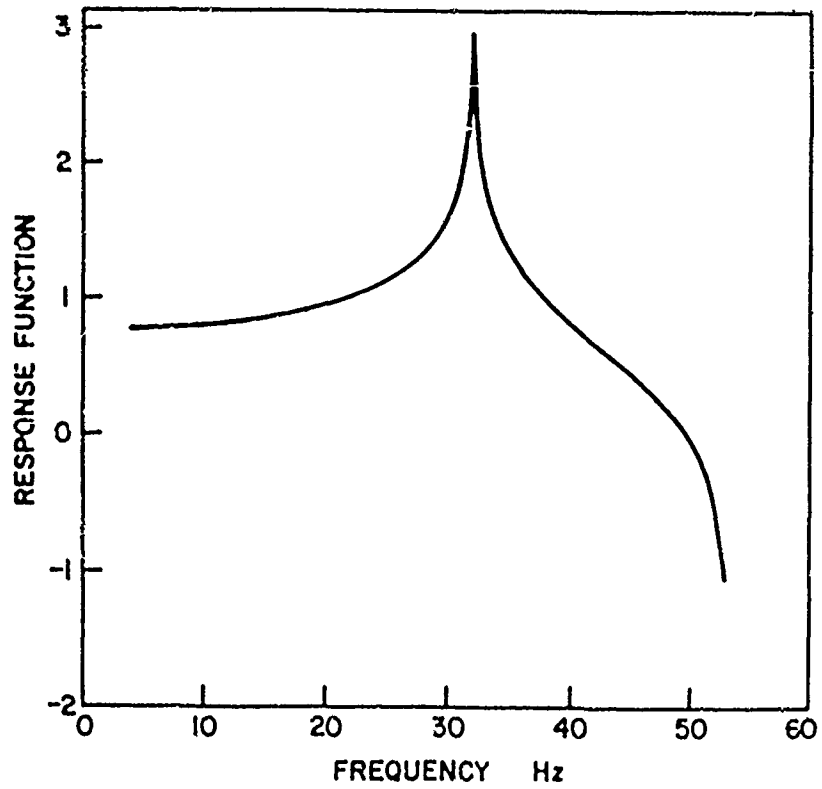
FIG. 5 FREQUENCY RESPONSE FUNCTION FOR SHEAR STRESS ON RIGHT OF STATION 5 FOR EXCITATION AT STATION 2

GA-9

Here in terms of the power spectrum

$$\int_{-\infty}^{\infty} S(\omega)e^{i\omega(\tau-\Delta t_{ij})}d\omega$$

$$= \int_{-\infty}^{\infty} S_{ij}(\omega)e^{i\omega\tau}d\omega \tag{30}$$

where

$$S_{ij}(\omega) = S(\omega)e^{-i\omega\Delta T_{ij}} \tag{31}$$

is the cross spectral density function of the inputs at the ith and jth supports. Similarly

$$S_{ji}(\omega) = S(\omega)e^{i\omega\Delta t_{ij}} = S_{ij}^{*}(\omega) \tag{32}$$

4. Power Spectra and Variances of Stresses:

For a stationary excitation and response, the spectral density function of a response quantity, R, (such as bending moment, shear forces or stresses) can be written as (3):

$$S_{RR}(\omega) = \begin{Bmatrix} H_1(\omega) \\ \cdot \\ \cdot \\ H_m(\omega) \end{Bmatrix}^{T} \cdot \begin{bmatrix} S_{11}(\omega) & S_{1m}(\omega) \\ S_{21}(\omega) & S_{2m}(\omega) \\ S_{m1}(\omega) & S_{mn}(\omega) \end{bmatrix} \cdot \begin{Bmatrix} H_1(\omega) \\ \cdot \\ \cdot \\ H_m(\omega) \end{Bmatrix} \tag{33}$$

where, $S_{RR}(\omega)$ is the spectral density function of the response quantity R, $H_j(\omega)$ is the frequency response function of R due to unit excitation at j, and $S_{k\ell}(\omega)$ is the cross spectral density function of the acceleration excitations at masses k and ℓ (Eq. 27), and m the number of supports excited. Frequency response functions are obtained as described in the preceding sections. The variance of response quantity R is obtained using the following well known equation:

$$\sigma^2 = \int_{-\infty}^{\infty} S_{RR}(w) \, d\omega \tag{34}$$

Figs. 7 and 8, show typical spectral density function plots for bending and shear stresses on the right side of station 5 due to excitations at stations 2 and 8. Time lags between 0.01 secs and .15 secs. were used for these calculations. The temperature of the motor is taken as -45°C.

Table 2 shows the standard deviations of bending and shear stresses on the right side of station 5, obtained for various values of time lag between the excitations at stations 2 and 8. A time lag of .0312 secs in the table corresponds to the fundamental period of the system. (From the frequency response function . curves, Figs. 5-6, it is noted that the fundamental frequency is 32.1 cps. which corresponds to a fundamental period of .0312 secs.) It should be noted that the maximum standard deviation values occur for a time lag of zero seconds, that is for the case of simultaneous excitation at the two supports.
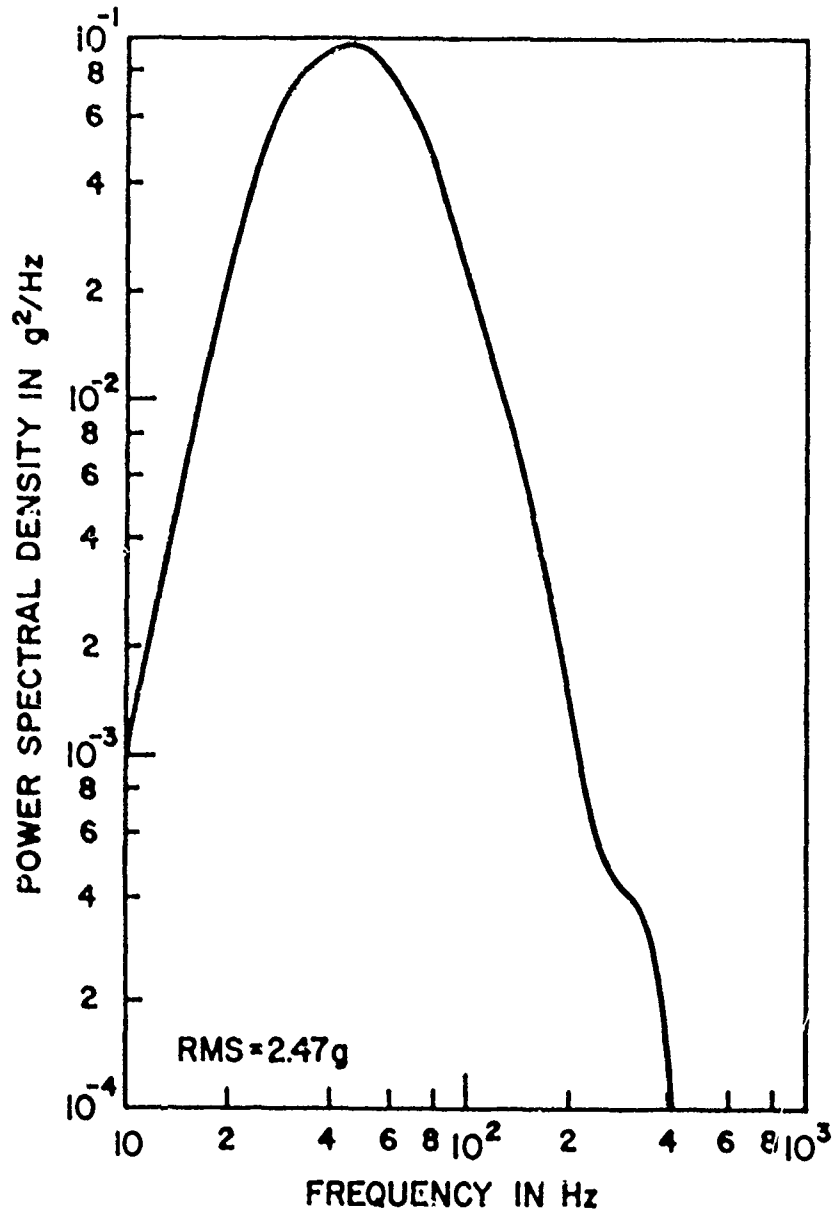
FIG. 6 ACCELERATION POWER SPECTRUM

GA-11
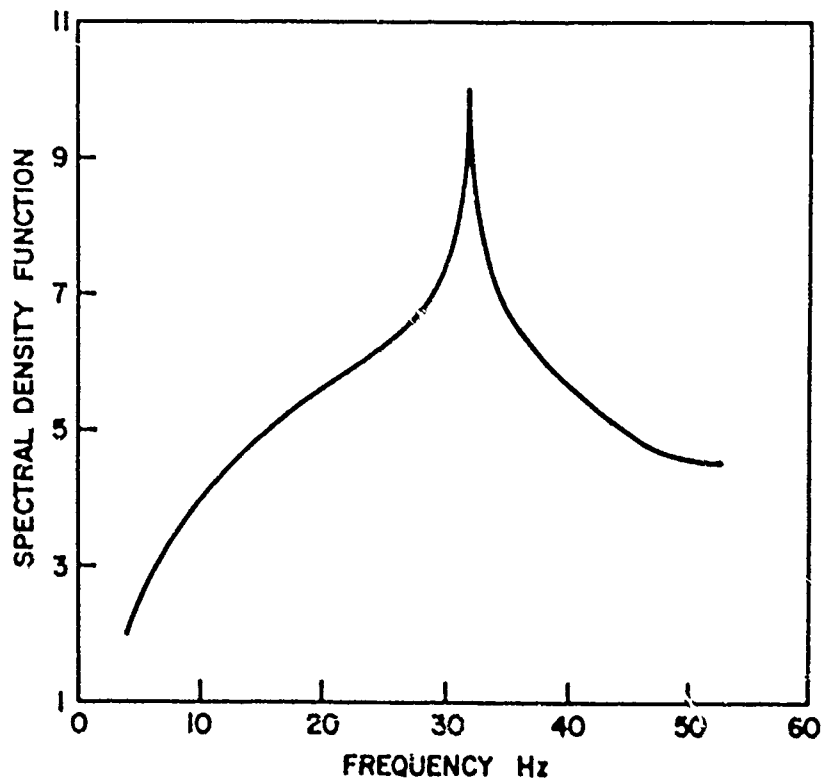
FIG. 7 SPECTRAL DENSITY FUNCTION FOR BENDING STRESS ON RIGHT OF
SECTION 5
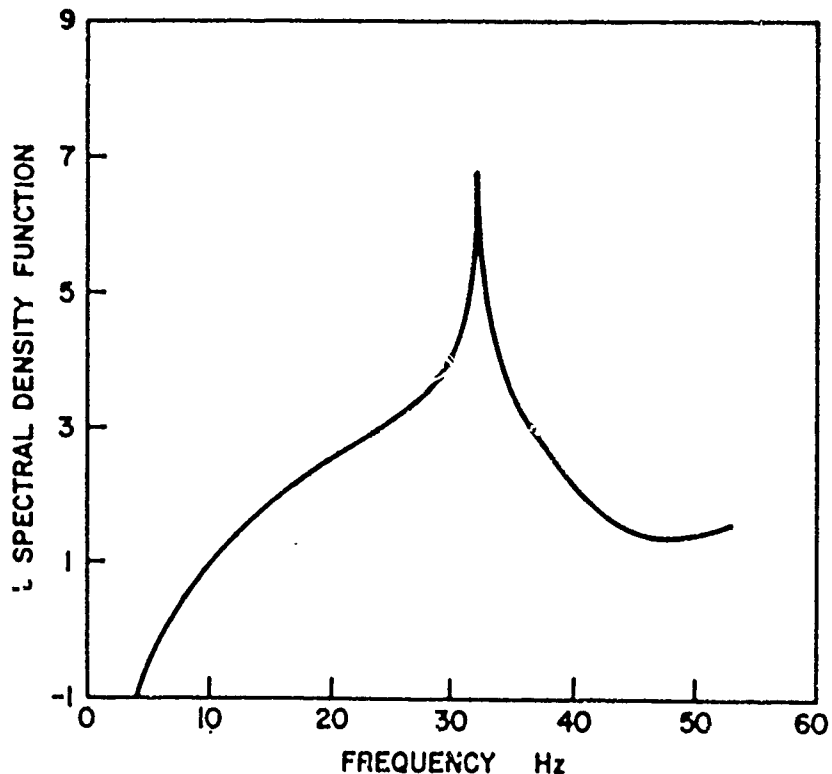
FIG. 8 SPECTRAL DENSITY FOR SHEAR STRESS ON RIGHT OF SECTION 5

5. Distribution of Peak Stresses

It is seen on Figs. 7 and 8 that both bending and shear stress power spectra are sharply peaked at the resonant frequency of 32.1 Hz which indicates that the response processes are narrow banded.

If it is assumed that the distribution of stress levels is Gaussian, with standard deviations given in Table 1, and zero mean, the distribution of peak stresses will follow the Raleigh distribution[3]

$$f_A(a) = \frac{a}{\sigma^2} e^{-\frac{1}{2}\left(\frac{a}{\sigma}\right)^2} \tag{35}$$

where a is the amplitude of the stress and σ is the standard deviation given in Table 1.

The average amplitude, $\bar{a}$, and the standard deviation of amplitudes, σ_a, may be calculated from Eq. 35 as

$$\bar{a} = 1.25\sigma \tag{36}$$

and

$$\sigma_a = .65\sigma \tag{37}$$

The average amplitudes and amplitude standard deviations for bending and shear stresses are also presented in Table 1.

While these stresses are relatively low, when superimposed on temperature induced and other stresses may be significant, particularly when the frequency of applications is also considered.

Table 1. Standard Deviations, σ, Mean Amplitudes, $\bar{a}$, and Amplitude Standard Deviations, σ_a, of Bending and Shear Stresses on the Right Side of Station 5 for Various Time Lags Between Inputs at Stations 2 and 8. Temperature -45°C.

Time Lag sec.	Bending Stress KN/m^2			Shear Stress KN/m^2		
	σ	$\bar{a}$	σ_a	σ	$\bar{a}$	σ_a
.0000	68.2	85.3	44.3	1.64	2.03	1.05
.0100	37.4	46.8	24.3	.89	1.11	.58
.0156	11.1	13.9	7.2	.26	.33	.17
.0312	68.0	85.0	44.2	1.61	2.01	1.05
.0500	25.1	31.4	16.3	.59	.74	.38
.1000	54.1	67.6	35.2	1.28	1.60	.83
.1500	56.7	70.9	36.9	1.34	1.68	.87

References

1. Lin, Y. K., "Probabilistic Theory of Structural Dynamics", McGraw-Hill Book Co., New York, 1967, pp. 169, 180.

2. Heller, R. A. and Singh, M. P., "Computer Code Using Random Probability Techniques for Rocket Motor Service Life Prediciton", Final Report, Part II, TR#RK-CR-80-1, Redstone Arsenal, May 1980.

3. Newland, D. E., "Random Vibrations and Spectral Analysis", Longman, London, 1975, pp. 42, 52.

4. Crandal, S. H. and Mark, W. D., "Random Vibration in Mechanical System", Academic Press, New York, 1963.

DAMPING PREDICTIONS USING MATERIAL PROPERTIES
FROM VARIOUS TEST METHODS

Michael L. Drake
University of Dayton
Research Institute
Dayton, Ohio

Matthew F. Kluesener
University of Dayton
Research Institute
Dayton, Ohio

ABSTRACT

There are a large number of tests which can be used to determine the damping characteristics of viscoelastic materials. All of the tests identify somewhat different damping properties when the same material is evaluated. The question immediately develops as to which set of damping properties generates the most accurate reduced frequency plot. The following paper addresses this question and illustrates one approach to determine the accuracy of the damping data in a specific temperature/ frequency range.

The approach taken to determine which of the material tests resulted in the most accurate damping data was to:

1) Generate a reduced temperature nomogram for each set of material data obtained from the various damping characterization tests;

2) Calculate the system damping for a cantilever beam model with a constrained layer damping system applied using each nomogram for material data input; and

3) Compare the predicted system response with the experimental test of the damped system.

Using the above approach, the BEAM test provided the lowest RMS error with the Rheometrics Mechanical Spectrometer as a close second in one instance.

INTRODUCTION

If one reviews the literature, one would find that there are a large number of test methods which can be used to determine the damping characteristics of viscoelastic materials.[1,2,3] Ideally, all the tests would identify the same damping properties when the same material was evaluated; however, in reality, there are variations in the properties measured.

The question immediately develops as to which set of damping properties is more correct over a given temperature and frequency range. A more appropriate question is which set of material properties generates the most accurate reduced frequency plot from which interpolations of damping properties over any frequency and temperature range can be made. The following paper addresses this question and illustrates one approach to determine the accuracy of the damping data in a specific temperature frequency range, but makes no claim to completely answer the question.

As part of the Relsat Program,* the University of Dayton Research Institute (UDRI) conducted a series of damping characterization tests on 3M's ISD-112 and GE's SMRD 100F90A.[2] As expected, each characterization test resulted in slightly different damping properties. The thrust of this paper is not a detailed investigation of the material data generated from each test (see Reference 2) but to evaluate the reduced temperature nomogram generated from each set of material data. The approach taken to determine which material test resulted in the most accurate damping data was to:

1) Generate a reduced temperature nomogram for each set of material data obtained from the various damping characterization tests;

2) Calculate the system damping for a cantilever beam model with a constrained layer damping system applied using each nomogram for material data input; and

3) Compare the predicted system response with the experimental test of the damping system.

The following paragraphs describe first the results from the ISD-112 data, then the results from the SMRD 100F90A data, and finally present the conclusions drawn from this work.

ISD-112 Results

The damping properties of ISD-112 were determined using:

1) The DuPont Dynamic Mechanical Analyzer (DMA),

---

* General Electric Space Systems Division prime contractor, Air Force Contract # F33615-82-C-3223.

2) The ASTM E-756-83 damping characterization standard-resonant cantilever beam (BEAM), and

3) The Rheometric Mechanical Spectrometer (RHEO).

All the ISD-112 material used in the material characterization tests and the damped system test was from the same material batch.

Figures 1, 2, and 3 are the reduced temperature nomograms for ISD-112 from the DMA, BEAM and RHEO tests respectively. The curves representing each material data set is shown in Figure 4 for comparison. There is obviously significant variation in the material properties determined by each test.

The DMA data on the ISD-112 only defines the properties into the beginning of the transition range. This limitation is typical of DMA data collected on very soft materials. Since the DMA collects data at only a single frequency at each temperature the data appear to have no scatter. The DMA test defined the highest modulus values and the lowest loss factor values found in the three test methods and had a temperature of peak loss factor approximately equal to that generated from the beam test.

The BEAM data for the ISD-112 do not extend far into the glass or rubber modulus plateaus which makes the curve fitting task more difficult. The lack of data in the glassy region are not typical for beam test data; however, limited data in the rubbery region are typical. The scatter seen in Figure 2 is typically of beam data.

The RHEO data for the ISD-112 extend into the glassy and rubbery modulus range approximately as far as the beam test data. The scatter in the data are quite small from the rubbery region through the transition region; however, as you start into the glassy region, the scatter begins to increase. This is believed to be caused by the test sample used. The Rheometric's data generated the lowest value of glassy modulus while the rubbery modulus compared well with the rubbery modulus from the beam test. The peak loss factor compared well with the value generated from the beam test although the temperature of peak damping was higher.

After reviewing these sets of material properties, one would indeed expect differences in the predicted damped response of a system using these three sets of data.

The damping system studied is shown in Figure 5. The steel cantilever beam was 9.5 inches long, 0.5 inches wide and 0.06 inches thick, the ISD-112 damping layer was 0.005 inches thick, and the constraining layer was 0.01 inch thick aluminum. This test system configuration was significantly different from that of the beam used in the ASTM standard characterization test.

The experimental test results, along with the fourth order beam theory predictions using each set of material properties, are shown in Figure 6 for the third mode (372.6 Hz) of the test system. The review of Figure 6 reveals that the DMA data do a very poor job of predicting the damped system test results. The RHEO data appear to predict better than the BEAM data but both predict a lower temperature of peak damping than is seen in the test results.

Figure 7 illustrates the comparison of predicted to test results for the sixth mode (1829.0 Hz) of the test system. Again, the DMA prediction is not good. The beam prediction using the BEAM data again has peak damping lower in temperature than seen in the test results but approximates the absolute value of peak damping very well. The RHEO data predict the temperature of peak damping correctly but under predict the maximum value of damping.

The BEAM and RHEO predictions seen in Figure 6 and 7 look reasonable and, in the past, would be accepted as good. However, analyzing the RMS error in modal loss factor for each mode across the temperature range tested revealed a rather large error. All the RMS error data are shown in Figure 8. The BEAM RMS error ranges from a high of 58.5 for mode 6 to a low of 45.0 for mode 4. The RHEO RMS error ranges from 48.6 at mode 2 to 30.7 at mode 4.

In view of these large RMS errors and after review the data are shown in Figures 6 and 7, RMS error was calculated for the data at 75°F, 100°F and 125°F which represents the three data points in the neighborhood of peak damping. In this range, the RMS error improved significantly, For the 3 point error (see Figure 9), the BEAM error now ranges from 42.5 for mode 2 to 13.9 for mode 6. The RHEO error range is 38.5 for mode 2 and 10.8 for mode 3.

Figure 10 presents the RMS error in the frequency prediction for all three material data sets. It is immediately apparent that the frequency prediction is significantly better than the loss factor prediction. The maximum error for both the BEAM and RHEO data are under 5 percent with most error values around 1 percent.

The first inclination was to assume that the reduced error in frequency means that the material characterization tests more accurately determine modulus than they do loss factor; however, more thought revealed this was not the case. A review of the energy dissipated per cycle equation, which is:

$$D_s = \int_{VOL} \eta\, G \gamma^2 dV \qquad (1)$$

revealed that both η and G strongly influence D and therefore ultimately modal loss factor in that

$$n_s = \frac{D_s}{U} \quad . \tag{2}$$

The damped resonant frequency, on the other hand, is much less sensitive to the modulus of the damping material.

An alternate way to look at the RMS error is to evaluate all the modes at a given temperature. This RMS error information is shown in Figure 11 for both loss factor and frequency data. Again, the DMA error is the largest while the RHEO has the lowest error for temperatures less than peak system damping and the BEAM has the lowest error for temperatures greater than peak system damping.

Figure 12 presents the total RMS error for all three material test methods. The RHEO data have the best overall RMS error for the system loss factor while the BEAM data have the best frequency RMS error. The 3 point data (data just around peak system damping) show that both the RHEO and BEAM have small errors in both loss factor and frequency predictions.

SMRD 100F90A RESULTS

The damping properties of 100F90A were determined using:

1) The DuPont Dynamic Mechanical Analyzer (DMA),

2) The ASTM E-756-83 damping characterization standard (BEAM),

3) The Rheometric Mechanical Spectrometer (RHEO), and

4) The Autovibron, a computer controlled Rheovibron, (AUTO).

All the 100F90A material used during the testing came from the same material batch.

Figures 13, 14, and 15, present the reduced temperature nomograms for the 100F90A for the DMA, BEAM, and AUTO tests respectively. All three nomograms were generated with the same T_0 which was 174.2°F. A comparison of the curve representations of each datum set is shown in Figure 16.

Figure 16 illustrates that the BEAM and DMA had good correlation in the glassy modulus value. The DMA data do not extend into the rubbery range and the BEAM data extend only into the beginning of the rubbery range. The AUTO data show a significantly softer glassy modulus value than either the DMA or BEAM; however, they do define a rubbery plateau. The BEAM and AUTO data correlate well in the rubber modulus area. The absolute value of loss factor is approximately the same for all three data sets; however, the BEAM indicates the lowest temperature of peak damping with the DMA predicting the highest temperature of peak damping.

Figure 17 presents the reduced temperature nomogram for the RHEO data. The data appear good from the glassy modulus into the transition

region. Note the glassy modulus corresponds well with the BEAM and DMA data and the absolute value of peak data correspond well with the other data. Also note that the T_0 used is 365F which is almost double that of the other material tests. Although the lower temperature portion of the nomogram by itself looks reasonable, the use of the very high T_0 is cause for concern. Figure 18 presents the RHEO data with the 174.2°F T_0 used in the other nomograms. This figure indicates the type of plot one would expect with too low a value of T_0 in that the modulus data show a shingling effect. The indication is simply that something is wrong with the RHEO data.

The damping system evaluated for the 100F90A is shown in Figure 19. Again, this damped cantilever beam is significantly different that the test specimen used in the BEAM test and the damping material thickness is different than that used in any of the material tests.

The experimental test results (system loss factor VS temperature) along with the fourth order beam predictions for each material data set are shown in Figure 20 for mode 3 (1200 Hz). It is immediately obvious that the variation in temperature of maximum material loss factor between the four data sets has a significant impact on the predicted temperature of peak system damping. Only the BEAM data predict the test results reasonably. Figure 21 presents similar data for mode 6 (5200 Hz) and illustrates the same trends seen in Figure 20.

Figures 20 and 21 indicate that only the BEAM data predict the r.   ad system response with a reasonable degree of accuracy. This c·   .sion is supported when we review the RMS error data presented in Figu.·e 22. The BEAM error ranges from 62.1% to 20.9%. All the other test method errors are totally unacceptable. As was seen in the ISD-112 data, the RMS error goes down when only the three temperatures around peak system damping are considered. For the BEAM, the 3 point data show RMS ranging from 37.3 to 19.1%.

The frequency data RMS are shown in Figure 23. Again, the frequency error is less than the loss factor error. The BEAM frequency RMS error for the 100F90A data are slightly higher than that seen with the ISD-112 data.

Figure 24 presents the RMS error for all the data sets across frequency at each temperature. The data again show the BEAM datum prediction to be the only acceptable one and indicate a similar trend as seen in the ISD-112 in that the BEAM RMS error is lower at temperatures below that of peak damping than it is above the temperature of peak damping.

Figure 25 presents the total RMS error and the conclusion is no surprise. The BEAM data most accurately predict the damped system test results.

CONCLUSIONS

Based on the RMS error presented in these two examples, the BEAM test provides the best material data to use in damping design and prediction of system damping. The authors feel that although this statement is factual, it is also misleading. The RHEO data from the ISD-112 produced excellent damped system predictions. The 100F90A RHEO test must be a bad test and if the test configuration was changed the RHEO data might produce prediction errors comparable to the ISD-112 results.

Other points of induced error are the errors in:

• The experimental measurements on the damped system,

• the fourth order beam theory used for damped system prediction, and

• the nomogram presentation of the material data.

If the experimental test on the damped system were run several times and the results averaged, this would most likely reduce any error introduced by the test results. The use of sixth order beam theory or finite element analysis to predict system damping instead of fourth order theory would reduce one source of error, but this error is not nearly large enough to explain the large differences between test and prediction. The authors feel that a large source of error, perhaps larger than that of the methods themselves, may be the nomogram presentation of the material properties. The nomograms presented in this paper used the Jones[4] α_T shift factor relationship.

The test methods considered in this paper determined material properties from approximately .01 Hz (for the RHEO) to greater than 5000 Hz (for the BEAM). Representing results from such a broad frequency range using the Jones α_T shift factor relationship may be stretching the range of applicability of this relationship since it was developed from data in the 100 to 5000 Hz range. Techniques are being developed which generate a shift factor for each material which may make the properties from various tests compare more favorably.[5]

The closing thoughts are that the BEAM test is used strictly for producing damping property data, and therefore, an experinced BEAM test operator is experienced in collecting damping data. The other test methods used are used for a variety of material property measurements and very seldom are they used to measure damping properties. The results of this fact implies that an experienced RHEO test operator most likely is not an experienced damping data collector, and therefore, may not consistantly generate reliable damping data. After some experience, this would obviously change.

It appears that most damping characterization methods are operator dependent and that experienced operators can produce reliable material property data (within the limitations of the particular test method) which

can be used in damped system design work. In critical situations a test series, as demonstrated in this paper, will be necessary to determine the most appropriate material characterization method for the damped system to be designed.

REFERENCES

1. Vibration Damping Short Course, presented by the University of Dayton, June, 1985.

2. Kluesener, M. F., "Comparison of Damping Material Properties by Various Test Methods," presented at the Vibration Damping Workshop II, March, 1986, and published in proceedings.

3. Jones, D. I. G., "A Critique of Complex Modulus Test Methods," presented at the Vibration Damping Workshop II, March, 1986, and published in proceedings.

4. King, C., "Computerized Processing and Graphic Representation of Viscoelastic Material Property Data," AFML-TR-79-4099, Wright-Patterson AFB, 1979. Available from Defense Technical Information Center as ADA079914.

5. Rogers, L., private communications.
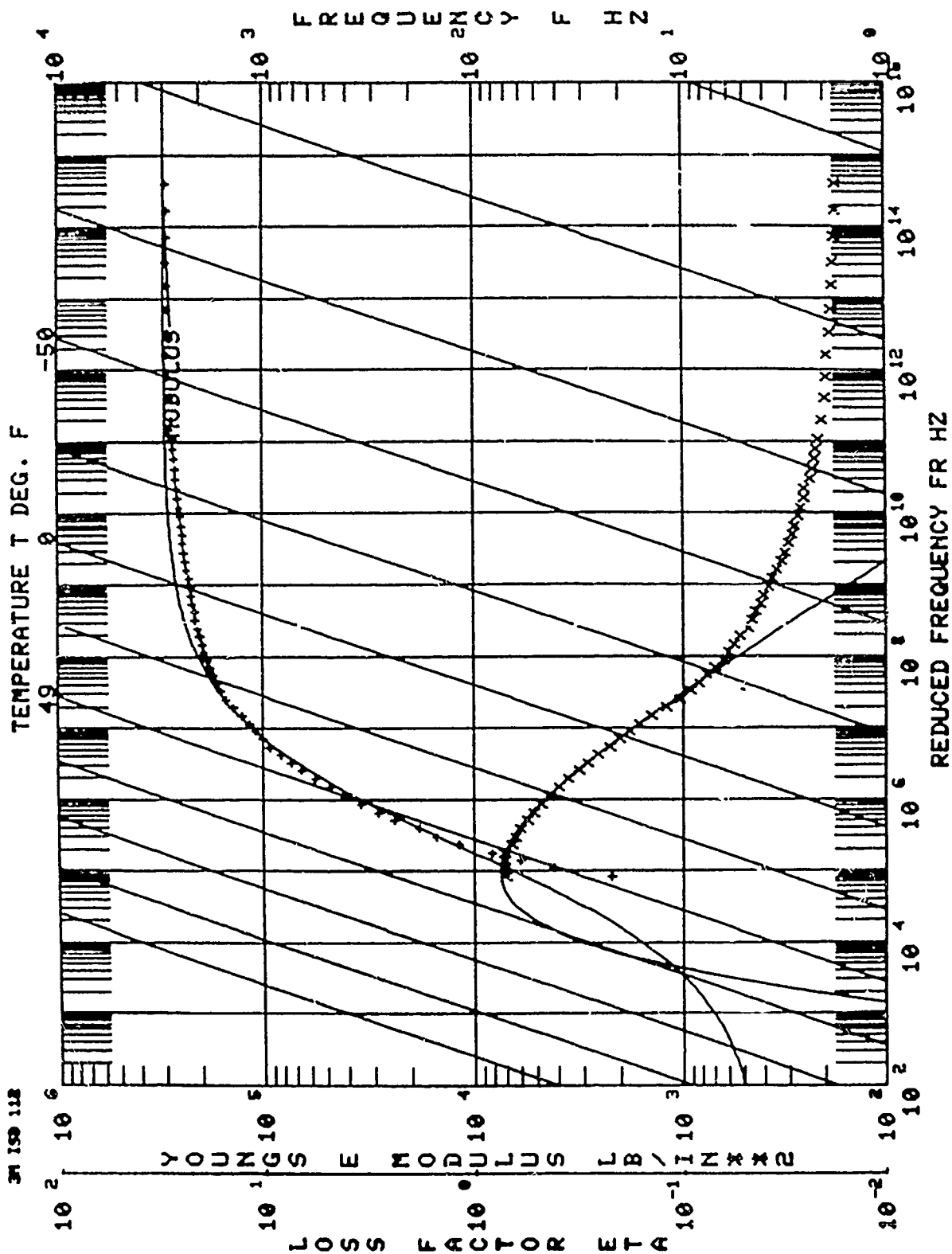
Figure 1 DMA Nomogram for ISD-112.
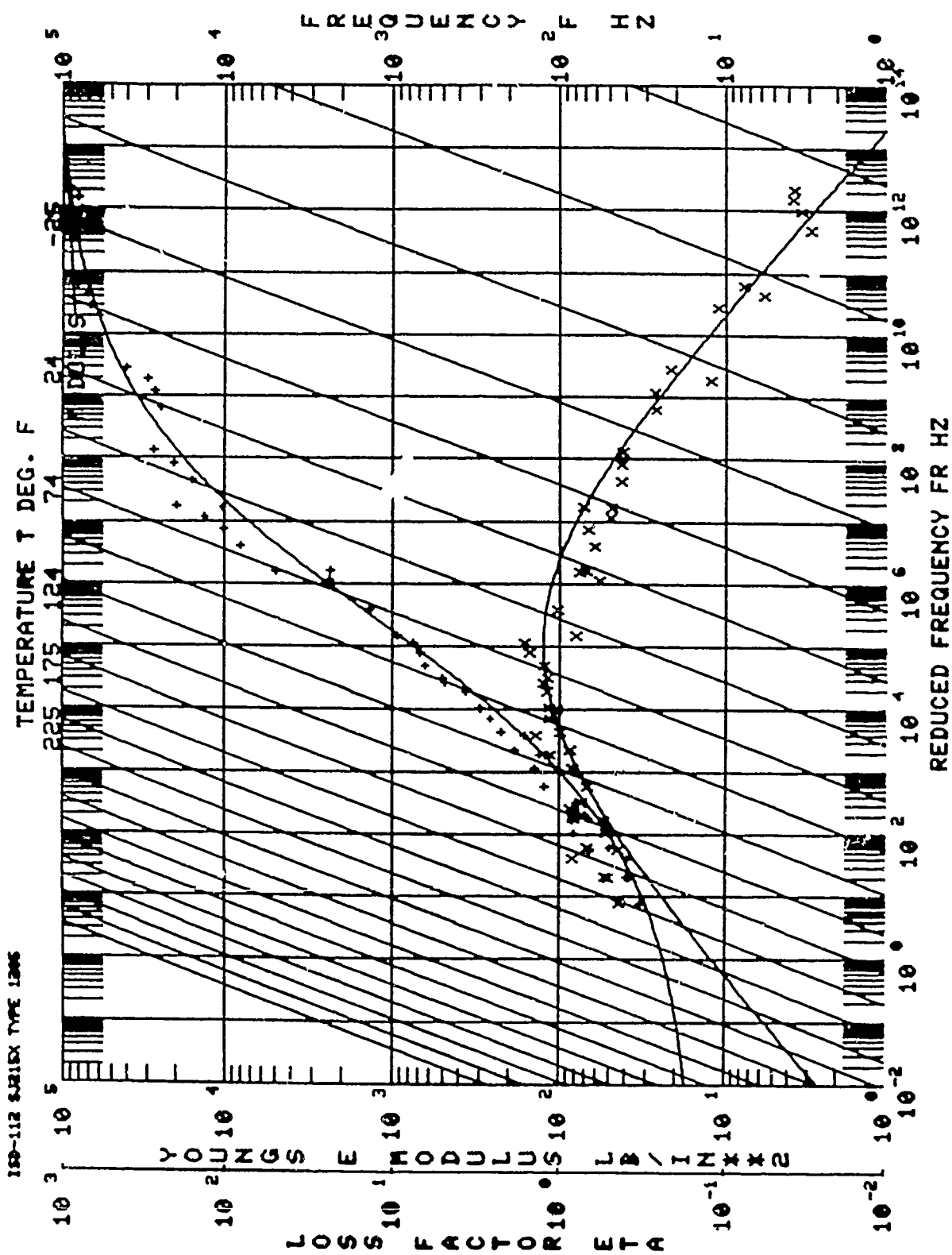
Figure 2 BEAM Nomogram for ISD-112.
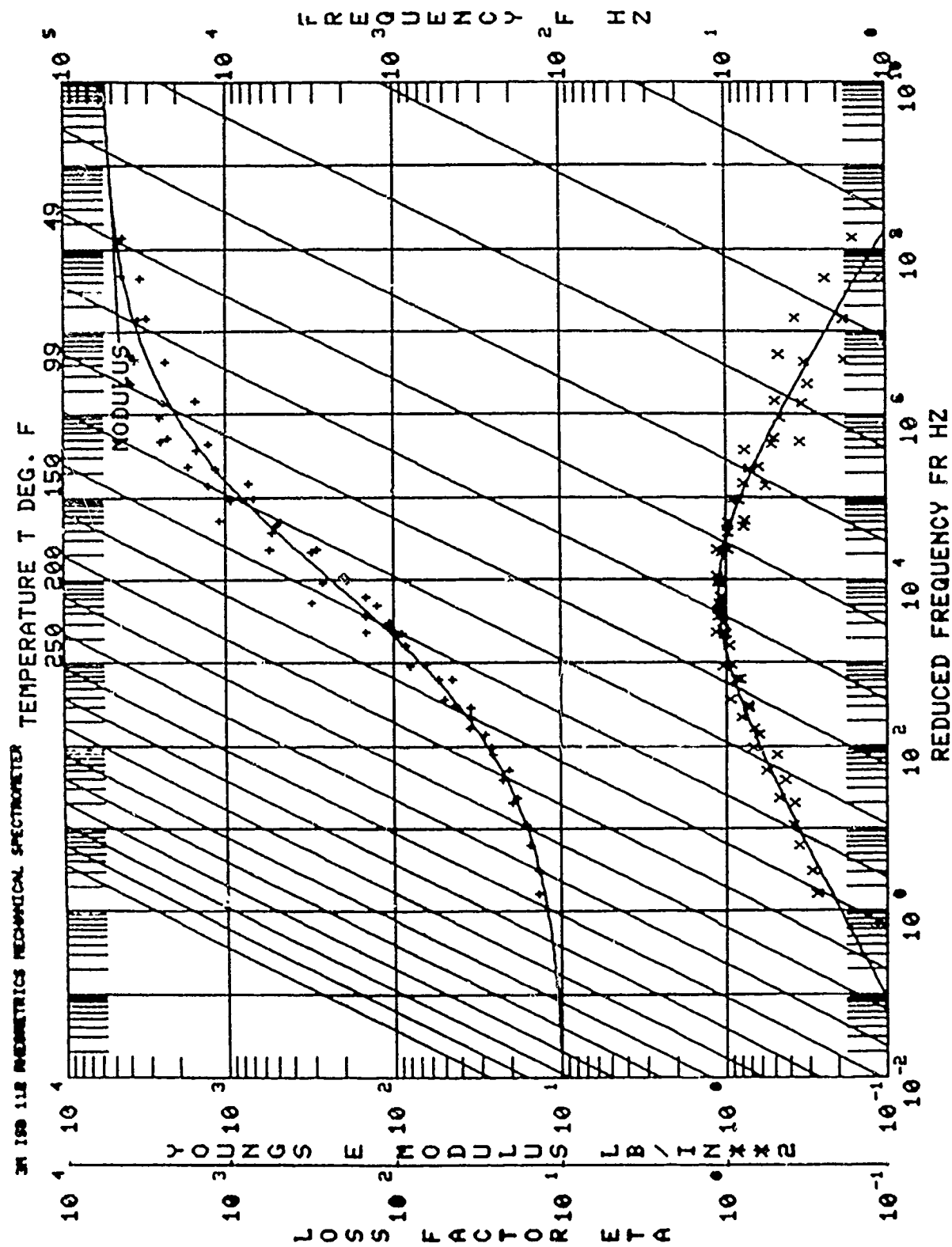
Figure 3 RHEO Nomogram for ISD-112.
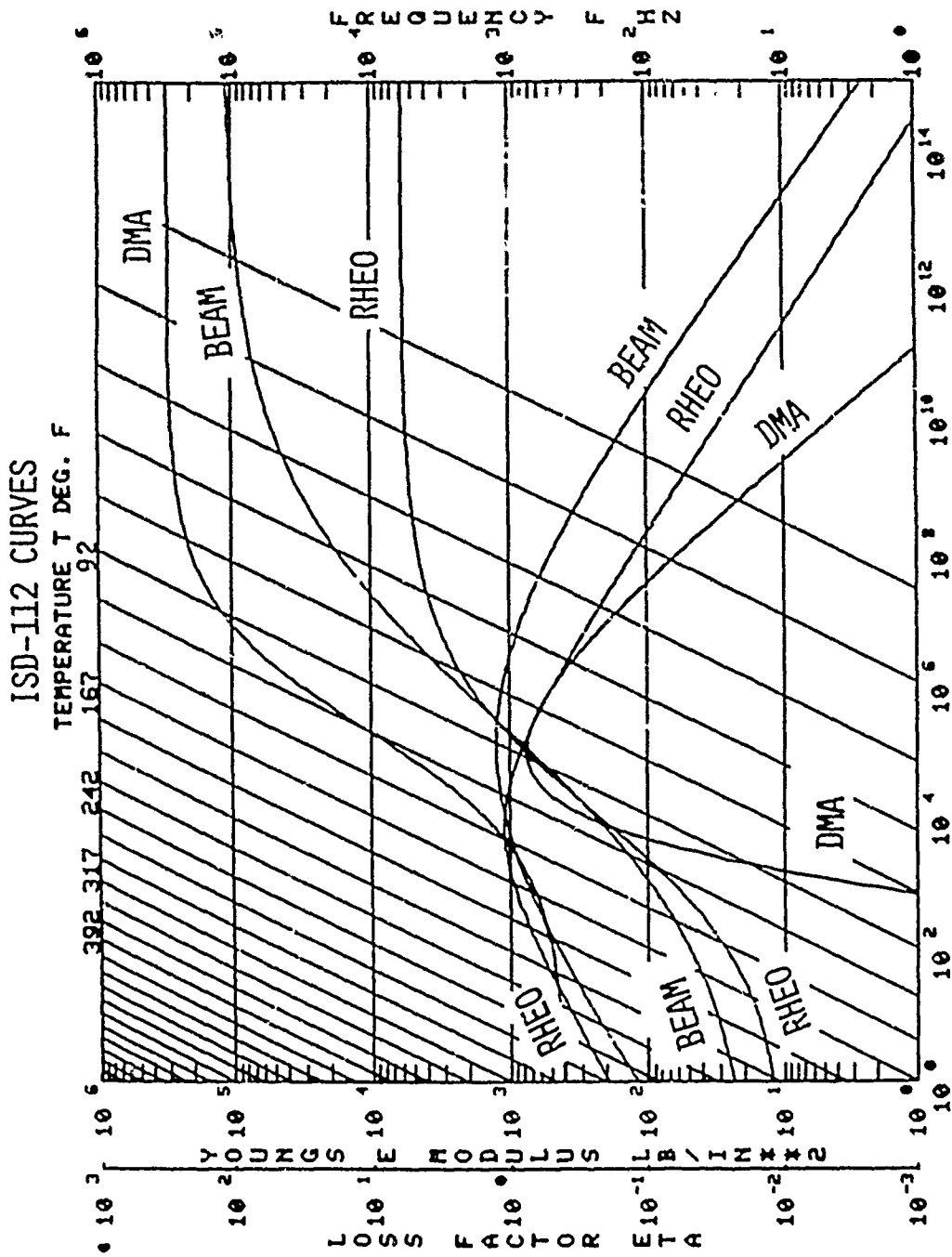
Figure 4 Comparison of Data Curves From the Three Test Methods
for the ISD-112 Material.
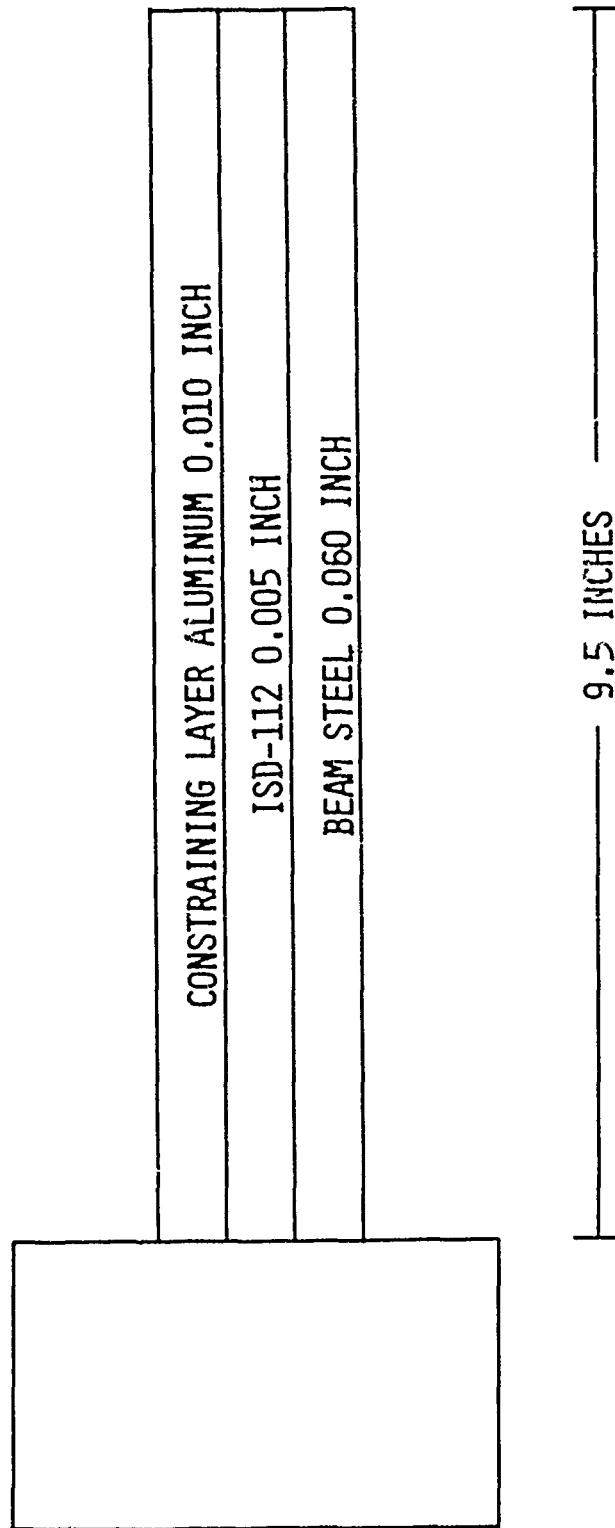
Figure 5 Damping System Tested With the ISD-112 Material.

CONSTRAINING LAYER ALUMINUM 0.010 INCH

ISD-112 0.005 INCH

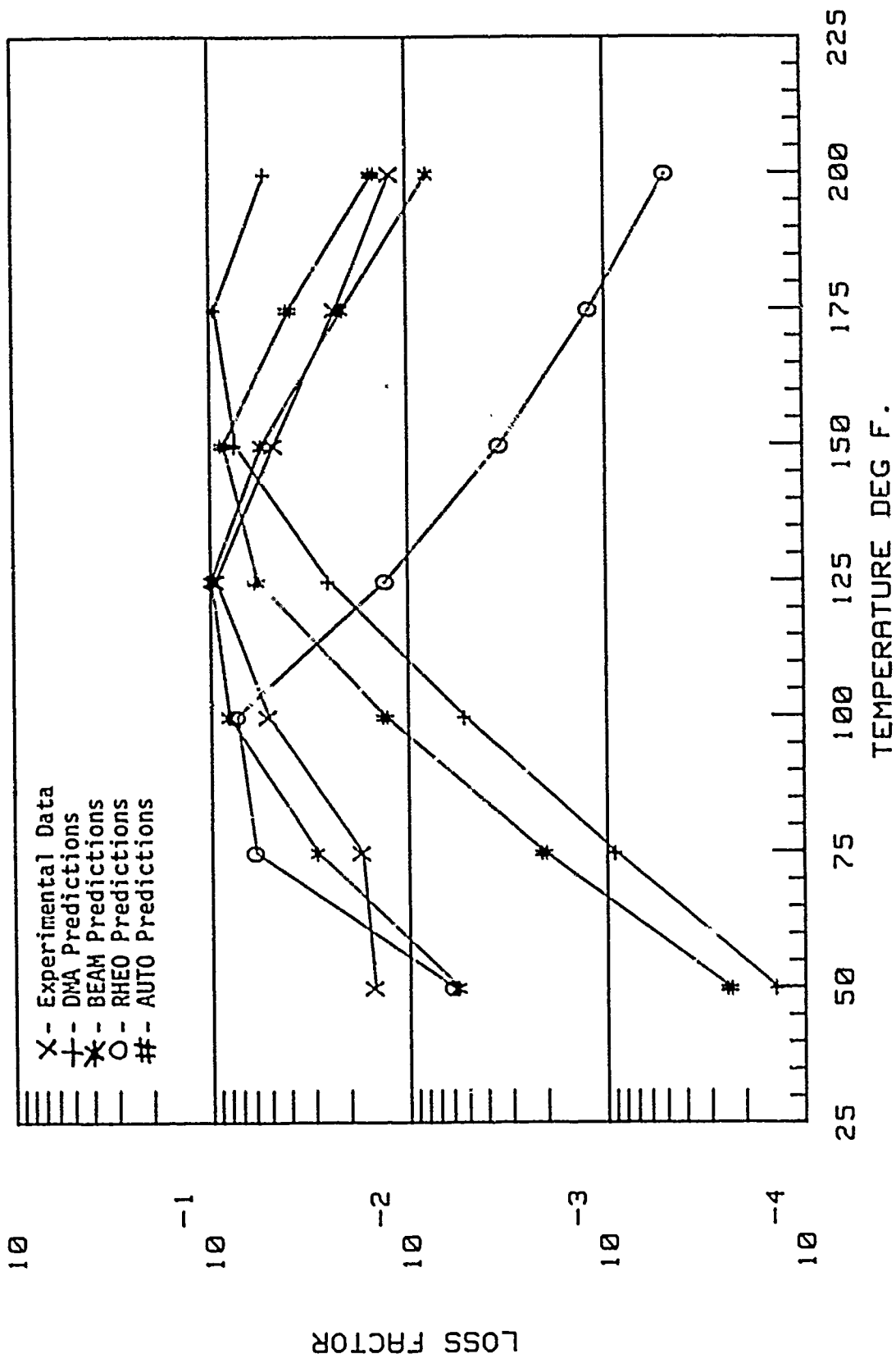BEAM STEEL 0.060 INCH

9.5 INCHES
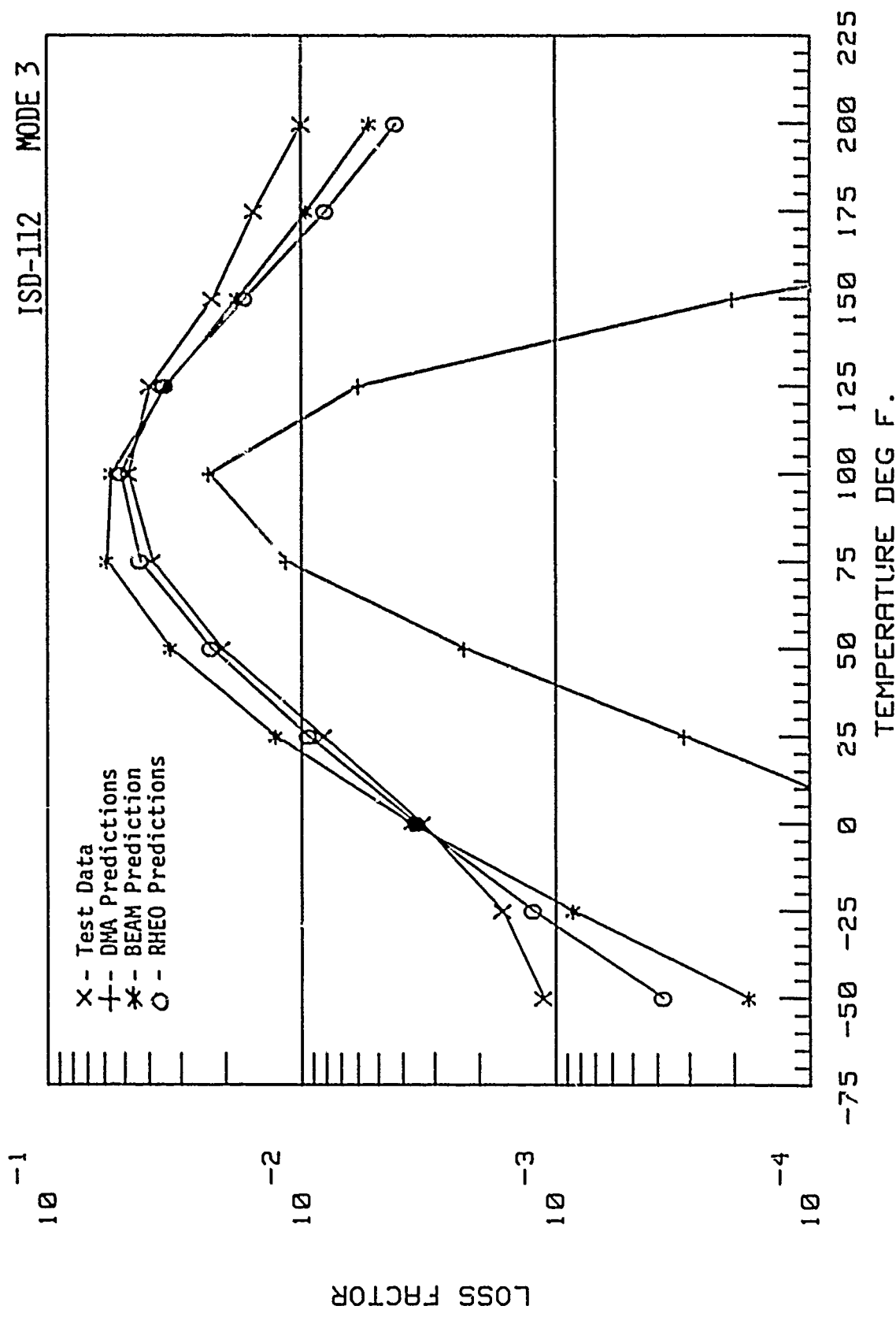
Figure 6 Comparison of Predicted Damping to Experimental Test Results for
ISD-112 for Mode 3.

GB-14
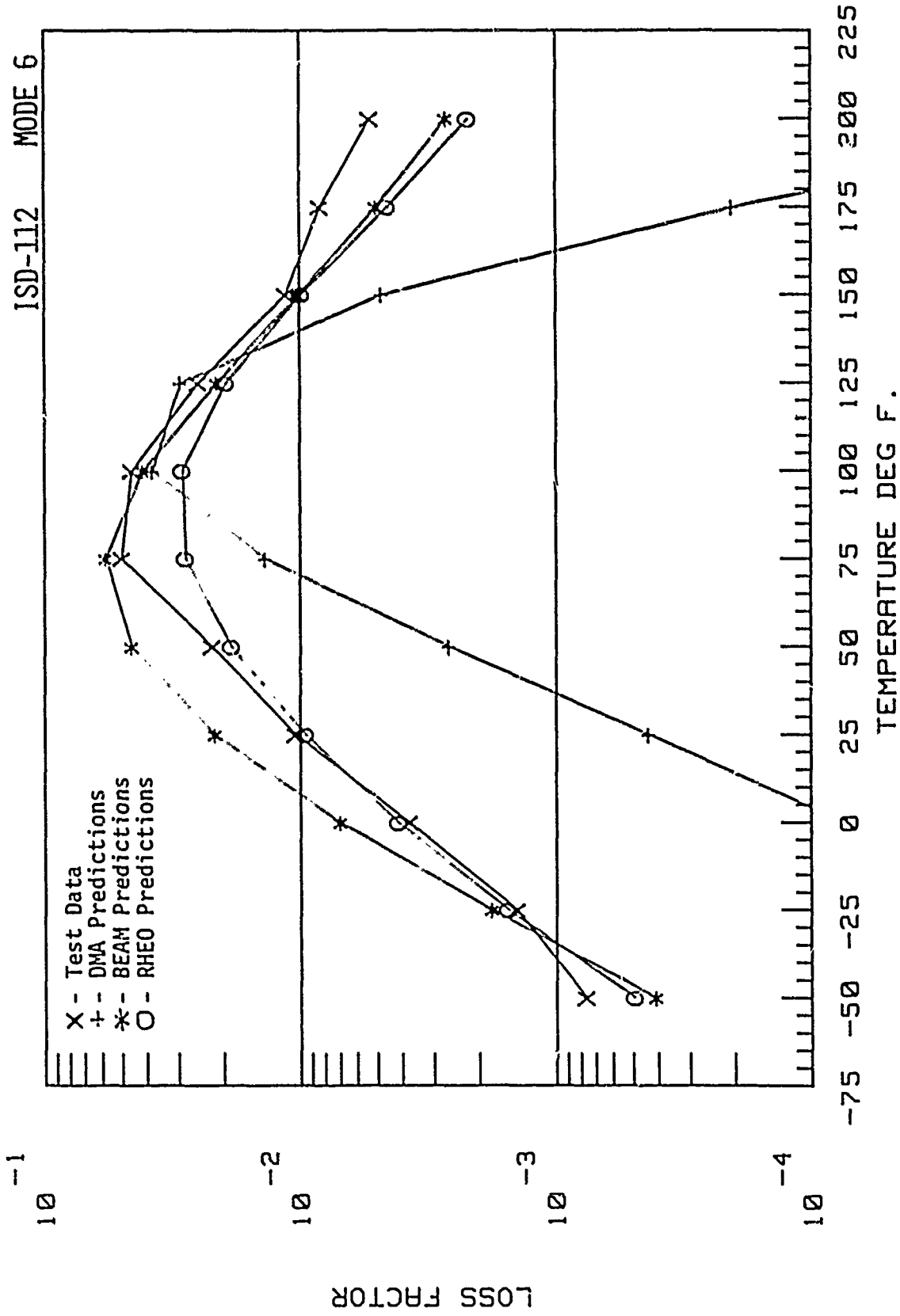
Figure 7 Comparison of Predicted Damping to Experimental Test Results for ISD-112 for Mode 6.

MODE NUMBER

	2	3	4	5	6
	ALL DATA	ALL DATA	ALL DATA	ALL DATA	ALL DATA
DMA	94.5	91.2	87.9	85.2	82.6
BEAM	50.4	45.7	45.0	50.3	58.5
RHEO	48.6	32.8	30.7	32.0	31.9

Figure 8   ISD-112 η_s RMS Error Across Temperature.

MODE NUMBER

	2	3	4	5	6
	3 + POINTS	3 POINTS	3 POINTS	3 POINTS	3 POINTS
DMA	83.6	70.4	54.8	45.5	44.3
BEAM	42.5	31.9	20.9	18.3	13.9
RHEO	38.5	10.8	11.8	25.9	35.4

+ 3 Points means RMS error calculated from the data at
75°F, 100°F, and 125°F

Figure 9   ISD-112 η_s RMS Error at 3 Temperatures Around
Peak Damping.

MODE NUMBER

	2		3		4		5		6	
	ALL DATA	3 POINTS	ALL DATA	3 POINTS	ALL DATA	3 POINTS	ALL DATA	3 POINTS	ALL DATA	3 POINTS
DMA	4.7	4.9	3.9	4.8	3.7	5.3	5.8	5.2	3.1	4.9
BEAM	0.9	1.0	0.6	0.3	0.6	0.1	4.6	0.6	1.1	0.9
RHEO	0.7	0.8	1.0	0.3	1.8	0.5	4.0	1.1	3.6	1.5

Figure 10 Frequency RMS Error Across Temperature for ISD-112

GB-18
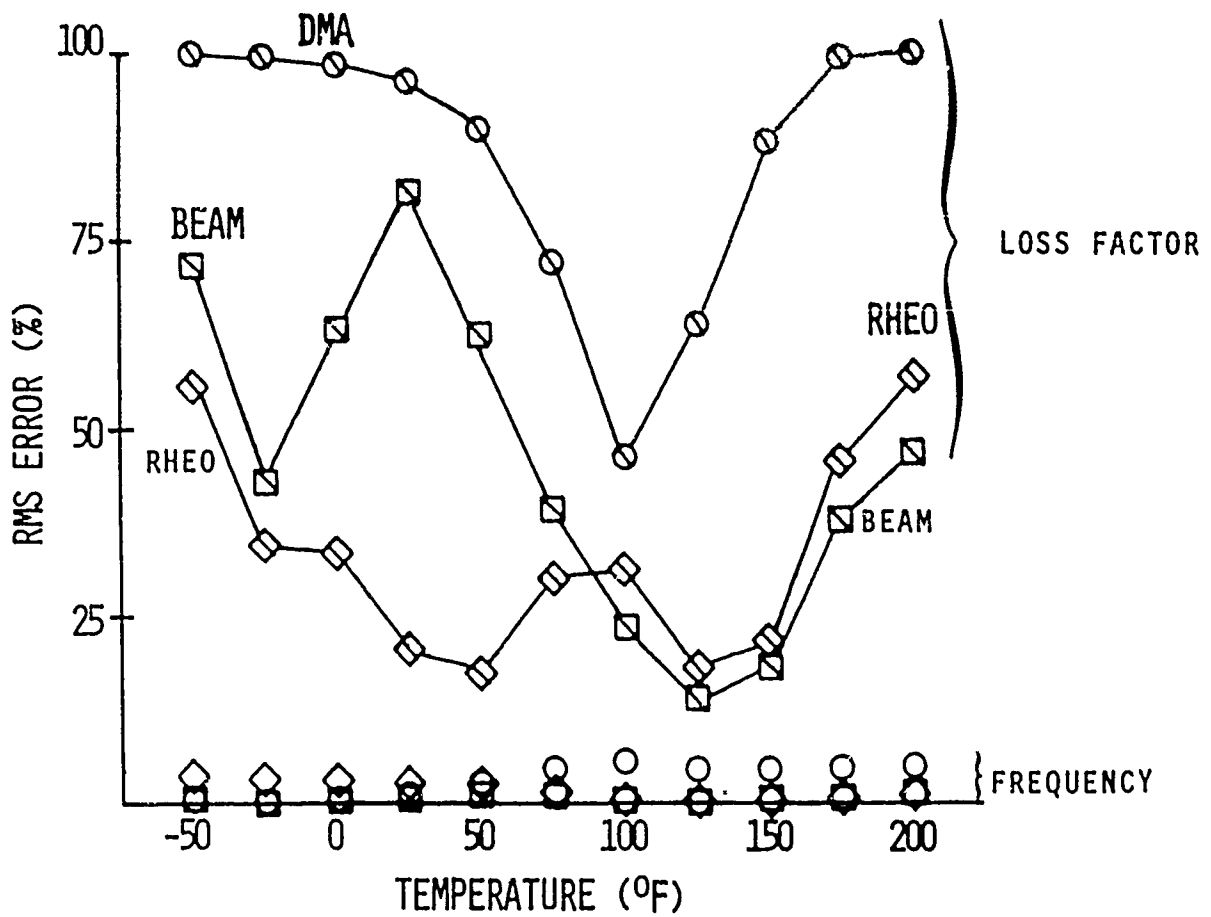
ISD-112

Figure 11   ISD-112 RMS Error at Each Temperature for all Modes.

ISD – 112

RMS ERROR

TEST	η_s		F	
	ALL DATA	3 POINTS	ALL DATA	3 POINTS
DMA	88.4	61.6	4.3	5.0
BEAM	50.2	27.5	2.2	0.67
RHEO	35.8	27.1	2.6	0.94

Figure 12 ISD-112 Total RMS Error
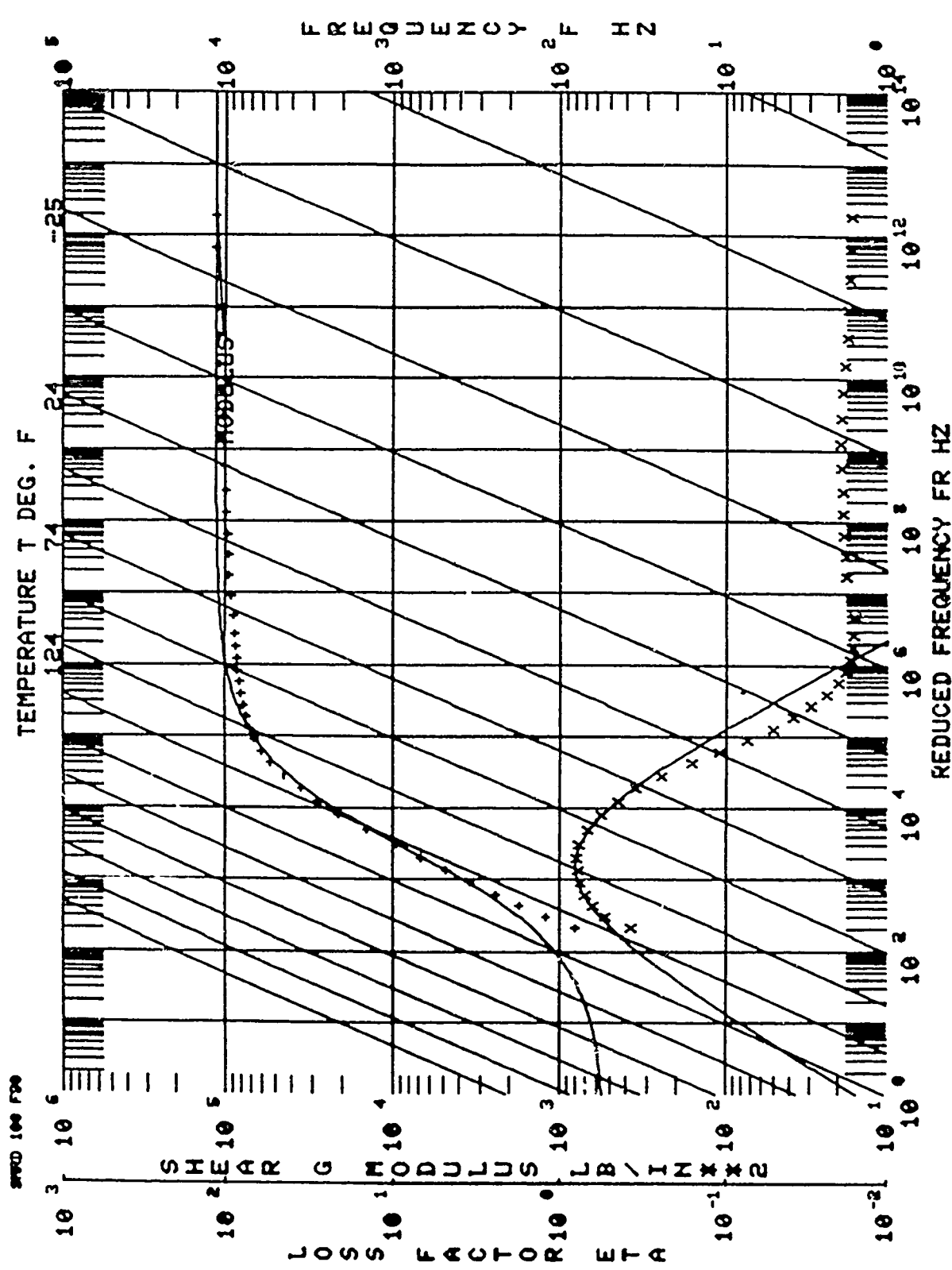
Figure 13 DMA Nomogram for SMRD 100F90A.
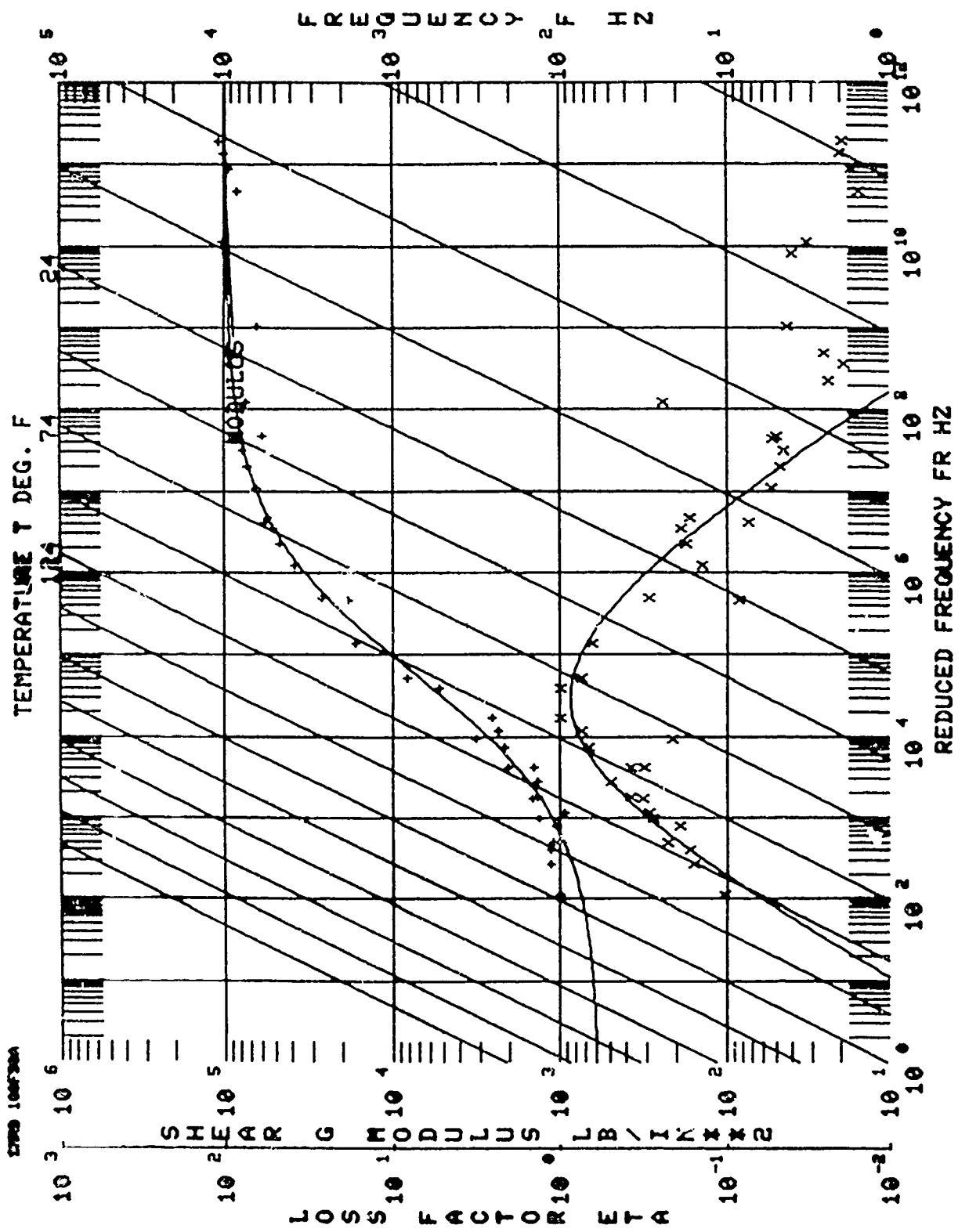
Figure 14 BEAM Nomogram for SMRD 100F90A.

Figure 15 AUTO Nomogram for SMRD 100F90A.
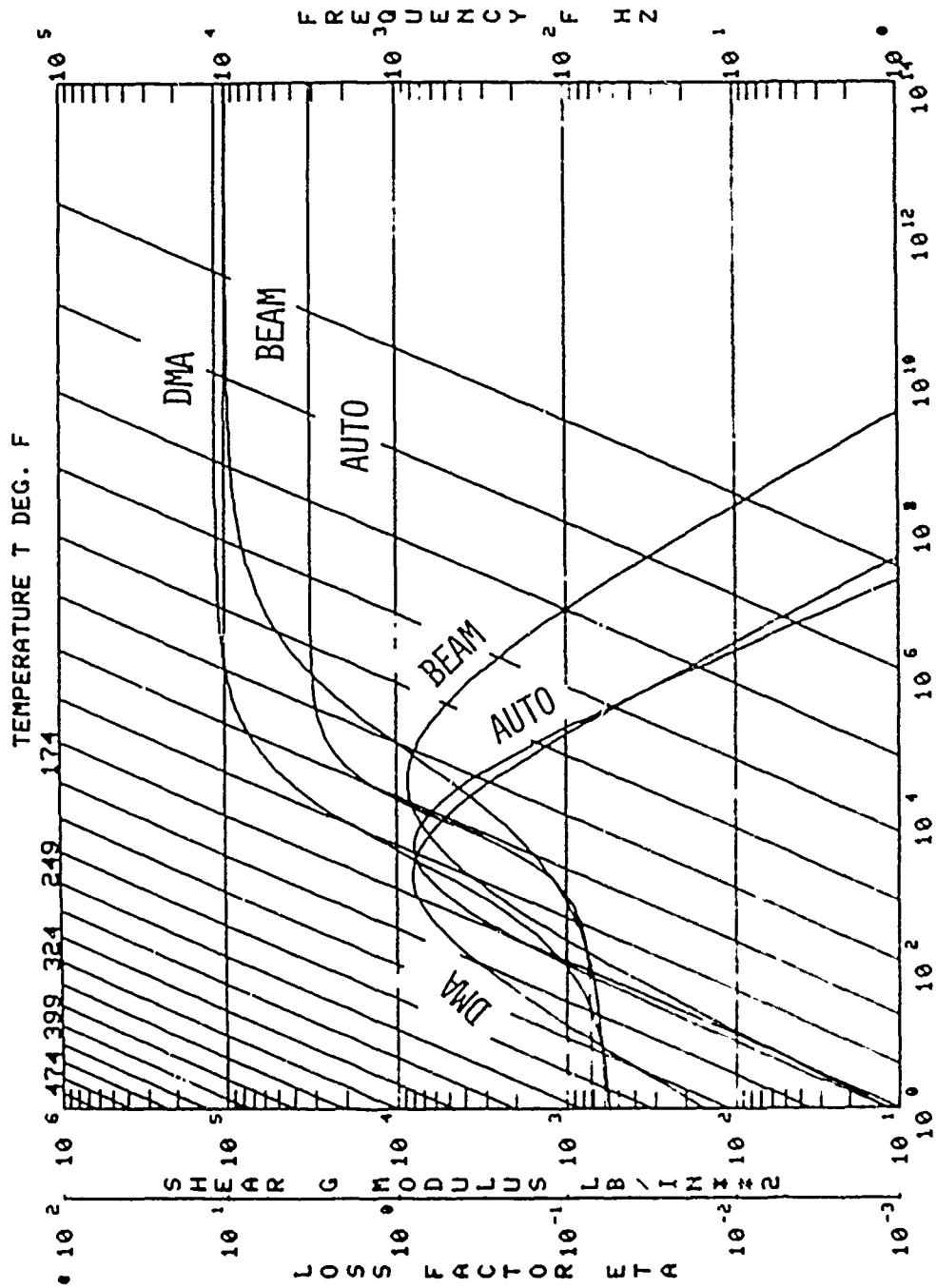
Figure 16 Comparison of Data Curves From Three Test Methods for SMRD 100F90A.
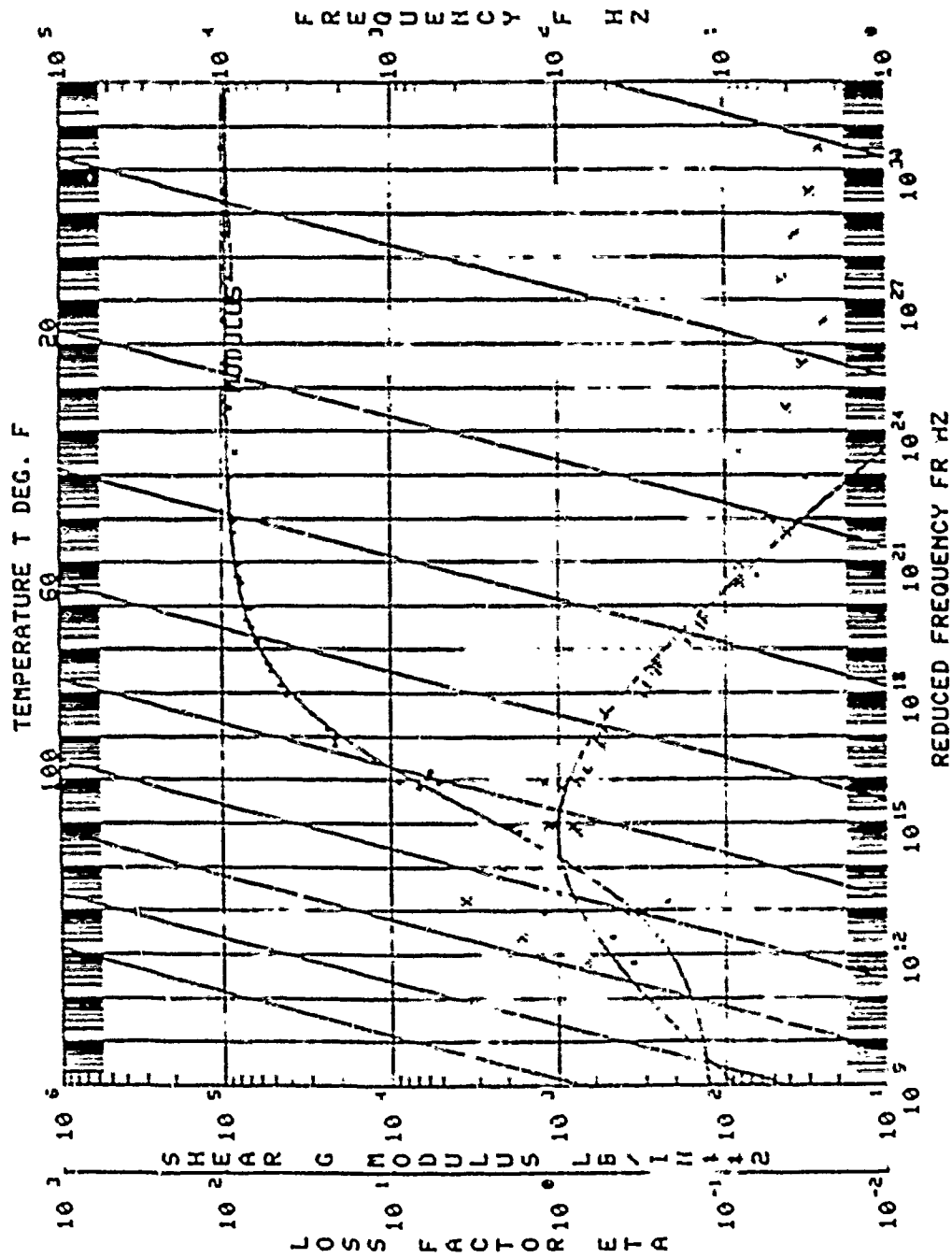
Figure 17 Nomogram From RHEO Data for SMRD 100F90A With T_0 = 356°F.
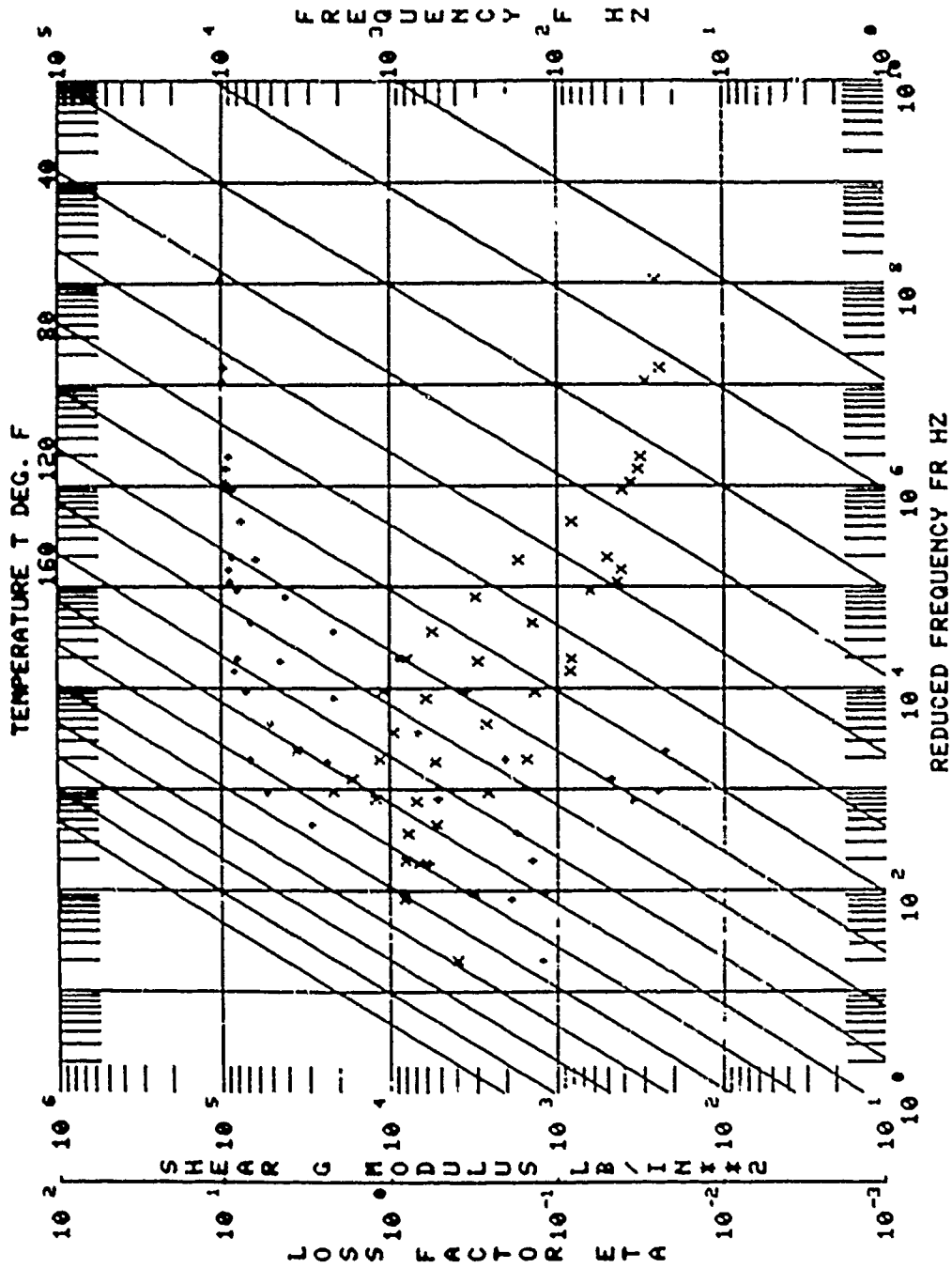
Figure 18 Nomogram for RHEO Data for SMRD 100F90A With T_0 = 174.2°F.

CONSTRAINING LAYER ALUMINUM 0.031 INCH

SMRD 100F90A 0.032 INCH

BEAM STEEL 0.125 INCH

8.125 INCHES
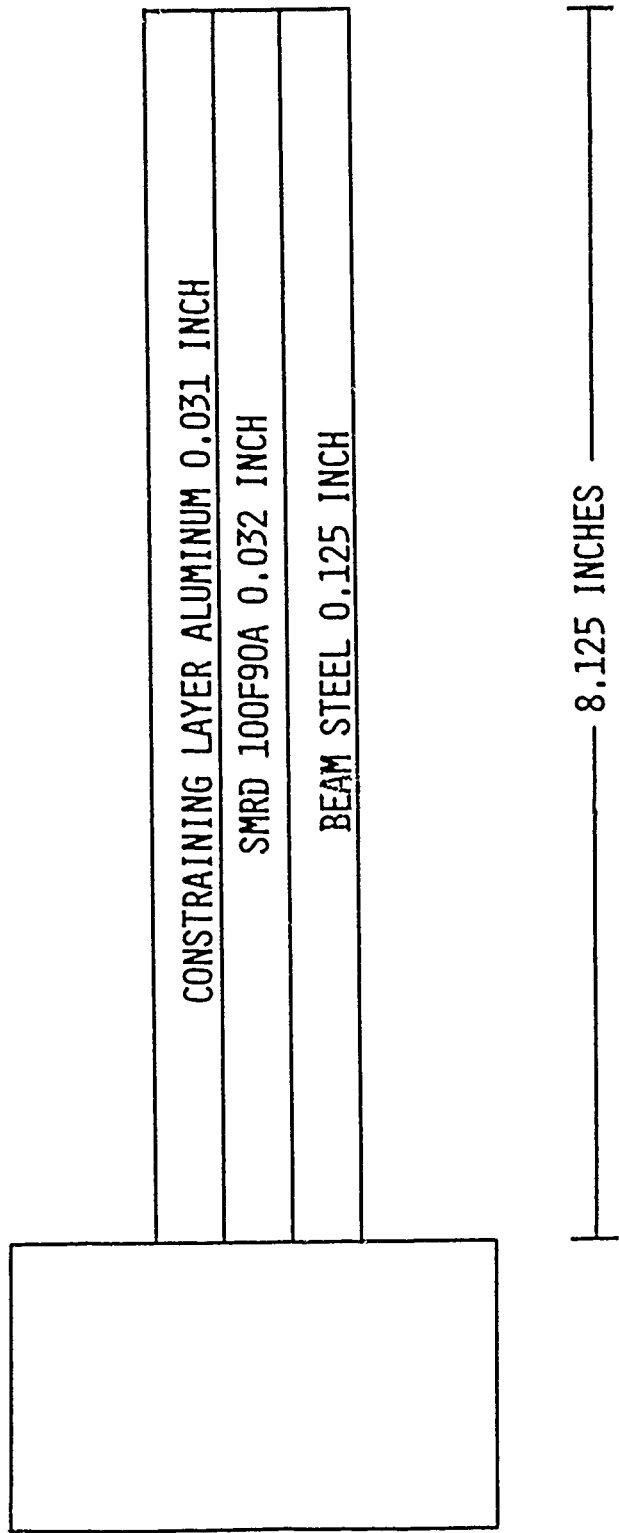
Figure 19 Damping System Evaluated for the 100F90A.

SMRD 100F90 MODE 3

X - Experimental Data
+ - DMA Predictions
* - BEAM Predictions
O - RHEO Predictions
- AUTO Predictions

LOSS FACTOR

10^{0} 10^{-1} 10^{-2} 10^{-3} 10^{-4}

TEMPERATURE DEG F.

25 50 75 100 125 150 175 200 225

Figure 20   Comparison of Predicted Damping to Experimental Test Results
For Mode 3.

GB-28

SMRD 100F90 MODE 6

X- Experimental Data
+- JMA Predictions
*- BEAM Predictions
O- RHEO Predictions
#- AUTO Predictions

LOSS FACTOR

TEMPERATURE DEG F.
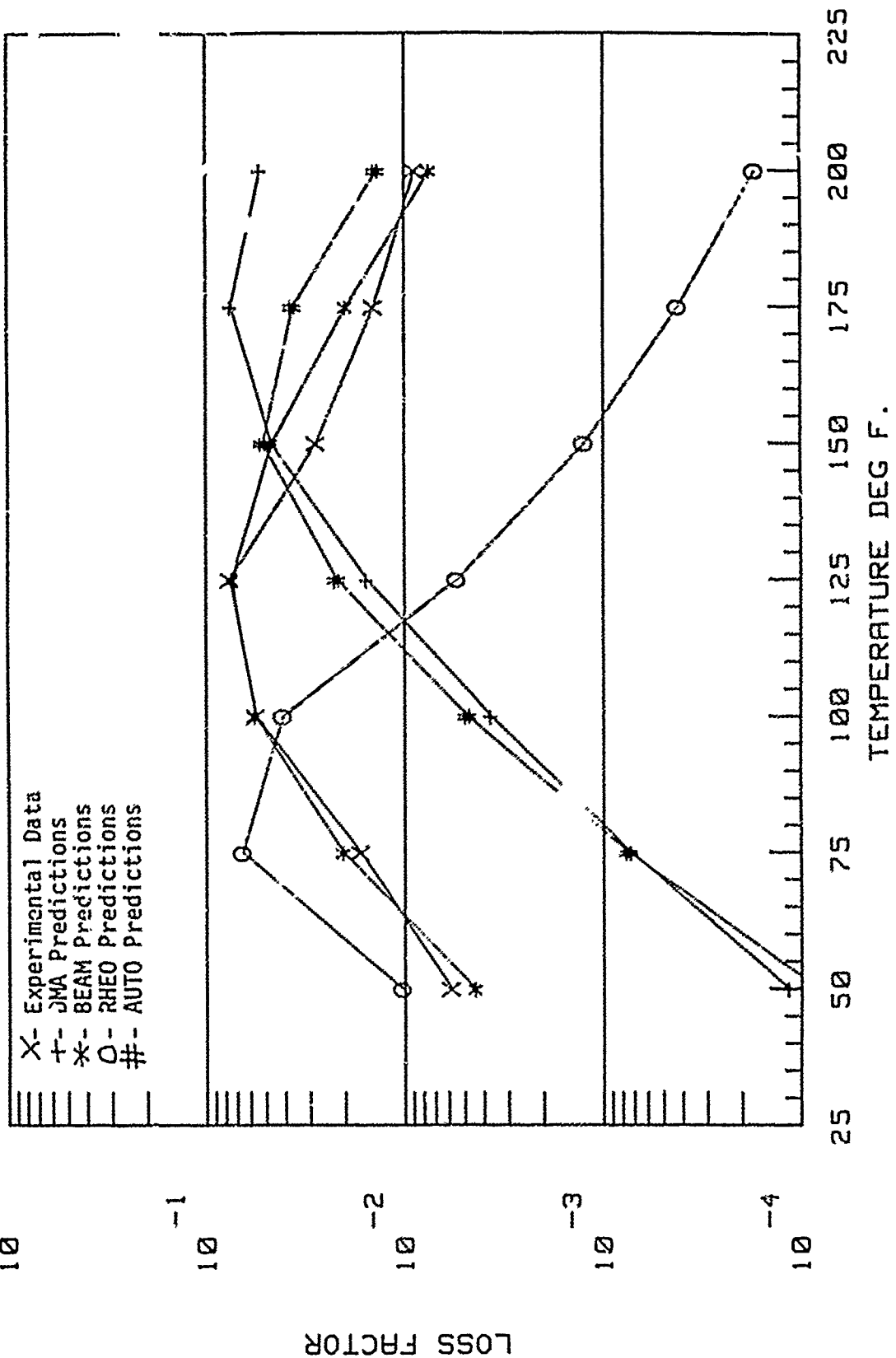
Figure 21   Comparison of Predicted Damping to Experimental Test Results
For Mode 6.

GB-29

MODE NUMBER

	2		3		4		5		6	
	ALL DATA	3 POINTS	ALL DATA	3 POINTS	ALL DATA	3 POINTS	ALL DATA	3 POINTS	ALL DATA	3 POINTS
DMA	166.1	74.7	186.6	74.7	241.4	77.8	244.2	78.4	260.3	81.5
BEAM	62.1	28.7	43.7	35.3	26.6	19.1	20.9	25.1	32.5	39.3
RHEO	105.1	84.9	119.3	77.7	125.1	75.9	117.0	78.4	136.0	78.5
AUTO	63.4	61.1	72.2	67.6	86.7	77.0	89.5	79.3	97.9	83.4

Figure 22 η_s RMS Error Across Temperature for SMRD 100F90A.

DE NUMBER

	2		3		4		5		6	
	ALL DATA	3 POINTS	ALL DATA	3 POINTS	ALL DATA	3 POINTS	ALL DATA	3 POINTS	ALL DATA	3 POINTS
DMA	5.5	7.9	7.3	10.4	7.7	10.9	7.7	10.9	7.5	10.6
BEAM	1.6	1.6	1.4	1.7	2.2	2.2	2.0	1.8	1.9	1.6
RHEO	8.9	12.3	7.8	11.2	7.4	10.5	6.5	9.1	5.9	8.13
AUTO	1.9	2.3	2.8	3.7	4.0	4.3	4.5	4.4	4.7	4.2

Figure 23 Frequency RMS Error Across Temperature for SMRD 100F90A.

GB-31
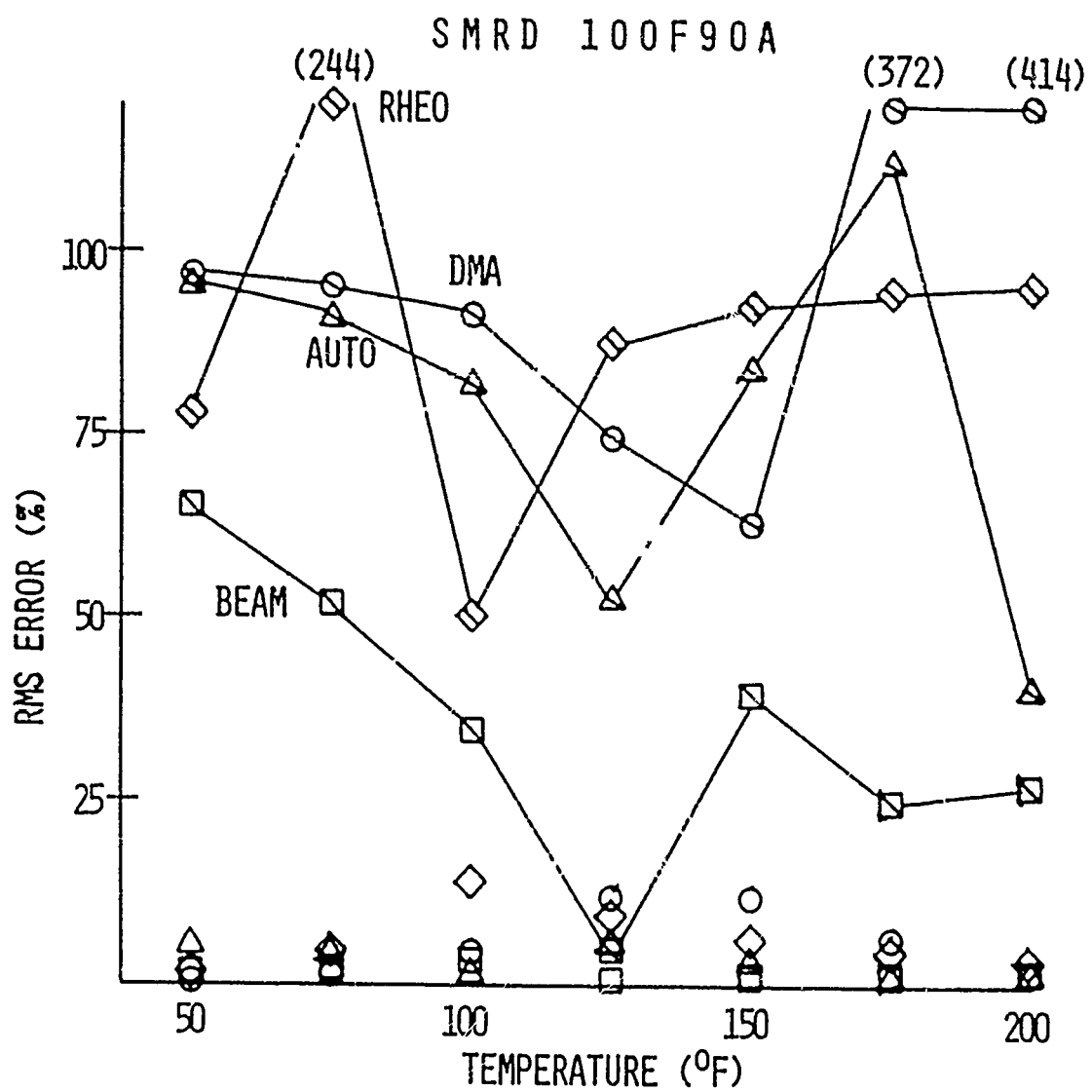
Figure 24 100F90A RMS Error at Each Temperature For All
           Modes.

SMRD - 100F90A

RMS ERROR

TEST	η_s		F	
	ALL DATA	3 POINTS	ALL DATA	3 POINTS
D M A	222.7	77.5	7.2	10.2
B E A M	39.9	30.4	1.8	1.8
R H E O	120.9	79.1	7.4	10.4
A U T O	82.9	74.1	3.7	3.9

Figure 25 SMRD-100F90A Total RMS Error.

THE PREDICTION OF TOTAL LOSS FACTORS OF COUPLED STRUCTURES

J.M. Cuschieri and E.J. Richards
Center for Acoustics and Vibrations
Department of Ocean Engineering
Florida Atlantic University
Boca Raton, FL. 33431

ABSTRACT

The total loss factor for coupled structures is estimated from
knowledge of the inherent loss factor of the structure material and the
coupling loss factor, that associated with the transfer of vibrational energy
from the substructure to other coupled substructures. The coupling loss factor
is estimated by using power flow methods. That is the flow of vibrational
energy is expressed in terms of the point and transfer mobilities of the
substructures, including if necessary mobilities for all six degrees of
freedom - three translational and three rotational. Additionally damping
mechanisms introduced at the joints between substructures can be included in
the model as massless damping mobility terms. Using these power flow
techniques expressions have been derived for the coupling loss factors for
general structures for which the extreme conditions, low and high inherent loss
factor relative to the coupling loss factor are considered. The results are
applied to estimate the total loss factor of a plate steel box where each side
is considered as a separate substructure, the analysis performed for both low
and high inherent loss factors of the individual panels. All of the
substructures have a high modal density which allowed the results obtained
to be compared to similar results obtained using the statistical Energy
Analysis technique. Also the results are compared to experimentally measured
values for the total loss factors. The total and inherent loss factors were
measured experimentally using the decay method. From comparison of the results
one can observe that for this case of a structure with high modal density, and
using mean values for the mobilities of the substructures good correlation
is obtained between the estimated loss factors using the analytical model and
the experimentally measured loss factors. Further work is currently in
progress on low modal density structures.

INTRODUCTION

In general structures are not of a single integral construction but are made up of substructures which are welded, bolted or rivited together. In defining a loss factor for one of the substructures, this will have contributions from the inherent loss factor, that is the loss factor associated with the structural material and additive damping mechanisms, and the loss factor associated in the energy transmitted or transferred to other substructures. The transmitted energy is a function of the inherent loss factors of the substructure and the other coupled substructures and the type of coupling between the substructures. These parameters will influence the way that vibrational energy will be throughout the global structure and also the extent to which control of the vibrational energy can be obtained by the introduction of damping treatment.

The analysis of coupled structures have, to some extent, already been done using Statistical Energy Analysis (SEA) methods[1]. However SEA methods are only useful in those frequency regions with high modal density for all of the substructures. Thus for low to medium frequencies where the modal density is not high enough to allow a statistical approach, only generalized results can be obtained using the SEA method. An alternative approach that will cover the whole of the frequency range, from low frequencies – low modal density – to high frequencies – high modal density – is by using power flow techniques[2]. That is the energy transmitted between substructures is expressed in terms of point and transfer mobilities. From such relationships one can define a coupling loss factor to compare to the inherent loss factor of the substructure. An additional advantage of using this technique is that damping mechanisms introduced at the joints between coupled substructures can be included in the model by introducing massless real mobility components in series with the joint to represent the energy losses at the joint.

ANALYTICAL APPROACH

Considering the general case of a substructure linked to other several substructures (Figure 1) with an excitation on one of the substructures. Vibrational energy will flow from the source substructure to the other substructures. This vibrational power flow will depend on the coupling between the substructures and the power flowing from the source substructure to the other substructures will in general have two components. A resistive or real component which represents the dissipated vibrational energy going into the connected substructure and a reactive or imaginary energy component which represents the fraction of vibrational energy that continuously flows back and forth between the two substructures. In energy terms, for $N + 1$ substructures, this can be represented using SEA notation by

$$E_{input} = E_{diss_s} + \sum_{i=1}^{N} \left(E_{t_{si}} - E_{t_{is}} \right) \tag{1}$$

Where E_{input} is the input energy to the source substructure; E_{diss_s}

is the dissipated energy in the source substructure; $E_{t_{si}}$ is the transferred energy component from the source substructure to substructure "i" and $E_{t_{is}}$ is the energy transferred back to the source substructure. For one of the substructures with no excitation

$$0 = E_{diss_i} + \left(E_{t_{is}} - E_{t_{si}} \right) + \sum_{\substack{j=1 \\ j \neq i}}^{N} \left(E_{t_{ij}} - E_{t_{ji}} \right) \tag{2}$$

These formulations for the energy balances for each substructure are set-up similar to SEA methods. Using power flow techniques each of the energy transfer component pairs for each joint between the substructures can be written in terms of the mobility functions at the joints.

Considering first a source substructure connected to a single receiver substructure (Figure 2). The transferred energy is given by the well known expression[2]

$$E_{tr_{SR}} = \left[\frac{|M_{S_o S_1}|^2}{|M_{S_1} + M_R|^2} \cdot \text{Real } [M_R] \right] |F|^2 \tag{3}$$

Where $M_{S_o S_1}$ is the transfer mobility between excitation location and attachment location on the source substructure; M_{S_1} is the mobility of the source substructure at the attachment location; M_R is the receiver mobility at the attachment location and $|F|^2$ is the excitation. The model shown here is a simplified model, that is one can expand this model to represent force and torque transmission in all directions and also include both line and point forces and torques[3]. In this case one can best represent all combinations of transfer mobilities using a matrix representation.

Considering next a source substructure connected to two receiver substructures (Figures 3). In this case there is some influence on the received energy by one substructure due to the presence of the second substructure. This can be included in the analysis by introducing cross coupling terms. However the influence of the other substructures on the receiver structure apart from the one with the excitation or the higher level of energy is insignificant[4] which therefore would imply that the cross coupling terms can be neglected. That is one can decompose each problem into one with a series of single receivers, each considered separately, for each substructural element.

By expressing the energy transferred from one substructure to another in terms of input and transfer mobilities, this will represent both energy transfer terms that is the energy transferred from substructure "i" to "j" and the energy transferred back from substructure "j" to substructure "i". That is from equation (3)

$$E_{tr_{ij}} = \left[E_{t_{ij}} - E_{t_{ji}} \right] \tag{4}$$

The total loss factor for each substructure can thus be given by dividing equation (1) by the energy level of the substructure

$$\eta_{ti} = \eta_{diss_i} + \sum_{\substack{j=1 \\ j \neq i}}^{N} \left(\frac{E_{tr_{ij}}}{\omega E_i} \right) \tag{5}$$

and

$$\frac{E_{tr_{ij}}}{\omega E_i} \simeq \frac{\text{Real } [M_{R_j}]}{|M_{ij} + M_{R_j}|^2 \, \omega m_i} = \eta_{c_j} \tag{6}$$

Where m_i is the mass of substructure "i" and η_{c_j} is the coupling loss factor of substructure "i" when coupled to substructure "j".

Therefore using the power flow approach, the coupling loss factor is expressed in terms of mobilities which can therefore be calculated provided the mobility terms can be either measured or computed. There are no limitations on the number of modes required. The values for the mobility terms can be either given in terms of mean levels which would be equivalent to the high modal density case and which would only depend on the general characteristics of the substructures, or alternatively given as exact functions of frequency which would then be dependent on the exact geometrics of the substructures.

EXPERIMENTAL ANALYSIS

Some preliminary experimental results have been obtained to verify the power flow approach in the prediction of the total loss factor of a simple multi component welded structure. The structure used in this analysis is a plate steel box of thickness 12 mm open on one side and with the dimension as shown in Figure 4. For this structure the two extreme conditions were investigated, that is for low inherent loss factor compared to the coupling loss factor and for a high inherent loss factor. The structure analyzed in this verification study had a high modal density and therefore the results do not demonstrate the applicability of this method to structures with a low modal density. Each panel of the box was considered as a substructure with connection to adjacent panel substructures.

SUBSTRUCTURES WITH LOW INHERENT DAMPING - STRONG COUPLING

In this case energy dissipation is only significant near the resonant frequencies of the substructures. Because of the strong coupling each substructure will accept all the energy that it can dissipate. Using the power flow approach we can substitute for the values of the mobilities for

the substructures by the mobilities at resonances. Thus from the mode solution for a structure vibrating at one of its resonant frequencies the mobility is given by;

$$M = \frac{1}{\omega_{mn} \, m_{mn} \, \eta_{mn}}$$

(7)

Where m_{mn} is the modal mass associated with th m, n th mode.

Near a resonance of substructure "j"

$$M_{jj} >> M_{ij}$$

(8)

and

$$\eta_{c_{ij}} \approx \frac{m_j}{m_i} \, \eta_j$$

(9)

Near a resonance of substructure "i"

$$M_{ij} >> M_{jj}$$

(10)

and

$$\eta_{c_{ij}} = \frac{mi}{mj} \, \frac{\eta_i^2}{\eta_j}$$

Where η_i is the total loss factor for substructure i. However the inherent loss factor is much smaller than the coupling loss factor and therefore

$$\eta_i \approx \eta_{c_{ij}}$$

(11)

and thus

$$\eta_{c_{ij}} = \frac{m_j}{m_i} \, \eta_j$$

(12)

and

$$\eta_{ti} = \eta_{diss_i} + \sum_{\substack{j=1 \\ j \neq i}}^{N} \frac{m_j}{m_i} \, \eta_j$$

(13)

Using the result in equation (13) the total loss factor of three of the box side panel is estimated from knowledge of the inherent loss factor of the individual panels. The measured inherent loss factor of individual panels is shown in Figure (5) for two of the panels of the box. Panels of equal dimensions had similar loss factor values. These measured loss factors were obtained using the decay method with the panels being impact excited with a calibrated hammer. Figure (6) shows the measured and calculated, using equation (13), total loss factors for three of the box panels. As can be observed from this figure good agreement exists between measured and calculated loss factors for this extreme case.

SUBSTRUCTURES WITH HIGH INHERENT DAMPING - WEAK COUPLING

In this case the structures are highly damped and therefore their mobilities can be represented by mean values which are in general real quantities.

Physically this will imply that most of the energy that is transferred from a substructure to a coupled substructure will be dissipated and not transferred back. In considering the types of mobilities, this will be dependent on the type of joint. Therefore for the box structure the substructures are connected along the edges and therefore line mobilities will be used.

To verify the results for this extreme case three sides of the box structure were covered with a 3 cm. layer of granular material (sand), (Figure 7), which increased the loss factor of these panels to approximately 0.1 (Figure 8). Using equation (6) and substituting for the line mobilities by mean mobility levels the estimated total loss factors for three of the box panels are shown in Figure (9), together with the measured total loss factors. In this case the agreement between measured and estimated loss factor is also good.

Some discrepancy exists between measured and estimated loss factors for plate 1 (Figure 9(a)). It should be noted that plate 1 has a low inherent loss factor, and coupled to other substructures (panels 2, 3 and 4) with a very high inherent loss factor, these panels are covered with the granular material. Thus in this case the assumption that the substructures had a high inherent loss factor which allowed the use of mean mobility levels starts to break down and a more accurate mobility function must be used in the expression for the coupling loss factor.

CONCLUSIONS

These preliminary results show that using power flow techniques the coupling loss factor of structures with low and high inherent loss factor, with a high modal density can be estimated. These results do not show the advantage of using this method over the SEA techniques. Infact the results obtained are the same as those obtained in reference[5] for the same structure using SEA techniques. However no restrictions were made with regards to the form of the mobility terms and therefore provided these can be measured or computed the energy transferred from a substructure to another when the modal density is low can be estimated. The application of this power flow method to finite structures with a low modal density will be the subject of a future paper.

The damping of the experimental steel box structure was increased by the introduction of a layer of granular material. For the results presented here the resulting loss factor was measured experimentally, however this can also be estimated using a similar power flow approach for two coupled substructures, that is by treating the sand layer as a structural component which has a complex speed of propagation of waves due to the energy lost between the grains of the material. In this case the appropriate mobility terms for the structure and the sand layer would be surface mobilities or impedances. Using this approach the increase of the loss factor of the structure can be estimated in

terms of the structure characteristics and the granular material layer
characteristics. This implies that alternative granular materials apart from
sand can be investigated which will allow the introduction of such damping
mechanism to other structures, apart from machinery components, where weight
may be a factor. This will also be a subject for future work.

ACKNOWLEDGEMENT

REFERENCES

1. R.H. Lyon (1983) Noise Control Engineering Journal 20 (3), 92-103,
    "Vibration Transmission in Machine Structures".

2. R.J. Pinnington, R.G. White (1981) Journal of Sound and Vibration 75 (2),
    179-197, "Power Flow Through Machine Isolators to Resonant and Non-
    resonant Beams".

3. J.W. Verheij (1982) Ph.D. Thesis, Institute of Applied Physics TNO-TH,
    Delft, The Netherlands, "Multi-path Sound Transfer from Resiliently
    Mounted Shipboard Machinery".

4. J.M. Cuschieri, E.J. Richards, S.E. Dunn (1985) Final Contract Report,
    Vector Research Corp., Bethesda, MD. "Development of an Acoustic Design
    Procedure for Sea Connected Pumped Fluid Systems Instituted in Navy
    Vessels".

5. J.C. Sun, E.J. Richards (1985) "Prediction of Total Loss Factors of
    Structures Part I, Theory and Experiment" submitted for publication
    to the Journal of Sound and Vibration.
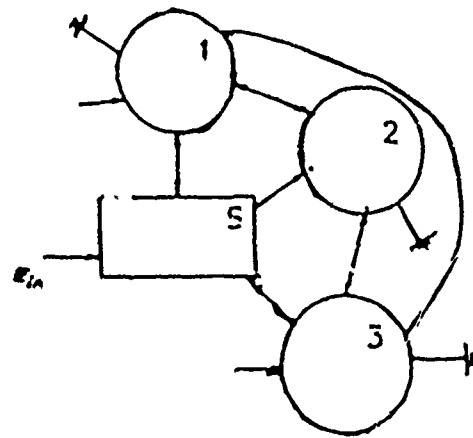
Figure 1. General structure configuration with a
source substructure connected to other substructures.
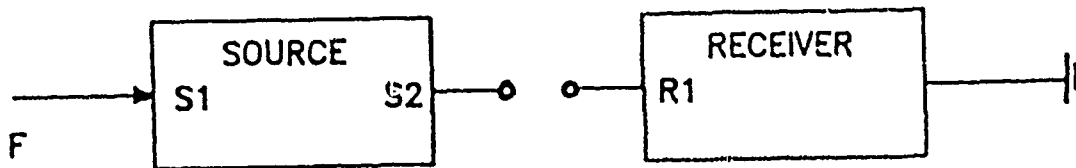
Figure 2. Single source - single receiver structural
combination.
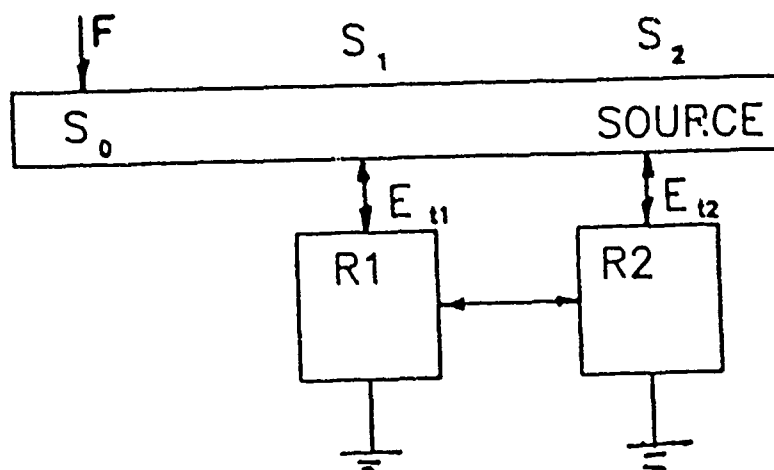
Figure 3. Single source - double receiver
structural combination.
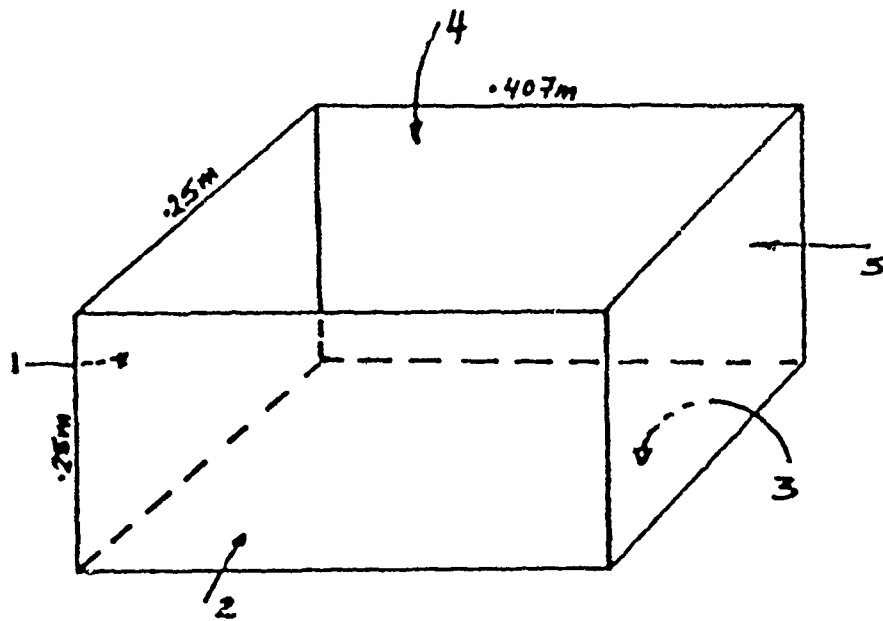
Figure 4.   Experimental box structure.
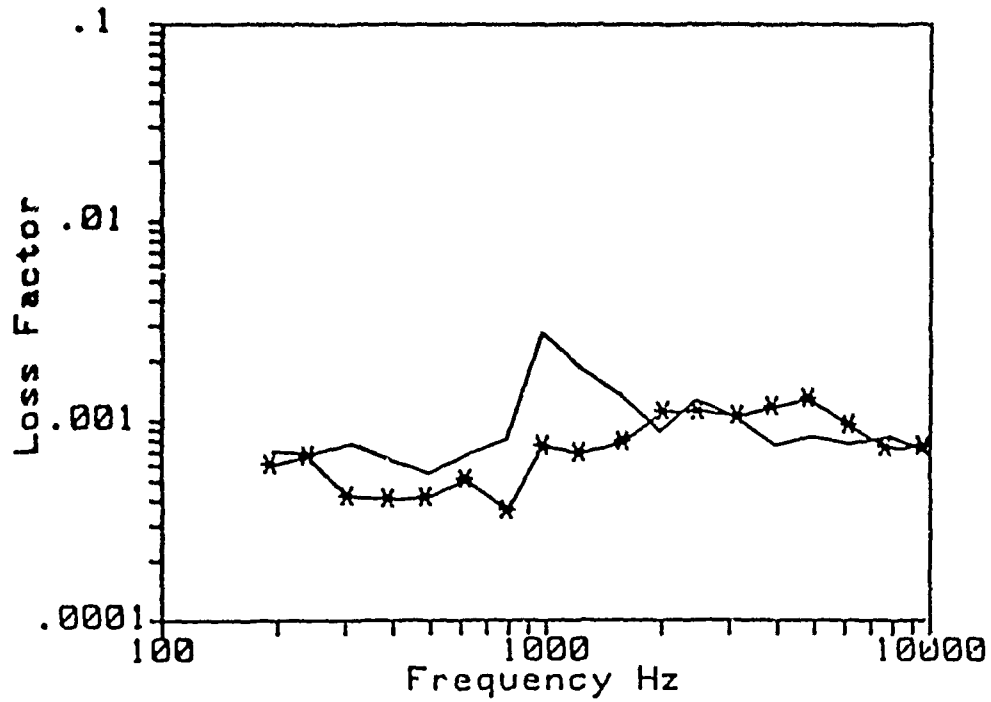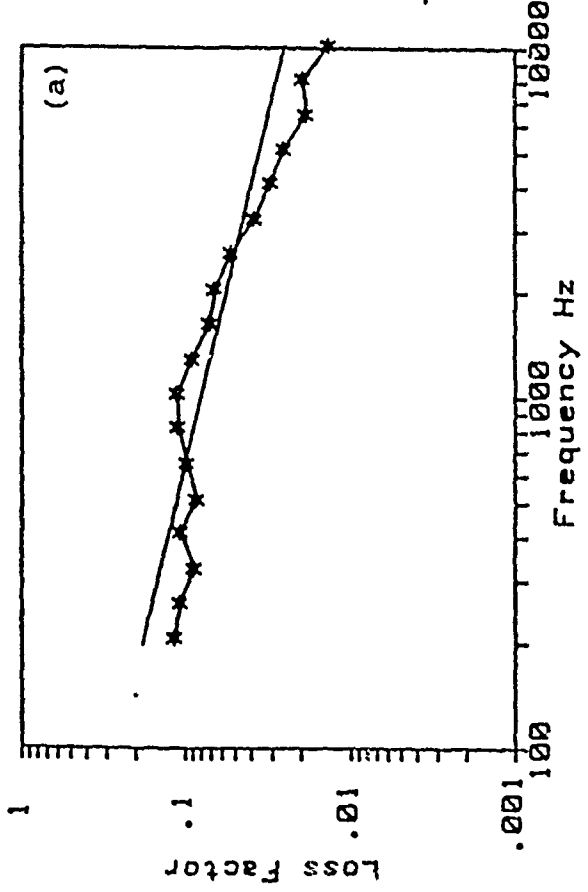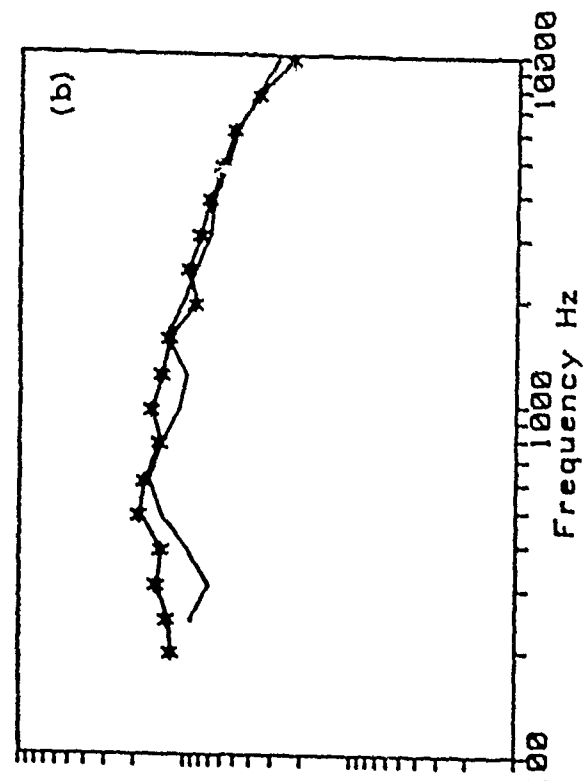

Figure 5.   Structural loss factor of two of the
box panels before assembly.
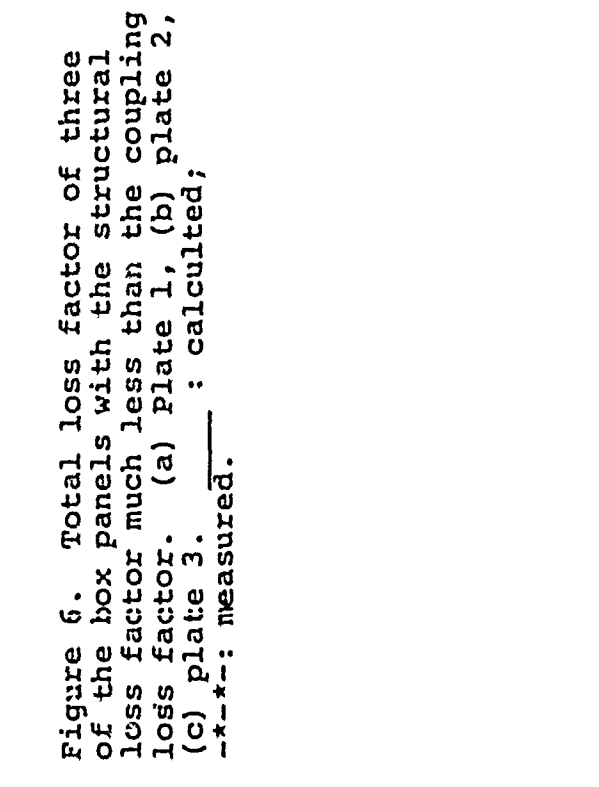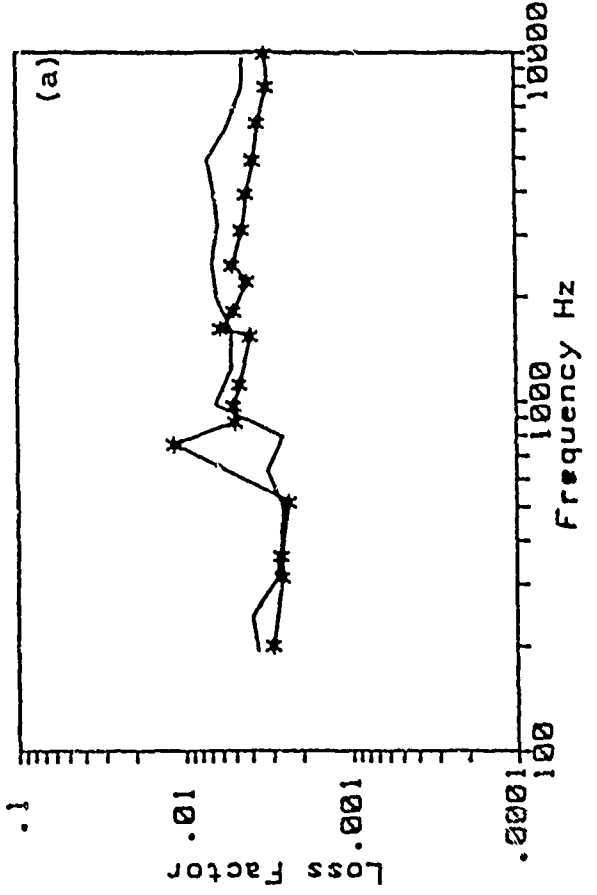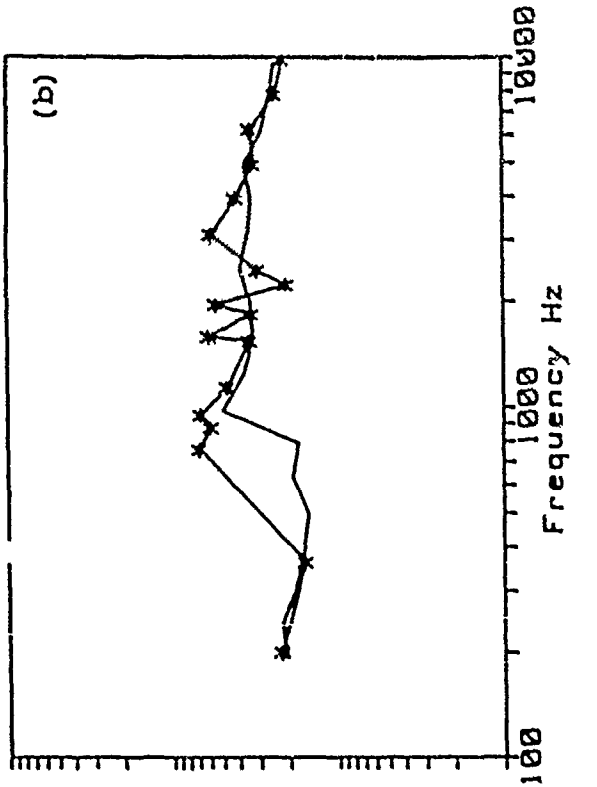
Figure 6. Total loss factor of three of the box panels with the structural loss factor much less than the coupling loss factor. (a) Plate 1, (b) plate 2, (c) plate 3. ───── : calculted; -*-*-: measured.
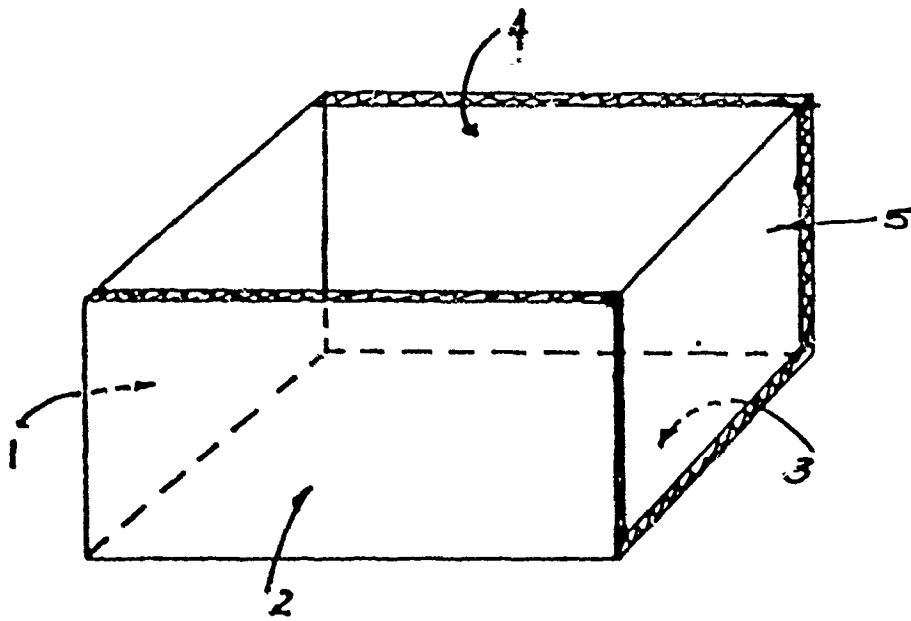
Figure 7.   Experimental box structure showing the three
sides which were covered with the granular material.
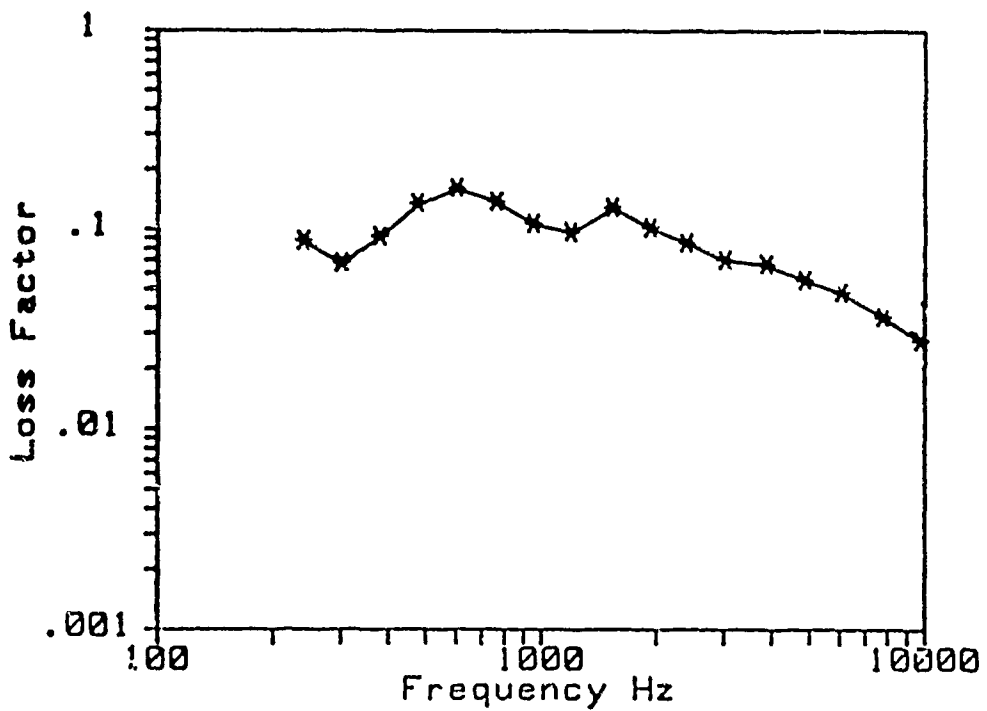
Figure 8.   Measured loss factor of the box panels covered
with the granular material before assembly.
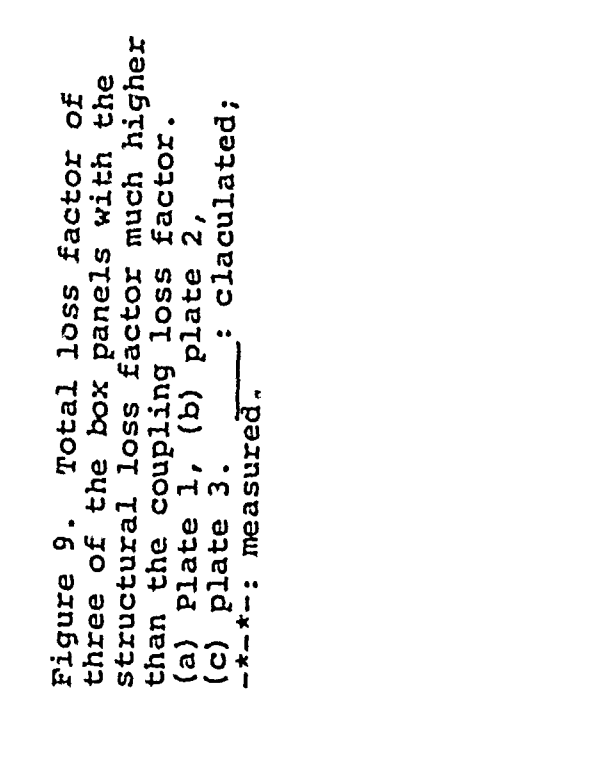
Figure 9. Total loss factor of three of the box panels with the structural loss factor much higher than the coupling loss factor. (a) Plate 1, (b) plate 2, (c) plate 3. -*-*-: measured. ———: claculated;

GC12

IDENTIFICATION OF MODAL DAMPING
OF FLEXIBLE SPACECRAFT APPENDAGES
USING SUBSTRUCTURE TECHNIQUES

Lawrence Slivinski

George A. Clark

Fei Hon Chu

RCA Astro-Electronics
Princeton, NJ 08540

ABSTRACT

Prediction of damping for large structures has been a
challenging problem, especially for flexible spacecraft
appendages. Because of the effect of air friction and
gravity, damping measurements for large flexible spacecraft
appendages are difficult to achieve using system level tests.
Several substructure coupling techniques have been proposed.
This paper presents a hybrid synthesis procedure using
combined experimental and analysis techniques. The damping
values for rigid joints, e.g. hinges, are obtained from
quasi-static load tests and the damping characteristics for
flexible components, e.g, panels, are determined using
analytical approaches based on the strain energy principle.
Modal synthesis techniques are used to predict modal damping
for the combined structure. A typical RCA-built deployed
solar array is used as an example to demonstrate the
procedure.

A test was developed to measure the damping values of solar
array hinges. The test consisted of input force and response
deflection measurements over a displacement range similar to
that experienced during system level oscillations. The
frequency of the applied force was also that of the operating
mode. To simulate these conditions, very sensitive
measurement instrumentation was required. To prevent test
fixture deflection from contaminating the data, all support
hardware was designed with a high degree of rigidity.
Acquired data was digitized and plotted in the form of force
vs displacement. Damping energy was calculated based on the
enclosed area of the above curve. Data acquisition and
processing was automated by a computer program.

The synthesis technique described here is similar to that
described in Ref. 1 except that component real modes are used
instead of complex modes as proposed by Soni. The structure
is broken down into a series of joints and flexible
components. Mass, stiffness, and damping characteristics are
represented in physical coordinates for the joints and modal
coordinates for the components. Coupling between components
is always done through the joints. Thus, physical degrees of
freedom are always available for coupling the substructures
even if free-free modes are used to represent the component.
Constraint equations are used to eliminate dependent degrees
of freedom. Then the system equations are solved for complex
eigenvalues and eigenvectors from which system modal damping
can be determined. This procedure is implemented using DMAP
alters and programs written for use with MSC/NASTRAN.

INTRODUCTION

Spacecraft appendages are getting larger. The demand for increased spacecraft power is forcing increased solar array size. The demand for greater sensitivity is forcing increased antenna and sensor sizes. As appendage sizes are increasing, appendage natural frequencies are dropping. The combination of larger size and lower frequency means that appendage dynamics have a greater effect on attitude control than in the past. In addition, spacecraft pointing accuracy and response requirements are becoming more stringent. These factors are placing heavy demands on the attitude control system. Accurate information about appendage natural frequencies and damping is, therefore, becoming more important for good attitude control design.

Testing would seem to be the most straightforward method of accurately determining appendage natural frequencies and damping. Typically, however, large spacecraft structures are designed to be deployed or assembled only when on-orbit, in zero gravity. In addition, because of the large surface area of many of these structures, the results can be contaminated by the presence of air.

Presented here is a hybrid synthesis method for predicting damping of large structures. The method allows the use of test and/or analytical data from the various structure components to be used to predict the system natural frequencies and damping. By using component level test data, the pitfalls of system level testing are avoided while maintaining a high degree of confidence in the predictions.

This method also encourages the representation of some substructures in physical coordinates and others in generalized coordinates. This fact can be used to advantage in substructure testing. Large, low damped components of the structure can be represented in generalized coordinates. Compact joint areas, where most of the system damping is concentrated, can be represented in physical coordinates.

ANALYTICAL METHOD

The hybrid synthesis technique described here is similar to that described by Soni in Reference 1. To better illustrate the technique, extensive reference will be made to an example problem. Figure 1 shows the example problem, a deployed solar array. It consists of four panels connected by pairs of interpanel hinges. Final connection to the spacecraft is made through the boom/hinge assembly. The solar array is considered fixed at the spacecraft interface for this example.

The first step in the hybrid synthesis method, as in any modal synthesis method, is the division of the structure into a series of substructures. In the hybrid synthesis method, however, the substructures are divided into two groups, those to be represented in physical coordinates and those to be represented in genralized coordinates. A requirement of this method is that substructures represented in generalized coordinates can only be connected to substructures represented in physcial coordinates.

Referring to the example solar array, this structure is readily divided into eight substructures. The boom/hinge assembly and the pairs of interpanel hinges are substructures that will be represented in physical coordinates. The panel assemblies will be represented in generalized coordinates. Note that the panel substructures are connected together through the hinge substructures fulfilling the above mentioned requirement. Also note the choice of substructures. The boom/hinge assembly and interpanel hinges are chosen to be respresented in physical coordinates. Hinges are compact, stiff components whose mass, damping, and stiffness properties are readily obtainable in physical coordinates. Conversely, the panel assemblies are most concisely represented in generalized coordinates using data from panel modal tests or finite element analyses.

The final goal of this procedure is to formulate the following system equation from the substructure data:

$$[M_{sys}]\{\ddot{P}\} + [C_{sys}]\{\dot{P}\} + [K_{sys}]\{P\} = 0 \qquad (1)$$

where:

$[M_{sys}]$ = system mass

$[C_{sys}]$ = system viscous damping

$[K_{sys}]$ = system complex stiffness

$\{P\}$ = system independent displacements in the assembly of substructure coordinates

This equation can then be solved to determine the system natural frequencies and damping.

The procedure to generate $[K_{sys}]$ is described below. The same procedure applies to generate $[M_{sys}]$ and $[C_{sys}]$. First, the substructure matrices are assembled as follows:

$$[K_{uncoupled}] = \begin{bmatrix} K_1 & & & & & \\ & K_2 & & & & \\ & & K_3 & & & \\ & & & K_4 & & \\ & & & & \ddots & \\ & & & & & K_j \end{bmatrix} \qquad (2)$$

where:

$[K_n]$ = substructure stiffness

For the example solar array problem $j = 8$; and matrices K_1, K_3, K_5, and K_7 would be in physical coordinates while K_2, K_4, K_6, and K_8 would be in generalized coordinates.

Any method can be used to obtain the generalized matrices. For example, fixed boundary flexible modes and constraint modes can be used to develop the transformation to generalized coordinates as in the Craig and Bampton modal synthesis procedure (Ref. 2). Free-free modes could also be used, and residual flexibility included, if needed (Ref. 3). In fact, different methods of obtaining the generalized matrices can be used on different substructures with no difficulty in developing the constraint equations that will be used to couple the substructures together. Also, it is not necessary to use complex modes to develop the generalized matrices. Real modes are entirely adequate, and accuracy will not be compromised if the off-diagonal terms of the viscous damping and complex stiffness are retained.

The matrix $[K_{uncoupled}]$ above is an assembly of uncoupled substructure stiffness matrices. If the free vibration equation formed of $[K_{uncoupled}]$ and the similarly assembled mass and damping matrices was solved, it would yield the individual substructure results. In order to form the system stiffness $[K_{sys}]$, the substructure matrices assembled in [Kuncpld] must be coupled together in some way. These matrices are coupled together by eliminating dependent degrees of freedom though the use of constraint equations. Let $\{P_{uncoupled}\}$ be partitioned as follows:

$$\{P_{\text{uncoupled}}\} = \begin{Bmatrix} P_1^I \\ --- \\ P_1^B \\ --- \\ P_2 \\ --- \\ P_3^I \\ --- \\ P_3^B \\ --- \\ P4 \\ \vdots \\ P_j \end{Bmatrix}$$

(3)

where:

$\{P_n\}$ = displacements of nth substructure in substructure generalized coordinates

$\{P_n^I\}$ = interior displacements of nth substructure in substructure physical coordinates

$\{P_n^B\}$ = boundary displacements of nth substructure in substructure physical coordinates

Note that $\{P_n^B\}$ are always dependent since these displacements can always be found from $\{P_n\}$, the generalized displacements of the neighboring substructure. A reduced set of independent degrees of freedom can be determined and a transformation defined such that:

$$
\begin{Bmatrix}
P_1^I \\
\hline
P_1^B \\
\hline
P_2 \\
\hline
P_3^I \\
\hline
P_3^B \\
\hline
P_4 \\
\vdots \\
P_j
\end{Bmatrix}
= [T]\{P\}
\tag{4}
$$

where:

$$
\{P\} =
\begin{Bmatrix}
P_1^I \\
\hline
P2 \\
\hline
P_3^I \\
\hline
P4 \\
\vdots \\
P_j
\end{Bmatrix}
= \text{displacements of independent degrees of freedom}
$$

The vector $\{P\}$ shown above is the same as that in equation (1) and transformation $[T]$ can be applied to $[K_{uncoupled}]$ to eliminate dependent degrees of freedom and determine the system stiffness as follows:

$$
[K_{sys}] = [T]^T [K_{uncoupled}][T]
\tag{5}
$$

The same procedure can be applied to determine the system mass $[M_{sys}]$ and viscous damping $[C_{sys}]$. With all the elements of equation (1) present, the equation can be solved, giving the system natural frequencies and damping information.

GD-7

TEST METHOD

A test method was developed to measure the damping and stiffness values of hinge assemblies. The test was run at various frequencies and displacements to understand how each of these parameters affects hinge performance. This part of the paper describes the various aspects of the test; test article, test set-up, results and discussion.

TEST ARTICLE

A solar array boom-to-boom hinge was the primary subject of the test. An interpanel hinge was also tested briefly because of limited availability. The boom-to-boom hinge is constructed of magnesium with two sets of ball bearing races. See Figure 2. Constant torque springs open the hinge. End of hinge travel is set with an adjustable stop. A viscous damper controls the rate of hinge deployment travel but, because of clearances is not effective over small ranges of displacement. The interpanel hinge is similarly constructed but resembles only one half of a boom-to-boom hinge. See Figure 2. The interpanel hinge has one bearing race and one spring. There are two hinges per panel.

TEST SET-UP

The hinge was attached through its mounting interface to a rigid test bed as shown in Figure 3. A 30 force pound shaker was used to input a force sine wave. The load was applied through a flexure assembly which allows load to be transmitted in only a single direction. A piezoelectric and a strain gage type load cell were used to measure the applied load. The resulting displacement was measured with a Linear Variable Differential Transformer (LVDT). A set of universal mounting fixtures were designed which allowed testing in six directions - three translation and three rotation.

The two signals - voltage proportional to load and voltage proportional to displacement - were routed to a digital computer. The computer digitized and stored the two simultaneously on magnetic disk. A program was written to read the stored time histories and plot them as force vs. displacement. The program automatically scales both axes of the plot such that the curves fill about 3/5 of the display area. The area enclosed by the curve is calculated on a point-by-point basis and converted to an equivalent linear viscous damping coefficient. The test discussion section

describes this formulation. The coefficient can be calculated over one or many load cycles. The equivalent linear stiffness coefficient is calculated by dividing the difference in the load required to achieve the maximum and minimum displacements by the differences of the maximum and minimum displacements.

TEST RESULTS

A sample of the computer generated output is shown in Figure 4. In general for these hinges, the viscous damping coefficient increases as the frequency of the applied load decreases. The viscous damping coefficient seems to have no consistent relationship with the level of applied load. The linear stiffness coefficient increases as the frequency of applied load increases and decreases as the level of applied load increases.

The parameter which has the most dramatic effect on these measured values is the direction the hinge is loaded. Each direction has a unique mechanism which provides the damping and stiffness. For example, direction #3 is the stiffest translation direction because the hinge is loaded against its stop. Direction #2 is the softest translation direction because there is a small amount of play which is exercised by loading in this direction. The presence of play or clearance in a particular direction has a dramatic effect on the equivalent stiffness. As the applied load is increased such that the hinge displaces through the clearance, the displacement increases with little change in load. Thus the equivalent stiffness goes down. The damping coefficient does not experience the same dynamic change because little energy is required or absorbed as the hinge displaces through the clearance.

DISCUSSION OF TEST

Because the applied load is small and the resulting displacement is very small (.0001 inch 0-Peak in some cases), the transducers must be very sensitive. Because the range of displacements varies dramatically (especially when clearance is introduced), the load vs displacement plotting routine must be flexible.

The enclosed area calculations depend directly on the phase between the force and displacement sine waves, thus a new problem is introduced. The phase between the two recorded signals cannot be contaminated in either the signal conditioning or recording section of the test. Precise checks must be made to ensure this. For example: The owners manual for the LVDT states that displacement measurements are good up to about 250 Hz. The displacement values are good to

250 Hz but the phase between the actual displacement and the measured value can be as much as 15° off. Filtering the data can also introduce phase errors. It is important to insure that any filters used add no phase bias. If a filter must be used which introduces phase bias, a phase matched filter must be used on the other channel to compensate.

Because the hinge damping and stiffness properties vary with load and frequency, it is important to run the test at parameters which are similar to the final systems parameters in this case the on-orbit oscillation parameters. The final system parameters, however, depend on the individual hinge properties so the hinge properties must be determined at several test conditions.

To convert the enclosed area of the force vs displacement curve to an equivalent linear viscous damping coefficient the following formulation is provided. The energy dissipated by the nonlinear damping force (the enclosed area) can be equated to the energy dissipated by a linear damping force which contains the proportional constant. The formulation is expanded in popular literature and yields:

$$C = A/\omega\pi d^2$$

where:

C = equivalent linear viscous damping coefficient

A = enclosed area of force vs deflection curve

ω = frequency of applied load

d = O-peak displacement

O Sinusoidal motion is assumed.

Similarly the enclosed area (energy dissipated) can be equated to velocity squared damping, Coulomb damping, etc.

RESULTS AND RECOMMENDATIONS

The results of this investigation, the deployed solar array natural frequencies and damping, are presented in Tables 1, 2, and 3. In these tables the results of the hybrid synthesis procedure are compared to a finite element analysis of the same system. Table 1 lists the results when only the panel damping is considered; Table 2 lists the results when only hinge damping is considered; and Table 3 lists the results when both panel and hinge damping are considered. Each table shows the synthesized results with and without residual flexibility included. Including residual

GD-10

flexibility improves the accuracy of the damping predictions because residual flexibility improves the accuracy of the system mode shapes. The amount of damping that the substructures in physical coordinates provide to the system is greatly affected by the system mode shapes.

When panel and hinge damping is included the results of the hybrid synthesis procedure compare very well with the finite element results. This correlation of results show that the hybrid synthesis technique is a good tool for predicting the natural frequencies, mode shapes and damping of large flexible (systems) appendages which are composed of well defined subsystems. This procedure is most cost effective when compared to very detailed finite element models. On-orbit data, when available, will also verify the procedure. The test derived component data will also be verified by the on-orbit data.

REFERENCES

1) M. L. Soni, "Prediction of Damping for Flexible Spacecraft Appendages," Proceedings of the Second International Modal Analysis Conference, 1984, pp. 218-222.

2) R. R. Craig and M. C. C. Bampton, "Coupling of Substructures for Dynamic Analysis", AIAA Journal, Vol. 6, No. 7, July 1968, pp. 1313-1319.

3) S. Rubin, "Improved Component-Mode Representation for Structural Dynamic Analysis", AIAA Journal, Vol. 13, No. 8, August 1975, pp. 995-1006.

TABLE 1. EXAMPLE PROBLEM RESULTS, ONLY PANEL DAMPING

| MODE | BASELINE | | SYNTHESIS | | | |
| | | | 10 PANEL MODES | | 10 PANEL MODES & RESID | |
	FREQUENCY (Hz)	DAMPING (C/CR)	FREQUENCY (Hz)	DAMPING (C/CR)	FREQUENCY (Hz)	DAMPING (C/CR)
1	0.139	0.00078	0.146	0.00098	0.138	0.00088
2	0.228	0.00015	0.232	3 E - 7	0.228	3 E - 7
3	0.663	0.00479	0.782	0.00767	0.661	0.00515
4	0.837	0.00237	1.07	0.00430	0.837	0.00212
5	2.25	0.00382	2.50	2 E - 6	2.25	0.00396
6	2.30	0.00070	2.69	0.00640	2.30	0.00003
7	2.52	0.00279	3.40	0.00476	2.51	0.00245

TABLE 2. EXAMPLE PROBLEM RESULTS, ONLY HINGE DAMPING

| MODE | BASELINE | | SYNTHESIS | | | |
| | | | 10 PANEL MODES | | 10 PANEL MODE & RESID | |
	FREQUENCY (Hz)	DAMPING (C/CR)	FREQUENCY (Hz)	DAMPING (C/CR)	FREQUENCY (Hz)	DAMPING (C/CR)
1	0.139	0.00376	0.146	0.00420	0.139	0.00353
2	0.228	0.0276	0.232	0.0291	0.228	0.0275
3	0.677	0.112	0.802	0.258	0.677	0.112
4	0.837	0.0161	1.07	0.0298	0.837	0.0154
5	2.28	0.271	2.46	0.346	2.28	0.271
6	2.52	0.0413	3.38	0.465	2.52	0.0404
7	2.67	0.220	3.39	0.0964	2.67	0.219

TABLE 3. EXAMPLE PROBELM RESULTS, PANEL AND HINGE DAMPING

			SYNTHESIS			
MODE	BASELINE		10 PANEL MODES		10 PANEL MODES & RESID	
	FREQUENCY (HZ)	DAMPING (C/CR)	FREQUENCY (HZ)	DAMPING (C/CR)	FREQUENCY (HZ)	DAMPING (C/CR)
1	0.144	0.0318	0.153	0.0442	0.144	0.0318
2	0.257	0.0453	0.263	0.0485	0.257	0.0452
3	0.641	0.0526	0.661	0.0612	0.641	0.0527
4	0.866	0.143	1.10	0.291	0.866	0.142
5	2.34	0.460	2.36	0.676	2.34	0.459
6	2.45	0.211	2.47	0.468	2.45	0.210
7	2.50	0.360			2.50	0.360
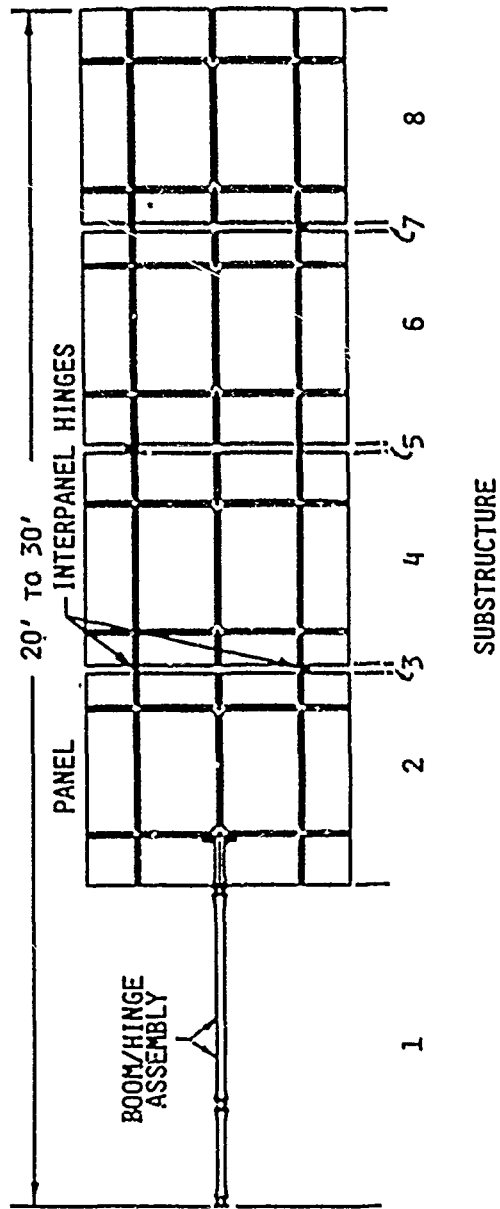
FIGURE 1. SOLAR ARRAY EXAMPLE PROBLEM.

Figure 2.   Solar Array Hinges

Constant Torque
Spring

Interpanel Hinge

Boom to Boom Hinge

LVDT

Load Interface Plate

Load Cell

Flexure Assembly

Hinge

Test Direction
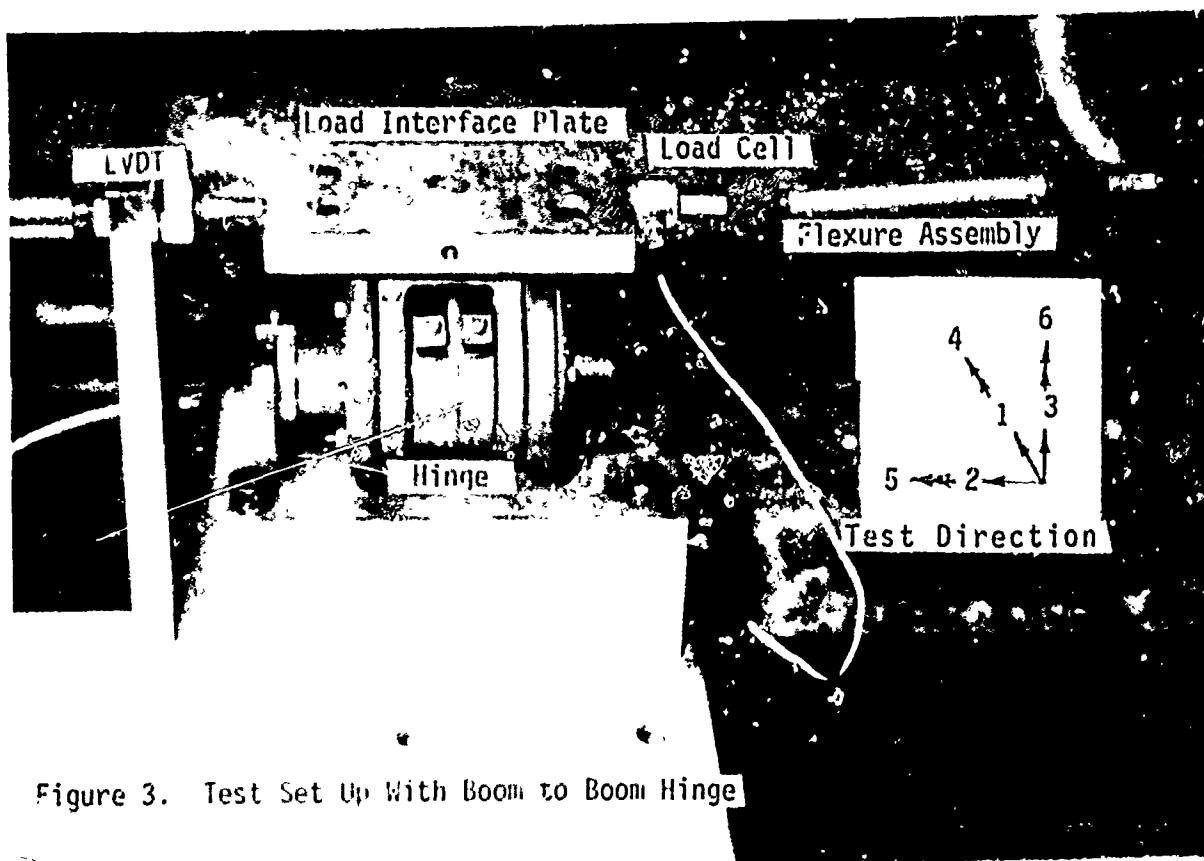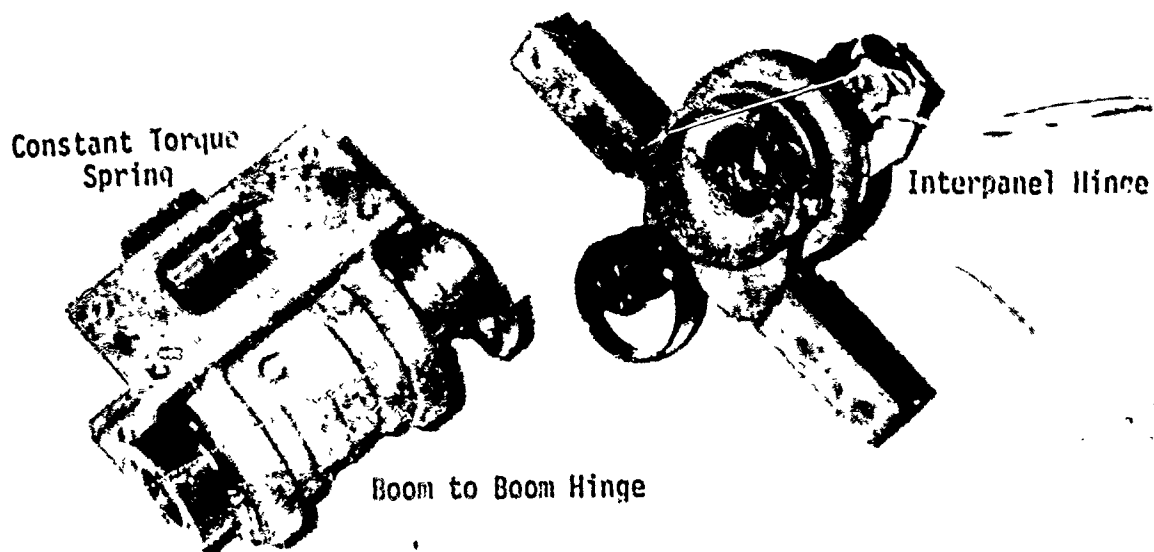
Figure 3.   Test Set Up With Boom to Boom Hinge

GD-15

FORCING FREQUENCY:
0.10 HZ
INPUT FORCE LEVEL:
7.41641 # 0-P
PEAK DISPLACEMENT:
-0.00416 IN. 0-P
CALCULATIONS BASED ON
1 CYCLES

ENCLOSED AREA=
7.22990E-02 POUND-INCHES
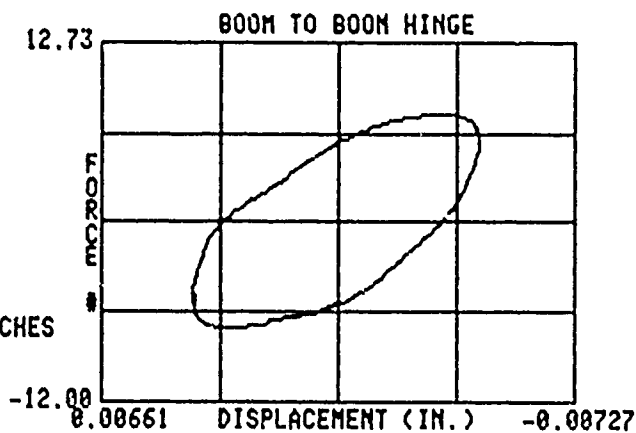
Equivalent Linear Viscous Damping Coefficient: 2.09E3 Pound Sec./Inch
Equivalent Linear Stiffness Coefficient: 1286.3 Pound/Inch

Figure 4.   Force Vs Deflection Curve for Boom to Boom Hinge
            Loaded in the #2 Direction

CONSTRUCTION OF A CONSISTENT DAMPING MATRIX

K. J. BUHARIWALA and J. S. HANSEN

Institute for Aerospace Studies
University of Toronto

ABSTRACT

A general method for constructing a material damping matrix in dynamical systems based on viscoelastic assumptions is presented. A generalization of the classical lamination theory, in particular, the consideration of viscoelasticity in the constitutive relation is considered. The discretized equations of motion for a laminated anisotropic viscoelastic plate using the finite element method are derived. The mass, damping and stiffness matrices are completely defined and arise consistently in the formulation of motion equations. Jacobi root perturbation method is employed to solve the viscoelastic eigenproblem. The technique is used to calculate the eigenvalues of an orthotropic, constrained, four-ply, balanced, symmetric, graphite reinforced epoxy shell element.

1   Introduction

Energy dissipation is an important consideration in the study of stabilization and control of structures, as even limited dissipation can result in fundamentally different requirements. A particularly important form of energy of dissipation in structures is material damping which is always present and is often either ignored or modeled crudely. The present paper is based on the premise that many material damping models currently used in the dynamical analysis are inadequate. The usual manner in which damping is incorporated in dynamical models is by first studying undamped models of the form,

$$\underline{M}\,\ddot{\underline{q}} + \underline{K}\,\underline{q} = \underline{f}(t) \tag{1}$$

for suitable generalized coordinates $\underline{q}$ and generalized loading $\underline{f}$. Methods for constructing the system inertia matrix $\underline{M}$ and the system stiffness matrix $\underline{K}$, for structural systems are well documented; for example reference may be made to Zienkiewicz [1]. In the usual procedure, material damping is accounted for by adding a linear viscous damping term $\underline{D}\,\dot{\underline{q}}$. The difficulty associated with this model,

$$\underline{M}\,\ddot{\underline{q}} + \underline{D}\,\dot{\underline{q}} + \underline{K}\,\underline{q} = \underline{f}(t) \tag{2}$$

is that in writing (2), one rarely comes across an algorithm for constructing the system damping matrix $\underline{D}$. Many studies involve quantifying the damping matrix from an experimentally measured set of information about the dynamic behavior of the system. Hanagud et al. [2], Caravani et al. [3], Caravani and Thompson [4] and Ibrahim [5] describe techniques for identifying the damping matrix in such a manner. Quantifying the damping matrix from an experimentally measured set of dynamic behavior is unattractive from an analytical point of view, since the damping matrix is not available at the design stage, unlike the mass and stiffness matrices.

Hence the present objective is to present a general algorithm for constructing a consistent material damping matrix without any knowledge about the dynamic behavior of the system. As depicted in Fig. 1, the present work endeavors to strengthen the weak link in the dynamical modeling process. In the development, it is shown that the motion equations are integro-differential in form rather than differential, (2). The present interest is directed towards the use of fiber-reinforced polymeric composite materials. The option available to structural engineers of selecting high stiffness, low or zero thermal coefficient of expansion and prescribed damping makes the weight efficient fiber-reinforced composites, a natural choice for a great number of structures. Polymeric materials which are used as the matrix in the composites are viscoelastic; thus the approach adopted is to model the composite as a viscoelastic material.

The viscoelastic stress-strain relation, of interest, for an anisotropic material is presented in Section Two. This is, first, specialized for an orthotropic lamina in Section Three. The stress and moment relations in terms of the membrane, coupling and stiffness operators are then stated in Section

Four for an orthotropic material. The equations of motion for the laminated cylindrical shell are presented in Section Five. In Section Six, using the finite element method, the discretized equations of motion are formulated for a cylindrical shell. The algorithm for constructing the damping matrix is provided explicitly.

2   Linear Viscoelastic Constitutive Relation

In order to derive a consistent damping matrix in a manner analogous to a stiffness matrix as in the Rayleigh-Ritz or a similar discretizing procedure, we require a constitutive relation which accounts for the energy dissipated in a material. The stress and strain are related linearly for a viscoelastic material. The viscoelastic constitutive relation can be represented by a differential or an integral form. In the present approach the stress-strain relation is given in an integral form. The linear, anisotropic, viscoelastic constitutive relation of interest is [6]

$$\sigma_{ij}(t) = \int_0^t \sum_{k,l=1}^{3} G_{ij}^{kl}(\underline{r}, t-\tau)\frac{\partial \varepsilon_{kl}}{\partial \tau} \, d\tau + C_{ij}^{kl}(\underline{r}) \, \varepsilon_{kl} \tag{3}$$

$$G_{ij}^{kl}(\underline{r}, t) = \int_0^\infty C_{ij}^{kl \, (*)}(\underline{r}, \theta)\gamma(\theta)e^{-\theta t} d\theta \tag{4}$$

where $\gamma(\theta)$ is the relaxation density distribution function and C_{ij}^{kl} and G_{ij}^{kl} are symmetric in all four indices (when Onsager's relations apply), and are positive-semidefinite.

3   Orthotropic Assumption

The stress-strain relations (3) and (4) apply to a viscoelastic material with an arbitrary degree of anisotropy. Here, the constitutive relations (3) and (4) take a simplified form, applicable for an orthotropic, material. These relations will be applicable for each lamina and a laminate will consist of a stack of laminae with various ply orientations, as shown in Fig. 2.

For a material in a state of plane stress, the orthotropic, viscoelastic constitutive relation becomes

$$\underline{\sigma}_k = \int_0^t \underline{G}(t-\tau)\frac{\partial \underline{\varepsilon}_k}{\partial \tau} \, d\tau + \underline{C} \, \underline{\varepsilon}_k \tag{5}$$

$$\underline{\sigma}_k^T = [\, \sigma_1 \quad \sigma_2 \quad \sigma_{12} \,] ; \quad \underline{\varepsilon}_k^T = [\, \varepsilon_1 \quad \varepsilon_2 \quad \frac{\gamma_{12}}{2} \,] \tag{6}$$

where γ_{12} is the engineering shear strain and

$$\underline{G}(t) = \int_0^\infty \begin{bmatrix} C_{11}^{(*)}(\theta) & C_{12}^{(*)}(\theta) & 0 \\ C_{12}^{(*)}(\theta) & C_{22}^{(*)}(\theta) & 0 \\ 0 & 0 & 2C_{66}^{(*)}(\theta) \end{bmatrix} \gamma(\theta)e^{-\theta t} \, d\theta \qquad (7)$$

$$\underline{C} = \begin{bmatrix} C_{11} & C_{12} & 0 \\ C_{12} & C_{22} & 0 \\ 0 & 0 & 2C_{66} \end{bmatrix} \qquad (8)$$

The indices in $\underline{G}(t)$ and $\underline{C}$ are ordered 1, 2 and 6 as done, by standard convention, in the analysis of composite materials. In general, the lamina principal axes (1,2) may not be coincident with the structural axes (x,y) as is evident from Fig. 2. Thus the transformation relating the two axes with respect to the structural axes for the kth lamina, as defined by Ashton et al. [7] is

$$\begin{bmatrix} \sigma_1 \\ \sigma_2 \\ \sigma_{12} \end{bmatrix}_k = \underline{T}_k \begin{bmatrix} \sigma_{xx} \\ \sigma_{yy} \\ \sigma_{xy} \end{bmatrix}_k \qquad (9)$$

and the transformation for the strain tensor is

$$\begin{bmatrix} \varepsilon_1 \\ \varepsilon_2 \\ \dfrac{\gamma_{12}}{2} \end{bmatrix}_k = \underline{T}_k \begin{bmatrix} \varepsilon_{xx} \\ \varepsilon_{yy} \\ \dfrac{\gamma_{xy}}{2} \end{bmatrix}_k \qquad (10)$$

GE-4

where the transformation matrix is

$$
\underline{T}_k = \begin{bmatrix} m^2 & n^2 & 2mn \\ n^2 & m^2 & -2mn \\ -mn & mn & m^2 - n^2 \end{bmatrix} \qquad (11)
$$

$$m = \cos(\theta_k) \text{ and } n = \sin(\theta_k)$$

In general, the fiber angle θ_k is different for each ply. Substituting the above transformation (9) and (10) in (5) gives the general orthotropic lamina constitutive relation,

$$
\underline{\sigma} = \int_0^t \underline{G}(t - \tau)\frac{\partial \underline{\epsilon}}{\partial \tau} d\tau + \underline{\overline{C}} \, \underline{\epsilon} \qquad (12)
$$

$$
\underline{\sigma}^T = [\, \sigma_{xx} \quad \sigma_{yy} \quad \sigma_{xy} \,] \qquad (13)
$$

$$
\underline{\epsilon}^T = [\, \epsilon_{xx} \quad \epsilon_{yy} \quad \gamma_{xy} \,] \qquad (14)
$$

and the entries of matrix $\underline{C}$ are given by

$$\overline{C}_{11} = C_{11}m^4 + 2(C_{12} + 2C_{66})m^2n^2 + C_{22}n^4$$

$$\overline{C}_{22} = C_{11}n^4 + 2(C_{12} + 2C_{66})m^2n^2 + C_{22}m^4$$

$$\overline{C}_{12} = (C_{11} + C_{22} - 4C_{66})m^2n^2 + C_{12}(m^4 + n^4)$$

$$\overline{C}_{66} = (C_{11} + C_{22} - 2C_{12} - 2C_{66})m^2n^2 + C_{66}(m^4 + n^4)$$

$$\overline{C}_{16} = (C_{11} - C_{12} - 2C_{66})m^3n + (C_{12} - C_{22} + 2C_{66})mn^3$$

$$\bar{C}_{26} = (C_{11} - C_{12} - 2C_{66})mn^3 + (C_{12} - C_{22} + 2C_{66})m^3n \qquad (15)$$

The entries of matrix $\underline{G}(t)$ are identical in form, with $G_{ij}(t)$ replacing C_{ij} and $\bar{G}_{ij}(t)$ replacing $\bar{C}_{ij}$. It is observed that matrices $\underline{G}(t)$ and $\underline{C}$ are fully populated.

The stress vector can now be related to the displacement vector by using the strain-displacement relation. The linear strain-displacement relation for a cylindrical shell of radius R, as shown in Fig. 3 [Langhaar 8] is

$$\underline{\epsilon} = \underline{\epsilon}^0 + z\underline{\kappa} \qquad (16)$$

where

$$\underline{\epsilon}^{0T} = \left[\ \frac{\partial u^0}{\partial x} \quad \left(\frac{\partial v^0}{\partial y} + \frac{w}{R} \right) \quad \left(\frac{\partial u^0}{\partial y} + \frac{\partial v^0}{\partial x} \right) \ \right] \qquad (17)$$

$$\underline{\kappa}^{T} = - \left[\ \frac{\partial^2 w}{\partial x^2} \quad \frac{\partial^2 w}{\partial y^2} \quad 2\frac{\partial^2 w}{\partial x \partial y} \ \right] \qquad (18)$$

4   Laminate Constitutive Equations

The laminate constitutive equations can be obtained by summing over the laminae. Using (16) in (12), we obtain

$$\underline{\sigma}^{(k)} = \int_0^t \underline{G}^{(k)}(t-\tau) \frac{\partial}{\partial \tau} [\ \underline{\epsilon}^0 + z\underline{\kappa} \ ]^{(k)} d\tau + \underline{\bar{C}}^{(k)} [\ \underline{\epsilon}^0 + z\underline{\kappa} \ ]^{(k)}$$

$$(19)$$

The stress and moment resultants taken over M laminae can then be expressed as

GE-6

$$
\begin{bmatrix}
N_{xx}(t) \\
N_{yy}(t) \\
N_{xy}(t) \\
\hline
M_{xx}(t) \\
M_{yy}(t) \\
M_{xy}(t)
\end{bmatrix}
=
\left[
\begin{array}{c|c}
\underline{A}(t) & \underline{B}(t) \\
\hline
\underline{B}(t) & \underline{D}(t)
\end{array}
\right]
\left[
\begin{array}{c}
\underline{\varepsilon}^0 \\
\hline
\underline{\kappa}
\end{array}
\right]
\tag{20}
$$

where

$$
\underline{A}(t) \triangleq \sum_{k=1}^{M} [\int_0^t \underline{G}^{(k)}(t-\tau)\frac{\partial}{\partial\tau}(.)d\tau + \underline{C}^{(k)}](h_k - h_{k-1}) \tag{21}
$$

$$
\underline{B}(t) \triangleq \frac{1}{2}\sum_{k=1}^{M}[\int_0^t \underline{G}^{(k)}(t-\tau)\frac{\partial}{\partial\tau}(.)d\tau + \underline{C}^{(k)}](h_k^2 - h_{k-1}^2) \tag{22}
$$

$$
\underline{D}(t) \triangleq \frac{1}{3}\sum_{k=1}^{M}[\int_0^t \underline{G}^{(k)}(t-\tau)\frac{\partial}{\partial\tau}(.)d\tau + \underline{C}^{(k)}](h_k^3 - h_{k-1}^3) \tag{23}
$$

$\underline{A}(t)$, $\underline{B}(t)$ and $\underline{D}(t)$ are the membrane, coupling, and bending matrix—operators respectively. If all plies are assumed to obey Hooke's law, that is, when $\underline{G}(t) \equiv \underline{0}$, then the membrane, coupling and bending terms are no longer matrix operators, but simply the standard $\underline{A}$, $\underline{B}$ and $\underline{D}$ matrices for composite materials.

It can be shown that for a balanced laminate (orthotropic plate), that is, a laminate where for each $+\theta$ lamina there exists an identical (in material properties and thickness) $-\theta$ lamina, terms $A_{16} = A_{26} = 0$. For a symmetric laminate, that is, a laminate where for each $+\theta$ lamina above the mid-plane there exists an identical $+\theta$ lamina at the same distance below the mid-plane,

$$
\underline{B}(t) \equiv \underline{0} \tag{24}
$$

Thus no coupling exists between stretching and bending for symmetric laminates.

5   Equations of Motion

Proceeding in the usual manner and making the standard assumptions for thin shells (constant thickness, small strains, negligible rotary inertia

terms, et cetera) as elucidated by Ashton and Whitney [9], the motion equations for a laminated cylindrical shell are

$$A_{11} \frac{\partial^2 u}{\partial x^2} + 2A_{16} \frac{\partial^2 u}{\partial x \partial y} + A_{66} \frac{\partial^2 u}{\partial y^2} + A_{16} \frac{\partial^2 v}{\partial x^2} + (A_{12} + A_{66}) \frac{\partial^2 v}{\partial x \partial y} + A_{26} \frac{\partial^2 v}{\partial y^2}$$

$$- B_{11} \frac{\partial^3 w}{\partial x^3} - 3 B_{16} \frac{\partial^3 w}{\partial x^2 \partial y} - (B_{12} + 2 B_{66}) \frac{\partial^3 w}{\partial x \partial y^2} - B_{26} \frac{\partial^3 w}{\partial y^3} + \frac{A_{12}}{R} \frac{\partial w}{\partial x}$$

$$+ \frac{A_{26}}{R} \frac{\partial w}{\partial y} = \rho \frac{\partial^2 u}{\partial t^2} \qquad (25)$$

$$A_{16} \frac{\partial^2 u}{\partial x^2} + (A_{12} + A_{66}) \frac{\partial^2 u}{\partial x \partial y} + A_{26} \frac{\partial^2 u}{\partial y^2} + A_{66} \frac{\partial^2 v}{\partial x^2} + 2 A_{26} \frac{\partial^2 v}{\partial x \partial y} + A_{22} \frac{\partial^2 v}{\partial y^2}$$

$$- B_{16} \frac{\partial^3 w}{\partial x^3} - (B_{12} + 2 B_{66}) \frac{\partial^3 w}{\partial x^2 \partial y} - 3 B_{26} \frac{\partial^3 w}{\partial x \partial y^2} - B_{22} \frac{\partial^3 w}{\partial y^3} + \frac{A_{26}}{R} \frac{\partial w}{\partial x}$$

$$+ \frac{A_{22}}{R} \frac{\partial w}{\partial y} = \rho \frac{\partial^2 v}{\partial t^2} \qquad (26)$$

$$D_{11} \frac{\partial^4 w}{\partial x^4} + 4D_{16} \frac{\partial^4 w}{\partial x^3 \partial y} + 2(D_{12} + 2D_{66})\frac{\partial^4 w}{\partial x^2 \partial y^2} + 4D_{26} \frac{\partial^4 w}{\partial x \partial y^3} + D_{22} \frac{\partial^4 w}{\partial y^4}$$

$$- B_{11} \frac{\partial^3 u}{\partial x^3} - 3B_{16} \frac{\partial^3 u}{\partial x^2 \partial y} - (B_{12} + 2B_{66})\frac{\partial^3 u}{\partial x \partial y^2} - B_{26} \frac{\partial^3 u}{\partial y^3} - B_{16} \frac{\partial^3 v}{\partial x^3}$$

$$- (B_{12} + 2B_{66})\frac{\partial^3 v}{\partial x^2 \partial y} - 3B_{26} \frac{\partial^3 v}{\partial x \partial y^2} - B_{22} \frac{\partial^3 v}{\partial y^3} - \frac{1}{R}\left(B_{12}\frac{\partial^2 w}{\partial x^2} + 2B_{26}\frac{\partial^2 w}{\partial x \partial y}\right.$$

$$\left. + B_{22} \frac{\partial^2 w}{\partial y^2}\right) + \rho \frac{\partial^2 w}{\partial t^2} = q \tag{27}$$

where q is the lateral pressure and ρ is the laminate density defined by

$$\rho \triangleq \sum_{k=1}^{M} \int_{h_{k-1}}^{h_k} \rho_0^{(k)} dz \tag{28}$$

Equations (25)-(27) are identical in form to those of laminated shells which obey the generalized Hooke's law, as can be seen by setting $G_{ij}(t) \equiv 0$, but now because of the definitions of A, B and D, eqns. (25)-(27) have the important embedded feature, namely, energy dissipation.

6   Equations of Motion: Finite Element Method – Virtual Work Formulation

In this section, we demonstrate explicitly the technique of constructing the damping matrix for a cylindrical shell element, Fig. 3, using the finite element method. We start with the principle of virtual work expressed as

$$\int_V \underline{X}^T \delta\underline{u} \, dV = \int_V (\delta\underline{\epsilon}^T \underline{\sigma} + \rho^0 \underline{\ddot{u}}^T \delta\underline{u})dV \tag{29}$$

where $\underline{X}$ and $\underline{u}$ are the externally applied load vector, and the displacement vector respectively defined by

$$\underline{X}^T = [\,0 \quad 0 \quad q\,]; \qquad \underline{u}^T = [\,u \quad v \quad w\,] \tag{30}$$

and the stress-strain and strain-displacement relations are obtained from (12) and (16), respectively. Using constitutive relation (19), we obtain

$$\int_V \sum_{k=1}^{M} \left[\rho^{0(k)} \; \underline{\ddot{u}}^T \delta\underline{u} + \delta(\underline{\epsilon}^{0T} + z\underline{\kappa}^T)^{(k)} \int_0^t \underline{\overline{G}}^{(k)}(t-\tau)\frac{\partial}{\partial \tau} \left[\underline{\epsilon}^0 + z\underline{\kappa}\right]^{(k)} d\tau \right.$$

$$\left. + \delta(\underline{\epsilon}^{0T} + z\underline{\kappa}^T)^{(k)} \underline{\overline{C}}^{(k)}(\underline{\epsilon}^0 + z\underline{\kappa})^{(k)} - \underline{X}^T \delta\underline{u} \right] dV = 0 \tag{31}$$

Integrating through the thickness of the laminate, the above can be written in terms of the membrane, coupling and bending matrix operators,

$$\int_0^a \int_0^b [\rho \, \underline{\ddot{u}}^T \delta\underline{u} + \delta\underline{\epsilon}^{0T} \underline{A}(t)\underline{\epsilon}^0 + \delta\underline{\epsilon}^{0T}\underline{B}(t)\underline{\kappa} + \delta\underline{\kappa}^T\underline{B}(t)\underline{\epsilon}^0$$

$$- \delta\underline{\kappa}^T\underline{D}(t)\underline{\kappa} - \underline{X}^T\delta\underline{u}] \, dxdy = 0 \tag{32}$$

where 'a' and 'b' are the axial and circumferential dimenions of the cylindrical shell structure. Here, $\underline{\epsilon}^{0T}\underline{B}(t)\underline{\kappa} \neq \underline{\kappa}^T\underline{B}(t)\underline{\epsilon}^0$ because of the integral nature of the coupling operator (22). Of course, for the elastic problem when $\underline{G} \equiv \underline{0}$, from the symmetry of matrix $\underline{C}$, we have $\underline{\epsilon}^{0T}\underline{B} \, \underline{\kappa} = \underline{\kappa}^T\underline{B} \, \underline{\epsilon}^0$.

The spatial dependence of the problem is discretized using the standard techniques of the finite element procedure. The trial functions chosen for the cylindrical shell segment are the polynomials,

$$u(x,y,t) = \sum_{i,j=0}^{1} a_{ij}(t)x^i y^j \tag{33}$$

$$v(x,y,t) = \sum_{i,j=0}^{1} b_{ij}(t)x^i y^j \tag{34}$$

$$w(x,y,t) = \sum_{i,j=0}^{3} c_{ij}(t)x^i y^j \tag{35}$$

where coefficients a_{ij}, b_{ij}, and c_{ij} are to be determined.

For convenience, in integrating the surface integral in (32), the normalized coordinates are introduced,

$$\xi = \frac{x}{a'}, \qquad \eta = \frac{y}{b'} \tag{36}$$

where a' and b' are the axial and circumferential dimensions of the finite shell element. Upon discretization, the principle of virtual work can be expressed as

$$\delta V[\, \underline{u} \,] = \sum_{i=1}^{n} \delta V_i [\, \underline{u} \,]$$

$$= 0 \tag{37}$$

where n is the total number of elements and V_i is the virtual work

corresponding to the ith discretized finite element. Integrating (32) over x and y in the principle of virtual work after using expressions (33) -- (35) yields the result

$$\delta V = 0$$

where

$$\delta V_i \triangleq \rho a'b' \delta \underline{\Delta}^T \underline{M}_1 \ddot{\underline{\Delta}} + \delta \underline{\Delta}^T \underline{E} \underline{\Delta} - \delta \underline{\Delta}^T \underline{F} \underline{\Delta} - \delta \underline{\Delta}^T \underline{F}^T \underline{\Delta} - \delta \underline{\Delta}^T \underline{f}_1 \qquad (38)$$

with

$$\underline{E} \triangleq \frac{\underline{D}_{11}(t)b'}{a'^3} \underline{N}_1 + \frac{\underline{D}_{12}(t)}{a'b'} (\underline{N}_2 + \underline{N}_2^T) + \frac{\underline{D}_{22}(t)a'}{b'^3} \underline{N}_3 + \frac{4\underline{D}_{66}(t)}{a'b'} \underline{N}_4$$

$$+ \frac{2\underline{D}_{16}(t)}{a'^2} (\underline{N}_5 + \underline{N}_5^T) + \frac{2\underline{D}_{26}(t)}{b'^2} (\underline{N}_6 + \underline{N}_6^T) + \frac{\underline{A}_{11}(t)b'}{a'} \underline{N}_7$$

$$+ \underline{A}_{12}(t) (\underline{N}_8 + \underline{N}_8^T) + \frac{\underline{A}_{22}(t)a'}{b'} \underline{N}_9 + \frac{\underline{A}_{66}(t)b'}{a'} \underline{N}_{10} + \frac{\underline{A}_{66}(t)a'}{b'} \underline{N}_{11}$$

$$+ \underline{A}_{66}(t) (\underline{N}_{12} + \underline{N}_{12}^T) + \frac{\underline{A}_{12}(t)b'}{R} (\underline{N}_{13} + \underline{N}_{13}^T)$$

$$+ \frac{\underline{A}_{22}(t)a'}{R} (\underline{N}_{14} + \underline{N}_{14}^T) + \frac{\underline{A}_{22}(t)a'b'}{R^2} \underline{N}_{15} + \frac{\underline{A}_{26}(t)a'}{R} (\underline{N}_{16} + \underline{N}_{16}^T)$$

$$+ \frac{\underline{A}_{26}(t)b'}{R} (\underline{N}_{17} + \underline{N}_{17}^T) + \underline{A}_{16}(t) (\underline{N}_{18} + \underline{N}_{18}^T) + \frac{\underline{A}_{16}(t)b'}{a'} (\underline{N}_{19} + \underline{N}_{19}^T)$$

$$+ \frac{\underline{A}_{26}(t)a'}{b'} (\underline{N}_{20} + \underline{N}_{20}^T) + \underline{A}_{26}(t) (\underline{N}_{21} + \underline{N}_{21}^T) \qquad (39)$$

and

$$\underline{F} = \frac{\underline{B}_{11}(t)b'}{a'^2} \underline{N}_{22} + \frac{\underline{B}_{12}(t)}{b'} \underline{N}_{23} + \frac{2\underline{B}_{16}(t)}{a'} \underline{N}_{24} + \frac{\underline{B}_{12}(t)}{a'} \underline{N}_{25}$$

GE-11

$$+ \frac{\underline{B}_{26}(t)b'}{Ra'} \underline{N}_{26} + \frac{\underline{B}_{22}(t)a'}{b'^2} \underline{N}_{27} + \frac{\underline{B}_{22}(t)a'}{Rb'^2} \underline{N}_{28} + \frac{2\underline{B}_{26}(t)}{b'} \underline{N}_{29}$$

$$+ \frac{2\underline{B}_{26}(t)a'}{R} \underline{N}_{30} + \frac{\underline{B}_{16}(t)}{a'} \underline{N}_{31} + \frac{\underline{B}_{16}(t)b'}{a'^2} \underline{N}_{32} + \frac{\underline{B}_{26}(t)a'}{b'^2} \underline{N}_{33}$$

$$+ \frac{\underline{B}_{26}(t)}{b'} \underline{N}_{34} + \frac{2\underline{B}_{66}(t)}{b'} \underline{N}_{35} + \frac{2\underline{B}_{66}(t)}{a'} \underline{N}_{36} \tag{40}$$

$$\underline{\Delta}^T = [\, a_{00} \quad b_{00} \quad c_{00} \quad c_{01} \quad c_{02} \quad c_{03}$$

$$a_{01} \quad b_{01} \quad c_{10} \quad c_{11} \quad \cdots \quad c_{33} \,] \tag{41}$$

The local 24 x 24 matrix $\underline{M}_1$, matrices $\underline{N}_1$, $\underline{N}_2$, ..., $\underline{N}_{36}$ and vector $\underline{f}_1$ can be inferred by integrating (32). Some typical $\underline{N}_j$ matrices are

$$\underline{N}_1 = \sum_{i=2}^{3} \sum_{j=0}^{3} \sum_{k=2}^{3} \sum_{l=0}^{3} \frac{ik(i-1)(k-1)}{(i+k-3)(j+l+1)} c_{ij}c_{kl}$$

$$\underline{N}_7 = \sum_{i=1}^{1} \sum_{j=0}^{1} \sum_{k=1}^{1} \sum_{l=0}^{1} \frac{ik}{(i+k-1)(j+l-1)} a_{ij}a_{kl} \tag{42}$$

$$\underline{N}_{22} = \sum_{i=1}^{1} \sum_{j=0}^{1} \sum_{k=2}^{3} \sum_{l=0}^{3} \frac{ik(k-1)}{(i+k-2)(j+l+1)} a_{ij}c_{kl}$$

Trial functions over each cylindrical shell element can also be expressed in terms of Hermite polynomials. The unknown coefficients a_{ij}, b_{ij} and c_{ij} in (33)-(35) can be related to the six degrees of freedom (u, v, w, w_x, w_y, and w_{xy}) per node, by taking the following trial functions:

$$u(\xi,\eta,t) = (1 - \xi)(1 - \eta)u_1 + \xi(1 - \eta)u_2 + \xi\eta u_3 + (1 - \xi)\eta u_4$$

$$\tag{43}$$

$$v(\xi,\eta,t) = (1 - \xi)(1 - \eta)v_1 + \xi(1 - \eta)v_2 + \xi\eta v_3 + (1 - \xi)\eta v_4$$

$$(44)$$

$$w(\xi,\eta,t) = \Theta(\xi)\Theta(\eta)w_1 + \Phi(\xi)\Theta(\eta)(w_x)_1 + \Theta(\xi)\Phi(\eta)(w_y)_1 + \Phi(\xi)\Phi(\eta)(w_{xy})_1$$

$$+ \Theta(\xi-1)\Theta(\eta)w_2 + \Phi(\xi-1)\Theta(\eta)(w_x)_2 + \Theta(\xi-1)\Phi(\eta)(w_y)_2$$

$$+ \Phi(\xi-1)\Phi(\eta)(w_{xy})_2 + \Theta(\xi-1)\Theta(\eta-1)w_3 + \Phi(\xi-1)\Theta(\eta-1)(w_x)_3$$

$$+ \Theta(\xi-1)\Phi(\eta-1)(w_y)_3 + \Phi(\xi-1)\Phi(\eta-1)(w_{xy})_3 + \Theta(\xi)\Theta(\eta-1)w_4$$

$$+ \Phi(\xi)\Theta(\eta-1)(w_x)_4 + \Theta(\xi)\Phi(\eta-1)(w_y)_4 + \Phi(\xi)\Phi(\eta-1)(w_{xy})_4 \qquad (45)$$

where the Hermite cubics are defined as

$$\Theta(\theta) = (|\theta| - 1)^2(2|\theta| + 1)$$

$$\Phi(\phi) = \phi(|\phi| - 1)^2 \qquad (46)$$

The transformation relating the degrees of freedom and the unknown coefficients in (33) - (35) is

$$\underline{\Delta} = \underline{H}\ \underline{q}_l \qquad (47)$$

where the local generalized coordinate vector is

$$\underline{q}_l^T = [\ u_1 \quad v_1 \quad w_1 \quad (w_x)_1 \quad (w_y)_1 \quad (w_{xy})_1$$

$$u_2 \quad v_2 \quad w_2 \quad (w_x)_2 \quad \cdots \quad (w_{xy})_4\ ] \qquad (48)$$

and the transformation matrix $\underline{H}$ as defined in (47) is given in the appendix. Using (47) the local virtual work corresponding to the ith element (38) becomes

$$\delta V_i = \rho a'b' \delta \underline{q}_1^T \underline{H}^T \underline{M}_1 \underline{H} \ddot{\underline{q}}_1 + \delta \underline{q}_1^T \underline{H}^T \underline{E} \underline{H} \underline{q}_1 - \delta \underline{q}_1^T \underline{H}^T (\underline{E} + \underline{E}^T) \underline{H} \underline{q}_1 - a'b' \delta \underline{q}_1^T \underline{f}_1$$

$$(49)$$

Upon assembly of the finite element equations and for an arbitrary generalized virtual displacement vector $\delta \underline{q}$, the unknown vector $\underline{q}$ is the solution of the integro-differential motion equations,

$$\underline{M} \ddot{\underline{q}} + \int_0^t \underline{R}(t-\tau) \frac{d\underline{q}}{d\tau} d\tau + \underline{K} \underline{q} = \underline{f} \tag{50}$$

subject to the appropriate boundary conditions.

Using expressions (21)-(23) in (39) and (40), the damping matrix $\underline{R}(t)$ and the stiffness matrix $\underline{K}$ are obtained from

$$\underline{R}(t) = \sum_{j=1}^{\alpha} \underline{R}_j g_j(t) \tag{51}$$

$$\underline{K} = \sum_{j=1}^{\alpha} \underline{K}_j \tag{52}$$

where upon comparing (39) and (40) term by term $\underline{R}_j$ and $\underline{K}_j$ are given by

$$\underline{R}_1 = \left[\frac{b'}{a'^3} \underline{H}^T \underline{N}_1 \underline{H} \right]_G \; ; \qquad g_1(t) = \frac{1}{3} \sum_{k=1}^{M} \overline{G}_{11}^{(k)}(t)(h_k^3 - h_{k-1}^3)$$

$$\underline{K}_1 = \left[\frac{b'}{a'^3} \underline{H}^T \underline{N}_1 \underline{H} \right]_G \left(\frac{1}{3} \sum_{k=1}^{M} \overline{C}_{11}^{(k)}(h_k^3 - h_{k-1}^3) \right)$$

$$\underline{R}_2 = \left[\frac{1}{a'b'} \underline{H}^T \underline{N}_2 \underline{H} \right]_G ; \qquad g_2(t) = \frac{1}{3} \sum_{k=1}^{M} \overline{G}_{12}^{(k)}(t)(h_k^3 - h_{k-1}^3)$$

$$\underline{K}_2 = \left[\frac{1}{a'b'} \underline{H}^T \underline{N}_2 \underline{H} \right]_G \left(\frac{1}{3} \sum_{k=1}^{M} C_{12}^{(k)}(h_k^3 - h_{k-1}^3) \right)$$

$$\underline{R}_{22} = [\ \frac{b'}{a'^2}\ \underline{H}^T\underline{N}_{22}\underline{H}\ ]_G\ ; \qquad g_{22}(t) = \frac{1}{2} \sum_{k=1}^{M} G_{11}^{(k)}(t)(h_k^2 - h_{k-1}^2)$$

$$\underline{K}_{22} = [\ \frac{b'}{a'^2}\ \underline{H}^T\underline{N}_{22}\underline{H}\ ]_G (\frac{1}{2} \sum_{k=1}^{M} C_{11}^{(k)}(h_k^2 - h_{k-1}^2))$$

$$\vdots \qquad\qquad\qquad\qquad (53)$$

where subscript G in (53) denotes the resulting global matrix upon assembly of the finite elements.

From (53) it is observed that the damping matrices $\underline{R}_i$ are derived consistently and are proportional to the stiffness matrices $\underline{K}_i$ but, because of the time dependence defined by $g_i(t)$, the damping matrix $\underline{R}(t)$ in (51) is not in general proportional to the stiffness matrix $\underline{K}$, and tends to zero for arbitrarily large time. The discretized motion equations (50)-(53) determine the instantaneous viscoelastic response of a general shell laminate which depends on the entire history of the response. The upper limit α in the summation (51) and (52) can be deduced from the symmetry of ply orientations in the composite material:

$\alpha = 36$ for the general cylindrical shell laminate

$\alpha = 21$ symmetric, cylindrical shell laminate

$\alpha = 15$ balanced, symmetric, cylindrical shell laminate

$\alpha = 12$ balanced, symmetric flat laminate

The formulation of the integro-differential motion equations (50) is now complete. The damping matrix $\underline{R}(t)$ is consistently defined and, as evident from (53), it is no more difficult to calculate than the stiffness matrix $\underline{K}$. Hence, an existing computer code of a purely elastic structure ($\underline{M}, \underline{K}$ system) can be easily modified for analysis of a corresponding viscoelastic structure ($\underline{M}, \underline{R}(t), \underline{K}$ system). The only aspect remaining to be specified, in the model, is the material decay distribution function $\gamma(\theta)$, which is implicit in function $g_i(t)$.

7   Eigenproblem

One method of solving the equations of motion of a viscoelastic structure is to use modal analysis, for which the eigenmodes of the structure are required. Our interest is to solve the eigenproblem for the viscoelastic structure, which cannot be solved by standard routines available on computer systems. The eigenproblem, of interest, can be formulated by taking either the Laplace transform or Fourier transform of the motion equation. We prefer to

work in the Laplace domain, so taking the Laplace transform of (50) (Laplace variable p), we obtain,

$$(p^2 \underline{M} + p \underline{\tilde{R}}(p) + \underline{K})\underline{\tilde{q}} = \underline{\tilde{f}} + \underline{M}(\underline{\dot{q}}(0) + p \underline{q}(0)) + \underline{\tilde{R}} \underline{q}(0) \qquad (54)$$

where

$$\underline{\tilde{R}}(p) = \sum_{i=1}^{\alpha} \underline{R}_i \; \tilde{g}_i(p) \qquad (55)$$

$$\tilde{G}_{ij}(p) = \int_0^\infty \frac{C_{ij}^{(*)}(\theta)\gamma(\theta)}{p + \theta} d\theta \qquad (56)$$

The solution for an arbitrary loading can be expanded in terms of the eigenmodes $\underline{u}$. Hence, for an N dimensional model, we can write the response as

$$\underline{q}(t) = \sum_{i=1}^{N} \underline{u}_i \; v_i(t) \qquad (57)$$

where the functions $v_i(t)$ depend on the initial conditions and force vector $\underline{f}(t)$. The eigenmodes $\underline{u}$ are independent of the initial conditions, therefore only the homogeneous counterpart of (54) need be considered. Hence, the eigenproblem, to be solved, becomes

$$(p^2 \underline{M} + p \underline{\tilde{R}}(p) + \underline{K})\underline{u} = \underline{0} \qquad (58)$$

As noted earlier, this problem cannot be solved by standard eigensolver routines available on computer systems. Numerical information for the eigenproblem, however, can be obtained by a root perturbation technique. The idea of root perturbation is not new. It was first introduced by Jacobi in 1846 [Aubrun, 10] and has been applied extensively, to evaluate root sensitivity to system parameter changes. The method is based on the observation that if a system is modified, for instance, by altering some parameter, then approximate analytical expressions of interest can be derived by treating the altered parameter as a perturbation about the reference point of the original system. The modification of the original system may entail a parameter change or, in our case, an addition of damping terms to the previously undamped system.

GE-16

8   Jacobi Root Perturbation Method

For convenience, the eigenproblem is cast in a first order form. So, first, consider the undamped eigenproblem (formulated from a purely elastic constitutive relation, $\underline{G} \equiv \underline{0}$),

$$(p^{0^2}\underline{M} + \underline{K})\underline{\upsilon}^0 = \underline{0} \tag{59}$$

where the N (total number of generalized coordinates in the finite element model) eigenvalues $(p^0)^2$ and eigenmodes $\underline{\upsilon}^0$ can be obtained from standard eigensolver routines available in most computer software packages. It is observed that the eigenvalues are purely imaginary and occur in complex conjugate pairs. From (59) we observe,

$$p^0 = \pm j\omega_\alpha^0 \tag{60}$$

where

$$\omega_\alpha^0 = \left(\frac{\underline{\upsilon}_\alpha^{0^T} \underline{K} \underline{\upsilon}_\alpha^0}{\underline{\upsilon}_\alpha^{0^T}\underline{M} \underline{\upsilon}_\alpha^0} \right)^{1/2} > 0 \tag{61}$$

For a constrained structure, the undamped frequencies ω^0 as given by (61) are positive, since the mass $\underline{M}$ and stiffness $\underline{K}$, matrices are positive-definite. The usual orthonormality conditions are

$$\underline{\upsilon}_\alpha^{0^T}\underline{M} \underline{\upsilon}_\beta^0 = \delta_{\alpha\beta} \qquad \alpha,\beta = 1,2,\ldots,N \tag{62}$$

and

$$\underline{\upsilon}_\alpha^{0^T}\underline{K} \underline{\upsilon}_\beta^0 = (\omega_\alpha^0)^2\delta_{\alpha\beta} \qquad \alpha,\beta = 1,2,\ldots,N \tag{63}$$

Therefore, there exists a transformation which simultaneously diagonalizes the mass and stiffness matrices. So let

$$\underline{Q}^0 = \text{row} \begin{bmatrix} \underline{v}_1^0 & \underline{v}_2^0 & \cdots & \underline{v}_N^0 \end{bmatrix} \tag{64}$$

then using

$$\underline{v} = \underline{Q}^0 \underline{\phi} \tag{65}$$

the viscoelastic eigenproblem (58) can be expressed as

$$(p^2 \underline{1} + p\hat{\underline{R}}(p) + \hat{\underline{k}})\underline{\phi} = \underline{0} \tag{66}$$

where

$$\underline{Q}^{0^T} \underline{M} \, \underline{Q}^0 = \underline{1} \tag{67}$$

$$\underline{Q}^{0^T} \widetilde{\underline{R}} \, \underline{Q}^0 = \hat{\widetilde{\underline{R}}} \tag{68}$$

$$\underline{Q}^{0^T} \underline{K} \, \underline{Q}^0 = \hat{\underline{k}} = \text{diag}\begin{bmatrix} \omega_1^{0^2} & \omega_2^{0^2} & \cdots & \omega_N^{0^2} \end{bmatrix} \tag{69}$$

where $\omega_1^0, \ldots, \omega_N^0$ are the frequencies of the undamped problem (59). A sufficient condition for the damping matrix R to be diagonal is that $\widetilde{R}$ be a linear combination of the mass and stiffness matrix. In general, $\widetilde{R}$ is not diagonal, since only sub-blocks of R are proportional to the corresponding sub-blocks of the stiffness matrix $\underline{K}$. The case where the damping matrix $\widetilde{R}$, as given by (68), can be diagonal is when $\alpha = 1$ (the upper limit of summation in (51) and (52)), that is, a one dimensional problem; for instance, a beam in pure flexure in which case $\underline{R}l \propto \underline{K}$ ($= \underline{K}l$), or when all g_j's are equal.

The eigenproblem (66) in first order form becomes

$$p\underline{x} - \widetilde{\underline{A}}(p)\underline{x} = \underline{0} \tag{70}$$

where

$$\widetilde{\underline{A}}(p) = \underline{A}^0 + \delta\widetilde{\underline{A}}(p) \tag{71}$$

$$\underline{A}^0 = \begin{bmatrix} \underline{0} & -\hat{\underline{K}} \\ \underline{1} & \underline{0} \end{bmatrix} \qquad \delta\tilde{\underline{A}}(p) = \begin{bmatrix} -\hat{\tilde{\underline{R}}}(p) & \underline{0} \\ \underline{0} & \underline{0} \end{bmatrix}$$

$$\underline{x} = \begin{bmatrix} p\underline{\phi} \\ \underline{\phi} \end{bmatrix} \qquad\qquad (72)$$

Thus, the damping matrix $\underline{R}(p)$ is treated as a first order perturbation of the undamped problem (59). We are considering small dissipation, hence the perturbation analysis, which involves perturbing about the periodic modes, will not yield purely dissipative modes. We can now apply Jacobi's root perturbation method. Let the eigenvalues and eigenmodes after the kth iteration be represented as

$$p^{(k)} = p^{(k-1)} + \delta p^{(k)}$$

$$= p^{(0)} + \sum_{i=1}^{k} \delta p^{(i)} \qquad k = 1,2,\dots$$

$$(73)$$

$$\underline{x}^{(k)} = \underline{x}^{(k-1)} + \delta\underline{x}^{(k)}$$

$$= \underline{x}^{(0)} + \sum_{i=1}^{k} \delta\underline{x}^{(i)} \qquad k = 1,2,\dots$$

$$(74)$$

where $p^{(0)}$ and $\underline{x}^{(0)}$ are the eigenvalues and eigenmodes respectively of the unperturbed, undamped problem

$$p^{(0)}\underline{x}^{(0)} - \underline{A}^0\underline{x}^{(0)} = \underline{0} \qquad (75)$$

For the ith unperturbed eigenvalue

$$p_i^{(0)} = j\,\omega_i^0 \qquad (76)$$

the ith eigenmode, by row reducing (75), can be shown to equal

$$\underline{x}_i^{(0)T} = [0 \quad 0 \quad \dots \quad j\omega_i^0 \quad 0 \quad \dots \quad 0 \mid 0 \quad 0 \quad \dots \quad 1 \quad 0 \quad \dots \quad 0]$$

(77)

where the only non-zero elements occur in position i and N+i.

Using expressions (73) and (74), the eigenproblem becomes

$$(p^{(0)} + \sum_{i=1}^{k} \delta p^{(i)})(\underline{x}^{(0)} + \sum_{i=1}^{k} \delta\underline{x}^{(i)}) \ - \ [\underline{A}^0 + \delta\underline{\tilde{A}}(p^{(0)} + \sum_{i=1}^{k} \delta p^{(i)})]$$

$$(\underline{x}^{(0)} + \sum_{i=1}^{k} \delta\underline{x}^{(i)}) = \underline{0} \qquad (78)$$

Expanding and neglecting second and higher order terms, yields

$$p^{(0)} \sum_{i=1}^{k} \delta\underline{x}^{(i)} + \sum_{i=1}^{k} \delta p^{(i)}\underline{x}^{(0)} - \underline{A}^0 \sum_{i=1}^{k} \delta\underline{x}^{(i)} - \delta\underline{\tilde{A}}(p^{(k-1)})\underline{x}^{(0)} = \underline{0}$$

(79)

Taking the left eigenvector of the unperturbed problem to be $\underline{y}^{(0)}$, that is,

$$p^{(0)}\underline{y}^{(0)T} - \underline{y}^{(0)T}\underline{A}^0 = \underline{0} \qquad (80)$$

where

$$\underline{y}_i^{(0)T} = [0 \quad 0 \quad \dots \quad 1 \quad 0 \quad \dots \quad 0 \mid 0 \quad 0 \quad \dots \quad j\omega_i^0 \quad 0 \quad \dots \quad 0] \qquad (81)$$

The perturbation in the nth eigenvalue after the kth iteration, after pre-multiplying (79) by $\underline{y}^{(0)T}$, gives

GE-20

$$\delta p_n^{(k)} = \frac{\underline{y}_n^{(0)T} \delta \underline{\tilde{A}}(p_n^{(k-1)}) \underline{x}_n^{(0)}}{\underline{y}_n^{(0)T} \underline{x}_n^{(0)}} - \sum_{i=1}^{k-1} \delta p_n^{(i)}$$

$$= -\frac{1}{2} \underline{u}_n^{(0)T} \underline{\tilde{R}}(p_n^{(k-1)}) \underline{u}_n^{(0)} - \sum_{i=1}^{k-1} \delta p_n^{(i)} \qquad (82)$$

The eigenvalues of the perturbed problem (58) are then obtained from (73). They are $2N$ in number and from the nature of matrix $\underline{R}(p)$, occur in complex conjugate pairs (denoted by an overscore), since

$$\overline{\tilde{G}_{ij}(p)} = \tilde{G}_{ij}(\overline{p}) \qquad (83)$$

To determine the perturbation in the eigenvector, we pre-multiply (79) by $\underline{x}^{(0)T} \underline{\Lambda}$ where $\underline{\Lambda}$ is a normalization weighting matrix such that

$$\underline{x}^{(0)T} \underline{\Lambda} \, \underline{x}^{(0)} = 1$$

$$\underline{x}^{(0)T} \underline{\Lambda} \, \delta \underline{x}^{(i)} = 0 \qquad i = 1,2,\ldots,k \qquad (84)$$

So (79) becomes

$$\sum_{i=1}^{k} \delta p^{(i)} - \underline{x}^{(0)T} \underline{\Lambda} \, \underline{A}^0 \sum_{i=1}^{k} \delta \underline{x}^{(i)} - \underline{x}^{(0)T} \underline{\Lambda} \, \delta \underline{\tilde{A}}(p^{(k-1)}) \underline{x}^{(0)} = 0$$

$$(85)$$

from which we obtain

$$\delta p^{(k)} = \underline{x}^{(0)T} \underline{\Lambda} \, \underline{A}^0 \sum_{i=1}^{k} \delta \underline{x}^{(i)} + \underline{x}^{(0)T} \underline{\Lambda} \, \delta \underline{\tilde{A}}(p^{(k-1)}) \underline{x}^{(0)} - \sum_{i=1}^{k-1} \delta p^{(i)}$$

$$(86)$$

Using this expression to eliminate $\delta p^{(k)}$ in (79) leads to the sought after expression for the perturbation in the eigenmodes

$$\delta\underline{x}^{(k)} = \left(\underline{A}^0 - p^{(0)}\underline{1} - \underline{x}^{(0)}\underline{x}^{(0)T}\underline{\Lambda}\,\underline{A}\right)^{-1}\left[\left(\underline{x}^{(0)}\underline{x}^{(0)T}\underline{\Lambda} - \underline{1}\right)\delta\widetilde{\underline{\Lambda}}(p^{(k-1)})\underline{x}^{(0)}\right.$$

$$\left. - \sum_{i=1}^{k-1} \delta\underline{x}^{(i)} \right] \tag{87}$$

The eigenmodes $\underline{x}$ of the viscoelastic problem (70) can then be obtained from (74).

The eigenmodes are only defined to within a multiplicative constant $re^{j\theta}$, that is, vectors $\underline{\eta}$ and $\underline{\upsilon}$ as given by

$$\underline{\eta} = re^{j\theta}\,\underline{\upsilon} \tag{88}$$

are the same eigenmodes. Thus for uniqueness, the eigenmodes are normalized to the mass matrix,

$$\underline{\upsilon}^T \underline{M}\,\underline{\upsilon} = 1 \tag{89}$$

This determines the scalar constant r in (88). To determine angle θ, we shall orient the eigenmode $\underline{\upsilon}_i$ so that the component with the largest magnitude is aligned with the real axis as illustrated in Fig. 4. If no single component can be identified as having the largest norm, then we shall orient the eigenmode $\underline{\upsilon}_i$ so that the component with the largest norm and smallest angle is aligned with the real axis.

9   Numerical Example

In this section we calculate the eigenvalues of a graphite reinforced epoxy shell element using the root perturbation method outlined in the previous section. The equation of motion, after spatial discretization for an orthotropic, balanced, symmetric shell laminate with six degrees of freedom per node (three displacements u, v, w, slopes w_x, w_y, and twist w_{xy}), is

$$\underline{M}\,\ddot{\underline{q}} + \int_0^t \underline{R}(t-\tau)\frac{d\underline{q}}{d\tau} + \underline{K}\,\underline{q} = \underline{f} \tag{90}$$

where

$$\underline{R}(t) = \sum_{i=1}^{15} \underline{R}_i \, g_i(t) \tag{91}$$

The corresponding eigenproblem is

$$\left(p^2 \underline{M} + p \, \underline{R}(p) + \underline{K}\right)\underline{u} = \underline{0} \tag{92}$$

The eigenvalues using the Jacobi root perturbation method are calculated for the following geometrical and material parameters

$a' = 0.254 \text{ m}$ (10")   axial length

$b' = 0.239 \text{ m}$ (9.4")   circumferential length

$R = 0.154 \text{ m}$ (6")   radius

$h = 5.08 \times 10^{-4} \text{ m}$ (0.02")   laminate thickness

$\rho = 1605 \text{ kg/m}^3$ (0.058 lbs/in^3) laminae density $\tag{93}$

for a balanced symmetric $(+\theta, -\theta)_s$ laminate with one edge (edge with nodes 1 and 4 in Fig. 3 (b)) fixed. The parameters chosen for the decay distribution functions $\gamma(\theta)$, shown in Table 1, are

Distribution	α	β
Uniform	1.0	10^8
Cauchy	1.2	$\theta_0 = 0$
Normal	$\mu = 8$	$\sigma = 0.1$
Beta	4.2	3.6
Gamma	0.2	3.5
Exponential	0.01	-
Weibull	0.01	1.4
Maxwell	3.0	-

Smith [11] has determined $C_{ij}^{(s)}$ and C_{ij} for several relaxation constants ρ for an othotropic graphite reinforced epoxy. These coefficients are tabulated in Table 2. From these data, the functional relationship $C_{ij}^{(*)}(\theta)$ can be obtained by performing a least squares fit to log $C_{ij}^{(s)}$ and log ρ_s for $\rho_s = 25$, 250, 2500, 2.5×10^4 and 2.5×10^5 seconds. This gives

	C_{11}	C_{22}	C_{12}	C_{66}	Pa. (Psi)
y intercept, b	7.26416 (3.42567)	7.93455 (3.78942)	6.91463 (3.07607)	7.54510 (3.70658)	
slope, m	0.082126 (0.082136)	0.086329 (0.086329)	0.104194 (0.104212)	0.071959 (0.071964)	
correlation coefficient	0.8556	0.8143	0.5907	0.9377	

$$C_{ij} = 10^b \, \rho^m , \quad \theta = 1/\rho$$

The variation in the norm of real part of the eigenvalues,

$$||\underline{\sigma}|| = (2 \sum_{i=1}^{12} \sigma_i^2)^{1/2} \tag{94}$$

as a function of the fiber angle θ is shown in Figure 5. All distributions except the uniform distribution exhibit the same functional relationship and vary over three cycles of the logrithmic scale. A plot $||\underline{\sigma}||$ vs. fibre angle would be useful to a designer as one could incorporate the optimal damping characteristic in a structure. Of course, a more general optimization would involve maximizing $||\underline{\sigma}||$ over as many fiber angles $\theta_1, \theta_2, \ldots, \theta_N$ as the number of plies in a laminate.

7   Conclusion

We have demonstrated explicitly an algorithm for constructing a material damping matrix using the finite element method. The assumptions made in the formulation of the damping matrix are: (1) the material behaves viscoelastically and (2) the stress-strain and strain-displacement relations are linear. The damping matrix is constructed in a manner analogous to the stiffness matrix, thus an existing computer code, which analyzes an elastic structure, can be easily modified to analyze a corresponding viscoelastic structure. The motion equations are no longer differential, but rather integro-differential in form, as depicted in the flowchart, Fig. 6.

The corresponding eigenproblem is solved by Jacobi's root perturbation technique. This method is demonstrated by calculating the eigenvalues of a constrained, four-ply, balanced, symmetric laminate.

REFERENCES

[1]   Zienkiewicz, O.C., The Finite Element Method, 3rd Edition, McGraw-Hill, 1977.

[2]   Hanagud, S., Meyyappa, M., Cheng, Y.P., and Craig, J.I., "Identification of Structural Dynamic Systems with Nonproportional Damping", AIAA/ASME/ASCE/AHS 25th Structures, Structural Dynamics and Materials Conference Proceedings, May 1984, Part 2, Paper No. 84-0993, pp. 283-291.

[3]   Caravani, P., Watson, M.L., and Thompson, W.T., "Recursive Least-Squares Time Domain Identification of Structural Parameters", Journal of Applied Mechanics, Vol. 44, No. 1, March 1977, pp. 135-140.

[4]   Caravani P., and Thompson, W.T., "Identification of Damping Coefficients in Multidimensional Linear Systems", Journal of Applied Mechanics, Vol. 41, No. 2, June 1974, pp. 379-382.

[5]   Ibrahim, S.R., "Dynamic Modeling of Structures from Measured Complex Modes", AIAA Paper No. 82-0770.

[6]   Buhariwala K.J., "Dynamics of Viscoelastic Structures", Thesis for the degree of Doctor of Philosophy, University of Toronto, Department of Aerospace Science, 1984.

[7]   Ashton, J.E., Halpin, J.C., Petit, P.H., Primer on Composite Materials: Analysis, Technomic publication, 1969, p. 19.

[8]   Langhaar, H.L., Energy Methods in Applied Mechanics, John Wiley and Sons, Inc., 1962.

[9]   Ashton, J.E. and Whitney, J.M., Theory of Laminated Plates; Progress in materials Science Series ... Vol. IV, Technomic publishing Co., Inc., 1970.

[10]   Aubrun, J. N., "Theory of the Control of Structures by Low Authority Controllers", AIAA Conference on Large Space Platforms: Future Needs and Capabilities, Sept. 1978.

[11]   Smith, B. A. W., "Polymer Matrix Composite Materials in Simulated Space Environment: Ultraviolet and Vacuum Effects", Thesis for the degree of Master of Applied Science, Institute for Aerospace Studies, University of Toronto, 1981.
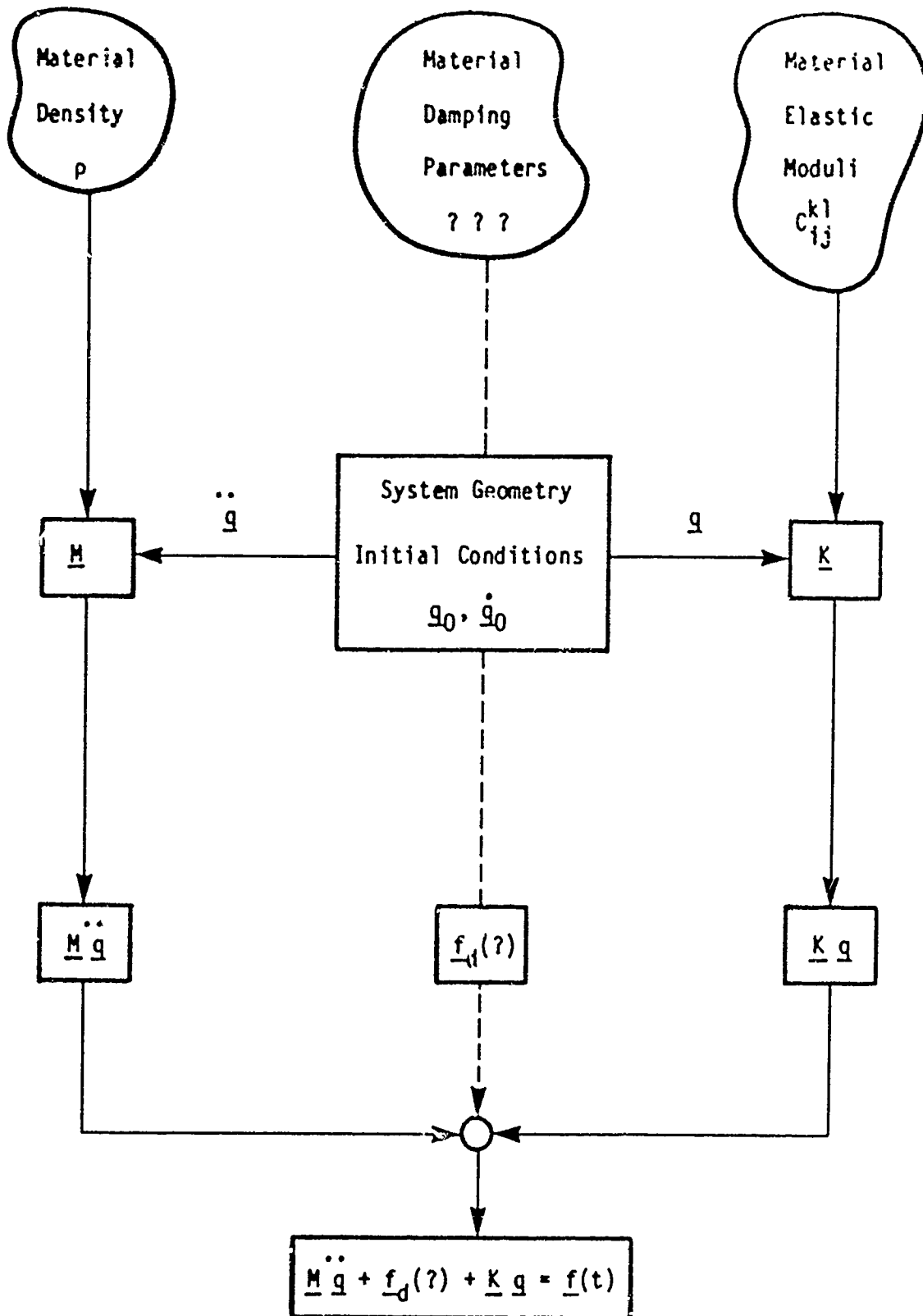
Fig. 1 Flow Chart for a Dynamical Model
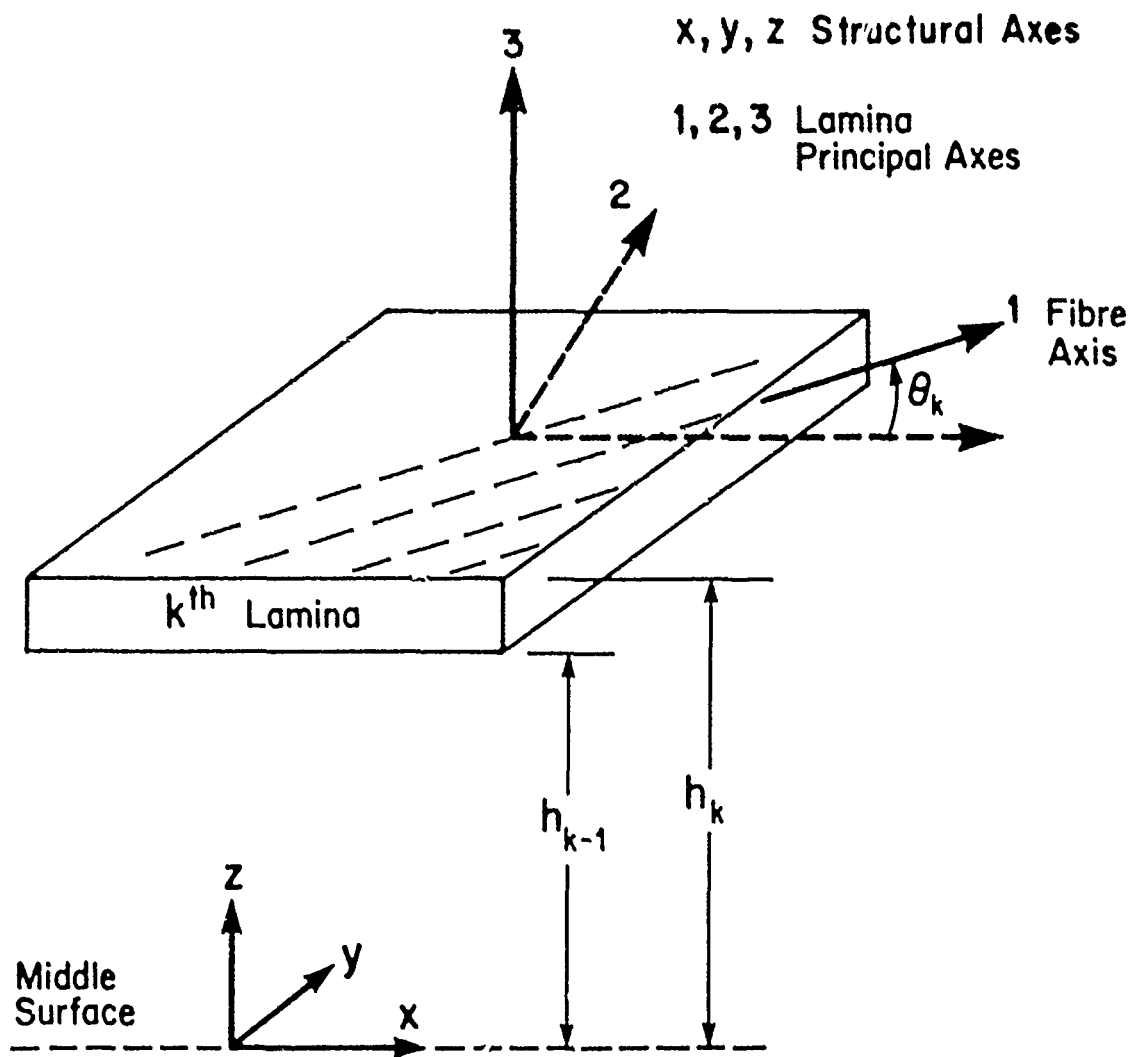
Fig. 2 k^{th} Lamina Relative to the Structural Axes
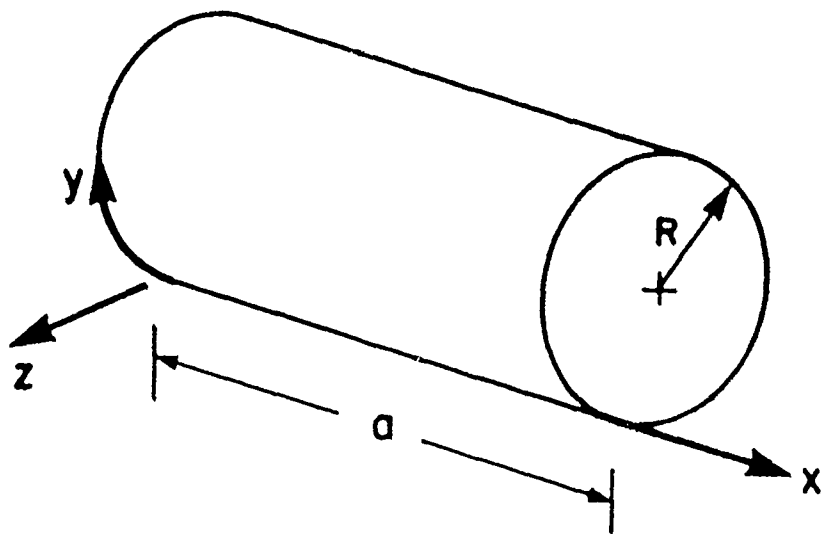
(a)
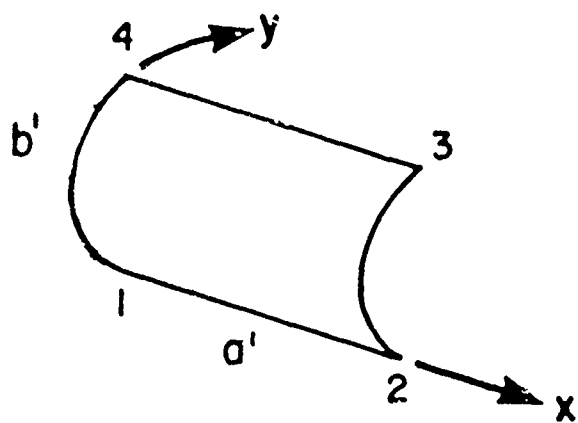
(b)

Fig. 3 Graphite Reinforced Epoxy Cylindrical Shell and
Cantilevered Shell Element

GE-28
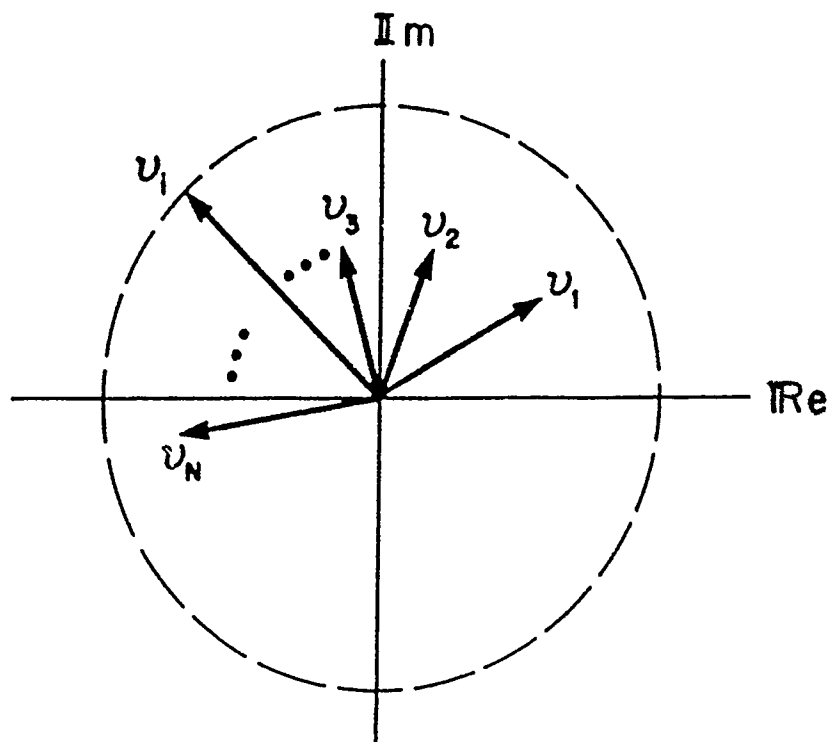
Fig. 4 a Components of the jth Viscoelastic Eigenmode
in the Argand Plane.
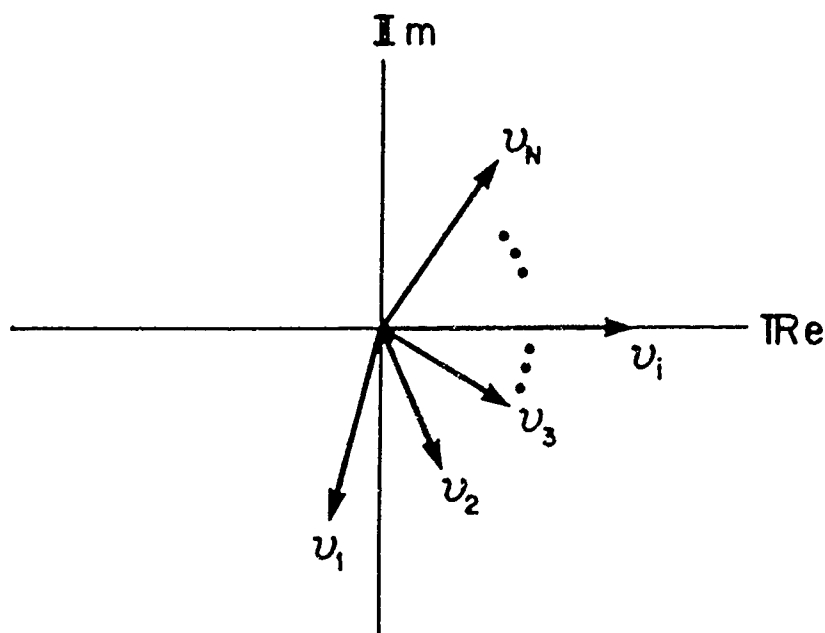
Fig. 4 b Component with the Largest Norm Aligned with
the Positive Real Axle.

Fig. 5 PLOT OF THE NORM OF THE REAL PART OF THE EIGENVALUES VS. FIBRE ANGLE FOR VARIOUS DISTRIBUTIONS

□ - UNIFORM
⊘ - CAUCHY
▲ - NORMAL
+ - BETA
× - GAMMA
◆ - EXPONENTIAL
✦ - WEIBULL
※ - MAXWELL

FIBRE ANGLE IN DEGREES

GE-30
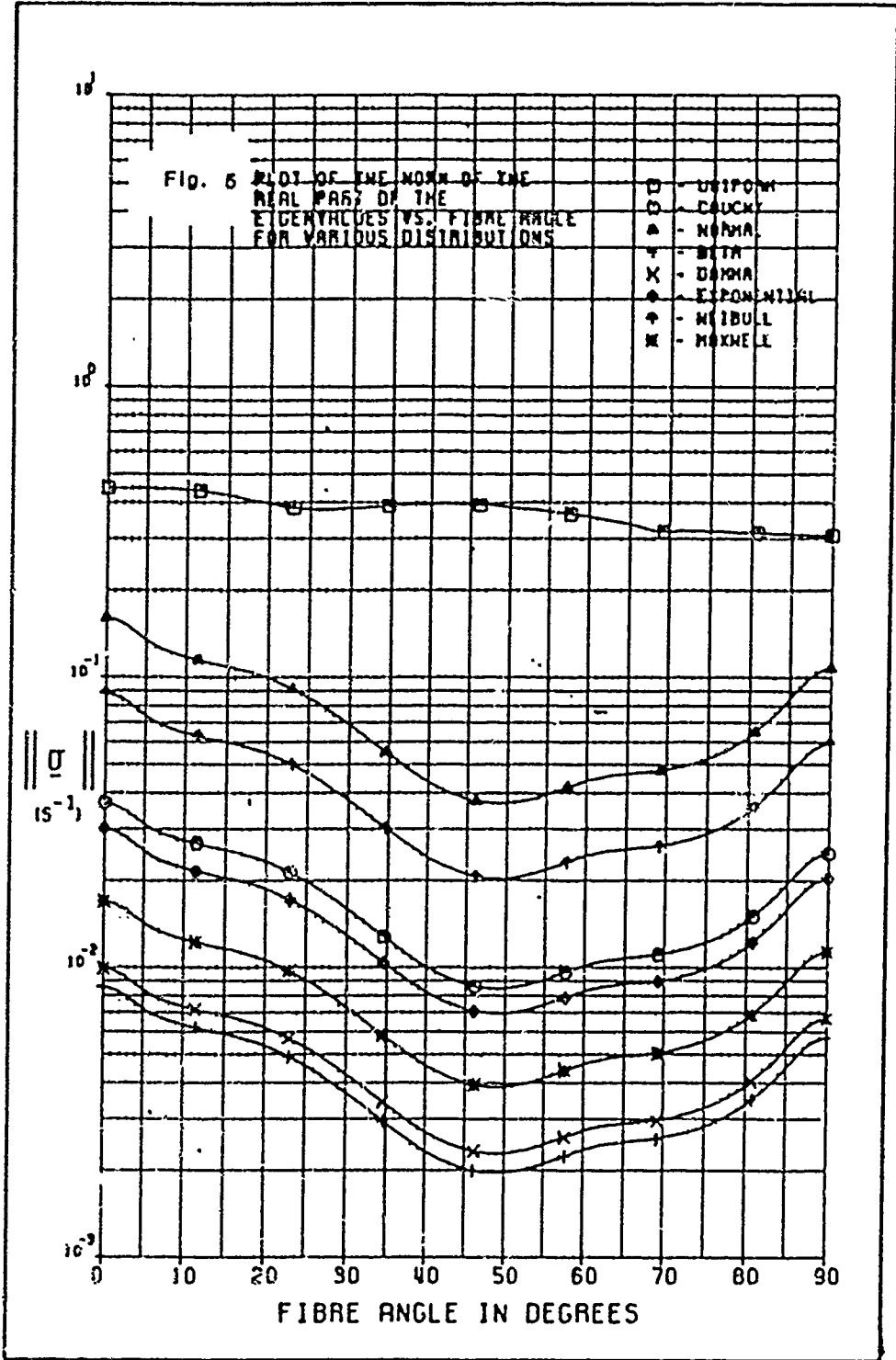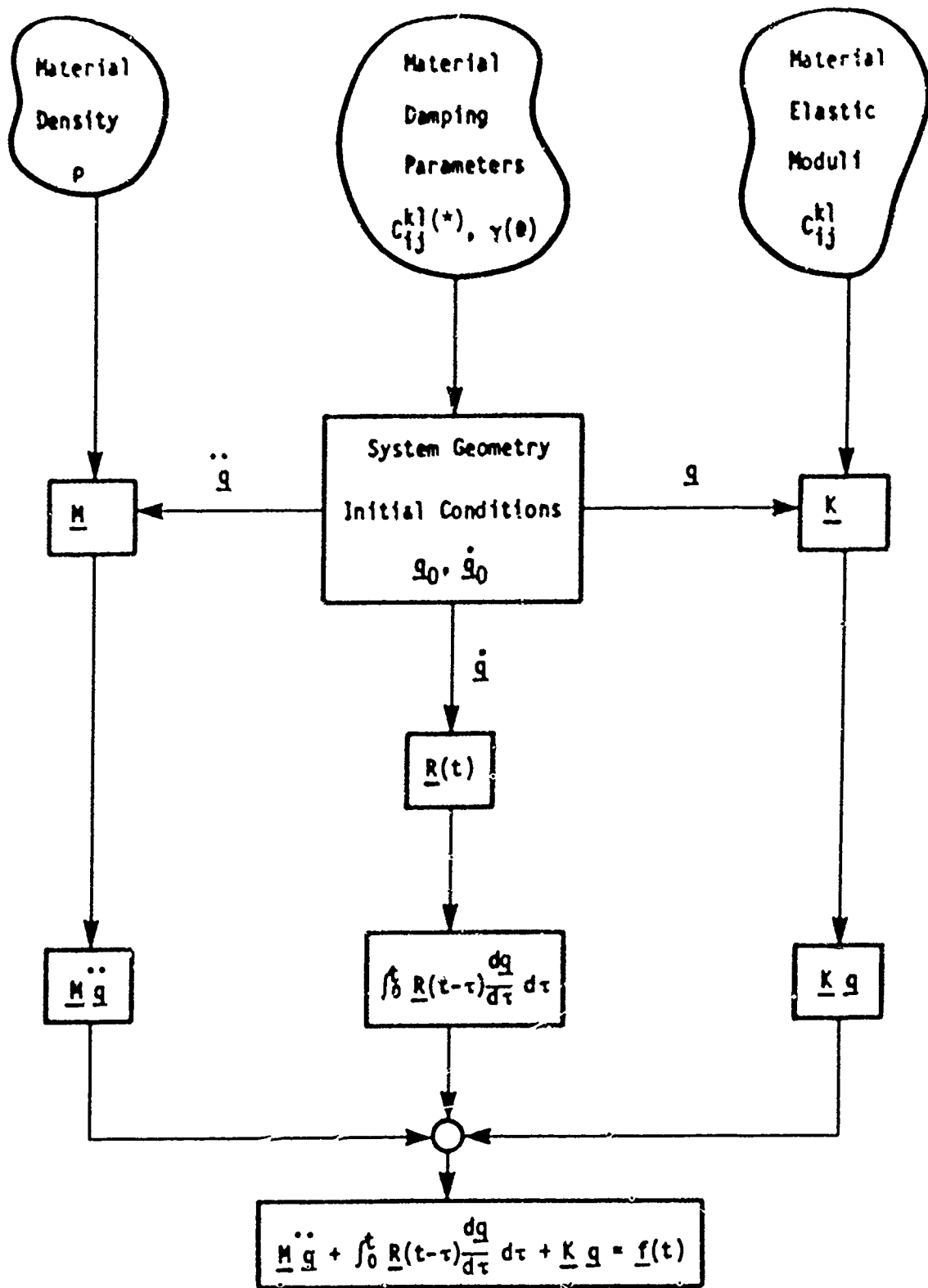
Fig. 6 Flow Chart for a Dynamical Viscoelastic Model

(Compare with Fig. 1)

Table 1 Decay density distribution functions and their corresponding mean and variances.

Distribution	Decay Density Distribution Function	Mean	Variance
Uniform	$\gamma(\theta) = \begin{cases} \dfrac{1}{\beta - \alpha} & \alpha < \theta < \beta \\ 0 & \text{otherwise} \end{cases}$	$\mu = \frac{1}{2}(\alpha + \beta)$	$\sigma^2 = \frac{1}{12}(\beta - \alpha)^2$
Cauchy	$\gamma(\theta) = \dfrac{\alpha}{\pi[(\theta - \theta_0)^2 + \alpha^2]} \quad \alpha > 0, \ -\infty < \theta < \infty$	The mean, variance, and higher moments do not exist	
Normal	$\gamma(\theta) = \dfrac{1}{\sigma\sqrt{2\pi}} e^{-(\theta - \mu)^2/2\sigma^2} \quad -\infty < \theta < \infty$	μ	σ^2
Beta	$\gamma(\theta) = \begin{cases} \dfrac{\theta^{\alpha-1}(1-\theta)^{\beta-1}}{B(\alpha,\beta)} + \theta_0, & 0 < \theta < 1 \ (\alpha,\beta > 0) \\ 0 & \text{otherwise} \end{cases}$ $B(m,n) = \int_0^1 u^{m-1}(1-u)^{n-1} du \quad m,n > 0$	$\mu = \dfrac{\alpha}{\alpha + \beta} + \theta_0$	$\sigma^2 = \dfrac{\alpha\beta}{(\alpha+\beta)^2(\alpha+\beta+1)}$
Gamma	$\gamma(\theta) = \begin{cases} \dfrac{\theta^{\alpha-1} e^{-\theta/\beta}}{\beta^\alpha \Gamma(\alpha)} & \theta > 0 \\ 0 & \theta < 0 \end{cases}$ $\Gamma(n) = \int_0^\infty t^{n-1} e^{-t}\, dt \quad n > 0$	$\mu = \alpha\beta$	$\sigma^2 = \alpha\beta^2$
Exponential	$\gamma(\theta) = \begin{cases} \alpha e^{-\alpha\theta} & \theta > 0 \\ 0 & \text{otherwise} \end{cases}$	$\mu = \dfrac{1}{\alpha}$	$\sigma^2 = \dfrac{1}{\alpha^2}$
Weibull	$\gamma(\theta) = \begin{cases} \alpha\beta\theta^{\beta-1} e^{-\alpha\theta^\beta} & \theta > 0 \\ 0 & \theta < 0 \end{cases}$	$\mu = \alpha^{-1/\beta}\Gamma\left(1 + \frac{1}{\beta}\right)$	$\sigma^2 = \alpha^{-2/\beta}[\Gamma(1 + 2\delta) - \Gamma^2(1 + \delta)] \ ; \ \delta = 1/\beta$
Maxwell	$\gamma(\theta) = \begin{cases} \sqrt{\dfrac{2}{\pi}}\, \alpha^{3/2}\theta^2 e^{-\alpha\theta^2/2} & \theta > 0 \\ 0 & \theta < 0 \end{cases}$	$\mu = 2\left(\dfrac{2}{\pi\alpha}\right)^{1/2}$	$\sigma^2 = \dfrac{1}{\alpha}\left(3 - \dfrac{8}{\pi}\right)$

$\times 10^7$ Pa.
(Psi.)

ρ_S (s)

	2.5	25.0	250	2500	2.5×10^4	2.5×10^5	2.5×10^6
$c_{11}^{(s)}$	1.691 (2452.3)	2.933 (4254.3)	2.284 (3312.3)	3.094 (4488.1)	4.837 (7014.9)	5.188 (7524.5)	6.641 (9631.7)
$c_{22}^{(s)}$	3.398 (4929.1)	7.032 (10199.0)	5.326 (7725.0)	6.893 (9997.8)	12.738 (18475)	12.285 (17818)	17.403 (25241)
$c_{12}^{(s)}$	-0.295 (-429.7)	1.875 (2719.1)	0.8391 (1217)	1.200 (1740.8)	4.198 (6089.4)	2.782 (4034.5)	5.504 (7982.4)
$c_{66}^{(s)}$	5.036 (7340.2)	4.776 (6926.7)	4.847 (7030.2)	6.283 (9113.5)	6.419 (9310.4)	9.503 (13783)	9.372 (13593)

C_{11} 1.161×10^{11} (1.684×10^7)

C_{22} 7.943×10^9 (1.152×10^6)

C_{12} 2.432×10^9 (3.528×10^5)

C_{66} 3.192×10^9 (4.629×10^5)

Table 2   Viscoelastic coefficients for orthotropic GRE (Reference [11])

GE-33

APPENDIX

Matrix $\underline{H}$ as defined in (47)

$\underline{H}$

DAMPING IDENTIFICATION FROM NONLINEAR
RANDOM RESPONSES USING A MULTI-TRIGGERING
RANDOM DECREMENT TECHNIQUE

Samir R. Ibrahim
Professor of Mechanical Engineering and Mechanics
Old Dominion University
Norfolk, Virginia 35od

K. R. Wentz   and   J. Lee
Flight Dynamics Laboratory
Air Force Wright Aeronautical Laboraties
Dayton, Ohio 45433

ABSTRACT

The concept of multi-triggering random decrement technique is introduced.
Like the single triggering technique, it reduces multi-mode multi-measurement
stationary random responses to free decay responses but has the advantage of
increasing the apparent number of the resulting free decay time response
functions. The maximum number of these free decay responses is equal to the
square of the number of random measurements. These free decay responses are
then used in a linear time domain modal identification algorithm to extract
frequencies, damping factors and mode shapes of a structure under test. The
quasi linear modal approach is used to deal with nonlinearities by repeating
the linear identification process at different levels of inputs/responses.
The procedure is applied to rectangular panels subjected to acoustic random
input ranging from 130 to 157 db. The changes in frequencies and damping
factors with input level are reported. This application is part of a sonic
fatigue research program.

INTRODUCTION

Modal identification of structures, to experimentally determine natural frequencies, mode shapes and damping factors, is critical to the accurate mathematical modeling of structures. These extracted modal parameters, besides being directly related to the structure's physical parameters, are very useful in applications such as response and loads predictions, trouble shooting excessive vibrations, stability and control, verification and or modification of analytical dynamic models, structural integrity monitoring and incipient failure detection, fatigue design, among others.

While undamped natural frequencies and normal mode shapes can be approximately estimated from analytical models, damping characteristics of structures are determined mainly from experimentation. Even with the tremendous advances in the state-of-the art of modal identification in both frequency and time domains, the accuracy of damping identificatin, unlike frequencies and mode shapes, is an area of active current research efforts. Damping identification accuracy becomes more critical in applications such as incipient failure detection and structural integrity monitoring, flutter margin predictions and fatigue design.

To further complicate the problem of damping measurements, nonlinearities can cause unacceptable scatter of "error" bounds. Actually, the damping level may drastically vary with input and or response levels; a situation where the concept of a unique modal damping value can be erroneous and misleading.

Another application where damping, as well as modal, identification becomes more difficult is when a structure has to be tested under normal operating conditions wih unmeasureable or unknown random inputs.

The two main issues in this study to identify damping are:

1. The structure under consideration is highly nonlinear,

2. The input to the structure is unmeasureable or unknown stationary random force(s).

The approach under consideration is to deal with nonlinearities by using a quasi linear identification technique and with unmeasureable random input(s) by using the random decrement method. A linear time domain modal identification technique, which implements the free decay responses of the structure under test, is used for the identification process which is performed different levels of input to study the variation of modal parameters with the input level. The free decay time response functions are obtained from the random responses by using the random decrement technique[2-4].

The concept of multi-triggering in random decrement computation is introduced in this paper and shown to be advantageous for improving identification accuracy when the number of measurements on the structure is limited.

The entire approach is applied to strain and acceleration measurements of a rectangular panel subjected to acoustical input of varying level.

BACKGROUND

1. Time Domain Modal Identification

The linear time domain modal identification technique[1] used in this study uses the free decay responses of a structure and convert the indentification procedure to solving the eigenvalue problem

$$[A] \{\psi\} = \alpha \{\psi\} \qquad (1)$$

where the matrix of eigenvalues and eigenvectors, [A], is computed from the measured free decay time response functions of the structure. The eigenvalues α are directly related to the characteristic roots of the system from which frequencies and damping factors are determined. The eigenvectors ψ relate, or directly are, to the mode shapes at the measured coordinates.

2. Random Decrement Technique

The concept of random decrement technique was initially presented by Henry Cole[2]. The presentation or proof of the theoretical basis was rather imperical and intuitive but nevertheless, acceptable. The technique, when first presented, was designed to obtain a single mode signature of one single measurement.

Because of its simplicity and effectiveness, randomdec has subsequently gained a widespread use by the aerospace industry. Randomdec was later generalized to multi-measurements multi-mode responses[3], not to generate signature but rather to produce free decay response time functions that can be used in time domain modal identification of structures.

An excellent paper on randomdec is written by Professor J. K. Vandiver et al[4]. The paper offers a more rigorous proof on the theory of randomdec, analyzes errors and residuals and compares differnt methods of triggering ensembles.

Since the introduction of the concept of random decrement technique, efforts have been directed to investigate the theoretical grounds for accuracy and convergence and any inherent assumptions, conditions, or limitations. One main assumption in these theoretical proofs was that the random input forces(s) must be white noise.

The assumption of white noise input(s) is very convenient for theoretical proofs. The fact is, such white noise rarely exists in real life applications.

The strict condition of having white noise, or flat power spectrum

density, is not necssary, at least for the purpose of modal identification of structures. The only condition on the input random forces(s) is that it is of zero mean, stationary random[5].

Considering a multi-degree-of-freedom linear system with $[M]$, $[K]$, and $[C]$ as mass, stiffness and damping matrices and $\{y\}$ as the response vector to a random force input vector $\{f\}$, such a system is governed by the equation:

$$[M] \{\ddot{y}(t)\} + [C] \{\dot{y}(t) + K\{y(t)\} = \{f(t)\} . \qquad (2)$$

The above equation is valid for any time t and any set of initial conditions. Replacing time t with the expression $t_i + \tau$ where t_i's are selected according to the method of triggering the start of ensembles for the randomdec computations, then equation (1) can be written as

$$[M] \{\ddot{y}(t_i + \tau)\} + [C] \dot{y}(t_i + \tau) + [K] \{y(t_i + \tau)$$

$$= \{f(t_i + \tau)\} \; (i = 1,2\text{---}N) \qquad (3)$$

where N is the number of averages intended for use in randomdec computation. By summing all of the N equations, dividing by N and replacing $1/N \; \Sigma\{y (t_i + \tau)\}$ by $\{x(\tau)\}$, the resulting summation can be written as:

$$[M] \{\ddot{x}(\tau)\} + [C] \{\dot{x}(\tau)\} + [K] \{x(\tau)\} = \frac{1}{N} \sum_{i=1}^{N} \{f(t_i + \tau)\} \qquad (4)$$

Noting the since t_i's were selected according to a specific randomdec triggering ceriterion, the resulting response $\{x(\tau)\}$ will not average to zero. Now considering the right hand side of equation (4), if $\{f\}$ is a stationary random signal, then

$$\frac{1}{N} \sum_{i=1}^{N} \{f(t_i + \tau)\} = 0$$

and equation (4) will be:

$$[M] \{\ddot{x}(\tau)\} + [C] \{\dot{x}(\tau)\} + [K] \{x(\tau)\} = 0 \qquad (5)$$

Equation (4) implies that $\{x(\tau)\}$ is a free-decay response that resulted from applying randomdec to random responses due to a force input vector, $\{f\}$, where $\{f\}$ assumed to be only some stationary random signals with zero mean.

GF-4

Thus if $\{y(t)\}$ are the p measured random responses due to a stationary random input(s), then $\{x(\tau)\}$ are the randomdec, or free decay, time response functions where:

$$x_j(\tau) = \frac{1}{N} \sum_{k=1}^{N} y_j (t_k + \tau), \quad j = 1,2,\ldots p \quad\quad (6)$$

In equation (6) the times, t_j are determined according to an arbitary measurment, a leading station, $y_\ell(t)$ satisfying a selected triggering criteria; $t = t_j$ when $y_\ell(t)$ satisfies one of the following:

a) Constant level,
b) Zero crossings and positive slopes,
c) Zero crossings and negative slopes,
d) Positive
e) Negative

MULTI TRIGGERING RANDOM DECREMENT

The leading, triggering, measurement of equation (6) is totally arbitrary as long as all measurements are simultaneously recorded. For that reason y_ℓ can be anyone or everyone of the measurements. In such a case equation (6) becomes:

$$x_{j,\ell}(\tau) = \frac{1}{N} \sum_{k=1}^{N} y_j(t_k + \tau) \quad\quad (7)$$

$$j = 1,2,\ldots p \quad \text{and} \quad \ell = 1,2,\ldots p.$$

where t_k is determined when measurement $\ell, \ell = 1,2,\ldots p$, satisfies the specified triggering criterion.

It is obvious that equation (6) yields p free decay time response functions as compared to p^2 for equation (7). Considering that the size of identification model of equation (1) is usually larger than the number of measurements and or the number of modes in the responses, obtaining more randomdec functions becomes readily advantageous. It increases the apparent nunmber of measurements thus reduces the need to use more pseudo measurements (time delayed measurements). The delayed measurements, since they are free decay responses, contain higher noise to signal ratio than the original measurements.

This multi-triggering random decrement approach becomes increasingly effective when the number of measurements is limited especially with higher modal density and or higher noise levels. The approach has the advantages of:

1. Increasing the apparent number of measurements which is likely to

improve the identification accuracy.

2. When automated decreasing the effect of selecting one bad measurement as the leading measurement.

EXPERIMENTS AND RESULTS

The test structure in this series of experiments is a rectangular aluminum plate with dimensions of 25.4 x 50.8 x 0.16 cm. The panel is tested with all of its four edges clamped to the wall of the wideband noise test facility of the Sonic Fatigue Group at the Air Force Wright Aeronautical Laboratories. A sketch of the panel with instrumentation is shown in Figure 1. The panel in test configuration is shown in Figure 2 while Figure 3 shows the horse system for air modulation. The input level was changed from 130 to 160 db in steps of 3 db. Figure 4 shows a typical input spectrum.

For this study only five sensors were used. These are strain gages 1, 2, 3 and 8 and accelerometer 4. Four levels of input were used with rms of 130, 139, 148 and 157 db. Three seconds of random data were sampled at 4000 Hz. The accelerometer fell off at 154 db input, thus only the four strain gage responses were used for the 157 db input level. Typical output spectrums for the four different levels are shown in Figures 5, a, b, c and d. These spectrums indicate the nonlinearity as well as the difficulties associated with any attempts to measure modal damping especially at higher levels of input.

To prepare the random responses for use in the time domain identification algorithm, the multi-triggering randomdec technique was used to convert them to free decay response time functions. By using five random responses, twenty five free decay time functions were computed (16 for the 157 db input, no accelerometer). The record length of the randomdec functions was selected to be 0.25 sec (1000 samples) and the number of averages was limited to 500 using all positive points triggering. Thus the actual random record length used is about 2000 samples (0.5 sec.).

Figures 6, a, b, c and d show the random and randomdec functions (1000 samples each) for the five measurements.

The resulting free decay responses were used in the time domain identification with model sizes of 25, 25, 35 and 50 modes for the four levels of inputs. Higher number of modes for higher input levels were needed in order to deal with increasing nonlinearities.

Identification results indicated high modal densities of the system. Several of the identified modes were those of the acoustic chamber and suspension wall.

To correlate same identified modes at different levels to each other, neither frequencies nor damping factors can be used since they vary with input levels. For this purpose each mode shape at one input level was correlated to all mode shapes at each different input level. High correlation was used to

GF-6

indicate the same mode at different input levels.

Figure 7 shows the changes in the frequencies and damping factors of two modes denoted as modes m and n. Since the purpose of this paper is to only suggest a procedure, and not to study mechanisms of nonlinearities, the authors at this stage have no comments on the patterns of frequencies and damping changes with input level.

CONCLUDING REMARKS

The concept of multi-triggering in random decrement computation is introduced. By increasing the apparent number of free decay response measurements, up to the square of the number of random measurements used, this approach is likely to increase the modal identification accruacy of time domain techniques.

The use of a linear identification technique to identify, in a quasi linear sense, nonlinear system is shown to successfully work with highly nonlinear structures as indicated by the reported experiment of a panel subjected to a random acoustic excitation with varying level.

ACKNOWLEDGEMENT

REFERENCES

1. Ibrahim, S. R., "Time Domain Quasi Linear Identification of Nonlinear Dynamic Systemss," AIAA Journal, Vol. 22, No. 6, June 1984, pp. 817-823.

2. Cole, H. A., Jr., "On-Line Failure Detection and Damping Measurement of Aerospace Structures by Random Decrement Signature," NASA CR 2205, March 1973.

3. Ibrahim, S. R., "Random Decrement Technique for Modal Identification of Structures," Journal of Spacecraft and Rockets (AIAA), Vol. 14, No. 11, November 1977, pp. 696-700.

4. Vandiver, J. K., Dunwoody, A. B. and Campbell, R. B., "A Mathematical Basis or the Random Decrement Signature Analysis Technique," Journal of Mechanical Design, Vol. 104, April 1982, pp. 307-313.

5. Ibrahim, S. R., "Incipient Failure Detection From Random Decrement Time Functions," ASME Book NO. G00255, Random Vibrations - AMD - Vol. 65, December 1984, p. 69-81.
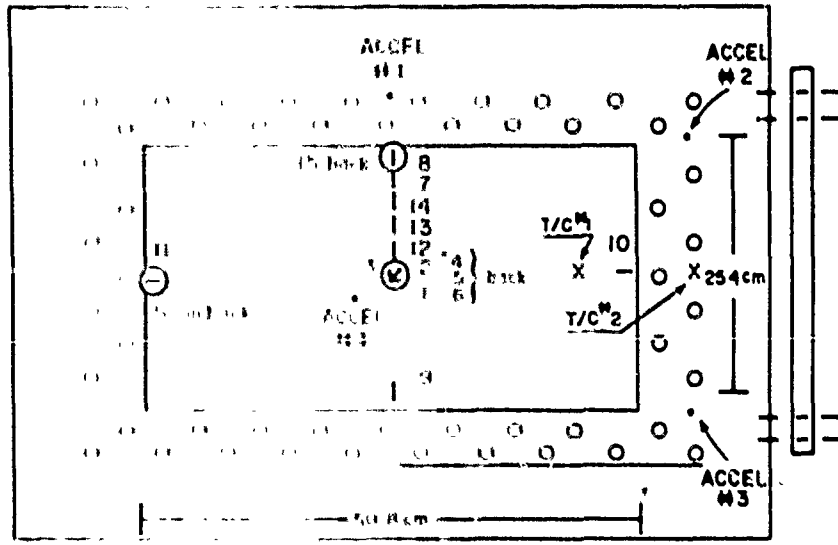
Figure 1 Schematics Sketch of Panel with Instrumentation.

Figure 2   Panel in Test Configuration.

Figure 3   Air Modulation System.
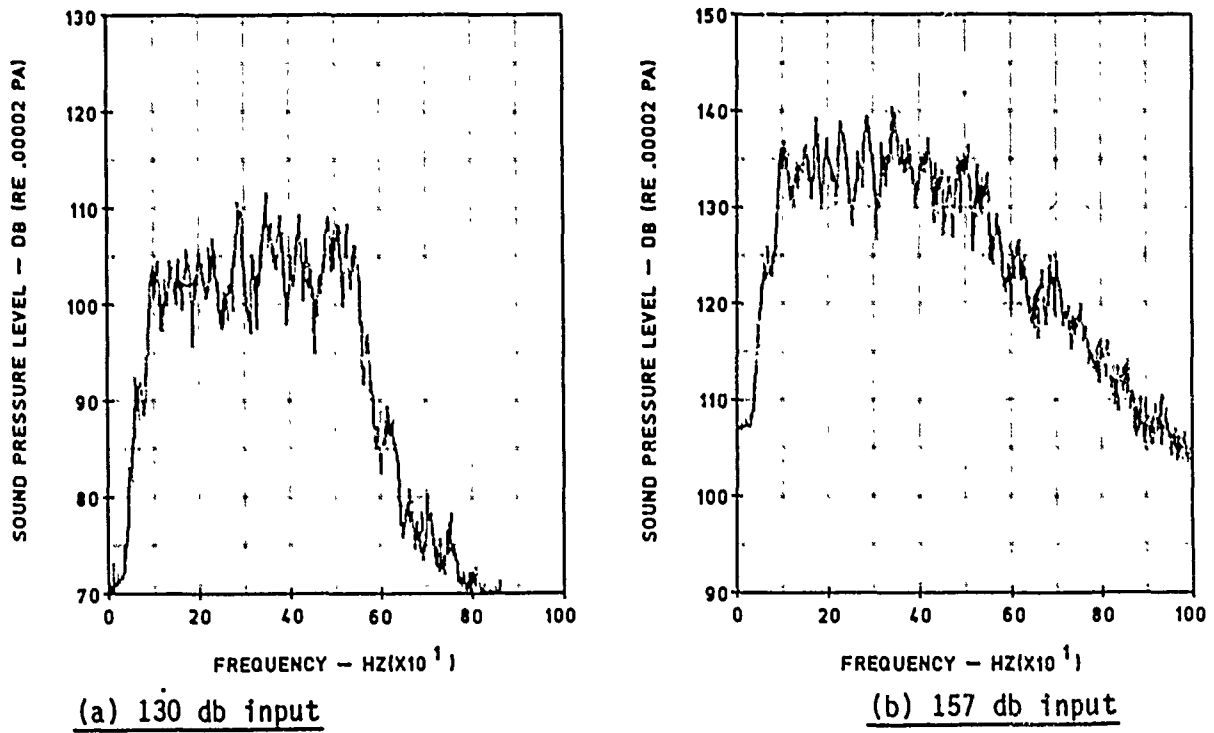
(a) 130 db input

(b) 157 db input

Figure 4   Input Sepctrums.
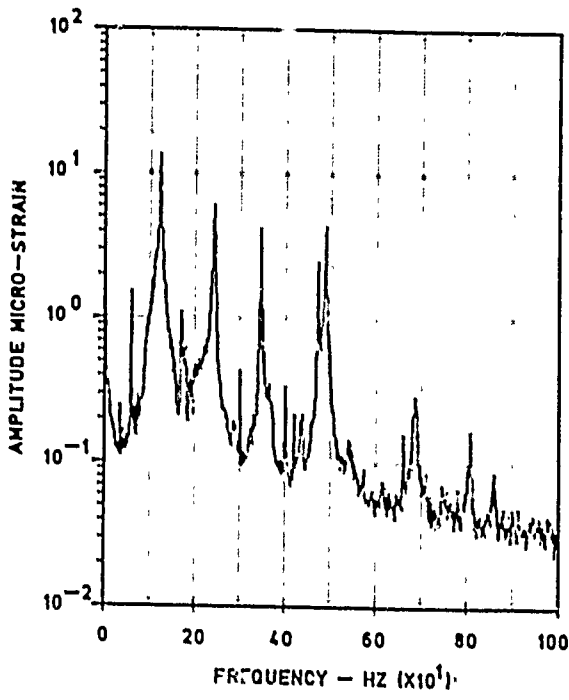
(a) 130 db input
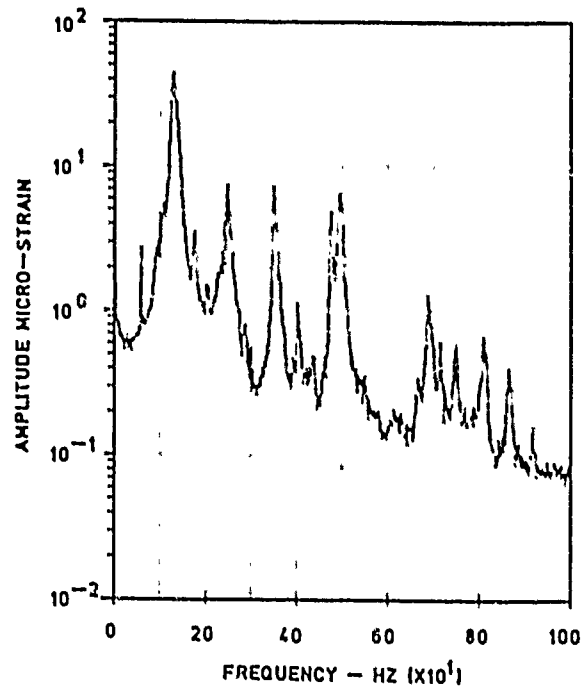
(b) 139 db input
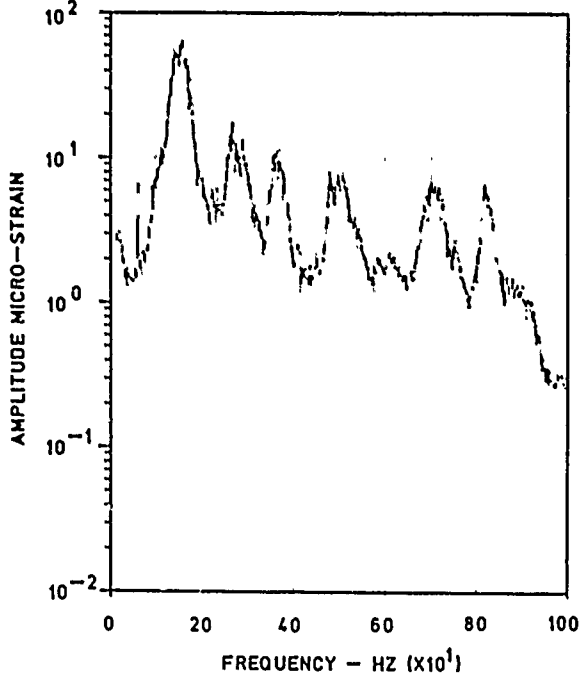
(c) 148 db input
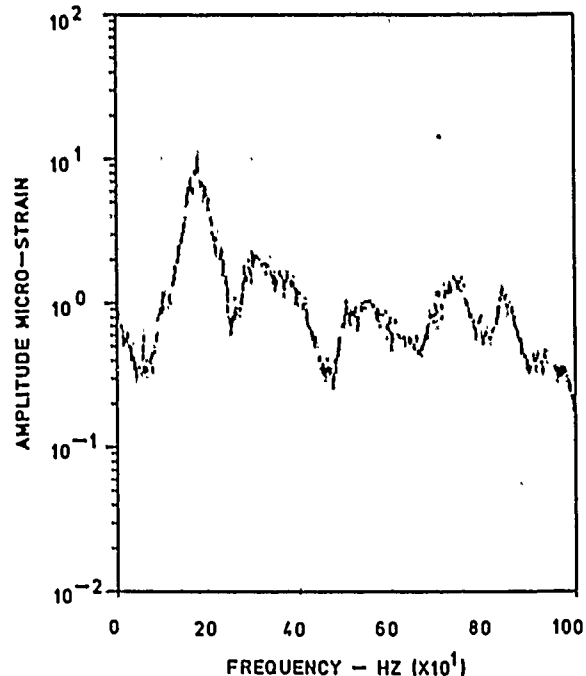
(d) 157 db input

Figure 5   Output Spectrums

GF-10
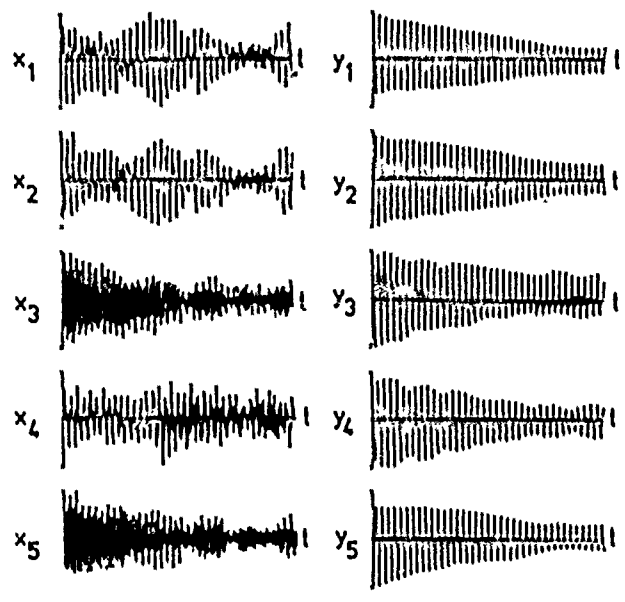
(6.a) 130 db input

(6.b) 139 db input

GF-11
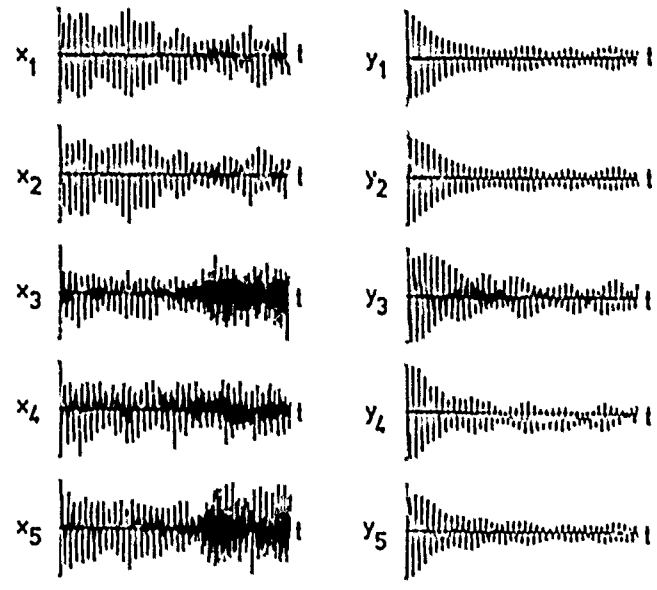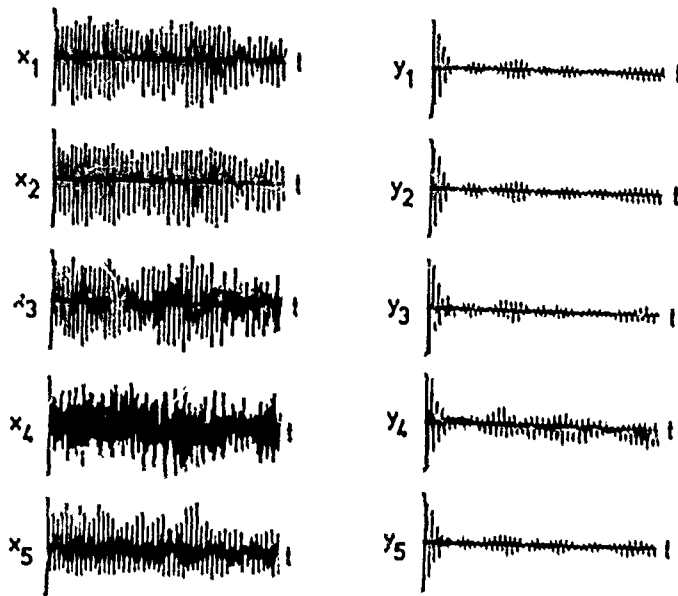
(6.c) 148 db input
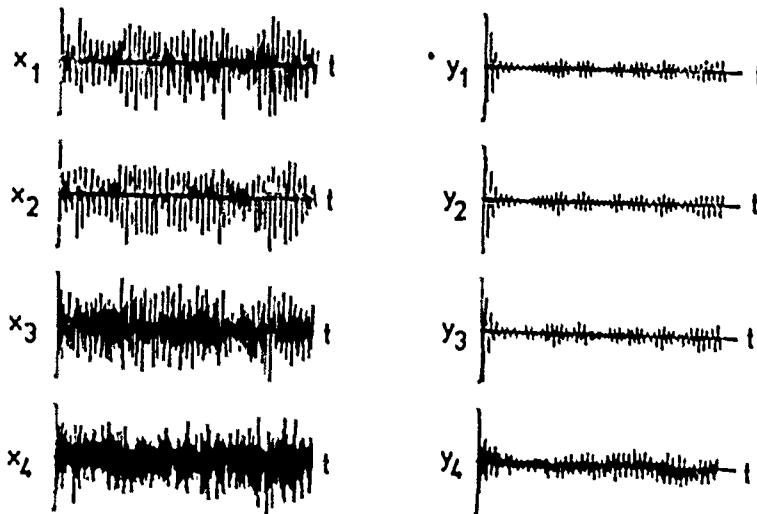
no x_5 (accelerometer gone)

(6.d) 157 db input

Figure 6 Random and Randomdec Time Response Functions.

GF-12
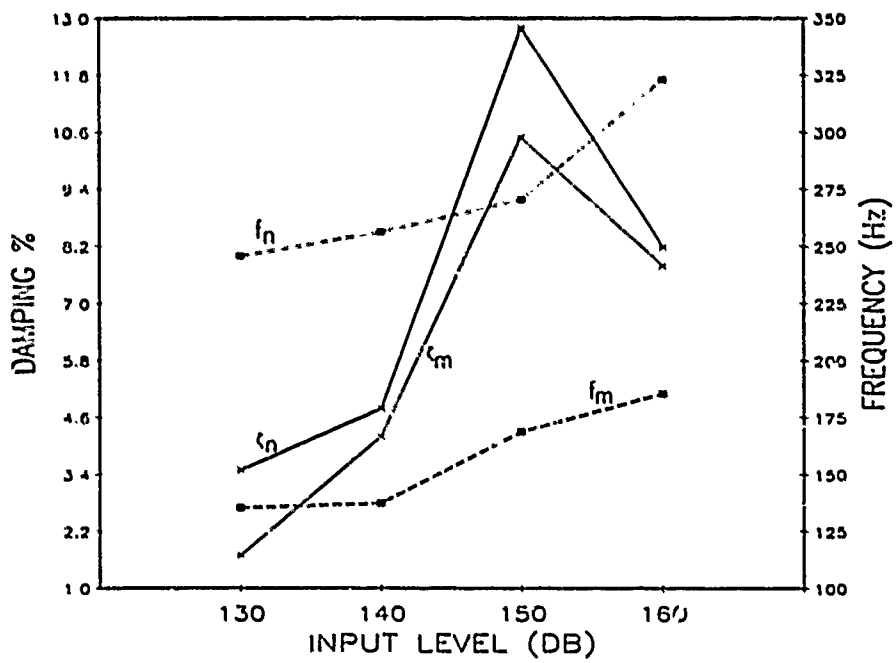
Figure 7   Changes in Identified Frequencies and Damping
Factors with Input Level.

DESIGN AND TESTING OF A SIXTY-FOOT DAMPED GENERIC SPACE TRUSS

Conor D. Johnson and David A. Kienholz

CSA Engineering, Inc.
560 San Antonio Road
Suite 101
Palo Alto, CA 94306

ABSTRACT

Two sixty-foot, viscoelastically damped generic space trusses have been de-
signed, fabricated, and tested for the PACOSS (Passive and Active Control of
Space Structures) Program. They are demonstration structures which use integral
viscoelastic damping for vibration control. Their purpose is to illustrate the
application of the technology to a type of structure important in space applica-
tions. The Modal Strain Energy method, implemented by finite elements, was used
to design the damping elements for the trusses. Damping due to the damping ele-
ments as well as hysteresis in the trusses' structural members was calculated by
the finite element model. A modal test of one of the trusses was conducted to
verify the model. Results of the analysis and test are compared and conclusions
are drawn relative to the design method and to the use of viscoelastic damping
for truss structures.

1.0 INTRODUCTION

Viscoelastic materials have been used to suppress vibration in many structures. However, most of these structures have been small and stiff in comparison to large space structures (LSS). LSS, by their very nature, will be highly flexible, have many low frequency modes, and have control systems that will couple strongly with the structure in the low frequency region. Suppression of structural vibration by use of passive damping will be a great aid in the design of stable control systems.

It is the purpose of this paper to demonstrate that existing technologies may be used to passively damp LSS's. The demonstration was performed on a less expensive, but convincingly similar structure. Trusses were chosen for the demonstration structures because of their natural suitability for large space structures. This type of structure could also be designed and built with the limited resources available. Before the large test structures were designed and built, a small damped truss was used to demons rate the damping concepts. This paper discusses the design analyses and test comparisons for both the full scale and small trusses.

2.0 MODAL STRAIN ENERGY METHOD

All of the damping analyses performed in the design of the structures used the Modal Strain Energy (MSE) method to estimate the structural damping for each configuration. This method was proposed by Rogers and implemented by Johnson and Kienholz[1] using finite element techniques. The method is based on approximating the complex eigenvectors by real eigenvectors calculated from purely elastic analysis (i.e. normal mode methods). The MSE method relates the structural damping to the strain energy distribution in the structure and to the material loss factors. This relationship has the form

$$\eta^{(r)} = \sum_i \eta_i (SE_i^{(r)}/SE^{(r)}) \tag{1}$$

where

η_i = Material loss factor for the i'th material

$SE_i^{(r)}$ = Strain energy in the i'th material when the structure deforms in its r'th mode

$SE^{(r)}$ = Total strain energy for the r'th mode

In a finite element formulation, the modal loss factor for the r'th mode is equal to the sum over all elements of the product of the material loss factor of each element and the fraction of strain energy in that element. A standard output option of many finite element codes is the percent strain energy in each element for each mode of interest.

Equation (1) leads to a simple approximate method for calculating structural loss factor for each mode using the undamped mode shapes and the material loss factor for each material. The approximation has been shown to be very good, even for very high material loss factors.[2] The basic advantages of the method are that only real normal modes and not complex modes need be calculated and that the energy distributions are of direct use to the designer. They serve to guide the choice of viscoelastic material as well as the most effective location for it.

3.0 THE DEMONSTRATION TRUSS

Prior to design and construction of the full scale trusses, a scaled truss was designed, built, and tested to demonstrate the feasibility of the damping concept and to verify the accuracy of the design method. The truss was constructed of one-quarter inch diameter Plexiglas rods, and was mounted in cantilever fashion to a fixed horizontal base. The truss was 49 inches high and the base was 4 inches square. The diagonal elements were arranged in a "K" pattern to obtain maximum flexibility and therefore obtain the lowest frequencies for the first modes.

Damping was incorporated into the truss in two ways; the truss was constructed of a material having a high loss factor (Plexiglas) and, more importantly, discrete, extensional damping elements were included in several diagonals. The discrete damper is designed to convert axial forces in the diagonal to shearing forces in a viscoelastic material. Figure 1 is a sketch of the discrete damper configuration used for this demonstration truss.
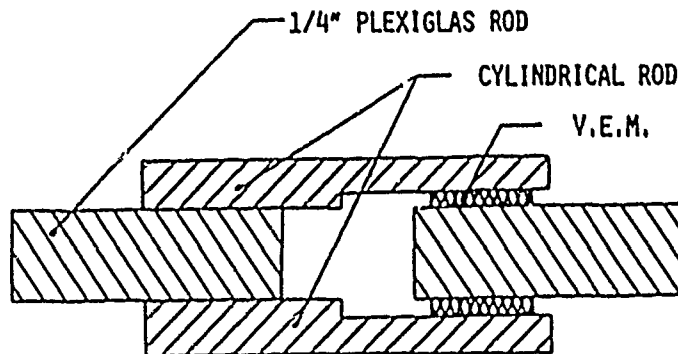
CYLINDRICAL SHEAR CONFIGURATION

Figure 1   Schematic of Discrete Dampers Used in the Demonstration Truss

HA-3

A truss was fabricated and tested with the discrete dampers in the bottom bay only. Table 1 shows the excellent agreement between predicted and measured results. The predictions include energy dissipation in the Plexiglas as well as the viscoelastic. To reduce the frequency of the first mode, an eight pound weight was added to the tip of the truss. Because of this large weight (the truss structure itself weighed only 1.8 lbs), large tip deflections occurred during the tests, possibly resulting in some non-linear behavior in the truss.

Table 1
Predicted and Measured Frequencies and Damping
for the First Mode of the Demonstration Truss

	No Additional Weight Added		8.0 Lb. Weight Added at Tip	
	Frequency (Hz)	Structural Damping	Frequency (Hz)	Structural Damping
Analysis	14.6	11.2 %	3.2	6.4 %
Experiment	15.5	11.5 %	3.1	4.9 %

4.0 DESIGN OF THE FULL SCALE GENERIC SPACE TRUSS

4.1 Modal Characteristics of the Undamped Truss

Initial goals for the full scale generic space truss were that the frequency of the first mode be in the range of 1.0 to 1.5 Hz, that the structure be fairly economical to build of readily obtainable materials, and that the truss should be capable of being deflected 6 inches at the tip with no member buckling. A number of truss designs were investigated in determining an overall size and configuration that would meet the requirements. Stability played a major role in this selection process.

The configuration selected was a cantilever truss 728 inches high with a square base plan of 40 inches. The truss was partitioned into three equal sections with four bays per section. Horizontal members were attached at each joint. All joints, including the base joints, were assumed to be clamped, as opposed to pinned. (When the trusses were constructed, all joints were either welded, cemented, or double bolted.) The vertical members and the horizontal members at the ends of each section are square 1.5 inch aluminum tubes with a wall thickness of 0.125 inches. The horizontal and diagonal members are Plexiglas 1.5 inch diameter tube with a wall thickness of 0.125 inches.

A finite element model of the truss is shown in Figure 2. A normal modes analysis of this undamped design predicted the first two bending modes of the truss at 1.64 and 1.71 Hz and the first torsional mode at 2.69 Hz. Due to the configuration of the diagonals in the truss, the first two mode shapes involve bending in vertical planes lying at 45 degrees to the truss sides. Therefore, the strain energy is the same in each of the four diagonal members of a bay. This same condition holds true for the horizontal members. The analysis predicted 34.5 percent (19.2 % in the lower section, 12.6 % in the middle section, and 2.7 % in the upper section) of the strain energy in the Plexiglas diagonals and 60.8 percent in the aluminum. The strain energy distribution for the first bending mode is shown in Table 2.

BAY NUMBER
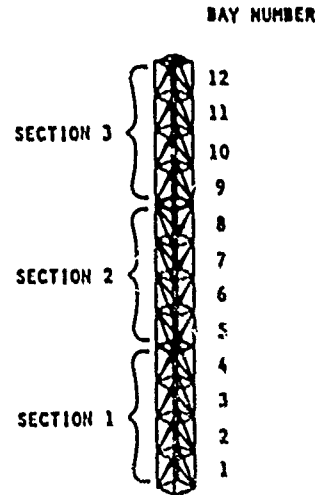
Figure 2   Finite Element Model of the Undamped Truss

Table 2
Strain Energy Distribution (Percent)
for Mode 1 of the Undamped Truss

Bay No.	Diagonals	Verticals	Hor(Al)	Hor(Plex)	Total
1 (Root)	4.431	18.733	0.000	0.870	24.034
2	5.285	14.498	0.000	0.923	20.706
3	5.068	10.941	0.000	0.343	16.852
4	4.422	8.009	0.311	0.000	12.742
Section 1	19.206	52.181	0.311	2.636	74.334
5	3.565	3.608	0.000	0.612	7.785
6	3.468	2.178	0.000	0.579	6.225
7	3.103	1.190	0.000	0.466	4.779
8	2.482	0.373	0.123	0.000	2.978
Section 2	12.6·8	7.349	0.123	1.677	21.767
Section 3	2.718	0.725	0.098	0.358	3.899
TOTAL	34.542	60.255	0.532	4.671	100.000

HA-5

4.2 Design of the Viscoelastic Discrete Dampers

Since the viscoelastic dampers installed on the diagonals performed well in the demonstration truss, the same concept was used in the damped design of the full scale truss. The calculated strain energy distribution without dampers showed that two-thirds of the strain energy in the Plexiglas diagonals was in the diagonals of the lower five bays. Dampers were designed for these five bays, but the dampers were incorporated in only two opposite sides of the truss. The design concept was that one bending mode would be damped primarily using only the Plexiglas material damping and the other would be damped using both material damping and the viscoelastic dampers. The strain energy distribution for the first bending mode of the undamped truss showed that 11.4 percent of the strain energy was in the ten diagonal members selected for replacement by the viscoelastic dampers. For the second mode, this percentage was 12.2 percent. However, as shown below, these fractions of strain energy can be changed greatly by varying the stiffness of the damped diagonals.

Figure 3 is a sketch of the discrete damper configuration. The design of the discrete damper follows that of the damping elements in the demonstration truss. This configuration converts the longitudinal motion of the diagonal dampers into shear strain in the viscoelastic material (VEM). Plexiglas tube of the same dimensions as the undamped diagonals was used for the connecting elements. Therefore, the purpose of the design analysis was to determine the optimum stiffness of the viscoelastic elements such that 1) the amount of strain energy in the viscoelastic materials was maximized, and 2) stability and other requirements were satisfied. The design of the viscoelastic dampers then reduced to determining the viscoelastic material and its geometric configuration (i.e. R_1, R_2, and W).

Two approaches will be discussed for the design of the discrete damping elements. The first approach uses the stiffness of the complete damped diagonal as a design parameter. The second approach models the viscoelastic material and uses the geometric and material properties of the VEM as the design parameters. For the design analysis, a value of 540,000 psi was used for the modulus of elasticity of Plexiglas.
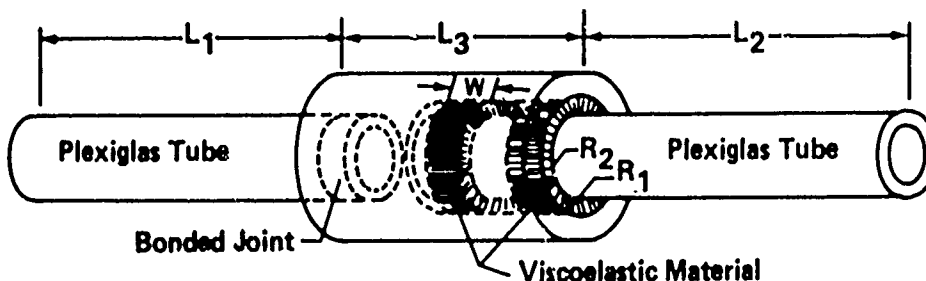
Figure 3   Schematic of Discrete Damper

4.2.1 Damper Diagonal Stiffness as a Design Parameter

Since the damper elements are only loaded axially, equations can be derived which relate the stiffness of the damper diagonals to the material and geometric properties of the damper. Also, an expression can be derived which relates the damper loss factor to the material loss factors and stiffnesses. Therefore, the truss loss factor can be determined once the strain energy distribution is known. Given these expressions, the properties of the VEM can be specified once the optimum stiffness of the damper diagonal is determined by the finite element analysis.

The stiffness of the damper shown in Figure 3 can be written (disregarding the compliance of the thick VEM housing) as

$$K_d = K_v K_p / (K_v + K_p) \tag{2}$$

where

$$K_v = \text{Stiffness of VEM}$$

$$K_p = \text{Longitudinal stiffness of the Plexiglas tube}$$
$$(A_p E_p / [L_1 + L_2]) \text{ where } L_1 \text{ and } L_2 \text{ are}$$
$$\text{shown in Figure 3)}$$

Once the desired stiffness of the damper diagonal is determined, the VEM properties can be determined by rewriting Eq. (2) as

$$K_v = G_v A_v / t_v = K_d K_p / (K_p - K_d) \tag{3}$$

where

$$G_v, A_v, t_v = \text{Shear modulus, cross sectional area, and}$$
$$\text{thickness of VEM in damper design}$$

$$E_p, A_p = \text{Modulus of elasticity and cross sectional}$$
$$\text{area of Plexiglas tube}$$

Following the definition of loss factor given by Eq. (1), the damper loss factor (η_d) is the sum of the Plexiglas loss factor (η_p) times its fraction of component strain energy and the VEM loss factor (η_v) times its fraction of component strain energy. This can be written as

$$\eta_d = \eta_p SE_p / SE_d + \eta_v SE_v / SE_d \tag{4}$$

where SE_i represents the summation of strain energy in all of the i'th type components (e.g., SE_p is strain energy in the Plexiglas components). Expressing strain energy in terms of the axial load and using Eq. (2), Eq. (4) for the loss factor of the damper can be expressed in terms of the stiffnesses as

$$\eta_d = \eta_p K_v / (K_v + K_p) + \eta_v K_p / (K_v + K_p) \tag{5}$$

HA-7
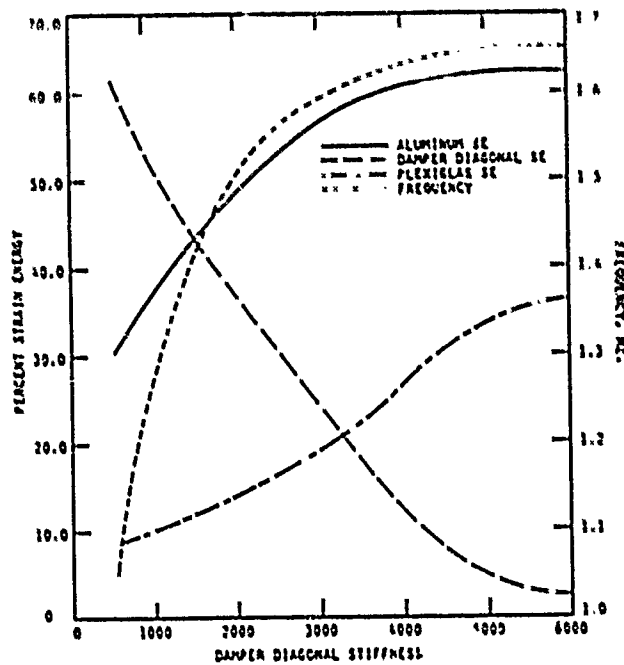
Figure 4   Variation in Strain Energy Distribution as a
Function of Damper Diagonal Stiffness

It is evident from Eq. (5) that it is highly desirable to make the structural link in series with the VEM as stiff as possible, i.e., η_d approaches η_v as K_p becomes very large.

The truss loss factor is the sum of the products of the fraction of the strain energy in each material or component times the corresponding loss factors for the material or component. Thus, the Plexiglas truss loss factor is

$$\eta_{Truss} = \eta_d(SE_d)/SE + \eta_p(SE_p)/SE + \eta_{al}(SE_{al})/SE \qquad (6)$$

where η_{al} is the loss factor of aluminum, and SE is the total strain energy in the truss.

Finite element analyses were performed with the stiffness of the ten damper diagonal members varied between 500 and 6,000 lbf/in. Figure 4 presents the variation of the frequency and strain energy distribution in the members as a function of damper diagonal stiffness. These curves show that the design with the maximum strain energy in the damper elements would be a design with a very low stiffness. However, as in the case with many designs of damping treatments, other factors influenced the final design. One design criterion stated that no member buckling should occur when the tip was deflected 6 inches. A stability analysis predicted the maximum allowable load in the aluminum vertical members as 12,334 lbf, and 248 lbf allowable in the Plexiglas diagonals. Analyses were run for a 6 inch tip deflection with various damper diagonal stiffnesses. A value of 1,775 lbf per inch produced 248 lbf axial force in the diagonal dampers and 2,667 lbf in the aluminum verticals. Therefore, the stability of the diagonals governed the design. The selected damper stiffness produced 46.5

HA-8

percent of the strain energy in the aluminum, 40.0 percent in the damper diagonals, and 13.5 percent in the other Plexiglas elements.

With the stiffness of the damper diagonal and the corresponding strain energy distribution known, the viscoelastic damper can be designed. From Figure 3 and the dimensions of the truss, the stiffness of the Plexiglas portion of the damper diagonal, K_p, can then be determined as 4,556 lbf/in. Substituting K_d = 1,775 lbf and K_p' = 4,556 lbf/in into Eq. (3) yields $G_v A_v/t_v$ = 2,908 lbf/in. This is the value of the design parameter for the viscoelastic damping element. The next step is the selection of a VEM that has a high loss factor in the temperature and frequency range of interest and has a shear modulus that will produce the desired design parameter value with reasonable dimensions. The selection of the actual VEM used will be discussed in a later section. Once the VEM is selected, the loss factor of the damper diagonal and the truss can be found by using the strain energy distribution and Eqs. (5) and (6).

4.2.2 VEM Properties as a Design Parameter

The previous section discussed the design analysis of a structure when a simple relationship can be found between the stiffness and loss factor of the damping elements, and the geometric and material properties of the elements. This was possible for the simple damper link of the truss, but the configuration of many structures and their damping design is usually too complex to find the required relationships. In those more typical cases, the finite element model must include elements representing not only the structure but also the viscoelastic material. This section will discuss the design of the damped truss by using the viscoelastic material properties directly as the design parameter.

A finite element model of the ten viscoelastic dampers shown in Figure 3 was created and joined with the model of the remaining truss. The viscoelastic material is represented by solid elements. The design variable is then $G_v A_v/t_v$. A number of analyses were performed varying this parameter and calculating the strain energy distributions. This was accomplished by choosing a reasonable A_v and t_v, and varying the shear modulus.

Figure 5 presents the variation of strain energies in the aluminum, Plexiglas, and viscoelastic materials as a function of viscoelastic stiffness. The maximum strain energy fraction in the viscoelastic occurs at a viscoelastic stiffness of 2,100 lbf/in. However, stability considerations again govern the final design. By simulating a tip deflection of 6 inches for various viscoelastic stiffnesses, a value of $G_v A_v/t_v$ = 2,990 lbf/in produced 248 lbf in the diagonal Plexiglas elements.

From Figure 5, for this value of viscoelastic stiffness, 45.5 percent of the strain energy is in the aluminum, 24.0 percent in the VEM, and 30.5 percent in the Plexiglas elements. The predicted frequency is 1.49 Hz.

The next step would be the selection of a VEM that has a shear modulus which, when using realistic geometric properties (A_v, t_v), would yield $G_v A_v/t_v$ = 2,990 lbf/in. The loss factor for the selected VEM should be high for a frequency of 1.49 Hz and for the temperature of interest. Once the VEM is selected, application of Eq. (1) yields the loss factor of the truss. The actual selection of the VEM will be discussed in a later section.

HA-9
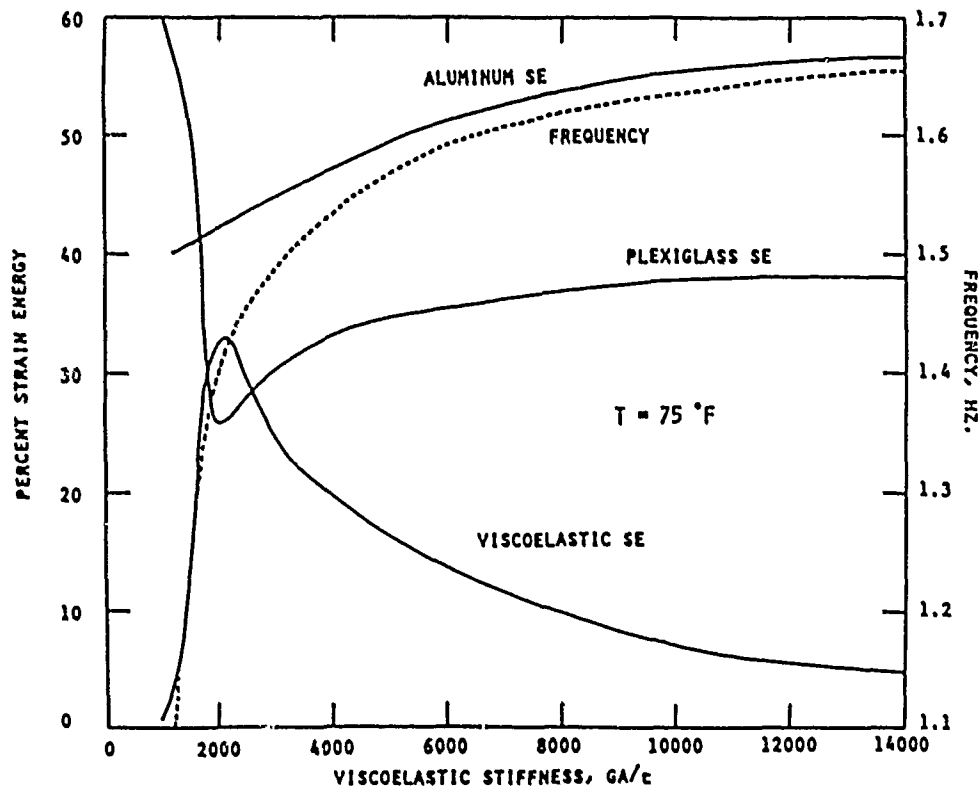
Figure 5   Strain Energy Distribution of the Plexiglas Truss
as a Function of Viscoelastic Stiffness

4.3   Performance Predictions for the Truss

The primary operating temperature of the trusses will be in the range of 60
to 80 degrees F. The maximum operating temperature was selected as 100 degrees
F. Recalling that the VEM design parameter was determined from stability condi-
tions, the VEM design value must be evaluated at this maximum temperature.
Therefore, the selected viscoelastic material should have a shear modulus that
would yield $G_v A_v / t_v$ = 2,990 lbf/in at 100 degrees F and 1.49 Hz.   The loss fac-
tor should be high in the temperature range of 60 to 80 degrees F.

A suitable viscoelastic material for this application is 3M Y-4205 Acrylic
Core Foam. Measured properties of this material are presented in Figure 6. The
shear modulus evaluated at 100 degrees F and 1.49 Hz is 70 psi.   This material
was applied to the damper elements shown in Figure 3 in two 1 inch wide strips
1.5 inches apart. Two strips were used to give more resistance to bending. The
thickness of the viscoelastic (t_v) was 0.240 inches.   Using the geometric
properties of the damper, the area (A_v) is found to be 10.136 square inches.
Therefore, $G_v A_v / t_v$ = 2,956 lbf/in.   Although this material satisfied the stiff-
ness conditions, it was probably not optimum for this application.   It's loss
factor peaks at a value of 1.3 at 25 degrees F for the frequency of 1.5 Hz.   At
55 degrees F, the loss factor has decreased to 0.70 with G_v =158 psi.

HA-10
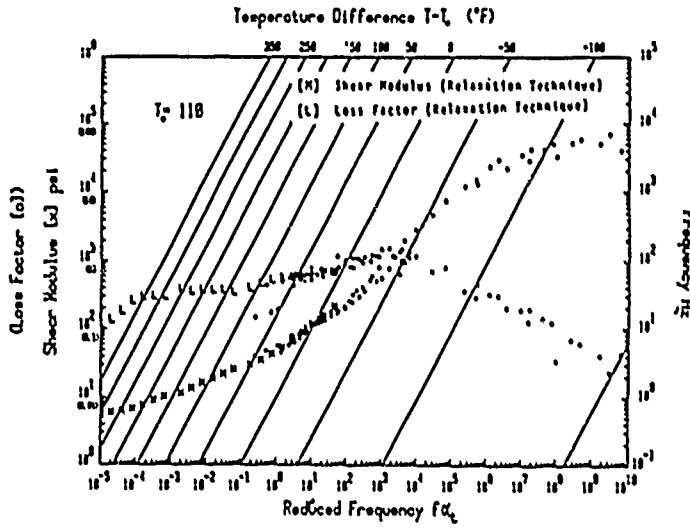
Figure 6   3M Y-4205 Acrylic Core Foam Material Data

Properties of the Plexiglas were determined in the frequency range of 1.0 to 2.0 Hz by hysteresis testing. With the Plexiglas and viscoelastic properties known as functions of temperature and frequency, finite element aralyses were performed to predict the performance characteristics of the truss. These analyses were performed with the material properties evaluated at temperatures between 50 and 100 degrees F. Strain energies in each element were calculated, and these strain energies were then added for each material. Applying Eq. (1), the modal damping for the truss was calculated. Results are shown in Figure 7. The predicted modal damping for the "damped" mode (the mode where the viscoelastic dampers are worked the most) increases by a factor of 2.8 when the temperature changes from 50 degrees to 100 degrees F. At 100 degrees F, the bending planes of the normal modes are almost perpendicular to the sides of the truss. At 50 degrees F, these planes are 29.6 degrees off the sides of the truss. When the stiffness of the damper diagonals equals the stiffness of the other Plexiglas diagonals, the angles are 45 degrees.
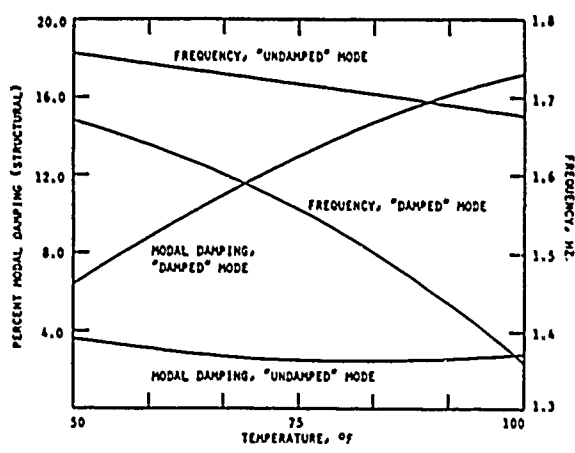
Figure 7   Modal Damping and Frequency of Plexiglas
Truss as a Function of Temperature

HA-11

5.0 MODAL TESTING

Two trusses were constructed, one as described above and the other using Lexan in place of Plexiglas. Both trusses used the discrete damper discussed above with Plexiglas connecting elements. Figure 8 shows the Plexiglas and Lexan trusses with the discrete dampers installed. The dampers are on the sides of the trusses perpendicular to the plane of the photograph. Further descriptions of the trusses are contained in Ref. [3].

A modal test was performed on the plexiglas truss for the purpose of verifying the finite element analysis. In particular, it was necessary to determine with high accuracy the modal loss factor of the fundamental bending mode in the damped direction. Additionally, the shape of the damped mode was measured to a level of detail that would allow diagnosis of any error in the analytical damping predictions.

Figure 8   Photograph of Trusses

HA-12

The test situation differed from a typical modal survey in several ways. Interest was concentrated on a single mode whose frequency and shape were essentially known in advance. Modes other than the first two bending modes were not important. The modal density was low and damping of the most important mode was relatively high. The measurement frequency range was extremely low and damping measurements of high confidence were required. Temperature of the test article, particularly the dampers, had a strong effect on its modal properties and had to be measured and controlled. These factors governed the planning and execution of the test.

5.1 Test Setup and Procedure

The test was performed using conventional frequency response methods. FRF measurements were made using single point, stationary random excitation. Two shaker locations were used sequentially. Both were at the junction of the middle and upper truss sections, 40 feet above the base. Input forcing was applied parallel to the truss sides, first in the well damped direction and then in the lightly damped direction.

FRF's were measured over the range of 0-8.0 Hz with a resolution of 0.02 Hz for excitation in the well damped direction. A total of 241 response degrees-of-freedom (DOF's) were used. These were: triaxial accelerations at each truss joint, triaxial accelerations on each damper, and relative axial displacements across the VEM for several circumferential locations on each damper. The latter was sensed by an LVDT mounted on the damper as shown in Figure 9.

Motions measured at the truss joints were used to determine the shape of the well damped mode. The accelerometer grid matches the finite element grid shown in Figure 2. Measurements of relative (shearing) displacements across the VEM were obtained because of their direct bearing on the modal loss factor. Redundant shearing measurements and triaxial motion of the dampers were obtained in order to detect any bending of the damping links due to initial misalignment. It was determined that while clearly visible, bending of the links was not sufficient to have a significant effect on damping.

Selected FRF measurements were made with excitation in the lightly damped direction. A frequency resolution of 0.0049 Hz was used. These were sufficient to determine the modal loss factor though not the shape of the lightly damped mode.

A single-function, multi-DOF curve fitting routine was used to determine modal loss factors for the first well damped and first lightly damped modes. A group of 17 FRF measurements was used, primarily from DOF's corresponding to motions on the upper 1/3 of the truss. Frequency and damping estimates from these functions were averaged to obtain final results. Single DOF (circle fitting) was used to obtain the shape of the well damped mode.

Temperatures of the damping elements were monitored and controlled during the test. Each discrete damper had a thermocouple embedded in the VEM and was wrapped in an electric heating pad. Voltage to the heaters was individually regulated to produce the desired temperature. The FRF's used to determine damping were taken during a time period when the temperature profile was particularly stable. Temperature of the Plexiglas was monitored via thermocouples at five points but was not controlled.

HA-13
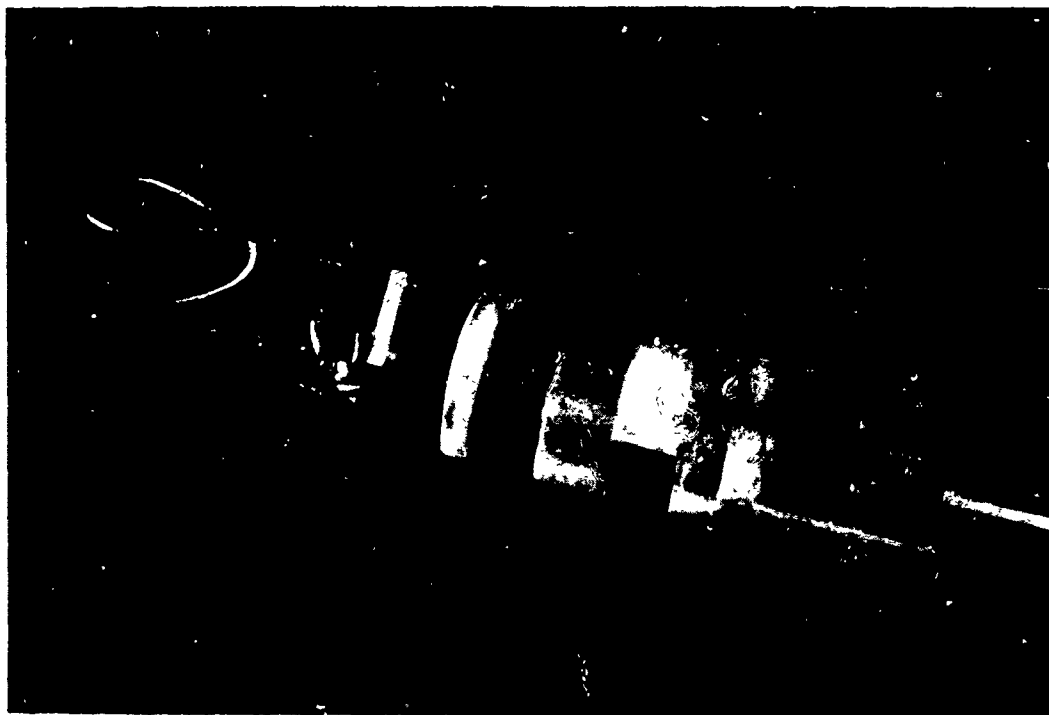
Figure 9   LVDT and Bracket Installed on a Damper

5.2 Test Results

A typical measured FRF and its fitted curve are shown in Figure 10.   Force input was in the well damped direction and the response acceleration was measured in the well damped direction near the top of the truss. Figure 10 is typical of the measurements used to estimate damping. The function is quite simple in form which made the curve fitting straightforward. The well damped mode at 1.63 Hz is dominant. A small contribution from the lightly damped mode is visible at 1.73 Hz as well as the second well damped bending mode at 5.7 Hz.

Figure 11 shows the measured shape of the well damped mode. It is essentially the first bending mode of a cantilever beam. There is no rotation about the beam axis but, due to asymmetry of the truss diagonals, the bending deformation is slightly out of the plane of the paper. A closer examination reveals the influence of the damping links. The upper seven bays of the truss deflect essentially as a classical Euler beam with the cross members remaining perpendicular to the stringers. Shearing behavior is clearly visible in the bottom five bays containing the damping links. It is greatest in the bottom bay where the upper cross member remains essentially horizontal. The transition from bending-shearing to pure bending is clearly visible between the fifth and sixth bays.

The mean of the measured modal loss factor and frequency of the first well damped mode were 0.0972 and 1.63 Hz, respectively. This mean was obtained from 17 FRF's and the standard deviation of the damping estimates was 2.6% of the mean. The average temperature of the dampers was 71.47 degrees F. More detailed results and comparisons with analytical predictions are given in the following section.

HA-14
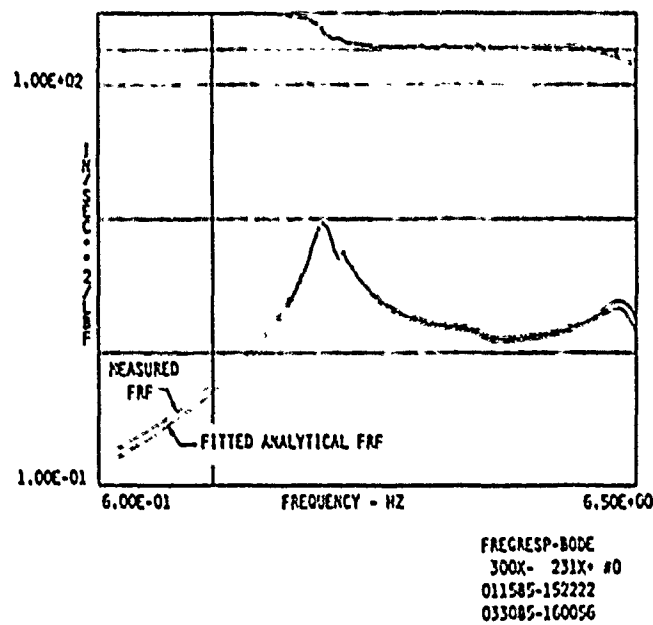
Figure 10   Typical Acceleration/Force FRF for the
             Plexiglas Truss with Excitation and
             Sensing in the Well Damped Direction
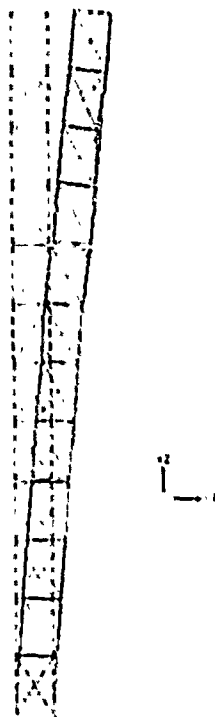
Figure 11   First Bending Mode of the Plexiglas Truss
             in the Well Damped Direction

HA-15

6.0 ANALYSIS/TEST CORRELATION

Three tests were chosen for comparison to the predicted results, as listed in Table 3. The truss was excited in the "damped" direction for Test No. 15-12 and 15-16, and in the "undamped" direction for Test No. 19-16.

The VEM and Plexiglas properties for the temperatures measured during each test were input to the finite element model. Loss factors of 0.045 for Plexiglas and 0.005 for aluminum were used for all analyses. An average temperature of 72 degrees F was used to determine the loss factor of the VEM. From Figure 6, the loss factor of the viscoelastic material was found to be 0.66 for 1.60 Hz, 0.68 for 1.73 Hz, and 0.98 for 6.2 Hz.

Using the material properties for the temperatures of Test No. 15-12, the finite element analysis predicted 13.3 percent of the strain energy in the VEM, 33.5 percent in the Plexiglas, and 53.2 percent in the aluminum for the "damped" mode. The truss loss factor can then be found by the application of Eq. (1) as the product of the strain energies and the loss factors for each material. It is η_{Truss} = (.133)X(0.66) + (.335)X(0.045) + (.532)X(0.005) = 0.1055. Similar calculations can be performed for the other test cases.

Comparisons of the predicted and measured damping and frequencies were made for the four cases shown in Table 3. For the "damped" first bending mode, the finite element model underpredicts the frequency by 2.2 percent, and overpredicts the structural damping by 4.0 percent. For the "undamped" mode, the finite element analysis accurately predicts the frequency, but underpredicts the damping by 16.2 percent. Apparently, the actual structure is working the discrete dampers more than the model predicts for this "undamped" mode. This may be due to random deviations from symmetry in the actual truss that are not reflected in the model. For the second bending mode, the predicted frequency is 11.4 percent low, while the predicted structural damping is only 1.7 percent high.

Table 3
Comparison of Experimental Results and Analytical
Predictions for the Plexiglas Truss

Test Number	Measured Frequency (Hz)	Predicted Frequency (Hz)	Measured Structural Damping, %	Predicted Structural Damping, %
"Damped" First Bending Mode				
15-12	1.628	1.592	10.14	10.55
15-16	1.632	1.600	9.98	10.03
"Undamped" First Bending Mode				
19-16	1.727	1.726	3.46	2.90
"Damped" Second Bending Mode				
15-16	6.235	5.522	17.25	17.54

7.0 CONCLUSIONS

It has been demonstrated that current passive damping design technology can be applied successfully to produce a large structure with significant damping when operated in its design environment. The analysis techniques presented here accurately predicted the structural damping of the truss. It is felt that this technique can be successfully used to design damping treatments for large space structures.

The analysis has shown that the truss would have been more highly damped in the "damped" direction if discrete dampers had been used in all planes. The most efficient series installation of VEM dampers is obtained when very stiff structural elements are used to connect the VEM to the remaining structure.

REFERENCES

1. Johnson, C.D., Kienholz, D.A., and Rogers, L.C., "Finite Element Prediction of Damping in Beams with Constrained Viscoelastic Layers," Shock and Vibration Bulletin, No. 50, Part 1, May, 1981, pp. 71-82.

2. Johnson, C.D. and Kienholz, D.A., "Finite Element Prediction of Damping in Structures with Constrained Viscoelastic Layers," AIAA Journal, Vol. 20, No. 9, Sept 1982, pp. 1284-1290.

3. "Vibration Damping Studied for Weapons in Space," published in Aviation Week & Space Technology, July 2, 1984, McGraw-Hill, Inc.

Y 4 /

THE DESIGN OF VISCOELASTIC PASSIVE DAMPING TREATMENTS

FOR SATELLITE EQUIPMENT SUPPORT STRUCTURES

by

Dr. Roy Ikegami

Mr. Derrick W. Johnson

Boeing Aerospace Company
P.O. Box 3999
Seattle, WA 98124

Abstract

This paper presents results of the Boeing Aerospace Company Reliability for Satellite Equipment in Environmental Vibration (RELSAT) program. A review of the program objectives, performance goals, and current status, is given. The design and analysis of viscoelastic passive damping treatments that will be applied to the Inertial Upper Stage Dynamic Test Vehicle (DTV) is described. These damping treatments will be used to damp the vibroacoustic response of avionics equipment mounted in the Equipment Support Section to the Space Shuttle launch environment. The design of the damping treatments was based on the results of a finite element and Modal Strain Energy method analysis of several damping concepts on a representative component test structure. The results of acoustic testing of the passive damping concepts applied to the component test structure are shown and compared with goals established from early tests on the DTV. The comparison was used to validate the effectiveness of the damping designs for subsequent use on the DTV. A damping design procedure based on the use of finite element analysis and component developmental testing is discussed.

Introduction

Expanding requirements for military surveillance and scientific observations in space have placed new and increasingly stringent design requirements on satellite systems. In general, the electronic equipment of these satellite systems must endure the harsh vibroacoustic environment of launch and then operate precisely in the relatively benign environment of space. In many cases, sophisticated electronic equipment has not survived the high acoustically induced vibration levels experienced during launch and, oftentimes, standard aerospace vehicle design practices do not identify these vibration problems until late in the design process. The objective of the RELiability for SATellite Equipment in Environmental Vibration (RELSAT) program is to develop and validate the application of passive damping technology for vibration control to increase satellite equipment reliability.

The application of viscoelastic passive damping techniques has the potential to provide cost effective minimum weight solutions to vibration problems. Modern analysis techniques utilizing finite element modeling and the Modal Strain Energy (MSE) method now allow a wide variety of different damping concepts to be analyzed on complex structures. The MSE method was first suggested by Johnson, Kienholz, and Rogers[1], and is becoming widely accepted as a valuable design tool.

The RELSAT program is a five year research and development program to demonstrate that early incorporation of viscoelastic passive damping technology into standard aerospace vehicle design practice can reduce vibration levels and increase equipment reliability without significantly affecting the vehicle weight or program cost and schedules. The program is approximately 50 percent complete with much of the damping concept development done and many of the viscoelastic materials to be used are characterized. This paper will present the approach being used to design and analyze passive damping treatments for the Inertial Upper Stage (IUS) baseline example system and show several damping treatments that were designed and tested on a representative test structure.

Baseline Satellite System

The IUS was selected as the baseline satellite system for this program for the following reasons:

1) The basic construction and weight to surface area ratio of the IUS is similar to other satellite systems.
2) The low weight to surface area ratio makes the IUS very susceptible to high vibroacoustic environments.
3) The IUS is designed to operate in the Space Shuttle and Titan launch vehicles in which the vibration levels are of the magnitude that degrade the reliability of avionics equipment.
4) There exists more than 500 IUS vibration and acoustic measurements which define equipment vibration environments for a variety of structural configurations.
5) The IUS dynamic test vehicle (DTV) is available for use in this study.

A sketch of the IUS is shown in Fig. 1. The IUS is basically a two stage vehicle consisting of two solid rocket motors, a cylindrical interstage, the spacecraft interface, and the equipment support section (ESS). The interstage and ESS are significant structural components because the large surface area of the interstage picks up acoustic radiation which in turn is transferred to avionics equipment through the ESS. The weight to surface area ratio of the IUS is approximately 0.008 pounds per square inch, similar to other satellites such as the Tracking and Data Relay Satellite, the Defense Support Program Satellite, and the

Defense System Communication Satellite.

The DTV was fabricated during the development phase of the IUS program to serve as a static and dynamic test article for development of the production vehicle. A picture of the DTV assembled for an acoustic noise test is shown in Fig. 2. The configuration and major structural components of the DTV are similar to the IUS flight vehicles. The equipment vibration design and test requirements for the IUS were obtained from acoustic tests on the DTV.

An important reason for choosing the IUS as a baseline was the large amount of available vibroacoustic data. More than 500 vibration and acoustic measurements were made to define the equipment vibration environments. These measurements were made during a series of five acoustic and modal survey tests performed on the DTV. The five tests are summarized in Table 1. More than one test was conducted because the magnitude of the noise induced vibration created avionics equipment design problems. During the tests, modifications were made to the DTV structure in an effort to reduce the vibration response and to understand the interaction between the structural response and the applied noise excitation. Viscoelastic damping material was applied during Test 3 and was found to reduce the vibration response. A modal survey was also conducted as part of Test 3 to examine significant vibration modes in the 50 to 300 Hz frequency range. Test 4 was conducted to determine whether the DTV vibration response was affected by the acoustic test facility characteristics. Test results showed that the vibration response was independent of the test facility. Test 5 was conducted as part of a study to design an IUS simulator for use in satellite equipment acoustic tests. The test consisted of measuring the vibration response with and without the interstage installed. The results indicated that the interstage was a significant contributor to the IUS ESS vibration environment.

The 145 dB noise level applied during the DTV acoustic tests was the design level for payloads carried in the Space Shuttle and the Titan launch vehicles. This acoustic noise level occurs during launch vehicle liftoff and flight. The IUS vibration response to this noise environment was the highest encountered during the IUS mission and thus defined the avionics equipment design vibration levels. Launch induced vibration levels of the magnitude experienced by the IUS can degrade equipment performance and reliability.

Goals and Requirements

Testing conducted on the IUS DTV indicated that viscoelastic damping treatments can be effective in reducing vibration. For this program it was desired to reduce the levels even further, so a set of performance goals were established for subsequent damping treatments to be designed for the DTV. These goals include the following:

1) Reduce overall vibration levels (20 to 2000 Hz) at IUS equipment location to 6 G rms or less.
2) Limit acceleration power spectral density levels in the 100 to 300 Hz frequency range to 0.1 g^2/Hz.

Figure 3 compares these goals with measured vibration spectra from the DTV. The spectra were measured at avionics support points during a 145 dB acoustic noise test.

These performance goals were chosen because the vibration reduction should be large enough to increase avionics reliability. Also, the 6 G rms level corresponds to the minimum vibration design level specified in MIL-STD-1540A. Reducing satellite vibration to this level would make it possible to incorporate MIL-STD-1540A qualified equipment into a new satellite system with no additional qualification testing. This could greatly reduce the cost of

future aerospace programs.

The 0.1 g²/Hz limit over the 100 to 300 Hz frequency range was chosen because of avionics equipment vibration characteristics. Avionics chassis and internal circuit boards characteristically have first mode resonant frequencies in this range[2]. Figure 3 shows that in the 100 to 300 Hz range the IUS DTV vibration input to avionics is high. Therefore, reducing these levels will significantly increase avionics reliability. These goals will require spectral peak reductions on the order of 10 dB.

Many different damping configurations can be used to meet these goals and reduce vibration levels, but they may be offset by degradation of performance and reliability in another part of the system. System requirements which are likely to impose constraints on the damping designs are contamination (outgassing), thermal and electrical conductivity, hardening (electromagnetic compatibility and electromagnetic interference), structural strength, structural deflection, and weight.

Design Procedure

Two basic design tools were chosen for damping treatment design in this program. They are closed form analytical solutions and finite element analysis with the Modal Strain Energy (MSE) method.

Closed form solutions are available for simple structures such as simple beams, flat plates, and cylindrical rings. The advantage of closed form solutions is that they can easily be programmed into the computer and a large number of design iterations can be performed at a relatively low cost. The disadvantage to closed form solutions is that they are useful only in analyzing simple structures.

Finite element analysis with the Modal Strain Energy method is the most useful tool for designing damping treatments for complex structures. In the MSE method, the complex eigenvectors which would normally be associated with analyzing a structure with damping, are approximated by real eigenvectors and the structural loss factor is then found from the equation

$$\eta^{(r)} = \frac{\sum_{j=1}^{N} \left(\eta_j \, SE_j^{(r)} \right)}{SE^{(r)}} \tag{1}$$

where

$\eta^{(r)}$ = structural loss factor for rth mode

η_j = material loss factor for the jth material

N = number of different materials in structure

$SE_j^{(r)}$ = total strain energy in jth material for rth mode

$SE^{(r)}$ = total strain energy in structure for rth mode

Since the eigenvectors are computed from an elastic finite element analysis, considerable computer time is saved as compared to a complex normal modes analysis. The advantage of the MSE method is that it can be used to analyze a wide variety of complex structures. The disadvantage is that the finite element models can be quite large and detailed and thus require a large amount of time and money to develop.

The most cost effective design procedure was to try to reduce the structure of interest into smaller components while still maintaining a representation of the original structure, and then design the damping treatments on the smaller structure. If it was at all possible it was

attempted to reduce the structure to the point where analytical solutions could be used. After the damping treatment is fully developed on the smaller structure, it could then be analyzed on the full size structure to determine the expected damping and to check for any undesirable interactions with other damping treatments. A design methodology based on this procedure is shown in Fig. 4.

Component Test Structure

From the previous vibroacoustic testing performed on the DTV, it was known that acoustically induced vibration was transmitted from the interstage through the ESS and to the avionics equipment. A component test sthucture, which was felt to be representative of the ESS, was designed and fabricated. Shown in Fig. 5, the component test structure isolates a 34 degree segment of the second stage structure between two of the spacecraft support longerons. It includes part of the ESS frame, the spacecraft interface, and the second stage motor support cone. A picture of the test structure with a simulated 3 lb electronic component mounted on the equipment deck is shown in Fig. 6. The structure is, basically, of aluminum skin and stringer construction with all rivets replaced by bolts to facilitate removal of portions of the structure to add damping treatments.

To assure that the test structure was, indeed, representative of the DTV, an acoustic test was performed to compare the response of the test structure to that of the DTV. Figure 7 shows the results of acoustic tests performed on the test structure and the DTV. A comparison indicates that the test structure is representative of the DTV in both shape of the power spectral density curve and the overall rms value. This information lends confidence that damping treatments developed on the test structure will provide similar results on the DTV.

Since the choice of damping treatments is dependent on the shape and frequency of the mode to be damped, a finite element model of the undamped structure was created and a normal modes analysis was performed. Two modes of interest are shown in Fig. 8. Both of these modes occur in the 200 Hz frequency range. The dynamic properties of 3M Y-966, shown in Fig. 9, indic--- --at it is effective for the 200 Hz and 70 degrees F range and was found to satisfy the outgassing requirements of the IUS baseline system[3]. Therefore, to simplify the damping treatment design, the viscoelastic material 3M Y-966 was selected for all damping treatments.

Damping Concepts

Several damping concepts have been developed for the component test structure and evaluated through acoustic testing. Add-on panel constrained layer damping treatments, web-type frame dampers, and integral sandwich panels were designed and evaluated in previous tests[3], and demonstrated that the response could be reduced very close to the established goals. The sandwich panels in which the original all-aluminum panels were replaced with a sandwich of a viscoelastic core with two aluminum face sheets proved to provide a large amount of damping with a minimal weight penalty. The damping concepts that will be explored in this paper include sandwich panels, constraining rib type frame dampers, and interface damping.

Sandwich panels were designed with a combination of closed form solutions and finite element analysis with the MSE method. A 10 inch square sandwich panel was analyzed with the closed form solutions by Abdulhadi[4] for varying thickness of 3M Y-966 viscoelastic core material with 0.016 inch aluminum face sheets. These results are shown in Fig. 10 with the results of a MSE analysis performed on the upper panel skin and stringer section isolated

away from the rest of the model. A limitation was imposed on the thickness of the viscoelastic material (VEM) by the reduced structural stiffness of the panels. A maximum VEM thickness of 0.006 inches was chosen for use on the test structure with reduced buckling allowables of approximately 50 percent. The resulting sandwich panel damping treatment consisted of replacing the original 0.032 inch aluminum panels with a sandwich of a 0.006 inch 3M Y-966 core with two 0.016 inch aluminum face sheets.

The constraining rib frame dampers consist of one inch square aluminum tubing (1/8 inch wall thickness) attached to the sides of the frame members beneath the simulated avionics box with 0.010 inch 3M Y-966. The frame dampers as they were applied to the component test structure are shown in Fig. 11. The frame dampers were designed using finite element analysis and the MSE method by isolating the ESS framework out of the undamped structure finite element model and iterating on several constraining rib and viscoelastic thickness combinations. It was known that for configurations where the viscoelastic does not lie in the neutral bending plane, the ideal constraining layer (or rib) should be as stiff as possible such that all relative motion between the frame member and the rib will be imparted into the viscoelastic. To determine the thickness of the viscoelastic, the constraining rib was considered to be a rigid body while iterating on the material thickness. Figure 12 shows the percent strain energy in the viscoelastic relative to the isolated ESS structure as a function of viscoelastic thickness for the two modes of interest. A VEM thickness of 0.010 inches was chosen from these results to be effective on both modes. In Table 2 the percent strain energy is shown as a function of the rib cross section while using a constant 0.010 inch VEM thickness.

In designing the interface damping treatments, separate studies were done[5] on free-free sandwich beams to determine the effects of various bolted beam parameters such as bolt torque and density on the damping. The idea of interface damping involves placing a thin layer of VEM between the mating surfaces of bolted or riveted joints, as shown in Fig. 13, in an effort to convert any slip in the joint into shear and thus damping in the viscoelastic. The most significant result of this study is that the same methods used for analyzing and designing unbolted sandwich beams can be used for bolted beams. Figure 14 compares the results of sixth order beam theory[6] and test results for a series of bolted and unbolted sandwich beams. The general shape of the curves indicates that the thickness and modulus of the VEM can be designed in the same manner as unbolted beams except that a reduction in the total structural loss factor can be expected. The damping treatment for the test structure was designed by isolating a lower panel stringer and the adjacent section of panel and analyzing it as a sandwich beam. The results indicated that the best damping occurred with 0.002 inch of the 3M Y-966. Subsequently, 0.002 inch of the VEM was used for all bolted joints.

Acoustic Testing

The acoustic testing was performed in a 16 ft x 24 ft x 20 ft reverberation room. The purpose of the testing was to evaluate the effects of the viscoelastic damping treatments on the response of the component test structure. The test structure was mounted in a bookend type vibration fixture and placed in the acoustic chamber. The Space Shuttle payload bay acoustic noise spectrum (145 dB overall) was then applied and acceleration responses were measured at the top and mounting points of the simulated avionics component. Acceleration power spectral densities were then calculated and compared to goals.

Four configurations of the test structure were tested in which various combinations of the damping treatments were used. The four configurations consist of the following:

1) Sandwich panels only.
2) Interface damping only.
3) Sandwich panels and frame dampers.
4) Sandwich panels, frame dampers, and interface damping.

Envelope power spectral density (PSD) levels for the first two configurations are shown in Figures 15 and 16. The envelopes consist of the maximum PSD levels versus frequency for all 12 of the accelerometers mounted on the test structure. Figure 15 shows that the sandwich panels were very effective in reducing response at the higher frequency levels which typically correspond to panel modes. They were not as effective, however, at the lower frequencies which correspond to vibration of the simulated avionics component. The response with the interface damping, shown in Figure 16, exhibits a general smoothing across the entire frequency spectrum which indicates a decoupling or isolation of the panel modes from the avionics component modes.

Combinations of the damping treatments were used to utilize the effectiveness of each damping treatment in its own frequency range. The sandwich panels were combined with the frame dampers to further reduce the response at the lower frequency levels. The response from this configuration, shown in Figure 17, is approaching our 6 G rms goal. The addition of the interface damping reduced the response, which is shown in Fig. 18, even further to be within 26 percent of the goal.

Summary

In summary, a procedure has been developed where, through the use of analytical tools, damping can be designed into a structure to provide reduced response to high level acoustic environments. By isolating the critical components of a structure down to a manageable size, both closed form solutions and the MSE method can be used to design damping treatments for use on the full scale structure. Finite element analysis with the Modal Strain energy method has proven to be an invaluable design tool in evaluating these damping treatments on complex structures.

The results of this study add to the catalog of damping concepts which will later be used on the DTV to damp the vibration response to the Space Shuttle acoustic noise environment. Integral damping treatments again show significant vibration reduction with little system level impact. Areas which still need to be addressed are to determine the impact of these damping treatments on structural strength, stiffness, and weight and to develop additional damping concepts which are agreeable to system designers. If the design of viscoelastic passive damping treatments can be incorporated early into the standard vehicle design cycle, the potential exists to increase system reliability, lower qualification test time and costs, and reduce overall equipment costs.

References

1. Johnson, C. D., Kienholz, D. A., and Rogers, L. C., "Finite Element Prediction of Damping in Beams with Constrained Viscoelastic Layers," *Shock and Vibration Bulletin*, No. 51, May 1981, pp. 78–81

2. Steinberg, D. S., Vibration Analysis for Electronic Equipment, Wiley, 1973, pp. 49,260

3. Ikegami, R., Johnson, D. W., et. al., "The Application of Viscoelastic Passive Damping to Satellite Equipment Support Structures," *Journal of Vibration, Acoustics, Stress, and Reliability in Design*, Vol. 107, Oct. 1985, pp. 367–374

4. Abdulhadi, F., "Transverse Vibrations of Laminated Plates with Viscoelastic Layer

Damping," *Shock and Vibration Bulletin*, Vol. 40, No. 5, Dec. 1969, pp. 90-104

5. Smith K. E., Kienholz, D. A., "Preliminary Investigation of Interface Damping," CSA Engineering report submitted to Boeing Aerospace Company, No. 85-06-05, June 1985

6. Rao, D. K., "Frequency and Loss Factors of Sandwich Beams Under Various Boundary Conditions," *Journal of Mechanical Engineering Science*, Vol. 20, No. 5, May 1978

Length 16.4 Ft.
Diameter 7.6 min.
9.5 max.

Weight
surface
area ratio's .008 lbs/in^2

Conical structure

Cylindrical structure

Solid Motors (SRM)

Equipment support section (ESS)- truss structure

Spacecraft interface
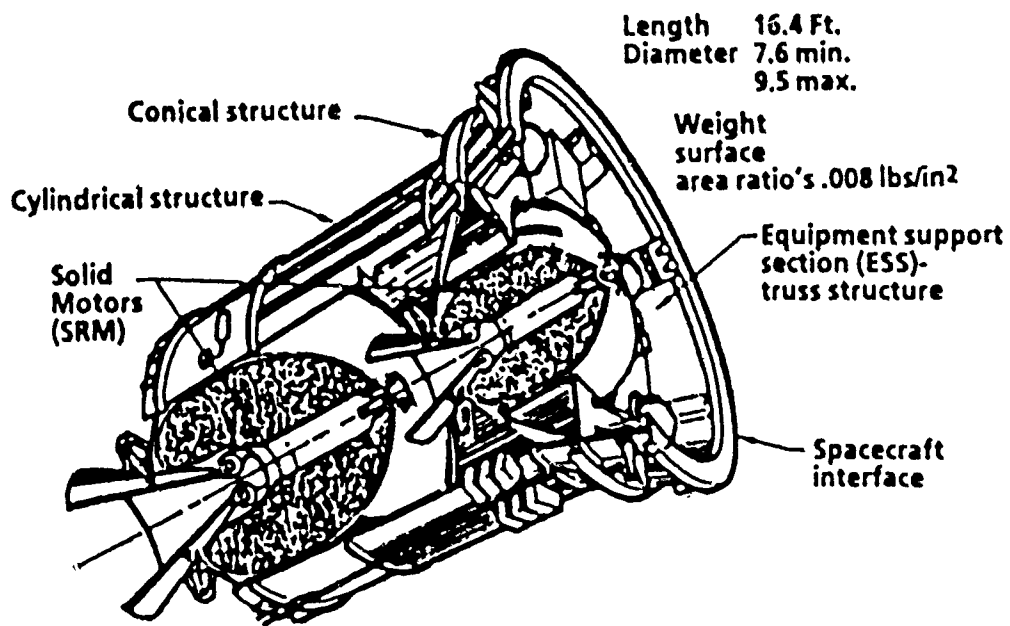
Figure 1.   Inertial Upper Stage (IUS) Selected for Baseline Satellite System

Figure 2. IUS DIV Assembled for Acoustic Noise Testing

| TEST NO. | PURPOSE | MEASUREMENTS | | TEST LEVEL |
		VIBRATION [1]	NOISE [2]	OVERALL SPL dB
1	Determine equipment vibration response	42	5	130 [3] 145
2	Determine equipment vibration response on a modified equipment support section	17	5	145 [3]
3	Determine equipment vibration response 1) One stage configuration 2) Two stage configuration 3) With and without viscoelastic damping Conduct modal survey	53	8	145 [3]
4	Determine equipment vibration response in a larger acoustic test facility	53	13	145 [4]
5	Determine equipment vibration response with and without the IUS interstage	38	5	145 [3]

[1] Vibration measured 20 to 2000 Hz [2] Noise measured 31.5 to 10,000 Hz
[3] Tested in Boeing 16 ft x 24 ft x 20 ft reverberation room
[4] Tested in Lockheed 86 ft x 50 ft x 44 ft reverberation room

Table 1.   IUS DTV Vibroacoustic Tests

IUS DTV		
	Item	Overall q_{rms}
○	3 lb box on ESS deck, ⊥ to deck	13
□	Interstage battery, tangential	10
◆	Battery on ESS deck, ⊥ to deck	8
△	Computer on conic, parallel to skin	8
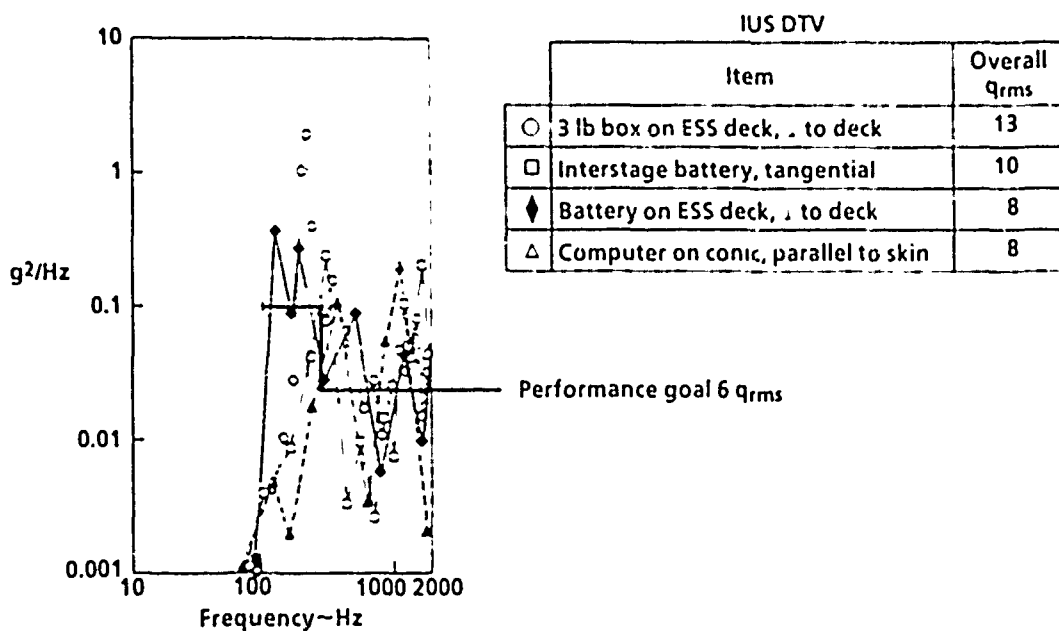
Figure 3.   Performance Goals for Redesigned DTV Compared With Baseline Vehicle Vibration

HB - 11
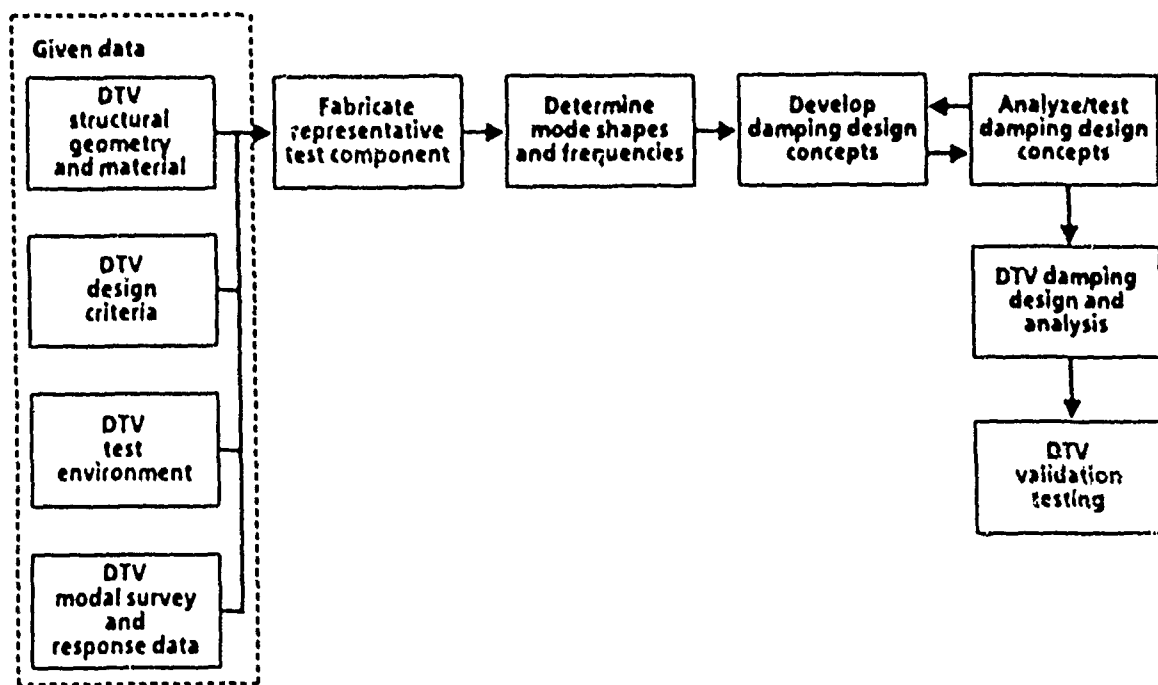
Figure 4. DTV Damping Design Methodology

- RELSAT Component Test Structure
  - Isolate Segment Between Two
    Spacecraft Support Longerons

    - ESS Frames
    - Spacecraft Interstage
    - 2nd Stage Motor Support Cone
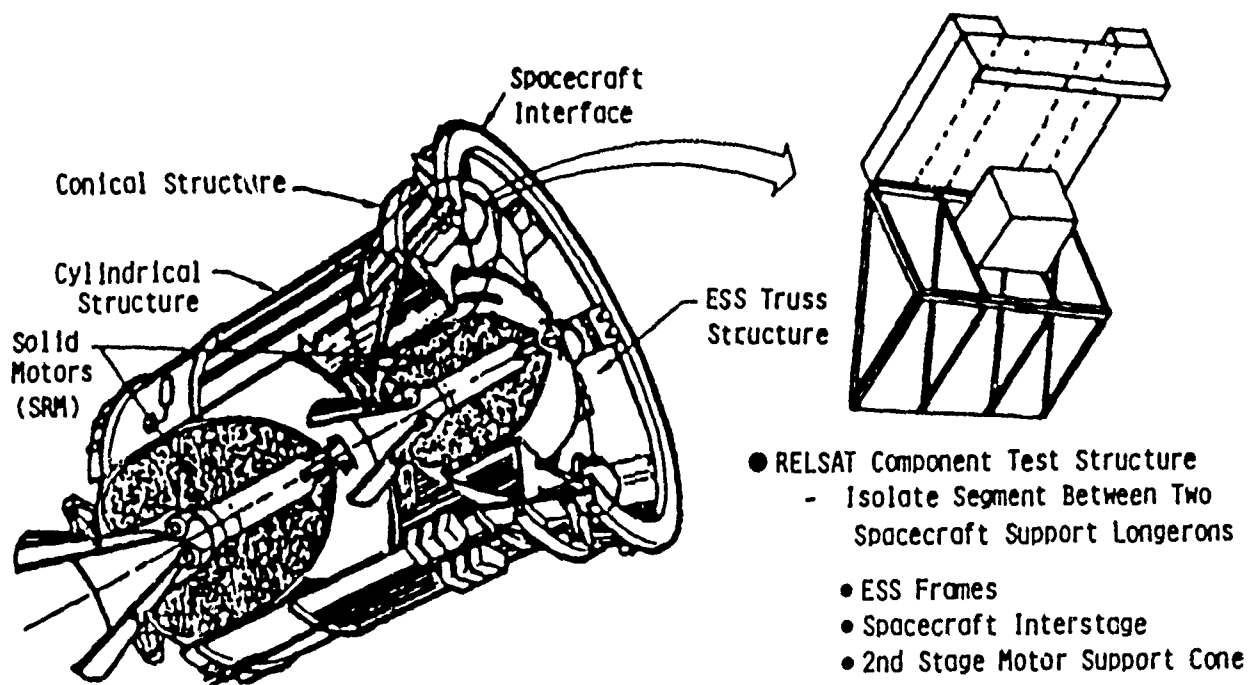
Figure 5. Component Test Structure for Developmental Testing

IUS RELSAT
TEST ASSEMBLY
Sk-830415
26 May 83
IR&D
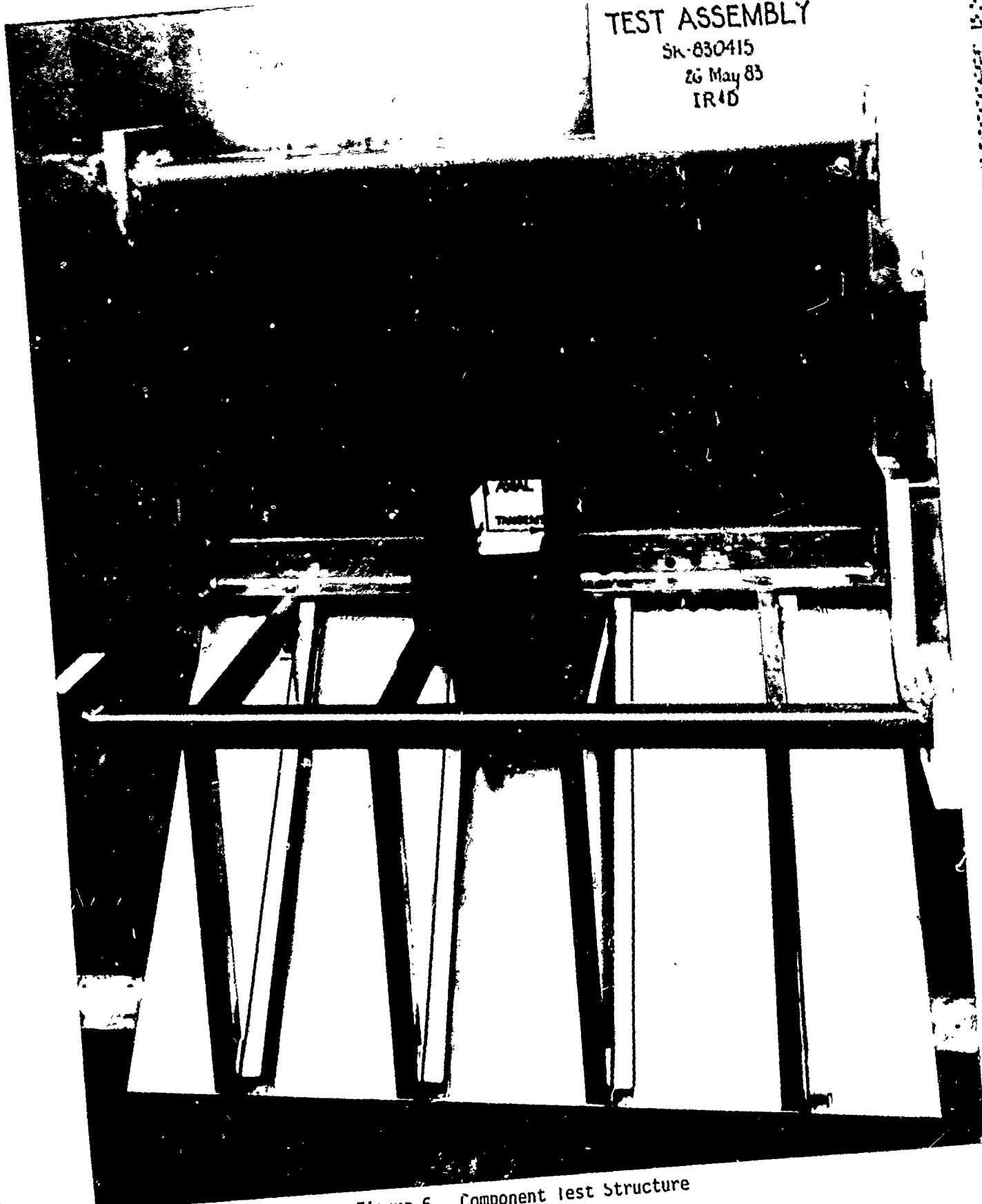
Figure 6.   Component Test Structure

HB - 13
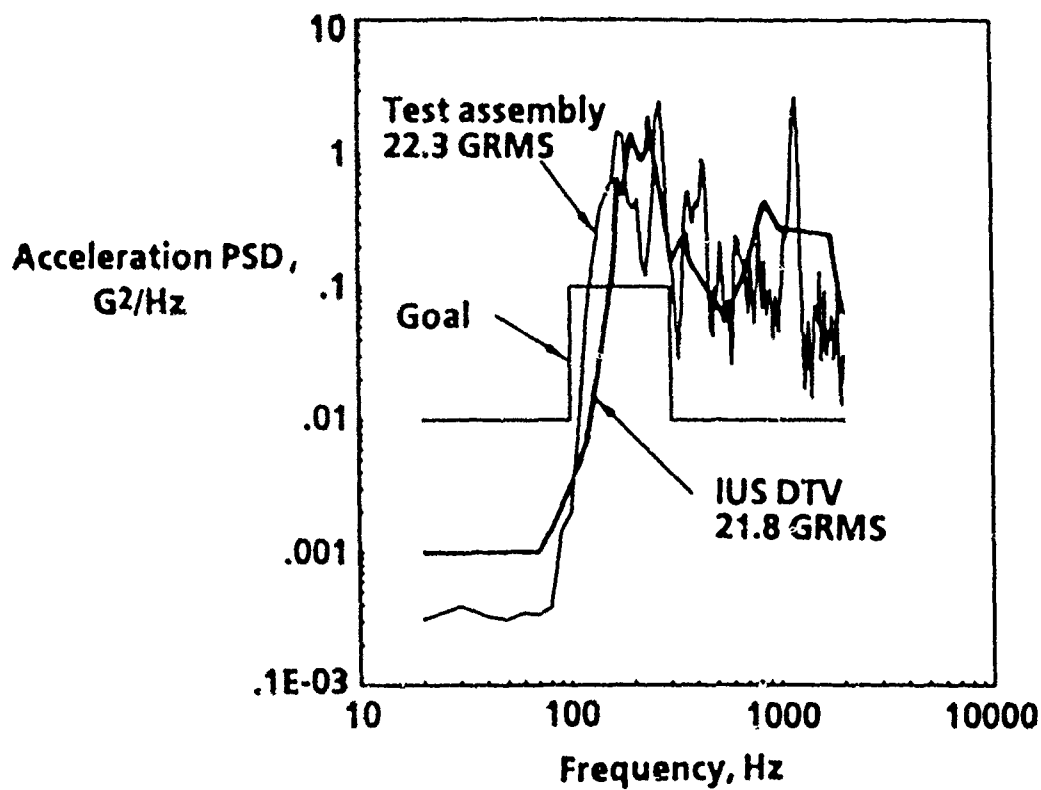
Figure 7. Comparison of Vibroacoustic Response of IUS DTV and Component Test Structure
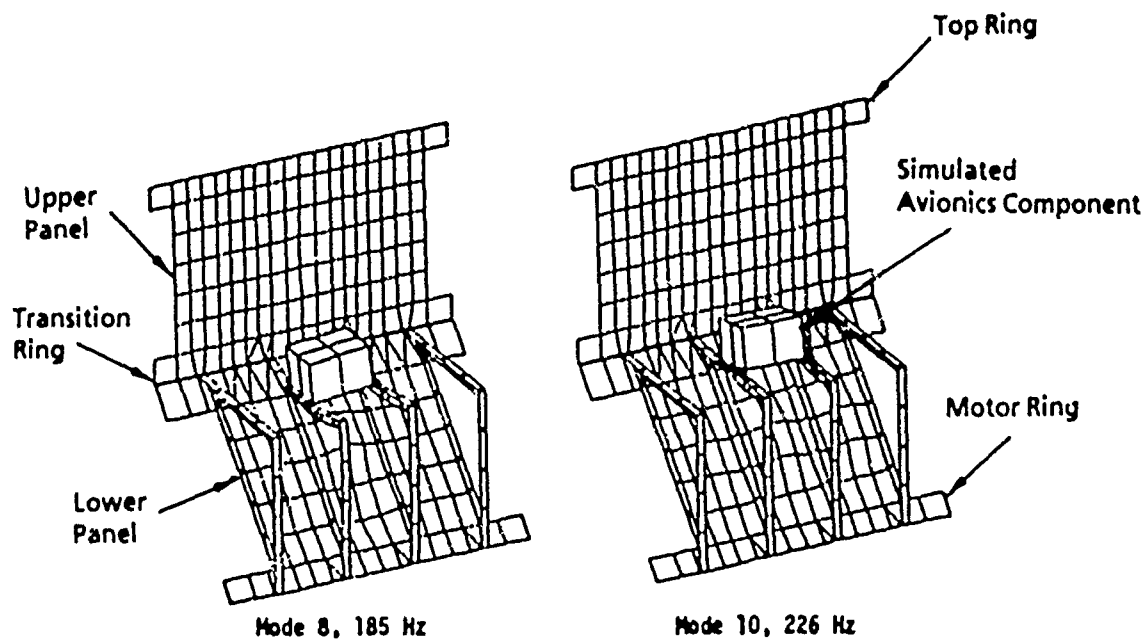
Figure 8. Representative Modes of Undamped Test Structure

HB - 14
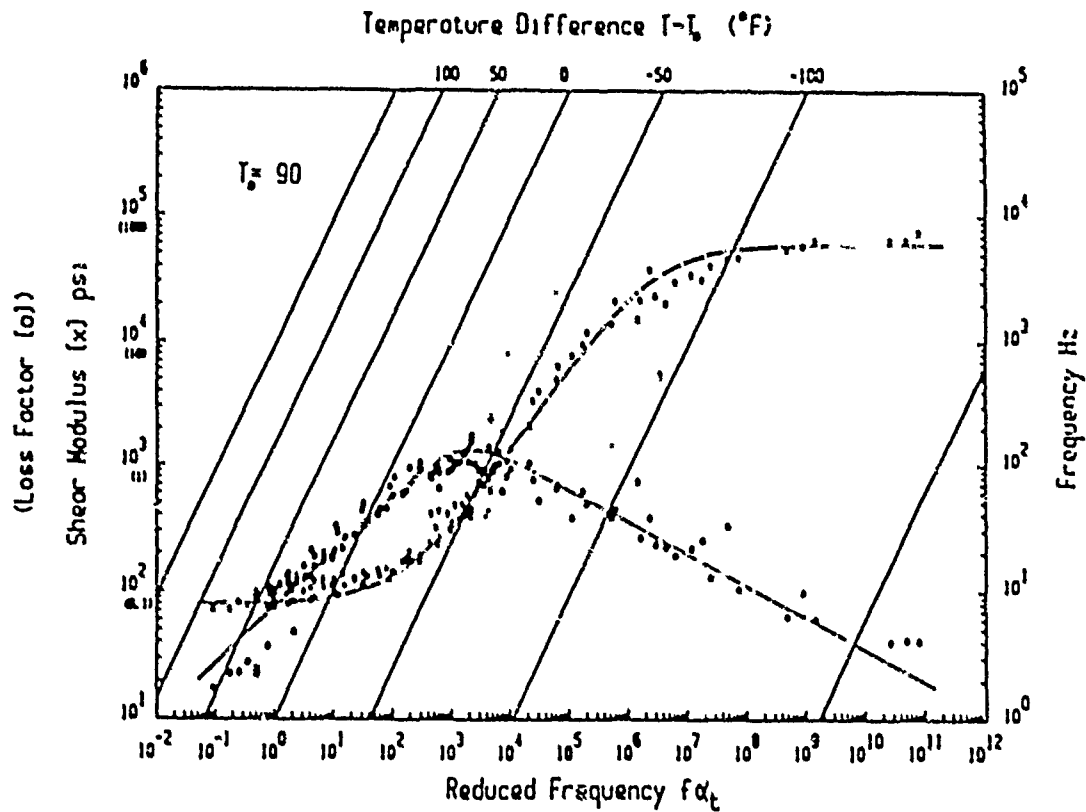
Figure 9. Dynamic Properties of 3M Y-966
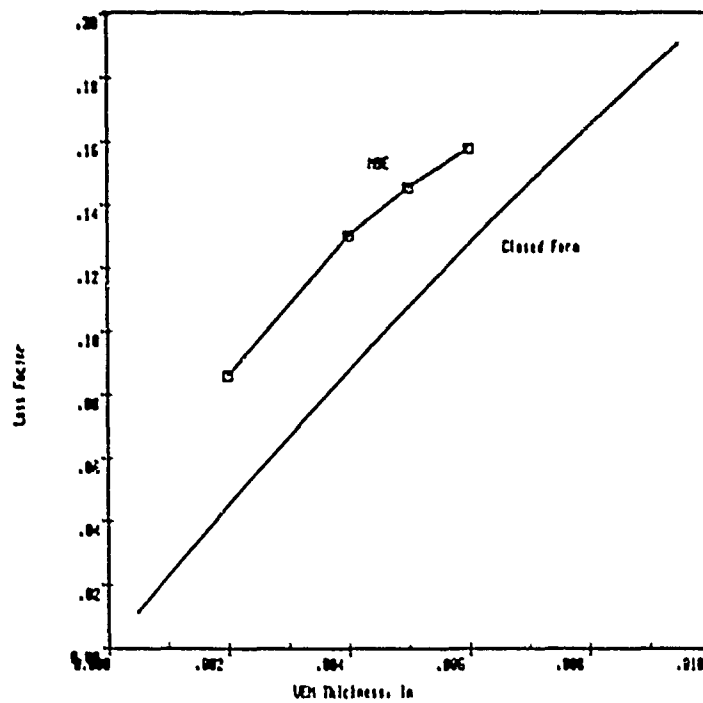
Figure 10. Results of Closed Form Analysis of a 10 inch Square Sandwich
Panel and MSE Analysis of Test Structure Upper Panel Section
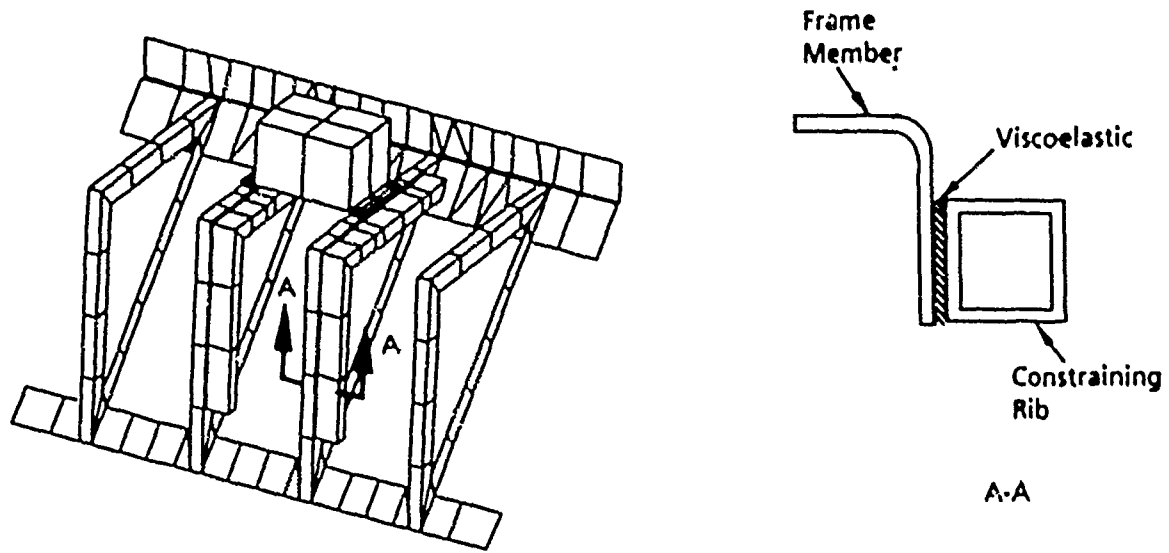
Figure 11. Constraining Rib-Type Frame Dampers
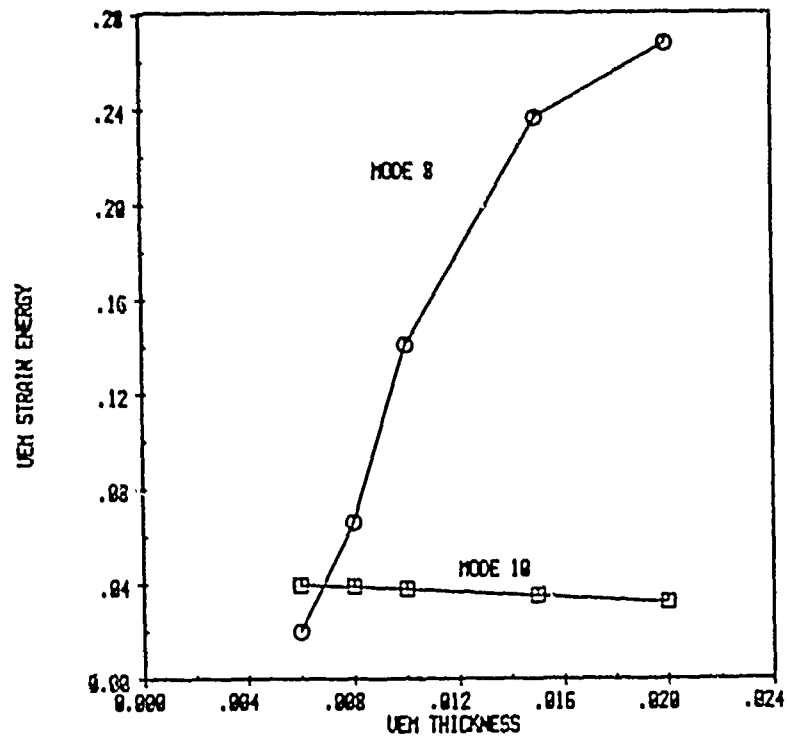
Figure 12. Strain Energy for Varying VEM Thickness and Rigid
Constraining Rib
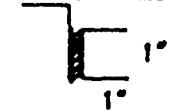
Cross Section	Wall Thickness	VEM Strain Energy Mode 8	VEM Strain Energy Mode 10
1″ / 1″	0.100	0.0319	0.0125
1″ / 0.5″	0.100	0.0548	0.0162
1″ / 1″	0.100	0.0652	0.0181
1″ / 1″	0.100	0.0865	0.0175
1″ / 1″	0.125	0.0946	0.0192
1″ / 1.5″	0.100	0.1133	0.0182
1″ / 1″	0.250	0.1245	0.0242

Table 2. Strain Energy for Several Constraining Rib Cross Sections
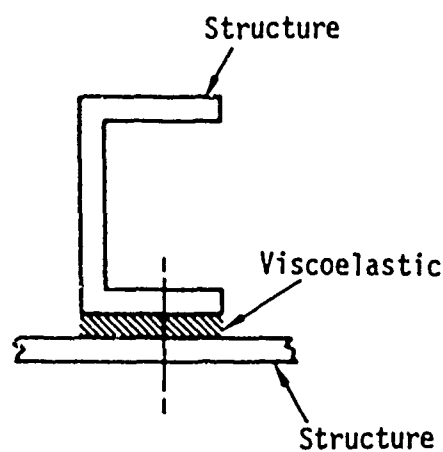
Figure 13. Interface Damping Treatment
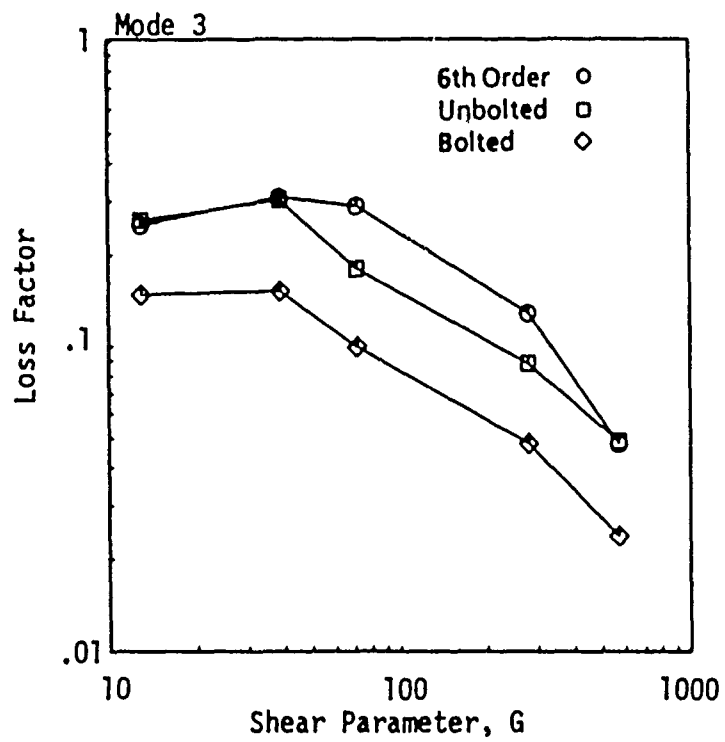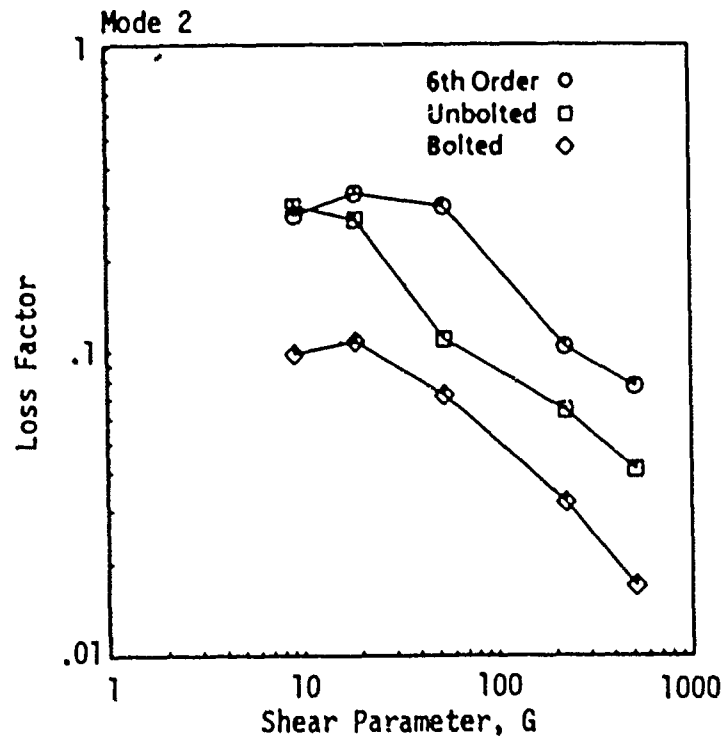
Figure 14. Loss Factors for Bolted and Unbolted Sandwich Beams
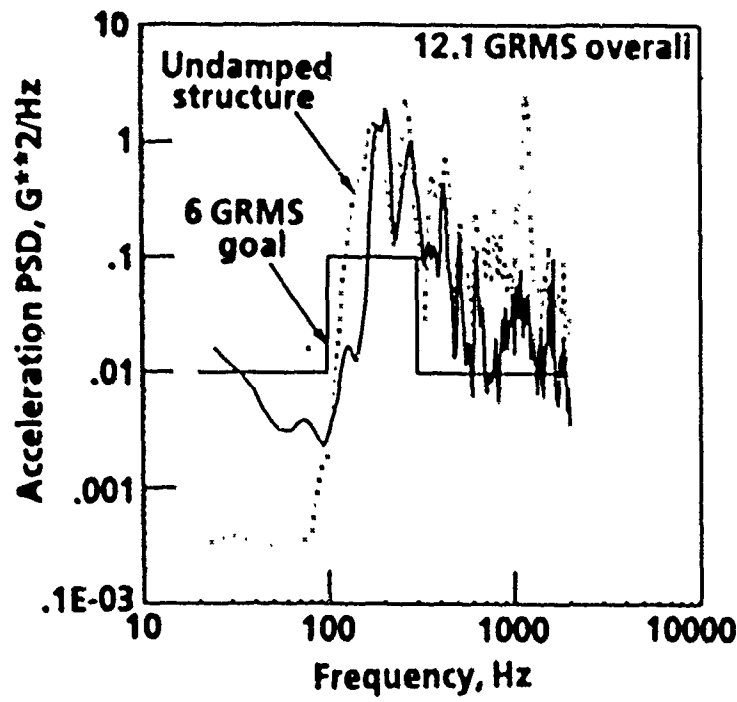
Figure 15. Acoustic Response with Sandwich Panel Damping
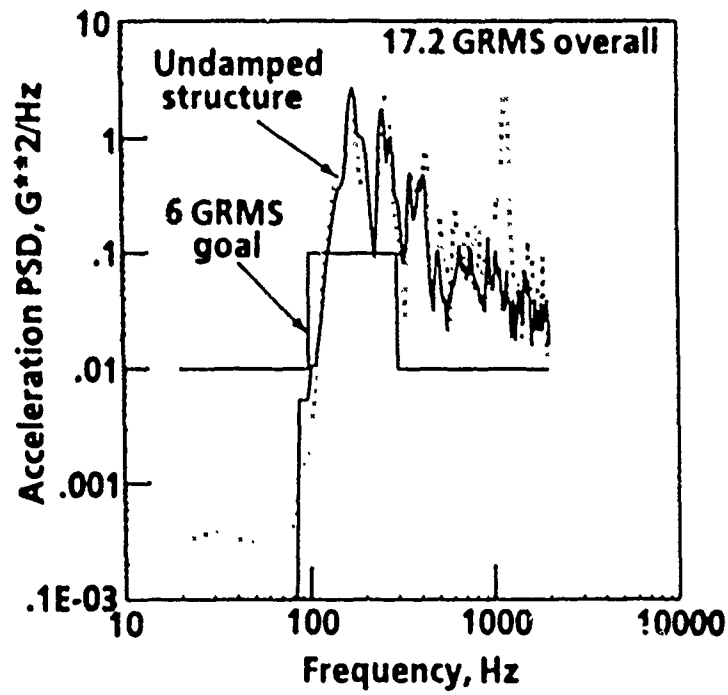
Figure 16. Acoustic Response with Interface Damping
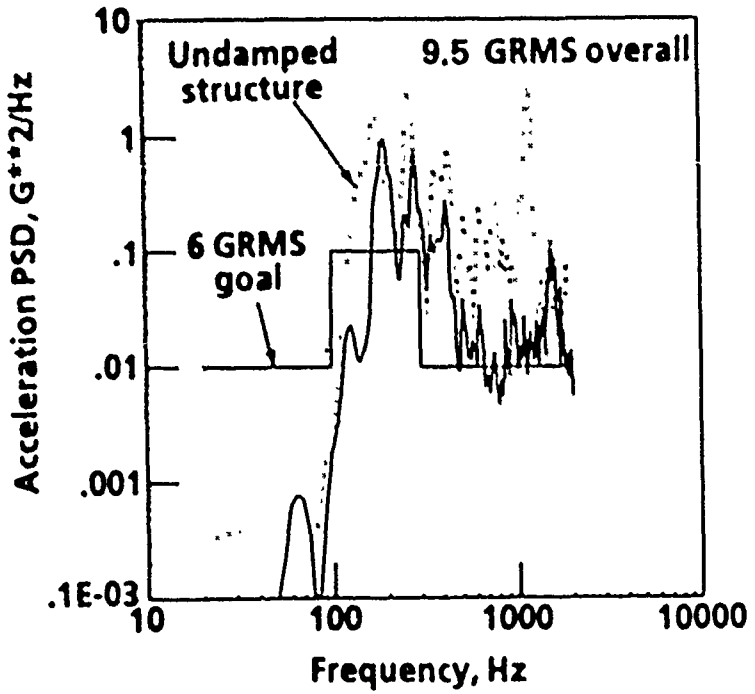
Figure 17. Acoustic Response with Sandwich Panels and Frame Dampers
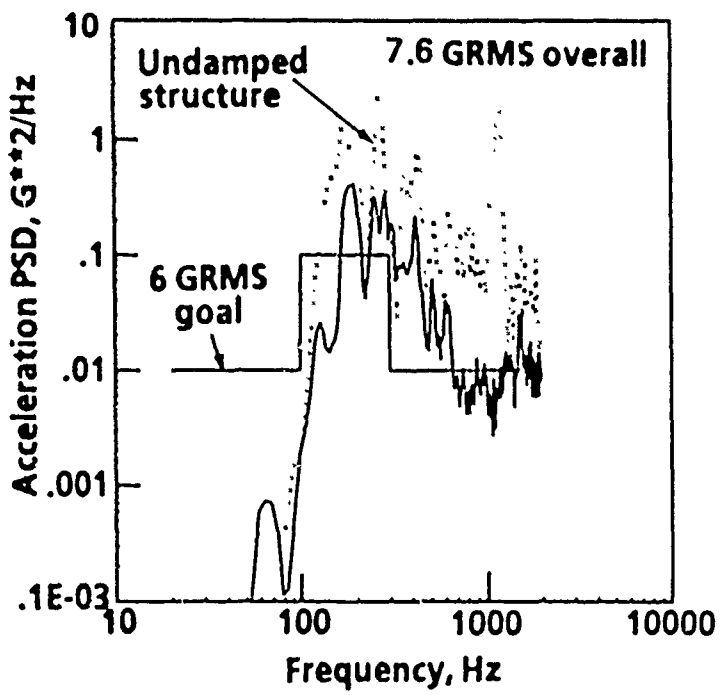
Figure 18. Acoustic Response with Sandwich Panels, Frame Dampers, and
Interface Damping

HB - 20

SHOCK AND VIBRATION ATTENUATION
IN VISCOELASTIC DAMPED STRUCTURE

Clark J. Beck, Jr.

Boeing Aerospace Company
Seattle, Washington

ABSTRACT

This paper presents the results of acoustic noise tests and pyrotechnic shock tests on space vehicle structure with and without viscoelastic damping. Vibration and shock spectra from the tests are compared to show attenuation provided by viscoelastic damping. Vibration levels were reduced by a factor of 2 or more. The shock was attenuated significantly. The damping treatments increased the weight between 0.5% and 5%.

INTRODUCTION

This report presents test data showing the attenuation of acoustic noise induced vibration in an aluminum structure treated with viscoelastic damping materials. Tests were also conducted to evaluate pyrotechnic shock attenuation in the damped structure. The test structure is representative of space vehicle aluminum structure. The structure was subjected to a 145 dB acoustic noise environment to provide vibration levels representative of current space vehicles. Pyrotechnic shock was simulated by dropping a steel ball onto the structure. Tests were conducted with and without damping treatment.

The shock and vibration response was measured with accelerometers placed at several locations on the structure. The accelerometer outputs were converted to acceleration power spectra and acceleration shock spectra. Comparison of the acceleration spectra from structure with and without damping treatment shows the effectiveness of the damping treatment over a broad frequency range.

This work was conducted as part of the RELSAT Program (RELiability of SATellite Equipment in Environmental Vibration). A description of the Boeing RELSAT Program is presented in the proceedings of the 1984 Vibration Damping Workshop[1]. The work was funded by the Air Force Wright Aeronautical Laboratories, Flight Dynamics Laboratory. Dr. Lynn Rogers and Mr. Robert Gordon are responsible for direction of the RELSAT Program.

TEST ARTICLE

The test article is an aluminum structure referred to as the RELSAT component test structure. A detailed description of the test structure is provided in Figure 1. Figure 2 is a closeup photograph of the test article. The RELSAT test structure represents a 34 degree segment of the Inertial Upper Stage (IUS) equipment support section (ESS) shown in Figure 3. The test article serves as a pilot model to demonstrate the effectiveness of various viscoelastic damping treatments in typical dynamic environments. The most promising treatments will be applied to the full IUS equipment support structure during the course of the RELSAT Program.

---

1. Application of Damping to Improve Reliability of IUS-Type Satellite Equipment - RELSAT Program, Proceedings of the 1984 Damping Workshop, (AFWAL-TR-84-3064), November 1984.

TEST CONFIGURATIONS

Four configurations of the RELSAT structure were tested. The configurations are referred to as DN, D1, D2 and D3. A description of each configuration follows.

DN - Nominal Damping

Configuration DN is the RELSAT structure as built without viscoelastic damping treatment. The damping is representative of a semi-monocoque riveted structure.

D1 - Add on Damper No. 1

Configuration D1 is the RELSAT structure with damping added to the lower panel and deck assembly, see Figure 4.

D2 - Add on Damper No. 2

Configuration D2 is the RELSAT structure with damping added to the upper panel, lower panel and deck assembly as shown in Figure 5.

D3 - Integral/Add on Damper

Configuration D3 is the RELSAT structure with integral damped panels and damping added to the deck assembly, Figure 6.

TEST DESCRIPTION

The test configurations were subjected to acoustic noise tests and pyrotechnic shock tests. The test setups and test instrumentation are described in the following paragraphs.

Acoustic Test Setup

The RELSAT test structure was installed in a massive steel test fixture. The structure and fixture were placed in a 16 ft. by 24 ft. by 20 ft. high reverberant acoustic test chamber.

Acoustic/Vibration Instrumentation

Accelerometers were attached to the test article at 4 locations. Three accelerometers were placed at each location (12 total) to sense acceleration in the axial, radial and tangential directions. Five (5) microphones were located around the test specimen to record the acoustic noise environment. The instrumentation locations are shown in Figure 7.

Shock Test Setup

The RELSAT test structure was installed in a massive steel test fixture. The pyrotechnic shock was simulated by dropping a 4 pound weight onto the longeron from a height of 24 inches.

Shock Instrumentation

Accelerometers were attached to the test article at 4 locations. Three accelerometers were placed at each location (12 total) to sense acceleration in three directions; axial, radial and tangential. The location schematic is shown in Figure 8.

TEST PROCEDURE

Acoustic Test Procedure

Three (3) test configurations (DN, D2 and D3) were subjected to a 145 db overall sound pressure level acoustic noise environment. Figure 9 shows the average 1/3 octave band sound pressure level spectrum for each test configuration. The spectra were obtained by averaging the output from five microphones. Each acoustic test was run for about 1 minute. The accelerometer and microphone outputs were recorded on magnetic tape throughout each test. All the bolts in the test structure were torqued prior to each acoustic test.

Shock Test Procedure

Three (3) test configurations were subjected to shock testing; DN, D1 and D2. At least 3 shocks were applied to each test configuration. Each shock was applied by dropping the 4 pound weight onto the longeron at the location shown in Figure 8. The accelerometer responses were recorded on magnetic tape. All the bolts in the test structure were torqued prior to application of the shocks on a new configuration.

DATA ANALYSIS

Sound Pressure Level

A one-third octave band sound pressure level spectrum was obtained from each microphone. Figure 9 shows the average spectrum for each test.

Acceleration Power Spectral Density

An acceleration power spectral density analysis was obtained from each accelerometer output for each test configuration. The analyses were performed on a Hewlitt Packard HP5451C analyzer using the following analysis parameters.

Frequency range	20 Hz to 2000 Hz
Bandwidth	10 Hz
Record Length	30 seconds
Spectral averages	64

Vibration Attenuation

The vibration attenuation due to the damping treatment was determined by calculating the square root of the ratio of the viscoelastic damped structure PSD to the PSD of the structure without viscoelastic damping.

Time Histories

The accelerometer outputs for each shock event were displayed as acceleration time histories.

Shock Spectra

A shock spectrum analysis was obtained for each of the shock events. The analyses were performed on an HP 5451C analyzer using the following analysis parameters.

Analyzer bandwidth	1/6 octave
Capture window	2 seconds
Maximum frequency	10,000 Hz
Damping	5% (Q = 10)

Shock Attenuation

The shock attenuation due to the damping treatment was calculated using the following relationship.

$$\text{Attenuation (db)} = 20 \log \text{ADN/ADA}$$

ADA = Acceleration response to shock for add on damper

ADN = Acceleration response to shock for nominal damping

TEST RESULTS

Acoustic Test

Both damping treatments significantly reduced the vibration level as evidenced by a comparison of Figures 10, 11 and 12. The overall acceleration levels were reduced by a factor of 2 for both the add-on-damper and the integral damper. The overall level is generally less than 6 grms for both dampers. The reduction of the overall level to 6 grms or less is one of the performance goals.

The add-on-damper was most effective at frequencies below 300 Hz while the integral damper was most effective above 300 Hz. Figures 13 and 14 show the damping trends for the add-on-damper and the integral damper at the component/deck interface.

The damping was accomplished with a weight increase of 2.3 pounds for the add on damper configuration, D2, and 0.2 pounds for the integral damping configuration, D3.

Shock Test

The test method produced consistent shock spectra as evidenced by the data shown in Figure 15. Note how the shock spectra from 3 different drop tests are almost identical.

Figure 16 contains a comparison of the RELSAT longeron response to shock versus the IUS longeron response to stage separation pyrotechnic shock. This comparison shows that the shock generated by dropping the weight on structure causes the same order-of-magnitude acceleration as stage separation shock.

The add-on-damping treatments provided significant shock attenuation in the axial and tangential directions at the equipment deck/component interface as shown in Figures 17 and 18. The attenuation varied with frequency and in some frequency ranges the additive damping caused a negative attenuation or increase in shock response relative to the undamped configuration. Add-on-damper number 1 (D1) was most effective at low frequencies (below 1000 Hz) while add-on-damper number 2 (D2) was more effective above 1000 Hz. Neither add-on-damper improved shock attenuation in the radial direction, Figure 19.

CONCLUSIONS

1. Both damping treatments evaluated during these tests reduced the noise induced vibration level by a factor of 2. The add-on-damper is most effective at frequencies below 300 Hz. The integral damper is most effective at frequencies above 300 Hz.

2. Both damping treatments reduce the mean overall grms vibration at the component/deck interface to a level which meets the RELSAT performance goal of 6 grms. Vibration spectra peaks for the damped structures do not fall within the RELSAT performance goal over the test frequency range, but the peaks are significantly lower than the undamped structure.

3. Structural response to pyrotechnic induced shock can be reduced by the use of viscoelastic add-on-dampers. Attenuation in the order of 6 dB relative to nominally damped structure was achieved during these tests. The attenuation varied as a function of frequency and direction of structural response. Unfortunately the addition of the damping material magnified the structural response in some frequency bands.

4. The add-on-damping treatment increased the structure weight by 2.3 pounds for a 5% weight increase relative to the test article weight. The integral damping treatment increased the structure weight by 0.2 pounds or a 0.5% weight increase relative to the test article weight.
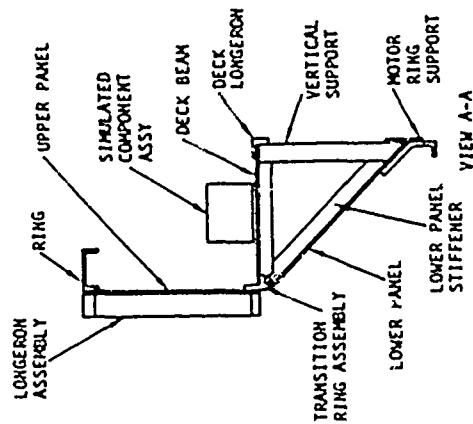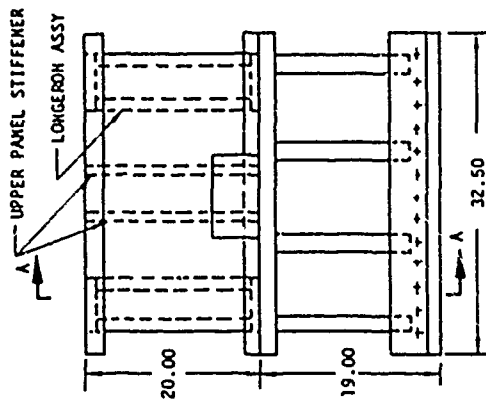
COMPONENT	REQD	DESCRIPTION	MATERIAL
RING	1	⊔ SHAPE, 0.25 THICK 2.25 X 6 X 32.5	△
LONGERON ASSEMBLY	2	END PLATES (2)6 X 2.25 X 0.80 CHANNELS (2) 0.25 THICK 1.3 X 2.25 X 18.2	△
UPPER PANEL STIFFENER	2	⊔ SHAPE, 0.100 THICK 0.87 X 1.25 X 19.9	△
UPPER PANEL	1	0.032 X 20 X 32.50	△
TRANSITION RING ASSEMBLY	1	A|B 0.25 THICK, X 32.50 A = 3.5 B = 2.0 C = 3.8	△
DECK BEAM	4	L SHAPE, 0.100 THICK 1.25 X 1.25 X 15.0	△
DECK LONGERON	1	L SHAPE, 0.100 THICK 2.25 X 1.25 X 32.5	△
VERTICAL SUPPORT	4	L SHAPE, 0.100 THICK 0.88 X 1.25 X 15.5	△
LOWER PANEL STIFFENER	4	⊔ SHAPE, 0.100 THICK 0.88 X 1.25 X 21.5	△
LOWER PANEL	1	0.032 X 21.5 X 32.5	△
MOTOR SUPPORT RING ASSEMBLY	1	A|B A = 0.100 X 6.2 X 32.5 B = 0.100 X 2.3 X 32.5	△
SIMULATED COMPONENT ASSEMBLY	1	BLOCK, 4 X 5 X 6.5 PLATE, 0.1 x 5 X 8.3	WOOD ALUMINUM

Notes:

△ All dimensions in inches.

△ 7/16 Dia. bolt/nut fasteners, class lll holes, spacing.

△ See SK830415 for detailed drawing.

△ 6061-T4 Aluminum

△ Structure weight 42.5 pounds

△ Simulated component assembly weight 3.5 pounds

FIGURE 1
TEST STRUCTURE DETAILS

IUS RELSAT
TEST ASSEMBLY
SK-630415
26 May 83
IR⅟10

FIGURE 2
RELSAT TEST STRUCTURE
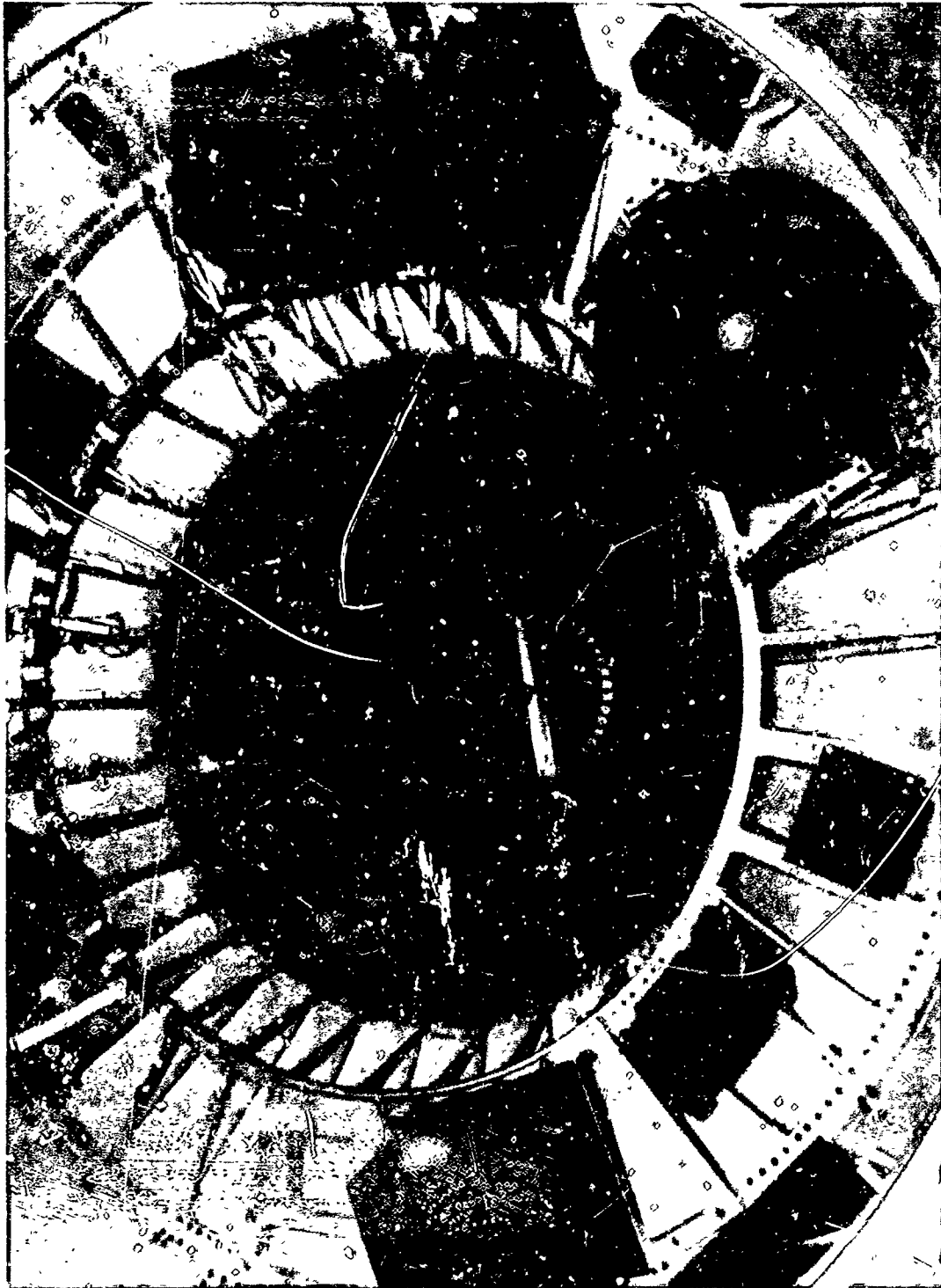
FIGURE 3
IUS EQUIPMENT SUPPORT SECTION
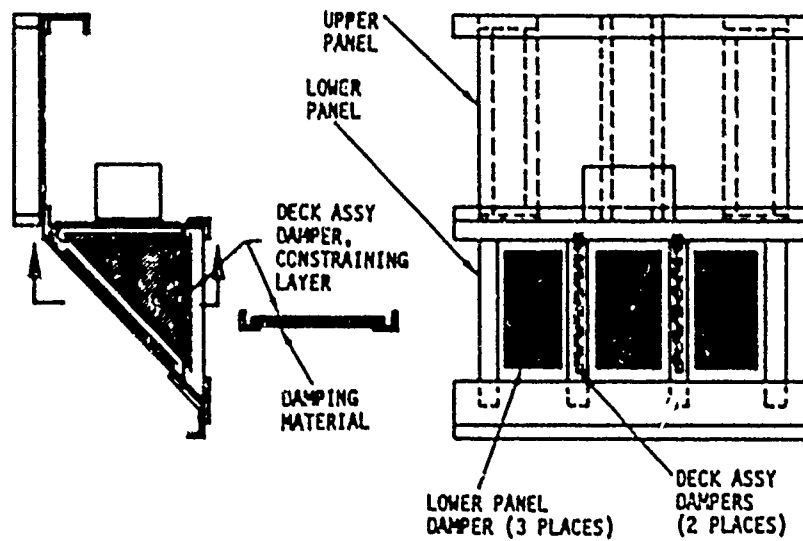
DAMPER	CONSTRAINING LAYER	DAMPING MATERIAL
LOWER PANEL	0.38 IN HONEYCOMB 5.0 X 10.0	0.010 LAYER OF ISD 112
DECK ASSY	0.38 IN HONEYCOMB 13.0 X 13.0 X 19.0	4 LAYERS, ISD 113 TOTAL 0.020 TO 0.030

All dimensions are in inches

FIGURE 4

ADD ON DAMPER D1
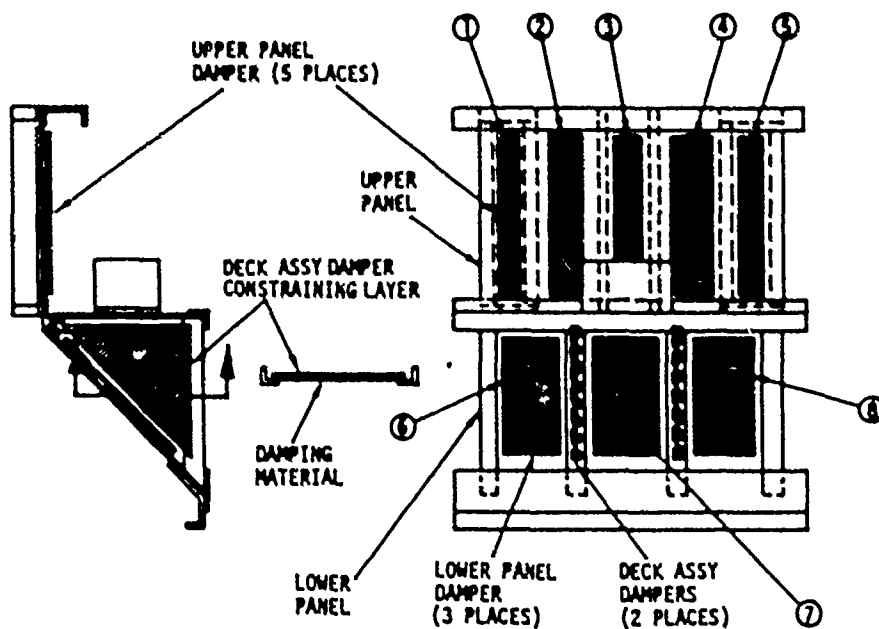
DAMPER	CONSTRAINING LAYER	DAMPING MATERIAL
DECK ASSY	0.38 IN HONEYCOMB 13.0 X 13.0 X 19.0	4 LAYERS, ISD 113 0.02 TO 0.03 TOTAL
PANEL ① · ② · ④ · ⑤	0.040 IN ALUMINUM 4.0 X 14.0	0.005, ISD 112
PANEL ③ · ⑥ · ⑦ · ⑧	0.040 IN ALUMINUM 6.0 X 14.0	0.005, ISD 112

All dimensions are in inches

FIGURE 5

ADD ON DAMPER D2
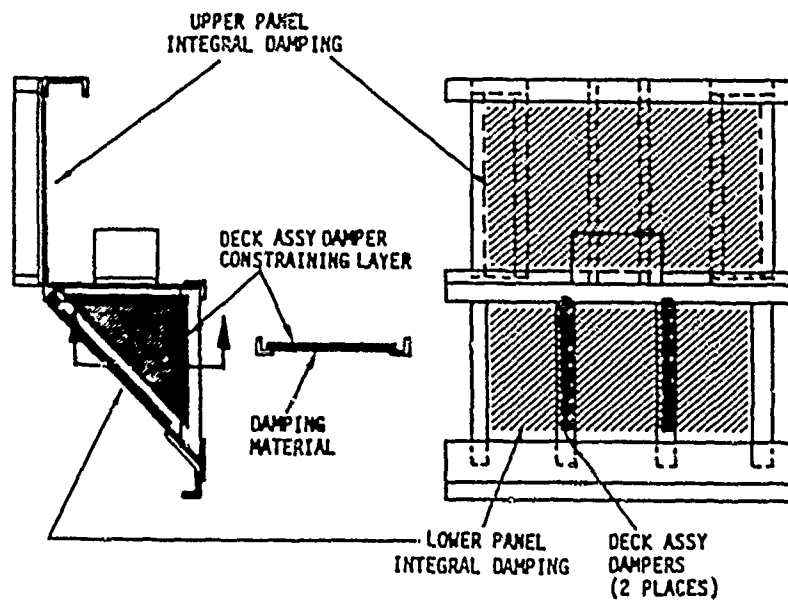
UPPER AND LOWER PANEL DAMPING	2 OUTER ALUMINUM SHEETS 0.016 THICK 0.002 THICKNESS OF XETHS L-35 BETWEEN THE SHEETS

DECK ASSY DAMPER	CONSTRAINING LAYER	DAMPING MATERIAL
	0.38 IN HONEYCOMB 13.0 X 13.0 X 19.0	4 LAYERS, ISD 113 0.02 TO 0.03 TOTAL

All dimensions are in inches

FIGURE 6

INTEGRAL/ADD ON DAMPER D3

SIMULATED
COMPONENT

ESS DECK

AXIAL(Z)

RADIAL(X)

VIEW A-A

A

AXIAL(Z)

TANGENTIAL(Y)

A
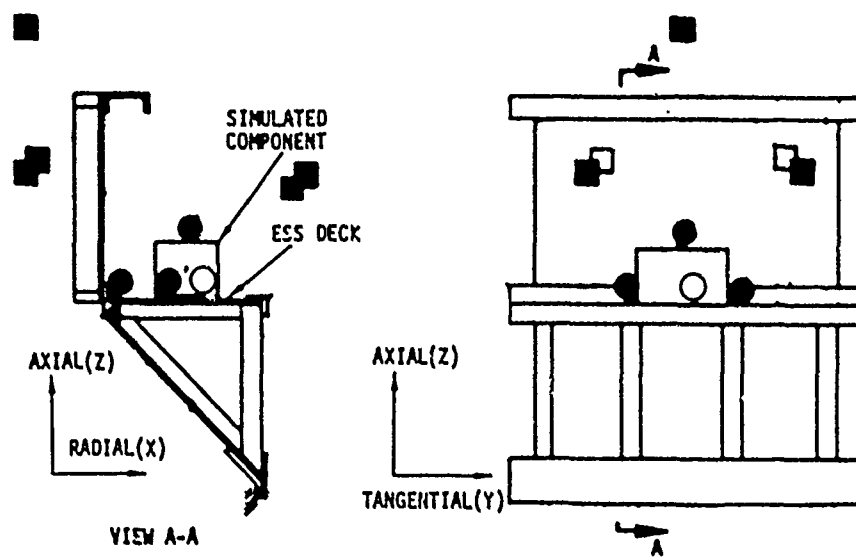
● ○ ACCELEROMETER LOCATIONS

■ □ MICROPHONE LOCATIONS

FIGURE 7

ACOUSTIC/VIBRATION INSTRUMENTATION
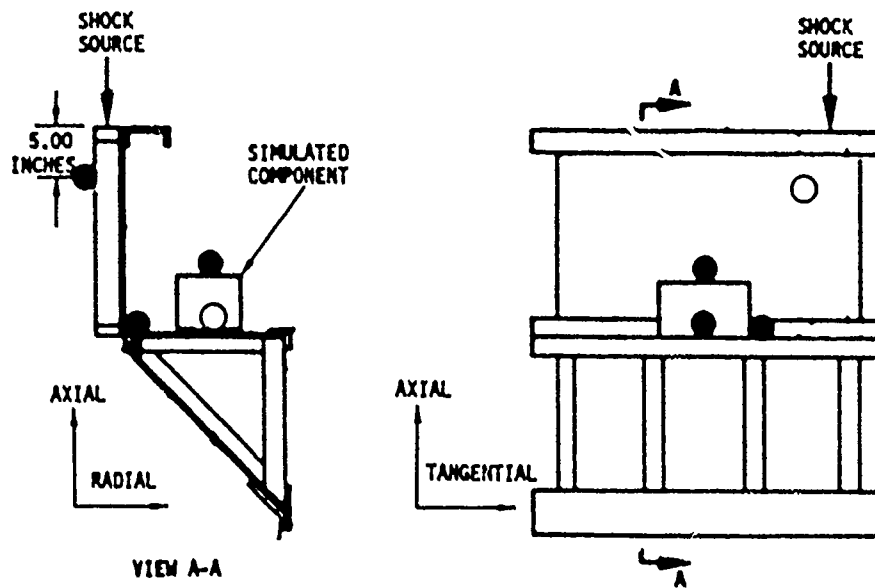
● ○ ACCELEROMETER LOCATIONS

FIGURE 8
SHOCK INSTRUMENTATION
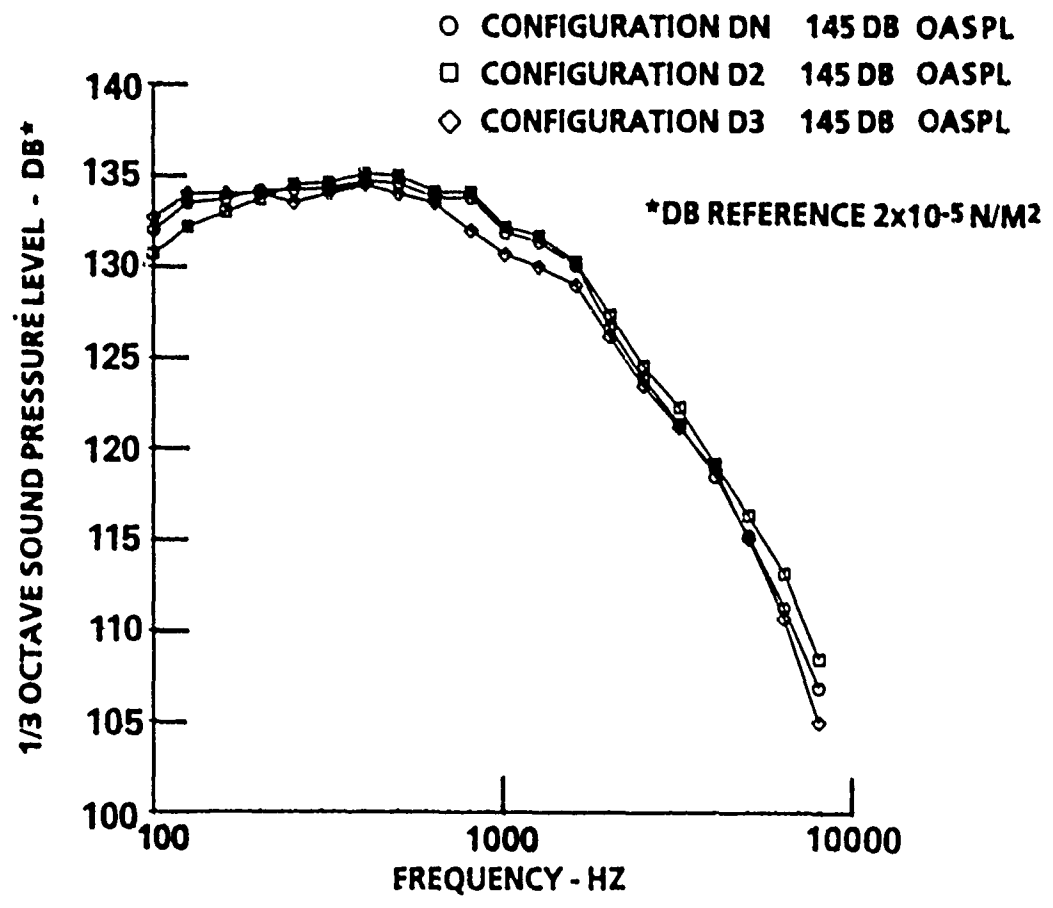
FIGURE 9
ACOUSTIC NOISE SPECTRA
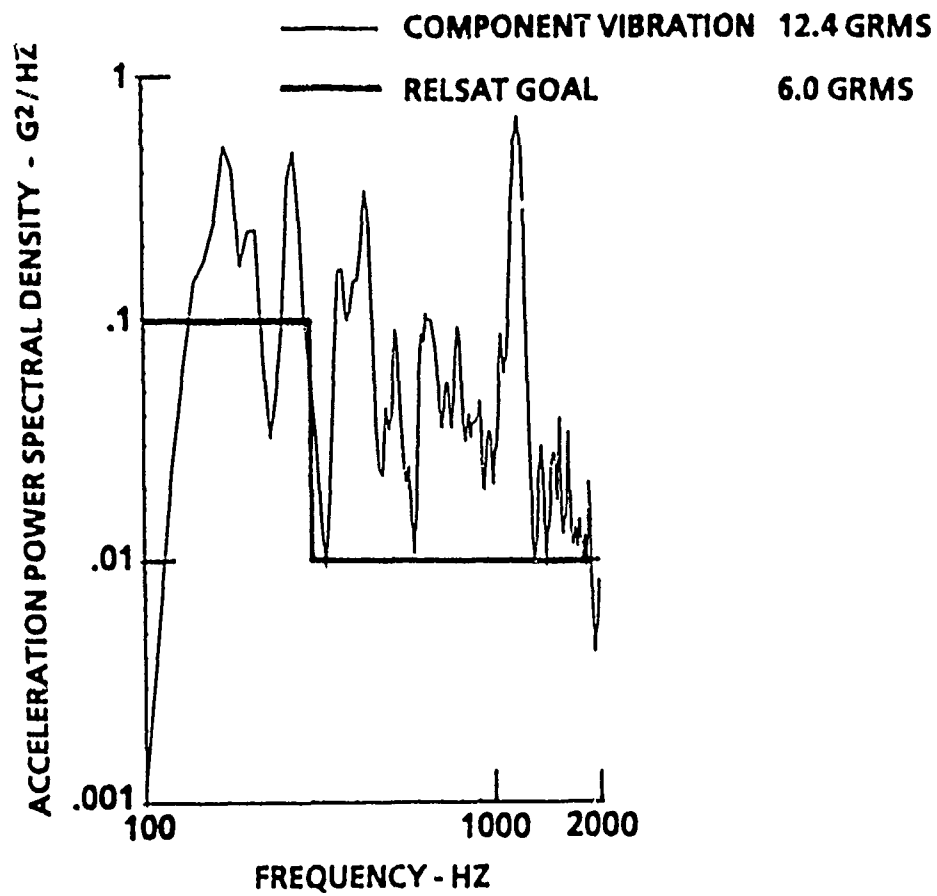
FIGURE 10

VIBRATION WITHOUT VISCOELASTIC DAMPING , DN
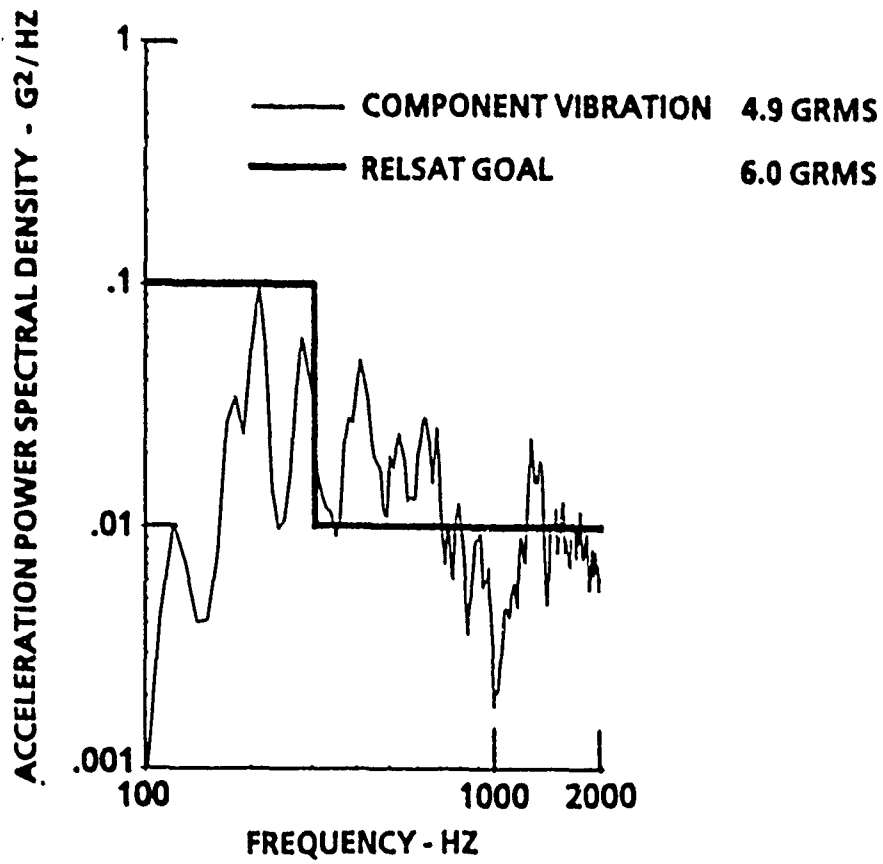
FIGURE 11

VIBRATION WITH ADD ON DAMPER, D2
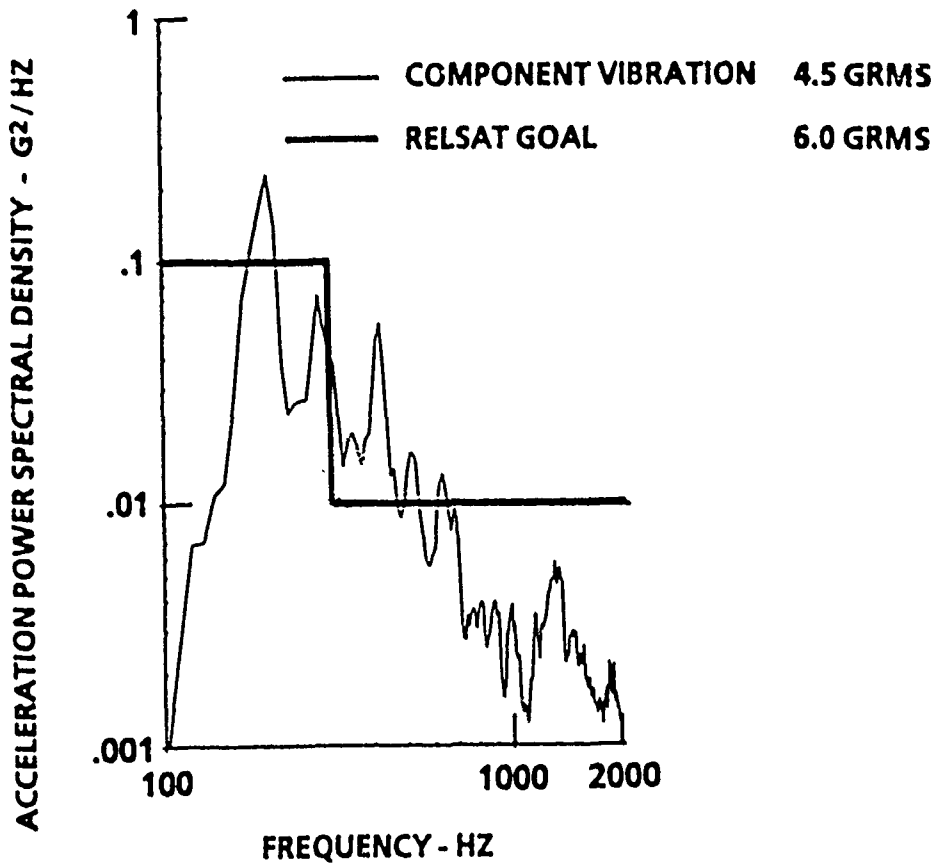
FIGURE 12
VIBRATION WITH INTEGRAL DAMPER , D3
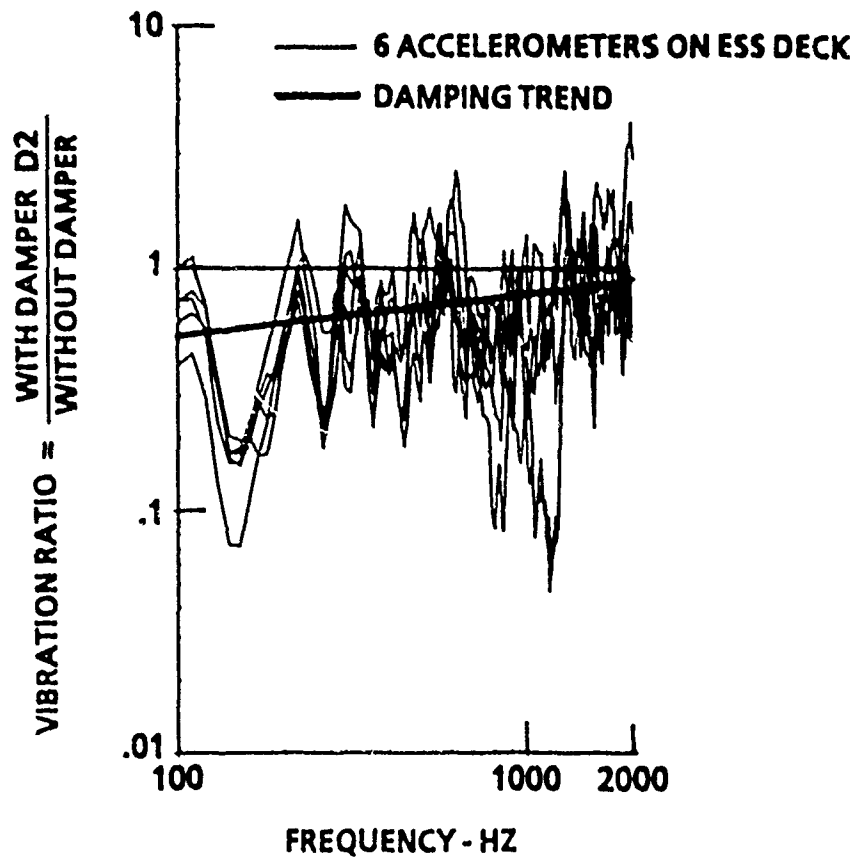
FIGURE 13
DAMPING TREND, ADD ON DAMPER, D2
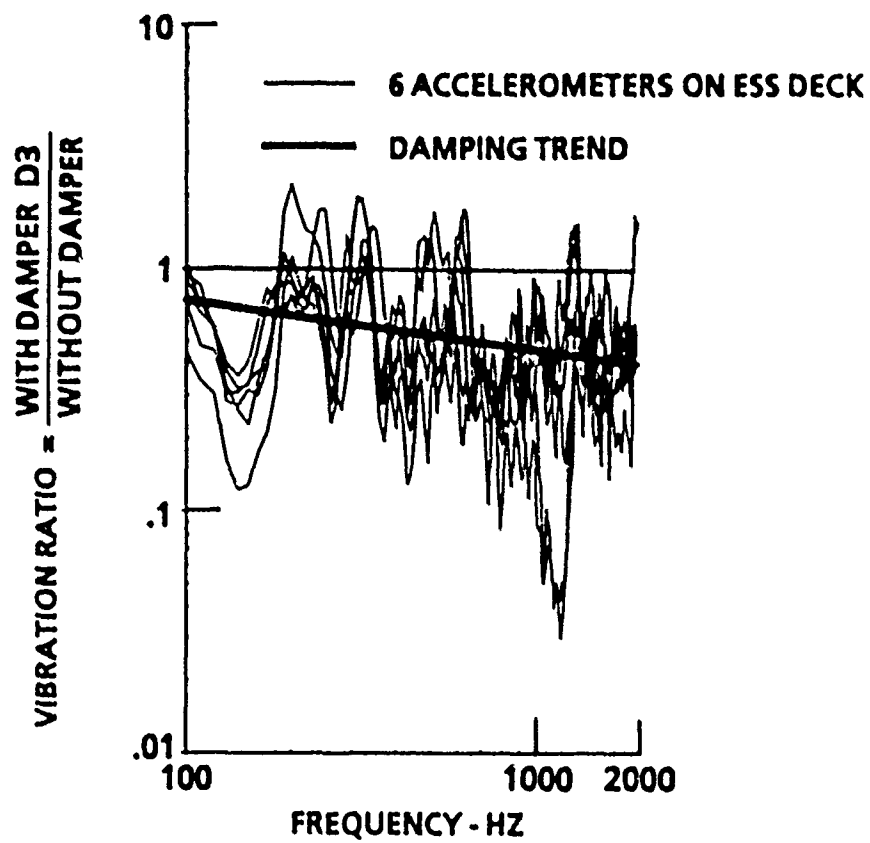
FIGURE 14
DAMPING TREND, INTEGRAL DAMPER, D3
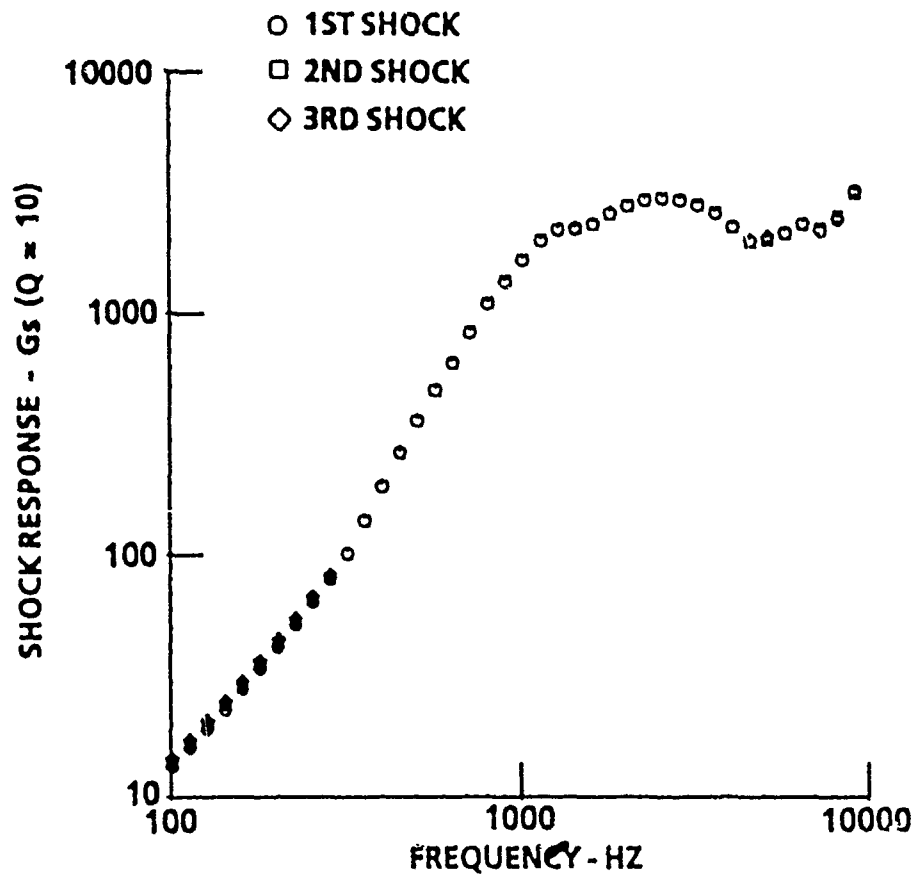
FIGURE 15
SHOCK SPECTRA REPEATABILITY
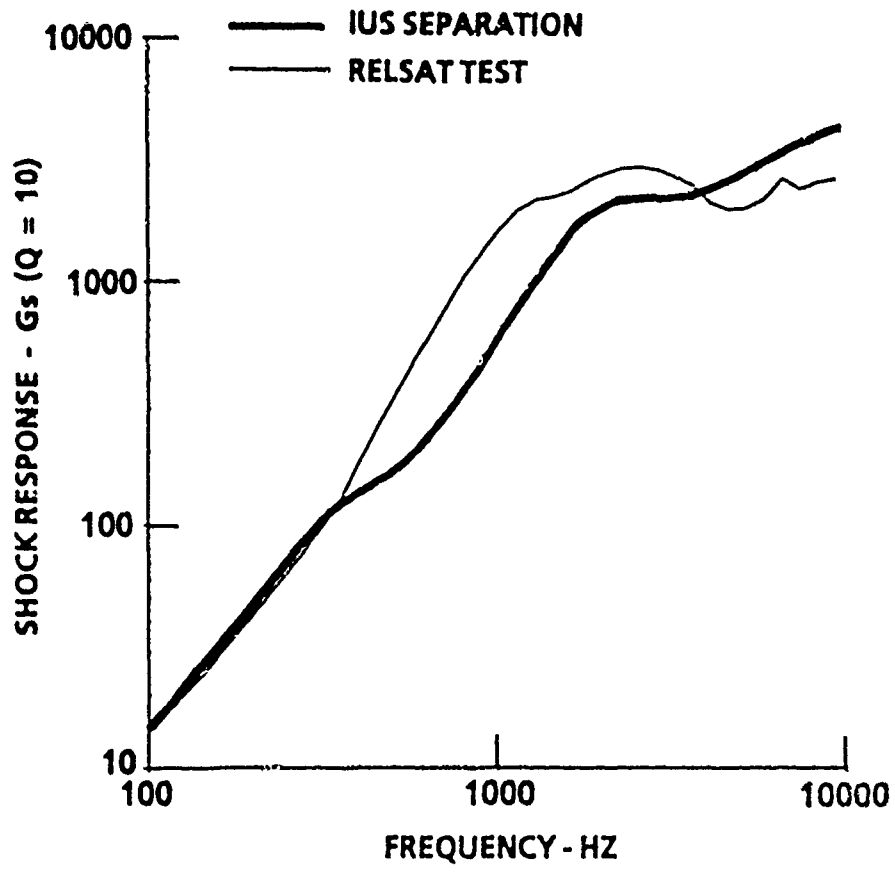
FIGURE 16
SHOCK RESPONSE COMPARISONS
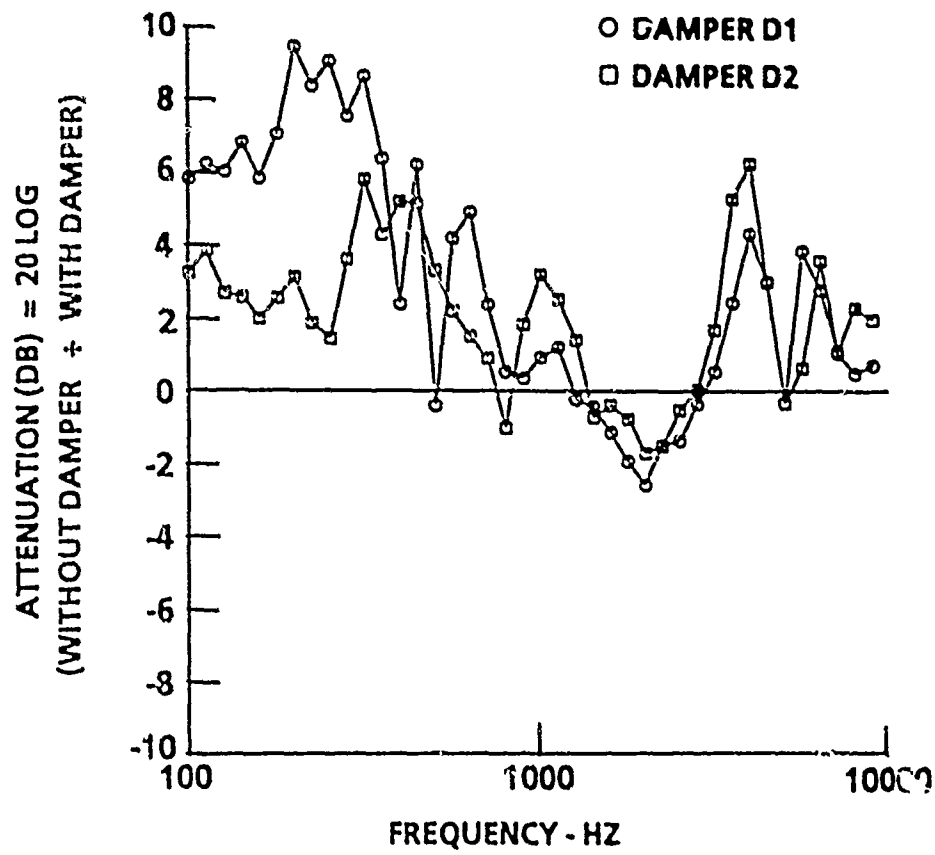
FIGURE 17
AXIAL SHOCK ATTENUATION
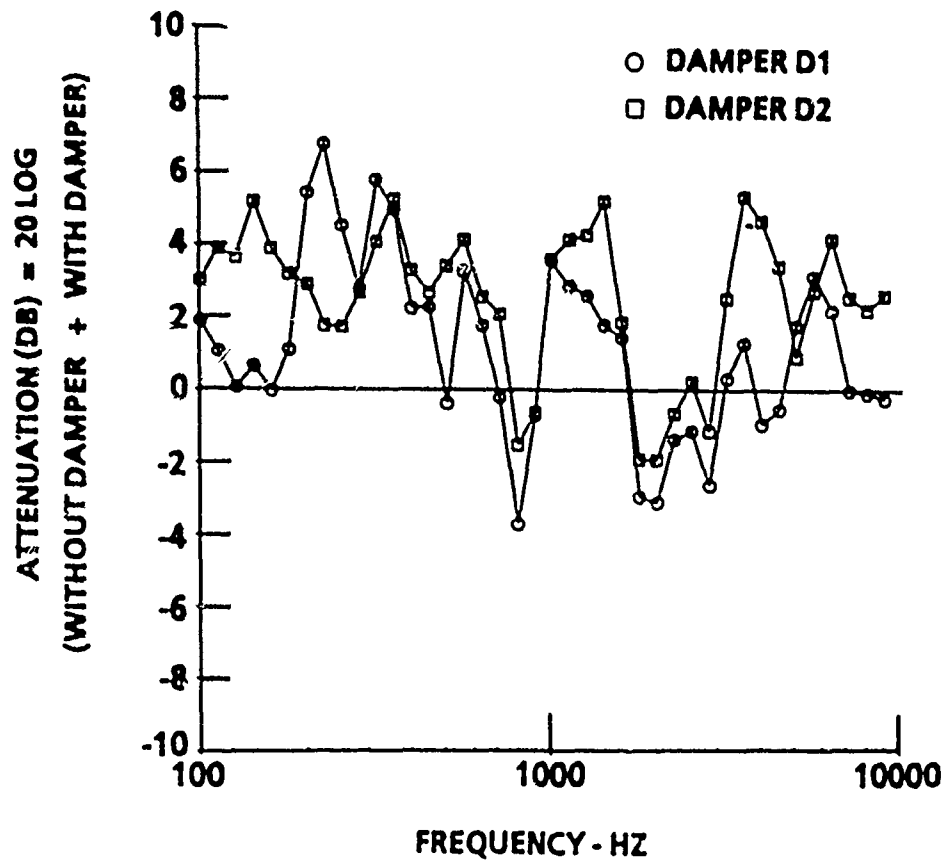
FIGURE 18
TANGENTIAL SHOCK ATTENUATION
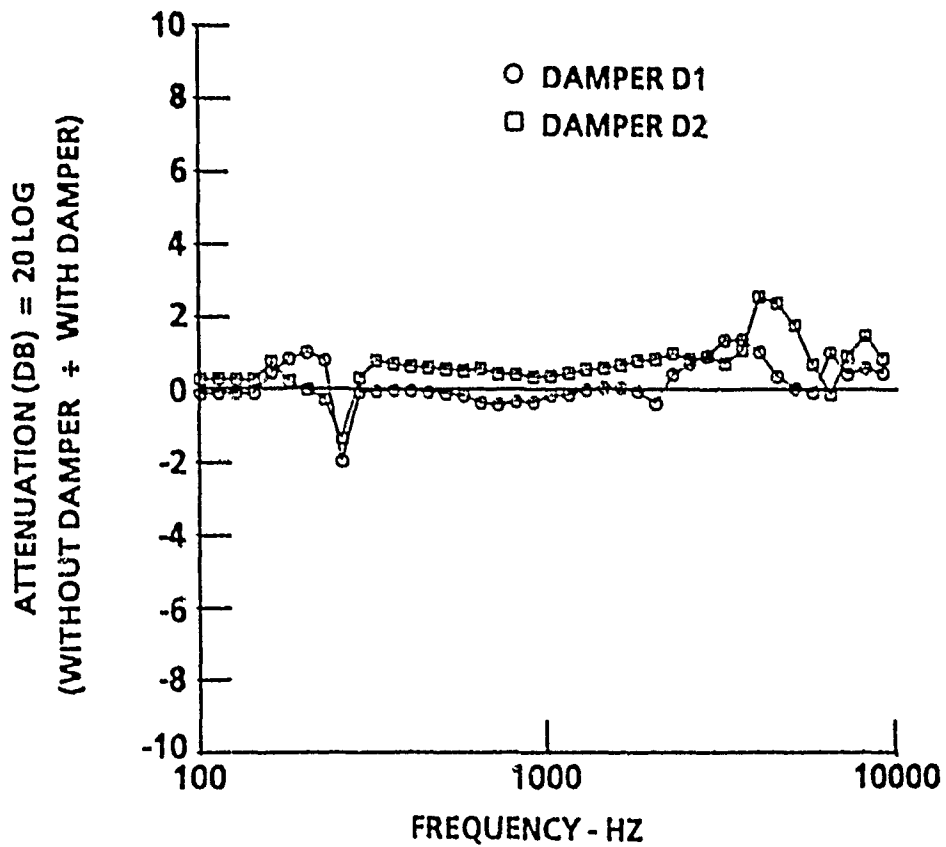
FIGURE 19
RADIAL SHOCK ATTENUATION

VIBROACOUSTIC AND SHOCK PERFORMANCE OF
DAMPED SPACECRAFT EQUIPMENT PANELS*

by

C. V. Stahle, J. A. Staley, and J. C. Strain

General Electric Space Systems Division

ABSTRACT

This paper presents performance results for viscoelastically damped satellite
equipment panel designs. Results show that launch vibroacoustic response
acceleration power spectral densities at component mounting locations are
reduced by up to 20 dB by damped panel designs. Corresponding derived
component random vibration test specification PSDs are reduced by about 13 dB
by damped panel designs. Component RMS response levels for the specifications
for damped panels are predicted to be reduced by over 50 percent compared to
baseline undamped panel designs based on a random response spectrum prediction
method. Damped panel designs showed low hysteresis under application and
removal of static loads. Test data show that viscoelastic material which had
been in space for about four years maintained good damping and stiffness
properties compared to materials which had not been in space. Viscoelastic
damping treatments appear applicable to alignment critical structures because
of low hysteresis under load application and removal and good property
stability under long term space vacuum exposure. Results shown demonstrate the
validity of methods used to design and fabricate viscoelastically damped
satellite equipment panels.

1.0 INTRODUCTION

Figure 1 shows a summary of the General Electric RELSAT program objective, approach and expected payoffs. The RELSAT program is aimed at improving satellite reliability by reducing satellite equipment failures due to effects of the launch vibroacoustic environment. The specific objective is to demonstrate the use of passive damping to control vibration of panel mounted equipment during launch. The approach is to design, fabricate, and test damped panels corresponding to Bay 3 of the DSCS (Defense Satellite Communication System) III Transponder Panel. This effort involved three major tasks: 1) evaluation of candidate damping material characteristics; 2) development and implementation of design concepts based on selected viscoelastic materials (VEMS); and 3) performing vibration, acoustic, static, and shock tests to evaluate the performance of damped equipment panel design concepts. This paper presents some of the performance results from the third task. Results from the first two tasks are reported in two other papers.[1,2] The payoffs which are expected to result from development of damped panel designs for satellite equipment panels include: 1) improved stability and pointing accuracy for alignment critical items which might be sensitive to effects of onboard disturbances and maneuvers; 2) a 20 percent increase in the satellite reliability on orbit as a result of a 50 percent reduction in the component vibroacoustic environment during launch; 3) a reduction in the potentially large number of ground test failures by 50 percent; and 4) a reduction of the spacecraft system development and operating cost by an estimated $40 million for a system consisting of a total of 14 DSCS III type satellites with a constellation of four satellites on orbit at any given time.

Figure 2 shows several key points relative to the RELSAT program. The DSCS III spacecraft shown is the system selected as the basis for the demonstration program. It is an Air Force communication satellite. Four are in geosynchronous orbit at any given time to give global communication coverage. The specific test article selected for study was Bay 3 of the DSCS III Transponder (North) panel. This bay has three 10 watt Traveling Wave Tube Amplifiers (TWTAs) and several smaller components mounted on it. Bay 3 is about 2 ft by 2 ft square and weighs about 50 lb including components and structure. The baseline panel structure consists of a magnesium base plate with two stiffeners. The design requirements for the panel include interdisciplinary constraints such as the need to radiate waste heat from the TWTAs through the base panel to space. Optical Solar Reflectors (OSRs) are mounted on the space side of the panel for solar radiation reflection and survivability. The panel must also have the structural integrity to withstand the steady state and low frequency accelerations during the launch phase. The center of Figure 2 shows a typical reduced temperature nomogram[3] for a VEM which might be considered for design of a damped equipment panel for the baseline DSCS III. The nomogram shows VEM shear modulus and damping properties as a function of frequency and temperature. An important requirement for VEMS for satellite applications is that they be space compatible, i.e., have low outgassing characteristics.[4] Figure 2 also indicates that the ultimate objective of the demonstration program is to develop damped stable platforms for satellite equipment and to develop damped stable platforms for satellite equipment and to demonstrate the technology for design and manufacture (fabrication) of such platforms.

2.0 DAMPING PAYOFFS

The interest in providing damping in satellite equipment panels has resulted from a history of failures after launch of a satellite and during ground development and production testing of a satellite, its subsystems, and its components. A significant number of spacecraft anomalies have been related to the launch vibration environment.[5] Figure 3 shows flight failures or malfunctions vs days after launch. Figure 3 also shows that about 40 percent of these are related to vibration. A reduction of these failures from 40 to about 20 percent and a corresponding reduction in ground test failures is expected to result in a total savings of about $40 million for a complement of 14 DSCS III type satellites. Vibration is also a major cause of failures occurring during ground environmental tests of spacecraft, its subsystems, and its components. Figure 4 shows that during design qualification, 64 percent of failures were related to vibration.[6] Following qualification of the satellite design, 30 percent of failures in production acceptance tests were vibration related. With damped equipment panel designs similar to those developed under the GE RELSAT program, a 50 percent reduction in vibration/acoustic related ground test failures is expected.

A cost/reliability model which can be used to determine payoffs from equipment panel damping is available in a computer program known as OCTAVE (Optimized Cost of Testing for Acoustic and Vibration Environments.[7,8] This computer program showed that a significant increase in reliability and decrease in satellite system cost could be obtained if the vibroacoustic responses during launch could be reduced by 50 percent. The cost and reliability improvements were based on a statistical decision theory model which in turn used a data base of cost/failure rate information for satellite components. A model of the spacecraft system was first developed which consisted of three major elements: 1) satellite housekeeping components; 2) the satellite structure; and 3) the payload (i.e., the communication system components). Various types of cost elements were incorporated in the model including direct and probablistic cost types. Ground test options were considered which would assure that the satellite had a high reliability on orbit at optimum cost. The value of 50 percent reduction in the launch vibroacoustic environment for components was assumed due to equipment panel damping. The results showed a 20 percent improvement in reliability on orbit and a $40 million savings for a 14 spacecraft production (DSCS III type system).

The history of increasing severity of vibration environments over the past decade for spacecraft components shows a smaller portion of spacecraft components passing vibration tests. This trend of increasing vibration environment is related to the increased acoustic sound pressure levels at launch and the need for increased vibroacoustic reliability. In particular, the Space Transportation System (STS) (or Space Shuttle) exhibits an increase in sound pressure levels in the low frequency range (below 300 Hz) compared to earlier expendable launch vehicles. Vibration requirements for new spacecraft currently being developed are higher than for previous spacecraft. Figure 5 shows: 1) a component random vibration test specification for a large diameter spacecraft being developed for launch on the Shuttle; 2) a corresponding specification for a small diameter (9 ft or less) spacecraft which was developed for launch on an expendable launch vehicle; and 3) the specification for the large diameter payload reduced by a factor of two on an RMS basis (by a factor of four or 6 dB on a PSD basis). Figure 5 shows that damping could reduce component random vibration levels for large diameter Shuttle payloads to

levels for smaller payloads developed for flight on expendable launch vehicles. Figure 5 also shows that the most significant random vibration environment is currently in the low frequency range (below 300 Hz) for shuttle launched payloads.

3. TEST PANELS

Damping materials were evaluated, damping materials were selected, damped panel design concepts were developed and evaluated, and baseline and damped panels corresponding to Bay 3 of the DSCS III transponder panel were designed and fabricated. Figure 6 shows a baseline panel consisting of a base plate with two stiffeners. Three mass simulated TWTAs are mounted directly to the base panel. Figure 7 shows a corresponding damped panel. This damped panel has damped honeycomb sandwich stiffeners. An aluminum core/aluminum face sandwich is bonded to the base plate to provide inherent stiffness of the panel independent of the damping treatment. The VEM is bonded to this honeycomb sandwich stiffener. An aluminum core/graphite-epoxy face sandwich is then bonded to the VEM to provide a constraining sandwich for the VEM. Damped panels were also made with hat stiffeners riveted to the base plate and with a VEM layer with a graphite-epoxy constraining layer bonded to the hat stiffener. Various tests were conducted on the baseline and damped panels. These included acoustic, sine vibration, static, creep, and pyro shock tests. Pyro shock test results are described briefly below. Results of acoustic tests are then discussed in some detail. Component random vibration test requirements are derived from the vibroacoustic tests for the baseline and damped panels. The implication for component random vibration test requirements are considered to be the primary result of the RELSAT satellite equipment panel damping demonstration effort.

4. PYRO SHOCK TESTS

Pyro shock tests were performed on the baseline and a damped panel. In separate tests, these panels were mounted in one bay of a dual bay simulator which is normally used to perform spacecraft separation shock tests for components mounted on the DSCS III transponder panel. The shock was produced by firing an explosive separation nut. In these tests, the separation nut was activated by a high pressure gas supply connected to the nut. This separation nut is used to separate the DSCS III from the IUS and from a second DSCS III spacecraft. Separation nuts are on bolts at either ends of the two longerons which form two ends of the DSCS III transponder panel. Three separation nut firings were made each for the baseline and a damped panel. Triaxial accelerometers were mounted at the shock source and two accelerometers were attached near the mounting locations of each of the TWTA masses on each of the panels tested. One of these two accelerometers was oriented normal to the test panel and the other was oriented in the in-plane direction of the panel in the direction of separation nut firing (in the direction of the longeron).

Figure 8 shows comparisons of damped and baseline shock spectra for the two accelerometers mounted near TWTA number 2 which was mounted in the middle of each panel. Results shown are envelopes for three firings, although results from the three firings for each panel showed little variation in the shock spectra. Figure 8 shows results for the out-of-plane and in-plane accelerometers. The figure shows that the shock spectra peak near 2200 Hz with

maximum levels on the order of 1000 g. This is above the frequency where significant damping occurs. Damping treatments were designed primarily to reduce vibroacoustic response in the out-of-plane direction in the 50 to 500 Hz range. Damping reduced the peak shock in the out-of-plane shock spectra by about 30 percent. The out-of-plane direction is the direction in which damping was intended to be provided by the damped panel design. Figure 8 shows that the peak in the shock spectra for the in-plane direction was increased by about 30 percent for the damped panel relative to the baseline. This may be due to the addition of stiffeners for the damped panel configuration which connect the longerons to the TWTA's.

5. VIBROACOUSTIC TESTS

Acoustic tests were conducted on the baseline and seven damped panel configurations. Panels with both hat and sandwich damped stiffeners were tested. The configurations included four different viscoelastic materials. Tests were conducted at temperatures ranging from 60 to 78 degrees F. Two tests were conducted with four panels suspended in the GE acoustic test facility for each test. Tests were conducted at 139.3 and 143.8 dB overall. Instrumentation on each panel consisted of 12 out-of-plane accelerometers and two in-plane accelerometers attached at component mounting locations. Thermocouples were used to monitor temperatures of viscoelastic materials. Four microphones were used to measure and control the acoustic test environment. Figure 9 shows one-third octave band qualification sound pressure levels for small diameter and large diameter shuttle payloads.[9,10] The acoustic environment used for acoustic tests corresponded to the shape of the 9 ft payload sound pressure level curve. Test vibroacoustic levels were scaled to correspond to acoustic levels shown in Figure 9. The 9 ft diameter levels correspond to a DSCS III qualification test level.

Figure 10 shows four of the damped panels suspended in the GE acoustic test facility. Each panel was mounted to a heavy aluminum frame which was supported by a low frequency suspension system. Figure 10 shows the location of four out-of-plane accelerometers at the mounting locations for each TWTA mass. Each panel had two in-plane accelerometers. In-plane vibroacoustic responses were small compared to out-of-plane responses. For each of the panels tested, the 12 out-of-plane accelerometers were analyzed statistically to obtain a 95 percentile level. The spectral content of the data were then scaled to acoustic levels shown in Figure 9 for the 9 and 15 ft diameter shuttle payload qualification acoustic test levels. Figure 11 shows results for the 9 ft diameter payload for test data for 72 degrees F. Results are shown for the baseline and a damped panel. Results for all damped panels were very similar. Results shown in Figure 11 are for the damped panel which gave the best results for all panels tested. Other damped panel designs had similar vibroacoustic responses but were slightly higher above 500 Hz. Figure 11 shows that damping reduces response by up to 20 dB. The largest peaks for the baseline panel were reduced the most and these peaks were in the low frequency range. Damping reduced responses significantly for frequencies up to about 400 Hz. Figure 12 shows results scaled for the 15 ft diameter shuttle payload acoustic environment at launch. These results indicate that damping can provide very significant benefits for large diameter shuttle payloads.

6. RANDOM VIBRATION SPECIFICATIONS

The Random Response Spectrum (RRS) method[11] was used to determine component random vibration test requirements corresponding to the 95th percentile out-of-plane random vibration levels determined from the acoustic tests for the baseline and best damped panels. The RRS method is similar to the shock spectrum concept. The RRS is the RMS response of a single-degree-of-freedom oscillator to a random vibration input spectrum vs the oscillator resonant frequency. A Q of ten was assumed for the component. The objective was to generate a random vibration test spectrum which had an RRS similar to the RRS for the actual component random vibration environment, i.e., for the 95th percentile out-of-plane random vibration spectrum. Random vibration specificatons were generated in this manner for the baseline and damped panel component random vibration environments. Figure 13 shows the out-of-plane random vibration spectrum and corresponding test spectrum for the 9 ft diameter payload (DSCS) baseline panel qualification level. The RRS for this specification level and the the 95 percentile out-of-plane data are also shown in Figure 13. The RRS for the specification is seen to envelope that for the actual baseline panel test data. The peak value of about 30 GRMS occurs for a component natural frequency just above 100 Hz. Note that the largest magnitudes of the test data, the specification, and the RRS are in the low frequency region (below 300 Hz). Corresponding results for the damped panel are shown in Figure 14. Damping significantly reduces the low frequency test and specification random vibration spectrum levels. The largest RRS level now occurs at about 2000 Hz for both the damped panel test data and specification. The peak GRMS at this frequency, however is now only about 13 g. Figure 15 compares the specifications for the damped and baseline panels shown previously in Figures 13 and 14. The maximum specification PSD has been reduced 13 dB using damping. The maximum GRMS has been reduced by 64 percent for the damped panel. Corresponding results for the 15 ft diameter shuttle payload are shown in Figure 16. Here the damped panel PSD is seen to be reduced by 14 dB relative to the baseline panel and the peak GRMS is reduced by 53 percent due to damping. This figure shows that major benefits from damping can be expected for large diameter payloads on the shuttle. Component random vibration test responses might be reduced from about 40 to about 20 GRMS by the addition of damping to equipment panels.

7. DAMPED PANEL HYSTERESIS AND LONG TERM VEM STABILITY

A static load test was conducted on a panel with damped hat stiffeners. A load was applied to each TWTA normal to the plane of the panel. The panel was loaded statically to an 11 g (550 lb) load in increments of approximately 1 g. The load was then removed in approximately 1 g increments. Deflections of the panel and strains in hat stiffeners were measured. Figure 17 shows a plot of strain in a hat stiffener vs total panel load for both the loading and unloading cycle. Figure 17 shows that very low hysteresis occurred. This result indicates that for the damped panel designs developed under RELSAT, viscoelastic treatments may be feasible for application to platforms requiring high alignment and pointing stability without introducing hysteresis during loading and unloading events such as launch, orbit transfer, deployments, and separations.

In April 1984, The Modular Attitude Control System (MACS) module was retrieved form the Solar Max Mission (SMM) spacecraft on a Shuttle repair mission. The SMM spacecraft was launced in January of 1980. The Attitude Control Electronics (ACE) component on the MACS module used viscoelastic materials

extensively for damping treatments. A piece of this material which had been in orbit for over four years was tested to determine its material properties after four years exposure to space environment. Figure 18 shows the measured loss factor and shear modulus (discrete data points) compared to properties of similar non-flight material (curves). The material retrieved from space is seen to have excellent damping properties (circles) which are nearly identical to the non-flight material. The shear modulus (squares) for the material which was in orbit is slightly stiffer than the similar material which was not flown. These results indicate that damping materials of the type used in the GE RELSAT damped panel designs will retain their viscoelastic characteristics for long periods of time when in orbit and could be quite useful for orbital damping applications.

8. SUMMARY AND CONCLUSIONS

The primary objective of the GE RELSAT program was to develop and demonstrate damped panel designs which would reduce the vibroacoustic response. An initial goal was to reduce the RMS response by 50 percent (6 dB). A reduction of this magnitude was estimated to result in a cost savings of $14 million for 14 spacecraft system (DSCS type). The most significant Shuttle vibroacoustic environments are in the low frequency range. The largest deflections and stresses of components are expected here. Pyro shock tests showed attenuation of out-of-plane shock spectra due to damping but an increase was seen in the in-plane shock spectra for damped panels. Vibroacoustic responses were reduced up to 20 dB for power spectral densities in the 50 to 300 Hz range. Corresponding component random vibration specificaiton levels were reduced about 13 dB. The expected component RMS acceleration responses to derived component random vibration specifications were reduced by 50 to 60 percent by damped panel designs. Low hysteresis in static load deflection tests indicates that damping may be applicable to alignment critical structures. Data recently obtained on viscoelastic material which had been in space for four years showed that long term space exposure had little or no effect on the material damping and stiffness properties. Materials of this type appear applicable to orbital damped panel designs for alignment critical structures.

9. ACKNOWLDEGEMENTS

The work for design, development, and testing of damped RELSAT satellite equipment panels was performed under AFWAL contract F33615-82-C-3223. Technical monitors are James Eichenlaub and Lynn Rogers who provided valuable guidance and assistance. Testing and test data reduction were performed by the General Electric Space Systems Division vibration and acoustic laboratory personnel. Harold Gongloff performed statistical analyses of vibroacoustic and shock spectra data and derived component random vibration test specifications using the Random Response Spectrum method.

10. REFERENCES

1. J. C. Strain, J. A. Staley, and C. V. Stahle, "Design and Experimental Verification of Damped Spacecraft Equipment Panels," Vibration Damping Workshop II, March 1986.

2. K. A. Schmidt, F. P. Curtis, E. F. Muziani, and L. Amore, "Fabrication of Damped Spacecraft Equipment Panels," Vibration Damping Workshop II, March 1986.

3. D. I. G. Jones, "A Reduced-Temperature Nomogram for Characterization of Damping Material Behavior," 48th Shock and Vibration Symposium, Oct. 1977.

4. R. Moss, "Using the Outgassing Test to Screen Materials for Contamination Potential," SAMPE Journal, March/April 1984.

5. A. R. Timmins and R. E. Heuser, "A Study of First Day Space Malfunctions," NASA TND-6474, September 1971.

6. R. B. Laube, "Methods to Assess the Success of Test Programs," October 1982 Aerospace Testing Seminar.

7. C. V. Stahle, H. R. Gongloff, J. P. Young, and W. B. Keegan, "Shuttle Payload Minimum Cost Vibroacoustic Tests," Proc. 1977 Annual Rel. and Maint. Symp.

8. C. V. Stahle, "Cost Effectiveness of Spacecraft Vibration Qualification Testing," Proc. of Inst. of Environmental Sci., 20th Annual Meeting, May 1974.

9. "Acoustic Requirements for DoD Shuttle Payloads Launched from KSC," Doc. No. DS-YV-0093, Rev. 1.

10. C. S. Tanner, "Acoustic Environments for DoD Payloads on the Shuttle," Proc. of the Shuttle Payload Dynamic Environments and Loads Predictions Workshop, JPL D-1347, 1984.

11. C. V. Stahle and H. R. Gongloff, "Development of Component Random Vibration Requirements Considering Response Spectra," The Shock and Vibration Bulletin, August 1976.

(RELIABILITY FOR SATELLITE EQUIPMENT IN ENVIRONMENTAL VIBRATION)

OBJECTIVE

- GENERICALLY DEMONSTRATE PASSIVE DAMPING CONTROL OF PANEL MOUNTED COMPONENT VIBRATION

APPROACH

- DESIGN, FABRICATE AND TEST DAMPED DSCS-III TRANSPONDER PANEL
  - EVALUATE MATERIAL PROPERTIES
  - DEVELOP AND IMPLEMENT DESIGN CONCEPTS
  - PERFORM VIBRATION, ACOUSTIC, SHOCK AND STATIC TESTS

PAYOFFS

- STABLE PLATFORM WITH HIGH POINTING ACCURACY FOR MANEUVERS AND ON-BOARD DISTURBANCES

- 20 PERCENT INCREASE IN RELIABILITY THROUGH 50 PERCENT REDUCTION IN VIBRATION ENVIRONMENT

- REDUCE LARGE NUMBER OF TEST FAILURES BY 50 PERCENT

- REDUCE SPACE SYSTEM DEVELOPMENT/OPERATING COST BY $40M

Figure 1.   RELSAT Program
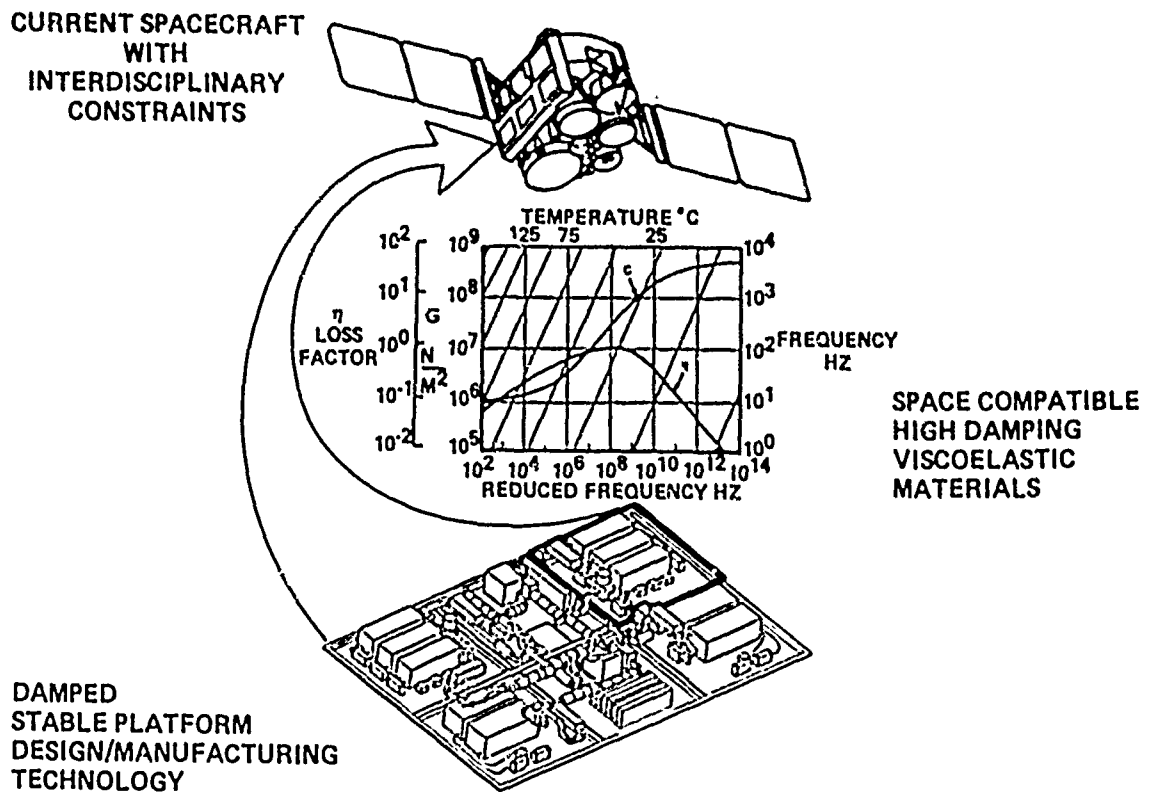
FIGURE 2.   RELSAT DSCS III Baseline System
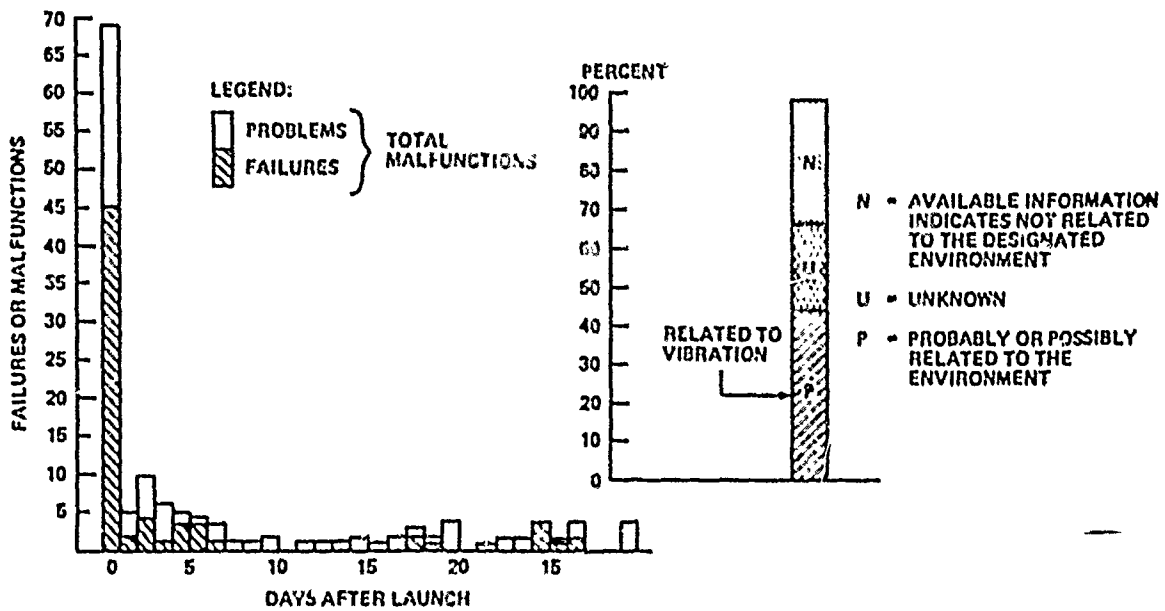
Figure 3. Spacecraft Flight Failures

DESIGN QUALIFICATION
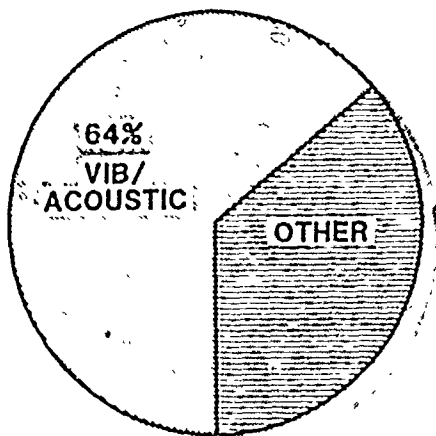
ACCEPTANCE

98 TEST FAILURES/SATELLITE
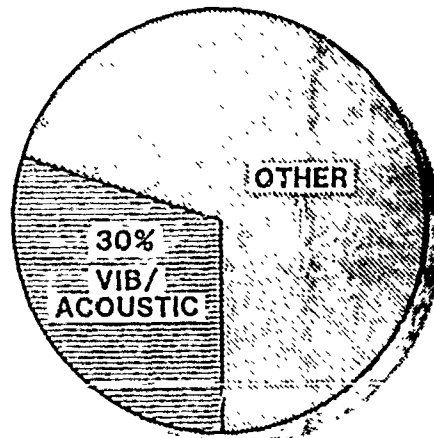
25 FAILURES/SATELLITE

REF: OCT 82 AEROSPACE
TESTING SEMINAR

A 50% REDUCTION IN VIB/ACOUSTIC
GROUND TEST FAILURES IS ESTIMATED

Figure 4. Environmental Test Failures
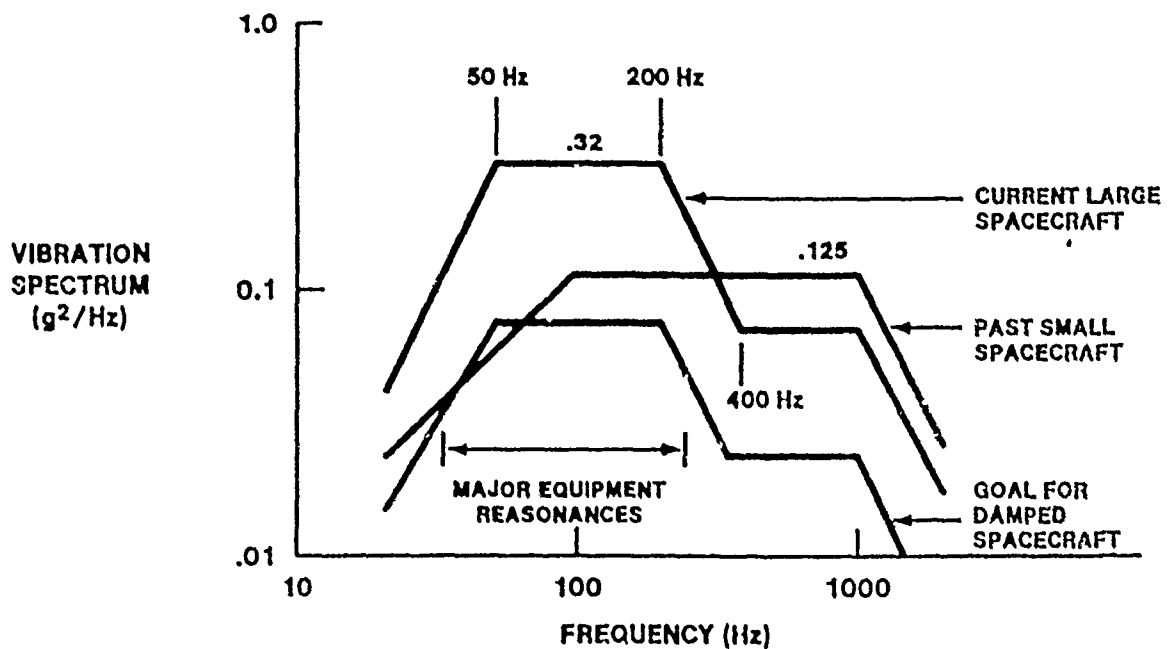
DAMPING COULD REDUCE SPECS FOR SHUTTLE
LARGE DIAMETER PAYLOADS TO SMALL DIAMETER LEVELS

Figure 5. Equipment Random Vibration Requirements

Figure 6. RELSAT Baseline
Panel

Figure 7. RELSAT Test Panel
With Damped Stiffeners

OUT-OF-PLANE DIRECTION   IN-PLANE DIRECTION
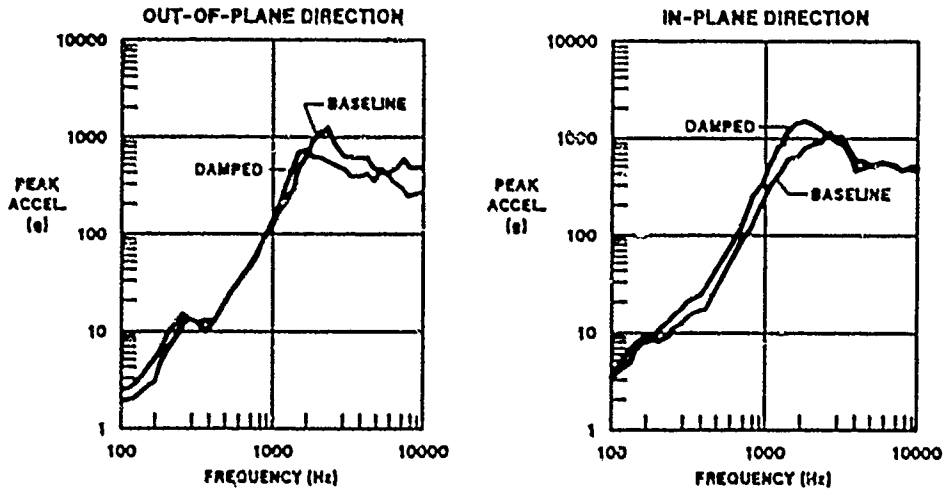
DAMPING TREATMENT REDUCES OUT-OF-PLANE SHOCK SPECTRA
AND INCREASES IN-PLANE SHOCK SPECTRA

Figure 8.   Pyro Shock Test Results
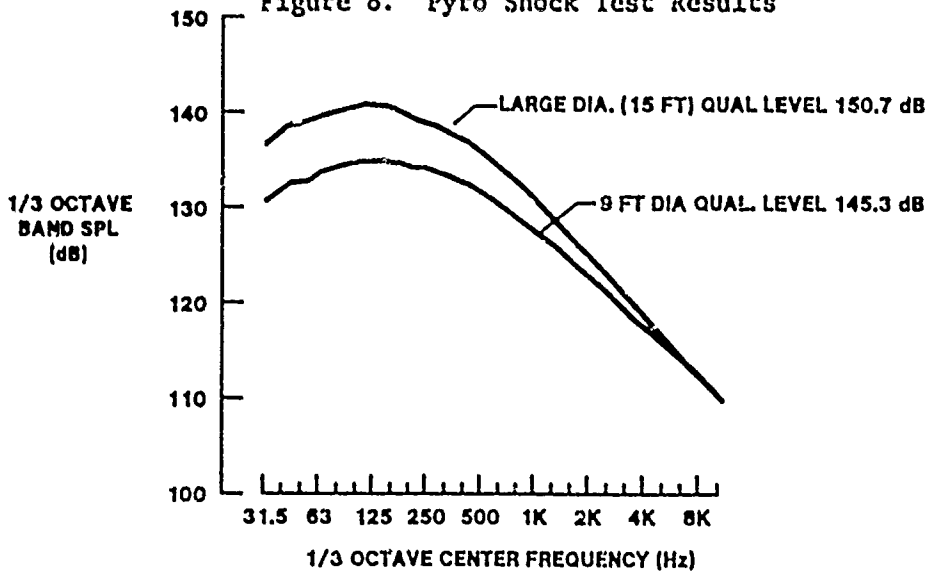
Figure 9.   Qualification Sound Pressure Levels
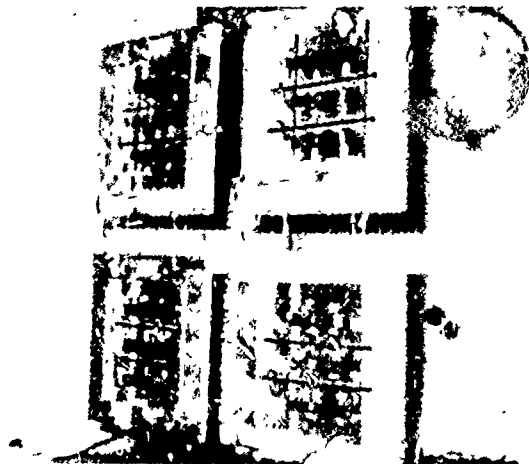
Figure 10.   RELSAT Panels in Acoustic Test Facility

95% LEVEL AT 72 DEG F
SCALED TO 145.3 dB QUAL. ACOUSTIC LEVEL
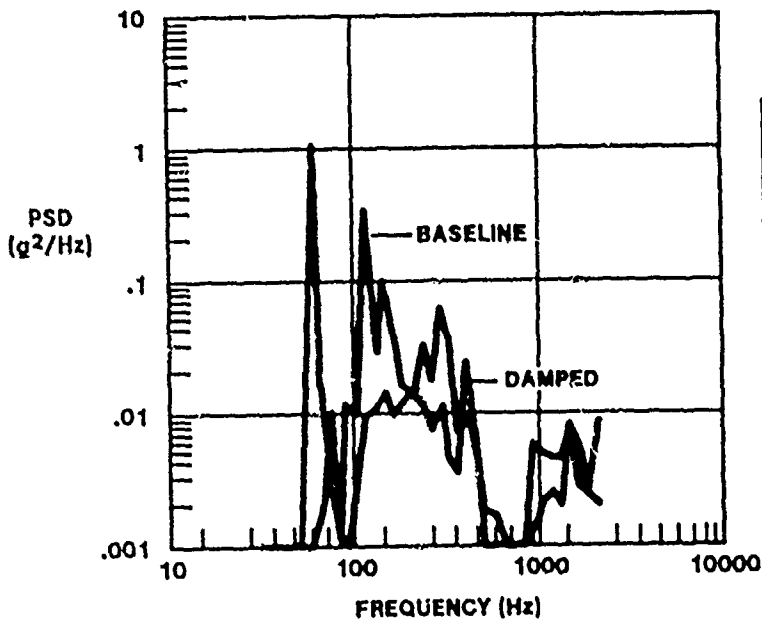
Figure 11. Out-of-Plane Vibroacoustic Response

95% LEVEL AT 72 DEG F
SCALED TO QUAL. ACOUSTIC LEVEL – 150.7 dB
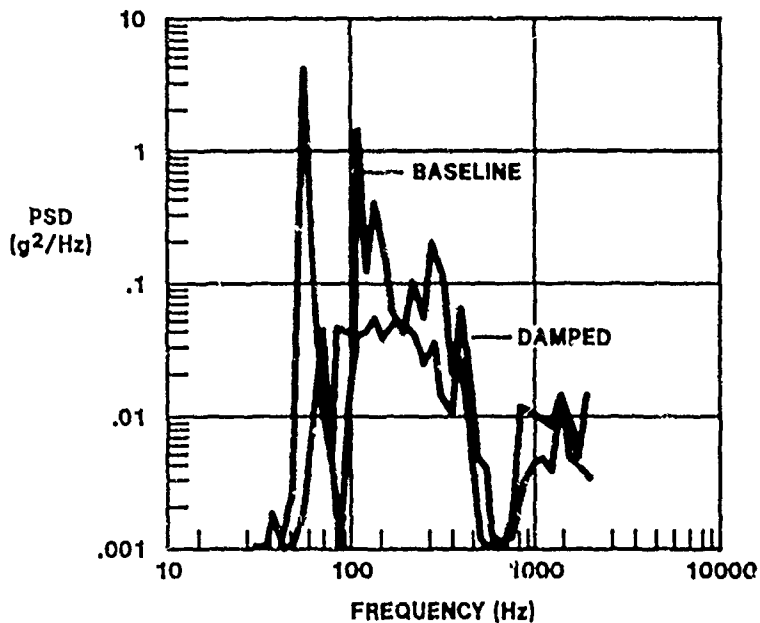
Figure 12. Vibroacoustic Response – Scaled for 15 Ft. Dia. Payload

COMPONENT SPEC & 95%
TEST LEVEL

RANDOM RESPONSE SPECTRA FOR
SPEC AND 95% TEST LEVEL

PSD
(g²/Hz)

G_RMS

95% TEST LEVEL

SPEC

SPEC

95% TEST LEVEL

FREQUENCY (Hz)

FREQUENCY (Hz)

LARGEST RESPONSE IN LOW FREQUENCY RANGE
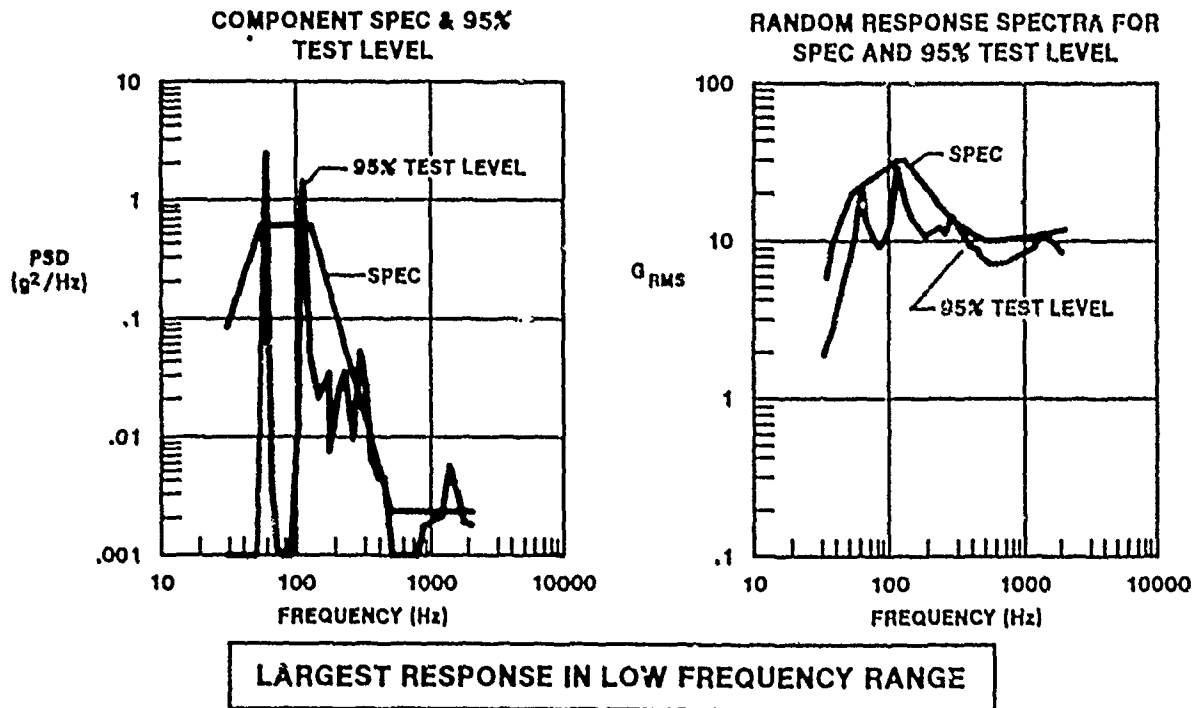
Figure 13. DSCS III Baseline Panel Random
Vibration Specification

COMPONENT SPEC & 95%
TEST LEVEL

RANDOM RESPONSE SPECTRA FOR
SPEC AND 95% TEST LEVEL

PSD
(g²/Hz)

G_RMS

95% TEST LEVEL

SPEC

SPEC

95% TEST LEVEL

FREQUENCY (Hz)

FREQUENCY (Hz)

LARGE REDUCTION IN RESPONSES IN LOW FREQUENCY RANGE
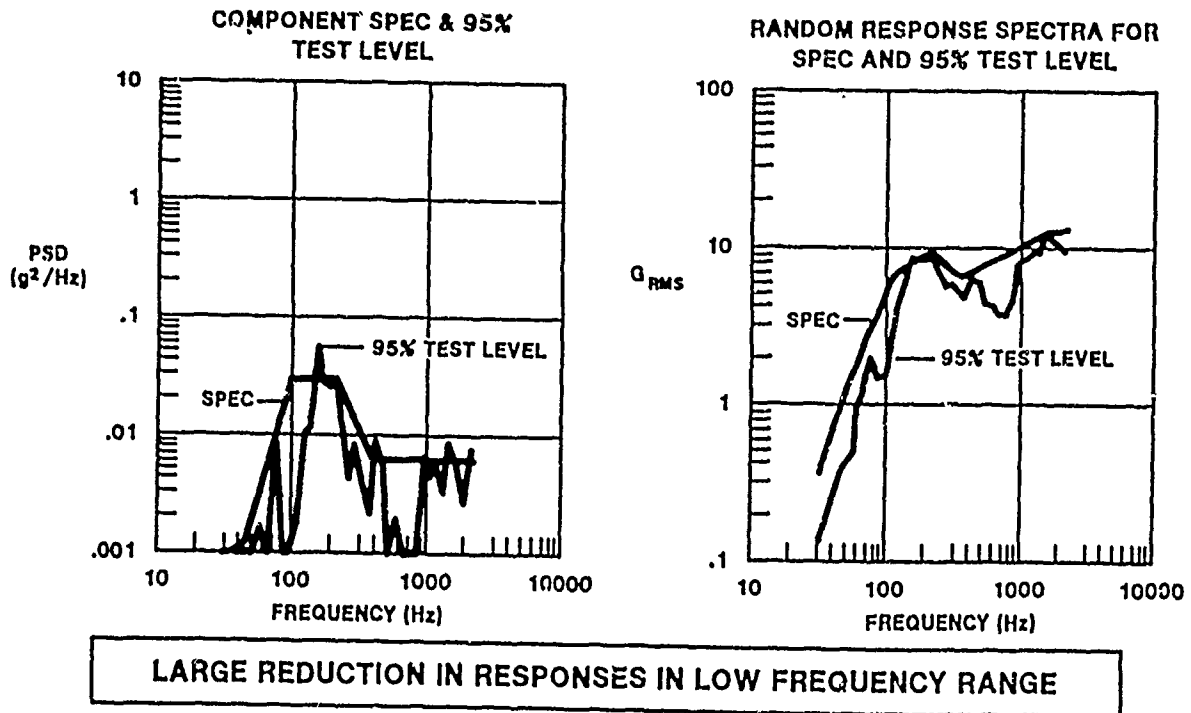
Figure 14. DSCS III Damped Panel Random
Vibration Specification

HD-14

OUT-OF-PLANE DIRECTION - SHUTTLE LAUNCH AT KSC

COMPONENT SPECS FOR BASELINE & DAMPED PANELS

RANDOM RESPONSE SPECTRA FOR BASELINE & DAMPED PANEL SPECS

DAMPING REDUCES COMPONENT SPEC LEVEL SIGNIFICANTLY
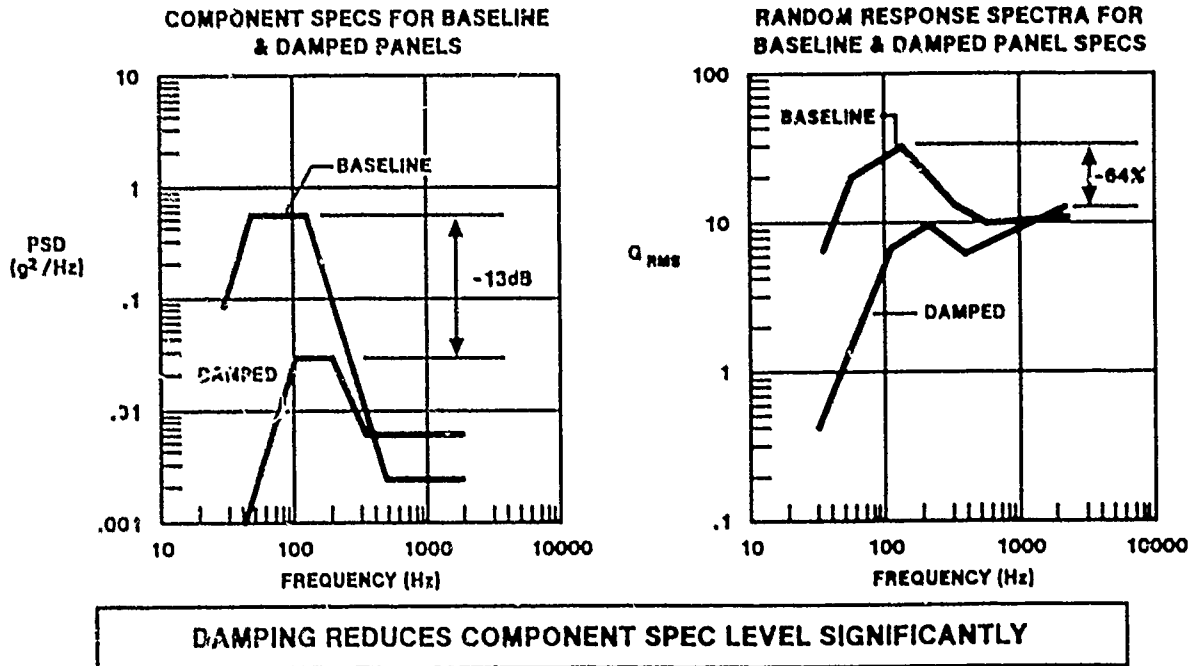
Figure 15.   DSCS III Baseline and Damped Panel Qualification Level
Random Vibration Specifications

OUT-OF-PLANE DIRECTION - SHUTTLE LAUNCH AT KSC

COMPONENT SPECS FOR BASELINE AND DAMPED PANELS

RANDOM RESPONSE SPECTRA FOR BASELINE & DAMPED PANEL SPECS

MAJOR BENEFITS OF DAMPING FOR LARGE DIAMETER PAYLOADS
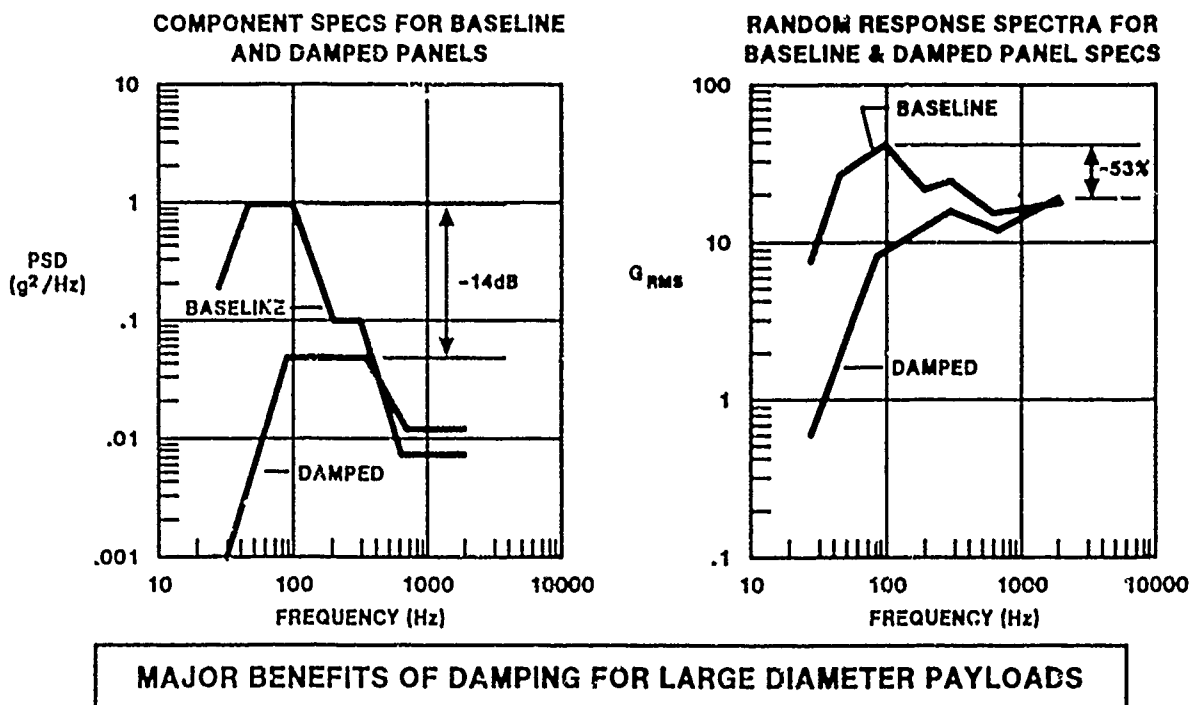
Figure 16.   Random Vibration Specifications -
15 Ft. Diameter Payload

- A RELSAT DAMPED PANEL WAS LOADED STATICALLY TO AN 11g LOAD IN APPROXIMATELY 1.0g INCREMENTS

- THE LOAD WAS THEN REMOVED IN APPROXIMATELY 1.0g INCREMENTS

- VERY LOW HYSTERESIS UNDER THE STATIC LOAD CYCLE WAS INDICATED BY A STRAIN GAGE ON A PANEL HAT STIFFENER

VISCOELASTIC DAMPING TREATMENTS MAY BE FEASIBLE FOR APPLICATION TO PLATFORMS REQUIRING HIGH STABILITY WITHOUT INTRODUCING HYSTERESIS DURING EVENTS SUCH AS LAUNCH, ORBIT TRANSFER, DEPLOYMENTS AND SEPARATION
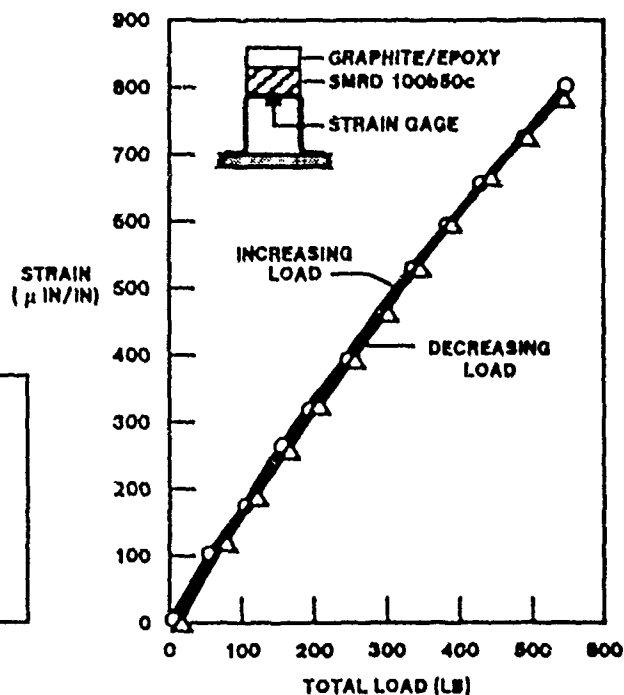
Figure 17. Static Test Hysteresis for a Damped Panel
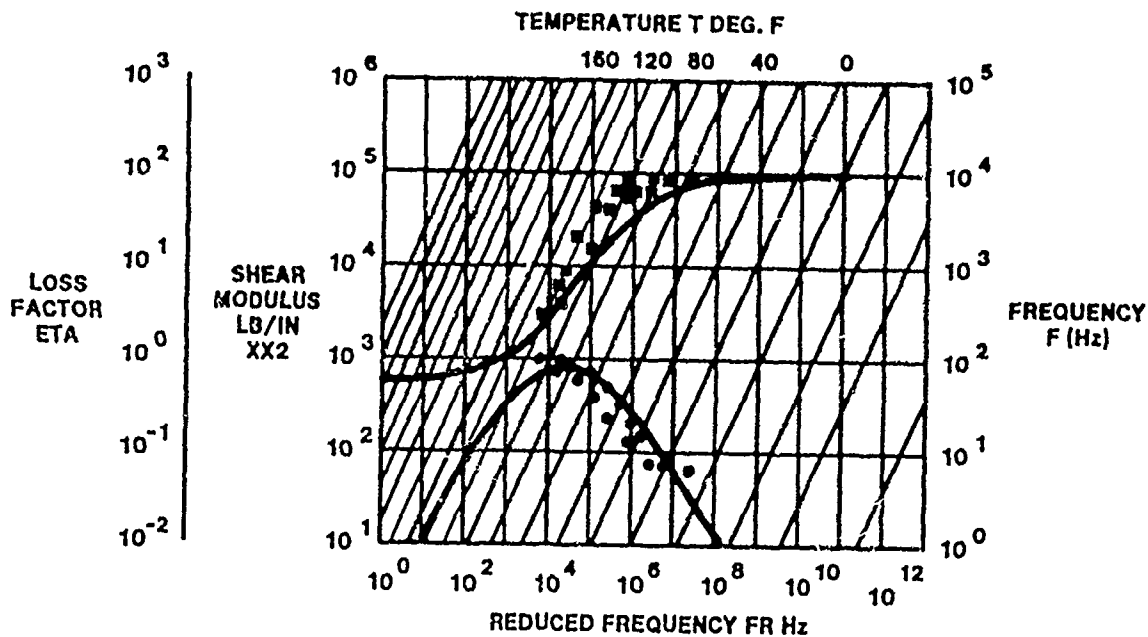
GOOD DAMPING PROPERTIES AFTER 4 YEARS IN SPACE

Figure 18. VEM Properties After Four Years in Space

DESIGN AND EXPERIMENTAL VERIFICATION OF DAMPED SPACECRAFT EQUIPMENT PANELS*

C. V. STAHLE
J. A. STALEY
and
J. C. STRAIN

GENERAL ELECTRIC SPACE SYSTEMS DIVISION
VALLEY FORGE SPACE CENTER
P.O. BOX 8555, PHILADELPHIA, PA 19101

ABSTRACT

The design, analysis and modal tests of viscoelastically damped spacecraft equipment panel structures are presented. The work was performed as part of the AFWAL RELSAT program and uses the DSCS III transponder panel to demonstrate the generic control of equipment vibration with passive damping. Highly effective integrally damped panel designs are achieved with small increase in structural weight. A damped stiffener approach is used that satisfies interdisciplinary constraints such as heat dissipation. Strength and deflection criteria are used that account for the load reduction and stiffness of the damped design. Two lightweight configurations are described: one using unidirectional graphite epoxy (G/E) constraining layers and the other using G/E honeycomb constraining layers with an aluminum honeycomb stiffener. Loss factors greater than 0.2 are obtained for low frequency modes using GE SMRD 100 damping materials. Damping is more than doubled in all modes below 500 Hz. The analysis uses NASTRAN finite element models with modal strain energy and can be applied to any complex design. Initial beam element tests compare analytical predictions with test results for the G/E constraining layer and honeycomb configurations using material properties from two different laboratories. Subsequent panel tests indicate damped panel analyses predict low mode resonant frequencies within 10 percent, damping loss factors within 30 percent and the temperature of maximum damping within 10 degrees F. The major source of prediction error appears to be material properties caused by measurement error, the temperature shift relation and the reference temperature. More accurate material property definition is recommended. The 20 dB attenuation of the vibroacoustic response, the material selection and panel fabrication are discussed in two other papers included in the proceedings.

1.0 INTRODUCTION

This paper discusses the design, analysis, and modal tests of viscoelastically damped spacecraft equipment panels. Examination of early spacecraft flight anomalies has indicated a large number are caused by the vibroacoustic launch vibration. As a result, vibration requirements have been increased which has led to a large number of ground test failures during component, subassembly and spacecraft random vibration and acoustic tests. Even after qualification tests of a spacecraft design have been successfully completed, subsequent acceptance tests of production units exhibit a large number of failures indicating a susceptability of the final designs to the vibroacoustic environment. Although damping has been used effectively within electronic packages to improve vibroacoustic reliability, its use to control equipment panel vibration has been limited and generally applied to existing designs. Because studies have shown that significant cost reductions can be obtained and that the vibroacoustic reliability can be significantly improved by reducing the random vibration environment, the RELSAT program (Reliability for Satellite Equipment in Environmental Vibration) has been initiated by AFWAL to generically demonstrate the passive damping control of panel mounted component vibration. Parallel RELSAT programs are being performed by Boeing and General Electric.

The approach used in the GE-RELSAT program is to design, fabricate and test a damped DSCS III transponder panel. The DSCS III (Defense Satellite Communication System) spacecraft was selected because the design is mature and enables interdisciplinary constraints to be readily defined. The goal is to achieve a reduction of 6 dB in the random vibration environment. As shown in Figure 1, large diameter shuttle spacecraft random vibration requirements exhibit high spectral amplitudes in the frequency range below 200 Hz where major equipment resonances occur. By obtaining a 6 dB reduction, the spectrum levels are reduced to those of current small diameter spacecraft. For any size spacecraft, the vibroacoustic reliability is significantly enhanced.

Three workshop papers are included in the proceedings covering different aspects of the GE-RELSAT program. This paper discusses the design and analysis of the panel and describes modal tests performed to verify the resonant frequency and modal damping predictions. The quantification of the cost reduction and reliability improvement, as well as the experimental results from acoustic and shock tests are presented in a second paper. The third paper discussed the selection of the viscoelastic material and describes the methods used in fabricating the damped panel.

The following sections discuss the panel design and analysis, the correlation of beam element tests with analytic predictions, comparison of panel modal test results with analytical results, and finally the conclusions reached in this portion of the RELSAT program.

2.0 TRANSPONDER PANEL DESIGN

The test article chosen for viscoelastic damping treatment was the North Panel Bay 3 of the Defense Satellite Communications System (DSCS) III, Figure 2. This equipment panel is approximately 27 inches square, constructed of magnesium thorium .18 inches thick and contains two integrally milled/riveted stiffeners. Three 10 watt traveling wave tube amplifiers (TWTA's) are mounted on it along with associated wave guides and electronics. These TWTA's place a

severe design constraint on the panel since the thermal requirement to dissipate their 30 watts of power makes the use of a lightweight honeycomb sandwich for the base panel impractical. Hence, the thick .18 plate which is required for thermal, not structural reasons.

The test articles for the RELSAT program utilize a .125 inch thick aluminum plate to simulate the stiffness of the actual .18 inch thick magnesium-thorium panel. The TWTA simulators are made of an aluminum block mounted to a steel plate. They provide the weight and center of gravity of the actual TWTA's and other components necessary to make the total panel weight equal to that of the actual flight hardware.

2.1 BASELINE UNDAMPED PANEL

This panel was designed to closely simulate the "as is" undamped North Panel Bay 3. It consists of the aluminum base plate and three TWTA simulators plus two aluminum hat section stiffeners in lieu of the integrally milled/riveted stiffeners on the flight hardware. These stiffeners were sized to provide a fundamental frequency near that of the actual DSCS panel. Figure 3 is a photograph of this test article, the NASTRAN model for which is shown in Figure 4. This model which contained 412 GRIDS and 259 ASET degrees of freedom (DOF) was constructed entirely of CQUAD4 elements with the exception of the TWTA's which were single 6 DOF nodes attached to the panel with rigid elements.

A modal test was performed on the baseline panel to provide a reference for damped panel measurements, and to verify analysis methods without the added complexity of modeling viscoelastic properties. Inaccuracies in the undamped panel model will be propagated in the viscoelastic properties used for damped panel analysis since these are very frequency dependent. These inaccuracies may result from both lack of detail in modelling, and from the unknown boundary condition.

2.2 DAMPED PANEL DESIGN

Two damped stiffener concepts were used in the designs. These were a honeycomb sandwich stiffener with a honeycomb sandwich constraining layer, and an aluminum hat section stiffener with a graphite constraining layer. Both of these concepts are illustrated in Figure 5. As in the baseline design, the aluminum hat section stiffener simulates the integrally milled/riveted stiffener on the actual DSCS III spacecraft equipment panel. The honeycomb sandwich stiffener is designed for lighter weight, and maximizes the strain energy in the viscoelastic material through a larger separation of the constraining layer neutral axis from the viscoelastic layer. One example, using each of these two concepts will be discussed in this section: a panel with honeycomb stiffeners and SMRD 100F90B damping material, and a panel with aluminum hat section stiffeners and SMRD 100B50A damping material.

A total of seven damped panels were designed for the RELSAT program. The scope of this paper is to describe the analysis used to design the panel damping treatments, and the correlation of the analysis to data from the modal test performed on one of the damped test articles.

2.2.1 DAMPED DESIGN CRITERIA

A primary objective of this effort is to demonstrate a 50% reduction of vibro-acoustic response by developing damped panel designs. A preliminary damping criteria which is expected to accomplish this is:

1) a minimum loss factor of 0.30 in the fundamental equipment panel mode, and

2) a minimum loss factor of 0.10 for all other major panel modes up to 500 Hz.

In addition to the damping criteria, structural design criteria must also be established.

A set of structural design criteria have been established for developing damped panel designs. These criteria are based on varying degrees of conservatism in the assumptions regarding: 1) the degree to which the vibroacoustic loads have been reduced, 2) limits on expected deflections, and 3) the degree to which the viscoelastic damping treatment is assumed to share in design loads for the panel structure.

Equivalent steady load factors are often used for satellite structure design. These load factors are usually composed of two parts: 1) a low frequency or quasi-steady part which consists of the nearly steady acceleration at liftoff plus a low frequency (typically of the order of two to fifty Hz) transient during liftoff; and 2) a higher frequency vibroacoustic portion induced by acoustic pressures caused by the propulsion system during launch. The sum of these two effects results in an equivalent design load factor which is used for design of secondary structures and components. The primary structure is generally designed by the quasi-steady portion only.

Three structural design criteria for the damped DTA designs are considered as shown in Table 1.

Criterion I - Baseline: Designs using this criterion represent "add-on" damping configurations. These designs consider neither the reduced dynamic loads due to damping nor the load carrying capacity of the damping treatment. For the DSCS III transponder panel the baseline structural design criterion consists of a 60 Hz minimum frequency requirement and a 35 G total load factor. The 35 G load is the sum of an 11.5 G quasi-static and a 23.5 G vibroacoustic load.

Criterion II - Conservative Integrally Damped: This criterion considers the reduction in dynamic loads due to damping, but does not allow for the load carrying capability of the damping treatment. The structural integrity of the panel is maintained by the undamped structure which is designed to a load factor which has now been significantly reduced by damping. The goal of the GE RELSAT program was to reduce the vibroacoustic portion of the dynamic loading by 50 percent. The total load factor for the criterion II design is therefore the sum of an 11.5 G quasi-steady load and a vibroacoustic load reduced to 11.8 G, or 23.3 G as compared to 35 G for the criterion I design. The stiffness of the undamped panel designed to this lower load factor will be less than that of the baseline panel, but it's deflection under the combined quasi-steady and vibroacoustic load of 23.3 G will be kept the same as that of the baseline panel under 35 G's.

Criterion III - Advanced Integrally Damped: This design criterion considers not only the reduction in vibroacoustic load due to damping, but also allows for the damping treatment's load carrying capability. This will provide the lightest weight damped design. The total design load factor remains at 23.3 G as in criterion II, but allowing the damping treatment to carry part of the structural loads will result in a lower weight design. For this criterion, the stiffness of the undamped panel may be further reduced using the requirement that the deflection under 23.3 G of the damped criterion III design does not exceed that of the undamped criterion II design under the same load.

Table 2 and Figure 6 illustrate the structural weight obtainable with the three criteria. This table compares preliminary design results using all three criteria to the undamped baseline. The first three damped designs utilized an aluminum hat section stiffener, with a graphite constraining layer, while the last used a honeycomb sandwich stiffener and constraining layer. The criterion II design with hat stiffeners is seen to provide a 2% structural weight reduction from the add-on, and the criteria III design with hat stiffeners provides an additional 2% reduction. Using honeycomb sandwich stiffeners in place of the aluminum hats, reduces the weight by another 8% so that it is comparable in in weight to the original undamped structure.

Final designs of the RELSAT test articles were all performed using criterion III.

2.2.2 DESIGN ANALYSIS METHODS

Design of the damped panels was performed primarily with MSC NASTRAN modal strain energy (MSE) calculations . The strain energy option in NASTRAN outputs tables of strain energy in each element of the NASTRAN finite element model, for each mode shape calculated. The viscoelastic material is modeled with solid brick elements having a shear modulus which is selected for a temperature and frequency. The ratio of the MSE in the viscoelastic elements, to the total MSE in the mode shape, multiplied by a material loss factor gives the composite loss factor. Since the resulting loss factor is correct only for the selected temperature and frequency several runs must be made using differend VEM shear moduli to get results for all modes of interest. A NASTRAN direct frequency response analysis will produce sinusoidal transfer functions which account for the frequency dependence of the shear modulus andloss factor in a single run. However, if the structure being analyzed does not have modes which are well enough separated to be considered as single-degree-of-freedom responses, the equivalent normal modal characteristics cannot be readily obtained.

Of all the variables in the finite element model, the shear modulus of the VEM, which is both frequency and temperature dependent, is the most difficult to quantify. The shear modulus was obtained from VEM test data which is reduced by a least squares fit to equations for shear modulus and loss factor as a function of frequency and reduced frequency. The reduced frequency is the frequency multiplied by a shift parameter which is a function of temperatures relative to a reference temperature, To. Experience has shown that this reference temperature is difficult to choose properly and that the size of typical discrepancies which often occur can produce significant differences in material properties using test data from different sources. An accurate and consistent method for choosing To has been determined to be a much needed development to increase the reliability of finite element damping calculations.

Another, much simpler but often useful analysis method is that described by Abdulhadi [8]. This is a "general analysis...for three layer plates consisting of two distinct plate type facings and a core that carries shear stresses only." A sixth order equation is solved to obtain composite frequency and loss factor for various boundary conditions. Abdulhadi's method is a useful method for optimization of damping treatments for uniform beams and plates. This anlaysis method was used to size sub-panel dampers. These graphite epoxy constraining layer damper strips were added to reduce the acoustic response of the sub-panels, which had frequencies calculated to be between 300 and 500 Hz.

2.2.3 SHRD 100F90B DAMPED, HONEYCOMB STIFFENED PANEL

This panel uses the aluminum baseplate and three TWTA simulators previously described, as do all of the test articles. It incorporates four honeycomb sandwich stiffeners in a "criss-cross" pattern. These are made from .4 inch thick Hexcel 1/8-5052-.002 aluminum honeycomb with a 5 mil aluminum lower face sheet and 30 mil aluminum upper face sheet. The damping is provided by .25 inch thick General Electric SHRD 100F90B viscoelastic damping material between the stiffeners and a honeycomb sandwich constraining layer. The constraining layer consists of .4 inch thick Hexcel 1/8-5052-.002 aluminum honeycomb with a lower face sheet of 5 mil uniaxial HMS/CE339 graphite epoxy and upper face sheet of 80 mils uniaxial HMS/CE339. A sketch of this stiffener/constraining layer is shown in Figure 5.

The .5 inch width of the stiffeners was chosen as a result of previous parametric analysis on a stiffened end supported plate which showed this width to provide optimum damping for the lowest weight, and the desire to use as little of the panel area as possible since most satellite equipment panels are very densely filled with components.

The panel stiffener height and face sheet are designed to provide a minimum frequency to satisfy the static deflection requirements of criterion III. The constraining sandwich layer is designed to provide adequate stiffness under the transient and vibroacoustic loads of criterion III and, along with the viscoelastic material, to provide a minimum loss factor of .3 in the fundamental mode, and .1 for all important modes below 500 Hz. Figure 7 is a photograph of this panel. The NASTRAN model used for correlation with the modal test data is shown in Figure 8. This model contained 674 GRIDs and 294 ASET DOF. A more coarse model with 303 GRIDs and 78 ASET DOF was used in performing the parametric analyses.

NASTRAN Modal Strain Energy (MSE) analyses were run to determine the first mode loss factors for the various parametric configurations, and to give a conservative estimate of the loss factors for the higher modes. Figure 9 shows the NASTRAN MSE in the VEM plotted vs. VEM thickness, with the chosen design point circled. NASTRAN MSE calculations were made for a wide range of VEM shear modulus to give the loss factors for all modes up to 500 Hz. The calculated composite loss factors are plotted vs. frequency in Figure 10 for a temperature range of 60° F to 70° F, the temperature range during launch.

2.2.4 SHRD 100B50A DAMPED, HAT SECTION STIFFENED PANEL

This design employs four aluminum hat section stiffeners in the same pattern as the stiffeners of the honeycomb stiffener panel. These are .5 inches high, .5 inches wide, and bent up from 1/32 inch aluminum. The damping is provided by .10 inch thick SHRD 100B50A viscoelastic damping material and a constraining layer of .25 inch thick uniaxial HMS/CE339 graphite epoxy. A photograph of this panel is presented in Figure 11 and the NASTRAN model containing 367 GRIDs and 78 ASET DOF is shown in Figure 5 along with a sketch depicting the stiffener/constraining layer configuration.

NASTRAN MSE analyses were run to determine the first mode loss factors for the various parametric configurations, and to give a conservative estimate of the loss factors for the higher modes. Figure 12 shows the NASTRAN calculated strain energy in the VEM vs. VEM thickness. Constraining layer thickness and test article total weight as calculated by NASTRAN are cross plotted. The point chosen for the design is circled. The hat section was designed to meet the static deflection requirements of criterion III and the final choice of stiffener, VEM, and constraining layer was checked to ensure the satisfaction of the total deflection requirements. The calculated loss factors are plotted vs. frequency for modes up to 500 Hz. in Figure 13. Results for a temperature range of 60° F to 70° F are presented. Values for each temperature were determined from a single NASTRAN run using the shear modulus at the fundamental frequency and are therefore conservatively low in both frequency and loss factor for the higher modes. A more detailed model than the coarse one shown in Figure 5 would be required to accurately calculate loss factors for the higher modes, but since it was decided that the honeycomb stiffener panel would be used for the modal test and the analysis correlation tasks, a larger model was not justified. The more coarse model is adequate for determining the loss factor of the lower modes and performing the parametric analyses to determine the design point.

3.0 BEAM ELEMENT FABRICATION AND EXPERIMENTAL EVALUATION

Several beam elements of candidate stiffener designs were fabricated and tested to: (1) verify fabrication methods planned for panels and (2) verify analytical predictions of performance. ISD112 and several GE-SHRD VEM's were used in a honeycomb sandwich configuration and in several hat stiffened configurations with unidirectional graphite-epoxy constraining layers. Results indicated ISD112 was not suitable for the stiffener configuration because of low bond strength. The SHRD materials were found to provide maximum performance close to room temperature but were slightly off on either the high or low side. Test results agreed reasonably well with analytical predictions using NASTRAN modal strain energy methods. Material properties appeared to be a major source of analysis error. Temperature was highlighted as the key variable effecting damping performance. These beam element tests are discussed in this section.

3.1 CANTILEVER BEAM ELEMENTS

3.1.1 TEST CONFIGURATIONS

A cantilever beam specimen was designed and fabricated to provide an early evaluation of candidate configurations, a preliminary correlation of analysis predictions with measured damping performance and identify unanticipated fabrication problems. The beam test article is shown in Figure 14. The honeycomb sandwich configuration was the lightest weight design using graphite epoxy (G/E) face sheets with thicknesses selected to provide inherent structural stiffness corresponding to criterion III. Honeycomb face sheet thicknesses were selected to maximize damping as discussed previously. Steel bars bonded to the bottom surface of the beam provided transverse stiffness and increased the weight so that the resonant frequencies would be in the range of panel designs. SMRD 100F90 material of 1/4 inch thickness was found to approximate the desired damping and is of the thickness used in other spacecraft applications. The beam width was abritrary. The aluminum thickness simulates the stiffness of the DSCS III magnesium panel.

The initial viscoelastic material selected for the honeycomb sandwich was ISD112 with a 10 mil thickness. This material uses a pressure sensitive adhesive and was found to come loose as a result of surface irregularities in the honeycomb pieces. This problem combined with concerns as to the bond strength in this stiffener application resulted in a change to SMRD 100F90. The The SMRD 100F90 uses a structural adhesive (HYSOL EA9309.3) known to exceed the VEM shear strength.

3.1.2 ANALYTICAL PREDICTIONS

A NASTRAN model of the Honeycomb cantilever beam configuration was used to estimate the damping and fundamental resonant frequency using the Modal Strain Energy method (MSE). The model was relatively coarse as shown in the SUPERTAB plots of Figure 15. The beam was divided into 10 spanwise segments and 7 crosswise segments using a single row of elements to represent the stiffeners and has 219 nodes. CQUAD4 elements were used for the aluminum baseplate and the honeycomb face sheets. The VEM and honeycomb core were modeled using CHEXA elements. Offsets were used in the CQUAD4 elements adjacent to the CHEXA elements so that common nodes could be used between the elements while simulating the neutral axis position. The steel bars were modeled using CBAR elements with offsets. All nodes at the cantilevered end were fixed which represented the interface with the test fixture, i.e. all DOF's at the end nodes of the plate, stiffener, VEM, and constraining layer. The model was reduced to 52 ASET DOF's of which approximately two-thirds were in the out-of-plane direction. The full mass matrix was calculated by NASTRAN using material densities for the various elements. A model check was made for the fundamental mode by increasing the number of nodes and dynamic DOF's by approximately 4; however, the much finer model results did not differ significantly from the coarse model. The Young's modulus for the G/E elements was 30E6 psi based on a 60 percent fiber volume fraction. The shear moduli for the honeycomb core were 135 Ksi and 54 Ksi representing the nominal value for 1/8-5052-.002 core material provided by Hexcel. The shear modulus of the viscoelastic material was varied over a range of values to determine the fundamental mode resonant frequency and loss factor as a function of temperature.

The analytical prediction of the fundamental resonant frequency and loss factor as a function of temperature were determined by combining NASTRAN results with the SHRD 100F90 properties displayed as a function of reduced frequency. The procedure is shown graphically in Figure 16. The VEM shear modulus, G, was varied in the NASTRAN analysis and the fundamental resonant frequency determined and plotted. The percent of modal strain energy in the VEM was also determined and plotted in the Figure. A resonant frequency was selected and the value of G determined from the NASTRAN results as indicated by Step 1. Using these values for F and G, the corresponding temperature is uniquely determined as shown. This also determines the VEM loss factor as indicated in the figure. The VEM loss factor and the NASTRAN modal strain energy are then combined as described previously to determine the composite loss factor. This procedure is repeated for various frequencies providing the analytical prediction of resonant frequency and composite loss factor as a function of temperature. The analytical results for the cantilever beam are shown in Figure 17.

The analytical results were determined using two different sets of material properties. The properties of SHRD100F90A have been determined by three different laboratories. Although the approaches used by each were similar, differences exist in the final properties. Two Reduced Temperature Nomographs are shown in Figure 18. The basic nomograms differ in shift parameters precluding direct comparison. The shear modulus and loss factor data from these two nomograms were used to define the properties at a temperature of 65° F and plotted vs. frequency in Figure 19. Also included is a third set of data measured from the same batch of VEM that was used for the Lab B measurements. The Lab A and Lab B measurements were both performed with sandwich beams and the data reduced with different α_T relations and different To constants. The Lab C measurements were obtained from a modified Oberst beam and reduced with the same α_T relation that was used for the Lab B data reduction, but with a different To.

It is apparent from the three curves of Figure 19 that more research should be be performed on VEM measurement and data reduction methods. There is considerable scatter in the raw data through which these curves were faired, and the choice of constant To in the temperature shift relation α_T is of great importance. Analyses were performed using the two reduced temperature nomograms and results were compared with test results.

The accuracy of these analytical predictions depends on the accurate modeling of the overall structure as well as the accurate representation of the VEM properties. Inherent in the procedure is the assumption that the model without the VEM accurately predicts the structural behavior. If the model of the non VEM structure is too stiff, then the analytical predictions will require a lower VEM shear modulus to match the measured resonant frequency. This will ultimately result in an apparent shift in the analytic results to a higher temperature. Similarly, higher strain energy in the non VEM structure will cause the analytical composite loss factor to be low. On the other hand, inaccuracies in the VEM properties could cause the analytical predictions to vary in either direction. When correlating analytical and experimental results, structural model error sources should be kept in mind and the overall difference should not be attributed solely to the VEM modeling.

3.1.3 EXPERIMENTAL RESULTS

The cantilever beam was tested using base excitation and circle fit techniques to accurately determine the resonant frequency and damping. The beam was clamped over a two inch span at the root and bolted to a Team Hydrostatic Table which was driven with an MB C-150 shaker. Three accelerometers were mounted to the tip of the beam to determine the phase and amplitude of the beam response. A single reference accelerometer was mounted to the vibration table to measure the input. The beam was excited sinusoidally. The accelerometers were recorded on magnetic tape and processed through the HP5423A Dynamic Analyzer. The analyzer determined the resonant frequency and damping of the beams at the fundamental resonance using a circle fit to the response with the input acceleration used as a reference. Because the fundamental mode was well separated from other resonances, this technique provided an accurate estimate of the loss factor and resonant frequency. The measurements were repeatable within approximately 1% and are not subject to inaccuracies associated with bandwidth measurements. Initial tests at input levels varying from 1/2 to 2 g's indicated that non-linear effects were small compared to temperature effects. Tests were subsequently performed with a single input level.

A crude method was used in these initial tests to vary temperature. The original intent was to test the beams only at room temperature. However, as the tests progressed, it was evident that the temperature should be varied to provide adequate data to evaluate the damping performance. This was accomplished by varying the room air conditioner setting to obtain low temperatures and using heat lamps to obtain higher temperatures. A thermocouple was taped to the VEM portion of the beam to determine the test temperature. Using these techniques, the temperature varied from approximately 55° to 100° F. The test results are shown in Figure 17.

3.1.4 COMPARISON OF ANALYTICAL AND EXPERIMENTAL RESULTS

The experimental results for the honeycomb sandwich beam cover a relatively wide temperature range and indicate reasonable agreement with analytical predictions but with an apparent temperature shift. The measured fundamental resonant frequency varied from 204 to 124 Hz which compares favorably with analytical variations from 209 to 118 Hz. There appears to be a 4 to 8 degree F shift in the resonant frequency curve but this could be caused by underestimating the cantilever beam stiffness (e.g. the analytical shear stiffness of the honeycomb was lower than actual). This tends to be substantiated by the asymptotic values. A similar shift in the temperature of maximum damping is also evident. The maximum measured loss factor is within 1 to 17 percent of predicted. The difference in the VEM properties obviously has a major effect on the accuracy of the analytical predictions.

The results of these initial tests indicated the need to obtain more detailed test data to evaluate performance and to consider other damping materials. The temperature was identified as a key parameter to correlate test and analytical results. A wide, well controlled temperature variation is needed to provide data on the analytical adequacy by checking both glassy and rubbery asymptotes, with more accurate measurements in the transition region. A test of the basic undamped structure would be helpful to verify analytical model accuracy. The observed peak damping was above the temperature range of interest indicating peak performance would require a different VEM material. Some

of the differences between test and analysis can be attributed to the uneven temperature distribution in the test article caused by the heat lamps.

3.2 END SUPPORTED BEAM ELEMENTS

Following the tests of the cantilever beam specimen, two end supported beams were fabricated and tested. The objective of these tests was to obtain better analytical correlation by using end supported test articles and by using a thermal chamber over the shaker so that the temperature could be controlled more accurately. In addition, one beam used SMRD 100B50 which has a lower transition temperature than SMRD 100F90.

3.2.1 TEST CONFIGURATIONS

The end supported beam test configurations are shown in Figure 20. The beams consisted of a 10 inch wide by 17 inch long 1/8 inch aluminum plate. Five steel bars were bolted and bonded to the plate to provide chordwise stiffness and beam resonance in the frequency range of interest. A single half inch wide hat section was riveted to the center of the beam simulating a criteria III stiffener. The viscoelastic material was bonded to the stiffener and a constraining layer of G/E with uniaxial fibers was bonded to the VEM. The VEM layers were 1/4 inch thick SMRD 100F90A and 0.10 inch thick SMRD 100B50C. The beam was bolted with washer stand-offs to aluminum bars which were attached to the 30 inch diameter head of an MB C-220 shaker. The end supported configuration was felt to be more readily analyzed than the cantilever arrangement used in the initial tests. The entire shaker head was enclosed in a small thermal chamber which contained a heater, a blower and a thermostatic control. Liquid CO_2 was vented into the chamber to cool the test article below ambient temperatures. Thermocouples sandwiched within a block of SMRD and attached to the outside of the block were used to determine when the temperature of the test article had stabilized.

3.2.2 ANALYTICAL PREDICTIONS

The analyses of the end supported beams were performed using NASTRAN and the MSE method described for the cantilever beam. The SUPERTAB plot of the FEM is shown in Figure 21. The model was finer than that used for the cantilever specimens having 18 elements in the spanwise direction and 9 elements chordwise. The model used CQUAD4 elements with offsets for all but the steel bars and VEM. The steel bars were modeled using CBAR elements with offsets. The VEM was modeled using CHEXA elements as in the cantilever model. The modulus of the VEM was varied in the NASTRAN analysis and the final results presented as a function of temperature using material property curves as described previously. An additional analysis was performed for the bare beam without the VEM to correlate with test results.

The analytical predictions for the hat stiffened beam are shown in Figure 22. The resonant frequencies of the first three modes are shown for both simply supported and clamped boundary conditions. Because of the dependance of the VEM model on that of the model for the basic stiffened beam, analysis and testing of this configuration was performed. The analytical results for the two damped beam configurations are shown in Figures 23 and 24 for the 1/4 inch

SMRD 100F90 and for the 0.10 inch SMRD 100B50 respectively. For the SMRD 100F90, analytical results are presented for both Lab A and Lab B material property data. For the SMRD100B50, only one set of material property data was available.

3.2.3 EXPERIMENTAL RESULTS

The experimental results are shown in Figures 22 to 24 for the various test conditions. The tests were performed in the same manner as the cantilever tests except that the MB C-220 shaker was selected because of its larger head diameter. The major change in the procedure was the use of the thermal chamber over the test article which improved the accuracy and range of test temperatures. The instrumentation consisted of three response accelerometers: two at midspan at the center and edge and one at quarter span in the center. The input was measured at one end of the beam. The response at the center mid-span was circle fit to measure the fundamental resonant frequency and damping. The other midspan accelerometer was checked for torsion which was found to be negligible at the fundamental resonance.

3.2.4 COMPARISON OF ANALYTICAL AND EXPERIMENTAL RESULTS

The first step in correlating the analysis and test results was to compare the resonant frequencies of the basic undamped beam, Figure 22. This was done by pl⁻ ⁻ing the ratio of the analysis to the test frequency for the first three bend. ⁻des. This comparison showed that there is excellent agreement in the fundu 1 resonant frequency when the analysis considers the beam to be clampc at the bolt attachments. There are, however, significant differences in the second and third resonant frequencies which were closer for pin constraints at the bolt attachments. In the interest of expediency, the results were considered satisfctory for analytical predictions of fundamental mode resonant frequency and damping. The decision was made to proceed but to limit comparisons to the fundamental mode only.

The analytical results for the beam with the 1/4 inch SMRD 100F90, Figure 23 agree reasonably well with test results for resonant frequency and temperature of maximum damping when Lab A material properties are used. Using Lab A material properties, the calculated temperature of maximum damping, 77° F, agreed with the test within measurement accuracy with less than 5 percent difference in the corresponding resonant frequency. The maximum damping, however, was 34 percent higher than measured. This agreement was considered to be partially the result of the accuracy of the beam-stiffener model which agreed within 2 percent of the measured resonant frequency. Using the Lab B material properties, the calculated temperature of maximum damping was approximately 77° F which was the same as predicted using Lab A properties. The analytical resonant frequency also agreed reasonably well. However, the maximum calculated damping was 21 percent higher than measured.

For the beam using the SMRD 100B50B, the analysis results agreed fairly well with measured values although only one estimate of material properties was available, Figure 24. The resonant frequency closely follows the measured values but shows a higher calculated asymptotic value at high temperature; this indicates a higher analytical stiffness of the basic beam than actual. The

temperature of maximum damping was 6° F lower than measured with the maximum calculated damping about 30 percent higher than measured. The resonant frequency of maximum damping agreed closely.

The summary of the beam test data is given in Table 3 and Figure 25 comparing the maximum loss factor and the corresponding temperature and resonant frequency. The maximum loss factor appears to be the most error prone with 30 percent variations between analysis and test. Calculated resonant frequencies and temperatures at the maximum damping point are generally within 15 percent and 3° F, respectively. The table indicates a high sensitivity of results to material properties. It will be noted that modeling errors of the basic stiffened beam are included in the calculations and the variations should not be considered to be solely VEM associated.

4.0   PANEL MODAL TESTS

4.1   TEST DESCRIPTION

The general arrangement of the modal tests is shown in Figure 26. The two test panels were the undamped baseline panel and the lightweight honeycomb configuration with a quarter inch layer of SMRD 100F90B between the inner aluminum honeycomb stiffener and the outer graphite epoxy honeycomb constraining layer. Each test panel had the simulated TWT'S installed and was bolted to a test frame along its four sides. The frame, in turn, was bolted to a massive rigid base. The frame had numerous openings machined around it to permit air to flow into the opening between the panel and the base fixture. (Initial tests indicated that the air trapped between the panel and the mounting base stiffened the test panel. After the openings were machined into the frame the fundamental panel mode was found to drop to nearly half the original test frequency.) A single Unholtz Dickie 50 pound permanent magnet shaker was attached to one of the TWT's through a flexible stinger which contained a piezoelectric force transducer and accelerometer at the TWT attachment end. The shaker was attached at the outer edge of one TWT for tests of both the baseline undamped panel and the damped panel. For the damped panel, a second shaker attachment at the center of the middle TWT was also used. Analytical predictions prior to performing the test indicated that these locations would effectively excite the modes of the panel below 300 Hertz. The shaker was suspended from a bungee sling attached to an overhead crane that could readily be positioned to align the shaker with the panel.

The instrumentation for the undamped baseline panel was limited to three accelerometers while 14 accelerometers were used for the damped panel. All of the accelerometers measured vibration normal to the panel except for two accelerometers mounted to the top of the center TWT on the damped panel. While a single accelerometer at the top center of each TWT measured the undamped panel responses, four accelerometers mounted at the bottom corners of the TWT's were used to measure the out of plane TWT response on the damped panel. The temperature of the damped panel was measured with a thermocouple attached directly to the viscoelastic material.

HE-13

A portable air conditioning unit was used to control the temperature by directing a flow of cooling air over the test panel. Data were obtained at 70° F. Endevco 2213 accelerometers and a Krystal force transducer were used to measure the response and excitation. Previous tests have shown negligible phase shifts between the transducers at frequencies above 5 Hz.

A pure random shaker excitation was applied over the frequency range from 20 to 500 Hertz. The force Power Spectral Density had a 6 dB/octave roll-up to improve the response signals in the higher modes. The transducer signals were analog recorded using a Spectral Dynamics multiplex system and played back for subsequent modal data processing. A shaker force of 8 pounds RMS was used to excite both the undamped and damped panel. The force amplitudes were arbitrarily selected to provide adequate response measurements.

The data were reduced using an HP5451B Fourier Analyzer with a University of Cincinnati (UCMIE) software package. The analog data were digitized and transfer functions generated using the Analyzer. The coherence was checked to assure accurate transfer function definition with zoom analysis performed to improve accuracy where needed. A typical transfer function is shown in Figure 27 and indicates the coherence was very close to unity in the resonant frequency range. Adequate frequency resolution was provided for both the undamped and damped panels. The UCMIE software option used for extracting modal parameters was the Least Squares Multi-Mode curve fit routine. This was necessary because of the large amount of modal overlap in the heavily damped modes as well as those panel modes which had closely spaced resonant frequencies. The mode shapes determined from the transfer functions were transferred by digital tape to the large mainframe computer for comparison with analytical predictions. Because of the limited number of measurements, the dot product between the test and analysis modes was used for comparison.

4.2 ANALYSIS TEST CORRELATION

The first seven out-of-plane analytical modes of the undamped panel with fixed edges are compared with the test results in Table 4. The modal dot products were calculated using only the Z motions normal to the panel for both the test and analysis modes. The dot products show good agreement between analysis and test mode shapes with those modes dominated by Z motion having values greater than 0.9. As would be expected, the agreement is not as good for modes having a large amount of rocking or X and Y motion. The resonant frequencies agree with test values to within approximately 10 percent. The test panel was bolted directly to the base plate at all locations which should have given it a nearly fixed boundary condition. The test loss factors were on the order of 0.03 or less showing the baseline structure to have relatively little damping.

The analytical predictions for the damped honeycomb panel are compared with the test results in Table 5 for a temperature of 70°F. The analysis is based on fixed boundary conditions along the four panel edges. As indicated in the Table and shown graphically in Figure 28, the resonant frequencies of the first four out-of-plane modes agree with test values within approximately 10% while larger errors are apparent in the higher modes. The coarseness of the NASTRAN model is believed to contribute to this error; however, it is apparent that the error in the resonant frequencies of the two highest modes are significantly greater than the error in undamped panel analysis. The modal dot products are compared in Figure 29 and show good agreement with only two of the damped panel

modes showing values lower than those of the undamped panel. The ratio of the measured to calculated loss factors is shown graphically in Figure 30. The comparison indicates that the calculated values tend to be less than the measured values but that the measured values are generally greater than two-thirds of the calculated values. The earlier element test results gave similar results with the agreement between calculated and measured loss factors being closer when maximum values were used. Subsequent panel tests using the base excitation method were performed over a wider temperature range to better correlate the analysis and test results.

The damped panel was excited sinusoidally by exciting it through its base using the MB C-220 shaker. The temperature was varied from approxmately 60° F to 90° F using the portable thermal chamber. The measured response was analyzed digitally using an HP5423A Fourier Analyzer to provide circle fits to the measured response. The input acceleration was used as the reference. Because of the overlap of the modal responses, circle fit results were only obtained for the fundamental mode. The results shown in Figure 31 agree with the previous test results and indicate that a maximum loss factor of 0.27 occurs at approximately 77° F. This is in closer agreement with the analytical predicted value of 0.35 but is shifted to a higher temperature.

The results of the modal test verify that a large amount of damping can be introduced into the panel with the damped honeycomb stiffeners. Although the maximum measured loss factors are less than the predicted values, the values agree within approximately 30 percent. The test results indicate that another viscoelastic material having a lower transition temperature would be more effective in damping the panel.

5.0 CONCLUDING REMARKS

Damped DSCS III Transponder equipment panel designs were developed using constrained layer viscoelastic materials (VEM's) on the panel stiffeners. Although preliminary studies indicated integrally damped honeycomb panels would be lighter and more effective, the damped stiffener design was selected because of thermal constraints caused by the high heat dissipating TWTA's. By using design criteria that accounted for the load reduction achieved by the damping, the weight impact was limited to 2 to 10 percent of the structural weight for the highly damped panel final designs. NASTRAN finite element analyses using Modal Strain Energy were used to systematically examine structural and VEM parameters to optimize the design. The VEM properties were represented with reduced frequency nomographs.

Reasonable agreement was obtained between analytical predictions and experimental results. Frequency and temperature were shown to govern the damping and resonant frequencies of VEM panel designs both analytically and experimentally. Analytical and measured modes shape agreement for the damped panel was nearly comparable to that of the undamped panel based on the dot product comparisons. There appeared to be shifts in the predicted temperature of maximum damping on the order of 3 to 10 degrees F. The resonant frequencies of the first seven panel modes agreed with analysis prediction within about 12 percent which was comparable to the agreement for the undamped panel. The maximum measured loss factor was within approximately 30 percent of analytical predictions with some values showing negligible variation. At specific temperatures, the measured

HE-15

loss factors were on the order of one half to two thirds of analytical predictions for the final panel design. Material property variations were shown to have a major effect on analytical predictions and could account for most of the differences between analysis and test results. Boundary conditions and inaccuracies in the finite element model of the basic structure also contribute to the test/analysis difference.

Large reductions in resonant magnifications were achieved with the damped stiffener designs. The first mode magnification measured on the undamped baseline panel was 26. The constrained layer damper design of the damped modal test panel reduced this Q of 26 to only 4.3 at the temperature of the modal test, (70° F) and to 3.7 at the temperature at which the peak loss factor was found during subsequent temperature sweep testing. These values compare to the Q of 3.0 which was calculated using NASTRAN MSE with VEM properties determined from a reduced temperature nomogram.

Subsequent acoustic test results showed that the damped panels were highly effective in reducing the random vibration environment. The initial goal of 6 dB reduction in the PSD was exceeded in the low frequency range by a large amount.

The results of this study demonstrate the effective application of viscoelastic material technology to the design of equipment panel structure.

6.0 REFERENCES

1. A. R. Timmins and R. E. Heuser, "A Study of First Day Space Malfunctions," NASA TND-6474, 1971.

2. R. B. Laube, "Methods to Assess the Success of Test Programs," Proc. of the 3rd Aersp. Testing Sem., Oct. 1982.

3. J. M. Medaglia, "Dynamic Integrity Methods Including Damping for Electronic Packages in Random Vibration," 50th Shock and Vib. Bull., 1980.

4. J. A. Staley and C. V. Stahle, "Damping in Support Structures for Equipment Reliability - RELSAT," Vibration Damping Workshop, Feb. 1984.

5. C. V. Stahle, "Cost Effectiveness of Spacecraft Vibration Qualification Testing," Proc. of Inst. of Env. Sci., 20th Annual Meeting, May 1974.

6. J. A. Staley, C. V. Stahle, J. C. Strain, "Vibroacoustic and Shock Performance of Damped Spacecraft Equipment Panels", Vibration Damping Workshop II, AFWAL March 1986.

7. K. A. Schmidt, F. Curtis, E. Muziani, L. Amore, "Fabrication of Damped Spacecraft Equipment Panels", Vibration Damping Workshop II, AFWAL March 1986.

8. F. Abdulhadi, "Transverse Vibrations of Laminated Plates with Viscoelastic Layer Damping," Shock and Vib. Bull. No. 4, Dec. 1969.

Table 1. Panel Design Criteria

A. LOAD FACTORS

CRITERION	STEADY (ZERO FREQ)	TRANSIENT (2 Hz)	VIBRO-ACOUSTIC	TOTAL	DEFLECTION
I. ADD-ON DAMPING - BASIC PANEL DESIGN-ED ASSUMING LOW DAMPING	3.0	8.5	23.5	35.0	ABOUT 0.10 INCH
II. INTEGRAL DAMPING - 50% REDUCTION IN VIBROACOUSTIC LOAD - NO LOAD CARRYING CAPABILITY OF DAMPING TREATMENT ASSUMED	3.0	8.5	11.8	23.3	ABOUT 0.10 INCH
III. INTEGRAL DAMPING - 50% REDUCTION IN VIBROACOUSTIC LOAD - DAMPING TREATMENT CARRIES TRANSIENT AND VIBROACOUSTIC LOADS	3.0	8.5	11.8	23.3	ABOUT 0.10 INCH

Header spanning: LOAD FACTOR (G)

B. DAMPING
- FUNDAMENTAL PANEL MODE LOSS FACTOR AT LEAST 0.3
- LOSS FACTOR FOR OTHER MODES UP TO 500 Hz AT LEAST 0.1

Table 2. Preliminary Design Weight Summary

PANEL DESIGN	STIFFENER/DAMPER		TOTAL STRUCTURE & DAMPER		TOTAL PANEL	
	LB	%	LB	%	LB	%
BASELINE-UNDAMPED	0.86	100	8.48	100	47.5	100
DAMPED STIFFENER* CRITERIA I	1.75	203	9.37	110	48.4	102
CRITERIA II	1.55	180	9.17	108	48.2	101
CRITERIA III (HAT STIFFENER)	1.33	155	8.95	106	48.0	101
CRITERIA III (HONEYCOMB STIFFENER)	0.72	84	8.34	98.3	47.3	99.7

*DAMPED STIFFENER DESIGNS USE P100 GRAPHITE (E=60E6, UNIAXIAL)

Table 3. Summary of Beam Test Results

TEST BEAM DESCRIPTION	MAX LOSS FACTOR (η)			RESONANT FREQ			TEMPERATURE			VIBROACOUSTIC MATERIAL
	TEST	ANAL	%DIFF	TEST(HZ)	ANAL(HZ)	%DIFF	TEST (F)	ANAL (F)	DIFF (F)	
CANTILEVERED H/C SANDWICH	0.46	0.465/ 0.38	+1.1/ -17.4	137	138/ 149	+0.7/ +8.8	100	88/ 95	12/ 5	1/4 INCH SMRD 100F90A
END SUPPORTED HAT-1/4 IN. VEM	0.29	0.39/ 0.35	+34.5/ +20.7	82	86/ 94	+4.9/ +14.6	77	76/ 76	1/ 1	1/4 INCH SMRD 100F90A
END SUPPORTED HAT - 0.10 IN. VEM	0.36	0.47	+30.6	90	91	1.1	37	33	6	0.10 INCH SMRD 100B50C

NOTES:
1) ANALYSIS VALUES SHOWN FOR LAB A AND LAB B 100F 90 MATERIAL PROPERTIES.
2) FUNDAMENTAL MODES ONLY.
3) VALUES OF PARAMETERS ESTIMATED FOR MAXIMUM LOSS FACTOR POINT.
4) CANTILEVER BEAM TEST TEMPERATURE NOT ACCURATELY CONTROLLED.

Table 4. Undamped Panel Modal Test Comparison

MODE NO	FIXED ANALYSIS FREQ (Hz)	TEST FREQ (Hz)	FIXED FREQ ERROR	MODAL DOT PRODUCT FIXED	TEST LOSS FACTOR (η)	MODE DESCRIPTION
1	55.4	49.7	11.5	1.000	.038	Z
2	117.4	106.1	10.7	.892	.016	Y - Z
3	123.4	110.3	11.9	.947	.022	Z - X
4	147.5	135.2	9.1	.946	.014	Z - X
5	210.6	213.5	- 1.4	.604	.020	X - Z
6	247.9	251.5	- 1.4	.975	.030	Y
7	279.8	270.3	3.5	.804	.027	X - Z
8	286.5	280.4	2.1	.810	.022	X - Z

NOTE: MODAL DOT PRODUCTS INCLUDE ONLY Z MOTIONS

Table 5. Modal Test Comparison for Damped Honeycomb Panel

70° F

MODE	RESONANT FREQ (HZ)		PERCENT FREQ ERROR	MODAL VECTOR DOT PDT	LOSS FACTOR(η)		LOSS FACTOR RATIO	$\dfrac{MEAS}{CALC}$
	FIXED ANAL.	TEST	FIXED ANAL.	FIXED ANAL.	FIXED ANAL.	TEST	FIXED ANAL.	
1	60.7	62.1	- 2.3	.991	.348	.231	1.51	.66
2	90.8	87.9	+ 3.3	.720	.261	.191	1.37	.73
3	127.4	140.1	-9.1	.921	.117	.081	1.47	.68
4	157.0	157.2	- .1	.937	.290	.176	1.50	.67
5	192.6	218.9	-12.0	.300	.121	.036	2.69	.37
6	216.5	195.8	+10.6	.775	.216	.184	1.02	.98
7	266.9	210.1	+27.0	.895	.068	.054	1.02	.98
8	298.6	248.5	+20.2	.978	.136	.091	1.14	.88
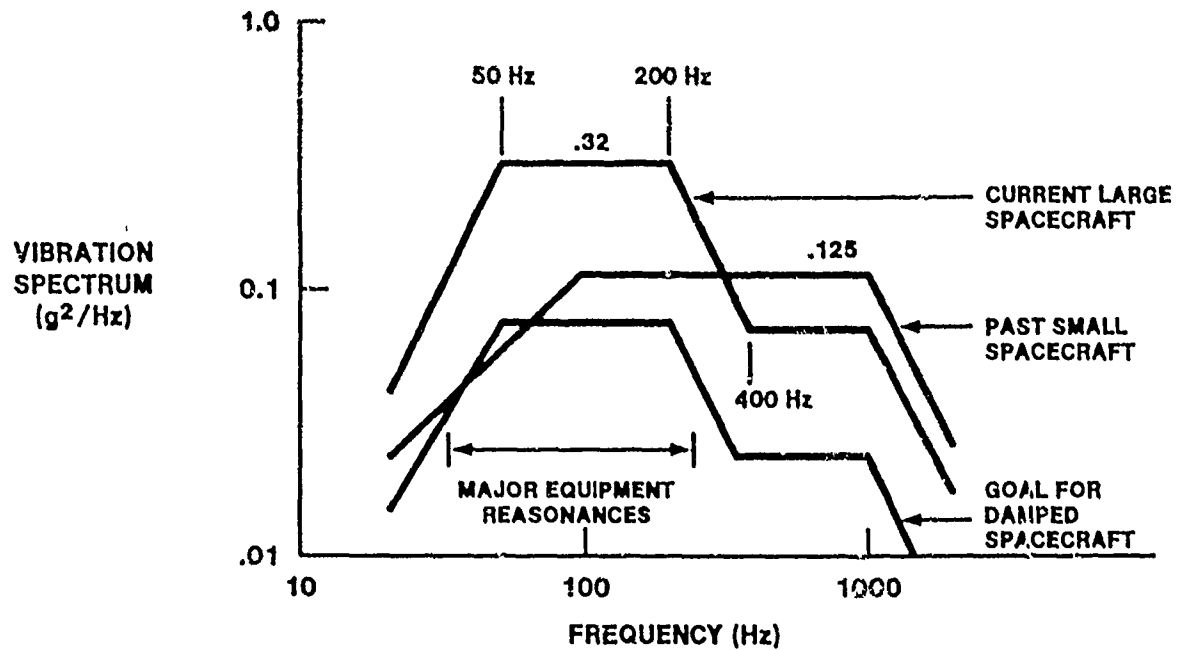
Figure 1. Equipment Random Vibration Requirements
With 6 dB Reduction Goal
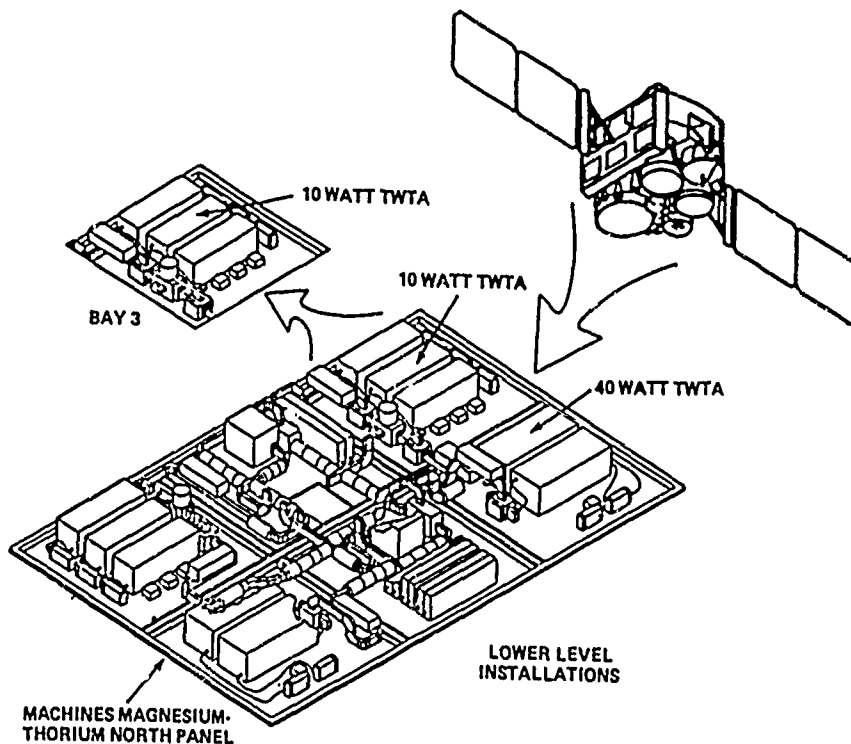
Figure 2. DSCS-III North Equipment Panel

Figure 3. Baseline Panel
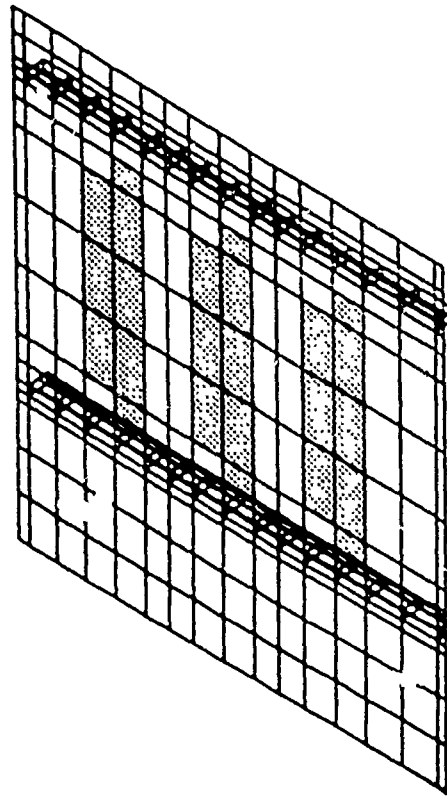
Figure 4. Nastran Model-Baseline
Undamped Panel

STIFFENER/DAMPER

GRAPHITE CONSTRAINING LAYER
SMRD VISCOELASTIC MATERIAL

ALUMINUM HAT SECTION

ALUMINUM BASE PLATE

HONEYCOMB SANDWICH WITH
GRAPHITE FACE SHEETS

SMRD VISCOELASTIC MATERIAL

HONEYCOMB SANDWICH WITH
ALUMINUM FACE SHEETS

ALUMINUM BASE PLATE
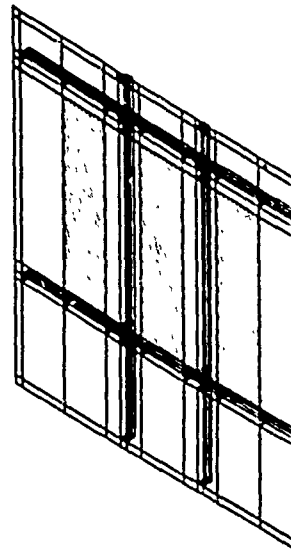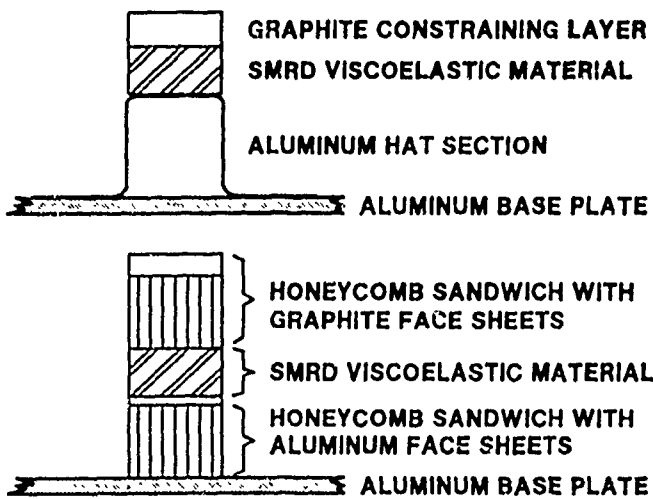
294 GRIDS
78 DYNAMIC DOF
209 CQUAD4
31 CHEXA

NASTRAN MSE USED TO ANALYZE THE DESIGNS

Figure 5. Damped Stiffener Concept and Parametric Study Nastran Model

PANEL DESIGN	STIFFENER/DAMPER	TOTAL STRUCTURE AND DAMPER	TOTAL PANEL
BASELINE UNDAMPED	100%	100%	100%
DAMPED STIFFENER			
CRITERION I			
CRITERION II			
CRITERION III HAT AND G/E			
CRITERION III HONEYCOMB			

CRITERION III PANEL WITH HONEYCOMB SANDWICH STIFFENERS WEIGHS APPROXIMATELY THE SAME AS BASELINE

Figure 6. Preliminary Design Weight Summary
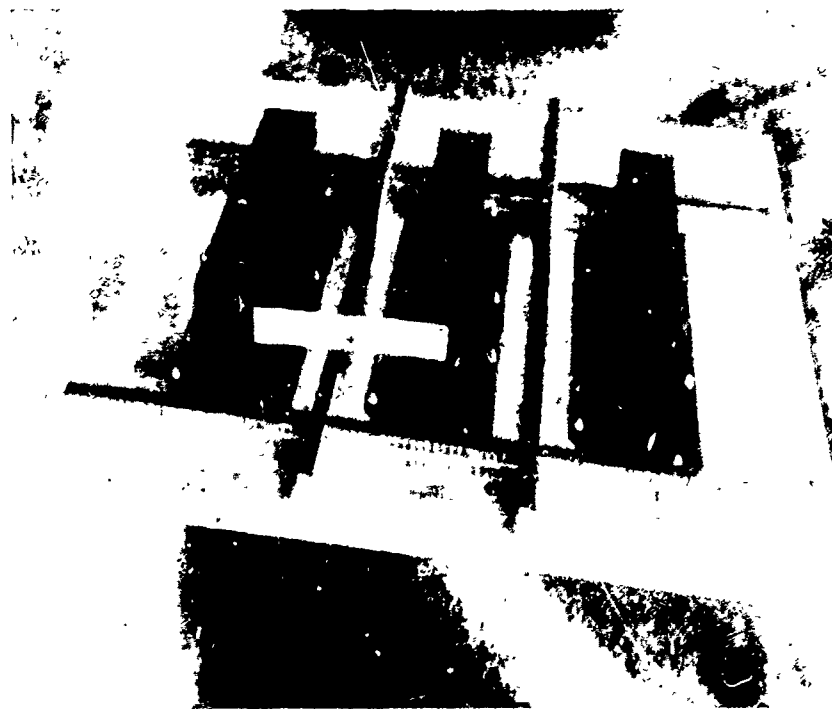
Figure 7. SMRD100F90B Damped Honeycomb Stiffener Panel

HE-21

STIFFENER/DAMPER

HONEYCOMB SANDWICH WITH
GRAPHITE FACE SHEETS

SMRD VISCOELASTIC MATERIAL

HONEYCOMB SANDWICH WITH
ALUMINUM FACE SHEETS

ALUMINUM BASE PLATE

674 GRIDS
294 DYNAMIC DOF
512 CQUAD4
168 CHEXA
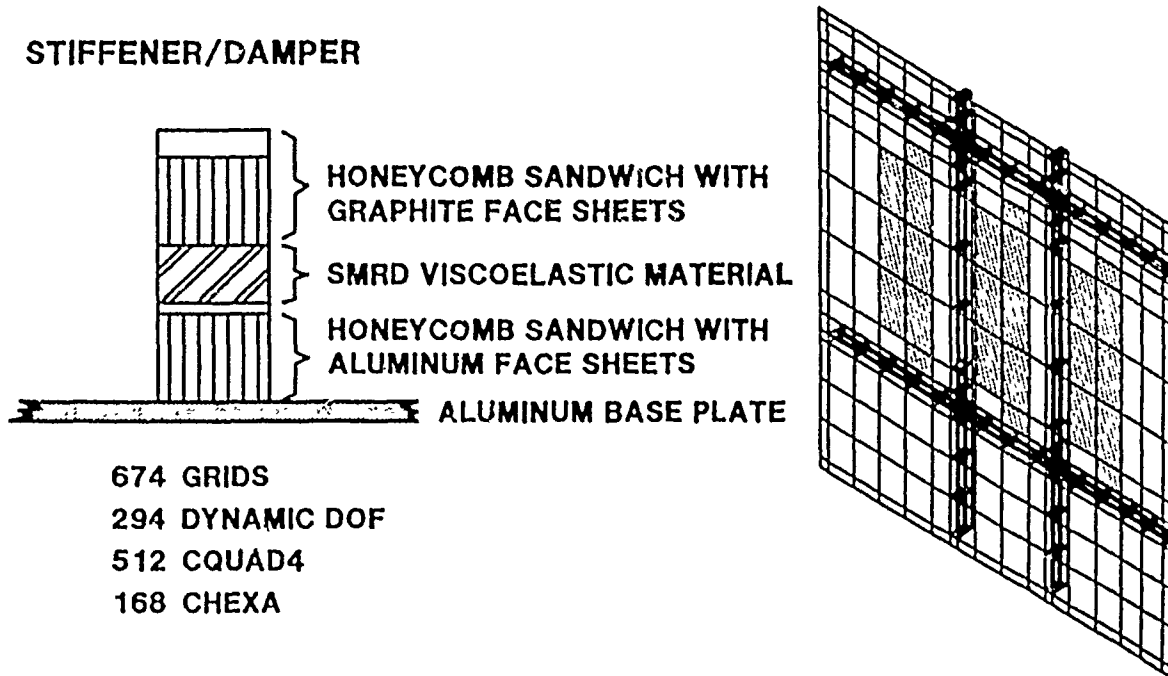
Figure 8.   Nastran Model – Damped Modal Test Panel

DESIGN
POINT

1ST MODE

SMRD 100 F90P2 @ 65°F
0.4" THICK HONEYCOMB STIFFENER &
CONSTRAINING LAYER

NASTRAN STRAIN ENERGY

SMRD THICKNESS (IN)

LOSS FACTOR VS. FREQUENCY
PANEL 2
0.25" SMRD 100F90B
HONEYCOMB SANDWICH STIFFENER AND
CONSTRAINING LAYER

O 65°F

BARS SHOW RANGE FOR
TEMPERATURES BETWEEN
60°F & 70°F

LOSS FACTOR

FREQUENCY (HZ)
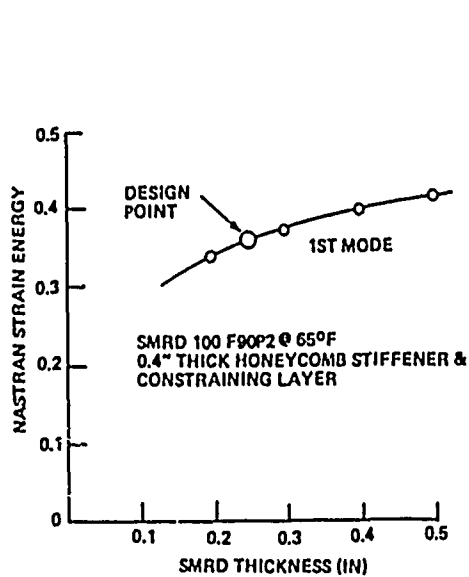
Figure 9.   Damped Modal Test Panel-
Nastran Model Strain Energy vs
VEM Thickness
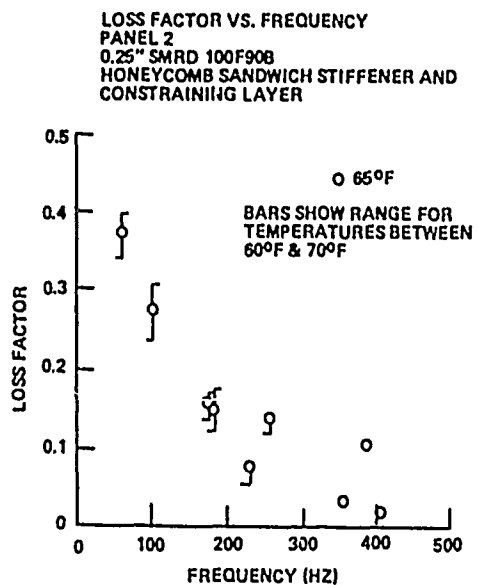
Figure 10.   Damped Modal Test Panel –
Preliminary Design Loss
Factors

HE-22

Figure 11.   SMRD100B50A Damped Hat Section Stiffened Panel
With 3 Subpanel Dampers

DESIGN GOAL: η_c > .3 1st MODE
.1 HIGHER PANEL MODES
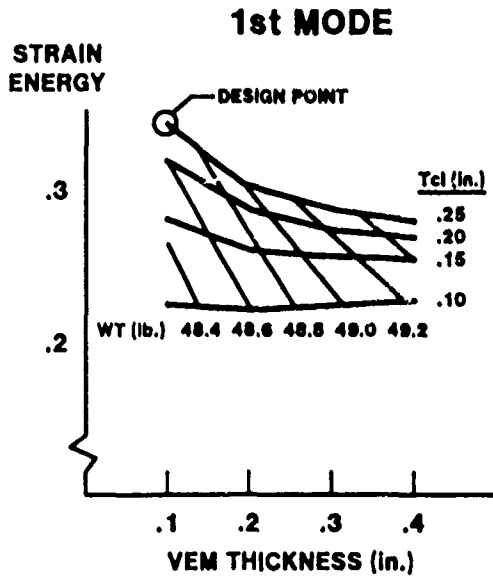
Figure 12.   VEM Strain Energy
vs. SMRD Thickness
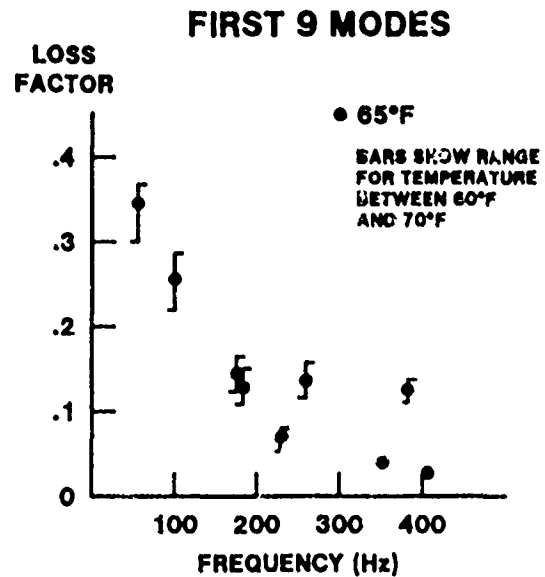
Figure 13.   Loss Factor vs Frequency
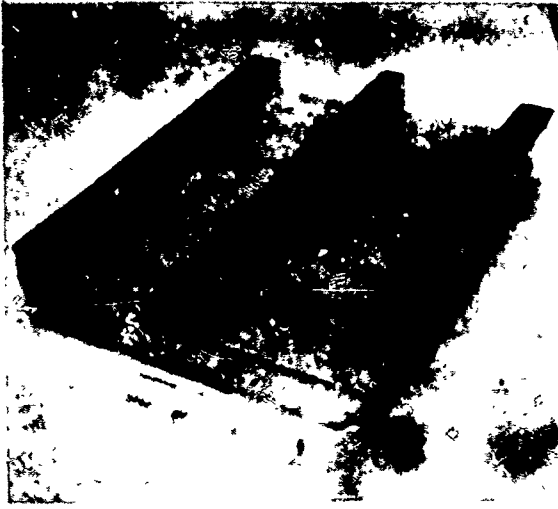
Figure 14. Cantilever Beam Test
Element
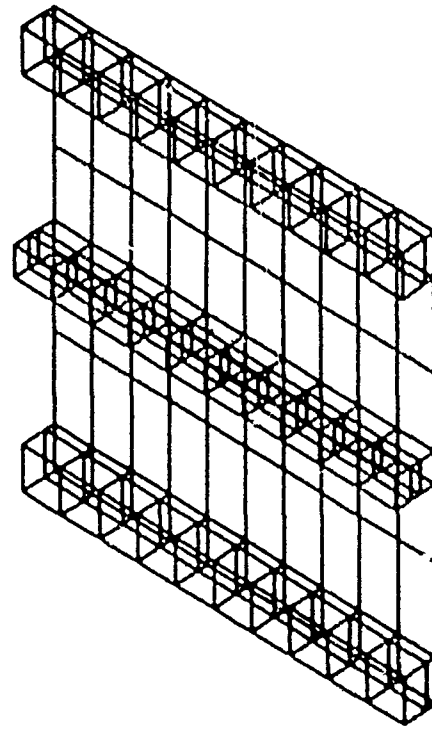
Figure 15. Nastran Model Honeycomb
Stiffened Panel
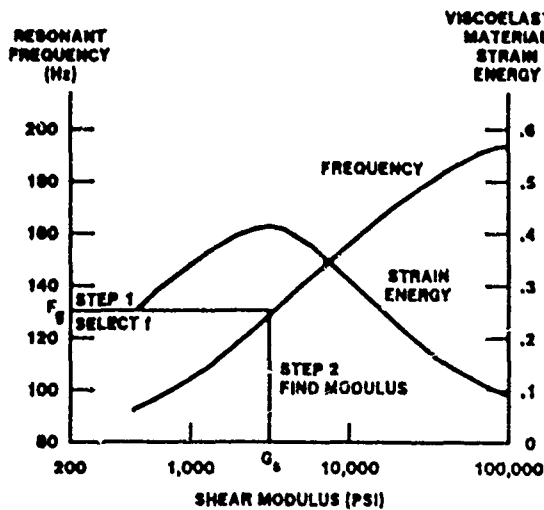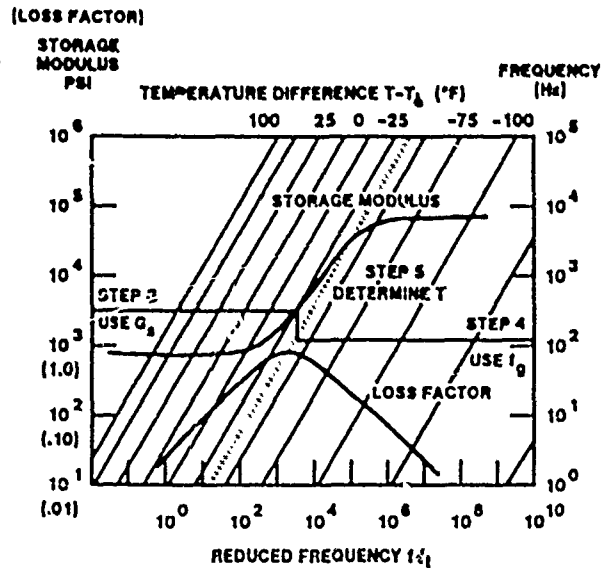
Figure 16. Methodology for Analysis/Test Comparison

HE-24
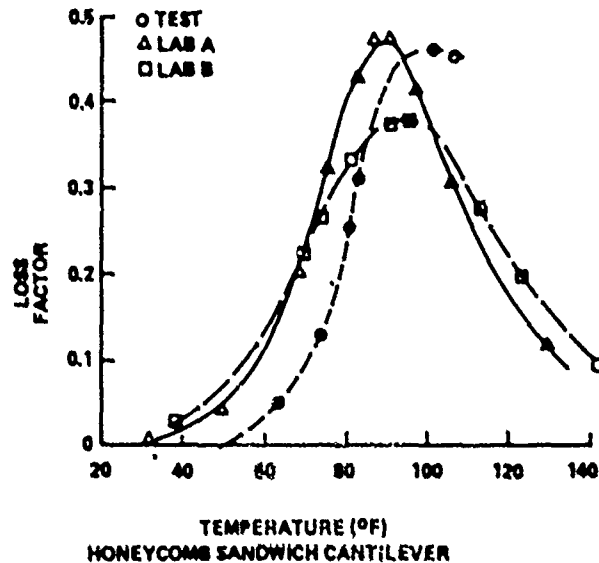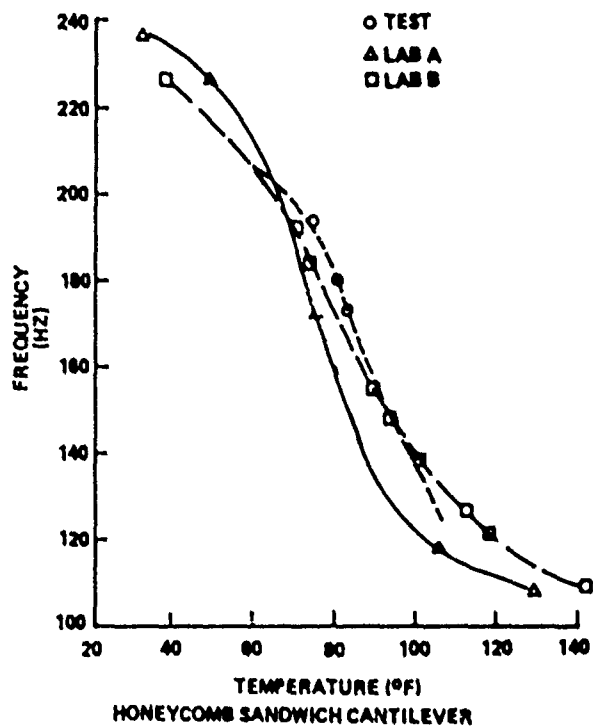
Figure 17.   Test/Analysis Comparison for Cantilevered
Honeycomb Stiffened Beam
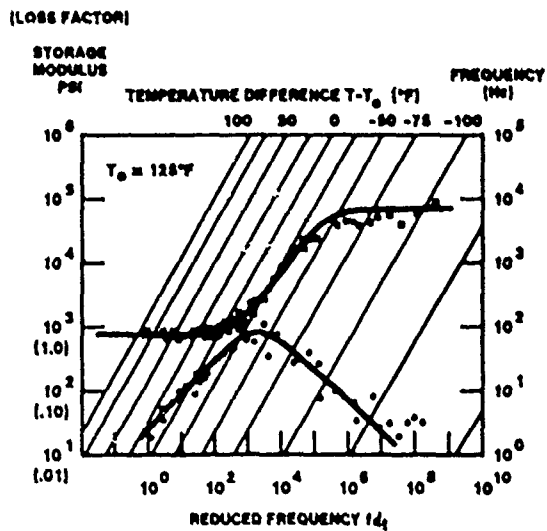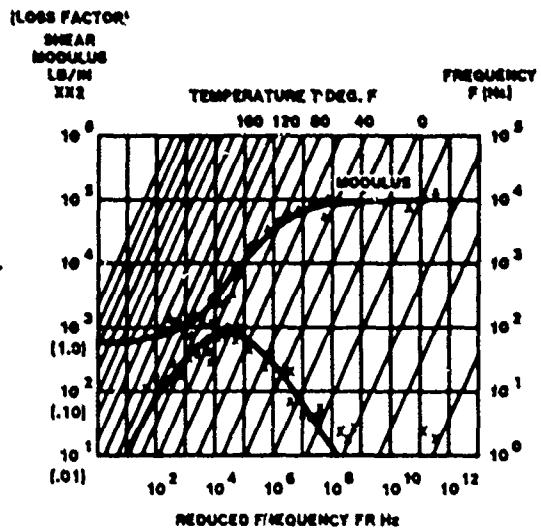
Figure 18.   Reduced Temperature Nomograms
SMRD100F90A
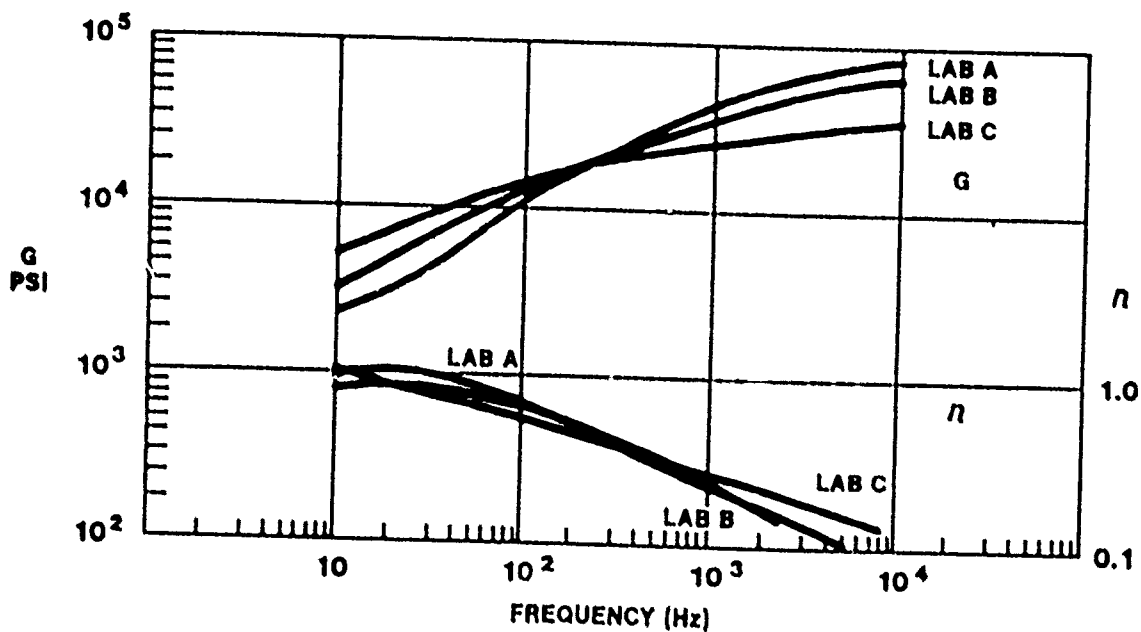
VEM PROPERTIES SHOW SIGNIFICANT VARIATIONS

Figure 19.   VEM Properties Show Significant Variations
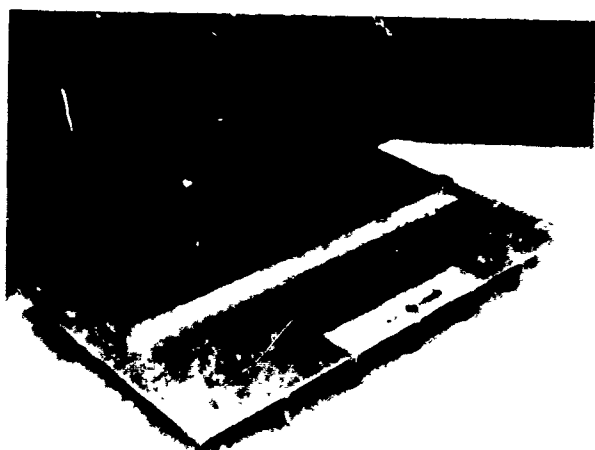
Figure 20.   End Supported Test Element
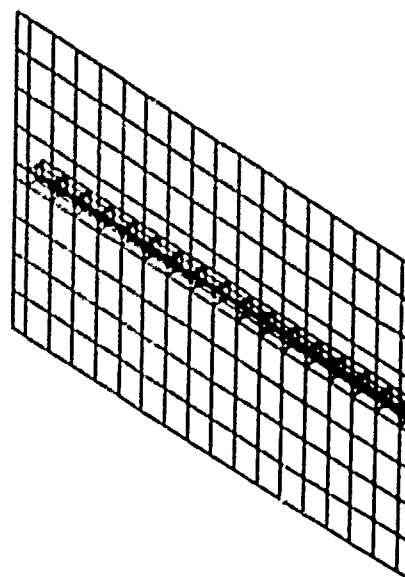
Figure 21.   Nastran Model of Hat Stiffened Beam
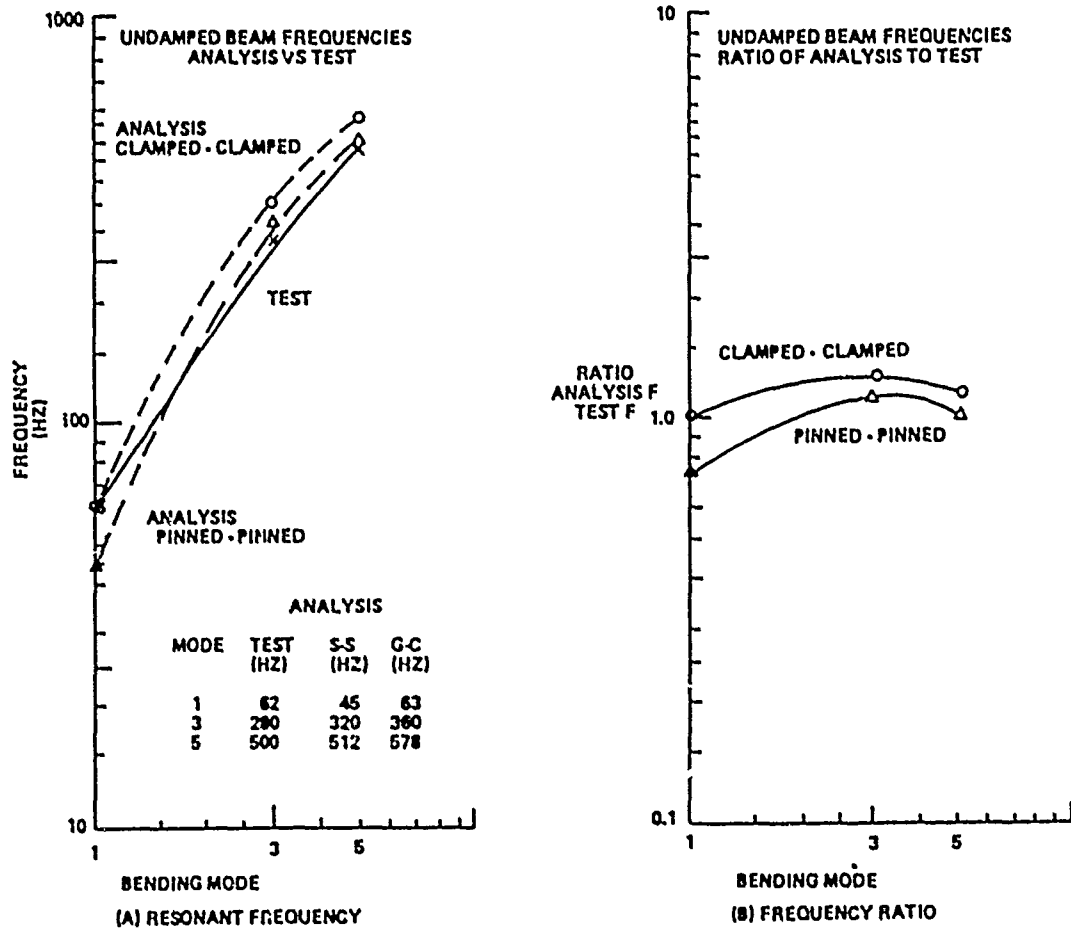
Figure 22. Analysis/Test Comparison for Undamped Beam
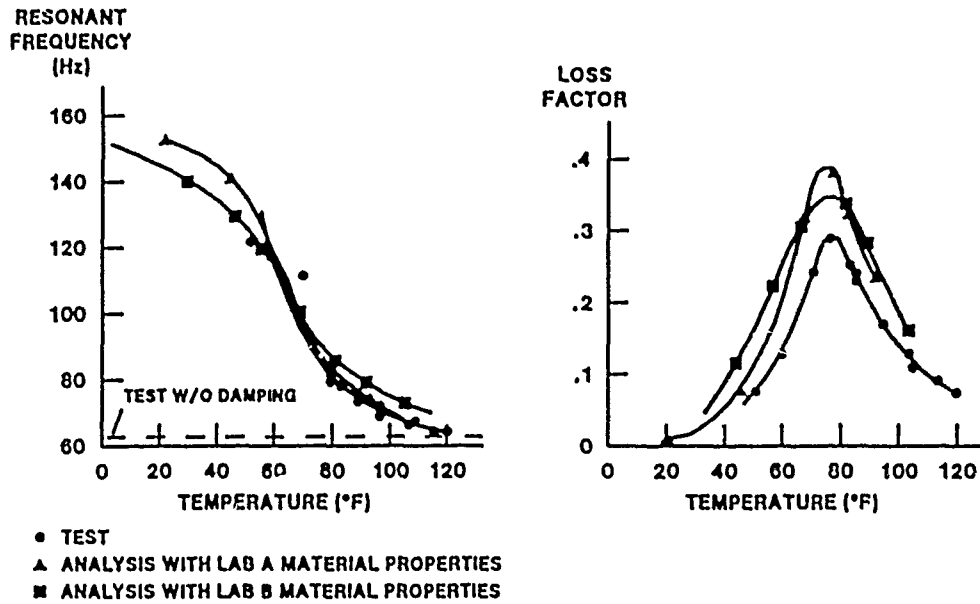
Figure 23. Test/Analysis Comparison for 1/4 Inch
SMRD100F90A Hat Stiffened Beam
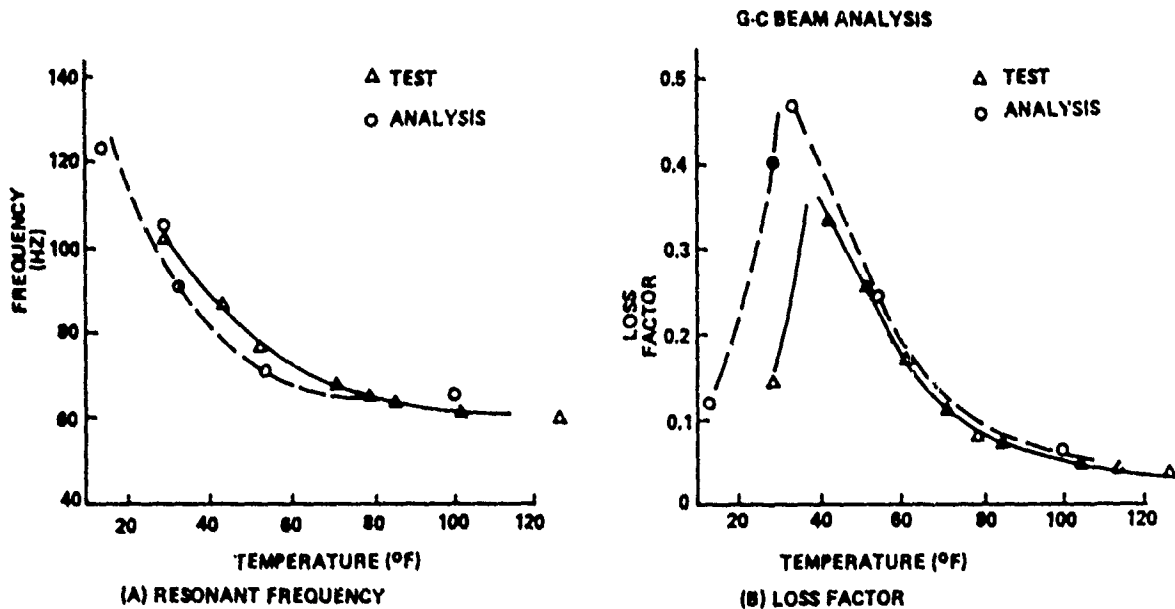
Figure 24.   Test/Analysis Comparison for 0.1"
SMRD100B50C Hat Stiffened Beam

Figure 25.   Summary of Elements - Analysis vs Test
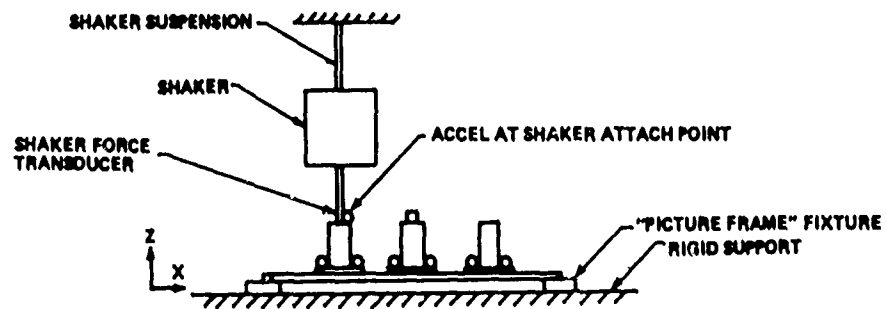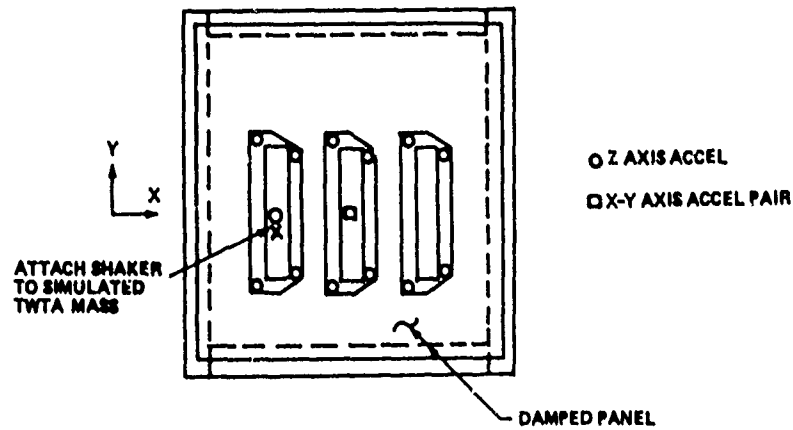
Figure 26. Panel Modal Test Arrangement
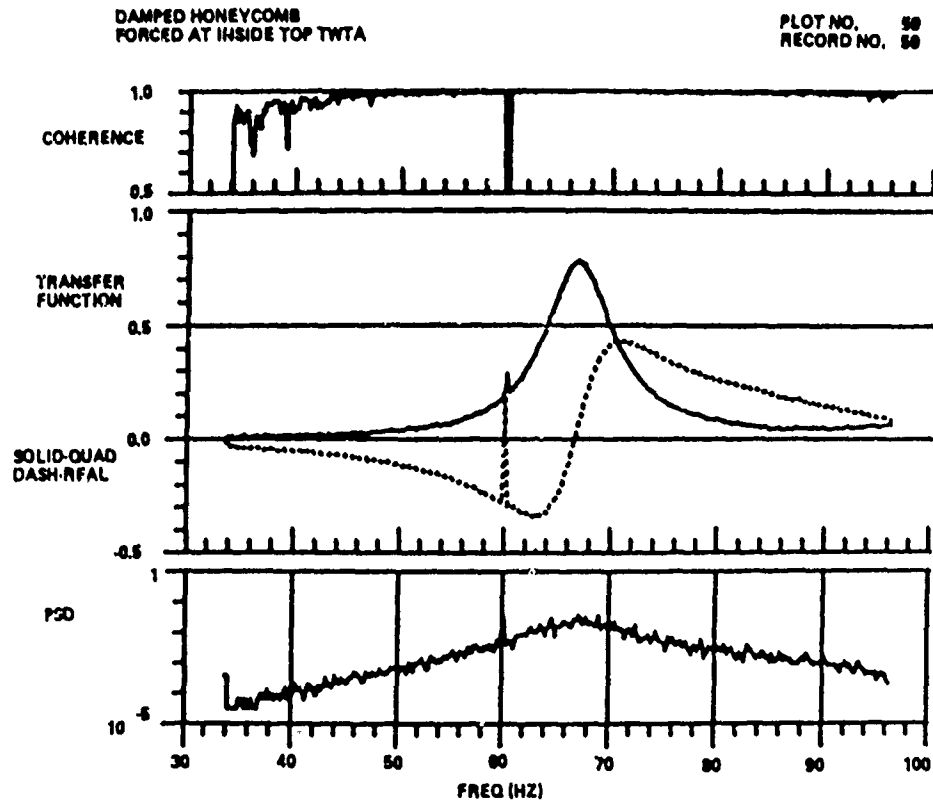
Figure 27. Typical Zoom Transfer Function

BASELINE

DAMPED HONEYCOMB STIFFENER
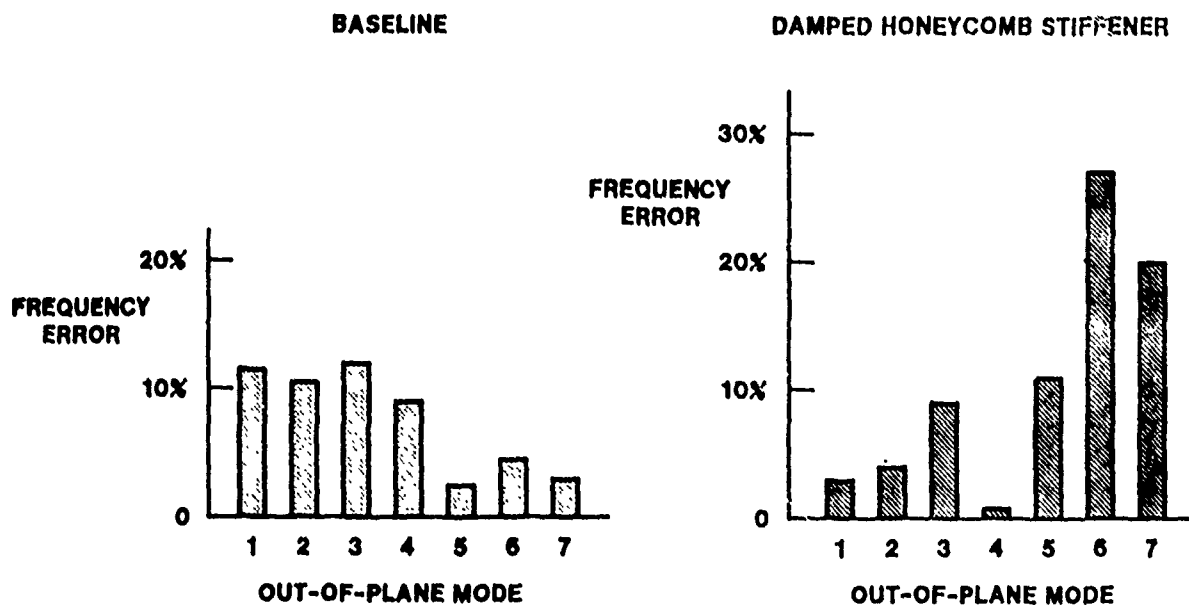
FREQUENCIES OF LOWER PANEL MODES CALCULATED WITHIN 12%

Figure 28. Resonant Frequency Comparison

BASELINE

DAMPED HONEYCOMB STIFFENER
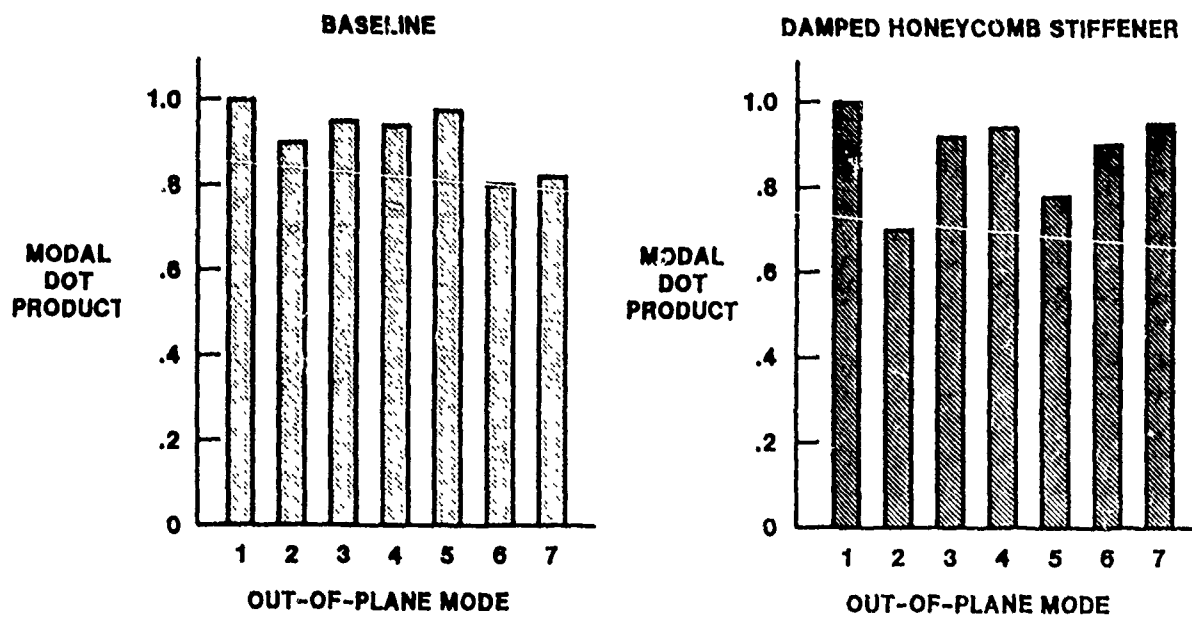
MODAL DOT PRODUCT > .7 FOR ALL OUT-OF-PLANE MODES

Figure 29. Modal Dot Product Comparison
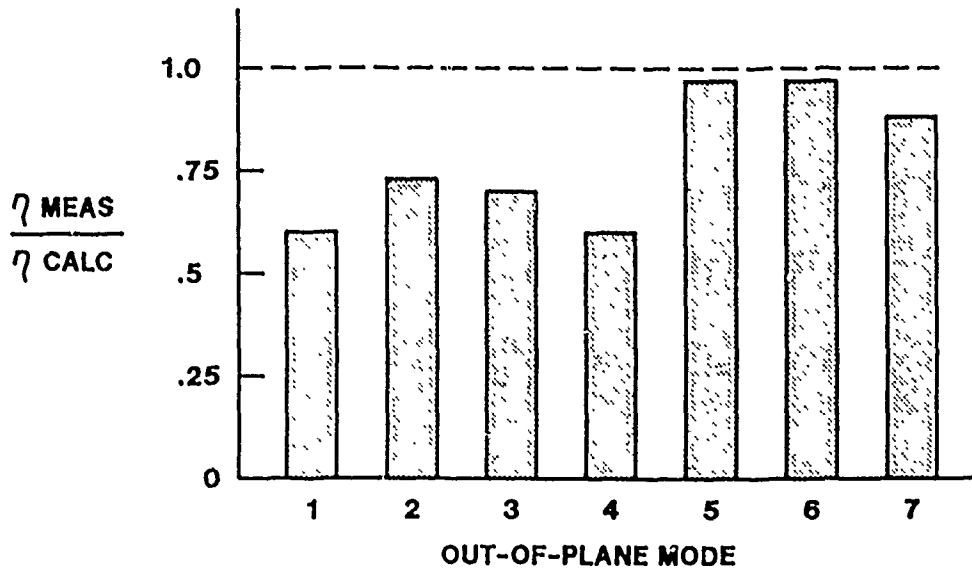
Figure 30. Loss Factor Comparison
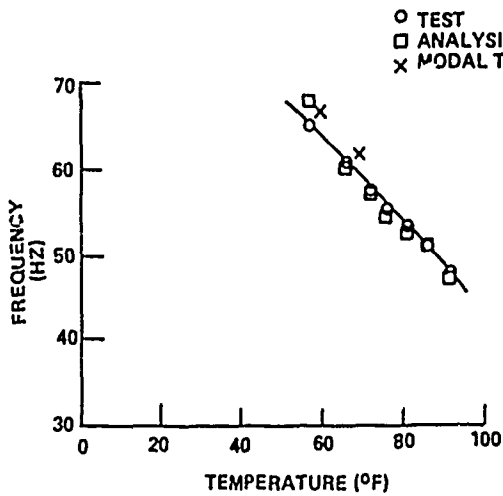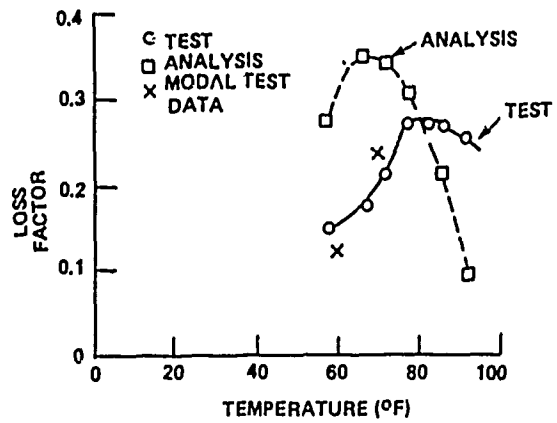
Figure 31. Damped Modal Test Panel Test/Analysis Comparison

FABRICATION OF DAMPED SPACECRAFT EQUIPMENT PANELS*

K. SCHMIDT, F. CURTIS, E. MUZIANI, L. AMORE

GENERAL ELECTRIC SPACE SYSTEMS DIVISION
VALLEY FORGE SPACE CENTER
P.O. BOX 8555, PHILADELPHIA, PA 19101

ABSTRACT

This paper discusses the material considerations and fabrication methods used in the GE RELSAT program and describes the technology needed to produce viscoelastically damped spacecraft equipment panels. Tests of the panels presented elsewhere in these proceedings indicate the damping is predictable and highly effective in reducing the vibroacoustic environment of electronic packages. The materials technology described herein builds on more than 15 years of GE experience in damping spacecraft electronic packages and other devices using a SMRD 100 viscoelastic epoxy. Material requirements are driven by prelaunch thermal vacuum testing, launch temperature of 60 to 72 degrees F, launch vibration frequency of 50 to 500 Hertz, and the need to survive 10 years in orbit without contaminating the spacecraft. GE SMRD 100 materials were selected that satisfied these requirements and were known to maintain their excellent damping properties after 4 years in orbit. Modulus and loss factor of candidate materials are compared at the temperature of interest for frequencies from 10 to 10,000 Hertz. Standard panel fabrication methods are used except for viscoelastic material (VEM) machining which uses diamond tooling. Quality control methods needed to assure panel structural integrity and damping performance rely on X-ray and and ultrasonic techniques to evaluate bonding and resonant beam measurements to determine material properties. Alternate fabrication methods that eliminate some bonding operations are presented. Because current measurements of VEM properties have a large variation, it is recommended that improved methods be investigated. Improved property measurement should address experimental errors, relations used to derive properties from test measurement, derivation of the reference temperature used in the shift relation, and VEM formulation controls that assure uniform properties.

INTRODUCTION

This paper presents the material considerations, basic fabrication techniques and quality control measures critical to the fabrication of damped spacecraft equipment panels. In conjunction with this paper, two others have been written, which address the design and testing of Dynamic Test Article (DTA) Panels.[1,2] The purpose of this effort, is to demonstrate the use of viscoelastic damping to reduce vibroacoustic environments for satellite equipment mounting structures in a launch environment. Research, testing and subsequent evaluation have shown that the technology and material resources are available to fabricate and implement constrained layer damping on spacecraft structures.

BACKGROUND

The formulation and application of viscoelastic materials in spacecraft has been under development at GE-SSD for over 15 years. SMRD (Spacecraft Materials Research and Development), a highly efficient damping compound developed by GE, was first flown on Landsat I Earth Observation Satellite where avionics reliability was enhanced by limiting relay panel vibrations.[3] Subsequent applications include Viking Lander, Acoustic Cannisters, Gimbals, and Camera Mounts.[4] In addition, it is used extensively on printed circuit boards, providing efficient damping and additional stiffening of the boards and/or components. Figure 1 shows a typical constrained layer damping strip installation. The board has a center strip extending from the edge to the connector and an additional strip bonded to the connector. A minimum amount of space is occupied by the strips which use unidirectional graphite epoxy constraining layers.

The constrained layer fabrication is shown in Figure 2. The constraining layers are bonded to the viscoelastic material (VEM). They are then machined to the final dimensions. Typical damping strips using SMRD 100F90 with unidirectional graphite epoxy constraining layers are shown in Figure 3 and can be made in a wide variety of shapes and sizes. Sizes range from a few inches to a few feet in length. The DSCS III spacecraft uses approximately 2000 damper strips. Most use unidirectional graphite epoxy constraining layers. The keel member shown in Figure 4 employs the use of a large damper strip to limit vibration levels so that vibration of adjacent packages stays within specified limits. This keel damper was added after acoustic tests indicated package qualification random vibration levels were being exceeded.

Currently, the concept of viscoelastic damping is being evaluated in relation to reducing vibroacoustic environments for satellite equipment mounting structures during launch. To date, testing has been conducted which has shown the damping to be highly effective in attenuating vibroacoustic response. In addition, the structural integrity of damped panels under static load, sinusoidal load and creep effects under steady state load were measured. The results of acoustic and shock tests, and the design, analysis and modal tests are presented in two other papers included in the proceedings.[1,2] This paper discusses the viscoelastic material requirements and properties, material selection, fabrication methods and quality control procedures.

RELSAT PANEL DESIGN APPROACH

The approach used in the design of the damped panel configuration is shown in
Figure 5. The original panel design provided integrally machined stiffeners
with riveted flange sections to support the panel components. The damped panel
design uses a similar concept with a constrained layer damper added to the
flange section. Although the figure indicates the same size stiffener, the
damped panel designs actually used smaller stiffeners using the VEM and
constraining layers to provide added stiffness. With this concept, the thermal
design of the panel is unaffected. Heat is conducted through the panel
structures and the VEM effect is negligable.

MATERIAL CONSIDERATIONS

Requirements

Key requirements to be considered when selecting damping materials for
spacecraft applications include space compatibility, weight, strength,
stiffness and high damping in the frequency and temperature range of interest.
These requirements are summarized in Table 1 for the various flight phases.
Prior to launch, the material is subjected to thermal cycling for an extended
period of time during subassembly and spacecraft tests. In addition, a storage
capability of 2 years is also required. The launch conditions are critical for
the damping performance of the material which requires high damping from 60 to
72 degrees F in the 50 to 500 Hertz frequency range. High shear strength is
required so that structural integrity is assured. A wide range of stiffness
values are acceptable although they influence the thickness of the damping
layer. During orbital flight, the VEM must not contaminate the spacecraft
during its 10 year life. This is reflected in the outgassing requirements of
ASTM E-595 which requires less than 1 percent mass loss and less than 0.1
percent collectable Volatile Condensible Materials under elevated temperature
and vacuum conditions. By selecting the dampened panel stiffener approach,
thermal conduction requirements are precluded.

Candidate Materials

The properties of candidate materials are compared in Table 2. The material
density varies from .028 to .066 pounds per cubic inch which affects the weight
but is not critical because of the small amount of material used. The
outgassing results, however, do eliminate the AF32 (SMRD 100F90A is an
acceptable material although it slightly exceeds the outgassing values).

Aging Effects

It is imperative that materials used on the spacecraft withstand the thermal
vacuum conditions imposed without changing stiffness and damping properties,
i.e. stability of the viscoelastic material properties is essential. In
addressing this requirement, SMRD panels are post cured under vacuum for 96
hours as a stabilization process. To verify the stability of GE developed
SMRD, recent events have enabled an evaluation of SMRD following four years in
space. The Solar Max Attitude Control Module launched in February of 1980 and
retrieved from space in April of 1984, used SMRD in its interior structure. A
sample recovered from the Attitude Control Electronics (ACE) package was tested

and found to have retained high damping properties after four years in space. Figure 6 compares SMRD 100F90 retrieved from space to standard SMRD 100F90 data. The individual data points shown for the SMM material were obtained from modified Oberst beam tests. The curves correspond to the original material before extended space exposure. The comparison indicates that the properties have not changed significantly. A maximum loss factor of approximately 1.0 was measured for the SMM material. This value is in close agreement with the maximum value for the corresponding curve. The data verify the stability of the SMRD material. Similar data are not available for the other materials in Table 2.

Damping and Stiffness Properties

This section addresses material characterization of VEM damping and stiffness. This information can be readily displayed on Reduced Temperature Nomograms (RTNs). Past research has shown that there is a definite correlation between many rheological materials in regard to behavioral similarities at different temperatures and frequencies. Measurements of the stiffness, E or G, and loss factor, η, as a function of frequency for various temperatures can be obtained. Using a shift parameter, α_T, and the data derived above, stiffness and loss factor information at various temperatures can be collapsed into a single curve. As a result, modulus and loss factor can then be plotted as two curves on a Reduced Temperature Nomogram.[5] This is illustrated in Figure 7. Ultimately, this nomogram can be used to determine material properties for the temperature and frequency of interest in a particular application. Figure 7 illustrates modulus and loss factor data at an average temperature of 65 degrees F, the temperature of interest, for various frequencies. Because the RTN includes the shift parameter which is material dependent, material comparisons and selections must be made using the material property curve shown on the right of Figure 7 which is independent of the temperature shift relation.

The accuracy of the material property measurements are also indicated by the individual data points in Figure 7. The temperature shift relations can be used to translate the properties from the RTN to the material properties at a specific temperature, including the curves and the original data points. The scatter in the data points provide an indication of the accuracy of the property measurements. Although the scatter appears small on the three cycle log scale, the scatter is relatively large with factors of two or more for many points. The scatter is particularly large for the loss factor.

In essence, the goal in searching for a good damping material is to find one whose high damping properties coincide with the temperature and frequency ranges of interest. In the specific case of DSCS III launch environment, the temperature and frequency ranges of prime importance for the North Panel Structure are 60 to 72 degrees F and 50 to 500 Hertz, respectively. In an attempt to attain the required stiffness and damping under these conditions, material formula variations were researched and tested. One way to evaluate the difference in damping properties between the material candidates is to compare them in relation to glass transition temperature. Modifications were made to the standard material in an attempt to shift the transition temperature, so that peak damping would occur in the desired temperature and frequency range. Figure 8 shows that SMRD material properties can be altered to meet specific requirements. Of the three materials shown in this graph,

SMRD 100F90C performed ideally for the RELSAT application. Peak damping occurred for about 50 to 500 Hertz at 65 degrees F.

In addition to the GE-SSD material formulations, commercial damping materials were investigated. Two materials selected for initial evaluation were DYAD 601 and 3M ISD112. Both materials satisfy the outgassing requirements, however, at 65 degrees F the peak damping for DYAD 601 was at a frequency above the range of interest for the DSCS III panel. Measured material properties from beam tests are shown in Figure 9. In addition, ISD112 properties were also measured, Figure 10. It appeared to be too soft, and required very thin layers to be effective. It did not have the required bond strength for the stiffener aplication. UDRI 3 was also considered, but was rejected because its tacky consistency posed fabrication problems and could cause contamination of the spacecraft. The final selection of candidate materials for panel fabrication and tests were four SMRD100 materials. The material properties are compared in Figure 11. The four prime material candidates are described below:

SMRD 100F90B is a modified 100F90 formulation which has significantly better outgassing characteristics and a temperature of peak damping closer to the ranges of interest than the original formulation. It is relatively stiff with a low density, and has been used by GE-SSD for electronic packages.

SMRD 100F90C is a further modification of 100F90, formulated in an attempt to reduce the transitiion temperature so that peak damping would occur in the temperature and frequency ranges of interest.

SMRD 100B50A has the damping properties which appear ideally suited for DSCS III transponder panel application. The material loss factor is high over a relatively broad frequency range and is nearly unity over the frequency range of interest. It has the same base resin system as 100F90, however it is modified by the addition of a conductive filler. The temperature of maximum damping at 100 Hertz is 63 degrees F and lies within the desired temperature range.

SMRD 100B50B - This is a modification of the previous material which is stiffer. At 65 degrees F, the frequency for peak damping is shifted to about 200 Hz, and has high damping over the frequency range of interest.

The decision to use the SMRD 100 materials was based on the fact that these materials satisfy the outgassing, strength, stiffness and damping requirements established. Refer to Table 3 for material selector parameters. In addition past experience in viscoelastic damping facilitates the application of various techniques used in damped printed wire boards to those for the damped spacecraft equipment panels.

DAMPED EQUIPMENT PANEL FABRICATION

VEM Fabrication Process

Both SMRD 100F90 and 100B50 are cast and cured in teflon coated aluminum molds in thicknesses ranging from 0.1" to 0.25". The sheets are stabilized and outgassed under vacuum at 135 degrees C for 96 hours; see Figures 12 and 13. The SMRD can be used as fabricated or milled to the desired dimensions. In the past, an aluminum oxide cup wheel was used to mill the SMRD. Due to obvious surface imperfections, diamond tooling replaced the former tool. Figure 14 is a photograph of a diamond compax end mill used primarily for milling smaller sections of VEM. The diamond flycutter shown in Figure 15 mills approximately a two inch wide strip per pass as compared to 1/2 inch strip produced with the end mill. This tool is used in larger applications.

Surface Preparation

Once the materials are machined to size, the SMRD can be bonded to constraining layers such as aluminum and graphite/epoxy laminates. To obtain optimum bond strength, an effective method of surface preparation is employed. The SMRD and constraining layers are abraded using 100 grit Aluminum Oxide paper. All surfaces are thoroughly cleaned with isopropyl alcohol and allowed to air dry.

Adhesive Selection/Bonding

Proper adhesive selection is essential in terms of space application. Once again, outgassing requirements, in addition to strength under rigorous environmental conditions are critical factors which must be considered. SMRD 100F90 and 100B50 bonded to both graphite/epoxy laminates and aluminum using epoxy adhesive, amine or polyamine cured epoxy resin. The adhesive selected for application was Hysol EA9309.3 commercial grade aerospace adhesive. material offered adequate strength and rigidity in addition to being comp with the materials under consideration.

Finally, the actual bonding of the SMRD to the constraining layers is a simple procedure. A thin film of adhesive is applied using a fingerprint roller. The materials are mated in such a manner as to preclude excessive air entrapment. The bonded sections are then cured under pressure.

Two damped panel configurations were designed and tested, one incorporated aluminum honeycomb stiffeners and the other aluminum hat section stiffeners. Figure 16 is representative of the honeycomb stiffener panel prior to completion. Aluminum honeycomb stiffeners are bonded to SMRD which will subsequently be bonded to a graphite/epoxy honeycomb constraining layer. Traveling wave tube amplifier (TWTA) mass simulators are bolted to the aluminum panel. Figure 17 shows a completed honeycomb panel prior to test. The aluminum hat section stiffener panel shown in Figures 18 and 19 consists of aluminum hat sections riveted to the aluminum base plate. A viscoelastic damping layer is bonded directly to the hat, followed by a graphite epoxy constraining layer. TWTA mass simulators are then added for dynamic testing.

The method of damping used on these panels simulates the predicted effect of constrained layer damping on the transponder panel of the DSCS III spacecraft.

FUTURE DAMPED PANEL FABRICATION

Looking into the future of constrained layer viscoelastic damping, a technique has recently been developed to eliminate the bond between the voscoelastic material, in this case SMRD, and the graphite epoxy laminate. Figure 20 compares the interfacial bonds between the VEM and laminate for adhesive and direct bond methods.

The new procedure incorporates the bonding process into the layup of the graphite epoxy laminate. As in the current process, the SMRD must be abraded and thoroughly cleaned. The graphite/epoxy prepreg is then layed up directly onto the surface of the SMRD sheet and cured under vacuum. The damper strip assemblies can then be machined to required dimensions. The benefits of this new procedure include improved bond strength, elimination of the bonding step and surface preparation of the graphite/epoxy laminate and most importantly, it virtually eliminates the possibility of interfacial voids because of high resin flow from the graphite/epoxy prepreg and the high pressure under which the composite is cured.

QUALITY CONTROL PROCEDURES

VEM Properties Confirmation

To validate the material properties of the SMRD, several tests were conducted. Hardness, using a Shore A durometer measured the materials resistance to indentation. It is a simple and effective means of monitoring changes in material stiffness. Density was determined through weight and dimensional measurement. Finally, to determine the damping properties of the viscoelastic material, the modified Oberst beam method of test was employed.[6] Specifically, the beams consisted of an aluminum layer sandwiched between two pieces of viscoelastic material. A series of beams were then mounted to a shaker and excited using base excitation. Damping properties of the materials under consideration, were determined over a wide range of frequencies and temperatures.

Structural Assessment

In addition to material property confirmation, non-destructive testing to determine structural integrity is critical. Delamination between the constraining layers or panel and the damping medium could cause a significant reduction in damping efficiency. As a result, it is important that non-destructive inspection techniques be employed to insure structural integrity. Three methods of test suggested are Ultrasonic Pulsed Echo techniques, Ultrasonic Impedance Plane Analysis and Real Time Radiographic Examination.

Ultrasonic and Contact Pulse Echo operates on the principle of pulsed ultrasonic waves. The waves are monitored as they interact with the material being inspected. A pulse ultrasonic beam is introduced into the part and the returning echos are monitored. This test method gives information regarding the type, size, location and depth of the defect. Figure 21 illustrates the difference between a bonded area and one with a known void. The large peak present on the photograph on the left is the back reflection of the aluminum

hat section. This peak diminishes when a voided area is contacted. Since this signal will not transmit through air, the last material the signal detects is the adhesive coated SMRD, signifying a void or debond as indicated in the photograph on the right.

Ultrasonic Impedance Plane Analysis using a Bonda Scope, is an alternate method of Non-Destructive Evaluation. The acoustical impedance plane method uses a small probe to generate a standing wave across the material thickness. The test frequency is selected to vibrate the laminate in such a fashion that the response to bondline and anomaly size is enhanced. The standing wave, which contains acoustical material information, affects the impedance value at the material surface. This value is then transformed through the probe's acoustic impedance into its electrical impedence. It is this electrical impedence which is subsequently processed for display on the acoustic impedance plane. Figure 22 illustrates a typical setup, where a bonded area appears as a dot located at the center of the grid and a non-bonded area shows up as a dot in one of the four quadrants depending upon depth and location of the anomaly.

Radiographic Examination or X-Ray, is another technique used to evaluate structural integrity. X-Rays are directed through the part being inspected and monitored with a screen or film sensitive to X-rays. Figure 23 shows an X-ray evaluation of a debonded area. Since a void will absorb fewer X-rays than a non-voided area, a dark spot will appear. Radiography can be performed through the thickness to detect anomalies or tangentially to detect delaminations.

CONCLUSIONS

As a result of this research and development effort, the following conclusions are made:

- The necessary technology is available to fabricate damped panel structures.

- Performance can be enhanced by altering material formulation to conform to application requirements.

- Key outgassing requirements can be satisfied.

- SMM damping material retains high damping properties after four years in space, verifying material stability.

- Standard fabrication methods can be used for all operations except VEM machining.

- Quality Control Methods are available to assure properties of the panel.

- The variation in measured VEM properties should be reduced.

- The VEM test method should be revised to reduce experimental errors.

- The VEM temperature shift relations should be improved.

- Material uniformity should be maintained within close tolerances.

REFERENCES

1. J. C. Strain, J. A. Staley, and C. V. Stahle, "Design and Experimental Verification of Damped Spacecraft Equipment Panels," Vibration Damping Workshop II, March 1986.

2. C. V. Stahle, J. A. Staley, and J. C. Strain, "Vibroacoustic and Shock Performance of Damped Spacecraft Equipment Panels," Vibration Damping Workshop II, March 1986.

3. C. V. Stahle and W. H. McCandliss, "Controlling Vibration of Viking Lander Electronic Packages," 44th Shock and Vibration Symposium, December 1973.

4. C. V. Stahle and J. M. Medaglia, "SMRD Damping Applications," SAMPE Series Volume 25, 1980, pp. 90-102.

5. D. I. G. Jones, "A Reduced-Temperature Nomogram for Characterization of Damping Material Behavior," 48th Shock and Vibration Symposium, Oct. 1977.

6. Ahid D. Nashif, "A New Method for Determining Damping Properties of Viscoelastic Materials," Shock and Vibration Bulletin No. 36, Pt. 4, 1967.

ACKNOWLEDGEMENTS

Table 1. VEM Requirements for DSCS III North Panel

PRE-LAUNCH
- COMPONENT/SUBASSEMBLY THERMAL CYCLING
- SPACECRAFT THERMAL CYCLING

  TEMPERATURE: -34 TO 71°C   TEMPERATURE: -17 TO 60°C
  VACUUM: 10⁻⁶ TORR   VACUUM: 10⁻⁷ TORR
  TIME: 10 DAYS   TIME: 25 DAYS

- STORAGE—COMPONENTS AS PART OF THE SATELLITE FOR 2 YEARS

LAUNCH
- TEMPERATURE (SHUTTLE BAY):   60 TO 72°F
- FREQUENCY OF HIGH DAMPING: 50 TO 500 Hz
- SHEAR STIFFNESS: 100 TO 1000 PSI
- SHEAR STRENGTH: 100 TO 10000 PSI AT 100 Hz

ORBIT
- SURVIVE ORBITAL ENVIRONMENT FOR 10 YEARS WITHOUT LOSS OF STRUCTURAL INTEGRITY OR CONTAMINATING THE SPACECRAFT
- OUTGASSING PER ASTM E-595
  - TOTAL MATERIAL LOSS: <1%
  - COLLECTIBLE VOLATILE CONDENSIBLE MATERIALS: <0.1%
- HEAT CONDUCTION: NOT A CONCERN BECAUSE OF DESIGN APPROACH

Table 2. Candidate Materials

MATERIAL	DENSITY (LB/IN³)	OUTGASSING VCM %	OUTGASSING TML %	PROPERTIES AT PEAK DAMPING G (PSI)	LOSS FACTOR	TEMP (°F) @ 250 Hz
ISD 112	.034	.02	.68	140	1.2	89
DYAD 601	.04	.01	.37	2.3K	1.0	35
AF 32	.0382	.46	1.97	76K	.9	84
UDRI 3	.034	.03	0.58	8K	1.0	62
SMRD 100F90A	.0285	.11	1.10	4.6K	1.0	98
SMRD 100F90D	.0296	.08	.81	2.7K	1.0	86
SMRD 100F90C	.0295	.05	.83	3.7K	1.0	71
SMRD 100B50A	.0613	.08	.57	4.1K	1.1	63
SMRD 100B50B	.0635	.10	1.17	4.2K	1.2	70
SMRD 100B50C	.0662	.05	.47	3.8K	1.0	74

Table 3. Material Selection

ISD 112
- LOW BOND STRENGTH
- FABRICATION DIFFICULTY

DYAD 601
- TEMPERATURE/FREQUENCY RANGE NOT MATCHED

AF 32
- EXCESSIVE OUTGASSING

UDRI 3
- FABRICATION DIFFICULTY (TACKY)
- CONTAMINATION

SMRD 100
- PROPERTIES CAN BE ALTERED TO MATCH APPLICATION
- FAMILIAR WITH FABRICATION METHODS
- HIGH BOND STRENGTH
- GOOD OUTGASSING REQUIREMENTS
- STABLE AFTER INITIAL VACUUM "BAKE OUT"

SMRD MATERIALS USE GE-SSD TECHNOLOGY BASE

Figure 1. Typical Damped Printed
Wiring Board

Figure 2. Constrained Layer
Damper Fabrication

Figure 3. Typical PWB Damper
Strips

Figure 4. DSCS III Application
to JLE Panel

STIFFENER

BASELINE

DAMPED CONCEPT
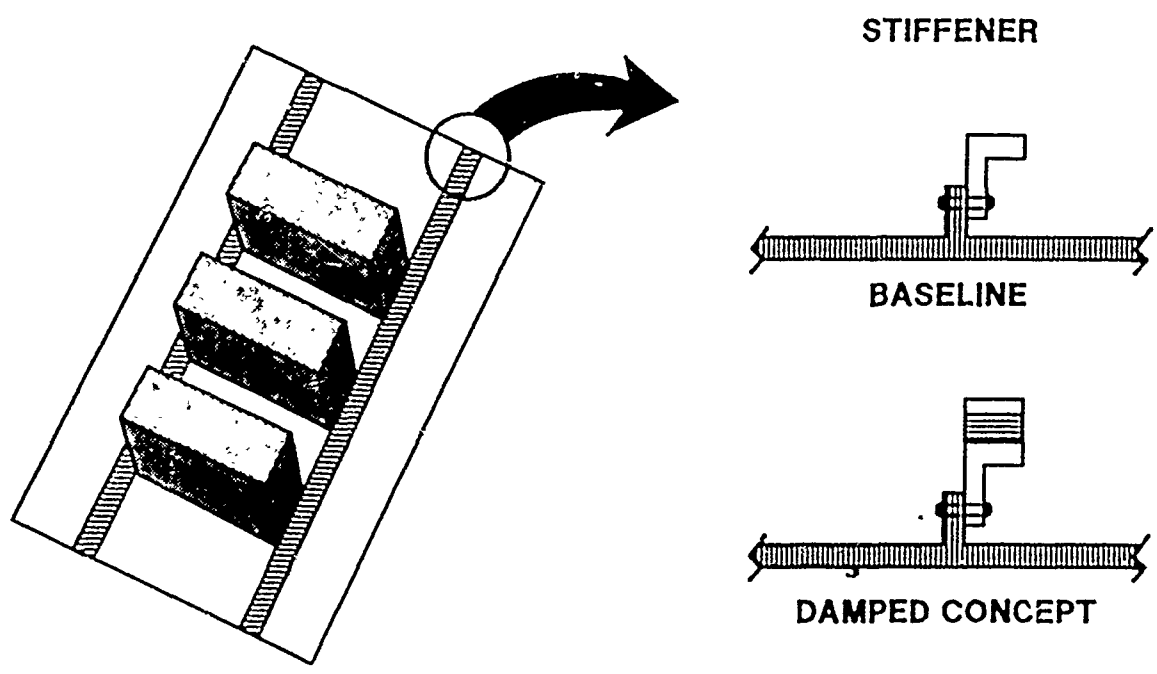
Figure 5. RELSAT Damped Panel Design Approach
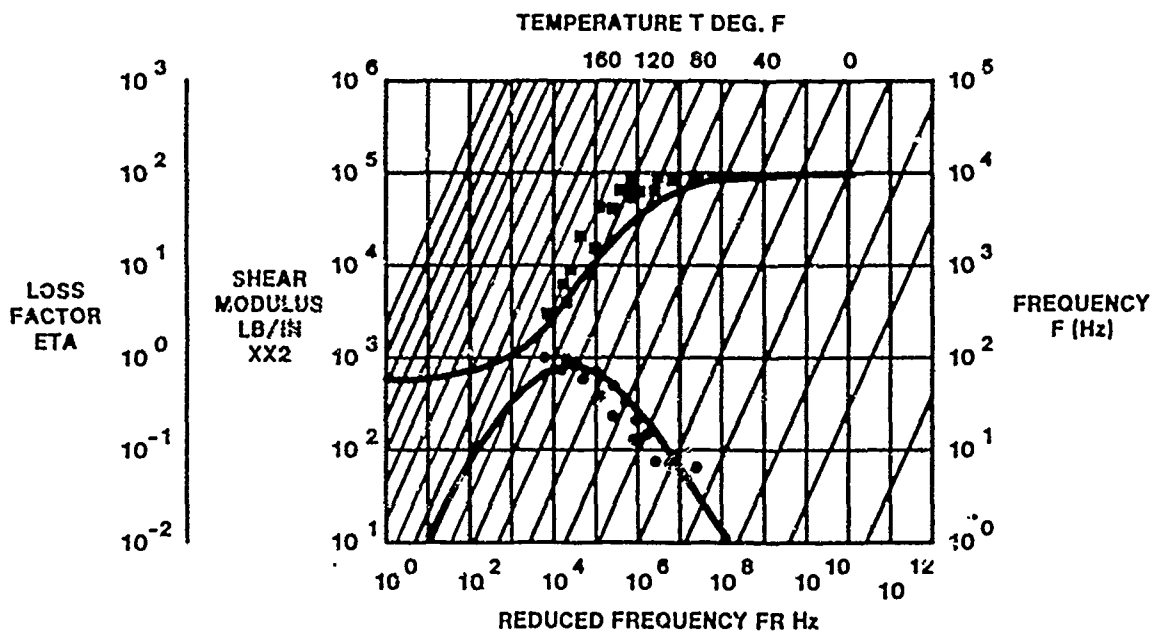
TEMPERATURE T DEG. F

GOOD DAMPING PROPERTIES AFTER 4 YEARS IN SPACE

Figure 6. Comparison of SMM and Current SMRD 100F90 Properties

HF-12

REDUCED TEMPERATURE NOMOGRAM OF SMRD100F90

MATERIAL COMPARISON TEMPERATURE = 65°F
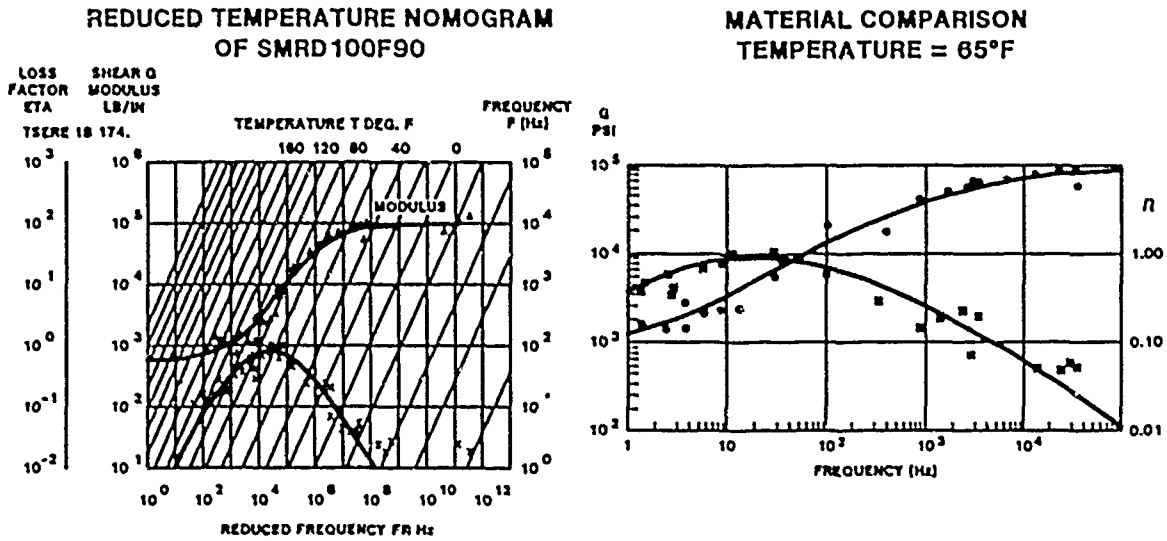
MATERIAL SELECTION MUST BE MADE USING
PROPERTIES AT TEMPERATURE OF INTEREST

Figure 7. Material Characterization
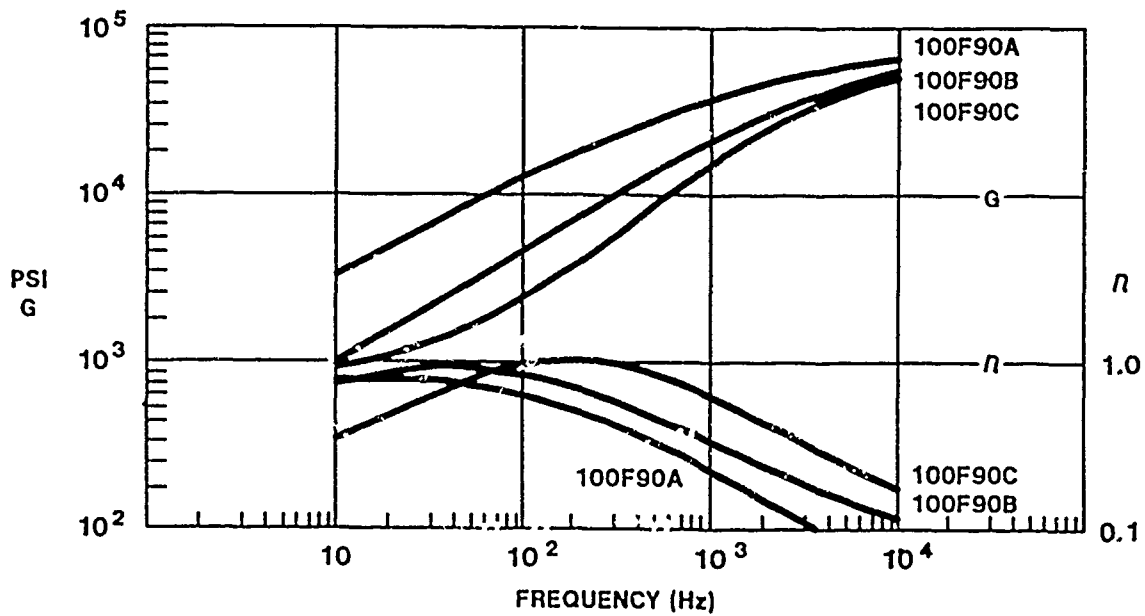
GE MATERIAL PROPERTIES CAN BE ALTERED TO MEET SPECIFIC
REQUIREMENTS. SMRD100F90C IS IDEAL FOR RELSAT.

Figure 8. Effect of SMRD 100F90 Formulation Changes

HF-13

(T = 65°F)
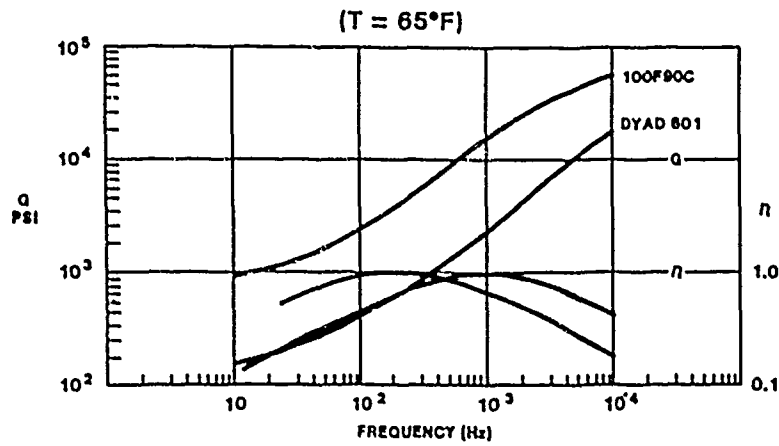
THE PEAK DAMPING FOR DYAD 601 IS ABOVE THE FREQUENCY RANGE
OF INTEREST. SMRD 100F90C COMES CLOSER TO DESIRED RANGE.

Figure 9.   Comparison of SMRD 100F90 and DYAD 601

(T = 65°F)
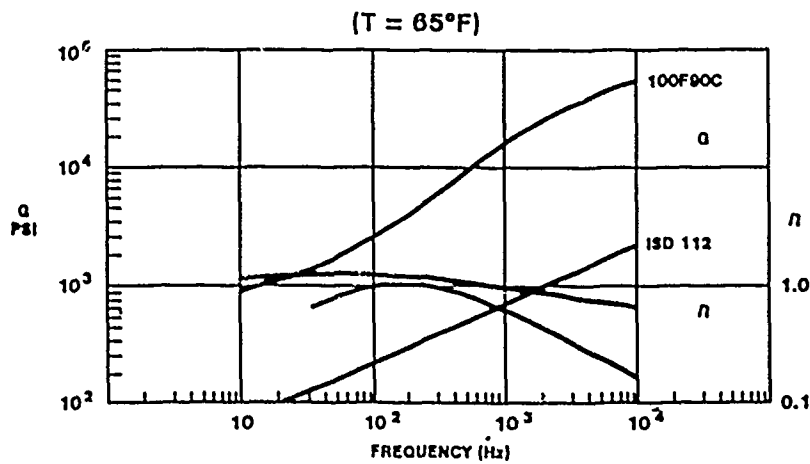
ISD 112 HAS A LOW MODULUS AND, CONFORMS TO RELSAT
TEMPERATURE/FREQUENCY RANGE

Figure 10.   Comparison of SMRD 100F90 and ISD 112

(T = 65°F)
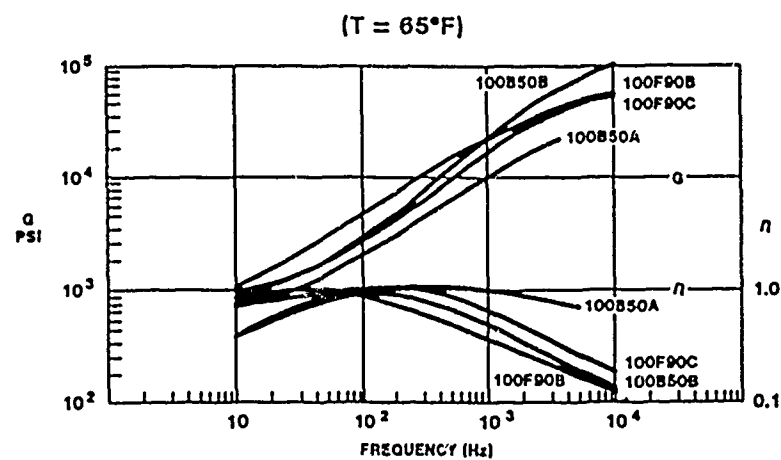
4 SMRD MATERIALS WERE SELECTED FOR PANEL FABRICATION & TEST

Figure 11.   Properties of Selected Materials at 65 Deg F

HF-14

- CAST AND CURED IN FLAT SHEETS

- STABILIZED AND OUTGASSED UNDER VACUUM AT 135°C FOR 96 HOURS

- BONDED TO CONSTRAINING LAYER

- MACHINED TO FINAL DIMENSIONS

- BONDED TO STRUCTURE

Figure 12.   VEM Damper Strip Fabrication Process

TEFLON COATED ALUMINUM MOLD
PRIOR TO CASTING
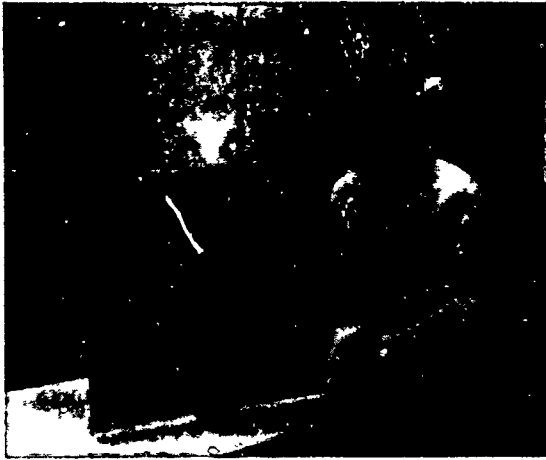
CURED MATERIAL
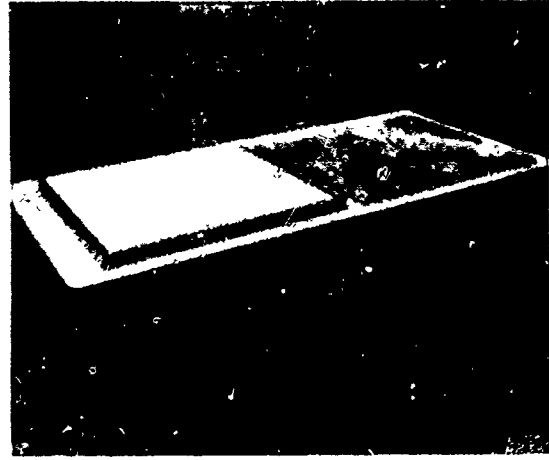
Figure 13.   SMRD Fabrication
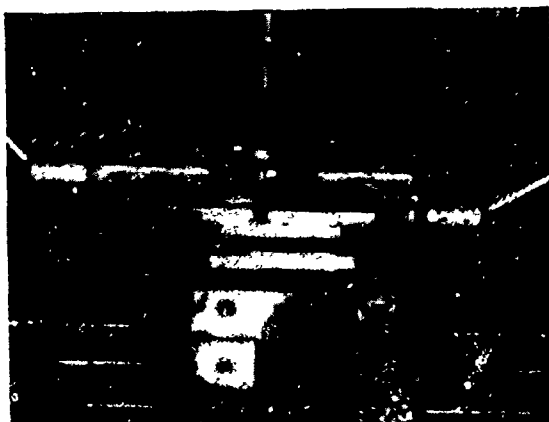
Figure 14.   SMRD 100F90 Milled with a Diamond Compax End Mill
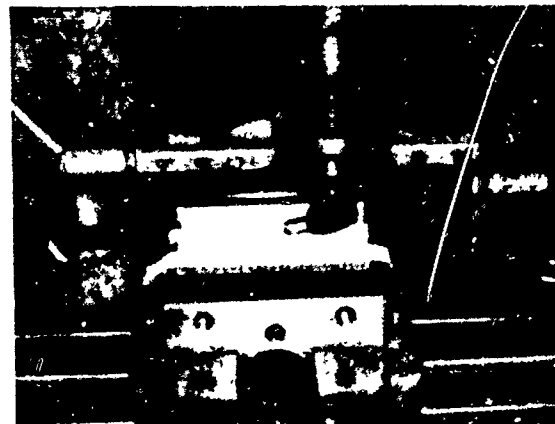
Figure 15.   SMRD 100F90 Milled With a Diamond Fly Cutter
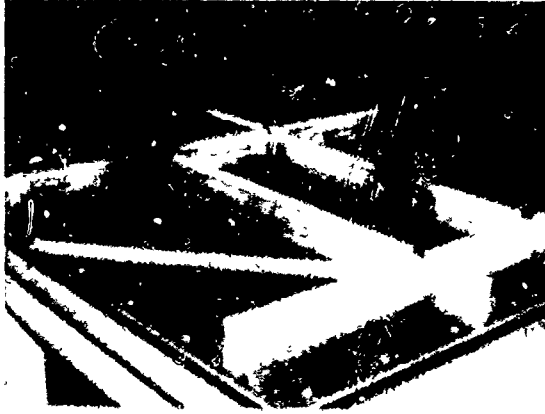
Figure 16. Honeycomb Stiffener Panel
Prior to Completion
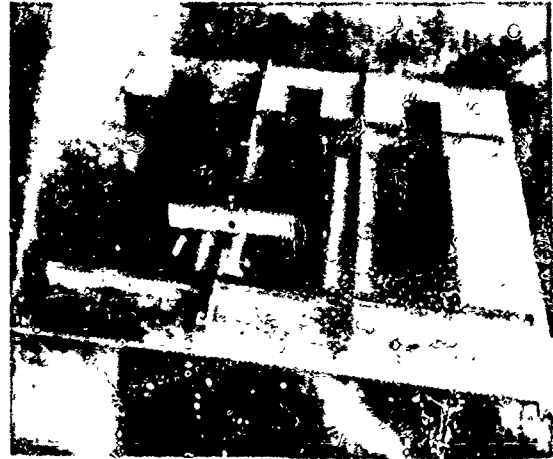
Figure 17. SMRD 100F90C Damped
Honeycomb Stiffener Panel
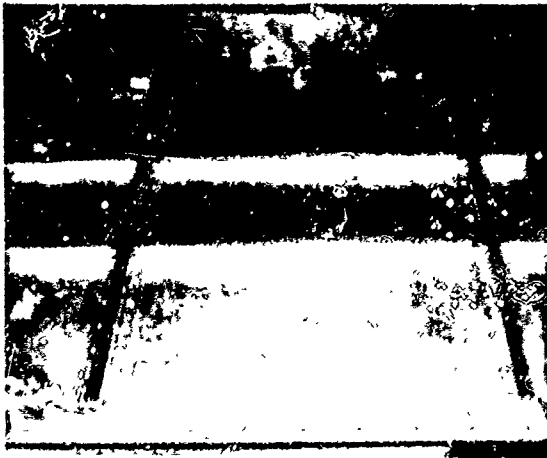
Figure 18. SMRD 100B50C Damped
Hat Section Stiffener Panel

Figure 19. Completed Hat Section
Stiffener Panel
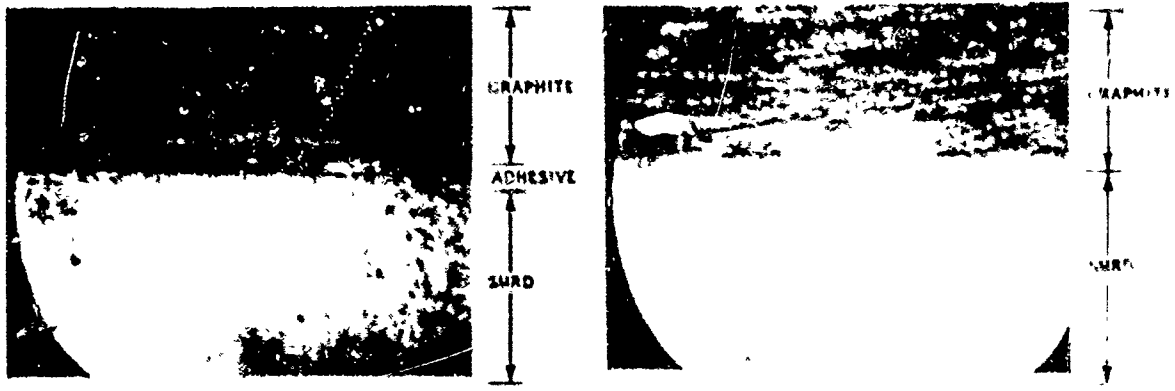
Figure 20.   Direct vs Adhesive Bonding of Graphite/Epoxy
Constraining Layer
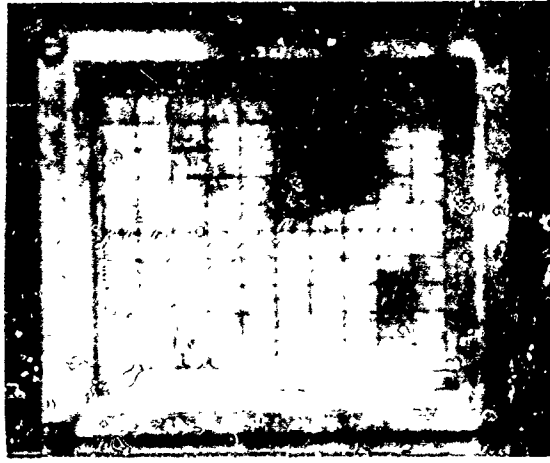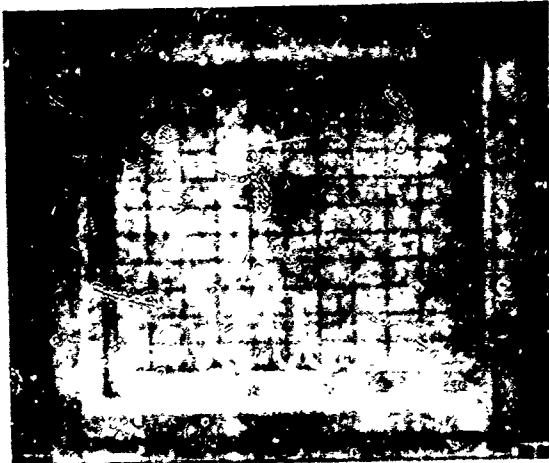
Figure 21.   Pulsed Echo Ultrasonic Method for
Assessing Bond

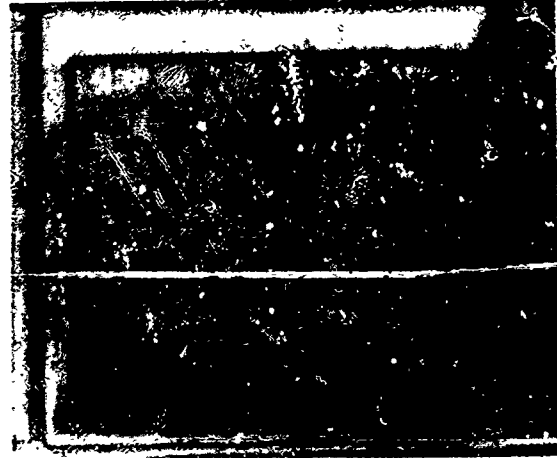BONDASCOPE   DETECTED VOID
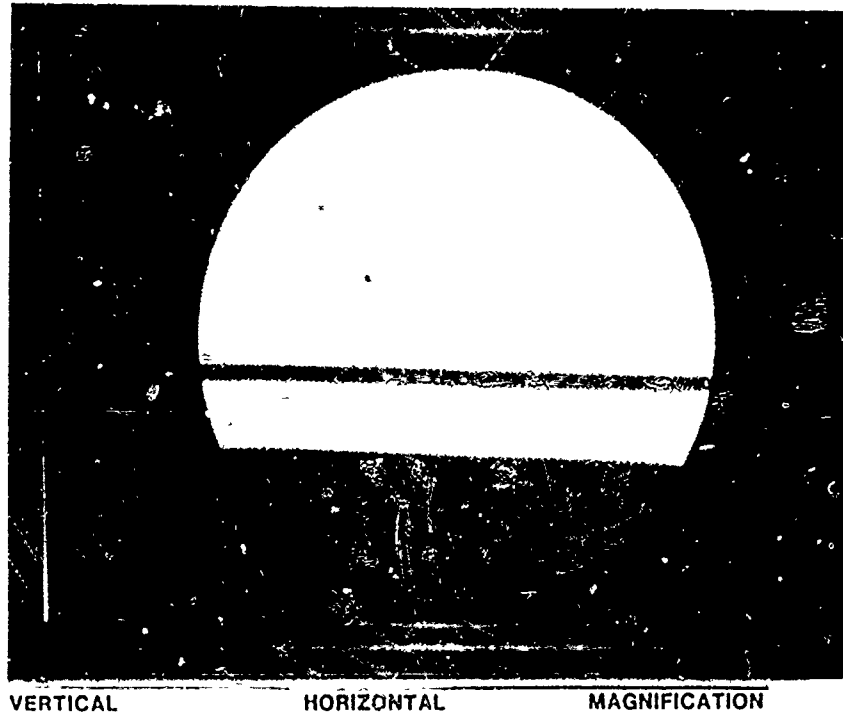

Figure 22.   Ultrasonic Impedance Plane Analysis

VERTICAL   HORIZONTAL   MAGNIFICATION

Figure 23.   Bond Evaluation by Real Time X-Ray

ADAMS, PROF. ROBERT D.
UNIVERSITY OF BRISTOL
DEPT. OF MECHANICAL ENGINEERING
QUEENS BUILDING - UNIVERSITY WALK
BRISTOL BS8 1TR
ENGLAND
0272-24161(W)

ALI, SYED A.
WASHINGTON UNIVERSITY
DEPT. OF CIVIL ENGINEERING
CAMPUS BOX 1130
ST. LOUIS, MO.
63130

ALLEN, DAVID H.
TEXAS A&M UNIVERSITY
AEROSPACE ENGINEERING DEPT.

COLLEGE STATION, TX.
77843

AMOS, DR. ANTHONY K.
AFOSR
NA
BOLLING AFB
WASHINGTON, D.C.
20332-6448
202-767-4937, AV 297 4937

ANDERSON, JIMMIE D.
GENERAL DYNAMICS
P.O. BOX 748
M/S 2851
FORT WORTH, TX.
76101

ANDRESS, LT. WALTER
AFWL
ARBH

KIRTLAND AFB, N.M
87117-6008
AV 244-2986, 505-844-2986

ARGIRO, LARRY J.
DAVID TAYLOR NAVAL SHIP R&D CTR.

MAIL CODE 274
BETHESEDA, MD.
20084-5000

ARRAJJ, B. MELISSA
MARTIN MARIETTA
DENVER AEROSPACE
P.O. BOX 179 M/S MO486
DENVER, CO.
80201

ASHLEY, PROF. HOLT
STANFORD UNIVERSITY
AERO/ASTRO DEPT.
DURAND BLDG., RM. 369
STANFORD, CA.
94305

AUSTIN, ERIC M.
CSA ENGINEERING, INC.

560 SAN ANTONIO RD. SUITE 101
PALO ALTO, CA.
94306

BAGLEY, MAJOR RONALD
4950 TESTW
FFCE

WPAFB, OH.
45433
513-257-6344

BAMPTON, MERV C.C.
BATTELLE

P.O. BOX 999
RICHLAND, WA.
99352

BANDA, DR. SIVA S.
AFWAL
FIGC

WPAFB, OH.
45433

BAUER, PROF. HELMUT F.
UNIV OF THE GERMAN ARMED FORCES

8014 NEUBIBERG
WERNER HEISENBERGWEG 39
FEDERAL REPUBLIC OF GERMANY

BAUER, JUDY A.
HONEYWELL AVIONICS
MAIL CODE 826-3
13350 U.S. HWY 19 SOUTH
CLEARWATER, FL.
33546

BAYARD, DAVID S.
JET PROPULSION LAB.

4800 OAK GROVE DR.
PASADENA, CA.
91109

BECK, CLARK J.
BOEING AEROSPACE CO.
P.O. BOX 3999
MAIL CODE 8C-72
SEATTLE, WA.
98124-2499

BERKMAN, E. FRANK
BBN LABORATORIES
PHYSICAL SCIENCES DIVISION
10 MOULTON ST.
CAMBRIDGE, MA.
02238

BERNHART, W.D.
WICHITA STATE UNIV.
DEPT. AERO ENGINEERING

WICHITA, KS.
67208

BITTERMAN, LT. BRUCE H.
AFWL
ARBH

KIRTLAND AFB, NM.
87117

BOLTON, H.L.
NASA
LANGLEY RESEARCH CENTER
MAIL CODE 356
HAMPTON, VA.
23665

BRENNAN, DR. TERRY J.
THE AEROSPACE CORP.

P.O. BOX 92957 M4/976
LOS ANGELES, CA.
90009

BUHARIWALA, KERMAN
UNIV. OF TORONTO
AEROSPACE STUDIES
4925 DUFFERIN ST.
DOWNSVIEW, ONTARIO M3H5T6
CANADA

BURKE, PAUL R.
BENDIX
GUIDANCE SYSTEMS DIVISION
WILLIAMS AVE. MAIL CODE 2/13
TETERBORO, NJ.
07608

BUTLER, MICHAEL J.
GENERAL DYNAMICS
ELECTRIC BOAT DIVISION
R.R. 1 WATSON ROAD
NORWICH, CT.
06360

CASEIRO, CHRIS A.
GENERAL DYNAMICS
ELECTRIC BOAT DIVISION
E. POINT RD STATION J-41 DEPT 443
GROTON, CT.
06340

CASTELLANI, ANTON
DIPARTIMENTO AEROSPAZIALE
UNIVERSITIA DI ROMA
VIA EUDOSSIANA 16
ROMA, ITALY
00186

CHANG, RON
TRW
MAIL CODE 92/3347
ONE SPACE PARK
REDONDO BEACH, CA.
90278

CHESNEAU, CHRIS
METRAVIB RDS
64 CHEMIN DES MOUILLES
MAIL CODE DP 182
69132 ECULLY CEDEX, FRANCE

78332253

CHONG, DARRYL G.
IBM CORP.
MAIL CODE H27-70B
5600 COTTLE RD.
SAN JOSE, CA.
95193

CHRISTENSEN, ERIC
AUBURN UNIV.

247 WILMORE LAB
AUBURN, AL.
36849

CRAWLEY, PROF. EDWARD F.
MASSACHESETTS INSTITUTE OF TECH.
ROOM 37-341
77 MASSACHUSETTS AVE.
CAMBRIDGE, MA.
02139

CREMA, PROF. BALIS LUIGI
DIPARTIMENTO AEROSPAZIALE
UNIVERSITA DI ROMA
VIA EUDOSSIANA 16
ROMA, ITALY
00168

CROCKER, PROF. MALCOLM J.
AUBURN UNIV.
DEPT. OF MECH. ENGINEERING

AUBURN, AL.
36849-3501
205-826-4820

CUNDY, DAVID R.
LOCKHEED-GA. CO.
ZONE 406, DEPT 72-73
86 S. COBB DR.
SMYRNA, GA.
30063

CUSCHIERI, JOSEPH M.
FLORIDA ATLANTIC UNIV.
CENTER FOR ACOUSTICS & VIB.-DEPT. OCE

BOCA RATON, FL.
33431
305-393-3438

CUTTING, FRED M.
HONEYWELL AVIONICS
MAIL CODE 826-3
13350 U.S. HWY 19 SOUTH
CLEARWATER, FL.
33546

DAHL, PHIL R.
THE AEROSPACE CORP.
P.O. BOX 92957
M4-895
LOS ANGELES, CA.
90009

DAVIS, HUGH W.
BALL
AEROSPACE SYSTEMS DIVISION
PO BOX 1062 M/S BE-6
BOULDER, CO.
80306
303-939-4022

DAVIS, L. PORTER
SPERRY
AEROSPACE & MARINE GROUP
21111 NORTH 19TH AVE.
PHOENIX, AZ.
85027
602-869-2085

DEVIS, DR. IR. B.
BERGOUGNAN-BENELUX-INSTRUMENTS
BRUGSESTEENWEG 7

9050 GENT
BELGIUM

DOLOWY, JR., JOSEPH F.
DWA COMPOSITE SPECIALTIES, INC.

21119 SUPERIOR ST.
CHATSWORTH, CA.
91311-4393

DORNSEIF, MARK J.
GENERAL DYNAMICS
C1-9530
KEARNY VILLA RD.
SAN DIEGO, CA.
92138

DOUGLAS, DR. BRUCE E.
DINSRDC

CODE 1961
BETHESDA, MD.
20084
202-227-4208

DRAKE, MICHAEL L.
UNIV. OF DAYTON
RESEARCH INSTITUTE
300 COLLEGE PARK/JPC-36
DAYTON, OH.
45469-0001
513-229-2644

DUKE, CAPT. JOHN
U.S. AIR FORCE ACADEMY
DFEM

U.S. AIR FORCE ACADEMY, CO.
80840

EDBERG, DR. DONALD L.
JET PROPULSION LAB.
MAIL CODE 157/316
4800 OAK GROVE DR.
PASADENA, CA.
91109

EICHENLAUB, JAMES A.
AFWAL
FIBA

WRIGHT PATTERSON AFB, OH.
45433

ELY, RICHARD A.
LTV AEROSPACE & DEFENSE
VOUGHT AERO PRODUCTS DIVISION
P.O. BOX 225907 M/S 194-51
DALLAS, TX.
75265
214-266-3959

EWING, MAJ. MARK
U.S. AIR FORCE ACADEMY
DFEM

U.S. AIR FORCE ACADEMY, CO.
80840

FERSHT, RENA S.
LITTON IND.
M/S 87
5500 CANOGA AVE.
WOODLAND HILLS, CA.
91367

FERSHT, SAMUEL N.
LITTON
G&CSD
5500 CANOGA AVE. - M/S 87
WOODLAND HILLS, CA.
91367

FOSTER, MATTHEW B.
MARTIN MARIETTA
DENVER AEROSPACE
P.O. BOX 179 M/S 1130
DENVER, CO.
80201

FRATER, NORMAN K.
IBM CORP.
DEPT E34, BLDG. 142
5600 COTTLE RD.
SAN JOSE, CA.
95193
408-256-6090

FRIGSTAD, ROBERT A.
3M
3M CENTER
BLDG. 220-7E-1
ST. PAUL, MN.
55144

GEHLING, RUSSELL N.
MARTIN MARIETTA
DENVER AEROSPACE
P.O. BOX 179 M/S MO486
DENVER, CO.
80201

GELDERLOOS, HENRY J.C.
HONEYWELL, INC.
MAIL STOP 809-5
13350 U.S. HWY 19 SOUTH
CLEARWATER, FL.
33546

GIBSON, PROF. RONALD F.
UNIVERSITY OF IDAHO
MECH. ENGRG. DEPT.
GEL 200
MOSCOW, ID.
83843

GLUCK, DR. RAFAEL
TRW
SPACE AND TECHNOLOGY GROUP
ONE SPACE PARK MAIL CODE R4/1408
REDONDO BEACH, CA.
90278
213-535-8751

GREEN, INGE
SAAB-SCANIA
AIRCRAFT DIVISION
S-581 88 LINKOPING
SWEDEN

+46 13 18 25 28

GREEN, ITZHAK
GEORGIA INST. OF TECH.
SCHOOL OF MECH. ENGRG.

ATLANTA, GA.
30332

GUBSER, DR. JOHN L.
MCDONNELL DOUGLAS ASTRONAUTICS CO.
DEPT E237-BLDG 106-RM 295, LEVEL 2
PO BOX 516
ST. LOUIS, MO.
63166
314-232-5123 (W)

GWINN, A. FORT
SVERDRUP TECH., INC.

600 WILLIAM NORTHERN BLVD.
TULLAHOMA, TN.
37388

HADAEGH, FRED Y.
JET PROPULSION LAB.
MAIL CODE 198-330
4800 OAK GROVE DR.
PASADENA, CA.
91109

HAISLER, WALTER E.
TEXAS A&M UNIV.
AEROSPACE ENGRG. DEPT.

COLLEGE STATION, TX.
77843

HALE, PROF. ARTHUR L.
GENERAL DYNAMICS
SPACE SYSTEMS DIV.
P.O. BOX 85357 M/Z C1-7130
SAN DIEGO, CA.
92138

HAMER, JEFFREY L.
CABOT CORP.
E-A-R DIVISION
7911 ZIONSVILLE RD.
INDIANAPQLIS, IN.
46268
317-872-1111

HANSEN, JORN S.
UNIV. OF TORONTO
INST. FOR AEROSPACE STUDIES
4925 DUFFERIN ST.
DONSVIEW, ONTARIO
CANADA M3H5TD

HARCROW, HARRY W.
MARTIN MARIETTA AEROSPACE
DENVER DIVISON
PO BOX 179 M/S M0486
DENVER, CO.
80201
303-977-8719

HARGIS, MARK
WILLIAMS INTERNATIONAL
P.O. BOX 200, M/S 4-5
2230 WEST MAPLE RD.
WALLED LAKE, MI.
48088

HARRIS, CHARLES E.
TEXAS A&M UNIVERSITY
AEROSPACE ENGRG. DEPT.
MAIL CODE 3141
COLLEGE STATION, TX.
77843

HARRISON, RICHARD W.
NAVAL SURFACE WEAPONS CENTER

10901 NEW HAMPSHIRE AVE.
SILVER SPRINGS, MD.
20903-5000

HASSELMAN, DR. T.K.
ENGINEERING MECHANICS ASSOCIATES
SUITE 318
3820 DEL AMO BLVD.
TORRANCE, CA.
90503
213-370-2551

HEDGEPETH, DR. JOHN M.
ASTRO AEROSPACE CORP.

6384 VIA REAL
CARPINTERIA, CA.
93013-2993

HELLER, PROF. ROBERT A.
VIRGINIA TECH.
ESM DEPT.

BLACKSBURG, VA..
24061
703-961-7483

HENDERSON, DR. JOHN P.
AFWAL
MLLN

WFAFB, OH.
45433
513-255-2689

HIGHSMITH, ALTON L.
TEXAS A&M UNIV.
AEROSPACE ENGRG. DEPT.

COLLEGE STATION, TX.
77843

HOLMAN, DR. ROBERT E.
HUGHES AIRCRAFT
ELECTRO OPTICAL DATA SYSTEMS
P.O. BOX 902, E11/V11D
EL SEGUNDO, CA.
90245

HOLMER, CURTIS I.
NKF ENGINEERING, INC.

12200 SUNRISE VALLEY DR.
RESTON, VA.
22091

HOSOMURA, TATEO
NISSAN MOTOR CO. LTD.

3-5-1, MOMOI
SUGINAMI-KU, TOKYO
JAPAN 167

HUGHES, PROF. PETER C.
UNIVERSITY OF TORONTO
INSTITUTE FOR AEROSPACE STUDIES
4925 DUFFERIN STREET
TORONTO, CANADA
M3H 5T6
416-667-7719

HUGHES, O. RICHARD
CELANESE RESEARCH CO.

86 MORRIS AVE.
SUMMIT, N.J.
07901

IBRAHIM, RAOUF A.
TEXAS TECH UNIV.
DEPT. OF MECH. ENGRG.

LUBBOCK, TX.
79409

IBRAHIM, PROF. SAMIR R.
OLD DOMINION UNIV.
DEPT. OF MECH. ENGRG.
MAIL CODE 1-ME00
NORFOLK, VA.
23508

IKEGAMI, DR. ROY
BOEING AEROSPACE CO.

MS 82-97 PO BOX 3999
SEATTLE, WA.
98124
206-773-9553

JAVID, AHMAD E.
IBM CORP.
HDA DEVELOPMENT - DEPT G39/BLDG. 70B
5600 COTTLE RD.
SAN JOSE, CA.
95193
408-284-0605

JOHNSON, DR. CONOR D.
CSA ENGINEERING, INC.
SUITE 101
560 SAN ANTONIO RD.
PALO ALTO, CA.
94306-4682
415-494-7351

JONES, DR. DAVID
AFWAL
MLLN

WPAFB, OH
45433
255-2689

KALYANASUNDARAM, SHANKAR
TEXAS A&M UNIV.
DEPT. OF AEROSPACE ENGRG.
TANU
COLLEGE STATION, TX.
77840

KIENHOLZ, DR. DAVID A.
CSA ENGINEERING, INC.
SUITE 101
560 SAN ANTONIO RD.
PALO ALTO, CA.
94306
415-494-7351

JACKSON, PETER A.D.
ANTIPHON, INC.

62 OMEGA DR.
NEWARK, DE.
19713
302-454-7666

JEWELL, RONALD E.
NASA
MARSHALL SPACE FLIGHT CENTER
ED-21
HUNTSVILLE, AL.
35812

JOHNSON, DERRICK W.
BOEING AEROSPACE CO.
P.O. BOX 3999
MAIL CODE 82-97
SEATTLE, WA.
98124

KALNIN, ILMAR L.
CELANESE RESEARCH CO.

86 MORRIS AVE.
SUMMIT, N.J.
07901

KERWIN, JR., DR. EDWARD M.
BBN LABORATORIES

10 MOULTON ST.
CAMBRIDGE, MA.
02238
617-491-1850

KILCULLEN, DR. ARTHUR F.
DAVID TAYLOR NSRDC
CODE 1962

BETHESDA, MD.
20084-5000
202-227-1520

KINRA, VIKRAM K.
TEXAS A&M UNIV.
DEPT. OF AEROSPACE ENGRG.

COLLEGE STATION, TX.
77840

KLUESENER, MATTHEW F.
UNIV. OF DAYTON
RESEARCH INSTITUTE
300 COLLEGE PARK/JPC-36
DAYTON, OH.
45469-0001
513-229-2644

LAMBERSON, CAPT. STEVEN E.
U.S. AIR FORCE ACADEMY
DFEM

U.S. AIR FORCE ACADEMY, CO.
80840

LARSON, CHARLES R.
ROCKWELL INTERNATIONAL
MAIL CODE AA57
12214 LAKEWOOD BLVD.
DOWNEY, CA.
90241

LAUGHLIN, MICHAEL J.
UNITED TECHNOLOGY RESEARCH CENTER
OATL
PO DRAWER 4181
WEST PALM BEACH, FL
33402
305-863-4077

LAYTON, JEFFREY B.
PURDUE UNIV.

254 HAWKINS GRAD. HOUSE
WEST LAFAYETTE, IN.
47906
317-743-0224

LESIEUTRE, GEORGE A.
SPARTA

23293 S. POINTE DR.
LAGUNA HILLS, CA.
92653

LEWIS, THOMAS M.
ANATROL CORP.

10895 INDECO DR.
CINCINNATI, OH.
45241

LORCH, DAN R.
DOUGLAS AIRCRAFT
202-15
7821 CONNIE DR.
LONG BEACH, CA.
90846

LU, DR. Y.P.
DAVID TAYLOR NAVAL SHIP R&D CTR.
MACHINERY DYNAMICS DIV.
CODE 2742
ANNAPOLIS, MD.
21402
301-267-2851

LYNCH, P.J.
AFWAL
FIGC

WPAFB, OH.
45433

MADIGOSKY, DR. WALTER M.
NAVAL SURFACE WEAPONS CTR.
WHITE OAK LABORATORY MAIL R 31
10901 NEW HAMPSHIRE AVE.
SILVER SPRING, MD.
20903-5000
202-394-2464, 301-394-2464, AV 290-34

MANSFIELD, WILLIAM E.
BARRY CONTROLS

700 PLEASANT ST.
WATERTOWN, MA.
02172

MATLA, MICHAEL J.
EASTMAN KODAK

901 ELM RD.
ROCHESTER, N.Y.
14650

MELDRUM, DEIRDRE R.
JET PROPULSION LAB.
MAIL CODE 198-330
4800 OAK GROVE DR.
PASADENA, CA.
91109

MILLER, A. KEITH
SANDIA NATIONAL LABS.
DIVSION 1524
P.O. BOX 5800
ALBUQUERQUE, N.M.
87185

MISRA, DR. MOHAN S.
MARTIN MARIETTA DENVER AEROSPACE
NEW TECH. MATERIALS ENGRG
PO BOX 179 M/S MO487
DENVER, CO.
80201
303-977-3000

MOELLER, MARK J.
GENERAL DYNAMICS
ELECTRIC BOAT
4 COURTLAND ST.
PAWCATUCK, CT.
06379

MASRI, PROF SAMI F.
UNIV. OF SOUTHERN CALIFORNIA
DEPT. OF CIVIL ENGINEERING, VHE 406

LOS ANGELES, CA.
90089-0242
213-743-2941

MCKAY, EUGENE L.
MARTIN MARIETTA
DENVER AEROSPACE
P.O. BOX 179 M/S D1744
DENVER, CO.
80201

MILES, RON N.
UNIVERSITY OF WASHINGTON
DEPT. OF MECH. ENGRG.
MAIL CODE FU-10
SEATTLE, WA.
98195

MILLER, DAVID W.
MASSACHUSETTS INST. OF TECH.
ROOM 37-327
77 MASSACHUSETTS AVE.
CAMBRIDGE, MA.
02139

MOBREM, MEHRAN
ASTRO AEROSPACE CORP.

6384 VIA REAL
CARPINTERIA, CA.
93013-2993

MOENING, CHARLES J.
THE AEROSPACE CORPORATION
VEHICLE AND CONTROL SYSTEMS DIV.
P.O. BOX 92957, M4/910
LOS ANGELES, CA.
90009
213-648-7202

MORGENTHALER, DANIEL R.
MARTIN MARIETTA
DENVER AEROSPACE
P.O. BOX 179 M/S M0486
DENVER, CO.
80201

MORRA, ROBERT G.
MARTIN MARIETTA CORP.
MP 313
6801 ROCKLEDGE DR.
BETHESDA, MD.
20817

NAMIRI, MANUCHER K.
JET PROPULSION LAB.
M/S 198-326
4800 OAK GROVE DR.
PASADENA, CA.
91109

NASHIF, AHID D.
ANATROL CORP.

10895 INDECO DR.
CINCINNATI, OH.
45241
513-793-8844

NELSON, PROF. FREDERICK C.
TUFTS UNIV.
DEAN COLLEGE OF ENGINEERING
105 ANDERSON HALL
MEDFORD, MA.
02155

NICHOLSON, DAVID W.
STEVENS INST. OF TECH.
DEPT. MECH. ENGRG.

HOBOKEN, N.J.
07030

NISHIMOTO, DR. TED S.
ROCKWELL INTERNATIONAL SSD
P.O. BOX 3644
MAIL CODE SL26
SEAL BEACH, CA.
90740-7644

NOKES, DR. DAVID S.
C.S. DRAPER LAB., INC.
M/S 27
555 TECHNOLOGY SQUARE
CAMBRIDGE, MA.
02139

NOTTORF, ERIC W.
TEXAS A&M UNIV.
AEROSPACE ENGRG. DEPT.

COLLEGE STATION, TX.
77843

OLKOWSKI, DAVID J.
AF ROCKET PROPULSION LAB
DYS
EDWARDS AIR FORCE BASE - STOP 24
EDWARDS AIR FORCE BASE, CA.
93523

PARIN, MIKE
ANATROL CORP.

10895 INDECO DR.
CINCINNATI, OH.
45241
513-793-8844

PASTERNAK, JOHN W.
LAWRENCE LIVERMORE NATIONAL LAB.
P.O. BOX 808
MAIL CODE L-194
LIVERMORE, CA.
94550

PEEBLES, JAMES H.
MCDONNELL DOUGLAS ASTRONAUTICS
MAIL CODE A3-267-13-3
5301 BOLSA AVENUE
HUNTINGTON BEACH, CA.
92647
714-896-3640

PERSH, JEROME
OUSDRE (R&AT/MST)
ROOM 3D1089
PENTAGON
WASHINGTON, D.C.
20301-3080

PETERSEN, DONALD H.
LTV
MISSILES & ADV. PROGRAMS DIV.
P.O. BOX 650003 M/S TH-85
DALLAS, TX.
75265-0003

PETERSON, SCOTT W.
LOCKHEED MISSILES & SPACE CO.
MAIL CODE 0/59-30, BLDG. 578
1111 LOCKHEED WAY
SUNNYVALE, CA.
94089

PILGRIM, STEVEN M.
PENN STATE UNIV.
MATERIALS RESEARCH LAB.
MAIL CODE 294 MRL
UNIVERSITY PARK, PA.
16802

PINSON, DR. LARRY D.
NASA-LANGLEY RESEARCH CENTER
STRUCTURES AND DYNAMICS DIV.
MAIL CODE 244
HAMPTON, VA.
23665
804-865-3121, FTS 928-3121

PINSON, EARL D.
LOCKHEED MISSILES & SPACE CO.
P.O. BOX BOX 3504
MAIL CODE B/104, 0/62-18
SUNNYVALE, CA.
94088-3504

PORTER, DAVIS L.
SPERRY
DV1-K
21111 N. 19TH
PHOENIX, AZ.
85036-1111

PRASAD, M.G.
STEVENS INST. OF TECH.

HOBOKEN, N.J.
07030

PREUMONT, ANDRE J.
VIRGINIA POLYTECHNIC INST. & STATE UN

215 RANDOLPH HALL
BLACKSBURG, VA.
24061

PROFFITT, DR. SHELBA J.
DASD-H-L

910 SOMMERSET RD.
HUNTSVILLE, AL.
35803

PRUCZ, PROF. JACKY
WEST VIRGINIA UNIV.
MECH. & AEROSPACE ENGRG. DEPT.
PO BOX 6101
MORGANTOWN, W.V.
26506-6010
304-293-3111

PUSEY, HENRY C.

4193 SUDLEY RD.
HAYMARKET, VA.
22069
703-754-2234

RAO, MOHAN D.
AUBURN UNIV.
DEPT. OF MECH. ENGRG. - WILMORE LABS

AUBURN, AL.
36849

RAZAVI, HAMID C.
SCIENTIFIC SYSTEMS, INC.
ONE ALEWIFE PLACE
35 CAMBRIDGE PARK DRIVE
CAMBRIDGE, MA.
02140

REISERT, T. DON
MARTIN MARIETTA AEROSPACE
BUSINESS DEVELOP. TECH. OPERATIONS
PO BOX 179 M/S 1130
DENVER, CO.
80201
303-977-4757

RICHARDS, JR., KENNETH E.
MARTIN MARIETTA
DENVER AEROSPACE
P.O. BOX 179 M/S MO486
DENVER, CO.
80201

RILEY, WILLIAM C.
ROI

2225 E. 28TH ST. BLDG 511
LONG BEACH, CA.
90806

RAO, DR. DANTAM K.
AFWAL
MLLN - MATERIALS LAB.

WPAFB, OH.
45433
513-255-2689

RAY, ASOK K.
TEXAS A&M UNIV.
OLD ENGRG. BLDG.

COLLEGE STATION, TX.
77843

REINHALL, PER G.
UNIV. OF WASHINGTON
DEPT. OF MECH. ENGRG.
MAIL CODE FU-10
SEATTLE, WA.
98195

REMINGTON, PAUL J.
BBN LABORATORIES
PHYSICAL SCIENCES DIV.
10 MOULTON ST.
CAMBRIDGE, MA.
02238

RIEGER, DR. NEVILLE F.
STRESS TECHNOLOGY, INC.

1800 BRIGHTON-HENRIETTA T1. RD.
ROCHESTER, NY
14623

ROBLEE, JEFFREY W.
LAWRENCE LIVERMORE NATIONAL LAB.
P.O. BOX 808
L-792
LIVERMORE, CA.
94550

ROGERS, DR. LYNN
AFWAL
FIBAA
AREA B. BLDG. 45, ROOM 257
WPAFB, OH.
45433-6553
513-255-5664

ROW, EUN
IBM CORP.
MAIL CODE E34/142
5600 COTTLE ROAD
SAN JOSE, CA.
95193

SACKMAN, PROF. JEROME L.
UNIV. OF CALIF. BERKELEY
DEPT. OF CIVIL ENGRG.

BERKELEY, CA.
94720
415-642-2950

SAFARI, AHMAD
PENN STATE UNIV.
MATERIALS RESEARCH LAB.

UNIVERSITY PARK, PA.
16802

SATTINGER, STANLEY S.
WESTINGHOUSE R&D CENTER
BUILDING 401/ROOM 2XPC
1310 BEULAH RD.
PITTSBURG, PA.
15235
412-256-1327

SCHAMEL, II, GEORGE C.
DEI - TECH, INC.
SUITE 500
11838 BUNKER BLVD.
NEWPORT NEWS, VA.
23606

SCHARNHORST, KURT P.
NAVAL SURFACE WEAPONS CENTER
WHITE OAK - MAIL CODE R31
10901 NEW HAMPSHIRE AVE.
SILVER SPRINGS, MD.
20903-5000

SCHMIDT, KATHRYN A.
GENERAL ELECTRIC CO.
SPACE DIV.
GODDARD BLVD. RM. U4201
KING OF PRUSSIA, PA.
19406

SCHOPPEE, MEREDITY M.
ALBANY INTERNATIONAL RESEARCH CO.

1000 PROVIDENCE HIGHWAY
DEDHAM, MA.
02056

SELL, WILLIAM
3M COMPANY
3M CENTER BUILDING 230-1F-02
457 HOLLY AVE., S.
ST. PAUL, MN.
55144-1000
612-733-6413

SELMER, LAWRENCE E.
ROCKWELL INTERNATIONAL
RB06
2250 MARIPOSA
EL SEGUNDO, CA.
90245

SESAK, DR. JOHN R.
LOCKHEED MISSILES & SPACE
ORG. 53-03, BLDG. 580
1111 LOCKHEED WAY
SUNNYVALE, CA.
94043

SHIN, PROF. YOUNG S.
NAVAL POSTGRADUATE SCHOOL
DEPT. OF MECH. ENGRG.
MAIL CODE 69 SG
MONTEREY, CA.
93943-5100

SINGH, RAMEN P.
DYNACS

2280 U.S. 19 NORTH #162B
CLEARWATER, FL.
33575

SKELTON, JOHN
ALBANY INTERNATIONAL RESEARCH CO.

1000 PROVIDENCE HIGHWAY
DEDHAM, MA.
02026

SLIVINSKY, LAWRENCE
RCA
ASTRO-ELECTRONICS
P.O. BOX 800 MAIL STOP 410-2-A36
PRINCETON, N.J.
08540

SOOVERE, DR. JAAK
LOCKHEED-CALIFORNIA
FLUTTER AND DYNAMICS - PO BOX 551
DEPT 76-12 PLANT A-1 BLDG 63G
BURBANK, CA.
91520-7612
818-847-2225 (W), 213-363-0292 (H)

SPANOS, JOHN T.
JET PROPULSION LAB.
M/S 198-326
4800 OAK GROVE DR.
PASADENA, CA.
91109

STAHLE, CLYDE V.
GENERAL ELECTRIC CO.
SPACE DIVISION
PO BOX 8555 M4018 BLDG. 100
PHILADELPHIA, PA.
19101
215-962-5838

STALEY, JAMES A.
GENERAL ELECTRIC CO.
VALLEY FORGE SPACE SYSTEMS
ROOM M4018/100 PO BOX 8555
PHILADELPHIA, PA.
19101
215-354-3442

STRAIN, JAMES C.
GENERAL ELECTRIC CO.
SPACE DIVISION
P.O. BOX 8555 M4018
PHILADELPHIA, PA.
19101

SUN, PROF. C.T.
UNIV. OF FLORIDA
DEPT. OF ENGRG. SCIENCES
231 AEROSPACE ENGRG. BLDG.
GAINESVILLE, FL.
32611

TONGUE, BENSON H.
GEORGIA INST. OF TECH.

ATLANTA, GA.
30332

TRAVASSOS, RICHARD H.
SYSTOLIC SYSTEMS

1065 EAST BROKAW RD.
SAN JOSE, CA.
95131

TUCKER, TENNA E.
THE AEROSPACE CORP.
MAIL CODE M4/915
2350 EAST EL SEGUNDO BLVD.
EL SEGUNDO, CA.
90245

UNGAR, DR. ERIC E.
BBN LABORATORIES, INC.

10 MOULTON ST.
CAMBRIDGE, MA.
02238
617-497-3261

VAICAITIS, PROF. RIMAS
COLUMBIA UNIV.
DEPT. OF CIVIL ENGRG.
610 S.W. MUDD
NEW YORK, N.Y.
10027

VAN VOOREN, ROBERT H.
TRW
R4/1098
ONE SPACE PARK
REDONDO BEACH, CA.
90278

VENNERI, SAMUEL L.
NASA HEADQUARTERS
MATERIALS AND STRUCTURES
CODE RM
WASHINGTON, D C.
20546

VOLIN, RUDOLPH H.
NAVAL RESEARCH LAB.
SHOCK & VIB. INFO. CENTER
MAIL CODE 5804
WASHINGTON, D.C.
20375-5000
202-767-3306, x2220, AV 297-3306

VOSS, H.M.
BOEING AEROSPACE CO.
STRUCTURES TECH.
P.O. BOX 3999, M/S 82-96
SEATTLE, WA.
98124

WADA, DR. BEN K.
JET PROPULSION LAB.
157-507
4800 OAK GROVE DR.
PASADENA, CA.
91109
818-354-3600

WEBB, BRADLEY A.
DWA COMPOSITE SPECIALTIES, INC.

2119 SUPERIOR ST.
CHATSWORTH, CA.
91311-4393

WEIMER, RAYMOND J.
CORDEC CORP.

8270-B CINDER BED RD.
LORTON, VA.
22079

WENDLER, BRUCE H.
TRW
ELECTRONICS & DEFENSE
ONE SPACE PARK BLDG. M1/1226
REDONDO BEACH, CA.
90278

WENTZ, KENNETH R.
AFWAL
FIBG

WPAFB, OH.
45433

WHEELER, PROF. ROBERT
VIRGINIA POLYTECHNIC INSTITUTE
DEPT. OF MATHEMATICS

BLACKSBURG, VA.
24061
703-961-5500

WHITE, CHARLES W.
MARTIN MARIETTA
DENVER AEROSPACE
P.O. BOX 179 M/S MQ486
DENVER, CO.
80201

WHITE, PROF. R.G.
UNIVERSITY OF SOUTHAMPTON
INST. OF SOUND & VIBRATION RES.
SO9 5NH
SOUTHAMPTON, ENGLAND

WILSON, ELLICK R.
NAVAL AIRCRAFT REWORK FACILITY
CHERRY POINT NAVAL AIR STATION
BLDG. 4033, CODE 315
MCAS CHERRY POINT, NC.
28533-5030

WILSON, JAMES F.
SPERRY CORP.
AEROSPACE & MARINE DIV.
P.O. BOX 21111, M/S N30D3
PHOENIX, AZ.
85036

WINTERHALTER, DAVID M.
MARTIN MARIETTA
DENVER AEROSPACE
P.O. BOX 179 M/S 0250
DENVER, CO.
80201

WOLFE, HOWARD F.
AFWAL
FIBGD - ACOUSTICS & SONIC FATIGUE GRO

WPAFB, OH.
45433
255-5229, 255-5573

WOLFENDEN, ALAN
TEXAS A&M UNIV.
MECH. ENGRG. DEPT.

COLLEGE STATION, TX.
77843

WONG, CATHERINE R.
DAVID TAYLOR NSRDC
ANNAPOLIS LAB.
CODE 2812
ANNAPOLIS, MD.
21402-5067
301-267-3128, x2842, AV 281-3128

WOO, RAYMOND
JET PROPULSION LAB.
MAIL CODE 198-330
4800 OAK GROVE DR.
PASADENA, CA.
91109

WREN, GRAEME G.
TEXAS A&M

P.O. BOX 1953
COLLEGE STATION, TX.
77841

YEDAVALLI, RAMA K.
UNIV. OF TOLEDO
DEPT. OF ELEC. ENGRG.

TOLEDO, OH.
43606

ZVOLANEK. IVO
MCDONNELL AIRCRAFT CO.
P.O. BOX 516
D335/B33/4N/425
ST. LOUIS. MO.
63166